





Gamma rays induced by interactions of fission neutrons measured with the FaNGaS instrument

Inaugural-Dissertation
zur
Erlangung des Doktorgrades
der Mathematisch-Naturwissenschaftlichen Fakultät
der Universität zu Köln

vorgelegt von

Niklas Ophoven
aus Düren

Jülich
2024

Diese Arbeit stellt eine von der Mathematisch-Naturwissenschaftlichen Fakultät der Universität zu Köln angenommenen Dissertation dar.

Berichterstatter:	Prof. Dr. Jan Jolie
(Gutachter)	Prof. Dr. Andreas Zilges
	PD Dr. Erik Strub

Tag der letzten mündlichen Prüfung: 11. Juni 2024

Abstract

Prompt Gamma Neutron Activation Analysis (PGNAA) using slow neutrons enables the non-destructive chemical element analysis of small samples. For large samples the Prompt Gamma Analysis based on Inelastic Neutron Scattering (PGAINS) complements PGNAA due to the higher penetration power of fast neutrons.

In this work, the PGAINS technique was studied with the FaNGaS (Fast Neutron-induced Gamma-ray Spectrometry) instrument installed at Heinz Maier-Leibnitz Zentrum (MLZ) in Garching.

Previously measured γ-ray spectra were analyzed to extract fast-neutron spectrum-averaged γ-ray production cross sections for all identified prompt γ-lines arising from the interaction of fast neutrons with the elements carbon (C), oxygen (O), chlorine (Cl), calcium (Ca), lanthanum (La), praseodymium (Pr), cerium (Ce), neodymium (Nd), samarium (Sm), terbium (Tb) and dysprosium (Dy). Additionally, relative intensities were compared to the work of Demidov et al. from 1978 and the elemental detection limits were estimated.

Numerical Monte Carlo simulations were performed to optimize FaNGaS for the irradiation of large samples. In order to reduce the flux of scattered neutrons and emitted γs reaching the detector crystal, a filter material must be placed into the collimator opening of the spectrometer. Therefore, the neutron and γ beam attenuation characteristics of different filters were investigated numerically and complemented by simple analytical models.

Furthermore, an analytical model was developed to estimate neutron self-shielding and γ-ray self-absorption in large rectangular-shaped samples of unknown composition.

In the frame of this work, a total of 779 different fast-neutron-induced prompt γ-lines were evaluated. Compared to the work of Demidov et al., the measurements resulted in 272 additional lines and identification of another 92 lines unreported in any nuclear data library adds decisive value to nuclear spectroscopy. Borated polyethylene with 20 weight percent boron oxide is proposed as filter material and the developed analytical model allows to estimate neutron self-shielding and γ-ray self-absorption in large samples with uncertainties of 2 and 1%, respectively.

Kurzzusammenfassung

Die Prompt Gamma Neutronen Aktivierungs-Analyse (PGNAA) mit langsamen Neutronen ermöglicht die zerstörungsfreie chemische Elementanalyse kleiner Proben. Für große Proben ergänzt die Prompt Gamma Analyse basierend auf Inelastischer Neutronenstreuung (PGAINS) die PGNAA auf Grund des höheren Durchdringungsvermögens schneller Neutronen.

In dieser Arbeit wurde die PGAINS Methode mit dem FaNGaS (Fast Neutron-induced Gamma-ray Spectrometry) Instrument am Heinz Maier-Leibnitz Zentrum (MLZ) in Garching untersucht.

Zuvor gemessene γ-Spektren wurden analysiert um schnelle Neutronenspektrum-gemittelte Wirkungsquerschnitte für die γ-Produktion aller identifizierten prompten γ-Linien aus Neutronenreaktionen mit den Elementen Kohlenstoff (C), Sauerstoff (O), Chlor (Cl), Calcium (Ca), Lanthan (La), Praseodym (Pr), Cer (Ce), Neodym (Nd), Samarium (Sm), Terbium (Tb) und Dysprosium (Dy) zu extrahieren. Zusätzlich wurden relative Intensitäten mit denen der Arbeit von Demidov et al. von 1978 verglichen und elementare Nachweisgrenzen geschätzt.

Numerische Monte Carlo Simulationen wurden durchgeführt um FaNGaS für die Bestrahlung großer Proben zu optimieren. Um den Fluß gestreuter Neutronen und emittierter γs auf den Detektorkristall zu reduzieren muss ein Filtermaterial in die Kollimatoröffnung des Spektrometers platziert werden. Deshalb wurden die Neutronen- und γ-Abschwächungseigenschaften verschiedener Filter numerisch untersucht und durch einfache analytische Modelle ergänzt.

Des Weiteren wurde ein analytisches Modell entwickelt mit welchem die Neutronen-Selbstabschirmung und die γ-Selbstabsorption in großen, rechteckförmigen Proben unbekannter Zusammensetzung bestimmt werden kann.

Im Rahmen dieser Arbeit wurden insgesamt 779 verschiedene prompte γ-Linien, induziert durch schnelle Neutronen, evaluiert. Verglichen zu der Arbeit von Demidov et al. wurden 272 zusätzliche Linien entdeckt sowie 92 weitere komplett neue Linien, was einen großen Mehrwert für die Kernspektroskopie bedeutet. Boriertes Polyethylen mit 20 Massenprozent Boroxid wird als Filtermaterial vorgeschlagen und das entwickelte analytische Modell erlaubt die Abschätzung der Neutronen-Selbstabschirmung und der γ-Selbstabsorption mit Unsicherheiten von 2 und 1 %.

Acknowledgements

The successful completion of this work is the result of unprecedented support I received from many colleagues and friends over a duration of 3 years. I am very thankful to each of them, but there are certain people whose assistance must be acknowledged by mentioning them here.

Without any doubt, my biggest thanks go to my local supervisor Dr. Eric Mauerhofer, who made this PhD project possible for me. The innumerable, fruitful and enjoyable discussions always pushed advance into my work and thereby also extended my scientific competence portfolio in the field of nuclear analytics. I am very thankful for his excellent and absolutely perfect supervision, which honestly could not have been better.

Furthermore, I want to express my gratitude to the institute heads Prof. Dr. Thomas Brückel and apl. Prof. Dr. Karen Friese for the endorsement of my PhD project as well as their trust into me. I am very thankful for their proofreading and helpful comments regarding publication manuscripts and conference abstracts.

I thank the former PhD student Zeljko Ilic a lot to provide me with many experimental data as well as for his help regarding the HYPERMET-PC software in the beginning. Owing the shutdown of FRM II, it is only thanks to Zeljko that this thesis contains also experimental data.

Many thanks go to the Thesis Committee. I thank Prof. Dr. Jan Jolie for taking over the duty of the first examiner, Prof. Dr. Andreas Zilges to be the second and PD Dr. Erik Strub to be the third examiner. I also thank my former supervisor of my Master Thesis, Prof. Dr. Christoph Langer, to be part of the committee as well as for his availability for questions regarding my project. I thank Prof. Dr. Mathias Wickleder to be the chairman of this great committee. I thank Mr. Jolie and Mr. Strub especially for the valuable input they provided me over all the time. I am very thankful having been part of Erik's great nuclear chemistry group and taking part in the weekly seminar. I associate nice memories to the barbecues and the christmas events I participated in.

I also want to thank Dr. Petra Neubauer-Günther from the BCGS at the University of Cologne for her very good and friendly assistance regarding the enrollment process at University of Cologne and any further organizational issues.

I thank Prof. Dr. Peter Reiter from the Physics Department that he took over the mandatory exam to get enrolled as a PhD student.

I also want to acknowledge the great support from the Munich people involved in the FaNGaS instrument working at FRM II: Dr. Zsolt Révay, Dr. Christian Stieghorst and Dr. Egor Vezhlev. I thank them all for their support regarding questions about the samples and the instrument itself as well as their helpful input to publications. I want to thank Zsolt and Christian in particular for the pleasant visit in Garching and providing me access to the restricted control area to see the FaNGaS instrument.

I am very thankful also to Dr. Jingjing Li and Dr. Tsitohaina Randriamalala, whose expertise in numerical simulations were of great value for me. I appreciate their assistance a lot in troubleshouting of my simulations and without their help I would not have been able to let a single simulation run on the JCNS cluster.

I thank the JCNS-2 secretary Barbara Daegener for all the support regarding non-disciplinary matters such as business travels.

I want to express great thanks also to Micha Hölzle, who helped me in any technical and IT problems. I am very thankful that you were able to recover my data from the faulty USB stick!

I also want to thank my daily office colleagues: Andreas Eich, Norberto Schmidt and Alexander Schwab for the nice atmosphere they spread and their help when I had problems.

Last but not least I want to express special thanks to my family and my girlfriend, who supported me throughout the whole time. Without their mental support this work would not have been possible.

Table of Contents

List of Tables **X**

List of Figures **XX**

List of Abbreviations **XXI**

List of Symbols **XXIII**

1 Introduction **1**

1.1 Prompt gamma-ray analysis with neutrons 1

1.1.1 Cold and thermal neutrons (PGNAA) 2

1.1.2 Fast neutrons (PGAINS) 3

1.2 Baghdad Nuclear Research Institute reactor 4

1.2.1 The IRT-reactor fast-neutron spectrum 5

1.3 History of the FaNGaS instrument 7

1.3.1 Scope of this work 8

1.4 Organization of this thesis 9

2 Fundamental radiation interactions **11**

2.1 Neutron interactions with matter 11

2.1.1 Energy group classification 13

2.1.2 Microscopic cross sections 14

2.1.3 Macroscopic cross sections 17

2.1.4 Integral cross sections 17

2.1.5 Reaction rates 18

2.1.6 Inelastic scattering (n,n'γ) 18

2.1.7 Moderation of fast neutrons 24

2.2 Photon interactions with matter 26

2.2.1 Photoelectric effect 26

2.2.2 Compton scattering 28

2.2.3 Pair production 29

2.2.4 Interactions in germanium detectors 32

3 Numerical tools and methods **33**

3.1 HYPERMET-PC . . . 33
3.1.1 Energy calibration . . . 33
3.1.2 Doppler-broadened peaks . . . 34
3.2 Simulation software . . . 35
3.2.1 MCNP code . . . 35
3.2.2 NJOY processing modules . . . 43

4 Methods **47**
4.1 Gamma-ray production cross sections . . . 47
4.2 Attenuation corrections . . . 48
4.2.1 Attenuation of gammas . . . 48
4.2.1.1 Simulation of gamma-ray self-absorption . . . 50
4.2.2 Attenuation of neutrons . . . 51
4.2.2.1 Simulation of neutron self-shielding . . . 52
4.3 Neutron moderation . . . 54
4.4 Interferences . . . 55
4.5 Comparison with literature data . . . 60
4.6 Limit of detection . . . 61

5 The FaNGaS instrument **63**
5.1 Fission neutron beam . . . 64
5.1.1 Neutron beam collimation . . . 64
5.2 FaNGaS spectrometer . . . 66
5.2.1 High-purity germanium (HPGe) detector . . . 67
5.2.2 Shielding configuration . . . 68
5.2.3 Sample irradiation . . . 69
5.3 Full-energy-peak (FEP) efficiency . . . 69
5.4 Radiation background . . . 70
5.5 Neutron-energy spectrum . . . 71

6 Experimental **75**
6.1 Sample description . . . 75
6.1.1 Stoichiometry verification . . . 76
6.2 Experimental flux reconstruction . . . 78
6.2.1 Neutron self-shielding factors . . . 79
6.2.2 Moderation factors . . . 80
6.2.3 Neutron flux . . . 82
6.2.4 Flux validation . . . 83
6.3 Results and Discussion . . . 89
6.3.1 Carbon (C) . . . 89
6.3.2 Oxygen (O) . . . 90
6.3.3 Chlorine (Cl) . . . 91

6.3.3.1 Polyvinylchloride (PVC) sample . . . 91
6.3.3.2 Rare earth chlorides . . . 94
6.3.4 Calcium (Ca) . . . 98
6.3.5 Lanthanum (La) . . . 102
6.3.6 Cerium (Ce) . . . 106
6.3.7 Praseodymium (Pr) . . . 109
6.3.8 Neodymium (Nd) . . . 113
6.3.9 Samarium (Sm) . . . 117
6.3.10 Terbium (Tb) . . . 123
6.3.11 Dysprosium (Dy) . . . 126
6.4 Detection limits . . . 132

7 Fast-neutron filter design **135**
7.1 Triangular peaks of Ge . . . 135
7.2 Filter materials . . . 136
7.3 Strategy . . . 138
7.4 Filter length estimation . . . 139
7.4.1 Analytical approach . . . 139
7.4.2 Numerical approach . . . 140
7.5 Scatter neutron spectrum . . . 145
7.5.1 Variance reduction approach . . . 146
7.5.2 Neutron flux at collimator opening . . . 147
7.5.3 Neutron flux at detector front surface . . . 151
7.6 Neutron performance . . . 153
7.7 Gamma-ray performance . . . 157
7.7.1 HPGe detector model . . . 157
7.7.2 Numerical full-energy-peak efficiency . . . 158
7.7.3 Analytical full-energy-peak efficiency . . . 159
7.8 Proposed material and method . . . 162

8 Large-sample analytics **165**
8.1 Concept . . . 165
8.2 Gamma attenuation . . . 166
8.2.1 Mass attenuation coefficient of concrete . . . 168
8.3 Neutron attenuation . . . 171
8.3.1 Three-step parametrization . . . 173
8.3.2 Uncertainty estimation . . . 178
8.4 Proposed approach . . . 179

9 Results and Discussion **183**
9.1 Experimental results . . . 183
9.2 Numerical results . . . 186

9.3 Outlook . . . 187

Appendices **189**

A. Gamma-ray self-absorption correction curves . . . 189
B. Average scattering factors . . . 191
C. Microscopic cross sections (tables) . . . 193
D. Microscopic cross sections (plots) . . . 196
E. Macroscopic cross sections . . . 200
F. Reaction rates . . . 201
G. Experimental gamma-ray spectra . . . 207
H. Gamma-ray production cross sections . . . 225
H.1 Isotopic partial . . . 225
H.2 Elemental . . . 255
I. HPGe detector data sheet . . . 265
J. Gamma-ray efficiency parametrization . . . 266
K. MCNP6 input files . . . 267

Publications **287**

Bibliography **289**

Erklärung zur Dissertation **305**

List of Tables

2.1 Classification of neutrons according to their kinetic energy after [45]. 13

3.1 Energy intervals with corresponding nuclides defining the boundaries for the linear energy calibrations according to Eq. (3.1) and the FEP energies given in HYPERMET-PC. 34
3.2 Basic quantities and units used in the MCNP code. 36

4.1 Average scattering factor $\overline{f_s}$ for the measured $TbCl_3 \cdot 6H_2O$ sample. . . 56

5.1 Neutron flux values at sample position for each considered neutron-energy range and different versions of the FaNGaS instrument. 73

6.1 Irradiation conditions and parameters for the measurements of C, O, Cl, Ca, La, Ce, Pr, Nd, Sm, Tb and Dy. 75
6.2 Verification of the stoichiometry for the $TbCl_3 \cdot 6H_2O$ sample. 77
6.3 Verification of the compound stoichiometry for all RE chloride samples. 77
6.4 Neutron self-shielding factors f_n derived with MCNP6 simulations for the measurement of the RE chloride samples. 80
6.5 Moderation factors derived with MCNP6 for the measurements of La, Pr, Sm, Dy and Tb. 81
6.6 Effective isotopic partial γ-ray production cross sections for identified neutron capture γ-rays of ^{150}Sm and ^{152}Sm. 86
6.7 Effective isotopic partial γ-ray production cross sections for identified neutron capture γ-rays of ^{139}La. 87
6.8 Effective isotopic partial γ-ray production cross sections for identified neutron capture γ-rays of ^{141}Pr. 88
6.9 Effective isotopic partial γ-ray production cross sections for identified capture γ-rays of ^{161}Dy, ^{162}Dy and ^{164}Dy. 89
6.10 Prompt (n,n'γ) γ-rays of ^{16}O and ^{18}O observed in different samples listed in Table 6.1. 91
6.11 Detection limits for all elements investigated within this work as well as effective γ-ray production cross sections for the most intense lines in this work and from thermal neutron capture (n,γ) reactions listed in [132]. 133

7.1 Threshold energy for inelastic scattering E_{thr} according to the ENDF/B-VII.1 library [50, 115] and γ-ray energy E_γ of Ge isotopes (^{A}Z). 136
7.2 Densities, total macroscopic cross sections and main γ-rays of considered filter materials. 137
7.3 Fraction of peak counts R_P of relevant γ-lines in % for all considered filter materials with a thickness of 10 cm. 144
7.4 Numerical simulations performed with the MCNP6 code to investigate the ^{208}Pb(n,n'γ)^{208}Pb reaction. 145
7.5 Absolute flux values of neutrons scattered towards the collimator opening derived by means of MCNP6 simulations for a Fe sample (S= 2.5 × 2.5 cm^2, d= 0.025 cm) for all considered neutron-energy ranges. 148
7.6 Ratio of the flux values from neutrons scattered by the Fe foil towards the collimator opening, i.e. Φ(scatter) to the experimental neutron flux values at sample position, i.e. Φ(incident). 148
7.7 Fraction of peak counts R_P of relevant γ-lines in % for boron-containing filter materials with a thickness of 10 cm. 155

8.1 Effective macroscopic cross sections for total (Σ_t) and scattering (Σ_s) reactions calculated after Eq. (2.14) for all samples considered in the numerical simulations and a fast-neutron-energy distribution corresponding to that one at sample position. 172
8.2 Comparison between the numerical neutron self-shielding factors f_n derived for the fast-neutron-energy distribution at sample position with the MCNP6 and PHITS codes for the case of an Al sample. . . . 173
8.3 Fit parameters $y_{0,i}$ and u_i of Eq. (8.3) for all parameters a_0 to a_3 defined in Eq. (8.2) for the dry and hydrated samples listed in Tab. 8.1. 177
8.4 Budgeting of the relevant uncertainties for the measurement of large samples with FaNGaS. 181

9.1 Overview on the final results of this work compared to the Atlas [27]. 184

List of Figures

1.1 Schematic illustration of Prompt Gamma Analysis (PGA) with cold or thermal neutrons (PGNAA, left side) and fast neutrons (PGAINS, right side). 2
1.2 Detection limits for PGNAA in the cold neutron beam from NIST (National Institute of Standards and Technology). 3
1.3 Experimental set-up at the IRT-M reactor used for irradiation experiments by Demidov et al. 4
1.4 The IRT-M reactor neutron flux in arbitrary units (a.u.) as a function of the neutron energy. 6

2.1 Classification of neutron interactions with matter. 11
2.2 Schematic representation of the concept of microscopic cross section. . 14
2.3 Discrete microscopic cross sections for ^{40}Ca (top) and ^{139}La (bottom) for the most important reaction channels. 16
2.4 Dependence of the inelastic threshold on atomic number Z. 19
2.5 Dependence of the inelastic threshold on proton and neutron number. 20
2.6 Relative angular distributions for the 847-, 1238- and 1810-keV γ-line from the ^{56}Fe(n,n'γ)^{56}Fe reaction. 22
2.7 Neutron-energy dependence of the ratio of the angular distribution factors for the three strongest γ-rays from the ^{56}Fe(n,n'γ)^{56}Fe reaction. 22
2.8 Doppler broadening observed in the $CaCO_3$ spectrum recorded with FaNGaS. 23
2.9 Schematic representation of the photoelectric effect. [73] 27
2.10 Schematic representation of the Compton Scattering. 28
2.11 Schematic representation of pair production in the vicinity of the electric field of a nucleus. 30
2.12 Predominating interaction type as a function of photon energy and atomic number Z (top, taken from [73]) and dependence of the cross section from various photon interactions on energy for Ge (bottom). . 31
2.13 Typical response function of an intermediate-size HPGe detector crystal. 32

3.1 Illustration of the peak integration method used in HYPERMET-PC to evaluate Doppler-broadened peaks. 34
3.2 The Monte Carlo principle of random walks in radiation transport problems. [106] 35
3.3 GUI of the MCNP6 geometry plotter. 38
3.4 GUI in JANIS 4.0 [123] for ^{12}C. 45

4.1 Dependence of the γ-ray self-absorption factor $f_{E\gamma}$ on the γ-ray energy E_γ for the measured $CeCl_3$ sample. 49
4.2 Numerical simulation of the γ-ray self-absorption factor $f_{E\gamma}$ for a 5 mm thick $CeCl_3$ sample with a surface area of 1.16 $\times$ 1.16 cm^2 and for different γ-ray energies E_γ. 51
4.3 Comparison between analytical and numerical neutron self-shielding factors obtained with the MCNP6 code for Al samples with thicknesses ranging between 0.025 and 10 cm. 53
4.4 Spatial YZX binning (100 $\times$ 100 $\times$ 1) of thermal, epithermal and fast neutrons inside the $TbCl_3{\cdot}6H_2O$ sample measured in this work. 54
4.5 Dependence of the average scattering factor $\overline{f_s}$ on the product of the effective macroscopic scattering cross section $\langle\Sigma_s\rangle$ and the effective thickness e for several samples (see text) that have been measured with FaNGas yet. 57
4.6 Determined correction curves for single and double escape peak interferences. 58

5.1 Schematic view of the fast-neutron facility at FRM II. 63
5.2 Schematic representation of the converter system utilized to produce fast neutrons at the entrance of neutron extraction channel SR10. [142] 64
5.3 Boron carbide (B_4C) and lead filters in the filter bench room located in front of the multi-leaf collimator (MLC) of MEDAPP. [34] 65
5.4 Old multi-leaf collimator (MLC) used for the previous version of FaNGaS [34, 138] (left) and the updated version which is currently in use for the FaNGaS version introduced in this work (right) [139]. 66
5.5 The FaNGaS spectrometer with the shielding at experimental position. 66
5.6 The DSPEC-50 digital spectrometer from ORTEC utilized for the measurements with FaNGaS. ©ORTEC 67
5.7 Schematic sectional view of the FaNGaS spectrometer perpendicular to the longitudinal detector symmetry axis showing the outer shielding (top picture) and sectional view along the detector symmetry axis showing the inner shielding (bottom picture). 68
5.8 Rear side of the FaNGaS spectrometer. 69

5.9 Dependence of the experimental full-energy-peak (FEP) efficiency of FaNGaS on the γ energy determined for the far-position at 67 cm away from the HPGe detector. [141] 70

5.10 Radiation background acquired with the FaNGaS spectrometer for 51,506 s counting live time. 71

5.11 The neutron-energy spectrum of FaNGaS at sample position. 72

6.1 Ratio between absolute γ-ray intensities for prompt lines of the ^{159}Tb(n,γ)^{160}Tb reaction observed in this work ($I_{E\gamma}(exp)$) compared to [132] ($I_{E\gamma}(th)$). 78

6.2 Ratio between absolute γ-ray intensities for prompt lines of the ^{159}Tb(n,γ)^{160}Tb reaction observed in this work ($I_{E\gamma}(exp)$) compared to [132] ($I_{E\gamma}(th)$). 81

6.3 Neutron-energy spectrum of FaNGaS at sample position as assumed in Chapter 5, i.e. Fig. 5.11, the version reconstructed in this chapter (red curve) and the volume-averaged sample flux derived from MCNP6 (green curve). 83

6.4 Ratio between absolute γ-ray intensities for lines of the ^{159}Tb(n,γ)^{160}Tb reaction observed in this work ($I_{E\gamma}(exp)$) compared to [132] ($I_{E\gamma}(th)$). 84

6.5 Ratio between absolute γ-ray intensities for lines of the ^{35}Cl(n,γ)^{36}Cl reaction observed in this work ($I_{E\gamma}(exp)$) compared to [132] ($I_{E\gamma}(th)$). 84

6.6 Relationship between the relative intensities I_R of the prompt γ-rays induced by fast-neutron inelastic scattering (n,n'γ) and (n,pγ) reactions on Cl (^{35}Cl, ^{37}Cl and ^{35}S) measured in this work and the relative intensities I_{RD} tabulated in the Atlas [27]. 92

6.7 Comparison of the relative intensities of the prompt γ-rays induced by fast-neutron inelastic scattering (n,n'γ) and (n,pγ) reactions on Cl obtained in this work with the data tabulated in the Atlas [27] in the form of a histogram of the residuals R in units of standard deviation (σ) calculated with Eq. (4.33). 93

6.8 Effective isotopic partial γ-ray production cross sections $\langle\sigma_{E\gamma}(90°)\rangle$ of the ^{35}Cl(n,n'γ)^{35}Cl (blue), the ^{37}Cl(n,n'γ)^{37}Cl (red) and the ^{35}Cl(n,pγ)^{35}S (green) reactions calculated after Eq. (4.1) as a function of the γ-ray energy E_γ. 94

6.9 Relationship between the relative intensities I_R of the prompt γ-rays induced by fast-neutron inelastic scattering (n,n'γ) and (n,pγ) reactions on Cl (^{35}Cl, ^{37}Cl and ^{35}S) averaged over all RE chloride samples and the relative intensities I_{RD} tabulated in the Atlas [27]. 96

6.10 Comparison of the relative intensities of the prompt γ-rays induced by fast-neutron inelastic scattering (n,n'γ) and (n,pγ) reactions on Cl for data averaged over all RE chloride samples with the data tabulated in the Atlas [27] in the form of a histogram of the residuals R in units of standard deviation (σ) calculated with Eq. (4.33). 97

6.11 Effective isotopic partial γ-ray production cross sections $\langle\sigma_{E\gamma}(90°)\rangle$ of the ^{35}Cl(n,n'γ)^{35}Cl (blue), the ^{37}Cl(n,n'γ)^{37}Cl (red), the ^{35}Cl(n,pγ)^{35}S (green) and ^{35}Cl(n,$\alpha\gamma$)^{32}P (pink) reactions calculated after Eq. (4.1) as a function of the γ-ray energy E_γ and averaged over all RE chloride samples. 97

6.12 Effective isotopic partial γ-ray production cross sections $\langle\sigma_{E\gamma}(90°)\rangle$ for all observed fast-neutron-induced γ-lines of Cl calculated after Eq. (4.1) for the PVC sample (blue) and averaged over all RE Cl samples (red) as a function of the γ-ray energy E_γ. 98

6.13 Relationship between the relative intensities I_R of the prompt γ-rays induced by fast-neutron inelastic scattering (n,n'γ), (n,pγ) and (n,$\alpha\gamma$) reactions on Ca measured in this work and the relative intensities I_{RD} tabulated in the Atlas [27]. 99

6.14 Comparison of the relative intensities of the prompt γ-rays induced by fast-neutron inelastic scattering (n,n'γ), (n,pγ) and (n,$\alpha\gamma$) reactions on Ca obtained in this work with the data tabulated in the Atlas [27] in the form of a histogram of the residuals R in units of standard deviation (σ) calculated with Eq. (4.33). 101

6.15 Effective isotopic partial γ-ray production cross sections $\langle\sigma_{E\gamma}(90°)\rangle$ of ^{40}Ca (blue), ^{42}Ca (red), ^{44}Ca (green), ^{40}K (grey) and ^{37}Ar (pink) calculated after Eq. (4.1) as a function of the γ-ray energy E_γ. 102

6.16 Relationship between the relative intensities I_R of the prompt γ-rays induced by fast-neutron inelastic scattering (n,n'γ) reactions on La (^{139}La) measured in this work and the relative intensities I_{RD} tabulated in the Atlas [27]. 104

6.17 Comparison of the relative intensities of the prompt γ-rays induced by fast-neutron inelastic scattering on La obtained in this work with the data tabulated in the Atlas [27] in the form of a histogram of the residuals R in units of standard deviation (σ) calculated with Eq. (4.33). 105

6.18 Effective isotopic partial γ-ray production cross sections $\langle\sigma_{E\gamma}(90°)\rangle$ of La (^{139}La) calculated after Eq. (4.1) as a function of the γ-ray energy E_γ. 105

6.19 Relationship between the relative intensities I_R of the prompt γ-rays induced by fast-neutron inelastic scattering (n,n'γ) reactions on Ce (^{140}Ce and ^{142}Ce) measured in this work and the relative intensities I_{RD} tabulated in the Atlas [27]. 107

6.20 Comparison of the relative intensities of the prompt γ-rays induced by fast-neutron inelastic scattering on Ce obtained in this work with the data tabulated in the Atlas [27] in the form of a histogram of the residuals R in units of standard deviation (σ) calculated with Eq. (4.33). 108

6.21 Effective isotopic partial γ-ray production cross sections $\langle\sigma_{E\gamma}(90°)\rangle$ of ^{136}Ce (blue), ^{140}Ce (red) and ^{142}Ce (green) calculated after Eq. (4.1) as a function of the γ-ray energy E_γ. 109

6.22 Relationship between the relative intensities I_R of the prompt γ-rays induced by fast-neutron inelastic scattering (n,n'γ) reactions on Pr (^{141}Pr) measured in this work and the relative intensities I_{RD} tabulated in the Atlas [27]. 110

6.23 Comparison of the relative intensities of the prompt γ-rays induced by fast-neutron inelastic scattering on Pr obtained in this work with the data tabulated in the Atlas [27] in the form of a histogram of the residuals R in units of standard deviation (σ) calculated with Eq. (4.33). 112

6.24 Effective isotopic partial γ-ray production cross sections $\langle\sigma_{E\gamma}(90°)\rangle$ of Pr (^{141}Pr) calculated after Eq. (4.1) as a function of the γ-ray energy E_γ. 112

6.25 Relationship between the relative intensities I_R of the prompt γ-rays induced by fast-neutron inelastic scattering (n,n'γ) reactions on Nd measured in this work and the relative intensities I_{RD} tabulated in the Atlas [27]. 114

6.26 Comparison of the relative intensities of the prompt γ-rays induced by fast-neutron inelastic scattering on Nd obtained in this work with the data tabulated in the Atlas [27] in the form of a histogram of the residuals R in units of standard deviation (σ) calculated with Eq. (4.33). 116

6.27 Effective isotopic partial γ-ray production cross sections $\langle\sigma_{E\gamma}(90°)\rangle$ of Nd calculated after Eq. (4.1) as a function of the γ-ray energy E_γ. 117

6.28 Relationship between the relative intensities I_R of the prompt γ-rays induced by fast-neutron inelastic scattering (n,n'γ) reactions on Sm measured in this work and the relative intensities I_{RD} tabulated in the Atlas [27]. 118

6.29 Comparison of the relative intensities of the prompt γ-rays induced by fast-neutron inelastic scattering (n,n'γ) reactions on Sm obtained in this work with the data tabulated in the Atlas [27] in the form of a histogram of the residuals R in units of standard deviation (σ) calculated with Eq. (4.33). 120

6.30 Intensity ratio of γ-lines induced by inelastic scattering in Sm compared to data listed in the Atlas [27] with (blue curve) and without (red curve) neutron capture corrections. 121

6.31 Comparison of the relative intensities of the prompt γ-rays induced by fast-neutron inelastic scattering (n,n'γ) reactions on Sm obtained in this work with the data tabulated in the Atlas [27] in the form of a histogram of the residuals R in units of standard deviation (σ) calculated with Eq. (4.33). 122

6.32 Effective isotopic partial γ-ray production cross sections $\langle\sigma_{E\gamma}(90°)\rangle$ of Sm calculated after Eq. (4.1) as a function of the gamma-ray energy E_γ. 123

6.33 Relationship between the relative intensities I_R of the prompt γ-rays induced by fast-neutron inelastic scattering (n,n'γ) reactions on Tb measured in this work and the relative intensities I_{RD} tabulated in the Atlas [27]. 124

6.34 Comparison of the relative intensities of the prompt γ-rays induced by fast-neutron inelastic scattering (n,n'γ) reactions on Tb obtained in this work with the data tabulated in the Atlas [27] in the form of a histogram of the residuals R in units of standard deviation (σ) calculated with Eq. (4.33). The values of R are given in Appx. H.1.31.125

6.35 Effective isotopic partial γ-ray production cross sections $\langle\sigma_{E\gamma}(90°)\rangle$ of Tb (^{159}Tb) calculated after Eq. (4.1) as a function of the γ-ray energy E_γ. 126

6.36 Relationship between the relative intensities I_R of the prompt γ-rays induced by fast-neutron inelastic scattering (n,n'γ) reactions on Dy measured in this work and the relative intensities I_{RD} tabulated in the Demidov Atlas [27]. 128

6.37 Comparison of the relative intensities of the prompt γ-rays induced by fast-neutron inelastic scattering (n,n'γ) reactions on Dy obtained in this work with the data tabulated in the Atlas [27] in the form of a histogram of the residuals R in units of standard deviation (σ) calculated with Eq. (4.33). 129

6.38 Intensity ratio of γ-lines induced by inelastic scattering in Dy compared to data listed in the Atlas [27] with (blue curve) and without (red curve) neutron capture corrections. 130

6.39 Comparison of the relative intensities of the prompt γ-rays induced by fast-neutron inelastic scattering (n,n'γ) reactions on Dy obtained in this work with the data tabulated in the Atlas [27] in the form of a histogram of the residuals R in units of standard deviation (σ) calculated with Eq. (4.33). 131

6.40 Effective isotopic partial γ-ray production cross sections $\langle\sigma_{E\gamma}(90°)\rangle$ of Dy calculated after Eq. (4.1) as a function of the γ-ray energy E_γ. 132

7.1 γ-ray spectra from MCNP6 simulations for a Ge cube of $5 \times 5 \times 5$ cm^3 irradiated with neutrons of energies: 0.01, 0.1, 0.6 and 1.2 MeV. . 136

7.2 Illustration of the strategy for the fast-neutron filter optimization of the FaNGaS spectrometer. 138

7.3 Dependence of the fast-neutron fraction R_N for 2 MeV neutrons on the thickness d of different filter materials obtained from analytical calculations according to Eq. (4.14). 139

7.4 Simplified model of the FaNGaS spectrometer for the simulation with the MCNP6 code. 140

7.5 Spatial neutron distribution in the XY plane at the front surface of the BPE shielding. 141

7.6 Dependence of the fast-neutron fraction R_N for 2 MeV neutrons on the thickness d of different filter materials obtained from numerical simulations with the MCNP6 code. 142

7.7 Simulated neutron-energy spectra at the detector front surface for all considered filter materials with a thickness of 10 cm induced by 2-MeV neutrons. 142

7.8 γ-ray spectra simulated in MCNP6 with F8 pulse-height tallies without a filter, a PE filter and a BPE filter with 20 wt% B_4C, each of 10 cm thickness. 143

7.9 MCNP6 model used to determine the spectrum of neutrons scattered from a Fe sample. 146

7.10 Neutron-energy spectrum and statistical uncertainties for each energy bin for the neutron scatter spectra obtained by numerical simulations with the MCNP6 code for collimator openings of 6 (left picture) and 10 cm (right picture) diameter. 147

7.11 Distribution of thermal, epithermal and fast scattered neutrons in a 15×15 cm^2 area (XY plane) centered at the collimator. 149

7.12 Variation of the scatter neutron spectrum at a collimator opening of 6 cm diameter for Fe foils of 0.25, 0.5 and 1 mm thickness as a function of the sample thickness (left picture). 150

7.13 Fast-neutron scatter spectra at a collimator opening of 6 cm for Al, Ti, Cu and Fe samples of 0.25 mm thickness and a surface area of 2.5 × 2.5 cm^2 obtained by numerical simulations with the MCNP6 code. 151
7.14 Dependence of the scatter fast-neutron flux at a collimator opening of 6 cm obtained by simulations with the MCNP6 code for Al, Ti, Cu and Fe samples of 1, 10 and 50 mm thickness. 151
7.15 Variation of the fast-neutron fraction R_N with the filter thickness d for the fast-neutron scatter spectrum derived at a collimator opening of 6 cm with MCNP6 for irradiation of a 0.25 mm thick Fe sample. . 153
7.16 Neutron-energy spectra obtained with a F1 (current) tally in the MCNP6 code at the front surface of the detector. 154
7.17 Simulated γ-ray spectrum for a BPE filter with 20 wt% B_2O_3 and different thicknesses (left plot), and the variation of the total counts below 3 MeV as a function of the thickness for the same filter material (right plot). 155
7.18 Fast-neutron flux fraction and peak-count fraction of a BPE filter with 20 wt% B_2O_3 for different γ-lines of Ge isotopes from inelastic scattering reactions. 156
7.19 Inelastic scattering cross sections (MT= 4) from the ENDF/B-VIII.0 [112] evaluation for every isotope of Ge. 157
7.20 HPGe detector model implemented into MCNP6. 158
7.21 Comparison of the experimental FEP efficiency curve with the simulated FEP efficiency curves obtained with MCNP6 for a single forward-focussed γ source and isotropic sources considering 26 γ energies between 10 keV and 8 MeV (left picture). 159
7.22 Geometrical illustration of the situtation for the determination of the analytical FEP efficiency. 160
7.23 Comparison between analytical and numerical solutions for the FEP efficiency for BPE filters with 20 wt% B_2O_3 and B_4C, respectively, as well as for a B_4C filter. Solid lines represent curve fits according to Eq. (5.1). 161
7.24 Analytically determined FEP efficiency for BPE filters with 20 wt% B_2O_3 and various thicknesses. 162
7.25 Dependence of the relative γ-ray efficiency (at 1.33 MeV from ^{60}Co), the scattered fast-neutron flux, the peak counts from inelastic scattering on Ge (averaged over all γ energies and isotopes) and the total counts (integrated between 0 and 3 MeV) on the thickness d of a filter made of BPE with 20 wt% B_2O_3. 163

8.1 Schematic representation of the irradiation of a large rectangular-shaped sample. 166

8.2 Comparison of the analytical γ-ray self-absorption factors $f_{E\gamma}$ for Al samples (μ_m values of Al taken from XCOM [92]) with a surface area of 2.5 $\times$ 2.5 cm^2 calculated after Eq. (4.10) with the values derived by numerical simulations with the MCNP6 code. 167

8.3 Comparison of the analytical γ-ray self-absorption factors $f_{E\gamma}$ for 5 cm long Al samples (μ_m values of Al taken from XCOM [92]) calculated after Eq. (4.10) with the values derived by numerical simulations with the MCNP6 code. 168

8.4 Dependence of the mass attenuation coefficient μ_m of ordinary concrete, $(C_2H_3Cl)_n$, $CaCO_3$, Fe and $LaCl_3{\cdot}7H_2O$ as a function of the γ-ray energy E_γ. 169

8.5 Dependence of the deviation in mass attenuation coefficients of several sample materials (averaged values) relative to these ones of ordinary concrete ($\Delta\mu_m$) on the γ-ray energy E_γ. 169

8.6 Dependence of the deviation in γ-ray self absorption factors $\Delta f_{E\gamma}$ on the γ-ray energy E_γ and the sample thickness d for a $(C_2H_3Cl)_n$, Ti, Cu and $LaCl_3{\cdot}7H_2O$ sample. 170

8.7 Dependence of the deviation in γ-ray self absorption factors $\Delta f_{E\gamma}$ on the γ-ray energy E_γ averaged over a $(C_2H_3Cl)_n$, $LaCl_3{\cdot}7H_2O$, $PrCl_3{\cdot}7H_2O$, Al, Ti, Fe, Cu, La and Ce sample for different sample thicknesses d (left plot) and dependence of the deviation $\Delta f_{E\gamma}$ averaged over all aforementioned samples and the thicknesses d for each γ-ray energy. 171

8.8 Dependence of the neutron self-shielding factor f_n on the sample length l and the quadratic surface area S for a Ca, Al, Cu and $LaCl_3{\cdot}7H_2O$ sample derived with numerical simulations assuming the fast-neutron-energy distribution at sample position. 174

8.9 Variation of the neutron self-shielding factor f_n as a function of the total macroscopic cross section Σ_t for a quadratic surface area S of 6 $\times$ 6 cm^2 at sample lengths l of 0.5, 2.5 and 7 cm for all sample materials listed in Table 8.1. 175

8.10 Variation of the slope u from Eq. (8.1) as a function of the sample length l for quadratic surface areas of 1, 6.25, 9 and 36 cm^2 for dry (hydrogen-free) and hydrated (hydrogen-containing) samples. 176

8.11 Variation of the fit parameters a_0 to a_3 from Eq. (8.2) as a function of the sample surface area S. 177

8.12 Dependence of the deviation in neutron self-shielding factors Δf_n on the sample length l and surface area S for a Ca, Al, Cu and $LaCl_3{\cdot}7H_2O$ sample. 178

8.13 Dependence of the deviation in neutron self-shielding factors Δf_n averaged over the samples listed in Table 8.1 for surface areas of 1 cm^2 and 6.25, 9 and 36 cm^2 (averaged) as a function of l for dry (left plot) and hydrated (right plot) samples. 179
8.14 Scheme of the proposed approach for γ and neutron attenuation corrections in large rectangular-shaped samples. 180

List of Abbreviations

ADC	Analog-to-Digital Converter
a.u.	arbitrary units
BPE	Borated polyethylene
DE	Double escape peak
DGNAA	Delayed Gamma Neutron Activation Analysis
DL	Detection limit
EHPs	Electron-hole pairs
ENDF	Evaluated Nuclear Data File
ENSDF	Evaluated Nuclear Structure Data File
EXFOR	Experimental Nuclear Reaction Data
FaNGaS	Fast Neutron-induced Gamma-ray Spectrometry
FEP	Full-energy peak
FRM II	Forschungs-Neutronenquelle Heinz Maier-Leibnitz
FZJ	Forschungszentrum Jülich GmbH
g.s.	ground state
HPGe	High-purity germanium
JANIS	Java-based nuclear information software
JCNS-2	Jülich Centre for Neutron Science
LANL	Los Alamos National Laboratory
MC	Monte Carlo
MCA	Multi-Channel-Analyzer
MCNP	Monte Carlo N-Particle code
MEDAPP	Medical Application
MLC	Multi-leaf collimator
MLZ	Heinz Maier-Leibnitz Zentrum
MR	Moderating ratio
MSDP	Macroscopic slowing down power
NECTAR	Neutron Computerized Tomography and Radiography
NIST	National Institute of Standards and Technology
PE	Polyethylene
PGA	Prompt Gamma Analysis
PGAINS	Prompt Gamma Analysis based on Inelastic Neutron Scattering

PGNAA	Prompt Gamma Neutron Activation Analysis
PHITS	Particle and Heavy Ion Transport code System
PTB	Physikalische-Technische Bundesanstalt
PVC	Polyvinylchloride
Rare earth	RE
SACS	Spectrum-averaged cross section
SE	Single escape peak
SM	Standard model
SR10	Strahlrohr 10
TANDEM	TransActinide Nuclear Data Evaluation and Measurement

List of Symbols

n.b.: only frequently used symbols are listed; meaning of the symbols unless otherwise stated in the text.

Symbol	Description	Unit
$\langle\rangle$	Indicates neutron-spectrum averaged quantities	
β	Fission spectrum attenuation law coefficient	
γ	Gamma-ray	
ϵ	Counting efficiency	
$\epsilon_{E\gamma}$	Full-energy-peak efficiency	
ζ	Reduced photon energy	
θ	Angle between neutron beam and detector	$^\circ$
λ_{tr}	Mean free transport pathlength	cm
$\mu(l)$	Linear attenuation coefficient	cm^{-1}
$\mu(m)$	Mass attenuation coefficient	$cm^2\ g^{-1}$
π	Level parity	
ρ	Mass density	$g\ cm^{-3}$
σ	Microscopic cross section	b
$\langle\sigma\rangle$	Microscopic effective isotopic reaction cross section	b
$\langle\sigma^Z\rangle$	Microscopic effective elemental reaction cross section	b
σ_a	Microscopic absorption cross section	b
σ_{cap}	Microscopic capture cross section	b
σ_{ch}	Microscopic charged particle cross section	b
σ_{el}	Microscopic elastic scattering cross section	b
σ_f	Microscopic fission cross section	b
σ_{inel}	Microscopic inelastic scattering cross section	b
σ_n	Microscopic neutral particle cross section	b
σ_s	Microscopic scattering cross section	b
$\sigma_{E\gamma}(E_n)$	Isotopic partial γ-ray production cross section	b
$\langle\sigma_{E\gamma}\rangle$	Neutron spectrum-averaged (effective) isotopic partial γ-ray production cross section	b
$\langle\sigma^Z_{E\gamma}\rangle$	Neutron spectrum-averaged (effective) elemental γ-ray production cross section	b

Σ	Macroscopic cross section	cm^{-1}
Σ_a	Macroscopic absorption cross section	cm^{-1}
Σ_{cap}	Macroscopic capture cross section	cm^{-1}
Σ_{el}	Macroscopic elastic scattering cross section	cm^{-1}
Σ_{inel}	Macroscopic inelastic scattering cross section	cm^{-1}
Σ_s	Macroscopic scattering cross section	cm^{-1}
Σ_t	Total macroscopic reaction cross section	cm^{-1}
Φ	Neutron flux	$cm^{-2}\ s^{-1}$
Φ_0	Incident neutron flux	$cm^{-2}\ s^{-1}$
Φ_{epi}	Epithermal neutron flux	$cm^{-2}\ s^{-1}$
Φ_{fast}	Fast neutron flux	$cm^{-2}\ s^{-1}$
Φ_s	Sample neutron flux	$cm^{-2}\ s^{-1}$
Φ_{th}	Thermal neutron flux	$cm^{-2}\ s^{-1}$
$\langle\Phi\rangle$	Integral neutron flux	$cm^{-2}\ s^{-1}$
Ω	Solid angle	sr
A	Mass number	
$B_{E\gamma}$	Area of background	counts
c	Speed of light	$m\ s^{-1}$
$\dot{C}_{E\gamma}$	Count rate of a γ-ray	counts s^{-1}
d	Sample thickness	cm
e	Effective thickness	cm
E_γ	γ-ray energy	eV
E_n	Neutron energy	eV
E_{thr}	Threshold energy	MeV
E^*	Level energy	MeV
$f_{E\gamma}$	γ-ray self-absorption factor	
f_{mod}	Neutron moderation factor	
f_n	Neutron self-shielding factor	
f_s	Scattering factor	
$\overline{f_s}$	Average scattering factor	
$g(t_b, t_c, t_{1/2})$	Effective counting time	s
h	Isotope abundance	
I_0	Initial beam intensity	
$I_{E\gamma}$	Absolute γ-ray intensity	
$I_{E\gamma,rel}$	Relative γ-ray intensity	
I_R	Relative γ-ray intensity in this work	
I_{RD}	Relative γ-ray intensity of Demidov et al.	
$I(x)$	Beam intensity after thickness x	
J	Angular momentum	$kg\ m^2\ s^{-1}$
l	Sample length	cm
M	Molar mass	$g\ mol^{-1}$

N_A	Avogadro constant	mol^{-1}
N'	Atomic density	atoms cm^{-3}
$P_{E\gamma}$	Net peak area of a γ-ray	counts
P_j	Legendre polynomials	
R	Residuals	σ
R_n	Nuclear radius	fm
R_N	Fast-neutron flux fraction	
R_F	Fermi radius	fm
R_P	Peak-count fraction	
R_{PB}	Total-count fraction	
S	Surface area	cm^2
t_b	Irradiation (real) time	s
t_c	Counting (live) time	s
$t_{1/2}$	Physical half-life	s
T	Temperature	K
u	Atomic mass unit	
v	Velocity	m s^{-1}
V	Volume	cm^3
$W(\theta)$	Angular-distribution correction factor	
x	Projectile	
X	Educt nucleus	
X^*	Compound nucleus	
y	Ejectile	
Y	Product nucleus	
Z	Atomic number	

1. Introduction

In this chapter the framework and background of this work is introduced. Fundamental physics aspects of applied methods are briefly presented and the state-of-the-art in this field is given by means of a literature review. In addition, general information on nuclear data retrieved from the literature for comparisons is presented and the objectives of the FaNGaS instrument are introduced within a brief historical review. Finally, this chapter also provides information on the structure of this work.

1.1 Prompt gamma-ray analysis with neutrons

Prompt Gamma Analysis (PGA) enables the non-destructive chemical element analysis of materials based on the detection of prompt γ-rays induced by neutron nuclear reactions within the considered sample matrix. The technique is characterized by an immediate γ-ray emission following the neutron interaction in a time scale not longer than pico- to femtoseconds (hence the nomenclature prompt). The term PGA includes both PGNAA (Prompt Gamma Neutron Activation Analysis) with slow neutrons using (n,γ) radiative capture reactions and PGAINS (Prompt Gamma Analysis based on Inelastic Neutron Scattering) with fast neutrons making use of the (n,n'γ) inelastic scattering reaction. The aforementioned processes are illustrated in Fig. 1.1.

The most fundamental equation used in PGA is described by a double integral depending on the volume V irradiated and the energy distribution of the neutrons. The variables within this integral are a function of the position r in the sample and the neutron (E_n) and γ-ray energy (E_γ), respectively [1]:

$$\dot{C}_{E\gamma} = \frac{P_{E\gamma}}{t_c} = \frac{N_A \cdot h}{M} \cdot \int_V \int_{E_{n=0}}^{\infty} \mu(r) \cdot \sigma_{E\gamma}(E_n) \cdot \Phi'(E_n, r) \cdot \epsilon'(E_\gamma, r) \cdot dE_n \cdot dr, \quad (1.1)$$

where $\dot{C}_{E\gamma}$ is the net count rate of a γ-ray with energy E_γ (counts s^{-1}), $P_{E\gamma}$ the net peak area (counts), t_c the counting (live) time (s), N_A the Avogadro constant (6.022 $\times$ 10^{23} mol^{-1}), h the isotopic abundance, M the molar mass (g mol^{-1}), $\mu(r)$ reflects the mass density of the examined element and accounts for inhomogeneity effects within the sample, $\sigma_{E\gamma}(E_n)$ the isotopic partial γ-ray production cross section (cm^2),

$\Phi'(E_n, r)$ the neutron flux (cm^{-2} s^{-1}) and $\epsilon'(E_\gamma, r)$ the counting efficiency. One should be aware that $\Phi'(E_n, r)$ in Eq. (1.1) already accounts for matrix effects such as neutron self-shielding, scattering and thermalization within the sample. The efficiency $\epsilon'(E_\gamma, r)$ also accounts for γ-ray self-absorption and the geometric efficiency.

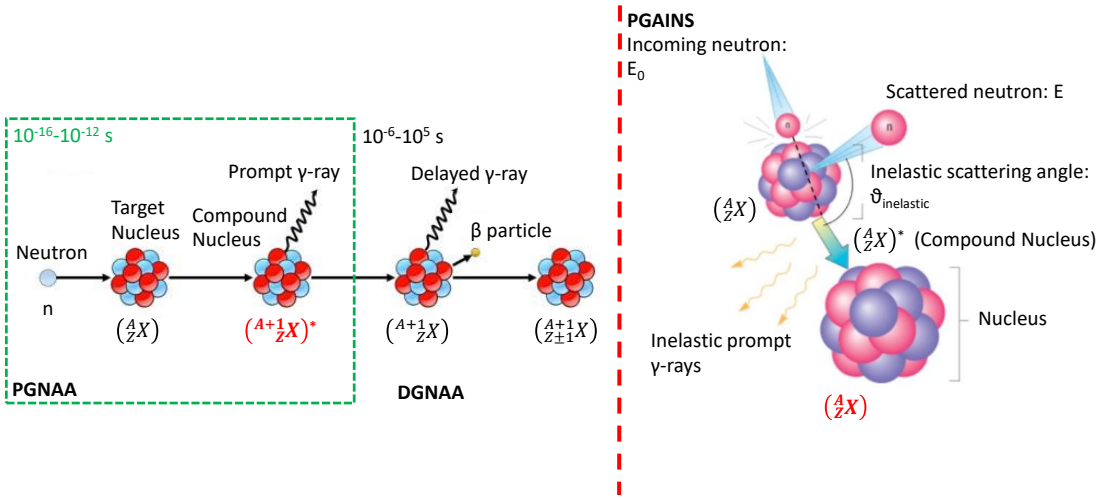


Figure 1.1: Schematic illustration of Prompt Gamma Analysis (PGA) with cold or thermal neutrons (PGNAA, left side) and fast neutrons (PGAINS, right side). DGNAA indicates Delayed Gamma Neutron Activation Analysis. The pictures were taken and modified from [2] (left side) and [3] (right side), respectively.

1.1.1 Cold and thermal neutrons (PGNAA)

Prompt gamma analysis using cold or thermal neutrons is called PGNAA (Prompt Gamma Neutron Activation Analysis) and the basic principle is depicted in Fig. 1.1. A neutron of negligible kinetic energy interacts with a nucleus X of a certain mass number A and atomic number Z (i.e. ${}^{A}_{Z}X$), denoted as (n,γ) reaction in nuclear physics notation. The neutron is captured by the nucleus and the surplus binding energy lifts it to an excited energy state, thereby creating a compound nucleus (denoted by an asterisk *). The nucleus deexcites then by the emission of prompt γ-rays. Since the formed nucleus has an additional neutron it is often unstable and decays via β decay, followed by the emission of delayed γ-rays used in DGNAA (Delayed Gamma Neutron Activation Analysis). The energy of the released γ radiation is characteristic for each element and isotope and hence acts as an unique fingerprint.

The great availability of intense thermal or cold neutron beams at facilities world-wide as well as compact Am-Be and ^{252}Cf neutron sources make PGNAA a powerful and well-established tool for an accurate and non-destructive chemical analysis in both industry and research [1, 4–8].

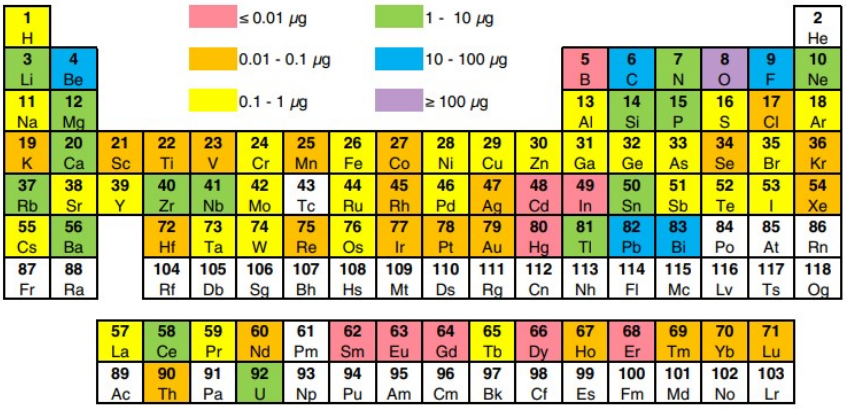


Figure 1.2: Detection limits for PGNAA in the cold neutron beam from NIST (National Institute of Standards and Technology). Values were calculated assuming matrix- and background freedom and a measurement of 24 h with 10% precision from counting statistics. [4]

High neutron capture cross sections in the low-energy range imply unprecedented sensitivities of this method with absolute detection limits reaching values below 0.01 μg for strong neutron absorbers such as cadmium (Cd) or gadolinium (Gd) (see Fig. 1.2). However, the high thermal cross sections up to 216 kb for ^{157}Gd [9] inherently imply short pathlengths of those neutrons. Consequently, PGNAA is a useful method for small and thin samples [1] and large objects might be investigated only to a certain extent [10–12]. Nevertheless, the penetration power of cold and thermal neutrons is limited and corrections for neutron and γ beam attenuation must be applied [12–15].

1.1.2 Fast neutrons (PGAINS)

As a consequence of the limited range of thermal and cold neutrons utilized in PGNAA, fast neutrons offer a better choice in the case of large samples owing their higher penetration power. The general feasibility to determine the elemental composition of thick samples by measuring fast-neutron-induced prompt γ-rays was demonstrated already several decades ago [16–19]. In contrast to low-energy neutrons, high-energy neutrons induce other reactions that are mostly associated with an energy threshold. Typical reactions are (n,n'), (n,p), (n,α) or (n,2n). The corresponding cross sections for the aforementioned reaction types are usually lower compared to thermal radiative neutron capture. However, at energies around the mean of fission neutrons (2 MeV) inelastic scattering reactions (n,n'γ) dominate since the intensity of (n,γ) reactions follows a $1/v$, with v as the neutron velocity, trend outside nuclear resonances. With respect to Fig. 1.1, a fast neutron scatters off from a target nucleus, thereby creating a compound nucleus which deexcites by the emission of prompt γ-rays. The crucial difference compared to PGNAA lies in the fact that the participating nucleus remains its identity, i.e. neither the mass nor the atomic number change in the reaction. Only (n,p), (n,α) or (n,2n) reactions induce

a low activity[a]. Therefore, the materials investigated with the PGAINS technique are not significantly activated in contrast to PGNAA. This facilitates the handling of irradiated materials for further investigations or sending back (e.g. in the case of museum samples) without the need of long storage and cooling times.

The cross sections for radiative neutron capture (n,γ) and hence the corresponding pathlengths of cold and thermal neutrons are observed to vary considerably depending on the considered material. In contrast to this, it will be shown within this work that the integral cross sections for fast-neutron inelastic scattering (n,n'γ) are nearly independent of the sample matrix. Although PGAINS complements PGNAA to allow accurate chemical analysis of large samples, in the frame of this work it is also demonstrated that PGAINS can offer higher sensitivity also in the case of thin samples composed of elements with very low cross sections for radiative neutron capture, in particular carbon, oxygen and cerium [1, 20, 21].

1.2 Baghdad Nuclear Research Institute reactor

In the mid 70s of the last century considerable efforts in the investigation of fast-neutron inelastic scattering reactions were made from the working group of A. M. Demidov at the Nuclear Research Institute in Baghdad (Iraq) [22–26]. The results of these investigations were compiled and published in the "Atlas of Gamma-ray Spectra from the Inelastic Scattering of Reactor Fast Neutrons", by Demidov et al. in 1978. [27]. This "Atlas" contains relative intensities and peak energies for 7375 γ-rays derived from irradiations at the IRT-M reactor[b] for 76 natural and 29 isotopically-enriched samples. The measuring angle between neutron beam and detector was 90° and the samples were tilted by 60° relative to the incident beam [22]. It is the only existing database in this field, although a relational database on (n,n'γ) data [28] based on [27] exists. Undoubtedly, the work and efforts of Demidov et al. are of great value but, unfortunately, they have never been validated.

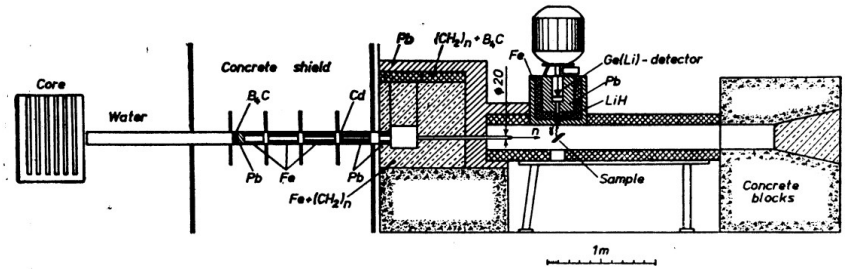


Figure 1.3: Experimental set-up at the IRT-M reactor used for irradiation experiments by Demidov et al. For the measurement of chlorine, also reported in this work, the set-up was slightly modified. [27]

[a] (n,n'γ) reactions could also induce low activities if a metastable state is formed.

[b] The reactor was also named "Osirak" by the French and completely destroyed by the Israeli airforce during operation opera in 1981.

The experimental irradiation set-up at the IRT-M reactor is illustrated in Fig. 1.3. The neutron beam produced in the light-water reactor open-core pool type was guided through a filter made of 9 cm lead (Pb), 1 cm of boron carbide (B_4C) and 1 mm of Cd. At sample position the beam diameter was approximately 30 mm, ensuring complete irradiation of the samples mounted in a holder of 25 × 25 mm^2. The utilized Ge(Li) detector had a shielding comprising of 10 cm lead (Pb), 5 cm iron (Fe), 8 cm paraffin with B_4C and 3 mm of ^{6}Li. A lithium hydride (LiH) filter, 20 mm in diameter and 110 mm long [22], inserted into the collimator of the Ge(Li) detector, was used to filter scattered fast neutrons. The prompt γ-ray spectra were recorded in the energy range of 0.12 to 3.4 MeV for most elements, with the exception of the light elements lithium, beryllium, boron, carbon, nitrogen, oxygen, fluorine, magnesium, silicon and calcium, whose spectra were measured up to 7 MeV. For the measurements either a 30 cm^3 (3.8 keV resolution at 1.2 MeV) or a 40 cm^3 (2 keV resolution at 1.2 MeV) Ge(Li) detector was used. The measurement time varied between 20 and 30 h. The efficiency of the spectrometer and the non-linearity of the detection system were determined with calibrated standard γ-sources, such as ^{75}Se, ^{182}Ta or ^{110}Ag. Relative intensities were also corrected for γ-ray self-absorption in the samples. Presence of γ-rays from the (n,γ) reaction was verified with the "Compendium of Thermal-Neutron Capture γ-Ray Measurements" [29, 30]. Unfortunately, however, any details regarding the correction of interferences with the capture reactions are missing in the Atlas [27]. Most elements were irradiated purely or as an oxide with sample masses typically above 10 grams [27].

In addition to relative intensities normalized to a certain transition of the considered isotope, the reference line of every element was also normalized with respect to the 847-keV line arising from the ^{56}Fe(n,n'γ)^{56}Fe reaction [27]. This normalization provides a unique reference point for every element.

1.2.1 The IRT-reactor fast-neutron spectrum

After filtering of the neutron beam by 10 cm of Pb the shape of the spectrum at sample position deviates from the fission spectrum produced in the core. A visualization of both spectra can be found in the Atlas [27]. The fission neutron spectrum can be approximated by an exponential law of the form $exp(\beta \cdot E_n)$. The value of β was given as -0.75 by Demidov et al. for neutron energies of $E_n > 1.5$ MeV [27]. In an earlier publication of Demidov et al. for $E_n > 1.5$ MeV the value of β was given as 0.72 [22]. Depending on the reactor type β can vary from -0.65 to -0.75 [31]. However, this variation does not really change relative γ-ray intensities emitted from levels above 0.5 MeV [27, 28] and therefore intensities from the Atlas [27] can be considered to be universal for the case of fission-based neutron sources using ^{235}U.

According to [28] the neutron flux $\Phi(E_n)$ of the IRT-M reactor can be described by the following expression:

$$\Phi(E_n) = \Phi_1(E_n) + \left(\frac{1 + tanh \cdot (K \cdot (E_n - 1.5))}{2}\right) \times (\Phi_2(E_n) - \Phi_1(E_n)), \quad (1.2)$$

where $\Phi_1(E_n)$ is the neutron flux in the energy region below E_n= 1.5 MeV and $\Phi_2(E_n)$ the neutron flux in the high-energy region, i.e. $E_n \geq 1.5$ MeV. The parameter K characterizes the infinitely smooth hyperbolic tangent function in Eq. (1.2).

In the energy region below E_n= 1.5 MeV, the neutron flux $\Phi_1(E_n)$ in Eq. (1.2) can be described by a Maxwellian distribution:

$$\Phi_1(E_n) = 2 \cdot A_1 \cdot \sqrt{\left(\frac{E_n}{\pi \cdot kT^3}\right)} \cdot exp\left(\frac{-E_n}{kT}\right), \quad (1.3)$$

where A_1 (a.u.) and kT (MeV) represent adjustable fitting parameters.

In the high-energy region of the spectrum, i.e. $E_n \geq 1.5$ MeV, the neutron flux $\Phi_2(E_n)$ can be reasonably described with an exponential of the form:

$$\Phi_2(E_n) = A_2 \cdot exp(-\beta \cdot E_n), \quad (1.4)$$

where A_2 (a.u.) and β are variables optimized in the fitting procedure [28].

For the overall fit depicted in Fig. 1.4 according to Eq. (1.2) the fit parameters were set to: K= 1, A_1= 84,500, kT= 0.39 MeV in the Maxwellian region and A_2= 36,600 and β= 0.76 in the exponential tail of the fit [28]. The average (flux-weighted) neutron energy of the IRT reactor spectrum was estimated as 0.631 MeV in [28].

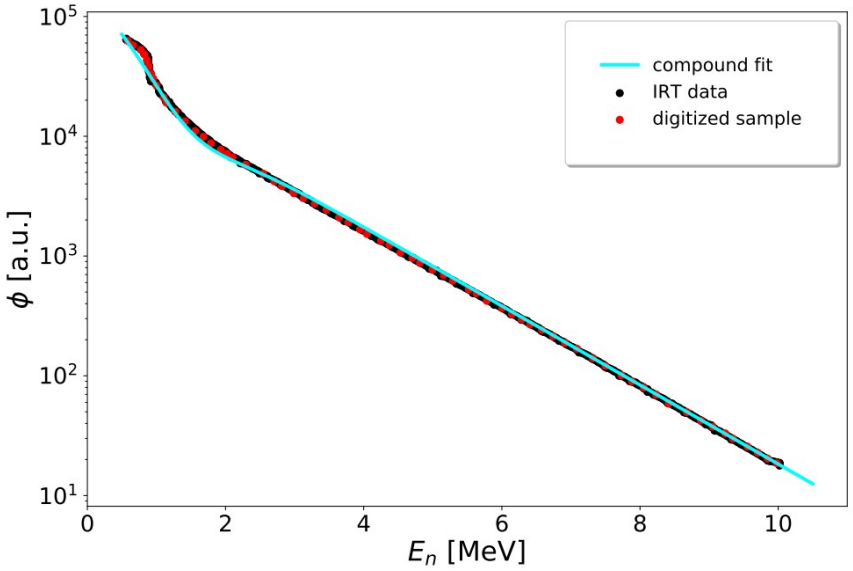


Figure 1.4: The IRT-M reactor neutron flux in arbitrary units (a.u.) as a function of the neutron energy. Black circles are digitized data points taken from [27] and red circles are a representative sample of these points required for fitting purposes. The solid line represents the fit described by Eq. (1.2) and taken from [28]. [28]

1.3 History of the FaNGaS instrument

The FaNGaS (Fast Neutron-induced Gamma-ray Spectrometry) instrument was developed at IEK-6 (Nuclear Waste Management and Reactor Safety) at the Forschungszentrum Jülich (FZJ) GmbH. Since 2014 it is installed at the SR10 (Strahlrohr 10) of the FRM II (Forschungs-Neutronenquelle Heinz Maier-Leibnitz) reactor at the MLZ (Heinz Maier-Leibnitz Zentrum) in Garching and from 2016 until today it is operated by JCNS-2 (Jülich Centre for Neutron Science). The idea of this instrument, however, was set a few years earlier. It originated from the TANDEM (TransActinide Nuclear Data Evaluation and Measurement) collaboration [32], initiated in 2011 by the prompt gamma activation analysis (PGAA) working groups at FZJ, the FRM II and the MTA EK (Hungarian Academy of Sciences Centre for Energy Research) by signing a Memorandum of Understanding (MoU). The absence of accurate nuclear reaction data of actinides, such as nuclear capture data of long-lived actinides like ^{237}Np, ^{242}Pu and ^{241}Am, served as the major motivation for this project [33]. Availability of such accurate data is crucial for the non-destructive assay and safe disposal of hazardous nuclear waste, especially for Germany that phased out nuclear energy.

The FaNGaS instrument resulted from three years successful cooperation and experiments at the neutron beam facilities in Budapest and Garching in the frame of TANDEM as well as financial support by the Bundesministerium für Bildung und Forschung (BMBF). This unique tool enables the non-destructive chemical analysis based on the detection of prompt γ-rays induced by fast-neutron reactions, mainly inelastic scattering, with actinides and other elements.

The long-range target of FaNGaS, as defined in [32], was the development of analytical techniques based on active neutron interrogation and γ-ray spectrometry for the non-destructive analysis of nuclear waste and its residues from dismantling activities. Now, the new goal is to use FaNGaS for chemical analysis of thin or large samples complementary to PGNAA. Therefore, much effort is put into: **(i)** the validation of nuclear data listed in the Atlas [27] and **(ii)** a continuous optimization of the instrument to improve its sensitivity by achieving higher peak-to-background ratios. In the frame of the aforementioned development and application of FaNGaS the relevant task is to determine neutron-spectrum averaged (effective) isotopic partial γ-ray production cross sections ($\langle\sigma_{E\gamma}\rangle$) for inelastic neutron scattering that are necessary to perform quantitative chemical analysis.

For this reason, a multitude of measurements were performed with the FaNGaS instrument at FRM II until the first quarter of 2020. Since then the reactor remained out of operation due to the global Corona pandemic and subsequent technical issues regarding the cold source and the cooling of the fuel. The measurements covered a multitude of elements, until the start of this work the following elements were measured: carbon (C), oxygen (O), sodium (Na), magnesium (Mg), aluminum (Al),

chlorine (Cl), potassium (K), calcium (Ca), iron (Fe), nickel (Ni), copper (Cu), zirconium (Zr), indium (In), lanthanum (La), cerium (Ce), praseodymium (Pr), neodymium (Nd), samarium (Sm), terbium (Tb) and dysprosium (Dy).

The measurement of Fe, published in [34], can be considered as an important milestone as it demonstrated that FaNGaS is a suitable tool for the investigation of fast-neutron-induced prompt γ-ray emission to create a reliable catalogue on (n,n'γ) reactions and to perform chemical analysis of large objects. With respect to data from Demidov et al. [27], the urgent need for a meticulous reevaluation was always pointed out in all works that followed so far [20, 21, 35–37].

Possible applications of the PGAINS technique utilized at FaNGaS cover a wide range of disciplines such as environmental research (e.g. nuclear waste), archaeology (e.g. amphoras), geology (e.g. rocks), industry (e.g. detection of clogs in pipelines [38]) and fundamental research (e.g. nuclear spectroscopy, astrophysics). From the aforementioned applications, in particular the field of nuclear spectroscopy benefits from measurements with FaNGaS, as incomplete decay schemes can be extended based on obtained experimental data. A part of the ongoing work is already adopted into the EXFOR (Experimental Nucler Reaction Data) [39] database.

1.3.1 Scope of this work

The main efforts of this work were the thorough analyses of prompt γ-ray spectra from the irradiation of various samples with the fission neutron beam at FaNGaS. These measurements were carried out by Zeljko Ilic, a former PhD student at MLZ, and basically include rare earth (RE) elements, i.e. La, Ce, Pr, Nd, Sm, Tb and Dy. As these samples were not irradiated elementary with a well-defined geometry, the analysis of those spectra was a demanding challenge that required the meticulous application of several analytical and numerical correction procedures. In addition to the aforementioned elements, also the analysis of prompt γ-ray spectra from C, O, Cl and Ca is presented. The analysis of all those experimental measurements was always the same and includes the calculation of relative γ-ray intensities and effective isotopic partial γ-ray production cross sections. The obtained nuclear data was compared to the work of Demidov et al. [27], particular emphasize in the discussions is on γ-lines that were absent in one of the two measurements.

Another major task tackled in the framework of this work was the optimization of the technical design of the instrument. Many endeavours were put into the development of a fast-neutron filter intended to be placed between sample and detector. This measure is necessary to reduce the undesired signatures in the γ-ray spectra induced by fast-neutron interactions inside the volume of the detector crystal on the one hand and to avoid saturation of the detector preamplifier in the case of the irradiation of large samples on the other hand. Suitable filter materials were studied numerically with standard Monte Carlo (MC) simulation software packages. Analytical approaches were applied to complement this work and to facilitate it.

A method for the quantification of large samples of any composition is also presented, supported by numerical simulations to estimate neutron self-shielding and γ-ray self-absorption. The limitations of this method are discussed.

1.4 Organization of this thesis

The introduction in Chapter 1 presents the background and motivation that has initiated this thesis. Besides concise introduction of some fundamental physics concepts it acts as a literature review and thereby introduces the Atlas [27] as well as the portfolio of the FaNGaS instrument, with emphasis on the importance of the aspects covered in this thesis.

The nuclear physics background is described in Chapter 2. Fundamental interactions of neutrons and photons relevant to this work, i.e. that govern fast-neutron induced prompt γ-ray spectrometry, are presented.

Chapter 3 provides information on applied numerical tools and methods. In particular, the γ-ray spectrum evaluation software, the software used to process nuclear data and numerical MC simulation codes used in this work are presented.

Chapter 4 describes the analytical methods. These concern the calculation of γ-ray production cross sections, corrections of neutron and γ attenuation, corrections of interferences, comparisons of the obtained data with literature and the estimation of elemental detection limits.

In Chapter 5 the FaNGaS instrument is described. Major focus is set to characterize the path of the neutrons from its creation to the interaction with the sample as well as the experimental configuration of the FaNGaS spectrometer.

The analysis and interpretation of experimentally obtained γ-ray spectra is given in Chapter 6. Apart from the description of the irradiated samples this chapter contains an experimental approach for the reconstruction of the thermal and epithermal spectrum part, as the spectrum is modified by a new multi-leaf collimator. In the frame of that, neutron self-shielding factors and moderation factors accounting for the presence of crystal water are given for the considered neutron-energy ranges and relevant samples.

The design of a fast-neutron filter inserted into the collimator of the spectrometer, to reduce signatures from fast-neutron inelastic scattering in the detector crystal and to prevent saturation of the detector preamplifier in the case of large samples, is presented in Chapter 7. After introduction of the theory suitable filter materials are selected based on the neutron and γ-ray performance of the considered filters.

The development of an analytical model for the neutron and photon attenuation corrections in large samples is presented in Chapter 8.

Chapter 9 summarizes the main outcomes and reached achievements, including a critical review and future outlook.

2. Fundamental radiation interactions

In the case of the PGAINS technique, a γ-ray spectrum represents the result of both the interactions of neutrons in a sample to produce the desired γ radiation and the subsequent interactions of these released γ-rays ending in the detector volume. Therefore, correct interpretation of a spectrum for the purpose of elemental analysis requires knowledge on the fundamental interactions of neutrons and photons in matter. This chapter intends to provide a solid physics background on basic interaction processes necessary to understand γ-ray spectrometry, with special regard to fast neutrons.

2.1 Neutron interactions with matter

According to the standard model (SM) of nuclear and particle physics, neutrons are subatomic particles that carry no net electrical charge and hence only interact via the strong short-ranged nuclear force [40]. Neutrons interact with matter through different types of interactions as illustrated in Fig. 2.1. These might be classified broadly into two categories: **scattering (i)** and **absorption (ii)**.

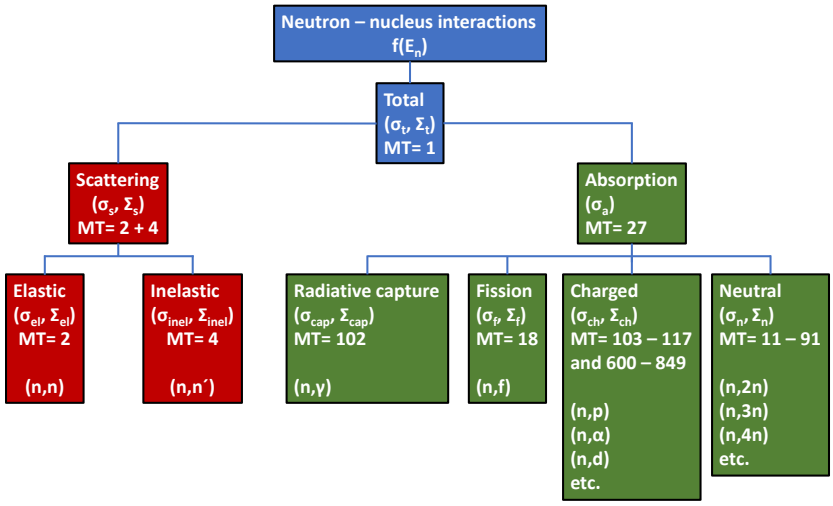


Figure 2.1: Classification of neutron interactions with matter. The MT number represents the reaction type specified by the evaluated nuclear data file (ENDF) [41]. The symbols σ and Σ denote microscopic and macroscopic cross sections, respectively.

Scattering (i) might be further divided into elastic and inelastic scattering. While total kinetic energy is usually conserved in the first reaction type, a certain fraction of energy is imparted to excite the nucleus in the second one. **Absorption (ii)** reactions remove a neutron from the incident beam and can be divided into radiative capture reactions, fission reactions and reactions with emission of a charged or neutral particle, respectively. Generally, reaction types can be characterized by a so-called MT number, ranging from 1 to 999. This number was introduced by the evaluated nuclear reaction databases (or evaluated nuclear data file, ENDF) [41] that store nuclear data from various libraries to ensure a uniform nomenclature. ENDF MT reaction numbers are the established standard for many nuclear data libraries.

Each of the interactions illustrated in Fig. 2.1 might occur in one of the three following fundamental interaction mechanisms: **compound nucleus formation**, **potential scattering** and **direct interaction**.

Compound nucleus formation

Neutrons with kinetic energies less than a few MeV are most likely to interact with all nucleons in a collective manner, i.e. with the nucleus as a whole. Absorption of a neutron results in an energy transfer to the whole nucleus and the release of binding energy, thereby creating a single excited state termed as compound nucleus. As the neutron lost all energy and momentum it becomes an indistinguishable part of the absorbing nucleus [42]. Compound nucleus reactions are binary two-step processes, that can be illustrated in the following way [43]:

$$x + X \rightarrow (x + X)^* \rightarrow y + Y, \tag{2.1}$$

where x and y denote the light projectile and ejectile, respectively, and X and Y represent the educt and product nucleus, respectively. The lifetime of compound nuclei exceeds the nuclear lifetime, i.e. the time the incident neutron would need to travel through the nucleus, by far. Consequently, the compound nucleus loses all information on its formation and the direction of the incident particle, resulting in an isotropic emission for all possible exit channels [43]. If, however, the compound state has non-zero total angular momentum (J), the distribution of emitted particles is anisotropic with symmetry to 90° relative to the incident particle beam axis [42].

Potential scattering

This type of scattering does not involve formation of a compound nucleus and it can be seen as a classical scattering process such as scattering of one billiard ball from another [44]. Potential scattering depends on the strong nuclear force, that in turn strongly depends on the size and shape of the nucleus. Therefore, it is sometimes also called shape elastic scattering.

Direct interaction

This type of nuclear reactions appears in a time scale that is comparable to the time of transit for the neutron through the nucleus [42]. Neutrons with kinetic energies above 40 MeV have de Broglie wavelengths comparable to single nucleons in a nucleus. As a consequence of that, such neutrons are most likely to interact with a single or a few nucleons only. If, for example, a neutron strikes a proton and gets completely absorbed, then this process would be called direct interaction (n,p) reaction. However, if the neutron would only transfer a small amount of energy just sufficient to elevate the proton into an excited state, this process would be termed direct interaction (n,n') reaction. This reaction type is not relevant for PGAINS.

2.1.1 Energy group classification

The induced reaction channel of a neutron strongly depends on its kinetic energy E_n, which is given in the classical regime as:

$$E_n = \frac{1}{2} \cdot m_n \cdot v_n^2, \tag{2.2}$$

where m_n and v_n are the mass and velocity of the neutron, respectively. In neutron physics it is common to classify neutrons into groups according to their kinetic energy. A standard classification system is given in [45] and it is shown in Table 2.1.

Table 2.1: Classification of neutrons according to their kinetic energy after [45].

Energy range	Name
0 - 0.025 eV	Cold
0.025 eV	Thermal
0.025 - 0.4 eV	Epithermal
0.4 - 0.6 eV	Cadmium
0.6 - 1.0 eV	Epicadmium
1 - 10 eV	Slow
10 - 300 eV	Resonance
300 eV - 1 MeV	Intermediate
1 - 20 MeV	Fast
$>$ 20 MeV	Relativistic

The names of the energy ranges given in Table 2.1 are given with respect to the temperature of the surrounding or specific nuclear reactions. A detailed description is given in [45]. For a neutron of 20 MeV energy, the fractional speed of light is already about 20%. For these relativistic (or ultrafast) neutrons the kinetic energy is no longer properly described by Eq. (2.2) and a relativistic treatment becomes necessary. The energy ranges in Table 2.1 are not strict and the groups are observed to vary in practice from research group to research group, depending on the very

specific needs. In nuclear reactor physics, neutron-energy spectra are often divided into three parts: thermal, epithermal (or resonance) and fast. The energy range of all other groups given in Table 2.1 is mostly included in these ranges, except the relativistic neutrons. For example, in the JANIS (Java-based nuclear information software) book of neutron-induced cross sections [9] thermal neutrons are defined with an energy range of 1×10^{-5} eV $\leq E_n \leq 10$ eV, resonance neutrons as 0.5 eV $\leq E_n \leq 100$ keV and fast neutrons as 1 keV $\leq E_n \leq 20$ MeV. In the frame of this work, thermal, epithermal and fast neutrons are considered with energy ranges spanning from 10^{-10} MeV to 1.42×10^{-7} MeV (thermal), 1.42×10^{-7} MeV to 0.06 MeV (epithermal) and 0.06 MeV to 20 MeV (fast).

The different types of reactions depicted in Fig. 2.1 depend on neutron energy and the most fundamental quantity used to describe any type of nuclear reactions is the microscopic cross section, denoted by the greek letter σ. It has the unit of area (cm^2) and it is often given in barns (1 barn= 10^{-24} cm^2) due to small nuclear dimensions. It reflects the probability of a certain reaction to occur.

2.1.2 Microscopic cross sections

The rate of a particular neutron reaction within a given material strongly depends on the kinetic energy of the incident neutron as well as on the nature of the target nuclei. Considering a nuclear reaction of the type $X(n, y)Y$ (where X and Y are the nuclei before and after the reaction, n is the incident neutron and y the ejectile) between a parallel monoenergetic neutron beam and a target (see Fig. 2.2), then the amount of particles emitted per unit time, $I(x)$, will be proportional to both the intensity of incident neutrons I_0 and the number of target nuclei N.

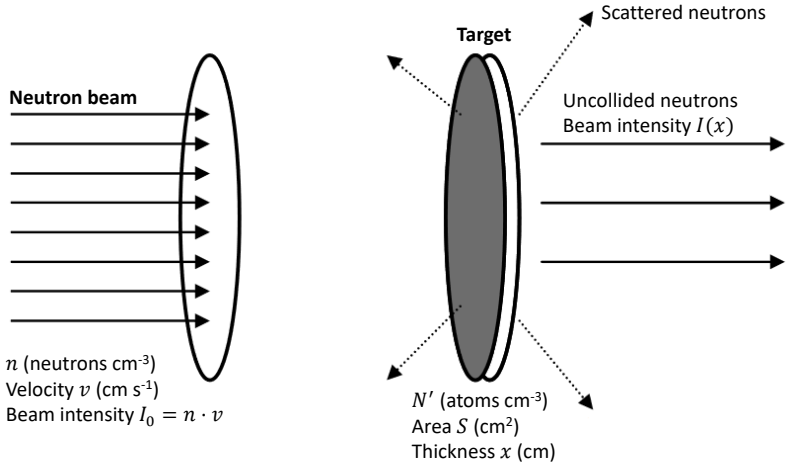


Figure 2.2: Schematic representation of the concept of microscopic cross section. Modified from [46].

The intensity I_0 is basically the product of the neutron speed v (cm s^{-1}) and the density of neutrons n (neutrons cm^{-3}). The proportionality factor is denoted as microscopic cross section σ [44, 46–48]:

$$I(x) \propto I_0 \cdot N \cdot \sigma \Leftrightarrow \sigma \propto \frac{I(x)}{I_0 \cdot N} = \frac{I(x)}{n \cdot v \cdot N' \cdot S \cdot x}. \tag{2.3}$$

The microscopic cross section σ characterizes the reaction probability between a single neutron and an individual particle or nucleus. According to Fig. 2.1, the total reaction cross section of a single neutron (σ_t) is expressed as the sum of scattering and absorption reactions:

$$\sigma_t = \sigma_s + \sigma_a. \tag{2.4}$$

Scattering (σ_s) and absorption reactions (σ_a) are further described by the sum of the following reactions depicted in Fig. 2.1:

$$\sigma_s = \sigma_{el} + \sigma_{inel}, \tag{2.5}$$

and:

$$\sigma_a = \sigma_{cap} + \sigma_f + \sigma_{ch} + \sigma_n. \tag{2.6}$$

For the case of a single nuclide and high neutron energies, the microscopic cross section for scattering might be reasonably estimated based exclusively on the geometrical area of the nucleus [46]:

$$\sigma_s = \pi \cdot R_n^2, \tag{2.7}$$

where R_n is the nuclear radius given by the Fermi equation [46]:

$$R_n = R_F \cdot A^{\frac{1}{3}}, \tag{2.8}$$

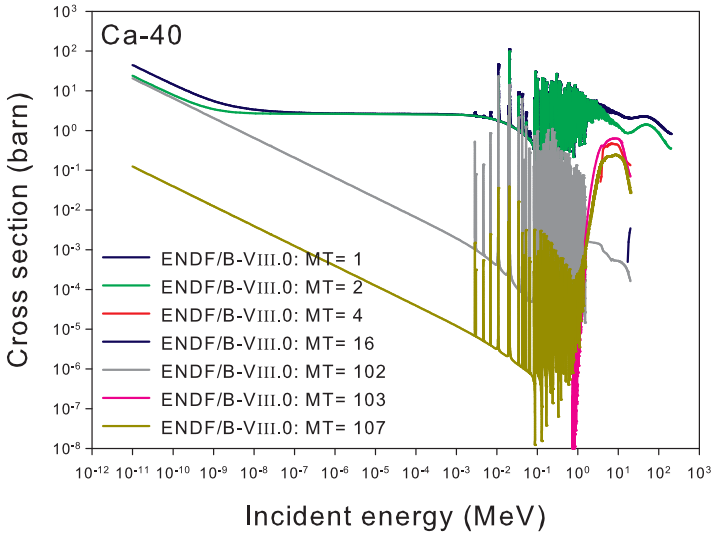
with $R_F = 1.2$ fm [46] as Fermi radius.

The variation of the microscopic cross section σ as a function of energy is called excitation function. In order to illustrate some basic features in the energy dependence of the most important neutron reactions, Fig. 2.3 shows the excitation functions for a light (^{40}Ca) and a heavy (^{139}La) nucleus.

For both, light and heavy nuclei, the elastic scattering cross section contributes most to the total cross section over the whole energy range. Only (n,γ) neutron capture reactions in the thermal regime and threshold reactions such as (n,n') at high neutron energies are competitive to elastic scattering. Owing their $1/v$ dependence, neutron capture cross sections are generally small for fast neutrons. The peaks in the epithermal energy regime are so-called resonances. At these energies the neutron energy matches exactly an excited compound nucleus state of long life time.

For light as well as heavy nuclei the relative contribution of the (n,n') reaction to the total cross section is substantial. From Fig. 2.3 one can also recognize that, for heavy nuclei like ^{139}La, cross sections for (n,p) and (n,α) reactions are

several orders of magnitude below those for (n,n') reactions. For light nuclei, such as ^{40}Ca, the respective cross sections might be in the same order of magnitude. This circumstance is reasoned in the fact that the Coulomb forces of the shell electrons are moderate in low-Z elements and hence the escape of charged particles as protons or alpha particles is less hindered [49]. In principle, reactions involving the emission of particles with a mass m such as (n,p) and (n,α) are endothermic and hence have a certain reaction threshold. For some nuclei, however, as for ^{40}Ca for the (n,α) reaction they are exothermic without any threshold.



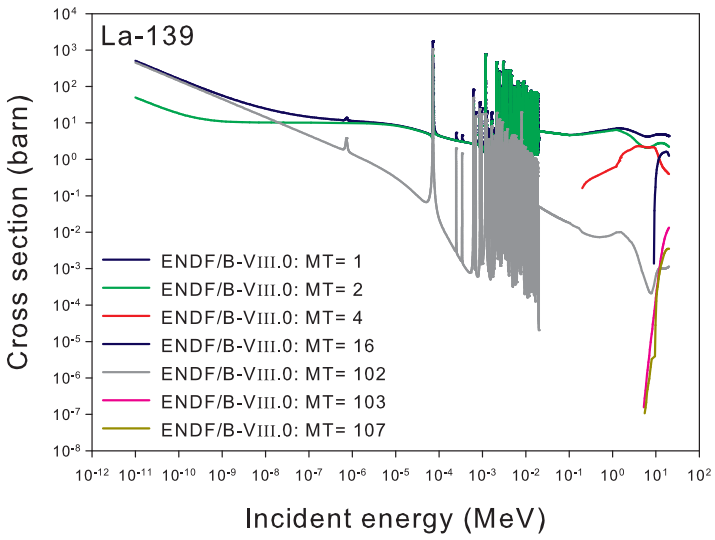


Figure 2.3: Discrete microscopic cross sections for ^{40}Ca (top) and ^{139}La (bottom) for the most important reaction channels. Data is taken from [50] and the reactions are denoted by the ENDF MT reaction numbers. MT= 1 is the (n,tot), MT= 2 the (n,elastic), MT= 4 the (n,n'), MT= 16 the (n,2n), MT= 102 the (n,γ), MT= 103 the (n,p) and MT= 107 the (n,α) reaction.

Indeed, in the experimental γ-ray spectrum of calcium carbonate ($CaCO_3$) presented within this work γ-lines from the ^{40}Ca(n,pγ)^{40}K and ^{40}Ca(n,$\alpha\gamma$)^{37}Ar reactions were observed. In contrast to that, examination of the measured lanthanum(III) chloride heptahydrate ($LaCl_3 \cdot 7H_2O$) spectrum did not reveal a single line from the ^{139}La(n,pγ)^{139}Ba and ^{139}La(n,$\alpha\gamma$)^{136}Cs reactions. The (n,2n) knockout reaction has a high energy threshold ($>$ 10 MeV), and the neutron spectrum at sample position of FaNGaS was not capable of inducing any single line attributed to this reaction channel yet, which is attributed to the low neutron flux around 10 MeV energy.

2.1.3 Macroscopic cross sections

The macroscopic cross section Σ (cm^{-1}) represents the effective target area of all nuclei from all elements and isotopes present in a material. It equals the probability of a neutron interaction per centimeter traversed in the material. For a material composed of a single nuclide the macroscopic cross section is expressed as:

$$\Sigma = N' \cdot \sigma = \frac{\rho \cdot N_A}{M} \cdot \sigma. \tag{2.9}$$

For a mixture of several nuclides the cross section can be calculated as [51]:

$$\Sigma = \frac{\rho \cdot N_A}{M} \cdot \sum_{i=1}^{n} \sigma_i \cdot n_i \cdot h_i = N' \cdot \sum_{i=1}^{n} \sigma_i \cdot n_i \cdot h_i, \tag{2.10}$$

where ρ is the density of the mixture (g cm^{-3}), N_A the Avogadro constant (6.022×10^{23} mol^{-1}), M the molar mass of the mixture (g mol^{-1}), σ_i the microscopic cross section (cm^2), n_i the number of atoms in the mixture (e.g. for H_2O, n_H= 2 and n_O= 1) and h_i the natural abundance of the ith nuclide.

It is noteworthy to mention that the inverse of the macroscopic cross section equals the mean free transport pathlength, which is the average distance the neutron has to travel through the considered material to induce a certain reaction of type j:

$$\lambda_{tr,j} = \frac{1}{\Sigma_j}. \tag{2.11}$$

2.1.4 Integral cross sections

In the previous sections microscopic and macroscopic cross sections were defined for discrete neutron energies. Both can also be evaluated as integral/effective quantities (denoted by angle brackets $\langle\rangle$) for a certain energy range limited by a minimum ($E_{n,min}$) and maximum neutron energy ($E_{n,max}$). Provided with an experimental or numerical neutron-energy spectrum of n bins in energy, a so-called spectrum-averaged or effective cross section (SACS) is defined as [34, 52, 53]:

$$SACS = \frac{\int_{E_{n,min}}^{E_{n,max}} \sigma(E_{n,i}) \cdot \Phi(E_{n,i}) \cdot dE}{\int_{E_{n,min}}^{E_{n,max}} \Phi(E_{n,i}) \cdot dE}, \tag{2.12}$$

where $\Phi(E_{n,i})$ is the differential neutron-flux density and $\sigma(E_{n,i})$ the microscopic cross section at a neutron energy in the interval $E_{n,min} \leq E_{n,i} \leq E_{n,max}$.

The integral microscopic cross section can be determined as an approximation of Eq. (2.12) as:

$$\langle\sigma\rangle = \frac{\sum_{i=1}^{n} \sigma_i(E_n) \cdot \Phi_i(E_n)}{\sum_{i=1}^{n} \Phi_i(E_n)}, \tag{2.13}$$

where $\Phi_i(E_n)$ is the neutron flux (cm^{-2} s^{-1}) and $\sigma_i(E_n)$ the microscopic cross section in the considered neutron-energy bin i, respectively. Integral values of macroscopic cross sections are simply obtained by setting $\langle\sigma\rangle$ from Eq. (2.13) equal to σ_i in Eq. (2.10):

$$\langle\Sigma\rangle = N' \cdot \sum_{i=1}^{n} \langle\sigma_i\rangle \cdot n_i \cdot h_i. \tag{2.14}$$

2.1.5 Reaction rates

With respect to Fig. 2.2 and Eq. (2.3) the reaction rate R (in units of s^{-1}) in a given volume traversed by a monoenergetic beam of free neutrons can be expressed as:

$$R = \sigma \cdot N' \cdot I = \sigma \cdot N' \cdot \Phi, \tag{2.15}$$

where the beam intensity I is called now neutron flux Φ (cm^{-2} s^{-1}). If the neutron-energy spectrum is divided into different neutron-energy ranges i, one can determine an integral reaction rate $\langle R_i\rangle$ in units of $atom^{-1}$ s^{-1} for every single group:

$$\langle R_i\rangle = \int_{E_{n,min}}^{E_{n,max}} \sigma(E_n) \cdot \Phi(E_n) \cdot dE = \langle\sigma_i\rangle \cdot \langle\Phi_i\rangle. \tag{2.16}$$

The sum of the reaction rates from all considered neutron-energy groups i must equal the total reaction rate $\langle R_t\rangle$ calculated with the integral flux covering the whole neutron-energy range of the spectrum:

$$\langle R_t\rangle = \sum_{i=1}^{n} \langle\sigma_i\rangle \cdot \langle\Phi_i\rangle, \tag{2.17}$$

where n might be 3 in the case of the neutron spectrum at sample position of FaNGaS with $i = 1$ for thermal, $i = 2$ for epithermal and $i = 3$ for fast neutrons.

Presence of the different nuclear reactions given in Fig. 2.1 and Fig. 2.3 ultimately depends on the product of the cross section and the corresponding neutron flux available at that energy, i.e. the reaction rate.

2.1.6 Inelastic scattering (n,n'γ)

Apart from direct interaction (n,n') reactions, inelastic scattering usually involves the absorption of the neutron and formation of a compound nucleus. If the com-

pound nucleus emits a neutron of lower energy, this process is termed as inelastic scattering. In contrast to the process of elastic scattering the total kinetic energy of the incident neutron is not conserved in an inelastic scattering event. As total energy, however, is conserved the energy loss of the neutron is transferred to the individual nucleons resulting in an excitation of the whole nucleus. Schematically, the process can be described by [54]:

$$n + {}^{A}_{Z}\mathrm{X} \rightarrow {}^{A+1}_{Z}\mathrm{X}^{*} \rightarrow {}^{A}_{Z}\mathrm{X}^{*} + n' \Rightarrow {}^{A}_{Z}\mathrm{X}^{*} \rightarrow {}^{A}_{Z}\mathrm{X} + \gamma. \tag{2.18}$$

As Eq. (2.18) illustrates, the neutron emission is not sufficient to remove the excitation energy completely. Rather, inelastic scattering reactions are accompanied by the emission of γ-rays, hence denoted as (n,n'γ) reactions.

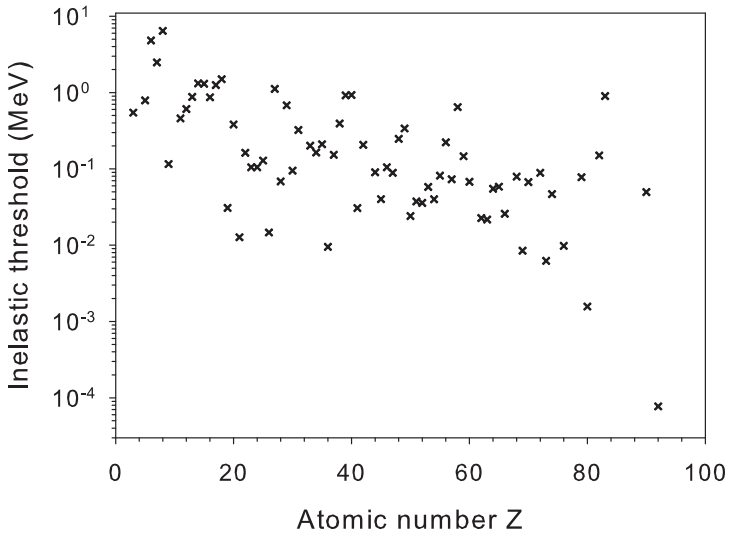


Figure 2.4: Dependence of the inelastic threshold on atomic number Z. Data points respresent elementary values averaged over naturally occuring isotopes and were taken from the JENDL-4.0 database [55].

Inelastic scattering is a threshold reaction and the associated threshold energy depends on the atomic number Z of the considered nucleus, as depicted in Fig. 2.4. In light nuclei, such as carbon for example, the excitation energy for the first excited state (ϵ_1) lies much higher above the ground state (g.s.) as in the case of heavy nuclei like uranium. In addition, Fig. 2.5 emphasizes that the threshold is isotope-specific and might vary considerably depending on the neutron number. Due to kinematics of the scattering process inelastic scattering cannot be induced by neutrons that just carry a kinetic energy equal to the energy of the first excited state. Rather, the kinetic energy of neutrons in the laboratory frame is connected to ϵ_1 as [28, 44]:

$$E_l = \frac{A+1}{A} \cdot \epsilon_1, \tag{2.19}$$

where E_l is also known as inelastic threshold. Obviously, for nuclei with $A \gg 1$ the

minimum energy for an inelastic scatter approaches the energy of the first excited level, i.e. $E_l \approx \epsilon_1$.

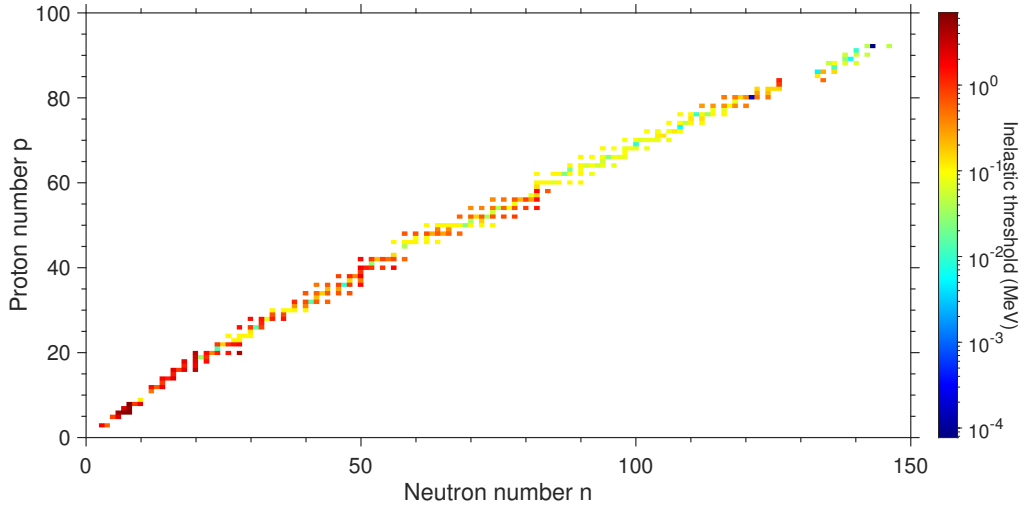


Figure 2.5: Dependence of the inelastic threshold on proton and neutron number. Values were taken from [55] but complemented by data from [50] when it was not available. For the elements At, Rn, Fr, Ra, Ac and Th only isotopes that are most abundant due to natural decay chains are depicted.

Anisotropic gamma-ray emission

In (n,γ) radiative neutron capture reactions the γ-rays are emitted isotropically (i.e. 4π solid-angle coverage). For isotropic distributions the angular-distribution correction factor, denoted as $W(\theta)$, is equal to one. In this case the result of a measurement is independent of the angle θ between neutron beam and detector and hence no correction is necessary to deduce the reaction cross section with respect to the differential cross section. Inelastic scattering of fast neutrons is anisotropic with $W(\theta) \neq 1$. The cross section for inelastic scattering is connected to the differential cross section as [28, 56]:

$$\sigma_{inel} = \frac{d\sigma(\theta)}{d\Omega} \cdot \frac{4\pi}{W(\theta)}, \tag{2.20}$$

where σ_{inel} represents the angle-integrated cross section for the inelastic scattering channel, $\sigma(\theta)$ is the differential inelastic scattering cross section measured under an angle of θ and Ω is the solid angle covered by the detector.

According to Grozdanov et al. [57], $W(\theta)$ is defined as the ratio of the net count rate measured at an angle θ to the net count rate measured at an angle of 90° with respect to the neutron beam axis for a considered γ-ray of energy E_γ. Therefore, it might be qualitatively defined as:

$$W(\theta) = \frac{\dot{C}_{E\gamma}(\theta)}{\dot{C}_{E\gamma}(90°)}, \tag{2.21}$$

where $\dot{C}_{E\gamma}(\theta)$ is the net count rate for a given γ-ray of energy E_γ at a measuring angle θ and $\dot{C}_{E\gamma}(90°)$ the net count rate at an angle of 90°, respectively.

In order to extract $\sigma(\theta)$ from Eq. (2.20), it can be rewritten to:

$$\sigma_{inel} \cdot \int_0^{4\pi} d\Omega = \frac{4\pi}{W(\theta)} \cdot \int_0^{\sigma(\theta)} d\sigma(\theta). \tag{2.22}$$

Integration of Eq. (2.22) yields:

$$\sigma(\theta) = \sigma_{inel} \cdot W(\theta). \tag{2.23}$$

For a certain transition from $J_i^{\pi_i} \rightarrow J_f^{\pi_f}$ (J denotes the spin and π the parity of the initial, i, and final, f, nuclear level) the angular-distribution function is properly described by the first three even terms of a Legendre polynomial [57]:

$$W(\theta) = 1 + \sum_{j=2,4} a_j \cdot P_j\left(\cos\left(\theta\right)\right), \tag{2.24}$$

where a_j are anisotropy coefficients [28, 58] and P_j are the Legendre polynomials of the order j. The polynomials are given as [28]:

$$P_0(\cos\left(\theta\right)) = 1, \tag{2.25}$$

$$P_2(\cos\left(\theta\right)) = \frac{1}{2} \cdot \left(3 \cdot \cos^2\left(\theta\right) - 1\right), \tag{2.26}$$

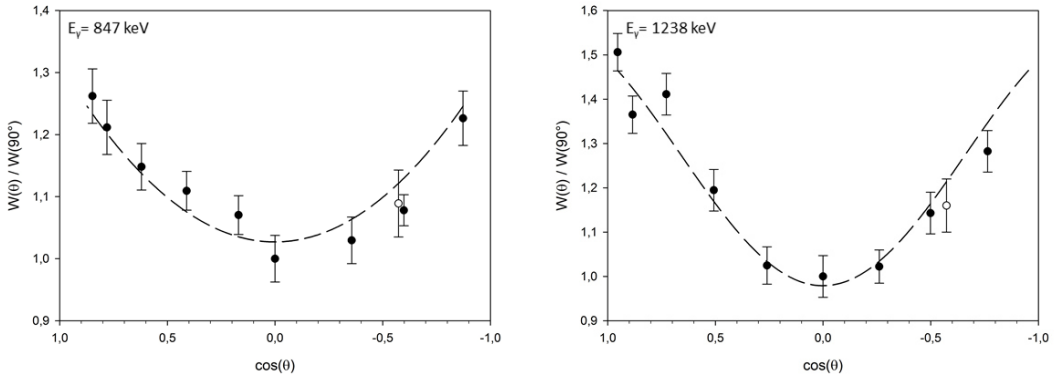
$$P_4(\cos\left(\theta\right)) = \frac{1}{8} \cdot \left(35 \cdot \cos^4\left(\theta\right) - 30 \cdot \cos^2\left(\theta\right) + 3\right). \tag{2.27}$$

As the solid angle Q_j subtended by the detector has an impact on the angular distribution of γ-rays [28], Eq. (2.24) can be modified to a more realistic equation:

$$W(\theta) = 1 + \sum_{j=2,4} a_j \cdot Q_j \cdot P_j\left(\cos\left(\theta\right)\right). \tag{2.28}$$

For a 4π detection system $Q_j \rightarrow 0$ and the nature of anisotropy in inelastic scattering disappears, whereas $Q_j \rightarrow 1$ for a point-like detector [28].

The anisotropy of inelastic scattering was investigated in the frame of the determination of the effective isotopic partial γ-ray production cross sections of the ^{56}Fe(n,n'γ)^{56}Fe reaction obtained with the FaNGaS instrument by irradiation of a thin Fe foil, as described in [34]. In Fig. 2.6 the relative angular distributions for the three strongest γ-rays from the ^{56}Fe(n,n'γ)^{56}Fe reaction (847, 1238 and 1810 keV) are depicted. Close symbols depict values determined at a neutron energy of 4 MeV and were taken from [59], open symbols represent values derived for an angle of θ= 125° with the fast-neutron spectrum average of FaNGaS. As the open symbols agree with the trend of the close symbols, the reliability of the FaNGaS instrument to derive partial γ-ray production cross sections at an angle of 90° between neutron beam axis and detector was demonstrated.



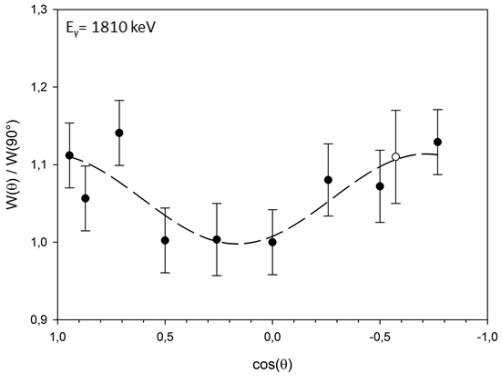


Figure 2.6: Relative angular distributions for the 847-, 1238- and 1810-keV γ-line from the ^{56}Fe(n,n'γ)^{56}Fe reaction. Close symbols are experimentally determined at a neutron energy of 4 MeV and were taken from [59]. Open symbols are values calculated for an angle of θ= 125°. Dashed lines are fits and serve to guide the eye.

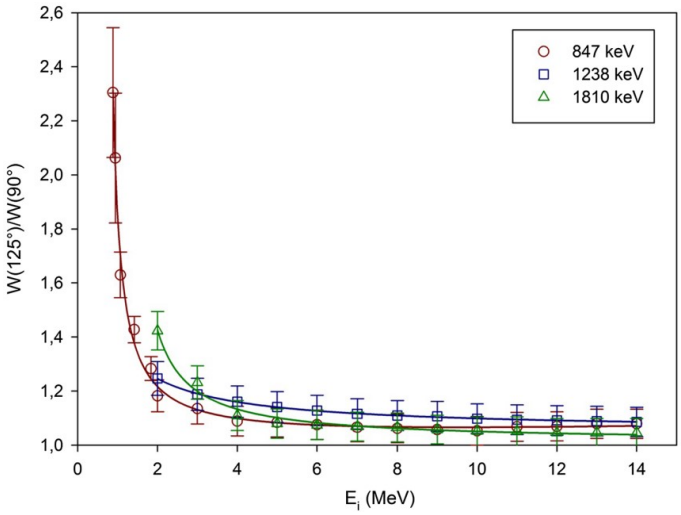


Figure 2.7: Neutron-energy dependence of the ratio of the angular distribution factors for the three strongest γ-rays from the ^{56}Fe(n,n'γ)^{56}Fe reaction. The data is taken from the FaNGaS measurement of Fe [34].

In addition, Fig. 2.7 also gives the dependence of the ratio of angular distribution factors from the three strongest Fe lines on the neutron energy. Apart from small differences arising from the γ-ray energy, the anisotropy decreases with increasing neutron energy.

Doppler broadening

As the inelastic scattering process also results in a certain transfer of kinetic energy to the resting nucleus involved in the (n,n'γ) reaction, the excited recoil nucleus might reach relatively high velocities of 10^8 up to 10^{10} cm s^{-1} [60]. If it is still moving at the time of γ-ray emission, the γ-rays are subject to Doppler broadening. This condition is met when the nuclear lifetime (τ_{nuc}) of the respective excited state is smaller than the time it takes for the recoil nucleus to lose all its kinetic energy and to come to rest (τ_{stop}), i.e. $\tau_{nuc} < \tau_{stop}$.

An established method to estimate the stopping time is provided by the computer code SRIM (The Stopping and Range of Ions in Matter) [61, 62]. Doppler broadening becomes visible in γ-ray spectra as broad peaks with a larger energy resolution than that of the detector itself. Although the width and shape depends on the composition and density of the absorber medium [63], it generally takes more time for light than heavier nuclei to spend all kinetic energy to the surrounding of the nuclei.

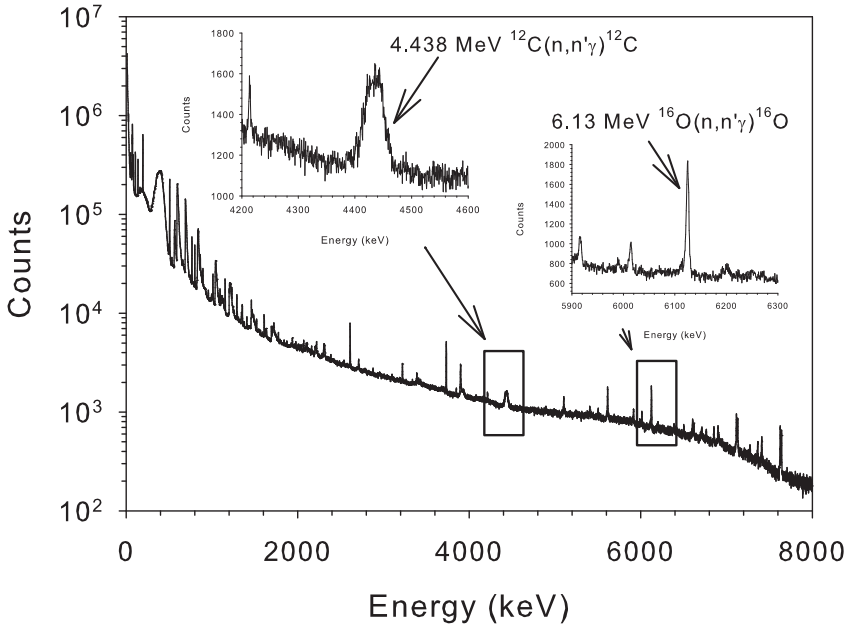


Figure 2.8: Doppler broadening observed in the $CaCO_3$ spectrum recorded with FaNGaS. The peak at 4.438 MeV from the ^{12}C(n,n'γ)^{12}C reaction shows a broadening compared to the sharp peak at 6.13 MeV from the ^{16}O(n,n'γ)^{16}O reaction. The broadening is associated to the short lifetime of the excited state (42.2 fs [64]) with respect to the time it takes the recoiled nucleus to stop.

As illustrated in Fig. 2.8, the γ-ray at 4.438 MeV from the ^{12}C(n,n'γ)^{12}C reaction clearly shows a broadening, in contrast to the γ-line at 6.13 MeV from the ^{16}O(n,n'γ)^{16}O reaction. This difference is reasoned in the different life time of the respective states. The $2^+ \rightarrow 0^+$ transition from the first excited state in ^{12}C takes place with τ_{nuc}= 42.2 fs [64], whereas the transition in ^{16}O from the second excited

state from $3^- \rightarrow 0^+$ takes 18.4 ps [65].

The additional spread in the line shape of a γ-line on top of the energy resolution of the detector equals the energy $E_\gamma^{'}$ [66] of the γ emitted in flight [67]:

$$E_\gamma^{'} = \frac{1}{2} \cdot \frac{E \cdot (E + 2 \cdot m \cdot c^2)}{E + m \cdot c^2} \cdot \sqrt{1 - \beta^2} \cdot \frac{1}{1 - \beta \cdot \cos(\delta)}, \tag{2.29}$$

where $\beta = v/c$ with v as the velocity of the recoil nucleus and c as the speed of light ($\approx 3 \times 10^8$ m s^{-1}), E is the transition energy and δ denotes the γ-ray emission angle relative to the velocity vector of the moving recoil nucleus. For the case that $\beta \ll 1$ and $E/m \cdot c^2 \ll 1$, Eq. (2.29) can be reduced to [67]:

$$E_\gamma^{'} \cong E_\gamma \cdot (1 + \beta \cdot \cos(\delta)), \tag{2.30}$$

where E_γ is the energy of a γ emitted by a nucleus at rest, given as [67]:

$$E_\gamma = E \cdot \left(1 - \frac{E}{2 \cdot m \cdot c^2}\right). \tag{2.31}$$

2.1.7 Moderation of fast neutrons

The slowing down of fast neutrons associated with the loss of kinetic energy in scattering reactions with nuclei is termed as moderation. In PGA this process could be reasonably neglected in most cases for sample thicknesses far below 1 mm, but it might be a severe issue for larger samples. If the samples also contain elements with small mass numbers A such as hydrogen in water, moderation can alter the shape of a neutron spectrum. For the analysis of γ-ray spectra of hydrated rare earth (RE) chlorides presented in this work, moderation effects were actually taken into account. Therefore, a brief introduction of fundamental quantities used to characterize the moderation process of fast neutrons is expedient.

Elastic scattering

Considering elastic scattering, the collision density is expressed in terms of lethargy u, a dimensionless quantity defined as [44, 68]:

$$u = \ln\left(\frac{E_0}{E}\right), \tag{2.32}$$

where E_0 is the inital and E the final neutron energy after moderation, respectively. The change in u, i.e. $\overline{\Delta u}$, is defined as the average logarithmic energy decrement given as [44]:

$$\xi = \overline{\Delta u} = \int_{\alpha E_0}^{E_0} \ln\left(\frac{E_0}{E}\right) \cdot P(E_0 \rightarrow E) dE = 1 + \frac{\alpha}{1 - \alpha} \cdot \ln(\alpha), \tag{2.33}$$

where α is a collision parameter resulting from the kinematics of the elastic scattering process [44]:

$$\alpha = \left(\frac{A-1}{A+1}\right)^2. \tag{2.34}$$

The required number of elastic collisions to moderate a fast neutron from an energy E_0 to E is expressed as [44, 68]:

$$n = \frac{1}{\xi} \cdot \ln\left(\frac{E_0}{E}\right). \tag{2.35}$$

The product of the average logarithmic energy decrement and the macroscopic cross section for elastic scattering (Σ_{el}) is called macroscopic slowing down power ($MSDP$) and it indicates how rapidly a neutron is slowed down in a material [68]:

$$MSDP = \xi \cdot \Sigma_{el}. \tag{2.36}$$

As a small macroscopic absorption cross section (Σ_a) is fundamental for an effective moderation, the efficiency of the moderation process is expressed by the moderating ratio (MR) [68]:

$$MR = \xi \cdot \left(\frac{\Sigma_{el}}{\Sigma_a}\right). \tag{2.37}$$

Inelastic scattering

Although elastic scattering contributes most to moderation, at very high neutron energies heavy nuclei are more effective to slow neutrons down via inelastic scattering. When a nucleus is hit by a neutron of energy E the probability that a neutron from inelastic scattering is emitted with an energy between E' and $E' + dE'$ can be approximated by [44]:

$$P(E \to E') \cdot dE' = \frac{E'}{T^2} \cdot \exp\left(\frac{-E'}{T}\right) \cdot dE', \tag{2.38}$$

where T (MeV) is the nuclear temperature defined as [44]:

$$T = 3.2 \cdot \sqrt{\frac{E}{A}}. \tag{2.39}$$

The average energy of an inelastically scattered neutron can then be expressed as [44]:

$$\overline{E'} = \int_0^\infty E' \cdot P(E \to E') \cdot dE' = 2 \cdot T. \tag{2.40}$$

Assuming that a 2-MeV neutron strikes a ^{139}La nucleus in a $LaCl_3{\cdot}7H_2O$ sample, the energy of the inelastically scattered neutron would be 0.77 MeV. Therefore, the

neutron would lose more than one half of its initial energy in a single inelastic scattering event (i.e. 1.23 MeV). As mean free transport pathlengths for elastic scattering, however, are generally smaller than that one for inelastic scattering, this kind of moderation can only play a significant role in the case of multiple neutron scattering in large samples.

2.2 Photon interactions with matter

According to the SM of nuclear and particle physics, photons are massless gauge bosons (force carriers) that mediate the electromagnetic interaction between charged particles [40]. They are quantized packages of light without physical mass and they obey the principles of quantum mechanics [69–71]. The different interaction mechanisms of photons heavily depend on their energy and the atomic number of the absorber material. The total reaction probability contains all relevant processes and is expressed by the total photon cross section σ_t:

$$\sigma_t = \sigma_{ph} + \sigma_{coh} + \sigma_{incoh} + \sigma_{pair} + \sigma_{trip} + \sigma_{ph.n.}, \tag{2.41}$$

where σ_{ph} is the cross section for the photoelectric effect, σ_{coh} the cross section for coherent scattering, σ_{incoh} the cross section for incoherent or Compton scattering, σ_{pair} the cross section for pair production in the electric field of electrons, σ_{trip} the cross section for triplet production in the field of a nucleus and $\sigma_{ph.n.}$ the cross section for photonuclear reactions. Since photons emitted in the frame of atomic and nuclear relaxation processes typically have energies between several hundreds of eV and a few MeV, for most practical purposes as in γ-ray spectrometry the three most relevant interaction processes of γ-rays are the **photoelectric effect**, **Compton scattering** and **pair production**. In the following, photons are preferably termed as γs or γ-rays since this nomenclature corresponds to the energy range covered in this work.

2.2.1 Photoelectric effect

In the photoelectric effect, a (γ,e) reaction in nuclear physics notation, an incoming γ is completely absorbed by a bound electron, denoted as photoelectron. This effect is illustrated in Fig. 2.9. Laws of momentum conservation exclude absorption by a free electron [72]. Since the γ energy exceeds the atomic binding energy, the photoelectron is ejected from the atom and the kinematics of the absorption two-body collision result in a complete transfer of the γ excess energy into kinetic energy of the released electron. Photoelectrons are monoenergetic, their discrete energy is given as [71]:

$$T_{e^-} = E_\gamma - W_i, \tag{2.42}$$

where T_{e^-} is the kinetic energy of the photoelectron, E_γ the energy of the incident γ and W_i the work function or ionization energy of the considered shell in the atom, i.e. the binding energy of the electron.

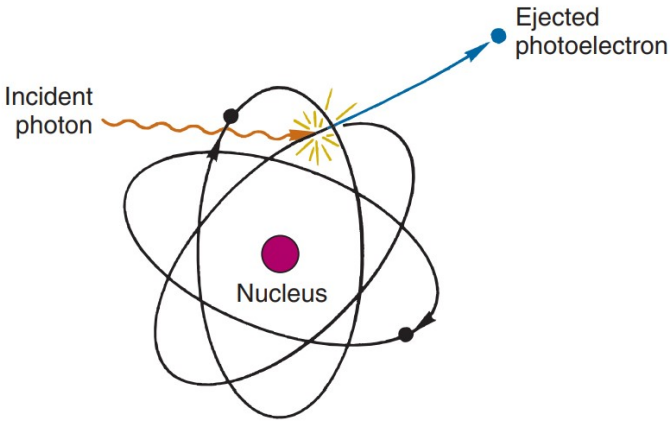


Figure 2.9: Schematic representation of the photoelectric effect. [73]

As the photelectric effect leaves an energetically-unfavourable vacancy in the atomic shell structure, it is always accompanied by electron movements from outer to inner shells in order to fill this gap in the deexcitation process. The difference in binding energy between involved shells is then either released in the form of characteristic X-rays or Auger electrons, which might be emitted as a cascade.

Generally, the cross section of the photoelectric effect σ_{ph} ($\mathrm{cm}^2 \cdot \mathrm{atom}^{-1}$) can be approximated as [74–77]:

$$\sigma_{ph} \cong constant \times \frac{Z^n}{E_\gamma^{3.5}}, \tag{2.43}$$

where Z is the atomic number with the exponent n varying between 4 and 5 in the energy range 0.1 MeV $\leq E_\gamma \leq$ 5 MeV as a function of energy [75, 76, 78]. As evident from Eq. (2.43), the photoelectric effect dominates at low γ energies E_γ [79] and for high-Z elements. If the γ energy coincides with the binding energy of a shell electron, the value of σ_{ph} assumes local maxima that are termed absorption edges [80]. The nomenclature of these depends on the involved shells and they are called K-, L_1-, L_2- and L_3-edge for example in the case of atomic electrons participating from the aforementioned shells. In fact, the expression for the cross section of the photoelectric effect given in Eq. (2.43) strongly depends on the γ energy with respect to the energy of absorption edges [54, 81], and it must be corrected at energies close to those [75].

For γ energies $E_\gamma > E_K$, where E_K represents the K-shell energy, the cross section for a photoelectric effect with a K-shell electron near to the nucleus is highest [73]. It is observed to decrease rapidly from inner to outer shells, i.e. $\sigma_{ph}^K/\sigma_{ph}^L \sim 5$ and $\sigma_{ph}^L/\sigma_{ph}^M \sim 4$ [82], where K, L and M denote the shell of the involved electron. Equations for L and M shells exist [83], but they are fairly complex and uncertain.

Strictly spoken, however, the complete cross section for the photoelectric effect is the sum over all participating shells [84]:

$$\sigma_{ph} \cong \sigma_{ph}^{K} + \sigma_{ph}^{L} + \sigma_{ph}^{M} + ... \tag{2.44}$$

2.2.2 Compton scattering

If the energy of a γ incident on an atomic shell electron is small compared to the rest-mass-energy equivalent of that electron (i.e. $E_\gamma < m_e \cdot c^2$), the resulting reaction is known as Thomson elastic scattering in the Thomson energy regime [85]. For γs with energy $E_\gamma \geq m_e \cdot c^2$, an inelastic scattering reaction with considerable energy transfer to the involved electron, depending on the reaction kinematics, is the result. This energy regime is called Klein-Nishina regime [85] and the process is known as incoherent or Compton scattering, which is illustrated in Fig. 2.10. Compton scattering dominates at intermediate γ energies.

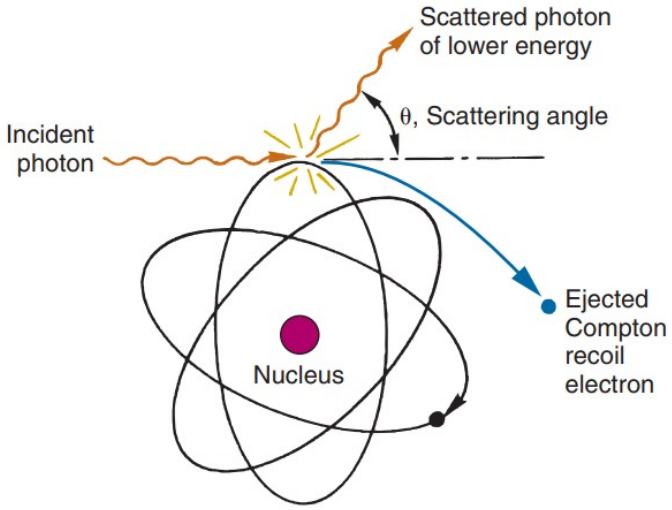


Figure 2.10: Schematic representation of the Compton Scattering. An incoming photon strikes a quasi-free electron and gets deflected by an angle θ. [73]

For the kinematics of the reaction the electron is assumed to be at rest and also to be quasi-free, which is justified as the energy of the incident γ greatly exceeds the binding energy of the electron [86]. The energy of the scattered γ ($E_\gamma^{'}$) is related to its scattering angle θ by the formula [74, 77, 80]:

$$E_\gamma^{'} = \frac{E_\gamma}{1 + \zeta \cdot (1 - \cos(\theta))}, \tag{2.45}$$

where $\zeta = E_\gamma / m_e \cdot c^2$ is the reduced γ energy. The energy transfer to the Compton electron has a minimum for $\theta = 0°$ (grazing collision) and a maximum for $\theta = 180°$ (γ backscattering). The transferred kinetic energy of the electron simply equals the energy loss of the γ due to laws of momentum conservation and assumptions made above [84]:

$$T_{e^-} = E_\gamma - E'_\gamma = \frac{E_\gamma \cdot \zeta \cdot (1 - \cos(\theta))}{1 + \zeta \cdot (1 - \cos(\theta))}. \tag{2.46}$$

The differential cross section for Compton scattering depends on the polarization of the γs [80, 87–89]. However, as common sources contain nuclei that are randomly oriented, the Compton scattering of unpolarized γs is the standard case [89]. The differential cross section per electron and unit solid angle ($cm^2 \cdot sr^{-1} \cdot electron^{-1}$) is expressed by the Klein-Nishina formalism [71, 74, 87]:

$$\left(\frac{d\sigma_C}{d\Omega}\right)_{E_\gamma, unpol} = \frac{r_e^2}{2} \cdot \left(\frac{E'_\gamma}{E_\gamma}\right)^2 \cdot \left(\left(\frac{E_\gamma}{E'_\gamma}\right) + \left(\frac{E'_\gamma}{E_\gamma}\right) - \sin^2(\theta)\right), \tag{2.47}$$

where r_e is the classical electron radius and $d\Omega = 2 \cdot \pi \cdot \sin(\theta) \cdot d\theta$ equals the solid angle into which the γ is scattered [89]. With increasing energy the γ tends to be forward-scattered and transfers less energy to the electron.

The total effective Compton cross section is obtained by taking all atomic electrons into account and often termed as incoherent scattering cross section σ_{incoh}. Integrating Eq. (2.47) over the whole solid angle yields [71]:

$$\begin{aligned}\sigma_{incoh} &= Z \cdot \int_\Omega \left(\frac{d\sigma_C}{d\Omega}\right)_{E_\gamma, unpol} \cdot d\Omega \\ &= Z \cdot \frac{\pi \cdot r_e^2}{\zeta} \cdot \left(\left(1 - \frac{2}{\zeta} - \frac{2}{\zeta^2}\right) \cdot \ln(1 + 2 \cdot \zeta) + \frac{1}{2} + \frac{4}{\zeta} - \frac{1}{2 \cdot (1 + 2 \cdot \zeta)^2}\right).\end{aligned} \tag{2.48}$$

Although the expression for the cross section strongly depends on the polarization and relativity in a complex manner, the following expression provides general validity and emphasizes the simple Z dependence of Compton scattering:

$$\sigma_C = constant \times Z. \tag{2.49}$$

Generally, Compton scattering depends on the number of electrons available as targets for scattering reactions [76].

2.2.3 Pair production

Pair production, denoted as (γ,e^-e^+) reaction, is the annihilation of a γ in the Coulomb field of a charged particle into an electron-positron pair (e^-e^+). As γs are massless, this process represents a conversion of pure radiant energy into matter. Pair production is the dominant interaction mechanism for high-energy γs and the process is illustrated in Fig. 2.11.

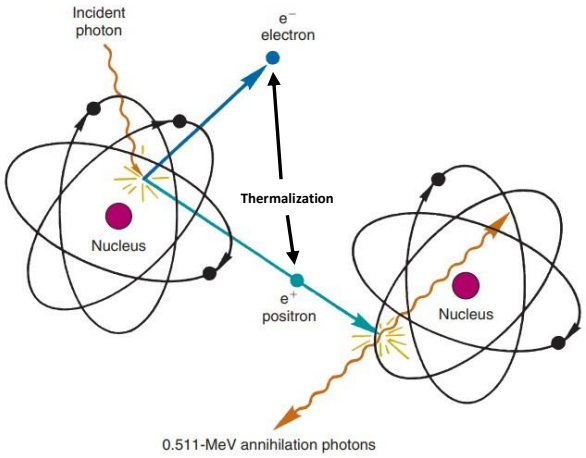


Figure 2.11: Schematic representation of pair production in the vicinity of the electric field of a nucleus. Picture taken from [73] and modified.

Applying conservation of energy and linear momentum, the minimum γ energy $E_{\gamma,min}$ required to overcome the associated reaction threshold is given by [77, 80]:

$$E_{\gamma,min} \geq 2 \cdot m_e \cdot c^2 \cdot \left(1 + \frac{m_e}{M_{nucleus}}\right) \cong 2 \cdot m_e \cdot c^2, \tag{2.50}$$

where $M_{nucleus}$ is the mass of the involved nucleus. The approximation of the reaction threshold as twice of the electron rest-mass-energy equivalent (1.022 MeV) is actually reasonable for all nuclei, since the ratio of proton to electron mass is $m_p/m_e \approx 1836$.

The recoiling nucleus is required to satisfy momentum conservation. Once the positron has deposited all its energy and comes to rest, it combines with a surrounding electron to form a positronium. This positronium is unstable and it is a hydrogen atom with a positron instead of a proton. After roughly 1.25×10^{-10} s it decays into two 511-keV γs (annihilation), but it might also decay into three γs forming a continuum [90].

No simple expression for the cross section of pair production exists as it depends on complex effects such as screening of the nuclear charge. A general expression, however, could be given as [77, 79]:

$$\sigma_{pair} = constant \times Z^2. \tag{2.51}$$

Pair production can also take place in the electric field of a bound electron, which is then termed triplet production to account for the recoiling electron as third particle. The threshold energy is still described by Eq. (2.50) but substituting $M_{nucleus}$ by the electron mass m_e it follows that the threshold for this reaction is $4 \cdot m_e \cdot c^2$, i.e. 2.044 MeV. As the cross section $\sigma_{pair} \propto Z^2$ but the cross section for triplet production $\sigma_{trip} \propto Z^1$ [91], the ratio of triplet to pair production is $\sigma_{trip}/\sigma_{pair} \approx 1/Z$. Therefore, triplet production can be neglected for high-Z materials.

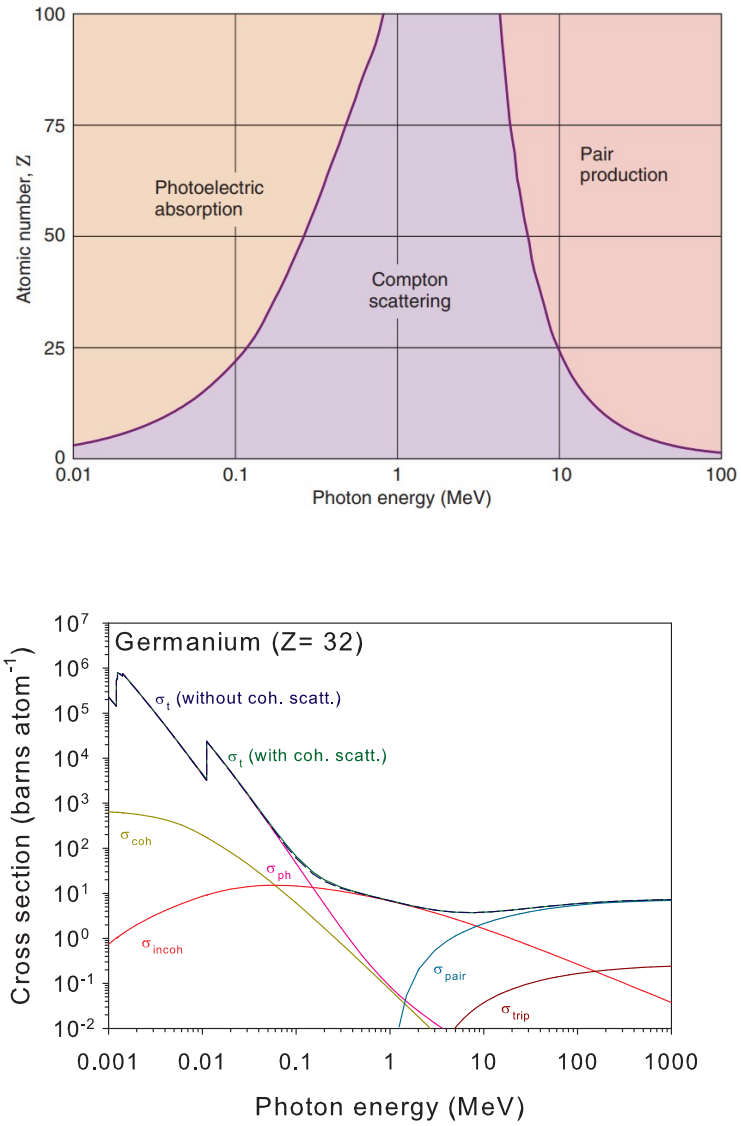


Figure 2.12: Predominating interaction type as a function of photon energy and atomic number Z (top, taken from [73]) and dependence of the cross section from various photon interactions on energy for Ge (bottom). The plotted data was taken from the photon cross section database XCOM of NIST [92].

All processes given in Eq. (2.41), except photonuclear reactions, are plotted in units of barns per atom as a function of the photon energy in Fig. 2.12 for Ge as absorber material. The term coherent scattering comprises elastic scattering with a single electron (Thomson scattering) and the whole atom (Rayleigh scattering) [77, 80] and might only play a role for low-energetic γs with energies below 50 keV [73]. Photonuclear reactions such as (γ,n), (γ,p) or (γ,f) require high threshold energies above the binding energy of the least bound nucleon. Usually a minimum of 6 to 7 MeV [80] is needed where the giant dipole resonance (GDR) can be induced.

2.2.4 Interactions in germanium detectors

The three main interactions of γs namely photoelectric effect, Compton scattering and pair production all take place in the crystal of a modern high-purity germanium (HPGe) detector and contribute to the overall recorded γ-ray spectrum (see Fig. 2.13). Their extent and relative proportions strongly depend on the geometrical size and arrangement of the detector crystal.

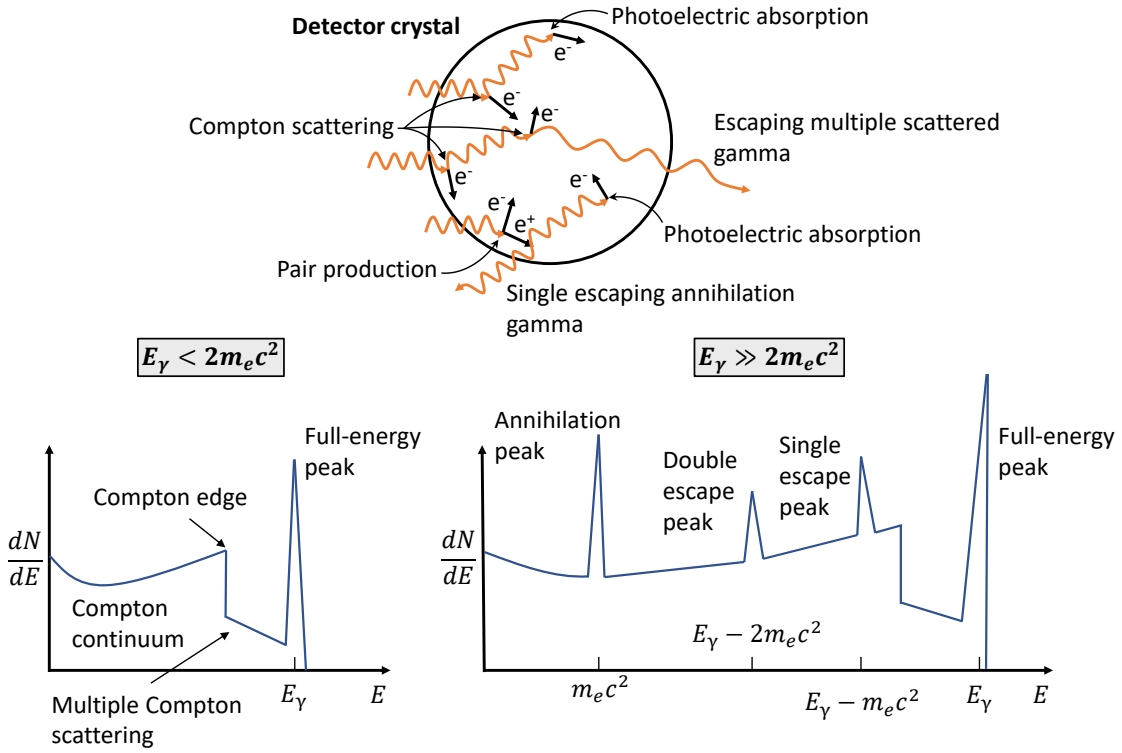


Figure 2.13: Typical response function of an intermediate size HPGe detector crystal. Inspired by [76].

The photoelectric effect is the main information carrier as it gives the complete energy of the γ (full-energy peak, FEP) and hence reflects the transition energy. The Compton effect results in the Compton continuum, which reflects the energy deposition of γs depending on the scattering angle θ. As the major component for background in a γ-ray spectrum it therefore defines the detection limit. In the case of a single backward scattering event (θ= 180°) a small peak, the Compton edge, is formed. This edge appears approximately at an energy of $E_C = E_\gamma -$ 255 keV [77] below the FEP of energy E_γ. Pair production results in single and double escape peaks, depending if one or both of the created 511-keV annihilation γs escape the crystal volume. These peaks might interfer with another FEP of interest. Additionally, if two γs reach the detector almost simultaneously, a peak at the sum of their energies becomes visibile in the spectrum (sum peak). In this work such sum peaks were not observed and in fact negligible due to the moderate counting rates and small solid angle subtended from the detector to the sample.

3. Numerical tools and methods

The various software packages used for the analysis and interpretation of the experimental data are described in this chapter.

3.1 HYPERMET-PC

The recorded γ-ray spectra were analyzed with the HYPERMET-PC software [93, 94]. The original version of this FORTRAN-based code was developed already in the early seventies of the last century at the Naval Research Laboratory in Washington D.C. Meanwhile it is provided by the Hungarian Institute of Isotopes [94] and it allows the automatic and efficient analysis of multichannel pulse-height spectra. The shape parameters for different peaks and background are found by a nonlinear fit starting with an initial trial value. The software supports a multitude of different multichannel spectrum formats, the one used in this work corresponds to that one from ORTEC (.chn files).

3.1.1 Energy calibration

By default, HYPERMET-PC uses a simple two-point linear energy calibration, that might be described by a first order polynomial:

$$E_\gamma = y_0 + y_1 \cdot x, \tag{3.1}$$

where y_0 is in units of keV, x in units of channels (ch) and the slope y_1 has units of keV ch^{-1}.

The electronics of detection systems, in particular the ADC (Analog-to-Digital Converter), are subject to nonlinearity effects [93, 95, 96]. Therefore, the software offers to read in a nonlinearity calibration file (.LIN file), which can be obtained by experimental measurements of various radioactive sources. As the nonlinearity of the current set-up of FaNGaS was not determined and hence a corresponding .LIN file is missing, initially two peaks were taken for the calibration. An energy calibration with background peaks at 140 keV from ^{75m}Ge and 7645 keV from ^{56}Fe according to Eq. (3.1) was observed to result in imprecise peak energies of prominent lines lying in between. The peak energy of the 2223-keV line of of the ^{1}H(n,γ)^{2}H reaction was found to deviate by more than 1 keV from the nominal value.

Therefore, the whole energy range (approximately 0 to 8 MeV) was divided into four different regions. These regions are given with their defining nuclides and energies taken from HYPERMET-PC in Table 3.1.

Table 3.1: Energy intervals with corresponding nuclides defining the boundaries for the linear energy calibrations according to Eq. (3.1) and the FEP energies given in HYPERMET-PC.

Interval	Nuclides	Energy range (keV)
I	^{75m}Ge, ^{208}Pb	139.680 - 2614.580
II	^{208}Pb, ^{56}Fe	2614.580 - 4218.270
III	^{56}Fe, ^{56}Fe	4218.270 - 5920.449
IV	^{56}Fe, ^{56}Fe	5920.449 - 7645.545

3.1.2 Doppler-broadened peaks

In the case of Doppler-broadened peaks the standard fit algorithm of HYPERMET-PC was not able to find a converging solution for one single Gaussian. Instead, the peak was fitted by several Gaussians. In principle, the sum of these individual peak areas gives a reasonable estimate for the total peak area. However, the internal "Peak Integration" mode was preferably used. For this mode one can define the integration limits. In a first run the peak area is determined, whereas the peak energy is resolved in a second run. Doppler-broadened peaks were observed in measurements of light elements such as C, Ca or Cl. The usefulness in using the peak integration method is depicted in Fig. 3.1 exemplary for the 3905-keV line from the ^{40}Ca(n,n'γ)^{40}Ca reaction, which has a lifetime of only 35 fs [97]. Alternatively to the aforementioned method, the variable peak width feature provided in HYPERMET-PC was used. In this, the fit algorithm increases the width of one single fitted Gaussian as long as it matches the distribution of measured counts with acceptable statistics.

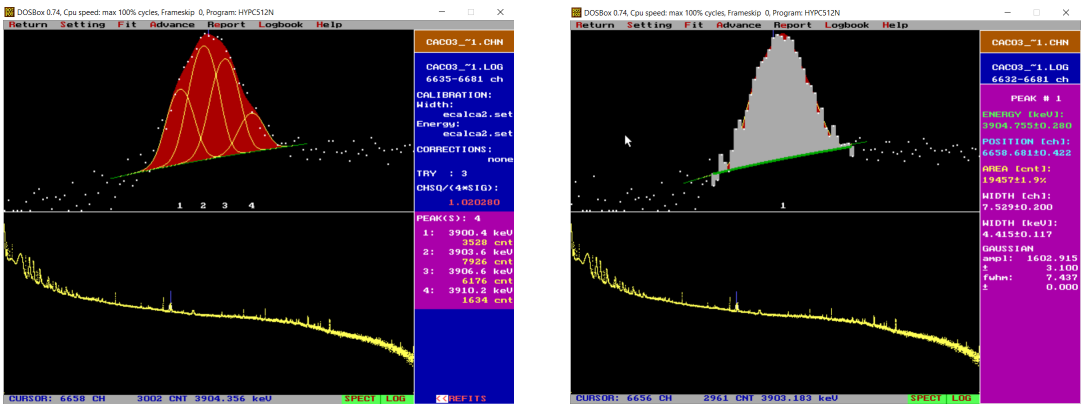


Figure 3.1: Illustration of the peak integration method used in HYPERMET-PC to evaluate Doppler-broadened peaks. The left picture shows the standard fit result and the right picture shows the result using the internal peak integration method.

3.2 Simulation software

The simulation software applied in the frame of this work is described in the following.

3.2.1 MCNP code

Processes that are governed by the random nature of radioactive decay and nuclear reactions cannot be solved reasonably with an analytical approach. Instead, they are routinely analyzed by the Monte Carlo (MC) method. In particular with respect to γ-ray spectrometry, a wide variety of MC codes is applied to quantify parameters such as the efficiency of a detector or the neutron and γ attenuation inside a sample [15, 98–105]. MC codes rely on a stochastic approach using random numbers: generally, a number N (e.g. particle histories) of independent calculations are accumulated and the desired result is obtained by taking the average.

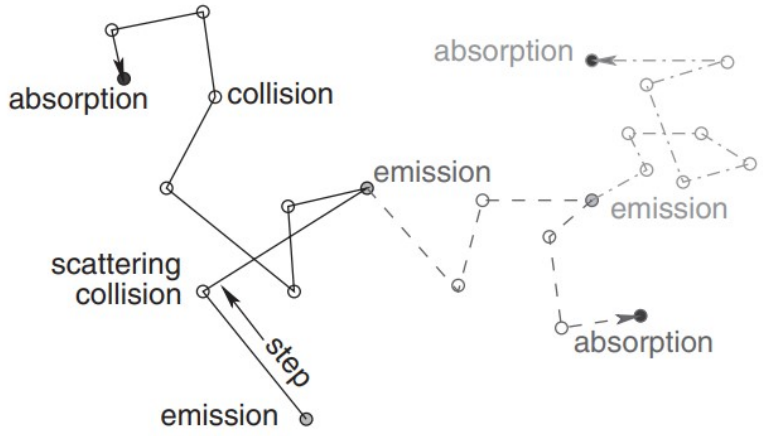


Figure 3.2: The Monte Carlo principle of random walks in radiation transport problems. [106]

The purpose of MC simulations is the derivation of average bulk parameters, either of the simulated particles itself (e.g. kinetic energy or number of particles crossing a certain surface) or of the traversed materials (e.g. deposited energy in a material) [106]. The basic principle of the MC method is illustrated in Fig. 3.2.

The program simulates the transport of each primary particle (also called "history") individually and independently from each other as a random walk in a step-by-step manner. Each particle can undergo different interactions, which might be termed as "events". The program decides these types of events based on nuclear data and probability density functions (PDFs) that are both manifested in the software. After each interaction certain parameters, such as kinetic energy for example, are redetermined by the code and the transport continues until the particle leaves the defined geometry, is absorbed or a cutoff value (e.g. in energy) is reached. In the

case of neutrons, the event type is basically determined by the ratio of the macroscopic cross section of the considered reaction to the value of the total macroscopic cross section, i.e. Σ_t.

Regarding the statistical uncertainty of MC simulations, the standard error σ depends inversely on the square root of the number of particle histories N:

$$\sigma \propto \frac{1}{\sqrt{N}}. \tag{3.2}$$

From Eq. (3.2) it follows that the statistical uncertainties of a numerical MC simulation can be reduced by a factor of 10 when the number of primary source particles is increased by a factor of 100.

In this work, the Monte Carlo N-Particle (MCNP) code (version 6.1) [107, 108] was used for numerical simulations. It is a general-purpose transport code qualified to simulate a wide variety of nuclear processes. It is capable to transport neutrons, photons, eletrons, ions and many other elementary particles up to an energy of 1 TeV/nucleon. It is developed and maintained by the Los Alamos National Laboratory (LANL) and optimized for reactor-physical calculations involving neutron transport. Table 3.2 gives the units used by MCNP for fundamental quantities.

Table 3.2: Basic quantities and units used in the MCNP code.

Quantity	Unit
Length	cm
Energy	MeV
Time	Shakes (10^{-8} s)
Temperature	MeV (kT)
Atomic density	Atoms b^{-1} cm^{-1}
Mass density	g cm^{-3}
Cross sections	b (10^{-24} cm^2)
Heating numbers	MeV $collision^{-1}$

Detailed and comprehensive information on the data cards and transport options is provided in the MCNP6 user manual [108]. In addition, Appx. K contains complete input files for selected simulations, also including descriptive comments. Therefore, in the following sections only some of the most relevant features used in the simulations for this work are considered briefly. For this purpose explanations are done based on short illustrative code-snippets taken from Appx. K.

Input structure

The input file (INP file) is written in text format (ASCII) and it contains information on the problem geometry, description of materials including cross-section libraries, particle type and source definition, type of desired output (termed as tallies) and

variance-reduction techniques for improved computing efficiency. The code structure can be generalized into three main blocks for any problem as:

```
----------------------------------------------------------------------
Message Block +
   blank line delimiter {optional}
One Line Problem Title Card
Cell Cards [Block 1]
   blank line delimiter
Surface cards [Block 2]
   blank line delimiter
Data Cards [Block 3]
   blank line terminator {optional}
----------------------------------------------------------------------
```

Running and geometry plotter

The run of an input file is initiated by the execution line, which has the general form:

```
----------------------------------------------------------------------
MCNP6 KEYWORD=value ... KEYWORD=value execution_option(s)
other_options TASKS=value
----------------------------------------------------------------------
```

where the KEYWORD represents default file names of MCNP6 to which a specific value can be assigned. The keyword INP, or just "i", indicates the user-supplied input file name, whereas OUT or just "o" indicates the corresponding output file name. Further keywords can be used to control for example the name of the cross-section directory file, a file from which plot commands will be read or a file that contains the desired tally results. The "execution_option(s)" provides six distinct execution models and "other_options" allows to add more flexibility by the user to the simulation. The TASKS option was used to enable CPU threading and thereby increasing the computing efficiency significantly. Simple simulations were usually run on a local laptop, whereas more advanced simulations requiring a high number of particle histories were transferred to the standard cluster of JCNS-2. Up to 12 nodes were available to submit jobs using the sinteractive command.

Typing "IP" right after "MCNP6" in the execution command line shown above calls the geometry plotter of MCNP6. Assuming that a X server is available for Microsoft Windows (e.g. with the software Xming) and the display variable is set properly, this option was frequently used to verify the written geometry and to ensure error-free input files. The geometry plotter is useful to show cells or surfaces and enables a quick debugging of incorrect geometries (see Fig. 3.3).

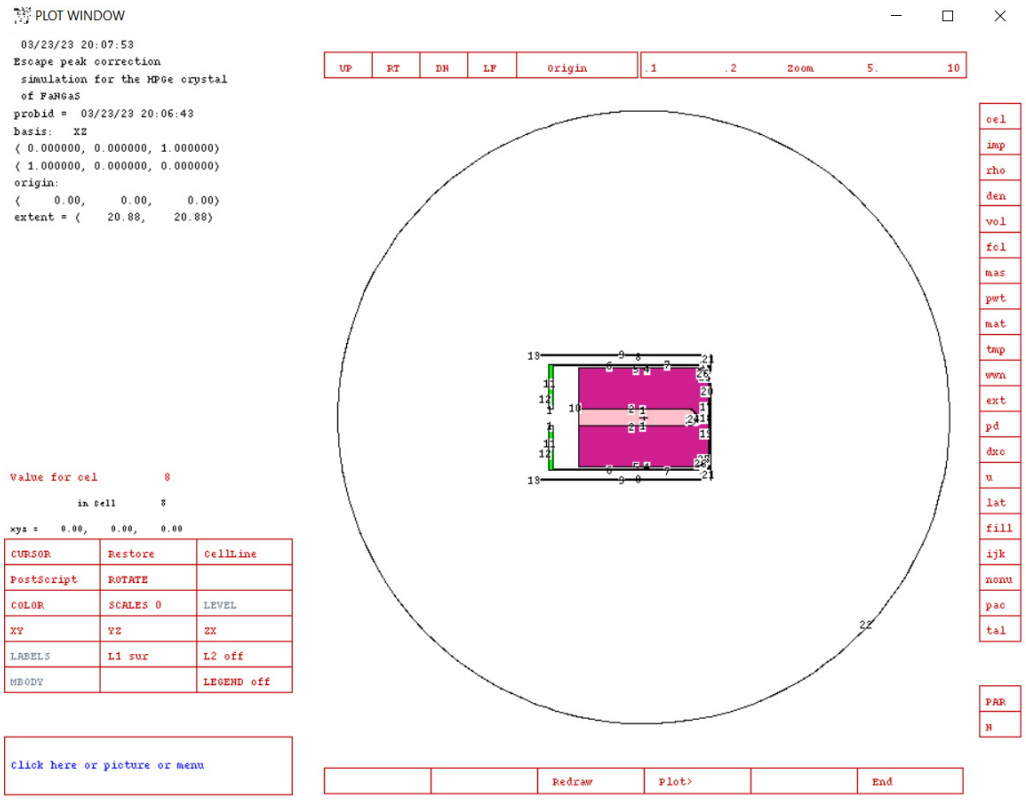


Figure 3.3: GUI of the MCNP6 geometry plotter. The HPGe detector model of FaNGaS is shown.

Cross-section nuclear data libraries

In order to depict physical neutron and γ interaction processes relevant to form a γ-ray spectrum properly, nuclear data libraries serve as an input for any numerical software packages. Generally, nuclear data libraries might be categorized into two broad sections [109]: (i) experimental nuclear data libraries and (ii) evaluated nuclear data libraries. The (i) experimental nuclear data library EXFOR (Experimental Nuclear Reaction Data) [39] is the most extensive compilation of experimental nuclear data, especially with regard to neutron reaction data. It is released and maintained by the Nuclear Data Section (NDS) of the International Atomic Energy Agency (IAEA). Since the discovery of the neutron in 1932 by James Chadwick data from over 20,000 experiments has been implemented. The (ii) evaluated nuclear data libraries combine available experimental nuclear data with accepted physics-based models to fill the gap left empty by experimental libraries. Experienced experts from the USA, Europe, Japan, Russia and China produce recommended libraries such as BROND (Russian evaluated neutron library) [110], CENDL (Chinese Evaluated Nuclear Data Library) [111], ENDF/B (Evaluated Nuclear Data Library) [112], JEFF (Joint Evaluated Fission and Fusion) [113] or JENDL (Japanese Evaluated Nuclear Data Library) [114], to name a few of them. Nuclear data from all of these libraries are compiled into ENDF (Evaluated Nuclear Data File) files, whose information is encoded by means of MT numbers associated to the corresponding nuclear reactions.

Each library obtains regular updates and in the frame of this work mostly current data from the ENDF/B library was used.

By default, version 6.1 of MCNP makes use of ENDF/B-VII.1 [115–117] cross-section libraries for neutrons and the MCPLIB84 library for γs [118]. The latest version of the neutron libraries is ENDF/B-VIII.0 [112]. Although the differences between these libraries were found to be minor, for some simulations the newer libraries were used. This was possible by downloading the Lib80x library [116] of version 6.2 of MCNP and placing it into the "xdata" folder. Cross sections from this library were used for example for the derivation of neutron moderation factors presented in Chapter 6. In the following, an excerpt from the file used for the terbium(III) chloride hexahydrate ($TbCl_3 \cdot 6H_2O$) simulation is shown:

```
-----------------------------------------------------------------------
M1 1001.00c 11.9988 1002.00c 0.0012 8016.00c 5.9856 8017.00c 0.0024 &
8018.00c 0.0120 17035.00c 2.2731 17037.00c 0.7269 65159.00c 1.0000
-----------------------------------------------------------------------
```

In the given example above (see Appx. K.2 for the complete input file), materials on the M1 card are characterized by the nuclide identification number "ZAID" with the general form ZZZAAA.nnX. The part "ZZZ" is the atomic number, "AAA" the mass number (000 for naturally-occuring elements), "nn" the cross-section identifier and X= c indicates the use of continuous-energy neutron tables. The value of nn= 00 indicates data evaluated at 293.6 K, i.e. room temperature.

Physics cards

The most fundamental physics treatment is set by the obligatory MODE card. This card acts to choose the particle types that are transported. The specification as:

```
-----------------------------------------------------------------------
MODE N,P
-----------------------------------------------------------------------
```

allows the transport of both neutrons and photons. However, if only the transport of one particle type influences the tally output, then the other particle was not transported in order to save computing time.

When no cross-section libraries are available for certain isotopes or when reactions exceed the maximum energy in a given library, then MCNP6 usually interrupts the run with a fatal error. To avoid this, model physics can be activated by:

```
-----------------------------------------------------------------------
MPHYS ON
-----------------------------------------------------------------------
```

Nevertheless, model physics were only used if necessary or when the computing time was reasonable, as CPU threading fails to work when they are activated.

By default, MCNP assumes energy cutoff values of 0 MeV for neutrons and 1 keV for photons. Transport of low-energy neutrons takes longer computing times

than needed for fast neutrons. Therefore, whenever thermal or epithermal neutron transport was not necessary a corresponding cutoff value was set. An example is shown for a fast-neutron filter simulation from Chapter 7 (see also Appx. K.4):

```
-----------------------------------------------------------------------
PHYS:N 20 $20 MeV energy upper transport limit
CUT:N 1E09 0.02 $10 s and 20 keV lower transport limit
-----------------------------------------------------------------------
```

In the given example, neutrons above 20 MeV as well as neutrons below 20 keV were "killed". In addition, a time cutoff was set in units of shakes (i.e. 10 s).

Geometry transformations

MCNP offers geometry tranformations via the TR card. The transformations can be applied to a defined surface or to the mesh grid of a FMESH tally. Since some of the samples were tilted by an angle of 45° with respect to the incident neutron beam axis, a TR card was used sometimes. As an example, in Chapter 6 the neutron moderation in the RE chloride samples that contain partially crystal water was investigated. For this purpose a TR card was applied to the corresponding macrobodies and FMESH tallies. A rotation was achieved by defining transformations as (see also Appx. K.2):

```
-----------------------------------------------------------------------
*TR1 0 0 0 45 90 90 90 0 90 45 90 90 1 $45° rotation around Y-axis
*TR2 0 0 -8.5 45 90 90 90 0 90 45 90 90 1 $45° rotation around Y-axis
-----------------------------------------------------------------------
```

The asterisk in front of TR enables to give the angles in the rotation matrix in degrees instead of cosines.

Source definition

The source definition is done by the SDEF card with various input parameters available in MCNP. In Chapter 7, the attenuation of the scatter-neutron spectrum by different filter materials was investigated. The code-snippet (Appx. K.6) showing the specifications of the SDEF card is shown and explained in the following:

```
-------------------------------------------------------------------------------
c Cone-focussed point source, longitudinal half-opening angle of ~ 4.80°
SDEF ERG=d1 POS=0 0 +71.255 PAR=1 X=0 Y=0 Z=+71.255 VEC=0 0 -1 DIR=d2
c FaNGaS neutron-energy bin structure with rel. probabilities of scatter spec.
SI1 H 6.60E-02 8.80E-02 1.10E-01 1.35E-01 1.60E-01 1.90E-01 2.20E-01 &
2.55e-01 2.90E-01 3.20E-01 3.60E-01 4.00E-01 4.50E-01 5.00E-01 5.50E-01    &
6.00e-01 6.60E-01 7.20E-01 7.80E-01 8.40E-01 9.20E-01 1.00E+00 1.20E+00    &
1.40e+00 1.60E+00 1.80E+00 2.00E+00 2.30E+00 2.60E+00 2.90E+00 3.30E+00    &
3.70e+00 4.10E+00 4.50E+00 5.00E+00 5.50E+00 6.00E+00 6.70E+00 7.40E+00    &
8.20E+00 9.00E+00 1.00E+01 1.10E+01
SP1 0.00 9.61E-03 9.19E-03 9.98E-03 1.09E-02 1.92E-02 1.37E-02 1.24E-02    &
1.16E-02 1.70E-02 1.55E-02 2.22E-02 2.53E-02 3.36E-02 2.62E-02 2.16E-02    &
2.98E-02 3.55E-02 3.97E-02 3.32E-02 2.77E-02 3.53E-02 7.88E-02 7.39E-02    &
```

```
4.99E-02 5.40E-02 3.85E-02 4.88E-02 5.60E-02 4.16E-02 3.77E-02 1.92E-02    &
1.42E-02 7.49E-03 7.52E-03 4.80E-03 2.52E-03 2.20E-03 1.27E-03 8.84E-04    &
7.20E-04 3.59E-04 5.31E-04
SI2 0.9964994810 1.0 $Cone-shaped beam into collimator
SP2 0 1
-------------------------------------------------------------------------------
```

The PAR parameter defines the source particle type, with PAR= 1 for neutrons. ERG specifies the energy, with d1 indicating a distribution tagged by 1. Each distribution requires a source information (SI) and source probability (SP) card. The H after SI1 indicates that histogram energy boundaries follow. The POS parameter sets the starting point in X, Y and Z of the particle, which is additionally done with X, Y and Z (redundant). VEC is a reference vector used for DIR in vector notation, which is another distribution (d2) and limits the particle emission to a cone restricted by a half-opening angle of 4.80° along Z-axis, as indicated above. Z= -1 indicates that the beam is emitted along negative Z-direction.

Tallies

The desired output is termed as a tally in MCNP and it is the equivalent to an experimentally measured quantity. The most frequent used tallies in the frame of this work comprise the F1, F4 and F8 tallies.

F1 tally

The F1 tally is a simple current tally, i.e. it counts the weight of the particles crossing a certain surface. If the particles' weights equal one, then the F1 tally output equals the absolute number of particles. In Chapter 7 simulations regarding a fast-neutron filter are presented. In one of these simulations, the current of fast neutrons arriving at the detector front surface was tallied (see Appx. K.4). This was defined as:

```
-------------------------------------------------------------------------------
F1:N 7 $Detector front surface
E1 1.90E-02 2.55E-02 3.20E-02 4.00E-02 &
5.25E-02 6.60E-02 8.80E-02 1.10E-01 1.35E-01 1.60E-01 1.90E-01 2.20E-01    &
2.55E-01 2.90E-01 3.20E-01 3.60E-01 4.00E-01 4.50E-01 5.00E-01 5.50E-01    &
6.00E-01 6.60E-01 7.20E-01 7.80E-01 8.40E-01 9.20E-01 1.00E+00 1.20E+00    &
1.40E+00 1.60E+00 1.80E+00 2.00E+00 2.30E+00 2.60E+00 2.90E+00 3.30E+00    &
3.70E+00 4.10E+00 4.50E+00 5.00E+00 5.50E+00 6.00E+00 6.70E+00 7.40E+00    &
8.20E+00 9.00E+00 1.00E+01 1.10E+01 1.20E+01 1.30E+01 1.40E+01 1.50E+01    &
1.60E+01 1.70E+01 1.80E+01 1.90E+01 2.00E+01
-------------------------------------------------------------------------------
```

In the example above, N indicates that neutrons are going to be scored at the surface specified by number 7. The F1 card is followed by an E1 card that provides the information on the desired energy binning of the result. Since no special tally treatment was applied, the F1 tally scores all neutrons, independent of the velocity

vector direction. A F2 tally works basically the same way, with the only difference that MCNP divides the tally output in each bin by the area provided by the user.

F4 tally

The F4 tally is a track-length tally and the output is given in units of primary^{-1} cm^{-2}. Supposing a particle of weight W and energy E makes a track length T in a defined cell of volume V, then this track length makes a contribution of $W \cdot T/V$ to the total fluence in the cell. In the frame of the neutron moderation simulations presented in Chapter 6 to investigate the effect of bound crystal water in some of the measured samples, the volume flux of neutrons in tilted samples was derived with a F4 tally. The description of this flux is given as (see Appx. K.2):

```
-------------------------------------------------------------------------------
F14:N 3
E14 1.00E-10 1.00E-09 1.00E-08 2.30E-08 5.00E-08 7.60E-08 1.15E-07 1.70E-07 &
2.55E-07 3.80E-07 5.50E-07 8.40E-07 1.28E-06 1.90E-06 2.80E-06 4.25E-06    &
6.30E-06 9.20E-06 1.35E-05 2.10E-05 3.00E-05 4.50E-05 6.90E-05 1.00E-04    &
1.35E-04 1.70E-04 2.20E-04 2.80E-04 3.60E-04 4.50E-04 5.75E-04 7.60E-04    &
9.60E-04 1.28E-03 1.60E-03 2.00E-03 2.70E-03 3.40E-03 4.50E-03 5.50E-03    &
7.20E-03 9.20E-03 1.20E-02 1.50E-02 1.90E-02 2.55E-02 3.20E-02 4.00E-02    &
5.25E-02 6.60E-02 8.80E-02 1.10E-01 1.35E-01 1.60E-01 1.90E-01 2.20E-01    &
2.55E-01 2.90E-01 3.20E-01 3.60E-01 4.00E-01 4.50E-01 5.00E-01 5.50E-01    &
6.00E-01 6.60E-01 7.20E-01 7.80E-01 8.40E-01 9.20E-01 1.00E+00 1.20E+00    &
1.40E+00 1.60E+00 1.80E+00 2.00E+00 2.30E+00 2.60E+00 2.90E+00 3.30E+00    &
3.70E+00 4.10E+00 4.50E+00 5.00E+00 5.50E+00 6.00E+00 6.70E+00 7.40E+00    &
8.20E+00 9.00E+00 1.00E+01 1.10E+01 1.20E+01 1.30E+01 1.40E+01 1.50E+01    &
1.60E+01 1.70E+01 1.80E+01 1.90E+01 2.00E+01
FT14 TAG 1
FU14 -1
-------------------------------------------------------------------------------
```

The input is identical to the case of a F1 or F2 tally, however, in this case an advanced tally treatment was also applied by means of a FT and FU card to filter for primary source neutrons only. The FT tally with the keyword TAG allows to separate a tally into components based on how and where the scoring particles were produced. The TAG keyword has one single parameter, which can have the values 1, 2 and 3. For the value of a= 1 "all collided particles will lose their tag and bremsstrahlung and annihilation photons will be included in the bin of collided particles" [119]. The FU card with the parameter -1 sets the source particle tag for all cells. As a result, the F14 tally above prints two outputs, i.e. total values including contributions of secondaries and primaries only.

F8 tally

For the numerical determination of the escape peak correction curves γ-rays were counted in MCNP6 with the F8 tally. This pulse-height tally works equivalent to a

standard multichannel analyzer. Only photons and electrons can be tallied with a F8 card, it cannot score neutrons due to their non-analog nature of transport. For the escape peak correction the tally was defined as (see also Appx. K.1):

```
----------------------------------------------------------------------
F8:P 1
E8 1E-03 8000i 8.0 $ ~ 1 keV intervals
----------------------------------------------------------------------
```

The P indicates that photons are scored and 1 implies that this scoring is done in cell number 1. The energy bins on the E8 card (1 keV to 8 MeV) are scored with 8000 bins of approximately 1 keV width.

3.2.2 NJOY processing modules

Nuclear data such as cross sections provided in ENDF files of different libraries is usually represented in a form of a physics viewpoint that is incapable to serve as a proper input for practical calculations. The NJOY nuclear data processing system [120, 121] is a numerical tool that enables the translation of cryptic information contained in ENDF files into a form needed for applications and being easily interpreted. The Fortran-based code was originally developed by Bob McFarlane in the 1970s at LANL, by which it is still being developed and maintained. For neutrons, photons and charged particles it can produce pointwise and multigroup nuclear cross sections and other quantities contained in evaluated nuclear data in the ENDF format. NJOY is the standard tool to produce libraries for MC-based particle transport and reactor analysis codes. In this work the version from 2016 (NJOY2016) [121] was used, which is distributed as open-source software.

NJOY was applied to obtain average (grouped) cross sections for every energy bin of the experimental neutron-energy spectrum. These were used to estimate neutron spectrum-averaged (effective) reaction cross sections according to Eq. (2.13).

Module sequence

Each processing task is handled separately by the NJOY code and denoted as a module. These modules are basically computer programs on their own and they are linked to each other by input and output files, respectively. In total, 24 different main modules exist, from which four were used in this work. Their meaning is exemplary explained based on the case of ^{12}C, for which the code is given as:

```
-------------------------------------------------------------------------
-- Copy ASCII input to binary.
MODER
 20 -21 /  'n/n_0625_6-C-12.zip'
--
-- Resonance reconstruction, to 0.1%.
RECONR
 -21 -22 /
```

```
 'pendf tape for carbon-12 from endf/b-viii'/
 0625 0 0 /
 0.001 /
 0 /
--
-- Doppler broaden to 300 K.
BROADR
 -21 -22 -23 /
 0625 1 0 0 0 /
 0.001 /
 300. /
 0 /
--
-- Group average, 300 K with group structure.
GROUPR
 -21 -23 0 91 /
 0625 1 0 2 1 1 1 1 /
 '6-C-12' /
 300. /
 1.0E10 /
 100 / # of groups, energy boundaries follow:
 1.000000E-4 1.000000E-3 1.000000E-2 2.300000E-2 5.000000E-2
 7.600000E-2 1.150000E-1 1.700000E-1 2.550000E-1 3.800000E-1
 5.500000E-1 8.400000E-1 1.275000E+0 1.900000E+0 2.800000E+0
 4.250000E+0 6.300000E+0 9.200000E+0 1.350000E+1 2.100000E+1
 3.000000E+1 4.500000E+1 6.900000E+1 1.000000E+2 1.350000E+2
 1.700000E+2 2.200000E+2 2.800000E+2 3.600000E+2 4.500000E+2
 5.750000E+2 7.600000E+2 9.600000E+2 1.275000E+3 1.600000E+3
 2.000000E+3 2.700000E+3 3.400000E+3 4.500000E+3 5.500000E+3
 7.200000E+3 9.200000E+3 1.200000E+4 1.500000E+4 1.900000E+4
 2.550000E+4 3.200000E+4 4.000000E+4 5.250000E+4 6.600000E+4
 8.800000E+4 1.100000E+5 1.350000E+5 1.600000E+5 1.900000E+5
 2.200000E+5 2.550000E+5 2.900000E+5 3.200000E+5 3.600000E+5
 4.000000E+5 4.500000E+5 5.000000E+5 5.500000E+5 6.000000E+5
 6.600000E+5 7.200000E+5 7.800000E+5 8.400000E+5 9.200000E+5
 1.000000E+6 1.200000E+6 1.400000E+6 1.600000E+6 1.800000E+6
 2.000000E+6 2.300000E+6 2.600000E+6 2.900000E+6 3.300000E+6
 3.700000E+6 4.100000E+6 4.500000E+6 5.000000E+6 5.500000E+6
 6.000000E+6 6.700000E+6 7.400000E+6 8.200000E+6 9.000000E+6
 1.000000E+7 1.100000E+7 1.200000E+7 1.300000E+7 1.400000E+7
 1.500000E+7 1.600000E+7 1.700000E+7 1.800000E+7 1.900000E+7
 2.000000E+7 /
 3 /
 0 /
 0 /
 stop
---------------------------------------------------------------------------
```

As the starting module, MODER converts plain text files (ASCII, 20 in the code snippet above) into binary files (-21), which increases the computing efficiency. The

RECONR module ensures that the cross sections are obtained with a certain tolerance by linear interpolation. Therefore, it reads the ENDF file (-21) and produces the union grid, which is a common energy grid for all reactions. Resonance cross sections are reconstructed with a tolerance of 0.1%. The produced pointwise cross sections are written into a PENDF (point-ENDF) file, i.e. file number -22. The BROADR module, based on the SIGMA1 code [122], Doppler-broadens the data by means of the accurate point-kernel method. This was done for room temperature (300 K). As the last module, GROUPR processes the pointwise cross sections produced by all previous modules into the multigroup form determined by the binning structure of the energy boundaries that is put in.

Grouped cross sections

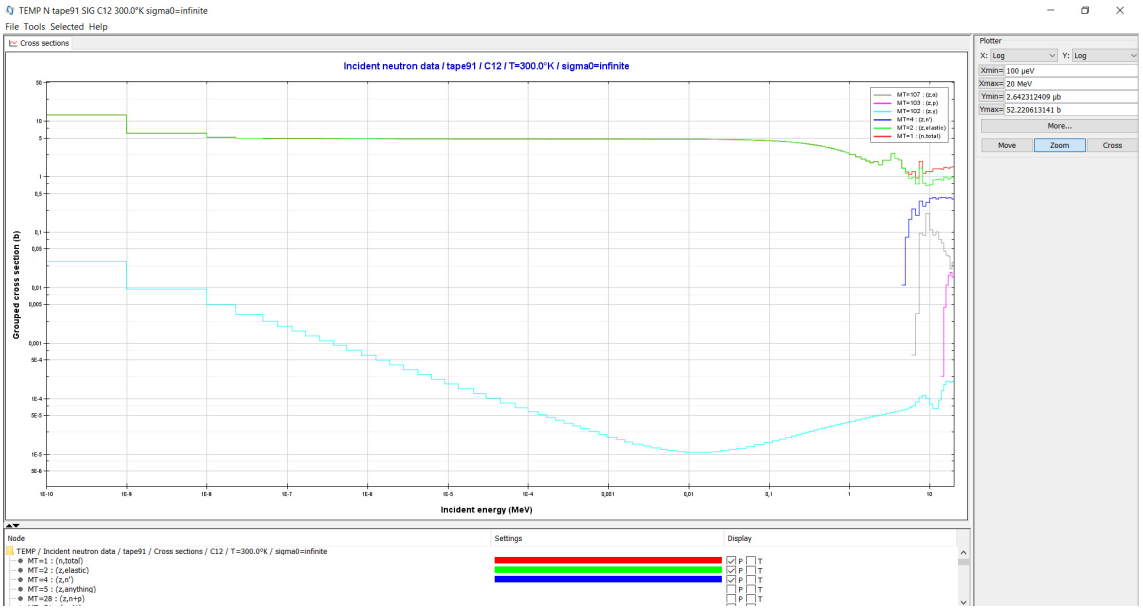


Figure 3.4: GUI in JANIS 4.0 [123] for ^{12}C.

The GROUPR module produces a fille called "tape91" in the code given above (could be also every other number between 20 and 99 not used in the previous modules). This file contains all the information on the grouped cross sections. Version 4.0 of the software JANIS (Java-based Nuclear Information Software) [123] is a display program that enables to access nuclear data processed with NJOY. It is developed by the OECD Nuclear Energy Agency and since it is written in the JAVA language it runs on almost all operating systems. It allows to access numerical values and graphical representations without prior knowledge of the storage format.

The graphical user interface (GUI) of the software is depicted in Fig. 3.4 for the case of ^{12}C. Numerical data for the reactions of interest (identified by their corresponding ENDF MT numbers) were exported into a MS Excel sheet for post-processing. Grouped cross sections of relevant reactions are plotted in Appx. D for every element covered in this work.

4. Methods

This chapter is devoted to the determination of γ-ray production cross sections. Necessary corrections concerning γ and neutron attenuation as well as various interferences are described. The approach to compare the obtained results with available literature data is presented also. Futhermore, the method to derive an estimate of the elemental detection limit is given.

4.1 Gamma-ray production cross sections

The count rate $\dot{C}_{E\gamma}$ in Eq. (1.1) can be simplified in practice, assuming a homogeneous and regularly-shaped sample. Regardless the reaction channel and the energy of the considered neutrons, the net peak area $P_{E\gamma}$ of a given γ-ray is generally described as:

$$P_{E\gamma} = \frac{m}{M} \cdot N_A \cdot h \cdot \epsilon_{E\gamma} \cdot \langle \sigma_{E\gamma} \rangle \cdot \langle \Phi \rangle \cdot g(t_b, t_c, t_{1/2}) \cdot f_{E\gamma} \cdot f_n \cdot f_{mod}, \qquad (4.1)$$

where m (g) is the mass of the considered element, M is the molar mass (g mol^{-1}), N_A the Avogadro constant (6.022×10^{23} mol^{-1}), h the isotopic abundance, $\epsilon_{E\gamma}$ the full-energy-peak (FEP) efficiency, $\langle \sigma_{E\gamma} \rangle$ the neutron spectrum-averaged (effective) isotopic partial γ-ray production cross section, $\langle \Phi \rangle$ the integral neutron flux in the considered energy range (cm^{-2} s^{-1}), g the effective counting time (s), $f_{E\gamma}$ the γ-ray self-absorption factor, f_n the neutron self-shielding factor and f_{mod} the moderation factor required in the case of samples that contain water. If more than one isotope is found to feed a certain γ-line (multi-isotope lines) the sum of the abundances of all involved isotopes i is used in Eq. (4.1), i.e. $h = \sum_i h_i$.

The factor $g(t_b, t_c, t_{1/2})$ is different for prompt and delayed γ-rays. For a prompt γ-ray it equals the counting live time t_c, i.e. $g(t_b, t_c, t_{1/2})|_{Prompt} = t_c$. In the case of delayed γ-rays the factor $g(t_b, t_c, t_{1/2})$ in Eq. (4.1) might be described by:

$$g(t_b, t_c, t_{1/2})|_{Delayed} = t_c - \frac{t_c \cdot t_{1/2}}{t_b \cdot \ln(2)} \cdot \left(1 - \exp\left(\frac{(\ln(2) \cdot t_b)}{t_{1/2}}\right)\right), \qquad (4.2)$$

where t_b denotes the irradiation time (s) and $t_{1/2}$ the half-life (s) of the formed activation product.

γ-ray production cross sections calculated after Eq. (4.1) are denoted as iso-

topic partial as the abundance h is considered. The effective cross sections for γ-ray production $\langle\sigma_{E\gamma}\rangle$ are linked to the effective cross section $\langle\sigma\rangle$ of the considered reaction for the isotope through the intensity of the γ-ray (i.e. $I_{E\gamma}$), containing the contribution of internal conversion, as:

$$\langle\sigma_{E\gamma}\rangle = \langle\sigma\rangle \cdot I_{E\gamma} \cdot W(\theta), \tag{4.3}$$

where $W(\theta)$ is the angular-distribution correction factor. For reactions with isotropic γ-ray emission, such as radiative neutron capture (n,γ), $W(\theta)$= 1. In the case of anisotropic emissions, such as the (n,n'γ) inelastic scattering reaction, however, the value of $W(\theta)$ is unequal to one, i.e. $W(\theta) \neq 1$, and can be calculated according to Eq. 2.24.

The effective cross section of the considered reaction for the element $\langle\sigma^Z\rangle$ can be obtained by connecting the effective cross section of the isotopes $\langle\sigma_i\rangle$ as given in Eq. (4.3) with their abundance:

$$\langle\sigma^Z\rangle = \sum_i^n h_i \cdot \langle\sigma_i\rangle, \tag{4.4}$$

where n is the number of isotopes of the considered element.

Effective isotopic partial γ-ray production cross sections determined in this work are given in Appx. H.1.

4.2 Attenuation corrections

Entering a material of thickness d, the intensities I of γ and neutron beams are attenuated exponentially as a function of the thickness. According to the Beer-Lambert law [124], the attenuation of a parallel and monoenergetic beam of incident intensity I_0 can be expressed by:

$$I(d) = I_0 \cdot \exp\left(-Z(E) \cdot d\right), \tag{4.5}$$

where $Z(E)$ is the attenuation coefficient being different for γs and neutrons. Scattering reactions in the tarversed absorber medium remove particles from the initial beam intensity. The fraction of the particles surviving a certain thickness d is called uncollided beam intensity and it is expressed in terms of the transmission B [124]:

$$B = \frac{I(d)}{I_0} = \exp\left(-Z(E) \cdot d\right). \tag{4.6}$$

4.2.1 Attenuation of gammas

For γ-rays the factor $Z(E)$ from Eqs. (4.5) and (4.6) equals the total linear attenuation coefficient μ_l (cm^{-1}), which is defined as:

$$\mu_l = \frac{\sigma_t \cdot \rho}{u \cdot A}, \tag{4.7}$$

where σ_t is the total cross section for γ-ray interactions, ρ the material density, u denotes the atomic mass unit (1/12 of 1 g of ^{12}C, i.e. 1.66 $\times$ 10^{-24} g) and A is the mass number. Division of μ_l by the value of ρ yields the total mass attenutation coefficient μ_m [76]:

$$\mu_m = \frac{\mu_l}{\rho}. \tag{4.8}$$

According to Eqs. (4.5) and (4.8) the beam intensity of γs after passing through a material of thickness d can be expressed as:

$$I(d) = I_0 \cdot \exp\left(-\mu_m \cdot \rho \cdot d\right). \tag{4.9}$$

Depending on the sample thickness, density and atomic number Z the γs might suffer substantial attenuation already within the sample matrix they are produced in. Attenuation of γ-rays within the sample is known as γ-ray self absorption, which is quantified with the $f_{E\gamma}$ factor introduced in Eq. (4.1). In the case of slab-shaped samples it might be given as [1, 125]:

$$f_{E\gamma} = \frac{1 - \exp\left(-\mu_m \cdot \rho \cdot d\right)}{\mu_m \cdot \rho \cdot d}, \tag{4.10}$$

where d is the thickness of the sample along the symmetry axis of the detector.

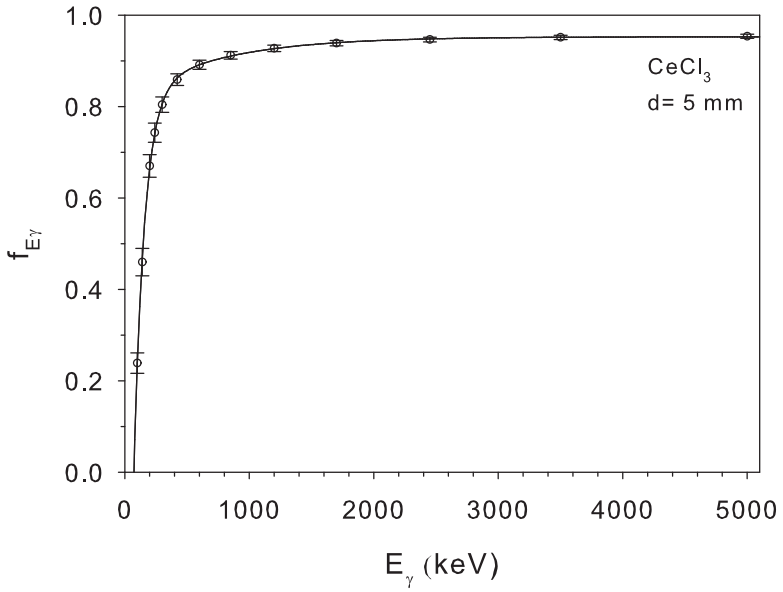


Figure 4.1: Dependence of the γ-ray self-absorption factor $f_{E\gamma}$ on the γ-ray energy E_γ for the measured $CeCl_3$ sample. The solid line represents the fit of the data with Eq. (4.12). The fit coefficients are a_0= -1.4201 $\pm$ 0.1571, a_1= 2.2959 $\pm$ 0.1499, a_2= 0.0197 $\pm$ 0.0008, a_3= 0.1008 $\pm$ 0.0098 and a_4= 0.0020 $\pm$ 0.0003.

In the case that the sample is tilted by an angle of 45° relative to the neutron beam axis, the effective thickness e must be used instead of d:

$$e = \frac{d}{cos(45°)}. \tag{4.11}$$

To correct for the γ-ray self-absorption, the values of μ_m were taken for several γ-ray energies between 100 keV and 5 MeV from the Photon Cross Sections Database XCOM from NIST [92]. The resulting data points were fitted with a double exponential function with 5 parameters of the form:

$$f_{E\gamma} = a_0 + a_1 \cdot (1 - \exp(-a_2 \cdot E_\gamma)) + a_3 \cdot (1 - \exp(a_4 \cdot E_\gamma)), \tag{4.12}$$

where a_0 to a_4 represent the fit parameters.

Figure 4.1 exemplary illustrates the dependence of $f_{E\gamma}$ on the γ-ray energy E_γ for the measured cerium(III) chloride ($CeCl_3$) sample. For γ-rays with energies below 100 keV the value of $f_{E\gamma}$ was calculated with Eq. (4.10) instead of (4.12). Correction curves for other measured samples are provided in Appx. A.

4.2.1.1 Simulation of gamma-ray self-absorption

Complementary to analytical estimates, numerical simulations are frequently applied to derive γ-ray self-absorption factors [15, 102, 103, 126]. In principle, an uniformly distributed source over the sample volume with several discrete γ-ray energies, each of equal emission probability, must be defined. At a position corresponding to the distance between the sample and the detector (67 cm at FaNGaS) a reference volume must be provided with a surface area equal to that one of the detector. This surface can be used to derive the value of $f_{E\gamma}$ at different energies by means of two F1 (current) tally results in the MCNP6 code as:

$$f_{E\gamma}(MCNP6) = \frac{F1(sample)}{F1(void)}, \tag{4.13}$$

where F1(sample) is the F1 tally result at the detector front surface with the sample material being present and F1(void) the result with void in the sample, i.e. zero density. In fact, the result of F1(void) corresponds to the geometrical point source efficiency at a given γ-ray energy. Contributions of secondary γs can be disregarded by setting a narrow (i.e. 1 keV) energy binning of the F1 tallies. For this purpose, the latter were modified by corresponding FT and FU cards in addition. By default, the MCNP6 code uses photoatomic cross sections from the MCPLIB84 library [118].

Exemplary, Fig. 4.2 shows the simulated $f_{E\gamma}$ values for the measured $CeCl_3$ sample. A thickness of 5 mm, tilted by 45° relative to the incident neutron beam, was simulated with a front surface area of 1.16 × 1.16 cm^2. The mass of the 5 mm thick sample equals that one irradiated experimentally (i.e. 2.66 g, see Table 6.1).

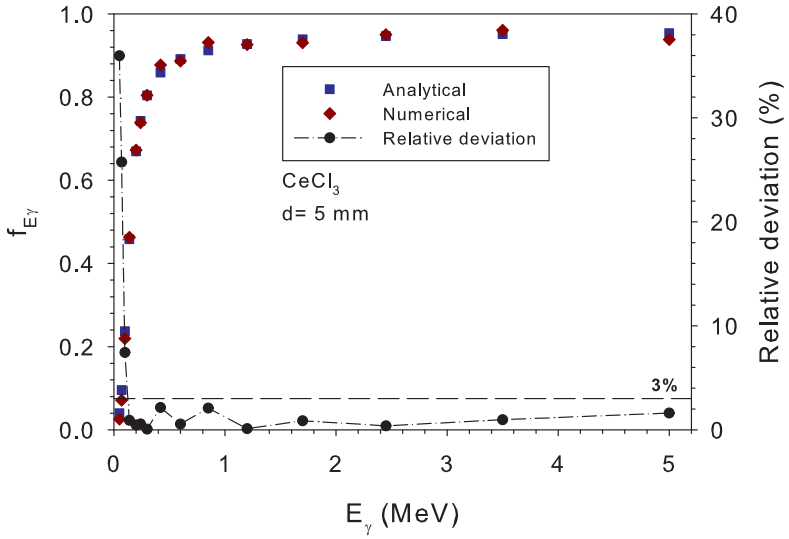


Figure 4.2: Numerical simulation of the γ-ray self-absorption factor $f_{E\gamma}$ for a 5 mm thick $CeCl_3$ sample with a surface area of 1.16 × 1.16 cm^2 and for different γ-ray energies E_γ. The sample was tilted by 45° relative to the symmetry axis of the detector and a total of 10^9 primary γs were run.

Generally, a good agreement is observed between the analytical solution and the simulation within an energy range between 100 keV and 5 MeV. The average value of the relative deviation in the aforementioned energy range is 1.4%, whereas it increases below 100 keV with decreasing energy of the γs to a maximum value of about 36% at 50 keV. Since the photoatomic cross sections used in MCNP6 (MCPLIB84 library [118]) were found to be almost identical to these ones of XCOM, a faulty or incomplete γ transport in the simulations with the MCNP6 code was assumed. In fact, various works in the literature suggest problems with the framework conditions specified above and hence support this assumption [127–130].

4.2.2 Attenuation of neutrons

For neutrons, the factor $Z(E)$ from Eqs. (4.5) and (4.6) equals the total macroscopic cross section Σ_t. Therefore, according to the Beer-Lambert law [124], the attenuation of a parallel and monoenergetic neutron beam of incident intensity I_0 traversing a material of thickness d can be expressed by:

$$I(d) = I_0 \cdot \exp\left(-\Sigma_t \cdot d\right). \tag{4.14}$$

When a beam of free neutrons enters matter the individual particles undergo various nuclear reactions depending on their kinetic energy and the nuclear properties of the traversed material. Besides (n,xn) reactions leading to an increase of the net neutron-flux density within the considered material, any other type of nuclear reactions ultimately removes neutrons and hence results in a reduction of the initial number of neutrons. Assuming thin samples of thicknesses much smaller than 1 mm

and neutron energies around a few MeV, the neutron flux averaged over the sample thickness (Φ_s) could be reasonably approximated by the incident neutron flux Φ_0. For samples with thicknesses greater than 1 mm the sample flux Φ_s can be given as [51]:

$$\Phi_s = \Phi_0 \cdot f_n, \tag{4.15}$$

where f_n is called neutron self-shielding factor.

Assuming that absorption reactions dominate over scattering processes, for a monoenergetic and parallel beam of neutrons impinging on a slab-shaped sample the neutron self-shielding factor can be estimated by [51]:

$$f_n = \frac{1 - \exp\left(-\Sigma_t \cdot d\right)}{\Sigma_t \cdot d}, \tag{4.16}$$

where d is the sample thickness along neutron beam direction.

For absorber materials where scattering is not negligible the self-shielding factor (denoted as $f_{n,s}$ in this case) might be estimated with the following expression [51]:

$$f_{n,s} = \frac{f_n}{1 - \frac{\Sigma_s}{\Sigma_t} \cdot (1 - f_n)}, \tag{4.17}$$

where f_n is calculated after Eq. (4.16) and Σ_s corresponds to the macroscopic scattering cross section.

4.2.2.1 Simulation of neutron self-shielding

For monoenergetic and parallel neutron beams Eqs. (4.16) and (4.17) could be used to determine self-shielding factors, but they fail to yield reliable values in the case of a neutron-energy distribution, i.e. a spectrum. The use of effective macroscopic cross sections calculated after Eq. (2.14) in the aforementioned equations results also in wrong values. This is reasoned in the fact that a certain fraction of neutrons with energy E_n that have interacted in the sample could still undergo reactions in another neutron-energy bin at energies of E'_n, resulting in multiple tracklength contributions per source neutron. This effect is not accounted for in the simple analytical model. Additionally, for large samples multi-neutron scattering cannot be neglected. Therefore, numerical simulations are routinely applied to derive spectrum-averaged self-shielding factors [15, 98].

The limitations of Eqs. (4.16) and (4.17) are illustrated in Fig. 4.3 for the case of a 2.3-MeV neutron beam and a neutron beam with the energy distribution corresponding to fast neutrons at sample position impinging on Al samples with a surface area of 2.5 × 2.5 cm^2 and thicknesses between 0.025 and 10 cm.

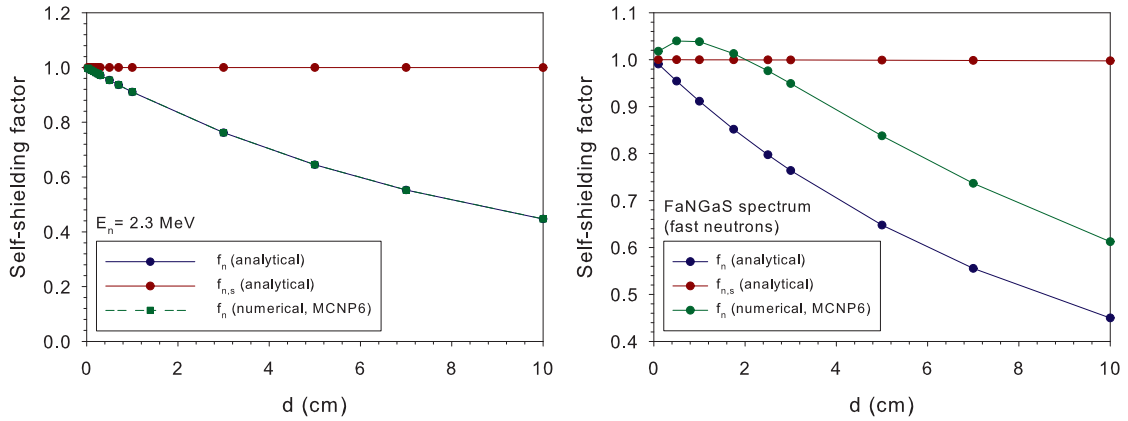


Figure 4.3: Comparison between analytical and numerical neutron self-shielding factors obtained with the MCNP6 code for Al samples with thicknesses ranging between 0.025 and 10 cm. The left picture gives the results for a monoenergetic neutron beam of 2.3 MeV energy and the right picture gives the results for the fast-neutron-energy distribution at sample position. The blue curves (f_n) give analytical self-shielding factors according to Eq. (4.16) and the red curves ($f_{n,s}$) according to Eq. (4.17). A total of 10^8 primary neutrons were run in the simulations.

Generally, assuming a thick and inhomogeneous sample, the self-shielding factor for fast neutrons can be expressed as [15]:

$$f_n = \frac{\int_V \int_{E_{min}}^{E_{max}} \Phi_r(E,\bar{r}) \cdot \sigma_t(E) \cdot \rho_r(\bar{r}) \cdot dE \cdot d\bar{r}}{\int_V \int_{E_{min}}^{E_{max}} \Phi_d(E,\bar{r}) \cdot \sigma_t(E) \cdot \rho_d(\bar{r}) \cdot dE \cdot d\bar{r}}, \tag{4.18}$$

where V is the volume, Φ denotes the neutron flux, σ_t the total microscopic cross section, ρ the density and $\bar{r}$ indicates dependence on the position within the sample volume. The subscript r indicates a sample case with the physical density ρ_r and the index d indicates a diluted-sample case with a density $\rho_d \ll \rho_r$, respectively.

For a homogeneous sample the spatial dependence of the density in Eq. (4.18) cancels out:

$$f_n = \frac{\int_V \int_{E_{min}}^{E_{max}} \Phi_r(E,\bar{r}) \cdot \sigma_t(E) \cdot \rho_r \cdot dE \cdot d\bar{r}}{\int_V \int_{E_{min}}^{E_{max}} \Phi_d(E,\bar{r}) \cdot \sigma_t(E) \cdot \rho_d \cdot dE \cdot d\bar{r}}. \tag{4.19}$$

As the total cross sections $\sigma_t(E)$ are constant in each considered neutron-energy bin, the expression for the self-shielding factor in numerical simulations might be generally simplified as [98]:

$$f_n = \frac{\int_{E_1}^{E_2} dE \cdot \Phi_s}{\int_{E_1}^{E_2} dE \cdot \Phi_0}, \tag{4.20}$$

where Φ_0 is the flux impinging on the sample front surface and Φ_s the sample flux also described by Eq. (4.15). The volume-averaged flux is obtained in simulations

with the MCNP6 code by means of the F4 (volume) flux tally, that simply divides the track length made of a neutron (cm) in a certain energy bin by the corresponding volume (cm^3) of the given cell or voxel element. Therefore, an estimate for spectrum- and sample-averaged self-shielding factors can be obtained as:

$$f_n = \frac{F4\,tally(\rho_r)}{F4\,tally(\rho_d)} \approx \frac{F4\,tally(\rho_r)}{F4\,tally(void)}. \tag{4.21}$$

As literature suggests to take diluted sample densities ρ_d of $10^{-6} \cdot \rho_r$ [131], it was found that it is reasonable to approximate the diluted-sample case by filling the sample with void, i.e. density zero, as indicated in Eq. (4.21).

4.3 Neutron moderation

Samples with an effective thickness above 1 mm and containing water enable neutron moderation leading to an increase of the thermal and epithermal neutron flux within the sample. In contrast to the neutron self-shielding, these moderation effects lead to an increase of the respective neutron-flux values in each considered neutron-energy range. Since some of the RE chloride samples presented within this work contain a considerable weight fraction of water, i.e. approximately 30 wt% (see Table 6.1), the neutron moderation was investigated numerically with the MCNP6 code.

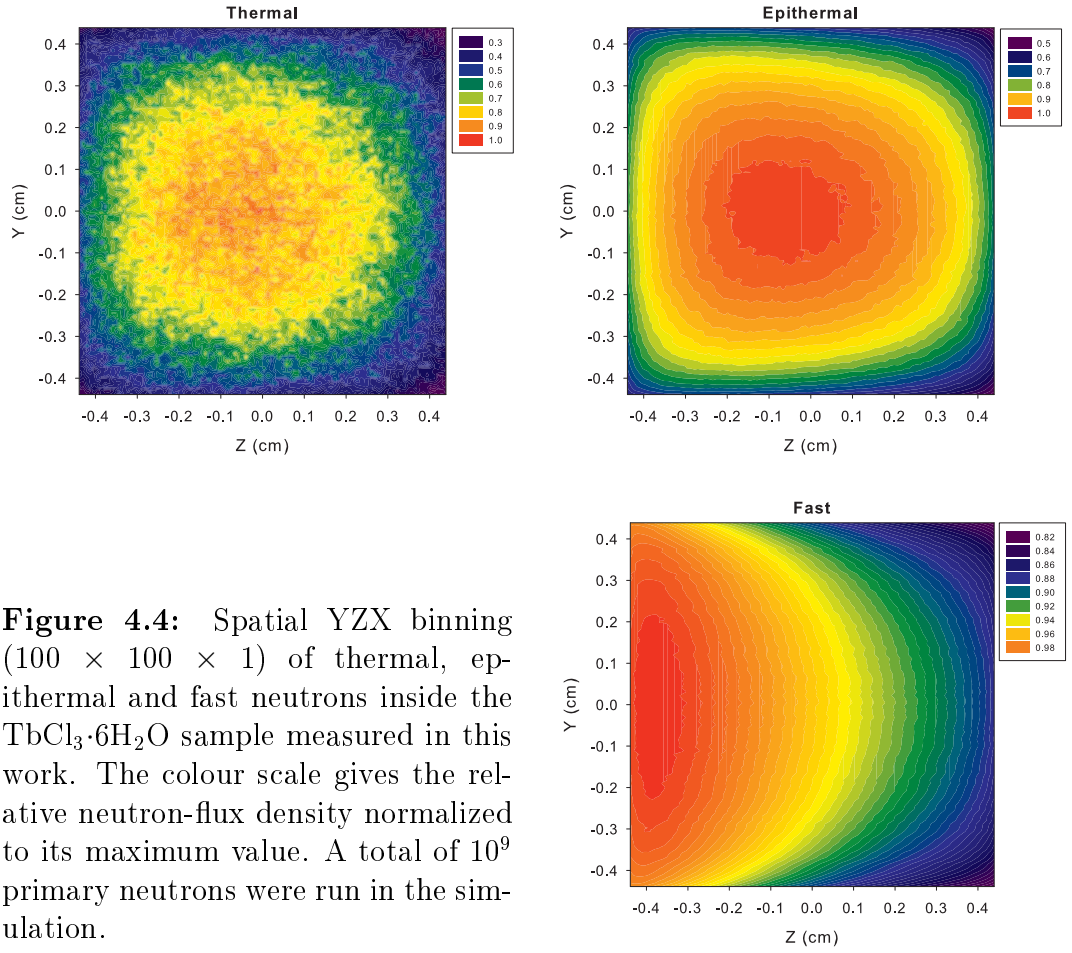


Figure 4.4: Spatial YZX binning (100 × 100 × 1) of thermal, epithermal and fast neutrons inside the $TbCl_3{\cdot}6H_2O$ sample measured in this work. The colour scale gives the relative neutron-flux density normalized to its maximum value. A total of 10^9 primary neutrons were run in the simulation.

For the case of the terbium(III) chloride hexahydrate ($TbCl_3 \cdot 6H_2O$) sample measured in this work a FMESH4 tally was applied to make 100 × 100 × 1 spatial binnings of the neutron-flux density within the sample for XYZ, XZY and YZX binnings. The $TbCl_3 \cdot 6H_2O$ sample was modeled with a thickness of 6 mm and a surface area of 0.886 × 0.886 cm^2 (X-axis: horizontal sample axis, Y-axis: vertical sample axis) corresponding to the measured mass of 2.049 g (see Table 6.1). The FMESH4 tally as well as the sample were both tilted by 45° relative to the incident neutron beam axis. The neutron source was simulated with the corresponding neutron-energy distribution at sample position and the neutrons were emitted along negative Z-axis to hit the complete sample front surface. The results for the YZX binning are depicted in Fig. 4.4.

Absence of moderation would imply that the neutron-flux density decreases as a function of thickness for all three considered neutron-energy ranges. The fact, however, that the highest neutron density, in contrast to fast neutrons, is not found at the front surface of the sample in the case of thermal and epithermal neutrons is a clear indication for relevant moderation processes.

As moderation had to be considered in the analysis of the hydrated RE chloride samples with respect to Fig. 4.4, the MCNP6 code was used to quantify the moderation in terms of moderation factors, denoted as f_{mod}. These factors were determined with three simulations and neutron-energy distributions: thermal (10^{-10} MeV $\leq E_n \leq 1.42 \times 10^{-7}$ MeV), epithermal (1.42×10^{-7} MeV $\leq E_n \leq 0.06$ MeV) and integral (10^{-10} MeV $\leq E_n \leq 20$ MeV). F4 tallies were applied to obtain the respective sample fluxes Φ_s in each neutron-energy bin. The moderation factors were then estimated for thermal neutrons as:

$$f_{mod,th} = \frac{(\Phi_{th})_{integral}}{(\Phi_{th})_{thermal}}, \tag{4.22}$$

and for epithermal neutrons, respectively, as:

$$f_{mod,epi} = \frac{(\Phi_{epi})_{integral}}{(\Phi_{epi})_{epithermal}}. \tag{4.23}$$

An input file used for the $TbCl_3 \cdot 6H_2O$ sample is attached in Appx. K.2. Moderation factors determined according to Eqs. (4.22) and (4.23) are given for all hydrated RE chloride samples in Table 6.5 in Chapter 6.

4.4 Interferences

Calculation of precise and accurate nuclear data from experimental γ-ray spectra requires the application of correction procedures. Necessity of these corrections arises if the difference in energy between a γ-line at energy E_γ and an interference at an energy of E'_γ falls below the energy resolution of the detector, i.e. the detector cannot distinguish the individual lines from each other.

Generally, the following interferences were relevant for this work: **(i) background lines**, **(ii) single and double escape peaks**, **(iii) prompt gamma lines** and **(iv) delayed gamma lines from activation products**.

Prompt gamma lines represent the most frequent interferences, followed by background lines, delayed gamma lines and single and double escape peaks, respectively. Details for the corresponding correction procedures are given in the following.

Background lines

As a certain fraction of neutrons scatters from the sample towards the detector and interacts with the shielding material of the spectrometer and the Ge crystal, an increase in the count rate from γ-lines associated to the beam background was observed. The extent of this scattering process depends on the thickness and density of the considered sample but also is a strong function of the ratio of the macroscopic scattering to the macroscopic absorption cross section, i.e. Σ_s/Σ_a. The observed ratio between the count rate with and without sample yields a scattering factor, denoted as f_s, which can be used to account for the aforementioned processes.

For the determination of average scattering factors ($\overline{f_s}$), relevant background lines associated to materials of the spectrometer were considered. The determination of that factor is exemplary illustrated in Table 4.1 for the case of the measured $TbCl_3{\cdot}6H_2O$ sample, for which a value of $\overline{f_s}$= 1.53 ± 0.32 was determined.

Table 4.1: Average scattering factor $\overline{f_s}$ for the measured $TbCl_3{\cdot}6H_2O$ sample.

E_γ	Reaction	Source material	Count rate (s^{-1})		f_s
(keV)			Background	$TbCl_3{\cdot}6H_2O$	
139.7	^{74}Ge(n,γ)^{75m}Ge	HPGe crystal	9.84 ± 0.11	17.58 ± 0.16	1.79 ± 0.03
1014.2	^{27}Al(n,n'γ)^{27}Al	HPGe housing	0.68 ± 0.01	1.31 ± 0.03	1.94 ± 0.05
1696.8	^{74}Ge(n,n'γ)^{74}Ge	HPGe crystal	0.24 ± 0.01	0.25 ± 0.01	1.04 ± 0.07
2222.8	^{1}H(n,γ)^{2}H	BPE shielding	0.23 ± 0.01	0.35 ± 0.02	1.51 ± 0.09
2614.6	^{208}Pb(n,n'γ)^{208}Pb	Lead shielding	0.66 ± 0.02	0.91 ± 0.02	1.37 ± 0.05
Average value $\overline{f_s}$					**1.53 ± 0.32**

The dependence of the average scattering factors on the product of the effective macroscopic scattering cross section ($\langle\Sigma_s\rangle$) and the effective thickness (e) is illustrated in Fig. 4.5 for several samples that have been measured with FaNGaS, comprising: Al, Ti, Fe, Cu, In, $(C_2H_3Cl)_n$, $CaCO_3$, $LaCl_3{\cdot}7H_2O$, $CeCl_3$, $PrCl_3{\cdot}7H_2O$, $NdCl_3$, $SmCl_3{\cdot}7H_2O$, $TbCl_3{\cdot}6H_2O$ and $DyCl_3{\cdot}6H_2O$.

In principle, it can be concluded that the value of $\overline{f_s}$ is observed to increase with increasing values of $\langle\Sigma_s\rangle \cdot e$. In fact, however, the shape of the scattered neutron spectrum reaching the detector could differ from sample to sample depending on its macroscopic excitation function. Taking the excitation function for the reaction of a considered γ-line into account, the increase in the net counts is strongly influenced whether a high number of neutrons is provided at energies around the maximum of

the respective excitation function or not. The average scattering factors $\overline{f_s}$ for all γ-ray spectra analyzed within this work are provided in Appx. B.

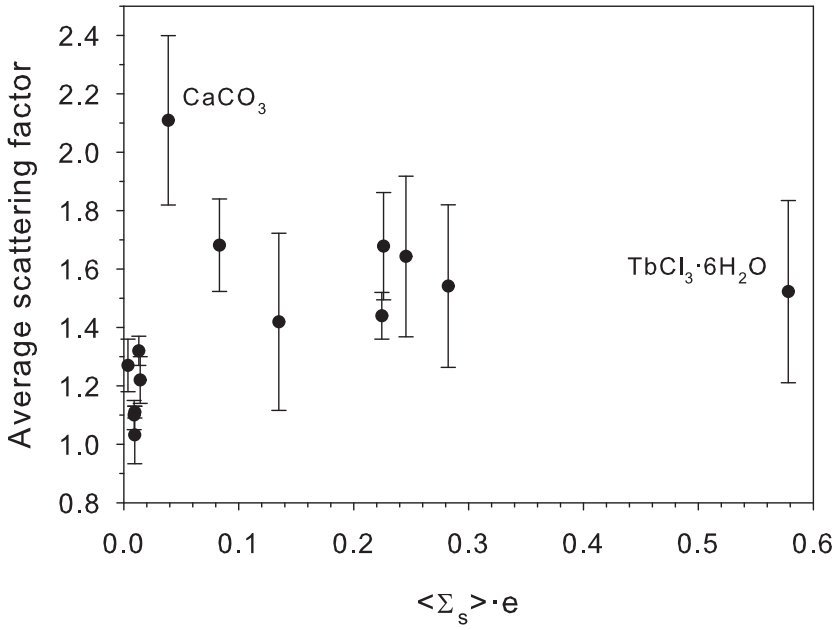


Figure 4.5: Dependence of the average scattering factor $\overline{f_s}$ on the product of the effective macroscopic scattering cross section $\langle\Sigma_s\rangle$ and the effective thickness e for several samples (see text) that have been measured with FaNGas yet.

Escape peak lines

γ-rays of energy $E_\gamma \geq 1.022$ MeV are likely to interact via pair production, resulting in the creation of two 511-keV γs. If one of them escapes from the detector crystal, a single escape peak (SE) at an energy of E_γ - 0.511 MeV is produced. If both escape, a double escape peak (DE) at an energy of E_γ - 1.022 MeV becomes visibile in the spectrum. In order to correct for the contribution of aforementioned interactions in the HPGe crystal to the net counts of a given FEP, the dependence of the SEs and DEs on the energy of the considered FEP must be characterized.

The correction curves for SEs and DEs were obtained by means of numerical simulation with the MCNP6 code and the results were checked with available experimental data. For the simulation the implemented HPGe detector model as given in Chapter 7 (see also Fig. 7.20) was used. A circular disk source of homogeneous radial distribution and discrete γ-ray energies of 1.3, 1.5, 1.8, 2.3, 2.8, 3.5, 4.0, 5.0, 6.0, 7.0 and 8.0 MeV was simulated. Interferences between FEPs and escape peaks were excluded with this set of discrete energies. A total of 10^8 primary γs were run to meet acceptable statistics with uncertainties below 1% in the peaks.

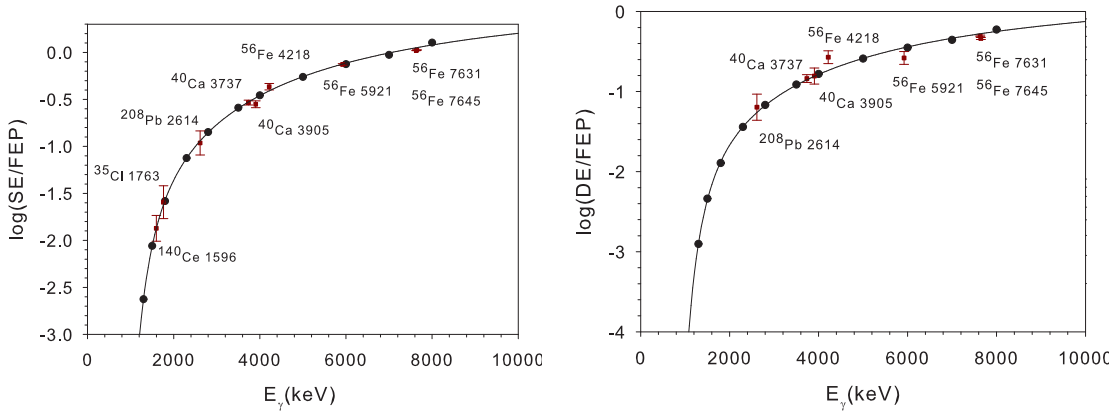


Figure 4.6: Determined correction curves for single and double escape peak interferences. Round values in black represent data points obtained by means of numerical simulation with MCNP6. The solid line in black is the curve fit according to Eq. (4.24). Square symbols in red with error bars represent experimental values. A total of 10^8 primary γs were run in the simulation (see Appx. K.1 for details).

The data points depicted in Fig. 4.6 obtained by numerical simulation were fitted with the following equation:

$$log\left(\frac{SE}{FEP}\right) \, or \, log\left(\frac{DE}{FEP}\right) = b_0 + \left(\frac{b_1}{E_\gamma}\right) + \left(\frac{b_2}{E_\gamma^2}\right) + \left(\frac{b_3}{E_\gamma^3}\right), \tag{4.24}$$

with b_0= 0.7737 ± 0.0385, b_1= (-6.3758 ± 0.3493) × 10^3, b_2= (7.3210 ± 0.8957) × 10^6 and b_3= (-6.2095 ± 0.6781) × 10^9 for SE correction and b_0= 0.4463 ± 0.0432, b_1= (-6.3979 ± 0.3912) × 10^3, b_2= (7.4241 ± 1.0031) × 10^6 and b_3= (-6.1875 ± 0.7594) × 10^9 for DE correction with E_γ in units of keV.

As depicted in Fig. 4.6 a good agreement between measured and calculated values is obtained, thereby justifying the use of Eq. (4.24).

Prompt gamma lines

For the case that the peak energy E_γ of a prompt γ-line interferes with a fast-neutron-induced γ-line of interest, the net counts $P_{E\gamma}$ of the interfering line were calculated in the case there is no neutron moderation as:

$$P_{E\gamma} = \frac{m}{M} \cdot N_A \cdot h \cdot \epsilon_{E\gamma} \cdot I_{E\gamma} \cdot \langle\sigma\rangle \cdot \langle\Phi\rangle \cdot t_c \cdot f_{E\gamma} \cdot f_n, \tag{4.25}$$

where the γ-ray intensity $I_{E\gamma}$, in the case of (n,γ) reactions, can be derived according to Eq. (4.3) with the effective cross section $\langle\sigma\rangle$ of the considered reaction given in [132, 133]. The values of $\langle\sigma_{E_\gamma}\rangle$ were obtained by dividing the effective elemental cross sections provided in [132] and [133] by the respective isotopic abundance h.

In the case of samples that contain a significant mass fraction of water the contribution of each neutron-energy range was considered individually taking into

account neutron moderation. In this case, complementary to Eq. (4.25), the net counts of a prompt line were determined as:

$$P_{E\gamma} = \frac{m}{M} \cdot N_A \cdot h \cdot \epsilon_{E\gamma} \cdot f_{E\gamma} \cdot I_{E\gamma} \cdot t_c \cdot \left(\sum_{i=1}^{n} \langle \sigma_i \rangle \cdot \langle \Phi_i \rangle \cdot \langle f_{n,i} \rangle \cdot \langle f_{mod,i} \rangle \right), \quad (4.26)$$

where the subscript i refers to the considered neutron-energy range, i.e. thermal, epithermal and fast. For a given (n,γ) line produced by epithermal neutrons the intensity can be reasonably estimated by taking that one for thermal neutrons (denoted as $I_{E\gamma,th}$) provided in [132, 133], as demonstrated by the measurement of In [36]. The same intensity was assumed also for fast neutrons.

In the case of interferences between fast-neutron-induced prompt γ-lines, the affected lines were evaluated for the reaction that had the major contribution to the net counts. In principle, two methods were applied to correct for the aforementioned interferences: (i) either the relative γ-ray intensities listed in the Atlas [27] or (ii) these given in the NuDat 3.0 database [65] were used. Since intensities in the latter one are mostly level-specific, the second method is particularly useful in cases where several γ-lines of a certain level are detected. $\langle \sigma_{E\gamma}(90°) \rangle$ values determined from a $(C_2H_3Cl)_n$ spectrum analyzed in this work were used to correct for fast-neutron-induced interferences arising from Cl.

The net counts related to a fast-neutron-induced line can be deduced with Eqs. (4.1), (4.25) and (4.26). Nevertheless, for the purpose of elemental analysis in spectrometry, it might be practical to define a production cross section that contains the unfiltered information of both the fast-neutron-induced and the (n,γ) reaction. To simplify for cases where aforementioned reactions originate from two different isotopes, the abundance was neglected and for water-free samples involving only prompt γ-lines an elemental cross section was defined as:

$$\langle \sigma^Z_{E\gamma} \rangle = \frac{P_{E\gamma} \cdot M}{m \cdot N_A \cdot \epsilon_{E\gamma} \cdot \langle \Phi \rangle \cdot t_c \cdot f_{E\gamma} \cdot f_n}, \quad (4.27)$$

where $\langle \Phi \rangle$ is the integral neutron flux.

For hydrated samples, the net counts were (i) splitted between the fast-neutron and the radiative neutron capture reaction. Secondly (ii), the net counts of the latter one were distributed between thermal, epithermal and fast neutrons according to their relative reaction rates. The elemental cross section was then given as:

$$\langle \sigma^Z_{E\gamma} \rangle = \frac{P_{E\gamma} \cdot R_{fast} \cdot M}{m \cdot N_A \cdot \epsilon_{E\gamma} \cdot \langle \Phi \rangle \cdot t_c \cdot f_{E\gamma} \cdot f_n} + \sum_{i=1}^{n} \left(\sum_{j=1}^{3} \frac{P_{E\gamma} \cdot R_{i,cap} \cdot R_j \cdot M}{m \cdot N_A \cdot \epsilon_{E\gamma} \cdot \langle \Phi \rangle \cdot g(t_b, t_c, t_{1/2}) \cdot f_{E\gamma} \cdot f_{n,j} \cdot f_{mod,j}} \right), \quad (4.28)$$

where R_{fast} is the relative reaction rate for the considered fast-neutron-induced reaction, $R_{i,cap}$ the relative reaction rate for the ith interfering radiative neutron capture reaction and R_j the relative reaction rate of thermal (j= 1), epithermal (j= 2) and fast neutrons (j= 3) in the ith radiative neutron capture reaction, respectively. For dry samples, Eq. (4.28) reduces to Eq. (4.27). As per definition, $f_{mod,fast}$= 1. Effective elemental γ-ray production cross sections are given in Appx. H.2. for lines interfered by (n,γ) reactions with a contribution to the net counts above 1%.

If several nuclides contribute to a certain γ-line (e.g. ^{35}Cl and ^{159}Tb in a $TbCl_3{\cdot}6H_2O$ sample), then the different masses m and the molar masses M must be considered in Eqs. (4.27) and (4.28). In addition, the net counts must be split between the nuclides according to the relative reaction rates. Nevertheless, Appx. H.2. provides also values of $\langle\sigma^Z_{E\gamma}\rangle$ for those aforementioned cases.

Delayed gamma lines

Radiative neutron capture reactions (n,γ) but also fast-neutron-induced reactions such as (n,pγ) or (n,$\alpha\gamma$) can result in the accumulation of radioative activation products emitting delayed γ-rays. In the absence of neutron moderation the net counts of the interfering lines can be calculated by:

$$P_{E\gamma} = \frac{m}{M} \cdot N_A \cdot h \cdot \epsilon_{E\gamma} \cdot I_{E\gamma} \cdot \langle\sigma\rangle \cdot \langle\Phi\rangle \cdot g(t_b, t_c, t_{1/2}) \cdot f_{E\gamma} \cdot f_n, \tag{4.29}$$

where $g(t_b, t_c, t_{1/2})$ is the effective counting time for delayed γ-lines specified in Eq. (4.2). In the case of samples that contain water the net counts of the interfering lines are given by:

$$P_{E\gamma} = \frac{m}{M}{\cdot}N_A{\cdot}h{\cdot}\epsilon_{E\gamma}{\cdot}f_{E\gamma}{\cdot}I_{E\gamma}{\cdot}g(t_b, t_c, t_{1/2}){\cdot}\left(\sum_{i=1}^{n}\langle\sigma_i\rangle \cdot \langle\Phi_i\rangle \cdot \langle f_{n,i}\rangle \cdot \langle f_{mod,i}\rangle\right). \tag{4.30}$$

4.5 Comparison with literature data

The results derived from the experimental measurements presented in this work were compared to that one of Demidov et al. [27]. Therefore, γ-ray intensities were determined relative to the same reference line as chosen in [27]. Relative γ-ray intensities ($I_{E\gamma,rel}$) in percent were calculated as:

$$I_{E\gamma,rel} = \frac{P_{E\gamma,i}/\left(\epsilon_{E\gamma,i} \cdot f_{E_{\gamma,i}}\right)}{P_{E\gamma,ref}/\left(\epsilon_{E\gamma,ref} \cdot f_{E_{\gamma,ref}}\right)} \cdot 100\%, \tag{4.31}$$

where the subscripts i and ref refer to the considered and the reference (100%) line.

Plotting the relative intensity determined in this work (I_R) versus the intensity

obtained by Demidov et al. (I_{RD}) provided a first overview on the agreement between the two data sets. To quantify the agreement, the data points were fitted by:

$$I_R = a \cdot (I_{RD})^b, \tag{4.32}$$

where the fit coefficients a and b were given to the second digit.

To prove the consistency of the two data sets in a more detailed manner, the residuals R in units of standard deviation (σ) were calculated and plotted in a histogram. These residuals were calculated as:

$$R = \frac{I_R - I_{RD}}{\sqrt{(s_{I_R})^2 + (s_{I_{RD}})^2}}, \tag{4.33}$$

where s_{I_R} and $s_{I_{RD}}$ represent the standard devation of the relative intensities in this work and the work of Demidov et al. [27], respectively. The histograms were fitted by a simple Gaussian of the general form:

$$R = a \cdot exp\left(-0.5 \cdot \left(\frac{R - R_0}{\sigma}\right)^2\right), \tag{4.34}$$

where σ provided the agreement level in units of standard deviation. The parameter R_0 gives the shift of the Gaussian centroid with respect to zero and indicates a possible systematic deviation.

4.6 Limit of detection

There exist many different approaches in the literature defining a limit of detection (LOD) or detection limit [134–136]. In this work, the detection limit (DL) was defined as the minimum mass of a pure element that has to be irradiated for a certain time in order to give a net signal above the background with a certain standard deviation σ. For a certain counting live time t_c and neglecting any neutron and γ beam attenuation effects, it can be calculated with Eq. (4.1) from the minimum peak area $P_{E\gamma}(c)$ that might be estimated according to [137] as:

$$P_{E\gamma}(c) = \frac{\sqrt{2 \cdot B_{E\gamma}}}{c}, \tag{4.35}$$

where $B_{E\gamma}$ is the area of the background below the γ-line of interest and c a predefined value for the relative uncertainty of the peak area. The value of c was set to 0.5, assuming a peak area uncertainty of 50%.

In the presence of an interfering peak, $P_{E\gamma}(c)$ can be expressed as:

$$P_{E\gamma}(c) = \frac{\sqrt{2 \cdot (P_{int} + 2 \cdot B_{E\gamma})}}{c}, \tag{4.36}$$

where P_{int} equals the net area of the interfering peak.

5. The FaNGaS instrument

This chapter is devoted to a detailed description of the FaNGaS instrument. First of all, the path of the fission neutrons produced in the moderator pool of the reactor to the experimental measurement position is described. The shielding configuration and detector specifications of the spectrometer are presented along with a characterization of the full-energy-peak (FEP) efficiency. Furthermore, the active radiation background and the neutron-energy spectrum at sample position are introduced.

Figure 5.1 provides a schematic overview on the fast-neutron facility at FRM II. The fast neutrons are produced with two uranium converter plates placed in front of the beam tube used for extraction. After filtering and collimation of the neutron beam within a filter bench bunker it enters the MEDAPP (Medical Application) irradiation room [138, 139], in which the spectrometer of FaNGaS is installed. The NECTAR (Neutron Computerized Tomography and Radiography) facility [140] depicted in Fig. 5.1 is located in the following irradiation bunker. Details of Fig. 5.1 are dicussed in the subsequent sections.

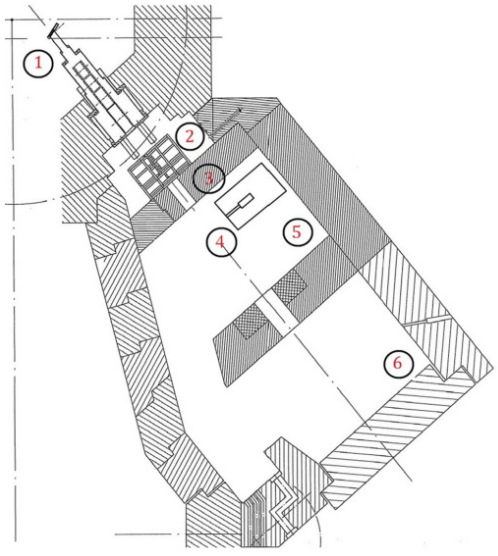


Figure 5.1: Schematic view of the fast-neutron facility at FRM II. (1) converter plate made of 498 g of highly-enriched uranium (93% of ^{235}U) plunged into the reactor pool at a distance of about 1 m from the reactor core; (2) filter bench bunker containing the collimator of FaNGaS; (3) multi-leaf collimator of the MEDAPP facility; (4) FaNGaS spectrometer at measuring position; (5) bunker of the MEDAPP facility; (6) bunker of the NECTAR facility. [34]

5.1 Fission neutron beam

The FRM II is a pool type reactor in which heavy water serves as both moderator and coolant. Thermalized neutrons induce fission of ^{235}U contained in the fuel (U_3Si_2 dispersed in Al). The latter one is enveloped in a central fuel rod of 1.3 m length and 24 cm diameter, providing about 8 kg of highly-enriched uranium (93% of ^{235}U). In the vicinity of the neutron beam extraction channel SR10 (Strahlrohr 10) used for FaNGaS, two highly-enriched uranium converter plates (93% of ^{235}U) of 15 × 15 cm^2 [139, 141] are installed to produce the fission neutron beam. The converter system is illustrated in Fig. 5.2.

The converter plates are positioned by a mechanical drive in front of the 275-cm long helium-filled beam tube SR10 and they can be moved in and out from its entrance to obtain fast or thermal neutron beams, respectively [141]. The cooling of the plates is ensured by light water (H_2O) and a beam shutter is available for rapid closure of the beam tube.

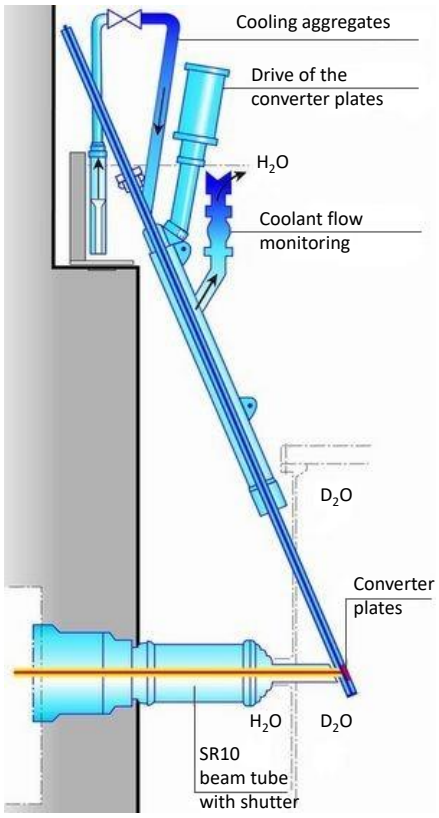


Figure 5.2: Schematic representation of the converter system utilized to produce fast neutrons at the entrance of neutron extraction channel SR10. [142]

5.1.1 Neutron beam collimation

The fast neutrons produced in the uranium converter plates are extracted through the SR10 into a filter bench bunker used for pre-collimation and beam shaping. This bunker is located between the experimental bunker (MEDAPP facility) and the end

of SR10 (see also Fig. 5.1). At the exit of SR10 a 1 cm thick thermal neutron filter made of borated polyethylene (BPE) is placed [141]. Therefore, the generated neutrons can be assumed to be pure fission neutrons whose energy spectrum is adequately described by the Watt distribution [143, 144]. Different set-ups of filters can be mounted on the bench and electropneumatically driven in or out from the neutron beam axis. In the current version of FaNGaS used to measure the γ-ray spectra analyzed in this work, the neutron-beam collimator consisted of a sequence of polyethylene (PE), boron carbide (B_4C) and lead (Pb of high purity, i.e. $> 99.99\%$). The number of sequences is five with thicknesses of 5 cm for PE, 1 cm for B_4C and 3 cm for Pb, resulting in a total length of about 45 cm [141]. In addition, a filter made of a 1 cm thick B_4C plate and two Pb plates with a total thickness of 5 cm are placed at the upstream beam side in order to absorb thermal neutrons from the fast-neutron beam and to attenuate hard γ radiation released from the reactor core [34]. The arrangement of the aforementioned collimator produces a fast-neutron beam with an effective diameter of about 6 cm [141]. The configuration of the filter bench bunker relevant to this work is shown in Fig. 5.3.



Figure 5.3: Boron carbide (B_4C) and lead filters in the filter bench room located in front of the multi-leaf collimator (MLC) of MEDAPP. [34]

The filter bench bunker is separated from the experimental measurement position of FaNGaS by a 70 cm thick biological-shield wall made of concrete. Within this wall a multi-leaf collimator (MLC) is installed that enables to adjust the size and shape of the neutron beam. In a previous version of FaNGaS [34], the technical specifications of the MLC were described in [138] as: it consisted of movable 50 cm long and 1.5 cm wide leaves, which are made in beam direction of a sequence of Fe, PE and Pb. The aforementioned description of the MLC is referred to as "old MLC" in the following.

Now, those leaves have a length of 62 cm and their thickness varies between 1.15 and 1.75 cm [20, 139] (this version is termed as "new MLC", hereafter). In beam direction, they consist of a sequence of Fe, BPE (20 wt% B_2O_3), Fe with BPE inlays, Al and BPE [20]. For measurements with FaNGaS described in this work, the aperture of the MLC was set to $S = 5.8 \times 5.8$ cm^2. A photograph of the old and the new versions of the MLC, respectively, is depicted in Fig. 5.4.

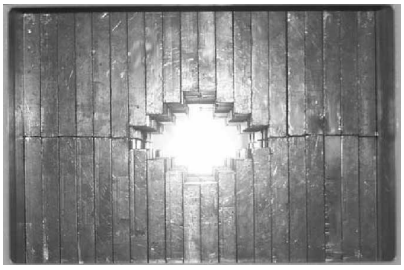




Figure 5.4: Old multi-leaf collimator (MLC) used for the previous version of FaNGaS [34, 138] (left) and the updated version which is currently in use for the FaNGaS version introduced in this work (right) [139].

5.2 FaNGaS spectrometer

The FaNGaS spectrometer is installed in the bunker of the MEDAPP facility. Any given specifications refer, unless indicated otherwise, to the last upgrade of the spectrometer. The experimental set-up is depicted in Fig. 5.5 and, in principle, the spectrometer consists of two components: **(i)** a **high-purity germanium (HPGe) detector** to measure the γ radiation released in the interaction of the fast neutrons in an irradiated sample and **(ii)** a **shielding** of different materials to protect the detector from the induced radiation background.



Figure 5.5: The FaNGaS spectrometer with the shielding at experimental position. (1) front side of the MEDAPP multi-leaf neutron beam collimator; (2) HPGe detector shielding (made of BPE with 20 wt% B_2O_3); (3) detector collimator ($\varnothing$ 6 cm); (4) PTFE sample holder; (5) iron support frame; (6) Digital spectrometer.

5.2.1 High-purity germanium (HPGe) detector

For the detection of prompt γ radiation induced by a fast-neutron beam, FaNGaS utilizes a well-shielded coaxial n-type HPGe detector (GMX50-83 from ORTEC). This detector provides a relative efficiency of 50%. In order to optimize the detector dead time without a significant decrease in the peak resolution a shaping time of 3 μs was set for the measurements presented in this work to achieve an energy resolution of 2.1 keV (FWHM, full width at half maximum) at 1.33 MeV [141]. The electromechanical cooling is ensured by an electronic cryostat (CFG-X-COOL-III from ORTEC). The signals generated by the preamplifier of the detector (Transistor-Reset) are processed using a Digital Spectrometer DSPEC-50 (from ORTEC, see Fig. 5.6) by a 16 k channels Multi-Channel-Analzyer (MCA) interfaced to a personal computer via USB or Ethernet connection. DSPEC-50 is entirely software-controlled and it is configured and operated using the software application MAESTRO (Multichannel Analyzer Emulation Software) from ORTEC.



Figure 5.6: The DSPEC-50 digital spectrometer from ORTEC utilized for the measurements with FaNGaS. ©ORTEC

In principle, HPGe detectors are PIN diodes with an external voltage applied in the reverse-biased mode [77, 86, 145–147]. Hence, the working principle of HPGe detectors relies on the collection of electron-hole pairs (EHPs) at the cathode and anode, respectively. The EHPs are created in the Ge crystal by the energy deposition of γs, with the number of EHPs and hence the height of the corresponding net electronic pulse being proportional to the amount of deposited energy. N-type Ge detectors are characterized by an excess of donor impurities (electron excess), i.e. the hole collection process is only of secondary importance. The damage mechanisms related to fast-neutron irradiation of semiconductor detectors are well understood [148–151]: they mainly create hole trapping centers. In coaxial detectors most interactions occur near the surface of the Ge crystal. As the holes are collected at the outer contact in n-type HPGe detectors, the utilized GMX50-83 detector shows a high radiation resistance. In fact, as a threshold above which significant energy resolution degradation due to neutron damage is observed, a fluence of about 10^9 cm^2 is often quoted [152]. In addition, as the fast-neutron-induced defects are unstable, the energy barrier preventing a rearrangement in the crystal structure can be lowered by raising the temperature of the Ge crystal, which is known as (off-line) annealing and can lead to a recovery of the initial energy resolution [153, 154].

5.2.2 Shielding configuration

The shielding material of the FaNGaS spectrometer serves two purposes: (i) the shielding for scattered fast neutrons and (ii) the shielding for high-energy γ-rays originating from the activated background in the experimental bunker. A schematic view of the FaNGaS spectrometer is shown in Fig. 5.7.

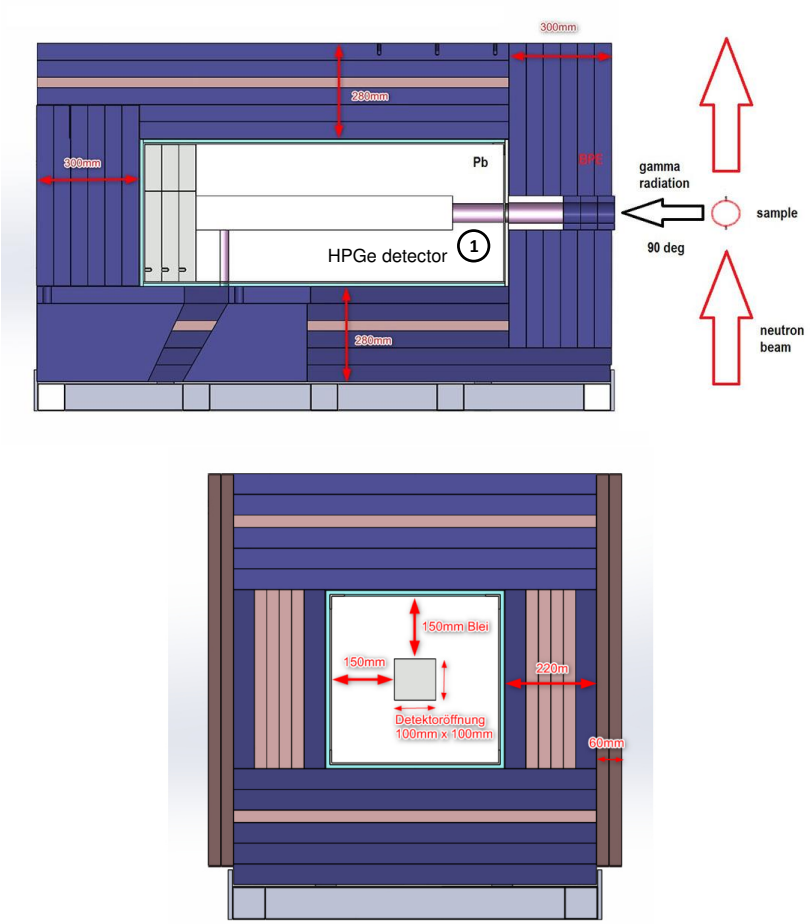


Figure 5.7: Schematic sectional view of the FaNGaS spectrometer perpendicular to the detector symmetry axis showing the outer shielding (top picture) and sectional view along the detector symmetry axis showing the inner shielding (bottom picture). The shielding was designed and constructed by Johannes Pfeil and Linus Willerding from the FRM II infrastructure group.

The outer shielding is made of BPE (20 wt% B_2O_3), which is 30 cm thick for the front and rear side and 28 cm thick for the vertical and horizontal sides, with respect to the longitudinal symmetry axis of the detector (see Fig. 5.7). In fact, the aforementioned thickness along the horizontal side is realized by use of additional BPE plates (6 cm thick, see Fig. 5.7) that are mounted on plate hooks. Optionally, it is possible to fix two additional BPE plates with a thickness of 3 cm on the sides of the shielding. The cylindrical aperture at the front side has an opening diameter of 10 cm. It is filled with a removable BPE collimator of 6 cm diameter, 2 cm wall thickness and 20 cm length.

For γ attenuation the detector is enclosed by 15 cm thick blocks of lead-copper (Pb99.94Cu, standardized nomenclature according to DIN17640-1 [155]). Compared to a previous version that used lead-antimony bricks the production of the long-lived radionuclide ^{124}Sb ($t_{1/2}$= 60.3 d) is avoided. The first 10 cm in the front collimation tract (starting from detector) are filled by a lead collimator of 6 cm length and 2 cm wall thickness. Therefore, the collimation of the spectrometer is 6 cm.

As depicted in Fig. 5.8 the rear part of the spectrometer shielding consists of two doors that can be opened to facilitate the access to the detector. The whole spectrometer has a weight of about 4 tons and it is supported by a massive iron frame (see Fig. 5.5).

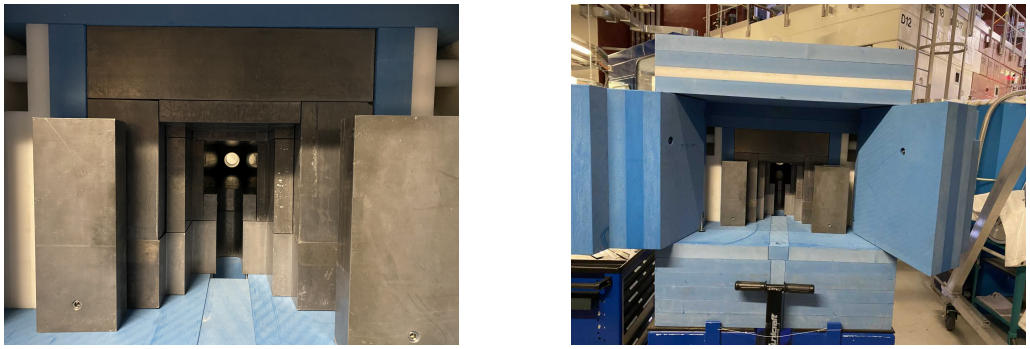


Figure 5.8: Rear side of the FaNGaS spectrometer. Two doors can be opened to facilitate the access to the HPGe detector and the lead shielding blocks.

5.2.3 Sample irradiation

Thin foil or powder samples are contained in a small PTFE (Polytetrafluorethylene) bag, attached to a thin PTFE rod. Irradiation of the whole sample surface is ensured by a laser-assisted alignment. At irradiation position the distance of the sample towards the detector endcap is 67 cm. The distance from the sample towards the uranium converter plates is 591 cm. The leaves of the MLC were adjusted to allow the maximum beam dimension of 5.8 × 5.8 cm^2 impinging on the sample front surface. The surface area of the samples is typically about 2.5 × 2.5 cm^2. Large samples are placed on a heavy table for irradiation [38].

5.3 Full-energy-peak (FEP) efficiency

The full-energy-peak (FEP) efficiency is defined as the quotient of the number of detected γs in the photopeak of energy E_γ and the total number of emitted γs of same energy E_γ [156]. The dependence of the FEP on the γ energy is depicted in Fig. 5.9. It was determined with various calibrated radioactive sources such as ^{60}Co, ^{137}Cs, ^{133}Ba and ^{152}Eu provided by the Physikalische-Technische Bundesanstalt (PTB) as well as prompt γs induced by (n,γ) reactions of ^{35}Cl, ^{54}Fe and ^{56}Fe. Aforementioned sources from PTB were used to cover the energy region below 2 MeV. Prompt

γ-lines of Cl induced by the ^{35}Cl(n,γ)^{36}Cl reaction were measured irradiating a polyvinylchloride (PVC) sample with thermal neutrons delivered from the SR10 beam tube after removing the uranium converter plates.

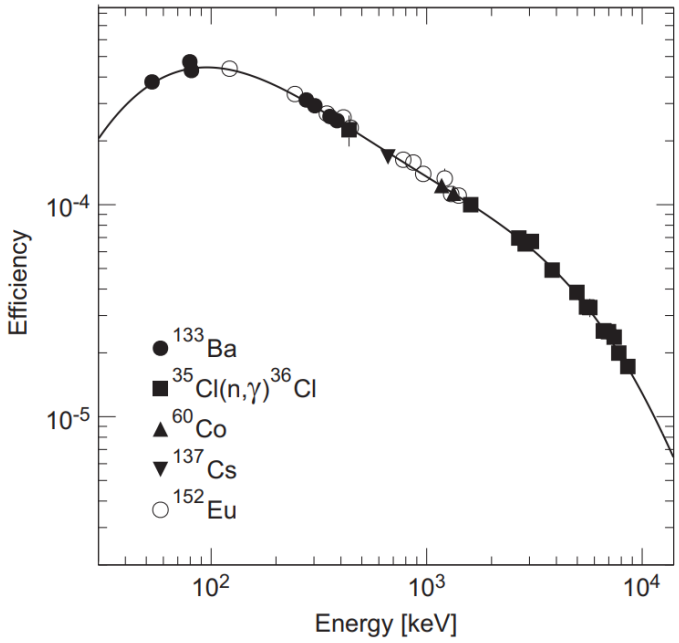


Figure 5.9: Dependence of the experimental full-energy-peak (FEP) efficiency of FaNGaS on the γ energy determined for the far-position at 67 cm away from the HPGe detector. [141]

The obtained efficiency curve is expressed by a 8th-degree polynomial fit as:

$$\epsilon_{E\gamma} = exp\left(\sum_{i=0}^{8} a_i \cdot \ln\left(E_\gamma\right)^i\right), \tag{5.1}$$

where the fit coefficients a_0 to a_8 are given in Appx. J.1.

5.4 Radiation background

The active radiation background, i.e. the background during irradiation without sample, was counted for 14.3 h (live time) for an irradiation time of 15.7 h (real time). The measurement includes signatures from both prompt and delayed γ-rays. A detailed analysis of the radiation beam background can be found in [34, 141] and some of the most intense background lines are depicted in Fig. 5.10. The active background is mostly associated to the emission of prompt γ-rays. However, strongly depending on the irradiation time and the half-life of the considered radionuclide, a few delayed lines also contribute to the active background. γ-lines were observed from the interaction of neutrons with the HPGe detector (Ge, Al, Cu, In), the shielding (B, H, Pb), the iron supporting frame (Fe), the sample holder made of PTFE (F) and the surrounding air (N, O). Prominent lines from the active

background are for example the 2223.2-keV line from the $^{1}H(n,\gamma)^{2}H$ reaction and the 2614.4-keV line arising from the $^{208}Pb(n,n'\gamma)^{208}Pb$ reaction [141]. The most prominent delayed lines come from metastable states of In, which is present in the electronics of the detector and characterized by relatively short half-lives (not more than a few hours). For example, a line at 1097.4 keV emitted from $^{116m1}In$ ($t_{1/2}$= 54.3 min [141]) is observed with good statistics.

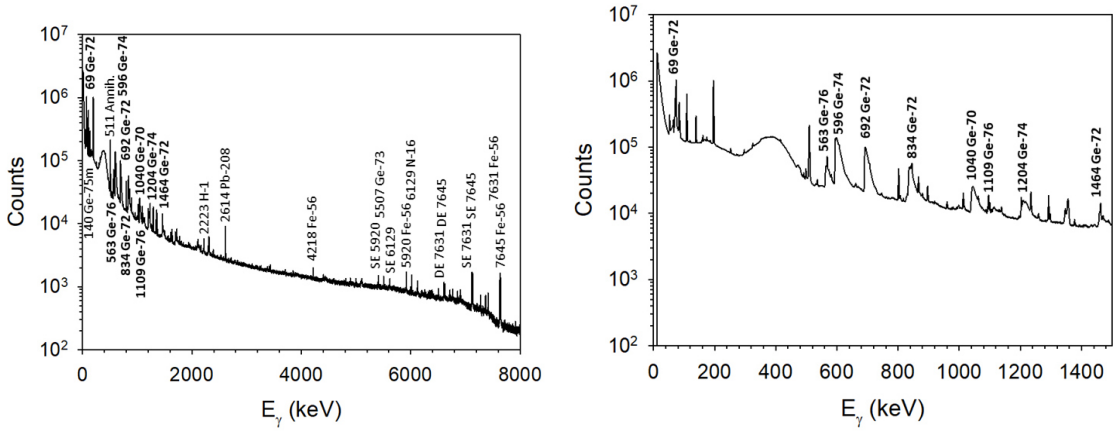


Figure 5.10: Radiation background acquired with the FaNGaS spectrometer for 51,506 s live time. Prominent background peaks are marked accordingly. The left picture shows the complete spectrum with the most intense background lines, whereas the right picture shows triangular peaks of Ge induced by fast-neutron inelastic scattering interactions within the Ge crystal of the HPGe detector.

The interaction of scattered fast neutrons in the Ge crystal leads to so-called triangular-shaped peaks. The energy of these peaks is illustrated in Fig. 5.10. The reduction of these peaks is crucial for an accurate chemical analysis as the fitting procedure of overlaid peaks can be drastically hindered. Minimization of those peaks by means of the design of a filter is the subject of Chapter 7.

5.5 Neutron-energy spectrum

The neutron-energy spectrum at sample position was determined in a previous work [34] by means of the foil activation technique, as described in [34]. High-purity metal foils of Al, Ti, Fe, Ni, Zr and In were irradiated and the induced activity was measured at a distance of 17 cm away from the HPGe detector. The HYPERMET-PC software was used for analysis of the measured γ-ray spectra and the corresponding reaction rates R were calculated. The spectrum unfolding was performed by processing the obtained values of R with the software STASYL PNNL [157], which utilizes the generalized least-square method. The neutron spectrum determined in [141] was used as an initial guess with 100 neutron-energy groups. An average energy of 2.30 MeV and a fast-neutron flux of (1.40 $\pm$ 0.05) $\times$ 10^{8} cm^{-2} s^{-1} were obtained [34].

The neutron-energy spectrum at sample position is given in Fig. 5.11. It covers a total energy range between 10^{-10} and 20 MeV with 100 neutron-energy bins and it is split into three energy ranges designated as thermal (10^{-10} MeV $< E_n <$ 1.42 $\times$ 10^{-7} MeV, 7 energy bins), epithermal (1.42 $\times$ 10^{-7} MeV $< E_n <$ 0.06 MeV, 42 energy bins) and fast (0.06 MeV $< E_n <$ 20 MeV, 51 energy bins). It is similar to a fission spectrum (kT= 0.35 MeV) and differs from a classical reactor spectrum as used by Demidov et al. (see Fig. 1.4).

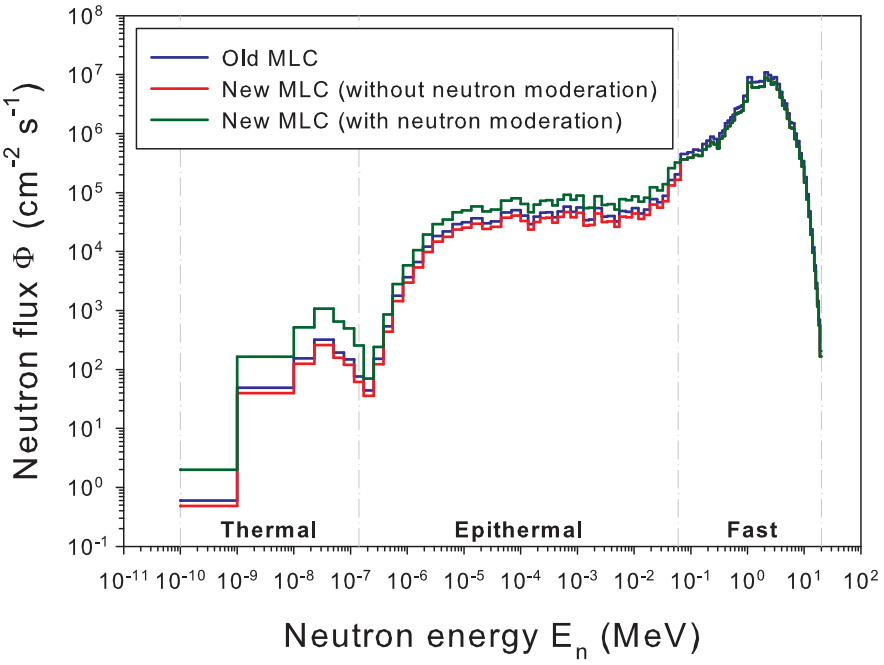


Figure 5.11: The neutron-energy spectrum of FaNGaS at sample position. The blue curve represents the spectrum related to the old version of the MLC [34, 35]. The red and green curves represent the spectrum associated to the upgraded MLC without [20, 21] and with [37] neutron moderation, respectively.

In the frame of a general upgrade program the MEDAPP facility was provided with a new MLC. This new MLC is electronically operated and, as shown in Fig. 5.4, the new MLC protrudes around 30 cm from the biological-shield wall. Consequently, the spectrometer was shifted 43 cm away from the wall, leading to an increased distance between sample-irradiation position and uranium converter plates from h_{old}= 548 cm to h_{new}= 591 cm. Besides the fact that the distance between sample and detector is kept unchanged to 67 cm, the aforementioned increase is expected to behave proportional to the corresponding ratio in solid angle subtended from the neutron source to the sample and is expressed by the following equation:

$$\frac{\Phi_{new}}{\Phi_{old}} = \frac{(S/h^2)_{new}}{(S/h^2)_{old}}, \tag{5.2}$$

where S is the adjusted surface of the collimator opening, with S_{new}= 5.8 $\times$ 5.8

cm^2 and S_{old}= 6 × 6 cm^2. With a fast-neutron flux measured from the former irradiation geometry, i.e. Φ_{old}= (1.40 ± 0.05) × 10^8 cm^{-2} s^{-1} [34], Eq. (5.2) yields a new value of the fast-neutron flux of Φ_{new}= (1.13 ± 0.05) × 10^8 cm^{-2} s^{-1}. The new neutron flux value corresponds to a flux reduction by a factor of of 0.81 ± 0.02. The aforementioned value of Φ_{new} was also monitored via the measurement of the same Fe foil as reported in [34]. Comparing the count rates of the three strongest γ-lines of the ^{56}Fe(n,n'γ)^{56}Fe reaction at 846.9, 1238.3 and 1810.9 keV in the two experiments yields a mean value of the ratios of 0.807 ± 0.006. This value leads to a fast-neutron flux of (1.13 ± 0.04) × 10^8 cm^{-2} s^{-1}, which agrees very well with the value estimated from the change of the solid angle according to Eq. (5.2).

In addition, the new version of the MLC was suspected to alter the neutron spectrum in the thermal and epithermal neutron-energy range. In fact, as a result of an experimental redetermination of the thermal and epithermal neutron flux a significant modification of the neutron spectrum was obtained in thermal and epithermal neutron-energy ranges, respectively. This modification is attributed to neutron moderation processes that are enabled by the composition of the new MLC. Details of the applied reconstruction approach are given in Chapter 6. Figure 5.11 shows the neutron-energy spectra corresponding to the work in [34], to the reduction related to the increased distance between converter plates and sample [20, 21] and the reconstructed spectrum that accounts for the modifications in the thermal and epithermal neutron-energy ranges associated to the new design of the MLC [37].

Furthermore, Table 5.1 provides the neutron flux values for all considered neutron-energy ranges (thermal, epithermal and fast) for the three spectra depicted in Fig. 5.11. In addition, integral (total) neutron flux values covering the whole considered neutron-energy range are given.

Table 5.1: Neutron flux values at sample position for each considered neutron-energy range and different versions of the FaNGaS instrument.

Neutron-energy range	Neutron flux (cm^{-2} s^{-1})		
	Old MLC Refs. [34, 35]	New MLC without neutron moderation Ref. [20]	New MLC with neutron moderation Ref. [37]
Thermal	(9.4 ± 2.8) × 10^2	(7.6 ± 2.3) × 10^2	(3.2 ± 1.3) × 10^3
Epithermal	(1.85 ± 0.09) × 10^6	(1.50 ± 0.07) × 10^6	(2.94 ± 0.77) × 10^6
Fast	(1.40 ± 0.05) × 10^8	(1.13 ± 0.04) × 10^8	(1.13 ± 0.04) × 10^8
Total	(1.42 ± 0.05) × 10^8	(1.15 ± 0.04) × 10^8	(1.16 ± 0.04) × 10^8

Thermal: (10^{-10} MeV < E_n < 1.42 × 10^{-7} MeV), Epithermal: (1.42 × 10^{-7} MeV < E_n < 0.06 MeV), Fast: (0.06 MeV < E_n < 20 MeV), Total: (10^{-10} MeV < E_n < 20 MeV)

6. Experimental

This chapter is dedicated to the analysis of the γ-ray spectra of the following samples: $CaCO_3$, $(C_2H_3Cl)_n$, $LaCl_3{\cdot}7H_2O$, $CeCl_3$, $PrCl_3{\cdot}7H_2O$, $NdCl_3$, $SmCl_3{\cdot}7H_2O$, $TbCl_3{\cdot}6H_2O$ and $DyCl_3{\cdot}6H_2O$. All aforementioned samples were measured by Zeljko Ilic in 2020. The samples and the experimental conditions are described including the verification of the stoichiometry of the rare earth chlorides. In order to correct for possible interferences from (n,γ) neutron cature reactions the thermal and epithermal flux was determined experimentally, supported by numerical simulations to evaluate the neutron self-shielding and neutron moderation factors.

Finally, relative intensities and effective isotopic partial as well as elemental cross sections for the production of γ-rays induced by (n,n'γ), (n,pγ) and (n,$\alpha\gamma$) reactions are presented including comparisons with available literature data.

6.1 Sample description

Mass and thickness of the aforementioned samples as well as the corresponding irradiation and measurement times are given in Table 6.1.

Table 6.1: Irradiation conditions and parameters for the measurements of C, O, Cl, Ca, La, Ce, Pr, Nd, Sm, Tb and Dy. The parameters t_b and t_c denote the irradiation (real) and counting (live) times, respectively.

Sample[a]	Mass (g)	Element (g) (Atlas) [27]	Thickness (cm)		t_b (h)	t_c (h)
			d[b]	e[c]		
$CaCO_3$	2.402	Ca: 0.962 (11.3), C: 0.288 (9.6), O: 1.152 (17.7)	0.1	0.14	8.6	6.5
$(C_2H_3Cl)_n$	0.145	Cl: 0.082 (5.2), C: 0.056 (9.6)	0.02	0.028	17.0	15.4
$LaCl_3{\cdot}7H_2O$	1.514	La: 0.566 (18.1), Cl: 0.434, O: 0.457, H_2O: 34.0 wt%	0.4	0.57	13.1	10.9
$CeCl_3$	2.655	Ce: 1.509 (30.2), Cl: 1.146	0.5	0.71	3.4	2.7
$PrCl_3{\cdot}7H_2O$	1.486	Pr: 0.561 (9.2), Cl: 0.423, O: 0.446, H_2O: 33.8 wt%	0.4	0.57	7.6	6.3
$NdCl_3$	1.865	Nd: 1.074 (5.5), Cl: 0.792	0.3	0.42	3.1	2.5
$SmCl_3{\cdot}7H_2O$	1.880	Sm: 0.739 (4.3), Cl: 0.522, O: 0.550, H_2O: 32.9 wt%	0.4	0.57	3.6	2.8
$TbCl_3{\cdot}6H_2O$	2.049	Tb: 0.872 (1.7), Cl: 0.584, O: 0.527, H_2O: 29.0 wt%	0.6	0.85	9.7	7.7
$DyCl_3{\cdot}6H_2O$	1.865	Dy: 0.804 (9.4), Cl: 0.526, O: 0.475, H_2O: 28.7 wt%	0.5	0.71	3.1	2.5

[a] Demidov et al. irradiated other samples, mostly thin metal foils or oxides [27]
[b] maximum thickness estimated with a caliper, except for the $(C_2H_3Cl)_n$ foil (nominal thickness)
[c] effective thickness due to tilting of the sample by 45° relative to the neutron beam axis

The samples were irradiated as a powder conditioned in small PTFE bags, except

for the $(C_2H_3Cl)_n$ (Polyvinylchloride, PVC) sample (thin foil). Most of the rare earth (RE) chlorides contained crystal water. All samples were tilted by 45° with respect to the incident neutron beam axis.

6.1.1 Stoichiometry verification

Anhydrous RE chlorides are hygroscopic and hence tend to bound water molecules from the surrounding atmosphere. Samples that already contain water might further take up water molecules or release them, thereby changing the compound stoichiometry. Therefore, for the RE chlorides listed in Table 6.1 the composition was checked with the help of the $(C_2H_3Cl)_n$ sample as a reference by determining the mass of Cl based on a comparison of count rates from certain γ-rays induced by inelastic scattering.

For the (n,n'γ) reaction a linear dependency between count rate and mass can be reasonably assumed over a wide mass region due to the high penetration power of fast neutrons [141]. Consequently, for a given γ-line of energy E_γ, the ratio in the net count rate $\dot{C}_{E\gamma}(RE)$ from a RE chloride and $\dot{C}_{E\gamma}(PVC)$ from the PVC sample, respectively, must be in agreement with the ratio of the respective Cl amounts. Therefore, the experimental Cl mass ($m_{RE}(Cl)$) is expressed as:

$$m_{RE}(Cl) = \frac{\dot{C}_{E\gamma}(RE)}{\dot{C}_{E\gamma}(PVC)} \cdot m_{PVC}(Cl), \tag{6.1}$$

where RE denotes the respective RE chlorides and $m_{PVC}(Cl)$ is the Cl mass of the PVC sample (82 mg).

For the stoichiometry verification only interference-free γ-lines were used and if the value of a single line strongly disagreed with the trend of all other lines it was disregarded. The intense γ-lines at 1185, 1219, 1763, 2645, 2694, 3002, and 3163 keV from the ^{35}Cl(n,n'γ)^{35}Cl reaction as well as the lines at 3086 and 3103 keV from the ^{37}Cl(n,n'γ)^{37}Cl reaction were considered to check the amount of Cl in the RE chloride samples. Given the mass of Cl after Eq. (6.1), the number of water molecules n (degree of hydration) in a RE chloride sample can be expressed as:

$$n = \frac{\left(3 \cdot M(Cl) \cdot \frac{m_{sample}}{m_{RE}(Cl)}\right) - (M(RE) + 3 \cdot M(Cl))}{M(H_2O)}, \tag{6.2}$$

where M denotes molar masses and m_{sample} equals the sample masses provided in Table 6.1.

In Table 6.2 the procedure is exemplary shown for the terbium(III) hexahydrate chloride ($TbCl_3 \cdot 6H_2O$) sample. In this case, except the lines at 1219 and 3002 keV, all lines yield Cl masses and values of n close to that one from the nominal composition of the hexahydrate as given in Table 6.1. The line at 1219 keV might contain a small unidentified interference arising from Tb not listed in NuDat 3.0 [65, 158]. For the line at 3002 keV the positioning of the baseline of the fit might

be somewhat inaccurate. Neglecting the 1219-keV line, the average value of the Cl mass is (583.8 ± 11.5) mg and the average value for the degree of hydration is 6.0 ± 0.4, respectively.

Table 6.2: Verification of the stoichiometry for the $TbCl_3{\cdot}6H_2O$ sample.

E_γ	Reaction	$\dot{C}_{E\gamma}$ (s^{-1})		$m_{RE}(Cl)$	n
(keV)		PVC	$TbCl_3{\cdot}6H_2O$	(mg)	
1185	$^{35}Cl(n,n'\gamma)^{35}Cl$	0.036 ± 0.006	0.256 ± 0.025	580.1 ± 105.1	6.1 ± 1.1
1219	$^{35}Cl(n,n'\gamma)^{35}Cl$	0.827 ± 0.016	6.162 ± 0.031	612.9[a]± 12.0	5.0 ± 0.1
1763	$^{35}Cl(n,n'\gamma)^{35}Cl$	0.778 ± 0.009	5.622 ± 0.079	594.4 ± 11.0	5.6 ± 0.1
2646	$^{35}Cl(n,n'\gamma)^{35}Cl$	0.123 ± 0.005	0.885 ± 0.019	593.0 ± 26.8	5.7 ± 0.3
2694	$^{35}Cl(n,n'\gamma)^{35}Cl$	0.079 ± 0.005	0.561 ± 0.016	585.8 ± 39.0	5.9 ± 0.4
3002	$^{35}Cl(n,n'\gamma)^{35}Cl$	0.089 ± 0.019	0.608 ± 0.020	559.8[b]± 118.5	6.9 ± 1.5
3086	$^{37}Cl(n,n'\gamma)^{37}Cl$	0.051 ± 0.011	0.371 ± 0.017	597.0 ± 127.6	5.5 ± 1.2
3103	$^{37}Cl(n,n'\gamma)^{37}Cl$	0.050 ± 0.009	0.351 ± 0.013	574.9 ± 105.6	6.3 ± 1.2
3163	$^{35}Cl(n,n'\gamma)^{35}Cl$	0.064 ± 0.005	0.456 ± 0.023	585.7 ± 51.2	5.9 ± 0.5

E_γ is the γ-ray energy, $\dot{C}_{E\gamma}$ the net count rate, $m_{RE}(Cl)$ the experimental Cl mass calculated with Eq. (6.1) and n is the determined number of crystal water molecules calculated with Eq. (6.2)
[a]small interference arising from Tb not listed in NuDat 3.0 [65, 158] might be possible
[b]maybe imprecise peak fit

The result of the stoichiometry verification for all analyzed RE chloride samples is given in Table 6.3. Considering the uncertainties, the obtained masses show a good agreement with these from the assumed stoichiometries and number of crstal water molecules listed in Table 6.1. Furthermore, this example shows that analytics using a comparison with reference materials works. Therefore, analytics of small size samples can be performed using a comparison with references.

Table 6.3: Verification of the compound stoichiometry for all RE chloride samples.

Sample	E_γ(Cl) (keV)	$\overline{m_{RE}}(Cl)$ (mg)	$\bar{n}$
La$Cl_3{\cdot}7H_2O$	1185, 2646, 2694, 3002, 3086, 3103	430 ± 20	7.2 ± 1.0
CeCl_3	2645, 3002	1146 ± 5	0 ± 0.1
Pr$Cl_3{\cdot}7H_2O$	1185, 2645, 3002	430 ± 10	6.7 ± 0.5
NdCl_3	1185, 1763, 2645, 3002, 3086	792 ± 4	0 ± 0.1
Sm$Cl_3{\cdot}7H_2O$	1184, 1764, 2646, 3002, 3086, 3103	530 ± 11	6.7 ± 0.4
Tb$Cl_3{\cdot}6H_2O$	1185, 1763, 2645, 2694, 3002, 3085, 3103, 3163	584 ± 11	6.0 ± 0.4
Dy$Cl_3{\cdot}6H_2O$	1763, 2645, 3002, 3085, 3103, 3163	533 ± 8	5.7 ± 0.3

E_γ is the γ-ray energy of considered Cl lines, $\overline{m_{RE}}(Cl)$ is the average experimental Cl mass calculated with Eq. (6.1) and $\bar{n}$ the average number of crystal water molecules determined with Eq. (6.2). The γ-ray energies slightly deviate from measurement to measurement as evident from the measured spectra (see Appx. G)

6.2 Experimental flux reconstruction

As evident from the recorded γ-ray spectra of the RE elements, given in Appx. G, several lines from (n,γ) reactions in Cl and the respective RE elements were identified. Presence of those lines is mostly attributed to the thermal, and especially the epithermal, neutron-flux component in the spectrum at sample position. With respect to data provided in [132, 133] and [65], many lines from (n,n'γ) reactions were potentially interfered. In addition, the thermal and epithermal neutron-flux values could differ compared to these ones assumed in [20, 21], since neutron moderation is enabled by the composition of the new MLC. Therefore, as a modification of the neutron-energy spectrum was considered as possible and suspicious, the thermal and epithermal neutron fluxes were checked. This flux reconstruction was based on the measurement of $TbCl_3 \cdot 6H_2O$, as the corresponding γ-ray spectrum, shown in Appx. G.8, contains a multitude of prompt lines from the $^{35}Cl(n,\gamma)^{36}Cl$ and the $^{159}Tb(n,\gamma)^{160}Tb$ reactions, mostly with reasonable counting statistics.

The absolute intensity of aforementioned γ-rays was determined (denoted as $I_{E\gamma}(exp)$, hereafter) and compared to data given in [132] (denoted as $I_{E\gamma}(th)$). Taking the γ-ray self-absorption correction curve as given in Appx. A.5 and neglecting the neutron self-shielding factor for a total neutron flux of $(1.15 \pm 0.04) \times 10^8$ cm^{-2} s^{-1}, the intensities were obtained by division of the effective isotopic partial γ-ray production cross sections calculated after Eq. (4.1) and the value of the effective cross section for the $^{159}Tb(n,\gamma)^{160}Tb$ reaction obtained with NJOY, i.e. (413 ± 47) mb. The resulting intensity ratios are depicted in Fig. 6.1.

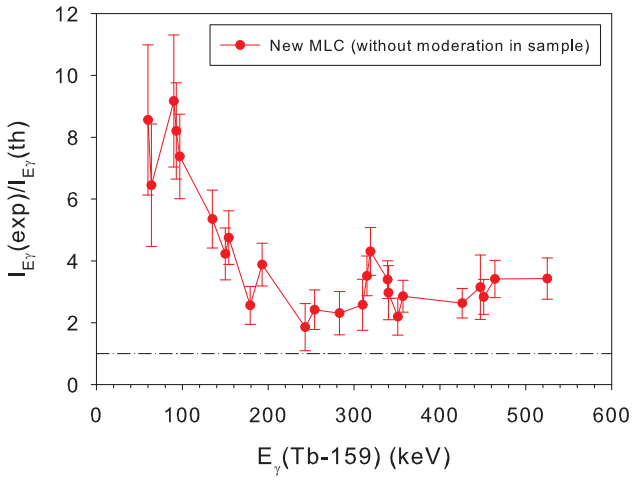


Figure 6.1: Ratio between absolute γ-ray intensities for prompt lines of the $^{159}Tb(n,\gamma)^{160}Tb$ reaction observed in this work ($I_{E\gamma}(exp)$) compared to [132] ($I_{E\gamma}(th)$). The neutron-energy spectrum assumed in [20, 21] (red curve in Fig. 5.11) is used with a total neutron flux of $(1.15 \pm 0.04) \times 10^8$ cm^{-2} s^{-1}.

Obviously, a strong disagreement in intensity was found, with an average ratio

of 4.3 ± 2.2 over all γ-lines. In addition, at γ-ray energies approximately below 200 keV the observed discrepancy increases further. This might be reasoned in either poor counting statistics or unidentified interferences.

Assuming that the intensities derived with [132] are correct, this disagreement might be the result of either sample- **(i) internal** or **(ii) external**, or both, neutron-energy spectrum modifications: first of all **(i)**, since the $TbCl_3{\cdot}6H_2O$ sample contains approximately 29 wt% water (see Table 6.1), internal neutron moderation effects are possible. Secondly **(ii)**, the constitution of the new MLC might lead to an external modification of the spectrum outside the sample.

The moderation was investigated numerically with MCNP6 as described within Chapter 4. Hence, each neutron-energy range, i.e. thermal, epithermal and fast, was considered separately. Therefore, effective isotopic partial γ-ray production cross sections were calculated with Eqs. (4.3) and (4.26) instead of Eqs. (4.1) and (4.3). For the further calculation of intensities, the effective isotopic partial cross sections were estimated as following:

$$\langle \sigma_{E\gamma} \rangle = \sum_{i=1}^{3} \frac{\Phi_i}{\Phi_{tot}} \cdot \langle \sigma^i_{E\gamma} \rangle, \tag{6.3}$$

where $\langle \sigma^i_{E\gamma} \rangle$ represents the effective isotopic partial γ-ray production cross section for thermal (i= 1), epithermal (i= 2) and fast (i= 3) neutrons. Φ_i is the neutron flux in the considered neutron-energy range and Φ_{tot} the total neutron flux (i.e. from 10^{-10} to 20 MeV).

6.2.1 Neutron self-shielding factors

As pointed out in Chapter 4, Eqs. (4.16) and (4.17) are invalid to estimate the neutron self-shielding for the case of a neutron-energy distribution. Therefore, for the RE chloride samples the values of f_n were derived from simulations as described within Chapter 4. Simulation details can be found in Appx. K.3.

A quadratic surface area S of the powder samples was assumed and calculated:

$$S = a^2 = \frac{m}{\rho \cdot d}, \tag{6.4}$$

where m is the sample mass given in Table 6.1, ρ the sample density given in Table 6.4 and d the estimated thickness.

As the samples were tilted by 45° along beam direction (Z-axis), the horizontal sample width perpendicular to that direction (i.e. X-axis) changes from a to d^*_x:

$$d^*_x = cos(45°) \cdot d + sin(45°) \cdot a. \tag{6.5}$$

Using the value of d^*_x instead of a for the definition of the neutron beam profile ensured complete irradiation of the sample surfaces in the simulations. The value

of d_x^* was confirmed by visual inspection of the geometry in the MCNP6 geometry plotter. For each RE chloride sample listed in Table 6.1, neutron self-shielding factors were derived for thermal, epithermal and fast neutrons. The obtained values are given in Table 6.4. A total of 10^8 primary source neutrons in each simulation was found to yield values with negligible uncertainties below 0.01%.

Table 6.4: Neutron self-shielding factors f_n derived with MCNP6 simulations for the measurement of the RE chloride samples. S is the quadratic surface area calculated after Eq. (6.4) and d_x^* the effective thickness horizontal and perpendicular (X-axis) to the neutron beam axis (Z-axis) determined after Eq. (6.5).

Sample	ρ	S	d_x^*	Neutron self-shielding factors f_n		
	(g cm^{-3})	(cm^2)	(cm)	Thermal	Epithermal	Fast
La$Cl_3 \cdot 7H_2O$	2.23	1.70	1.20	0.981	1.070	1.014
CeCl_3	3.97	1.34	1.17	0.798	1.010	1.006
Pr$Cl_3 \cdot 7H_2O$	2.25	1.65	1.19	0.976	1.069	1.014
NdCl_3	4.13	1.51	1.08	0.813	1.024	1.010
Sm$Cl_3 \cdot 7H_2O$	2.38	2.10	1.31	0.083	1.053	1.017
Tb$Cl_3 \cdot 6H_2O$	4.35	0.79	1.05	0.772	0.976	0.991
Dy$Cl_3 \cdot 6H_2O$	2.56	1.21	1.21	0.444	1.020	1.008

In general, scattering increases the value of f_n whereas capture reduces it. Therefore, the value of f_n behaves proportional to the ratio of the effective macroscopic scattering cross section and the macroscopic absorption cross section to the total macroscopic cross section, i.e. $\langle\Sigma_s\rangle/\langle\Sigma_t\rangle$ and $\langle\Sigma_a\rangle/\langle\Sigma_t\rangle$, respectively. As the value of $\langle\Sigma_a\rangle$ increases with decreasing neutron energy, the self-shielding factors are lowest for thermal neutrons. Except for the $TbCl_3 \cdot 6H_2O$ sample, the self-shielding factors of epithermal neutrons are slightly higher than those of fast neutrons. This observation is in agreement with the values of effective macroscopic cross sections provided in Appx. E.1 and, in fact, it is related to resonances of elastic scattering reactions. Besides the $SmCl_3 \cdot 7H_2O$ and $DyCl_3 \cdot 6H_2O$ samples with f_n values of 0.083 and 0.444, respectively, the self-shielding of thermal neutrons is relatively moderate. Actually, the high self-shielding for thermal neutrons in the aforementioned samples is reasoned in extraordinary large cross sections of (68,250 ± 557) b and (2,619 ± 2) b for the $^{149}Sm(n,\gamma)^{150}Sm$ and $^{164}Dy(n,\gamma)^{165}Dy$ reactions, respectively. Strong self-shielding of thermal neutrons is also reflected in the amount of produced capture γ-rays and interferences with lines arising from inelastic scattering.

6.2.2 Moderation factors

Neutron moderation effects are not negligible for the RE chloride samples due to the presence of crystal water. The moderation factors for thermal and epithermal neutrons, calculated according to Eqs. (4.22) and (4.23), are given in Table 6.5.

Table 6.5: Moderation factors derived with MCNP6 for the measurements of La, Pr, Sm, Dy and Tb. S is the quadratic surface area calculated after Eq. (6.4) and d_x^* the effective thickness horizontal and perpendicular (X-axis) to the neutron beam axis (Z-axis) determined after Eq. (6.5).

Sample	S (cm^2)	d_x^* (cm)	Moderation factors f_{mod}	
			Thermal	Epithermal
La$Cl_3 \cdot 7H_2O$	1.70	1.20	6.15 ± 2.78	1.59 ± 0.28
Pr$Cl_3 \cdot 7H_2O$	1.65	1.19	6.10 ± 2.76	1.59 ± 0.28
Sm$Cl_3 \cdot 7H_2O$	2.10	1.31	6.30 ± 2.82	1.62 ± 0.29
Tb$Cl_3 \cdot 6H_2O$	0.79	1.05	14.01 ± 6.32	2.12 ± 0.39
Dy$Cl_3 \cdot 6H_2O$	1.21	1.21	7.33 ± 3.21	1.73 ± 0.32

The f_{mod} factors depend strongly on the sample thickness. The $LaCl_3 \cdot 7H_2O$, $PrCl_3 \cdot 7H_2O$ and $SmCl_3 \cdot 7H_2O$ samples have an effective thickness of 0.57 cm and their corresponding f_{mod} values are very similar. The $DyCl_3 \cdot 6H_2O$ sample has a higher thickness of 0.71 cm and also higher values of f_{mod}. The thickest sample, i.e. $TbCl_3 \cdot 6H_2O$ with 0.85 cm, yields the highest moderation factors. However, the moderation factor for thermal neutrons is about twice that one of the other samples. This is reasoned in the large macroscopic scattering cross sections of the $TbCl_3 \cdot 6H_2O$ sample compared to the other samples (see Appx. E.1).

Consideration of the neutron self-shielding and moderation factors results in an improved ratio of intensities for the ^{159}Tb(n,γ)^{160}Tb reaction, as depicted in Fig. 6.2. However, an average intensity ratio of 2.6 ± 1.3 still shows a significant discrepancy. This implies a sample-external flux modification induced by the new MLC.

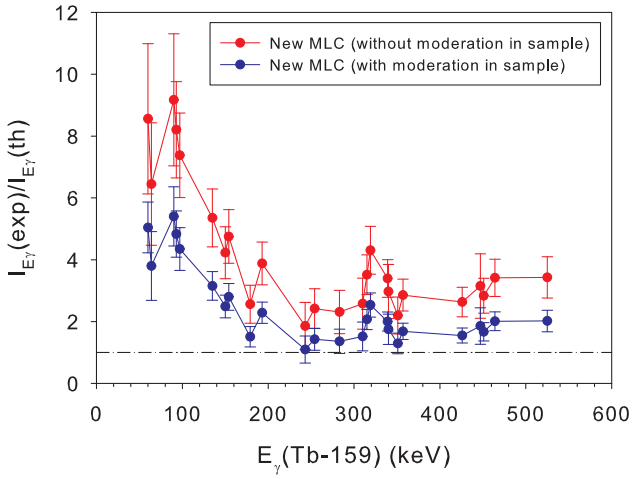


Figure 6.2: Ratio between absolute γ-ray intensities for prompt lines of the ^{159}Tb(n,γ)^{160}Tb reaction observed in this work ($I_{E\gamma}(exp)$) compared to [132] ($I_{E\gamma}(th)$). The neutron-energy spectrum assumed in [20, 21] (red curve in Fig. 5.11) is used. For the shown blue curve, in addition, self-shielding and moderation factors are considered and cross sections are calculated after Eqs. (4.26) and (6.3).

6.2.3 Neutron flux

As consideration of sample-internal moderation alone was insufficient to explain the observed discrepancy in γ-ray intensity depicted in Figs. 6.1 and 6.2, the neutron-energy spectrum was reconstructed in the thermal and epithermal energy region. This problem was solved in a semi-experimental way exploiting γ-lines from the ^{159}Tb(n,γ)^{160}Tb and ^{35}Cl(n,γ)^{36}Cl reactions. The major assumption of the used method is that the shape of the spectrum in the three considered neutron-energy ranges remains unchanged, i.e. only the absolute flux values change. With that being said, the total counts for a γ-ray peak are expressed as:

$$P_{tot} = P_{th} + P_{epi} + P_{fast}, \tag{6.6}$$

where P_{th}, P_{epi} and P_{fast} are the net counts induced by thermal, epithermal and fast neutrons, respectively, depending on the reaction rates, i.e. Eq. (2.16). For any γ-line used in the approach above, the net counts were first of all corrected for the contribution of the fast neutrons using a flux of 1.13 $\times$ 10^8 cm^{-2} s^{-1} and the effective cross sections provided in Appx. C. The remaining amount of counts was distributed between thermal and epithermal neutrons, depending on their effective reaction cross sections and reaction rates. Since the thermal and epithermal cross sections of the ^{159}Tb(n,γ)^{160}Tb reaction are approximately equal but the thermal flux is about four orders of magnitude less than the epithermal flux, one can reasonably neglect the contribution of thermal neutrons in the case of Tb. Therefore, the epithermal neutron flux was deduced directly from the lines of ^{159}Tb as:

$$\Phi_{epi} = \frac{m_{Tb} \cdot N_A \cdot h_{Tb-159} \cdot \epsilon_{E\gamma} \cdot t_c \cdot f_{E\gamma} \cdot I_{E\gamma}}{M_{Tb}} \cdot \frac{P_{tot} - P_{fast}}{\langle \sigma_{epi}^{Tb} \rangle \cdot f_{n,epi} \cdot f_{mod,epi}}, \tag{6.7}$$

where m_{Tb} is the mass of Tb in the $TbCl_3{\cdot}6H_2O$ sample, h_{Tb-159} the abundance of ^{159}Tb and M_{Tb} the molar mass of Tb. As Figs. 6.1 and 6.2 imply an increase in the intensity mismatch towards lower γ-ray energies, however, only the main neutron capture γs at 193, 243, 339, 357, 451, 464 and 525 keV were considered. These γ-rays yielded an average value of Φ_{epi}= (2.94 $\pm$ 0.77) $\times$ 10^6 cm^{-2} s^{-1} at sample position.

With the redetermined epithermal neutron flux after Eq. (6.7) the net counts produced by epithermal neutrons can be estimated according to Eqs. (4.1) and (4.3). Correction of the contribution of epithermal neutrons in γ-lines from Cl related to the ^{35}Cl(n,γ)^{36}Cl reaction allows to deduce the thermal neutron flux at sample position as:

$$\Phi_{th} = \frac{m_{Cl} \cdot N_A \cdot h_{Cl-35} \cdot \epsilon_{E\gamma} \cdot t_c \cdot f_{E\gamma} \cdot I_{E\gamma}}{M_{Cl}} \cdot \frac{P_{tot} - P_{fast} - P_{epi}}{\langle \sigma_{th}^{Cl} \rangle \cdot f_{n,th} \cdot f_{mod,th}}. \tag{6.8}$$

Using the intense lines at 1164, 1951 and 1959 keV of ^{35}Cl an average thermal

neutron flux of Φ_{th}= (3.16 ± 1.28) × 10^3 cm^{-2} s^{-1} was determined.

Comparison of the redetermined neutron-flux values with those assumed in a previous work [20, 21] yielded flux-scaling factors, by which the flux in each neutron-energy bin of the considered energy region has to be scaled. Factors of 4.14 ± 2.16 and 1.96 ± 0.57 were derived for the thermal and epithermal energy range.

The initially assumed spectrum as given in Chapter 5, the spectrum reconstructed within this chapter as well as the volume-averaged sample flux obtained from the MCNP6 simulations for the $TbCl_3 \cdot 6H_2O$ sample are depicted in Fig. 6.3.

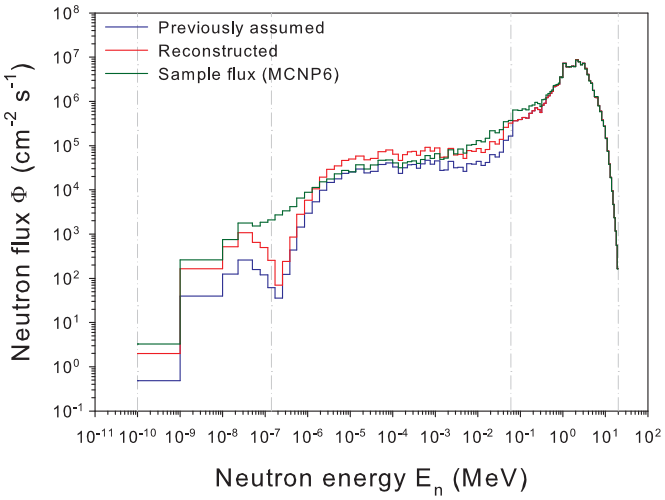


Figure 6.3: Neutron-energy spectrum of FaNGaS at sample position as assumed in Chapter 5, i.e. Fig. 5.11, the version reconstructed in this chapter (red curve) and the volume-averaged sample flux derived from MCNP6 (green curve).

Neglection of the f_n and f_{mod} factors in Eqs. (6.7) and (6.8) corresponds to experimental sample flux values Φ_s. A value of $\Phi_{s,th}$= (3.41 ± 1.38) × 10^4 cm^{-2} s^{-1} for the thermal and a value of $\Phi_{s,epi}$= (6.09 ± 1.61) × 10^6 cm^{-2} s^{-1} for the epithermal neutrons, respectively, was obtained. The corresponding sample flux values from the integral simulation (10^{-10} MeV ≤ E_n ≤ 20 MeV) in MCNP6 were (8.27 ± 2.54) × 10^3 cm^{-2} s^{-1} and (3.17 ± 0.43) × 10^6 cm^{-2} s^{-1} for the thermal and epithermal neutrons, respectively. As the experimental sample fluxes are higher than those from MCNP6, this is another proof for the external flux modification. In fact, this implies consistency of the simulations with respect to each other and the experimental data, since the ratios between the experimental and numerical sample flux values approximately equal the derived flux-scaling factors.

6.2.4 Flux validation

The determination of absolute radiative neutron capture γ-ray intensities of ^{159}Tb with the reconstructed epithermal neutron flux using Eqs. (4.1), (4.3) and (6.3) leads to reasonable agreement compared to data given in [132], as shown in Fig.

6.4. The average value of the absolute intensity ratios, considering all (n,γ) lines marked in Appx. G.8, is 1.4 $\pm$ 0.7. Consideration of only those lines used for the flux reconstruction process given above yields now an average value of 1.0 $\pm$ 0.2.

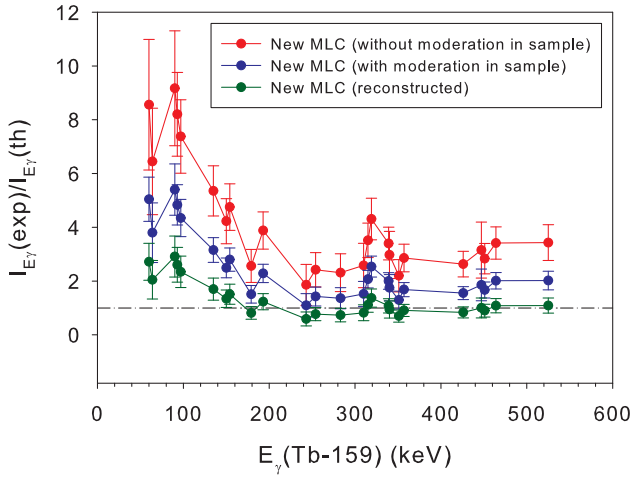


Figure 6.4: Ratio between absolute γ-ray intensities for lines of the ^{159}Tb(n,γ)^{160}Tb reaction observed in this work ($I_{E\gamma}(exp)$) compared to [132] ($I_{E\gamma}(th)$). The neutron-energy spectrum assumed in [20, 21] (red curve in Fig. 5.11) is used for the red and blue curves. In addition, the green curve corresponds to the reconstructed neutron spectrum.

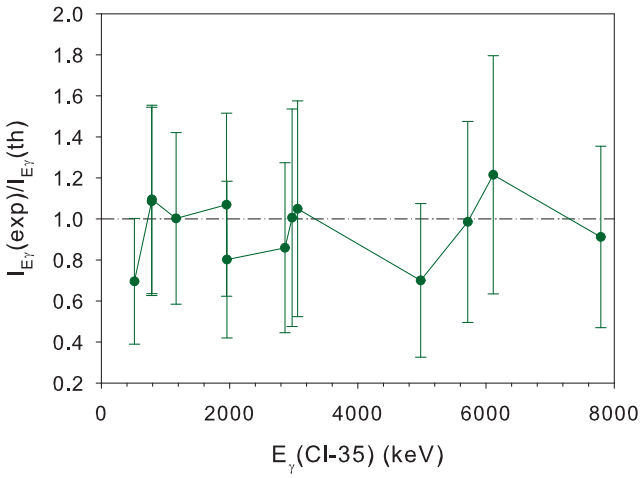


Figure 6.5: Ratio between absolute γ-ray intensities for lines of the ^{35}Cl(n,γ)^{36}Cl reaction observed in this work ($I_{E\gamma}(exp)$) compared to [132] ($I_{E\gamma}(th)$). The neutron-energy spectrum reconstructed within this work is used.

In addition, Fig. 6.5 shows the corresponding intensity ratios for all observed γ-lines from the ^{35}Cl(n,γ)^{36}Cl reaction, as marked in Appx. G.8. Besides the large uncertainties, the average value of 1.0 $\pm$ 0.2 indicates a good agreement, thereby confirming the reconstructed neutron-energy spectrum.

Except for the acquired $TbCl_3 \cdot 6H_2O$ spectrum, γ-rays from (n,γ) reactions attributed to other RE elements were relatively rarely observed. However, presence of certain lines from those elements in the measurements of $SmCl_3 \cdot 7H_2O$, $LaCl_3 \cdot 7H_2O$, $PrCl_3 \cdot 7H_2O$ and $DyCl_3 \cdot 6H_2O$ was exploited to verify the reconstructed spectrum.

Capture lines of ^{150}Sm, ^{152}Sm and ^{154}Sm

The measurement of the $SmCl_3 \cdot 7H_2O$ sample was used to check the incident thermal and epithermal neutron flux at sample position with a delayed γ-line detected at 104.2 keV (see Appx. G.7). According to [132], this line belongs to ^{154}Sm ($t_{1/2}$= 22.3 min) with an intensity of 75.7%. However, with respect to [159] this line contains a contribution of ^{153}Sm due to the neutron capture in ^{152}Sm. The isotope ^{153}Sm decays via β^- decay with a half-life of 46.3 h accompanied by emission of a 103.18-keV line ($I_{E\gamma}$= 30% [159]).

As the effectice reaction cross sections of both considered Sm isotopes are in the same order of magnitude for epithermal and thermal neutrons (see Appx. C.2), respectively, and in view of a thermal neutron self-shielding factor of 0.083 given in Table 6.4, one can reasonably neglect the contribution of latter ones.

In the case of γ-lines fed by the decay of two isotopes, mainly produced by epithermal and fast neutrons, the epithermal neutron flux at sample position can be expressed as:

$$\Phi_{epi} = \frac{m_{Sm} \cdot N_A \cdot \epsilon_{E\gamma} \cdot f_{E\gamma}}{M_{Sm}} \cdot \frac{P_{tot} - P_{fast}}{f_{n,epi} \cdot f_{mod,epi}} \cdot \frac{1}{\sum_{i=1}^{2} h_i \cdot \langle \sigma_{epi}^i \rangle \cdot g(t_b, t_c, t_{1/2})_i \cdot I_{E\gamma}^i}, \tag{6.9}$$

where i=1 refers to ^{152}Sm and i=2 to ^{154}Sm, respectively, and $g(t_b, t_c, t_{1/2})$ is the effective counting time according to Eq. (4.2).

A determined epithermal neutron-flux value of Φ_{epi}= (3.43 ± 1.04) × 10^6 cm^{-2} s^{-1} is in good agreement with the value derived from the $TbCl_3 \cdot 6H_2O$ spectrum, taking into account also the large uncertainties.

In addition to the delayed line, another 14 prompt γ-lines associated to the isotopes ^{150}Sm and ^{152}Sm were observed. For these, the effective isotopic partial γ-ray production cross sections ($\langle \sigma_{E\gamma} \rangle$) using Eqs. (4.1) and (6.3) were calculated and given in Table 6.6. They are compared to thermal neutron data from [132, 133] using the value of Φ_{epi} obtained from the $TbCl_3 \cdot 6H_2O$ measurement.

With sample-specific contributions of 90.2 and 98.9% of epithermal neutrons to the total (n,γ) reaction rate in ^{150}Sm and ^{152}Sm (see Appx. F.2), respectively, the detected γ-rays at 167.8 and 35.6 keV confirm the determined epithermal neutron flux. For all remaining lines listed in Table 6.6, however, the derived intensities are systematically lower compared to those in [132, 133] by about a factor of three, i.e. an intensity ratio of 0.30 ± 0.06. As the validity of the determined epithermal

neutron flux was proven with the delayed line already, two reasons could explain this observation: first of all **(i)**, the capture lines from levels in the produced ^{153}Sm isotope might be interfered by (n,n'γ) lines from other Sm isotopes. Except for the γ-rays above 5 MeV, this might be possible with respect to data in [65]. However, a relatively equal contribution of inelastic scattering as would be implied by all lines is considered as unlikely. Therefore, secondly **(ii)** the high resonance nature of Sm could result in different excitations induced by epithermal and thermal neutrons, respectively. In fact, this possibility was already mentioned by Demidov et al. [27].

Table 6.6: Effective isotopic partial γ-ray production cross sections for identified neutron capture γ-rays of ^{150}Sm and ^{152}Sm.

^{A}Z	E_γ (keV)		$P_{E\gamma}(90°)/$	$\langle\sigma_{E\gamma}\rangle$		$I_{E\gamma}$(This work)/
	This work	Refs. [132, 133]	$(\epsilon_{E\gamma} \times f_{E\gamma})$ $\times 10^{-8}$(count)	This work (mb)	Refs. [132, 133] (b)	$I_{E\gamma}$(Refs. [132, 133])
^{150}Sm	167.8	167.8 + 168.4	0.28 ± 0.01	68 ± 30	11.7 ± 3.4	1.11 ± 0.59
^{152}Sm	35.6	35.6 + 35.8 + 36.4	3.87 ± 0.61	244 ± 68	14.7 ± 5.9	1.03 ± 0.51
^{152}Sm	90.9	90.8 + 90.9 + 91.5	0.57 ± 0.08	36 ± 19	8.1 ± 3.0	0.27 ± 0.18
^{152}Sm	127.2	127.3	1.08 ± 0.04	68 ± 35	15.3 ± 1.1	0.28 ± 0.14
^{152}Sm	182.7	182.5 + 182.9	0.28 ± 0.03	17.4 ± 9.0	3.53 ± 1.12	0.31 ± 0.19
^{152}Sm	354.1	354.8	0.21 ± 0.02	13.0 ± 6.9	2.36 ± 0.41	0.34 ± 0.19
^{152}Sm	470.1	470.8	0.33 ± 0.05	21.1 ± 11.2	4.34 ± 0.79	0.30 ± 0.17
^{152}Sm	473.0	473.6	0.43 ± 0.07	27.4 ± 14.3	5.20 ± 0.93	0.33 ± 0.18
^{152}Sm	622.3	622.7	0.35 ± 0.04	22.2 ± 12.0	3.29 ± 0.82	0.42 ± 0.25
^{152}Sm	659.2	660.0	0.35 ± 0.04	22.3 ± 11.4	4.82 ± 0.86	0.29 ± 0.16
^{152}Sm	734.5	734.9	0.25 ± 0.03	15.7 ± 8.2	3.81 ± 0.75	0.26 ± 0.14
^{152}Sm	5238.2	5238.1	0.11 ± 0.01	6.94 ± 3.91	2.36 ± 0.41	0.18 ± 0.11
^{152}Sm	5740.7	5741.0	0.53 ± 0.13	34 ± 17	10.1 ± 1.9	0.21 ± 0.11
^{152}Sm	5831.5	5832.4	0.22 ± 0.02	14.1 ± 7.3	2.28 ± 0.41	0.38 ± 0.21

E_γ is the γ-ray energy, $P_{E\gamma}(90°)/(\epsilon_{E\gamma} \times f_{E\gamma})$ the net counts in the γ-ray peak divided by the full-energy-peak (FEP) efficiency and the γ-ray self-absorption factor, $\langle\sigma_{E\gamma}\rangle$ the effective isotopic partial cross section for γ-ray production calculated after Eqs. (4.1) and (6.3) and $I_{E\gamma}$ the absolute intensity of the γ-rays determined with Eq. (4.3)

Capture lines of ^{139}La

The measurement of the $LaCl_3 \cdot 7H_2O$ sample revealed several prompt and delayed γ-lines from the ^{139}La(n,γ)^{140}La reaction, as marked in the measured spectrum (see Appx. G.3.). For the identified 12 lines, Table 6.7 gives the values of $\langle\sigma_{E\gamma}\rangle$ calculated with Eqs. (4.1), (4.2) and (6.3). With 75.7% reaction rate of epithermal and 19.8% reaction rate of fast neutrons (see Appx. F.2), the contribution of thermal neutrons is negligible.

Generally, the absolute intensity of delayed γ-rays only depends on the physical half-life of the nuclide and the irradation time. Therefore, a found intensity ratio between this work and [132] close to one for the intense decay line at 487.3 keV ($I_{E\gamma}$= 30.9% [132]) confirms the incident epithermal neutron flux of Φ_{epi}= (2.94 ± 0.77) × 10^6 cm^{-2} s^{-1}. The disagreement for the line at 814.6 keV is unexpected. In fact, however, it implies an unidentified interference.

Table 6.7: Effective isotopic partial γ-ray production cross sections for identified neutron capture γ-rays of ^{139}La.

E_γ (keV)		$P_{E\gamma}(90°)/$	$\langle\sigma_{E\gamma}\rangle$		$I_{E\gamma}$(This work)/
This work	Ref. [132]	$(\epsilon_{E\gamma} \times f_{E\gamma})$ $\times 10^{-8}$(count)	This work (mb)	Ref. [132] (b)	$I_{E\gamma}$(Ref. [132])
155.2	155.6	0.20 ± 0.05	1.14 ± 0.46	0.192 ± 0.007	2.50 ± 1.05
218.1	218.3	0.46 ± 0.06	2.66 ± 0.99	0.78 ± 0.03	1.43 ± 0.60
235.2	235.8	0.21 ± 0.04	1.19 ± 0.47	0.111 ± 0.004	4.51 ± 1.84
237.3	237.7	0.28 ± 0.05	1.63 ± 0.62	0.320 ± 0.012	2.14 ± 1.16
287.9	288.3	0.40 ± 0.04	2.31 ± 0.85	0.73 ± 0.03	1.33 ± 0.57
487.3d[a]	487.0d	0.12 ± 0.03	6.86 ± 1.35	2.79 ± 0.04	1.03 ± 0.24
548.6	549.0	0.32 ± 0.04	1.83 ± 0.68	0.098 ± 0.004	7.83 ± 3.06
657.4	658.3	0.32 ± 0.06	1.83 ± 0.72	0.103 ± 0.004	7.47 ± 3.55
814.6d	815.8d	0.16 ± 0.04	8.71 ± 1.72	1.430 ± 0.012	2.56 ± 0.90
890.5	892.3	0.43 ± 0.04	24 ± 5[b]	0.033 ± 0.010	301 ± 69
4842.2	4842.7	0.39 ± 0.04	2.24 ± 0.83	0.661 ± 0.025	1.43 ± 0.55
5130.6	5130.9	0.21 ± 0.04	1.19 ± 0.47	0.0159 ± 0.0009	32 ± 15

E_γ is the γ-ray energy, $P_{E\gamma}(90°)/(\epsilon_{E\gamma} \times f_{E\gamma})$ the net counts in the γ-ray peak divided by the full-energy-peak (FEP) efficiency and the γ-ray self-absorption factor, $\langle\sigma_{E_\gamma}\rangle$ the effective isotopic partial cross section for γ-ray production calculated after Eqs. (4.1), (4.2) and (6.3) and $I_{E\gamma}$ the absolute intensity of the γ-rays determined with Eq. (4.3)
[a]corrected for a strong background interference (61% of net counts)
[b]value taken from [160]

Besides the decay lines, only for the most intense prompt lines at 218.1, 287.9 and 4842.2 keV an acceptable agreement in intensity was found, considering also the large uncertainties. However, the fact that there is no systematic deviation evident from Table 6.7, in contrast to Table 6.6, does not imply a wrong value of the epithermal neutron flux. Instead, it rather indicates that the absolute intensities for thermal neutron capture reactions as extracted from [132] are not always justified in the case of La for epithermal and fast neutrons. This hypothesis is supported by the clear presence of the lines at 890.5 and 5130.6 keV, which should be much less in intensity compared to [132, 160]. In fact, if the thermal radiative neutron capture intensities in [132, 160] are correct one would not expect lines with relevant counting statistics at those energies. In addition, based on the intensities derived from [132] it is unexpected and unclear why certain lines, e.g. those listed at 422.7 and 722.6 keV in [132], were not observed in the measured spectrum. As pointed out in [36], the actual intensity strongly depends on the nuclear properties of the transition such as multipolarity, spin, parity and angular momentum.

Capture lines of ^{141}Pr

Four prompt lines from ^{141}Pr(n,γ)^{142}Pr were observed in the $PrCl_3 \cdot 7H_2O$ spectrum (see Appx. G.5). The corresponding values of $\langle\sigma_{E\gamma}\rangle$ are listed in Table 6.8 with respect to [132]. Contributions of 2.4% for thermal, 75.9% for epithermal and 21.7% for fast neutrons were derived for the (n,γ) reaction in ^{141}Pr (see Appx. F.2).

For the lines at 126.7, 176.9 and 182.4 keV the intensities agree reasonably with [132] when considering the large uncertainties, hence confirming the incident epithermal neutron flux determined with the $TbCl_3{\cdot}6H_2O$ spectrum. For the line at 644.9 keV it is unclear why the discrepancy is higher than a factor of two. Besides an unidentified interference, use of γ-ray intensities taken from [132] might not be justified for this transition induced by epithermal and fast neutrons.

Table 6.8: Effective isotopic partial γ-ray production cross sections for identified neutron capture γ-rays of ^{141}Pr.

E_γ (keV)		$P_{E\gamma}(90°)/$	$\langle\sigma_{E\gamma}\rangle$		$I_{E\gamma}$(This work)/
This work	Ref. [132]	$(\epsilon_{E\gamma} \times f_{E\gamma})$ $\times 10^{-8}$(count)	This work (mb)	Ref. [132] (b)	$I_{E\gamma}$(Ref. [132])
126.7	126.8	0.18 ± 0.02	1.98 ± 0.71	0.307 ± 0.015	1.42 ± 0.52
176.9[a]	176.9	0.49 ± 0.11	6.02 ± 2.35	1.06 ± 0.04	1.26 ± 0.49
182.4[b]	182.8	0.23 ± 0.08	2.75 ± 1.21	0.377 ± 0.014	1.61 ± 0.71
644.9	645.7	0.14 ± 0.02	3.24 ± 1.19	0.311 ± 0.007	2.31 ± 0.85

E_γ is the γ-ray energy, $P_{E\gamma}(90°)/(\epsilon_{E\gamma} \times f_{E\gamma})$ the net counts in the γ-ray peak divided by the full-energy-peak (FEP) efficiency and the γ-ray self-absorption factor, $\langle\sigma_{E_\gamma}\rangle$ the effective isotopic partial cross section for γ-ray production calculated after Eqs. (4.1) and (6.3) and $I_{E\gamma}$ the absolute intensity of the γ-rays determined with Eq. (4.3)
[a]corrected for a strong background interference (37.9% of net counts)
[b]corrected for a strong background interference (40.7% of net counts)

Capture lines of ^{161}Dy, ^{162}Dy and ^{164}Dy

A total of 12 prompt lines were identified in the $DyCl_3{\cdot}6H_2O$ spectrum (see Appx. G.9): 4 from the ^{161}Dy(n,γ)^{162}Dy, 6 from the ^{162}Dy(n,γ)^{163}Dy and two from the ^{164}Dy(n,γ)^{165}Dy reaction, respectively. The values of $\langle\sigma_{E\gamma}\rangle$ are given in Table 6.9.

Besides the large uncertainties, the agreement for the lines at 5216.5 and 5450.1 keV is very good compared to [132, 133]. As 93.8 and 98.4% of the counts from radiative neutron capture in ^{161}Dy and ^{162}Dy (see Appx. F.2), respectively, are due to interactions of epithermal neutrons, this is considered as another verification for the epithermal neutron-flux value extracted from the $TbCl_3{\cdot}6H_2O$ spectrum.

For the lines at 5557.0 and 5606.3 keV from ^{164}Dy the determined intensities rather disagree with [132]. As 48.2% of the reaction rate comes from thermal neutrons (see Appx. F.2), this might imply inaccurate determination of the thermal neutron flux. In fact, self-shielding and moderation processes are much more sensitive with regard to the sample thickness as for the epithermal neutrons.

The line observed at 5216.5 keV is not listed in [132] but could correspond to a line at 5215.3 keV listed in [133], associated to the ^{162}Dy(n,γ)^{163}Dy reaction. Besides the fact that the lines below 1 MeV have rather large counting uncertainties, the intensity ratios fluctucate a lot. This might imply that thermal radiative neutron capture intensities derived from [132] are not correct for those transitions due to the strong resonances of Dy.

Table 6.9: Effective isotopic partial γ-ray production cross sections for identified capture γ-rays of ^{161}Dy, ^{162}Dy and ^{164}Dy.

^{Z}A	E_γ (keV)		$P_{E\gamma}(90°)/$	$\langle\sigma_{E\gamma}\rangle$		$I_{E\gamma}$(This work)/
	This work	Ref. [132, 133]	$(\epsilon_{E\gamma} \times f_{E\gamma})$ $\times 10^{-8}$(count)	This work (mb)	Ref. [132, 133] (b)	$I_{E\gamma}$(Ref. [132, 133])
^{162}Dy	289.1	289.5	0.10 ± 0.04	7.27 ± 4.41	2.67 ± 0.27	0.71 ± 0.44
^{162}Dy	318.8	318.1	0.11 ± 0.04	8.20 ± 5.05	6.50 ± 0.81	0.33 ± 0.21
^{161}Dy	321.4	321.8 + 321.9	0.11 ± 0.03	11.0 ± 5.9	13.5 ± 3.1	0.47 ± 0.27
^{162}Dy	375.6	376.5	0.13 ± 0.05	9.40 ± 5.83	3.12 ± 0.41	0.78 ± 0.50
^{162}Dy	398.2	399.0	0.12 ± 0.04	8.71 ± 5.27	3.10 ± 0.39	0.73 ± 0.45
^{161}Dy	768.2	768.8	0.07 ± 0.02	7.35 ± 3.85	3.07 ± 1.16	1.35 ± 0.88
^{162}Dy	819.9	820.8	0.15 ± 0.03	10.5 ± 5.6	1.88 ± 0.24	1.45 ± 0.79
^{161}Dy	936.4	937.2	0.08 ± 0.02	7.85 ± 4.27	7.40 ± 2.64	0.60 ± 0.39
^{162}Dy[a]	5216.5	5215.3	0.24 ± 0.05	17.5 ± 9.4	1.49 ± 0.20	0.99 ± 0.55
^{161}Dy	5450.1	5450.3	0.19 ± 0.02	18.4 ± 8.9	2.1 ± 0.4	0.94 ± 0.49
^{164}Dy	5557.0	5557.3	0.21 ± 0.04	11.0 ± 3.2	28.7 ± 1.4	1.52 ± 0.45
^{164}Dy	5606.3	5607.7	0.35 ± 0.03	17.8 ± 4.9	35.9 ± 1.6	1.96 ± 0.55

E_γ is the γ-ray energy, $P_{E\gamma}(90°)/(\epsilon_{E\gamma} \times f_{E\gamma})$ the net counts in the γ-ray peak divided by the full-energy-peak (FEP) efficiency and the γ-ray self-absorption factor, $\langle\sigma_{E\gamma}\rangle$ the effective isotopic partial cross section for γ-ray production calculated after Eqs. (4.1) and (6.3) and $I_{E\gamma}$ the absolute intensity of the γ-rays determined with Eq. (4.3)
[a]uncertain assignment

6.3 Results and Discussion

In this section the results of the measurements with regard to fast-neutron-induced prompt γ-lines are given element by element in the order of increasing atomic number. The agreement with the data from the Atlas [27] is discussed, with particular emphasize dedicated to γ-lines being absent in one of the two measurements.

6.3.1 Carbon (C)

Prompt γ-rays emitted in fast-neutron-induced reactions with C were analyzed by the measurement of the $CaCO_3$ [21] and the PVC sample [20] as described in Table 6.1. In both measurements one single γ-ray from the ^{12}C(n,n'γ)^{12}C was observed. The γ-ray, emitted from the first 2^+ level in ^{12}C with 4439.8 keV above g.s. [161], was determined with a peak energy of 4441.14 ± 0.41 keV in the $CaCO_3$ and 4440.96 ± 0.15 keV in the PVC measurement. Due to the short life time of the excited level (42.2 fs [64]) this peak shows a strong Doppler broadening [64, 162]. γ-ray data of C are given in Appx. H.1.1 and H.1.2.

Cross sections of (14.4 ± 3.3) mb [20] and (12.8 ± 2.3) mb [21] for the $CaCO_3$ and the PVC measurement, respectively, demonstrate reproducibility of FaNGaS. An average value of (13.3 ± 1.9) mb [21] was deduced from those two measurements.

Since ^{12}C emits only one single γ-ray from inelastic scattering, division of the effective isotopic partial γ-ray production cross section $\langle\sigma_{E\gamma}(90°)\rangle$ by the effective reaction cross section obtained from NJOY (see Appx. C.1), i.e. (12.5 ± 1.1) mb, results in an angular-distribution correction factor of $W(\theta)$= 1.1 ± 0.2. In the Atlas [27] a γ-ray intensity of 109% is given [27]. Probably Demidov et al. derived this

value with their effective reaction cross section, as the FaNGaS measurement yielded a corresponding ratio of 107%. In fact, however, the γ-ray intensity cannot exceed 100% and in accordance with Eq. (4.3) one has to divide the value of $\langle\sigma_{E\gamma}(90°)\rangle$ also by the value of $W(\theta)$.

6.3.2 Oxygen (O)

Two γ-rays issued from the fast-neutron inelastic scattering on O were observed in the $CaCO_3$ spectrum [20]. The γ-ray data are given in Appx. H.1.1. One γ-ray at 6129.3 keV from the ^{16}O(n,n'γ)^{16}O reaction and another one at 1981.7 keV from the ^{18}O(n,n'γ)^{18}O reaction were identified. The γ-line at 6129.3 keV interfered with the decay line of ^{16}N (E_γ= 6128.6 keV, $I_{E\gamma}$= 67%, $t_{1/2}$= 7.13 s [159]), that is formed via the ^{16}O(n,pγ)^{16}N reaction. However, the interference could be neglected since the cross section (fission spectrum average for kT= 1.35 MeV, taken from [9]) of the ^{16}O(n,p)^{16}N reaction (44.72 μb [9]), is considerably lower than that of the ^{16}O(n,n'γ)^{16}O reaction (4.92 mb [9]) and its contribution to the net count rate was only (1.36 $\pm$ 0.20)%. Effective isotopic partial γ-ray production cross sections of (201 $\pm$ 28) mb and (2.20 $\pm$ 0.37) mb were obtained for the lines at 1981.7 and 6129.3 keV, respectively.

The two prompt γ-rays of O were also observed in the measurement of RE chloride samples, as some of them contained crystal water according to Table 6.1. The interference from ^{16}N was neglected due to the lower irradiation times and smaller masses of O compared to the $CaCO_3$ measurement. The corresponding values of $\langle\sigma_{E\gamma}(90°)\rangle$, calculated after Eq. (4.1), are given in Table 6.10. Compared to the $CaCO_3$ measurement, average cross-section values of (200 $\pm$ 24) mb for the 1982-keV line and (2.56 $\pm$ 0.20) mb for the 6129-keV line confirm the values obtained from $CaCO_3$. In addition, presence of the O lines is considered as another proof that the RE chloride samples listed in Table 6.1 contained crystal water, whereas absence of those lines in the measured spectra of $CeCl_3$ and $NdCl_3$ confirms freedom of water. Furthermore, the well agreement between the values also confirms the assumed compound stoichiometries, in particular the number n of crystal water molecules for each sample.

With respect to data from the Atlas [27] the relative intensities between both O lines, relative to the 1982-keV line from ^{18}O (100%), agree reasonably taking into account the uncertainties. Nevertheless, the cross sections derived from the $CaCO_3$ measurement are proposed. Besides better counting statistics, interferences are less likely.

With effective reaction cross sections of (8.49 $\pm$ 0.72) and (347 $\pm$ 32) mb (see Appx. C.1) as well as an angle of 90° between neutron beam axis and detector, angular-distribution correction factors of 0.26 $\pm$ 0.05 and 0.58 $\pm$ 0.10 were estimated for the inelastic scattering on ^{16}O and ^{18}O, respectively.

Table 6.10: Prompt (n,n'γ) γ-rays of ^{16}O and ^{18}O observed in different samples listed in Table 6.1.

This work					From Atlas [27]	
Sample	E_γ (keV)	$P_{E\gamma}(90°)/(\epsilon_{E\gamma} \times f_{E\gamma})$ $\times$ 10^{-8} (count)	I_R(relative) (%)	$\langle\, \sigma_{E_\gamma}(90°)\, \rangle$ (mb)	E_γ (keV)	I_R(relative) (%)
^{18}O(n,n'γ)^{18}O						
$CaCO_3$	1981.69 ± 0.18	0.46 ± 0.05	100	**201 ± 28**	1983.0 ± 0.4	100
$LaCl_3{\cdot}7H_2O$	1981.61 ± 0.18[a]	0.26 ± 0.03	100	172 ± 22	1983.0 ± 0.4	100
$PrCl_3{\cdot}7H_2O$	1981.33 ± 0.19[a]	0.15 ± 0.02	100	180 ± 26	1983.0 ± 0.4	100
$SmCl_3{\cdot}7H_2O$	1982.39 ± 0.30[a]	0.10 ± 0.02	100	203 ± 55	1983.0 ± 0.4	100
$TbCl_3{\cdot}6H_2O$	1981.47 ± 0.11[a]	0.27 ± 0.05	100	213 ± 42	1983.0 ± 0.4	100
$DyCl_3{\cdot}6H_2O$	1982.58 ± 0.33[a]	0.09 ± 0.02	100	239 ± 50	1983.0 ± 0.4	100
^{16}O(n,n'γ)^{16}O						
$CaCO_3$	6129.32 ± 0.22[b]	2.50 ± 0.37	547 ± 121	**2.20 ± 0.37**	6129.3 ± 1.0	595 ± 120
$LaCl_3{\cdot}7H_2O$	6128.97 ± 0.14[b]	1.95 ± 0.16	743 ± 97	2.56 ± 0.29	6129.3 ± 1.0	595 ± 120
$PrCl_3{\cdot}7H_2O$	6128.72 ± 0.20[b]	1.15 ± 0.14	744 ± 131	2.69 ± 0.40	6129.3 ± 1.0	595 ± 120
$SmCl_3{\cdot}7H_2O$	6130.04 ± 0.19[b]	0.67 ± 0.12	687 ± 215	2.80 ± 0.55	6129.3 ± 1.0	595 ± 120
$TbCl_3{\cdot}6H_2O$	6128.75 ± 0.18[b]	1.38 ± 0.30	518 ± 146	2.22 ± 0.51	6129.3 ± 1.0	595 ± 120
$DyCl_3{\cdot}6H_2O$	6129.08 ± 0.22[b]	0.46 ± 0.09	518 ± 146	2.55 ± 0.54	6129.3 ± 1.0	595 ± 120

E_γ is the γ-ray energy, $P_{E\gamma}(90°)/(\epsilon_{E\gamma} \times f_{E\gamma})$ the net counts in the γ-ray peak divided by the full-energy-peak (FEP) efficiency and the γ-ray self-absorption factor, I_R the relative intensity of the γ-rays (relative to 1982 keV, 100%) and $\langle\sigma_{E_\gamma}(90°)\rangle$ is the effective isotopic partial cross section for γ-ray production at an angle of 90° between neutron beam axis and detector calculated after Eq. (4.1)

[a] corrected for contribution of the DE from the 3002-keV line of the ^{35}Cl(n,n'γ)^{35}Cl reaction

[b] corrected for background interference

6.3.3 Chlorine (Cl)

Fast-neutron-induced γ-rays of Cl were analyzed with the γ-ray spectrum obtained from the PVC measurement. Since the RE samples were irradiated as chlorides, the prompt γ-rays were also observed in these measurements and hence used to complement the analysis of the PVC measurement.

6.3.3.1 Polyvinylchloride (PVC) sample

A total of 14 γ-lines associated to fast-neutron-induced interactions on Cl were observed in the recorded PVC spectrum. These γ-rays are depicted in the measured spectrum given in Appx. G.1 and their data are given in Appx. H.1.2. From those, 7 were related to the ^{35}Cl(n,n'γ)^{35}Cl [163], 4 to the ^{37}Cl(n,n'γ)^{37}Cl [164] and 3 to the ^{35}Cl(n,pγ)^{35}S [163] reaction. Additionally, the main neutron capture lines from the ^{35}Cl(n,γ)^{36}Cl reaction were observed. With respect to [132], however, no relevant interferences with the aforementioned fast-neutron-induced lines were identified. Corrections of escape peak interferences were not necessary.

Intensities of the γ-lines were calculated relative to the 1219-keV line of ^{35}Cl (100%), emitted from the first $(1/2)^+$ level with 1219.3 keV above g.s. [163]. They are given together with the values determined in [27] in columns 4 and 7 of Appx. H.1.2. In this work, 14 of 27 listed lines in [27] were observed. The lines given at energies of 775.0, 930.5, 2180.8, 2840.3 and 3742.9 keV were observed in the measure-

ments of the RE chloride samples. Absence of these lines in the PVC measurement is attributed to the DL, which was not reached with the smaller Cl mass of 0.082 g being only partly compensated by the longer measurement time.

The lines listed at 637.2, 824.8, 882.3, 922.0, 1070.6, 1676.4, 2832.9 and 3195.6 keV [27] were not observed in any measurement of this work. The line at 882.3 keV was emitted from a level at 2645.7 keV [65, 163] in ^{35}Cl from which another line at 2646.1 keV was detected in this work. It was not identified due to interference with the 881-keV line of ^{206}Pb induced by inelastic scattering of fast neutrons with the Pb shielding [34]. The lines at 637.2 and 1070.6 keV had been assigned to the ^{35}Cl(n,$\alpha\gamma$)^{32}P reaction [27], which is justified with regard to [65, 165] as both lines originated from the same level in ^{32}P at 1149.4 keV above g.s. Those lines, however, were not observed in this work because of the higher DL.

The remaining lines at 824.8, 922.0, 1676.4, 2832.9 and 3195.9 keV had been reported as tentative assignments and were not placed in any decay scheme of Cl by Demidov et al. The fact that those lines were not observed in this work and missing data in [65] for most of them rather provides support that they do not belong to Cl. Data in [65] that involve levels above 7 MeV or absence of other intense lines arising from the same level was not regarded as a plausible possibility. According to [65, 165], the 1676.4-keV line could correspond to a direct g.s. transition from an excited level at E^*= 1755.0 keV in ^{32}P. The 3195.9-keV line could correspond to the SE of a line at 3707.9 keV, directly emitted to g.s. in ^{37}Cl [65, 164]. The clear presence of the 3195.9-keV line in Demidov's spectrum, shown only to about 3.5 MeV, together with the absence of a probable transition in [65] might support this assumption.

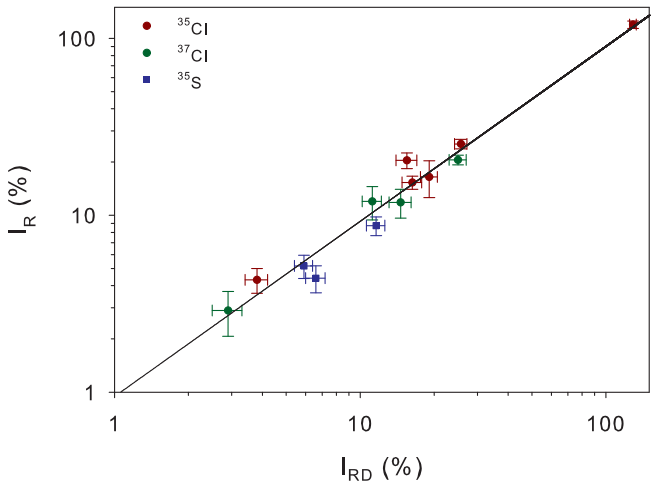


Figure 6.6: Relationship between the relative intensities I_R of the prompt γ-rays induced by fast-neutron inelastic scattering (n,n'γ) and (n,pγ) reactions on Cl (^{35}Cl, ^{37}Cl and ^{35}S) measured in this work and the relative intensities I_{RD} tabulated in the Atlas [27]. The solid line represents the fit of the data with Eq. (4.32).

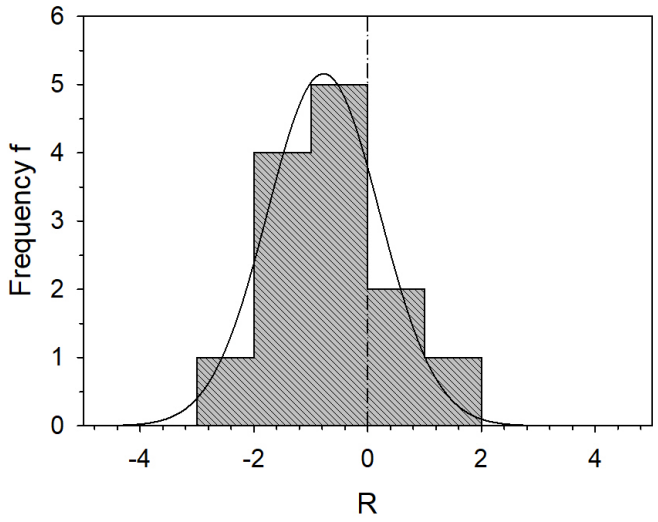


Figure 6.7: Comparison of the relative intensities of the prompt γ-rays induced by fast-neutron inelastic scattering (n,n'γ) and (n,pγ) reactions on Cl obtained in this work with the data tabulated in the Atlas [27] in the form of a histogram of the residuals R in units of standard deviation (σ) calculated with Eq. (4.33). The values of R are given in column 8 of Appx. H.1.2. The solid line represents the fit of the data with a Gaussian according to Eq. (4.34).

The PVC measurement did not result in the identification of new γ-lines compared to the measurement of Demidov et al. owing the small sensitivity. However, the γ-ray listed at 1184.7 keV in the Atlas [27] was unassigned. In fact, according to [65, 163] this line was found to represent a direction transition to g.s. from a level with E^*= 4347.8 keV in ^{35}Cl. Detailed analysis of the spectrum in the Atlas [27] and comparison to that one obtained in this work, unambiguously shows intense lines around 1164, 1951 and 1959 keV, which all belong to the ^{35}Cl(n,γ)^{36}Cl reaction with respect to [132]. This observation is a clear indication that the measurements in the work of Demidov et al. were accompanied by significant contributions from the radiative capture of thermal and epithermal neutrons.

The correlation between the relative intensities measured in this work and these given in [27] is depicted in Fig. 6.6 for all lines (this plot is termed as "intensity plot", hereafter). The values were fitted with Eq. (4.32), yielding the coefficients a= 0.94 ± 0.14 and b= 0.99 ± 0.06. The average intensity ratio I_R/I_{RD} is 0.94 ± 0.16, indicating a good agreement between the two measurements.

To prove the consistency of the two data sets in a more detailed manner, Fig. 6.7 shows a histogram of the residuals R in units of standard deviation (σ), calculated after Eq. (4.33) (this plot is termed as "residual histogram", hereafter). The fit of the data agrees at the 1.0σ level and the Gaussian centroid is aligned at R_0= -0.776 ± 0.072, indicating a probable systematic effect.

The effective isotopic partial γ-ray production cross sections, calculated with a fast-neutron flux of 1.13 × 10^8 cm^{-2} s^{-1} after Eq. (4.1), are given in column 5 of

Appx H.1.2 and they are plotted as a function of the γ-ray energy in Fig. 6.8. The total value of the partial cross sections is (175 ± 18) mb for the ^{35}Cl(n,n'γ)^{35}Cl, (86 ± 14) mb for the ^{37}Cl(n,n'γ)^{37}Cl and (10.7 ± 1.7) mb for the ^{35}Cl(n,pγ)^{35}S reaction. The effective reaction cross sections of fast neutrons derived with NJOY, as listed in Appx. C.1, are (238 ± 21) mb, (177 ± 15) mb and (119 ± 11) mb for the respective reactions. Except for the inelastic scattering on ^{35}Cl, the large discrepancy between aforementioned cross sections might imply a high anisotropy of Cl or incomplete γ-ray emission related to the small mass of Cl.

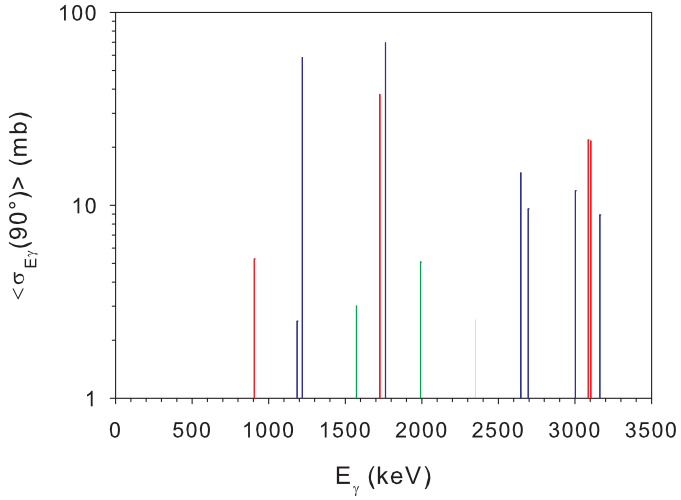


Figure 6.8: Effective isotopic partial γ-ray production cross sections $\langle\sigma_{E\gamma}(90°)\rangle$ of the ^{35}Cl(n,n'γ)^{35}Cl (blue), the ^{37}Cl(n,n'γ)^{37}Cl (red) and the ^{35}Cl(n,pγ)^{35}S (green) reactions calculated after Eq. (4.1) as a function of the γ-ray energy E_γ. Uncertainties are given in Appx. H.1.2.

6.3.3.2 Rare earth chlorides

Analysis with the spectra obtained from the RE chloride measurements resulted in many new lines compared to the PVC measurement and the Atlas [27]. Some lines were not observed in all measurements, which is associated to the different masses of Cl and irradiation times. The measurement of $CeCl_3$ provided the highest mass of Cl, i.e. 1.146 g, resulting in the observation of all fast-neutron-induced γ-rays of Cl, compared to the other samples. Identified γ-rays are marked accordingly in blue in the spectra provided in Appx. G. The tables with the γ-ray data for every RE chloride measurement are given in Appx. H.1.3 to H.1.9. Averaged data was obtained from all measurements, given in Appx. H.1.10. Lines marked in red were not considered for the average, as uncorrected interferences from (n,n'γ) reactions of the respective RE elements were suspected with respect to data in [65]. For the γ-ray at 1219.2 keV the cross section deduced from the PVC measurement is proposed, since the line was definitely free of any interferences and has reasonable counting statistics with 1.9% uncertainty in the peak fit. For all other observed γ-rays the

cross sections with the better R values, i.e. greater agreement in relative intensity with [27], are suggested. Proposed cross sections are written in bold in Appx H.1.2 and H.1.10.

In total, the analysis of the RE chloride spectra yielded 29 γ-lines from the interaction of fast neutrons with Cl. From these, 15 were assigned to the ^{35}Cl(n,n'γ)^{35}Cl [163], 8 to the ^{37}Cl(n,n'γ)^{37}Cl [164], 5 to the ^{35}Cl(n,pγ)^{35}S [163] and 1 to the ^{35}Cl(n,$\alpha\gamma$)^{32}P [165] reaction. In comparison to the PVC measurement, irradiation of the RE chloride samples resulted in the identification of 19 (14 in PVC) out of 27 lines given in the Atlas [27]. Absence of the 8 unidentified lines is discussed in the previous section.

Compared to [27], 10 new γ-lines of Cl were identified that are also reported in [65]. These include the lines at 1701.7, 3917.4, 4111.1, 4175.8 and 4622.6 keV for the ^{35}Cl(n,n'γ)^{35}Cl [163], the lines at 1900.6, 3625.9, 4011.0 for the ^{37}Cl(n,n'γ)^{37}Cl [164], the line at 2714.9 keV for the ^{35}Cl(n,pγ)^{35}S [163] and the line at 77.9 keV for the ^{35}Cl(n,$\alpha\gamma$)^{32}P [165] reaction. The latter line comes from the first excited level in ^{32}P with 78.1 keV above g.s. [165]. It could not be seen by Demidov et al. as their measurements had a lower energy threshold of 0.12 MeV [27]. The lines at 1701.7 keV and 4011.0 keV were emitted from levels at 4347.8 keV in ^{35}Cl [163] and 4010.0 keV in ^{37}Cl [164] above g.s. Their emission was accompanied by the γ-rays at 1184.7 keV and 905.8 keV, respectively, both clearly observed also by Demidov et al. [27]. While absence of the 4011.0-keV line in the Atlas [27] is simply reasoned in the upper energy range limit of 3.4 MeV, it is unclear why the line at 1701.7 keV had not been observed. The low intensities of the 1900.6- and 3625.9-keV lines resulted in poor fits. However, presence of both lines is justified and expected as they were both emitted from the same level, i.e. E^*= 3626.8 keV [164]. The high-energy γ-rays observed at 3917.4, 4011.0, 4111.1, 4175.8 and 4622.8 keV are reasonable and expected transitions directly to g.s. with respect to data provided in [65]. Besides the fact that these lines were out of the considered energy range in [27], at FaNGaS more neutrons with energies above the associated threshold energy are provided in comparison to the facility at the IRT reactor. The signals from those lines were, however, weak since most of them show Doppler-broadening and the observation was close to the corresponding DLs.

The assignment of the line at 4175.8 keV is somewhat uncertain with respect to data in [65]. In fact, it could have been also fed by two close-lying states at 4173.4 and 4177.9 keV above g.s. [163]. As both levels have life times in the femtosecond range, i.e. 34 and 25 fs [163], respectively, Doppler-broadening might have disturbed the resolution of the resulting doublet structure. According to [65, 163], those lines are accompanied by lines of 1479.7 and 2958.4 keV. However, these were not observed in this work. According to [65, 164], the 4175.8-keV line could also correspond to the ^{37}Cl(n,n'γ)^{37}Cl reaction. Nevertheless, presence of accompanied lines at 549.8 and 1090.5 keV (E^*= 4176.6 keV [164]) also could not clearly be confirmed with the

measured RE chloride spectra.

It is worth to mention that the line at 4111.1 keV, according to [65, 163], was accompanied by a line at 2348.8 keV of similar intensity. Therefore, the line at 2347.7 keV assigned to the ^{35}Cl(n,pγ)^{35}S reaction might be interfered to a certain extent by this transition.

For several lines the work of Demidov et al. suggests interferences with the (n,n'γ) reaction from isotopes of the respective RE element. Such interferences were found for the measurement of La, Ce, Sm and Dy. These interferences were corrected with the relative intensities given in the Atlas [27], except for ^{140}Ce where data from the corresponding ENSDF file [160] was preferred. Contributions of (4.2 ± 0.5)% for the 1762.9-keV line in $LaCl_3 \cdot 7H_2O$, (32.0 ± 5.3)%, (3.7 ± 0.3)%, (17.2 ± 3.1)% and (44.2 ± 2.7)% for the lines at 774.8, 1726.2, 1900.0 and 2347.6 keV in $CeCl_3$, (61 ± 5)% for the 929.9-keV line in $SmCl_3 \cdot 7H_2O$ and (8.1 ± 3.0)% and (23.7 ± 8.9)% for the lines at 1219.2 and 1725.7 keV in $DyCl_3 \cdot 6H_2O$ were determined.

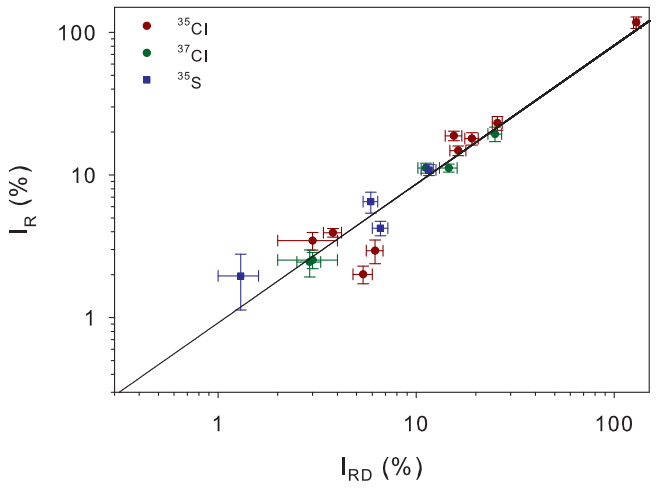


Figure 6.9: Relationship between the relative intensities I_R of the prompt γ-rays induced by fast-neutron inelastic scattering (n,n'γ) and (n,pγ) reactions on Cl (^{35}Cl, ^{37}Cl and ^{35}S) averaged over all RE chloride samples and the relative intensities I_{RD} tabulated in the Atlas [27]. The solid line represents the fit of the data with Eq. (4.32).

The intensity plot is shown in Fig. 6.9 for all lines. The values of the fit coefficients according to Eq. (4.32) are a= 0.92 ± 0.17 and b= 0.97 ± 0.08, respectively. The average intensity ratio I_R/I_{RD} is 0.91 ± 0.25, indicating a reasonable agreement between the two measurements. In fact, compared to the PVC measurement, the lines at 2179.4 and 2840.5 keV show the highest mismatch to Demidov data with intensity ratios of 0.48 ± 0.21 and 0.37 ± 0.18, respectively. Besides the fact that these lines had poor counting statistics in this work, the discrepancy for the line at 2179.4 keV might be due to an uncorrected contribution of the SE from the 2693.6-keV line in [27]. The FaNGaS spectrometer was able to resolve this doublet and

distinguish both peaks from each other. The fact that the FaNGaS measurements reproduce the same intensity mismatch for both lines over all measurements rather suggests a systematic error in one of the two data sets.

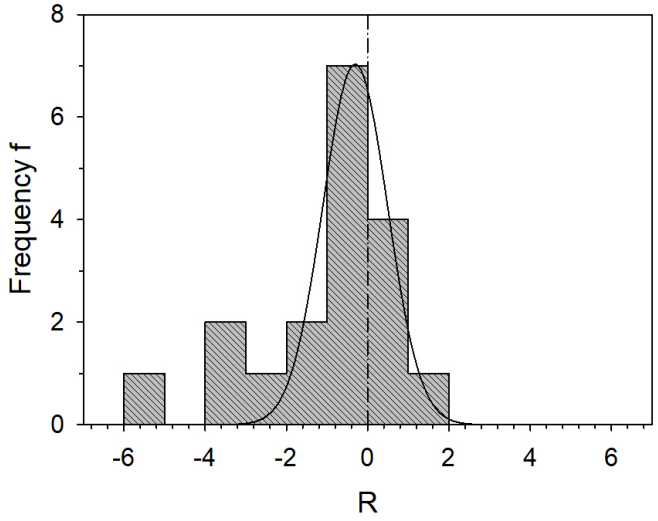


Figure 6.10: Comparison of the relative intensities of the prompt γ-rays induced by fast-neutron inelastic scattering (n,n'γ) and (n,pγ) reactions on Cl for data averaged over all RE chloride samples with the data tabulated in the Atlas [27] in the form of a histogram of the residuals R in units of standard deviation (σ) calculated with Eq. (4.33). The values of R are given in Appx. H.1.10. The solid line represents the fit of the data with a Gaussian according to Eq. (4.34).

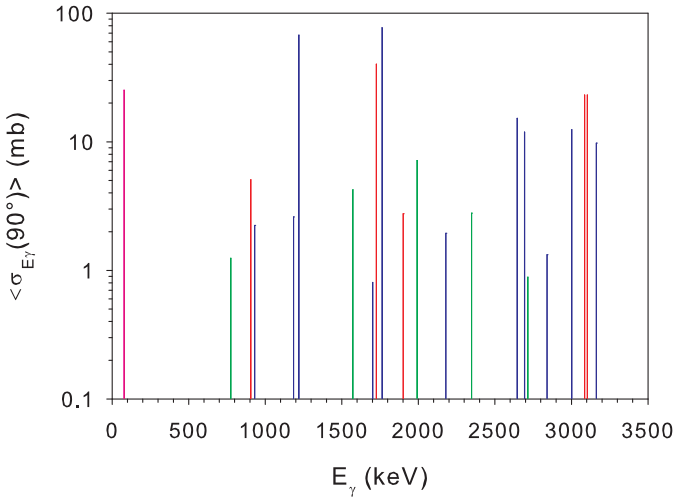


Figure 6.11: Effective isotopic partial γ-ray production cross sections $\langle\sigma_{E\gamma}(90°)\rangle$ of the ^{35}Cl(n,n'γ)^{35}Cl (blue), the ^{37}Cl(n,n'γ)^{37}Cl (red), the ^{35}Cl(n,pγ)^{35}S (green) and ^{35}Cl(n,$\alpha\gamma$)^{32}P (pink) reactions calculated after Eq. (4.1) as a function of the γ-ray energy E_γ and averaged over all RE chloride samples. Uncertainties are given in Appx. H.1.10.

The residual histogram is depicted in Fig. 6.10. The fit of the data agrees at the

0.8σ level and the Gaussian centroid is aligned at R_0= -0.307 ± 0.127, indicating a small systematic effect. The shift is caused mainly by the aforementioned lines observed at 2179.4 and 2840.5 keV.

The fact that the individual RE chloride samples yielded similar results and the agreement of averaged data to data from Demidov et al. is significantly improved relative to the PVC measurement emphasizes reproducibility and accuracy of the FaNGaS instrument.

The effective isotopic partial γ-ray production cross sections, calculated with a fast-neutron flux of 1.13 × 10^8 cm^{-2} s^{-1} after Eq. (4.1), are given in Appx. H.1.10. They are plotted as a function of the γ-ray energy in Fig. 6.11.

Furthermore, Fig. 6.12 shows the average cross sections in comparison to these derived from the PVC measurement. The error margins overlap for all lines except those at 1572.2 and 1991.0 keV, for which the better counting statistics in the RE chloride spectra resulted in smaller uncertainties.

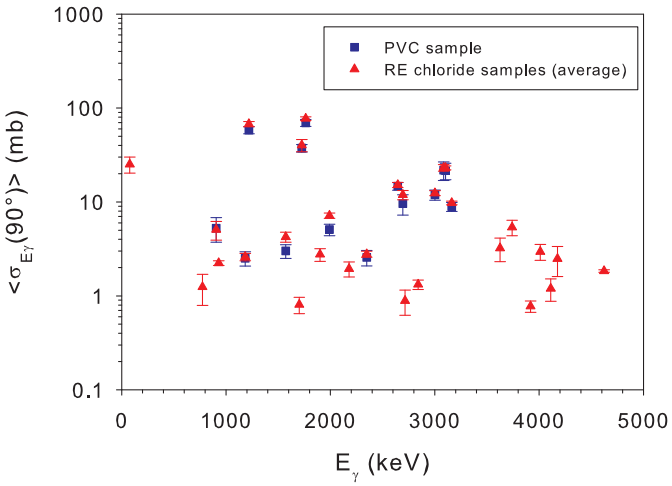


Figure 6.12: Effective isotopic partial γ-ray production cross sections $\langle\sigma_{E\gamma}(90°)\rangle$ for all observed fast-neutron-induced γ-lines of Cl calculated after Eq. (4.1) for the PVC sample (blue) and averaged over all RE chloride samples (red) as a function of the γ-ray energy E_γ.

6.3.4 Calcium (Ca)

The measurement of the $CaCO_3$ sample resulted in the identification of 35 prompt γ-lines related to fast-neutron-induced reactions on Ca. These γ-rays are depicted in the recorded spectrum, provided in Appx. G.2. Their corresponding data is given in Appx. H.1.1. From all 35 lines, 12 were found to belong to (n,n'γ), 20 to (n,pγ) and 3 to (n,$\alpha\gamma$) reactions. From the 12 (n,n'γ) reactions, 7 lines were assigned to the ^{40}Ca(n,n'γ)^{40}Ca [97], 1 to the ^{42}Ca(n,n'γ)^{42}Ca [166] and 4 to the ^{44}Ca(n,n'γ)^{44}Ca [167] reaction. The (n,pγ) and (n,$\alpha\gamma$) reactions both originated from the ^{40}Ca isotope, i.e. the reactions ^{40}Ca(n,pγ)^{40}K [97] and ^{40}Ca(n,$\alpha\gamma$)^{37}Ar [164]. As a light

nucleus, some lines of Ca are subject to Doppler broadening [64]. Indeed, the line at 3904.8 keV from the ^{40}Ca(n,n'γ)^{40}Ca reaction showed a broadening due to the short life time of 35 fs [97] at the respective state. Neutron self-shielding and γ-ray self-absorption corrections were neglected owing the small effective sample thickness of 0.14 cm. Only for the line observed at 29.8 keV the self-absorption was corrected with Eq. (4.10). With respect to data in [132], only the strongest neutron capture line from the ^{40}Ca(n,γ)^{41}Ca at 1943 keV (see Appx. G.2) might have been present close to the background line at 1940 keV from ^{74}Ge and ^{27}Al [34]. However, as other main capture lines given in [132] were not observed and as the intensity for lines at energies of potential interferences is about one order of magnitude below the 1943-keV line, interferences arising from neutron capture were reasonably neglected. In addition, no escape peak interferences were identified.

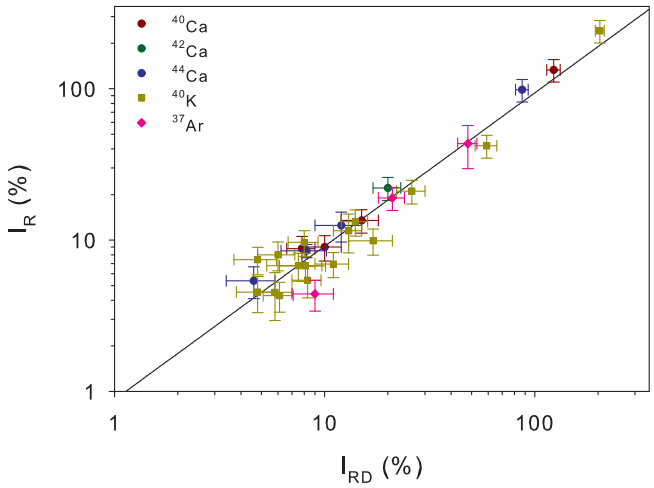


Figure 6.13: Relationship between the relative intensities I_R of the prompt γ-rays induced by fast-neutron inelastic scattering (n,n'γ), (n,pγ) and (n,$\alpha\gamma$) reactions on Ca measured in this work and the relative intensities I_{RD} tabulated in the Atlas [27]. The solid line represents the fit of the data with Eq. (4.32).

Intensities of γ-lines were calculated relative to the 3905-keV line of ^{40}Ca (100%), emitted from the first 2^+ level at 3904.4 keV above g.s. [97]. They are given together with the values determined in [27] in columns 4 and 7 of Appx. H.1.1. In this work, 29 of 35 listed lines in [27] were observed. The lines listed at energies of 1345.6, 1369.5, 2951.9, 5250, 5628 and 5902 keV in the Atlas [27], respectively, were not observed in this work. According to [65, 97], the lines at 1345.6 and 5250 keV belong to the same excited level, E^*= 5248.8 keV, of the ^{40}Ca(n,n'γ)^{40}Ca reaction. As depicted in Appx. D.4 and as given in [55, 114], the energy threshold for this reaction is around 3.44 MeV, which exceeds the mean neutron energy of 2.30 MeV in this work. The fast-neutron flux, as defined from 60 keV $\leq E_n \leq$ 20 MeV, overlaps only partly with the corresponding excitation function. The effective activation flux, integrated over the limits of the excitation function, was (2.19 $\pm$ 0.08) $\times$ 10^7 cm^{-2}

s^{-1}. Hence, only 19.4% of the defined fast-neutron flux of $(1.13 \pm 0.04) \times 10^8$ cm^{-2} s^{-1} induced inelastic scattering reactions on ^{40}Ca. Although the mean neutron energy was lower in the Atlas [28], a much higher Ca mass (11.3 g [27] vs. 0.962 g in this work) had been irradiated for a longer time (24.2 h [27] vs. 6.46 h counting live time). Therefore, it might be possible that the DL was not reached in this work.

The ENSDF file of the ^{40}Ca(n,n'γ)^{40}Ca reaction [97] available in [65] gives differential cross sections $d\sigma/d\Omega$ for a measuring angle of 125° and various discrete neutron energies between 4.85 and 8.05 MeV from the work of Dickens [168]. From the FaNGaS measurement of Fe [34] one can deduce that the correction for the anisotropy is negligible at high energies, i.e. the angular-distribution correction factor $W(125°)/W(90°) \approx 1$. For the energy range between 6.45 and 8.05 MeV in [168], the ratio in percent of differential cross sections between the lines at 5250 and 3905 keV is (21.8 ± 6.4)%, which agrees well with the relative intensity of (27 ± 5)% given in the Atlas [27]. Hence, although the spectrum is not shown beyond 3 MeV in [27] and the relative intensity of the 5250-keV line was in the range of other lines clearly observed in this work, it is plausible that Demidov et al. had observed this line owing their higher Ca mass [27]. The line listed at 1369.5 keV had been unassigned in the Atlas and belongs probably to the background as no peak with significant statistics was found and no relevant transition is proposed in [65]. For the unassigned γ-ray listed at 2951.9 keV in [27] no proper transition was found. Curiously, in the spectrum of Demidov et al. this line was neither seen nor marked accordingly, providing support for a misattribution. The γ-lines at 5628 and 5902 keV of the ^{40}Ca(n,n'γ)^{40}Ca reaction [97] should have been present in the Demidov spectrum due to the higher irradiated mass and longer exposure time. Presence of these lines in [27] is supported since the differential cross-section ratios [168] relative to the 3905-keV line are (14.8 ± 3.2)% for the 5628- and (9.6 ± 3.2)% for the 5902-keV line, respectively. Aforementioned values are in good agreement to the relative intensities of (21 ± 5)% and (16 ± 5)% tabulated in [27], taking into account also the large uncertainties. Nevertheless, those lines require high excitation energies above 5 MeV. In principle, this requirement is better fulfilled with the neutron-energy spectrum of FaNGaS due to the higher mean neutron energy.

On the other hand, compared to [27] 6 new γ-lines of Ca were identified. These comprise the lines at 29.8, 843.5, 1307.5, 1613.6, 2009.8 and 3683.8 keV. The line at 29.8 keV could not be seen by Demidov et al. as in their measurement the γ energy threshold was about 120 keV. The line at 843.5 keV was strongly interfered by a line of ^{27}Al in both data sets [27, 34]. However, comparison with the background spectrum and data in [65] clearly implied a relevant contribution from the ^{40}Ca(n,pγ)^{40}K reaction. In fact, this line was emitted from the same level (E^*= 1643.6 keV [97]) as the line at 1613.6 keV. The latter one could not have been observed uniquely by Demidov et al. as the doublet with the close-lying line at 1611.2 keV in [27] from the ^{40}Ca(n,$\alpha\gamma$)^{37}Ar reaction could not be resolved. Radiative neutron capture was

excluded for the line at 2009.8 keV and a proposed transition observed in a (p,p'γ) reaction on ^{40}Ca [169] was excluded also due to the high level energy of 7623.1 keV and 12 MeV neutron energy used in [169]. This line was rather cautiously assigned to the ^{40}Ca(n,n'γ)^{40}Ca reaction assuming it represents a transition not listed in [65, 97] yet. The lines at 1307.5 and 3683.8 keV were assigned to the ^{40}Ca(n,n'γ)^{40}Ca and the ^{40}Ca(n,pγ)^{40}K reaction, respectively. As they correspond to direct transitions to g.s. without other intense lines, probably these levels had not been excited in the work of Demidov et al.

The line at 2289.7 keV had been assigned to the ^{40}Ca(n,pγ)^{40}K reaction by Demidov et al. although, according to [65, 97], it might have been also fed by the inelastic scattering reaction in ^{40}Ca. However, as the respective level energy of 6025.5 keV is far above the mean neutron energy in this work, this contribution should be negligible.

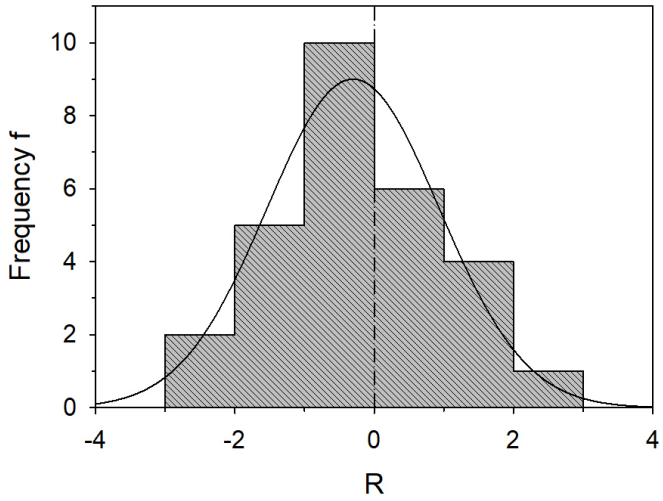


Figure 6.14: Comparison of the relative intensities of the prompt γ-rays induced by fast-neutron inelastic scattering (n,n'γ), (n,pγ) and (n,$\alpha\gamma$) reactions on Ca obtained in this work with the data tabulated in the Atlas [27] in the form of a histogram of the residuals R in units of standard deviation (σ) calculated with Eq. (4.33). The values of R are given in Appx. H.1.1. The solid line represents the fit of the data with a Gaussian according to Eq. (4.34).

The intensity plot is depicted in Fig. 6.13 for all lines. The values for the fit coefficients of Eq. (4.32) are a= 0.88 ± 0.13 and b= 1.01 ± 0.05, respectively. The average intensity ratio I_R/I_{RD} is 0.94 ± 0.23, indicating a reasonable agreement between the two measurements.

The residual histogram is given in Fig. 6.14. The fit of the data agrees at the 1.2σ level and the Gaussian centroid is aligned at R_0= -0.302 ± 0.122, indicating a probable systematic effect.

The effective isotopic partial γ-ray production cross sections, calculated after Eq. (4.1) with a fast-neutron flux of 1.13 × 10^8 cm^{-2} s^{-1}, are plotted as a function of the γ-

ray energy in Fig. 6.15. Total values of aforementioned cross sections of (30 ± 3) mb, (355 ± 34) mb, (456 ± 46) mb, (217 ± 23) mb and (7.0 ± 0.7) mb were determined for the ^{40}Ca(n,n'γ)^{40}Ca, ^{42}Ca(n,n'γ)^{42}Ca, ^{44}Ca(n,n'γ)^{44}Ca, ^{40}Ca(n,pγ)^{40}K and the ^{40}Ca(n,$\alpha\gamma$)^{37}Ar reactions, respectively. The corresponding effective values for the reactions derived from NJOY as listed in Appx. C.1, i.e. (49 ± 4) mb, (495 ± 44) mb, (602 ± 55) mb, (122 ± 11) mb and (44 ± 4) mb suggest a highly anisotropic behaviour of Ca.

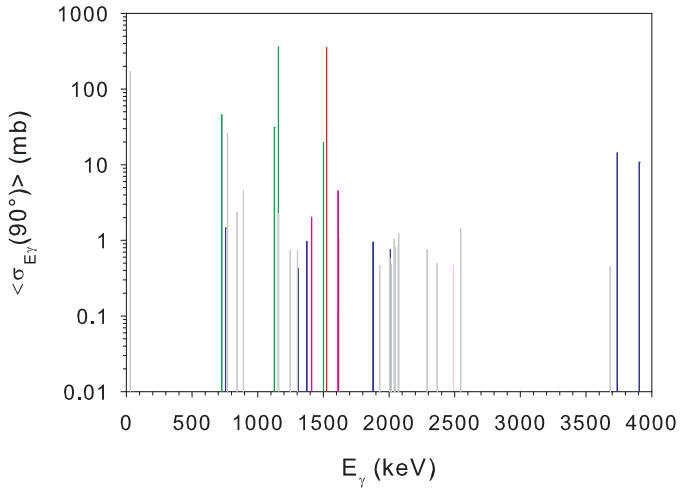


Figure 6.15: Effective isotopic partial γ-ray production cross sections $\langle\sigma_{E\gamma}(90°)\rangle$ of ^{40}Ca (blue), ^{42}Ca (red), ^{44}Ca (green), ^{40}K (grey) and ^{37}Ar (pink) calculated after Eq. (4.1) as a function of the γ-ray energy E_γ. Uncertainties are given in Appx. H.1.1.

6.3.5 Lanthanum (La)

A total of 54 prompt γ-lines from the ^{139}La(n,n'γ)^{139}La reaction were found. These γ-rays are depicted in the measured spectrum (see Appx. G.3) and their data are given in Appx. H.1.11. With respect to [132, 160, 170] and as given in Table 6.7, 12 lines from the ^{139}La(n,γ)^{140}La reaction were identified. Additionally, 18 out of 54 lines were found to have interferences from (n,γ) reactions on ^{35}Cl, ^{138}La and ^{139}La. Contribution of (n,γ) to the net counts was only corrected for the lines at 330.1 (1.3%), 495.2 (9.2%), 1370.5 (1.4%), 1595.2 (2.8%), 1600.3 (18.2%), 1625.6 (11.5%), 2812.1 (24.8%) and 3115.3 keV (23.7%). In all other cases the contribution was well below 1% and hence negligible. No relevant interferences arising from SEs and DEs were present.

Intensities of γ-lines were calculated relative to the 1420-keV line of ^{139}La (100%), fed by the two levels at 1420.3 and 1420.5 keV above g.s. with J^π values of $(11/2)^-$ and $(7/2)^+$ [170], respectively. They are given together with the values determined in [27] in columns 3 and 6 of Appx. H.1.11. In this work, 43 of 51 lines listed in [27] were observed. 24 lines in [27] had been listed without an assignment. Of these, the lines at 174.6, 232.5, 291.3, 308.3, 330.7, 363.1, 403.8, 425.2, 581.3, 1853.6,

2276.2 and 2385.6 keV were found to belong to the ^{139}La(n,n'γ)^{139}La reaction. The unassigned lines at 1626.7, 2071.4, 2210.5, 2244.6 and 2407.0 keV were observed in the FaNGaS measurement and assigned to the (n,n'γ) reaction in ^{139}La, as all other reaction channels were carefully excluded. The line at 2244.6 keV could indeed belong to a level at (2240 $\pm$ 12) keV above g.s. [170] from inelastic scattering, but without any associated γ-ray energies provided in [170] yet.

The γ-lines listed at energies of 846.8, 1462.6, 1613.6, 1766.0, 1951.4, 2298.0, 2314.2 and 2356.1 keV in [27] were not observed in this work. The lines at 846.8, 1462.6, 1613.6 and 2314.2 keV were all unassigned by Demidov et al. and not observed in the measurement performed with FaNGaS due to background interferences with lines of ^{56}Fe and ^{56}Mn, ^{72}Ge, ^{56}Fe and ^{14}N [34, 141], respectively. The fact that no data of those lines is available in [65, 170] provides support that they do probably not belong to ^{139}La. The lines at 1766.0 and 1951.4 keV were not observed due to interferences from Cl, i.e. the ^{35}Cl(n,n'γ)^{35}Cl and the ^{35}Cl(n,γ)^{36}Cl reactions. In fact, the line at 1766.0 keV was present and belongs to the same level at 1766.4 keV above g.s. [170] as the line reported at 1600.3 keV in Appx. H.1.11. The line at 1951.4 keV had been clearly observed by Demidov et al. and [170] provides an excited level of 1950 keV above g.s., without any listed γ-rays yet, to which this line might belong to. Assuming equal FEP efficiency and γ-ray self-absorption for the two lines at 1951 and 1959 keV from the ^{35}Cl(n,γ)^{36}Cl reaction, the ratio in net counts of 2.4 $\pm$ 0.1 (value of 1951-keV line to that of the 1959-keV line) is in disagreement with the ratio of cross sections given in [132], i.e. 1.5 $\pm$ 0.1. Hence, the assignment done by Demidov et al. seems plausible and is assumed to be correct. The line at 2356.1 keV might be emitted from a level at 2357 keV above g.s. [170]. The 2298.0-keV line is not given in [65], but might correspond to an unlisted line seen by Demidov et al. due to the higher mass of La irradiated (0.566 g vs. 18 g [27]).

On the other hand, this work resulted in the identification of 11 new lines. From these, only the lines at 97.1, 495.2 and 1254.1 keV are specified in [170]. The line at 97.1 keV could not be seen by Demidov et al. as the γ energy threshold was set to 120 keV [27]. The line at 495.2 keV was emitted from the same level, i.e. 2032.8 keV above g.s. [170], as the identified line at 232.6 keV listed in Appx. H.1.11. As Demidov et al. had observed the latter one it is unclear why this line had been absent in their measurement. The line at 1254.1 keV was emitted from the same level as the reference line at 1420.5 keV, i.e. 1420.5 keV above g.s. [170], and it is a doublet with the line measured in this work at 1256.6 keV. It could not be resolved by Demidov et al. due to the worse detector resolution. The lines at 153.4, 246.5, 1242.8, 2087.6, 2812.1, 3115.3, 3290.8 and 3789.5 keV are not listed in [65, 170]. However, as the peak statistics ranged between 9.5 and 26.7% and as any other reaction channels were excluded thoroughly, these lines are suggested as new ^{139}La(n,n'γ)^{139}La lines. In particular, the lines at 2812.1, 3115.3 and 3789.5 keV might correspond to direct

transitions to g.s. as the required level energies are known from ^{139}La(γ,γ')^{139}La reactions [170, 171] with incident γ energies between 1.2 and 4.1 MeV, matching well the mean neutron energy at FaNGaS.

At 890.5 keV a line was observed in the spectrum with counting statistics of 9.5%. This line had not been observed by Demidov et al. and it is not listed as a (n,n'γ) line in [170] and, according to [132, 133], this line does not belong to (n,γ) reactions in ^{138}La or ^{139}La. However, according to [160], this line probably refers to the thermal ^{139}La(n,γ)^{140}La reaction. Similar to the 5130.6-keV line in Table 6.7 it is assumed that the intensity of this line differs when induced by epithermal compared to thermal neutron capture as presence of the latter line was not expected based on a thermal neutron capture intensity of 0.37% (derived with a partial elemental cross section of 0.033 b in [160] and an effective isotopic reaction cross section of 9.04 b listed in [132]).

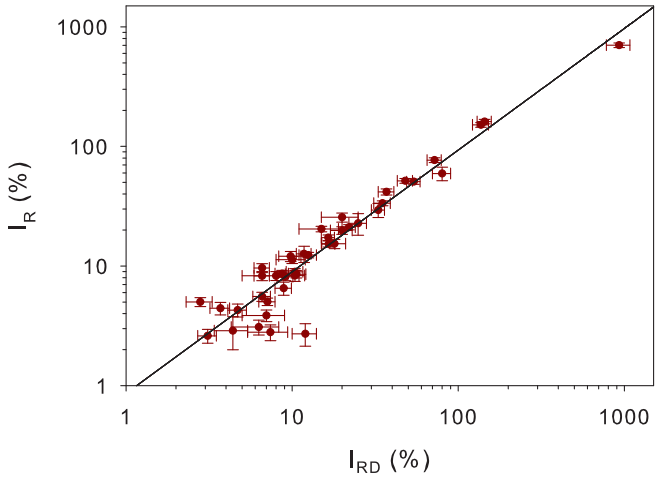


Figure 6.16: Relationship between the relative intensities I_R of the prompt γ-rays induced by fast-neutron inelastic scattering (n,n'γ) reactions on La (^{139}La) measured in this work and the relative intensities I_{RD} tabulated in the Atlas [27]. The solid line represents the fit of the data with Eq. (4.32).

The intensity plot is shown in Fig. 6.16 for all lines. The fit coefficients of Eq. (4.32) are a= 0.86 ± 0.12 and b= 1.02 ± 0.05, respectively. The average intensity ratio I_R/I_{RD} is 0.95 ± 0.27, indicating a reasonable agreement between the two measurements.

A large mismatch in relative intensity was found for the line at 2209.6 keV with a ratio of 0.23 ± 0.06. Owing the worse detector resolution in [27] this line might have been unresolved from the background line listed at 2206.8 keV in the Atlas [27] and maybe the background correction was not done correctly. As the mismatch in intensity is relatively large also for other γ-rays above 2 MeV it might also be a sensitivity issue related to counting statistics, which should be better in the case of Demidov et al. due to the higher mass of La irradiated. The intensity ratio of 1.36

± 0.37 for the 1042.9-keV line is attributed to the complicated peak fitting at the tip of the 1040-keV triangular peak from the ^{70}Ge(n,n'γ)^{70}Ge reaction [34].

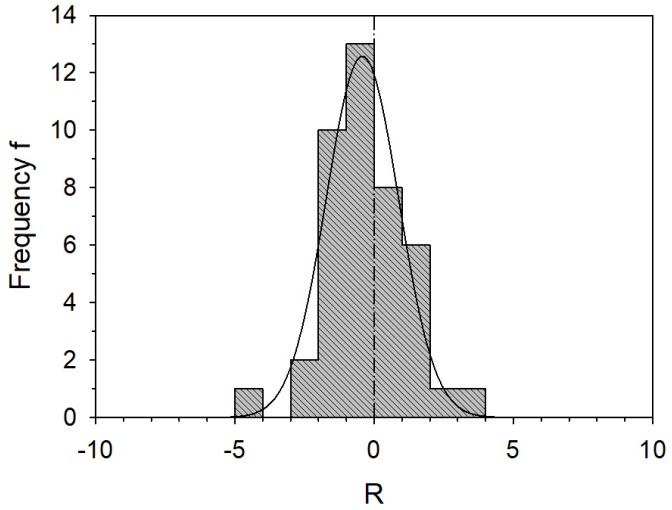


Figure 6.17: Comparison of the relative intensities of the prompt γ-rays induced by fast-neutron inelastic scattering on La obtained in this work with the data tabulated in the Atlas [27] in the form of a histogram of the residuals R in units of standard deviation (σ) calculated with Eq. (4.33). The values of R are given in Appx. H.1.11. The solid line represents the fit of the data with a Gaussian according to Eq. (4.34).

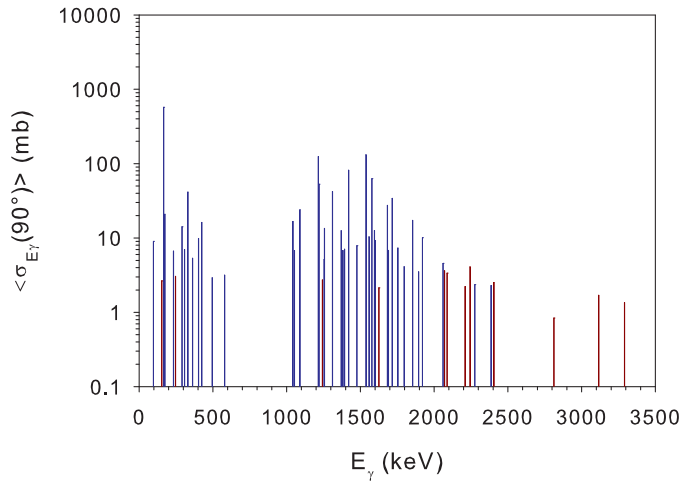


Figure 6.18: Effective isotopic partial γ-ray production cross sections $\langle\sigma_{E\gamma}(90°)\rangle$ of La (^{139}La) calculated after Eq. (4.1) as a function of the γ-ray energy E_γ. Lines in red are proposed as new lines with respect to data in [65]. Uncertainties are given in Appx. H.1.11.

For the line at 402.6 keV a relatively large difference in peak energy with respect to data from Demidov et al. [27] and [65, 170], i.e. 403.8 keV in both cases, was observed. However, as the fit in [65, 170] is characterized as a poor fit, the energy of this transition might have been determined more precisely in this work.

The residual histogram is depicted in Fig. 6.17. The fit of the data agrees at the 1.3σ level and the Gaussian centroid is aligned at R= -0.420 ± 0.119, indicating a probable systematic effect.

The values of $\langle\sigma_{E\gamma}(90°)\rangle$, calculated after Eq. (4.1) using a fast-neutron flux of 1.13 × 10^8 cm^{-2} s^{-1}, are given in Appx. H.1.11 and plotted as a function of the γ-ray energy in Fig. 6.18. The total value of the effective isotopic partial cross sections, (1.49 ± 0.14) b, is very similar to the effective reaction cross section derived with NJOY and listed in Appx. C.2, i.e. (1.33 ± 0.13) b. This might imply that the anisotropy, on average, was negligible at a measuring angle of 90° in the case of La.

6.3.6 Cerium (Ce)

In the analysis of the $CeCl_3$ spectrum 58 prompt γ-lines induced by fast-neutron inelastic scattering reactions were identified. One was related to ^{136}Ce [172], 41 to ^{140}Ce [160] and 16 to ^{142}Ce [173]. These γ-rays are depicted in the γ-ray spectrum shown in Appx. G.4 and their corresponding data are given in Appx. H.1.12 and H.1.13. With respect to [132] and Appx. G.4 a γ-ray marked at 661 keV from the ^{140}Ce(n,γ)^{141}Ce reaction, strongly interfered with the background, might have been present. However, no relevant interferences were identified and the cross sections σ and hence the absolute intensities $I_{E\gamma}$ of other lines reported in [132] are at least one order of magnitude less than for that one given at 662.0 keV (σ= 0.272 b and $I_{E\gamma}$= 47%).

Intensities of γ-lines were calculated relative to the 1596-keV line of ^{140}Ce (100%), emitted from the first 2^+ level at 1596.2 keV above g.s. [160]. They are given together with the values determined in [27] in columns 3 and 6 of Appx. H.1.12 and H.1.13. In this work, 31 out of 45 lines listed in [27], of which only 27 lines were originally assigned to fast-neutron reactions, were detected.

The γ-rays listed at energies of 337.0, 740.0, 774.0, 788.2, 846.3, 983.1, 1041.1, 1045.5, 1059.0, 1098.8, 1233.6, 1463.3, 1526.4, 1620.5, 1724.9, 1812.3, 1899.3 and 1958.5 keV in Demidov's Atlas [27] were reported as tentative assignments and unplaced in the decay schemes of Ce isotopes. The lines at 740.0, 983.1, 1059.0, 1233.6, 1526.4 and 1620.5 keV were observed in this work and assigned based on data provided in [65]. The 337.0-, 846.3-, 1041.1-, 1463.3- and 1958.5-keV lines are not specified in [65] and in addition the placement of the line at 1812.3 keV in the level scheme of ^{140}Ce is uncertain [160]. The lines at 337.0, 846.3, 962.2, 1041.1, 1045.5, 1098.8 and 1463.3 keV were not observed uniquely due to interferences with background lines [34, 141], i.e. from ^{115m1}In (336 keV), ^{56}Fe and ^{56}Mn (846 keV), ^{63}Cu (962 keV), ^{70}Ge (1040 keV), ^{70}Ge (1046 keV), ^{116m1}In (1097 keV) and ^{72}Ge (1463 keV), respectively [34, 141]. In fact, however, the levels of the lines at 1045.5 keV (E^*= 3394.9 keV in ^{140}Ce [160]) and at 1098.8 keV (E^*= 3001.1 keV in ^{140}Ce [160]) were excited as lines at 1404.9 and 982.2 keV, accompanying the respective emissions, were clearly identified. The lines at 788.2 and 1958.5 keV belong mainly

to the (n,γ) lines of ^{35}Cl and the lines at 774.8 and 2347.5 keV were essentially issued from the ^{35}Cl(n,pγ)^{35}S reaction. The latter lines had been both reasonably attributed to ^{140}Ce by Demidov et al. with regard to [65, 160]. In fact, the line at 774.8 keV was emitted from E^*= 3255.7 keV above g.s. [160] as the line observed at 739.6 keV in this work belongs to the same level. The 1724.9-keV line was not identified uniquely due to strong interferences with the 1726.2-keV line of ^{37}Cl and the background lines of ^{207}Pb and ^{56}Fe at 1725 keV [34]. The line at 1899.3 keV given in [27] was predominantly associated to the 1900.0-keV line of ^{37}Cl.

Escape peak corrections were necessary for several lines. The DEs of the lines at 1762.9 keV (^{35}Cl) and 2645.2 keV (^{35}Cl) as well as the SE of the line at 3625.5 keV (^{37}Cl) were found to interfere significantly with the lines at 739.6, 1623.6 and 3118.2 keV, respectively. Their contributions to the net count rates were estimated with Eq. (4.24) to be (34.9 $\pm$ 3.3)%, (41.9 $\pm$ 4.9)% and (14.5 $\pm$ 2.5)%, respectively. The contribution of the DE of the background line at 2614 keV (^{208}Pb) [34, 141] was negligible with (0.11 $\pm$ 0.02)%.

According to [65, 160], γ-lines of ^{140}Ce might be expected at energies of 1085 and 1252 keV. In fact, the recorded spectrum showed justified signals at these energies. However, by means of Eq. (4.24) these peaks were identified as pure escape peaks of the 1596.0-keV line of ^{140}Ce and the 1762.9-keV line of ^{35}Cl with contributions of (99.3 $\pm$ 7.3)% and (94.0 $\pm$ 10.3)% to the net counts, respectively. Hence, for the line at 1085 keV, actually given with a questionmark in [65, 160], the FaNGaS measurement can confirm that the signal is only produced by the SE of the 1596.0-keV line.

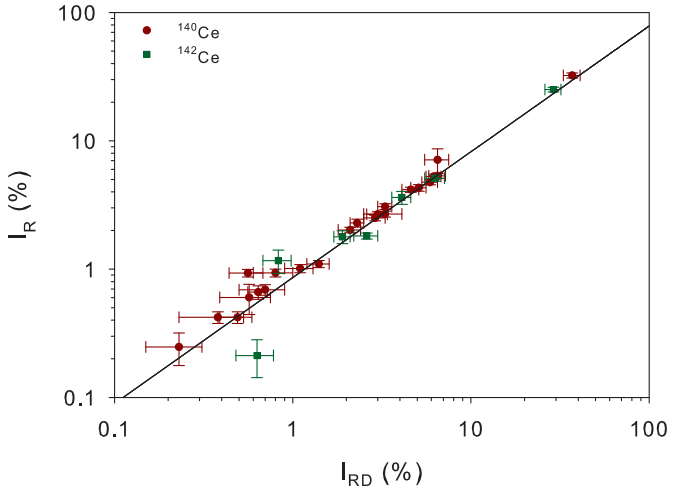


Figure 6.19: Relationship between the relative intensities I_R of the prompt γ-rays induced by fast-neutron inelastic scattering (n,n'γ) reactions on Ce (^{140}Ce and ^{142}Ce) measured in this work and the relative intensities I_{RD} tabulated in the Atlas [27]. The solid line represents the fit of the data with Eq. (4.32).

The line listed at 1724.9 keV in [27], emitted from E^*= 3319.7 keV in ^{140}Ce

[160], is accompanied by a line at 3319.3 keV. Absence of this line in the Demidov measurement could be related to the upper γ energy threshold of 3.4 MeV [27]. The line at 3120.4 keV in the Atlas [27] had been assigned to a level with E^*= 3120.4 keV and given with a relative intensity of (0.56 ± 0.12)%. However, with respect to the ENSDF file the relative intensity should be (10 ± 1)% [160]. Another line listed at 3118.5 keV from a level with E^*= 3318.5 keV was given with an intensity of (1.02 ± 0.05)%, which is in good agreement with the intensity evaluated in this work, i.e. (0.93 ± 0.06)%. Hence, the γ-line should belong in both data sets to the same level at 3118.5 keV. Identification of the line at 1058.1 keV of ^{142}Ce is accompanied with a line at 1637 keV according to [65, 173]. This line should be even more than twice stronger in intensity than the 1058.1-keV line, but no data was given due to an imprecise fit owing a strong interference with the Doppler-broadenend background line from the ^{14}N(n,n'γ)^{14}N reaction. The background line from N had not been reported in [27] and since the relative intensity of the line at 1058.1 keV strongly disagrees between the two data sets (0.21% vs. 0.63% in [27]), a faulty analysis of this line in [27] is assumed as the line at 1637 keV was not reported.

On the other hand, in comparison to [27] 27 new γ-lines were detected (one for ^{136}Ce, 17 for ^{140}Ce and 9 for ^{142}Ce) which are all specified in [65]. Owing the better detector resolution of the HPGe detector the doublets in the lines given by Demidov et al. at energies of 522.0, 894.8 and 1404.3 keV were resolved.

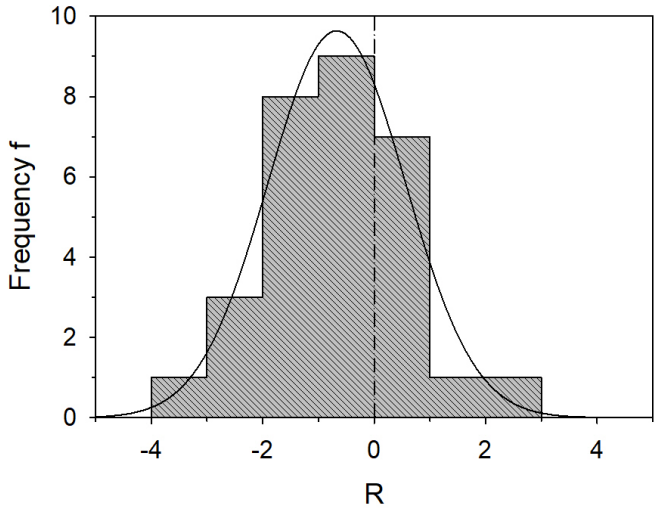


Figure 6.20: Comparison of the relative intensities of the prompt γ-rays induced by fast-neutron inelastic scattering on Ce obtained in this work with the data tabulated in the Atlas [27] in the form of a histogram of the residuals R in units of standard deviation (σ) calculated with Eq. (4.33). The values of R are given in Appx. H.1.12 and H.1.13. The solid line represents the fit of the data with a Gaussian according to Eq. (4.34).

The intensity plot is depicted in Fig. 6.19 for all lines. The values of the fit coefficients of Eq. (4.32) are a= 0.86 ± 0.06 and b= 0.98 ± 0.05, respectively. The

average intensity ratio I_R/I_{RD} is 0.93 ± 0.23, indicating a reasonable agreement between the two measurements.

The residual histogram is shown in Fig. 6.20. The fit of the data agrees at the 1.2σ level and the Gaussian centroid is aligned at R_0= -0.671 ± 0.084, indicating a probable systematic effect.

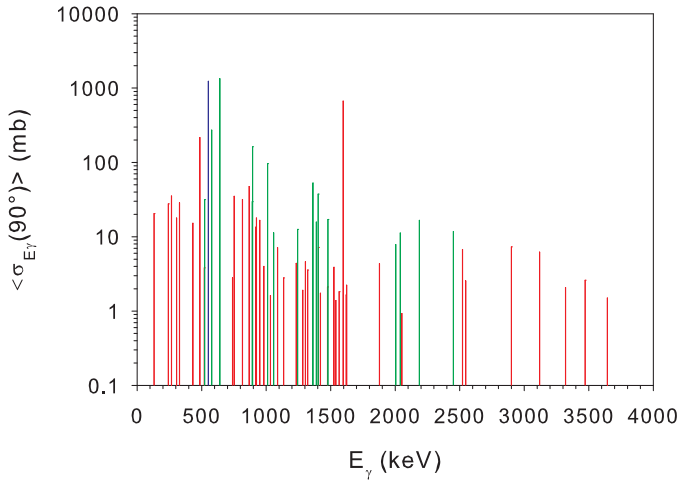


Figure 6.21: Effective isotopic partial γ-ray production cross sections $\langle\sigma_{E\gamma}(90°)\rangle$ of ^{136}Ce (blue), ^{140}Ce (red) and ^{142}Ce (green) calculated after Eq. (4.1) as a function of the γ-ray energy E_γ. Uncertainties are given in Appx. H.1.12 and H.1.13.

The values of $\langle\sigma_{E\gamma}(90°)\rangle$, calculated after Eq. (4.1) with a fast-neutron flux of 1.13 × 10^8 cm^{-2} s^{-1}, are plotted as a function of the γ-ray energy in Fig. 6.21. The total value of the effective isotopic partial cross sections was determined as (1.23 ± 0.17) b, (1.29 ± 0.13) b and (2.11 ± 0.20) b for the ^{136}Ce(n,n'γ)^{136}Ce, ^{140}Ce(n,n'γ)^{140}Ce and ^{142}Ce(n,n'γ)^{142}Ce reactions. The corresponding effective reaction cross sections obtained from NJOY as provided in Appx. C.2, i.e. (1.43 ± 0.14) b, (0.92 ± 0.08) b and (1.18 ± 0.11) b suggest moderate anisotropy in the case of ^{136}Ce and ^{140}Ce but a strong effect for ^{142}Ce. As from ^{136}Ce only one single γ-line was identified, an angular-distribution correction factor of $W(\theta)$= 0.86 ± 0.15 could be estimated for this transition.

6.3.7 Praseodymium (Pr)

The measurement of the $PrCl_3 \cdot 7H_2O$ sample yielded a total of 71 prompt γ-lines from the ^{141}Pr(n,n'γ)^{141}Pr reaction. These γ-rays are depicted in the spectrum given in Appx. G.5 and their data are given in Appx. H.1.14. With respect to [132] and as given in Table 6.8, 4 lines from the ^{141}Pr(n,γ)^{142}Pr reaction were identified. For 9 out of 71 γ-lines interferences with (n,γ) reactions on ^{35}Cl and ^{141}Pr were identified. The contribution of (n,γ) reactions to the net counts ranges between 1.4 and 33.9%.

Intensities of γ-lines were calculated relative to the 1126-keV line of ^{141}Pr (100%), which is a direct transition to g.s. from the level at 1126.8 keV with a J^π value of

$(3/2)^+$ [174]. They are given along with the values determined in [27] in columns 3 and 6 of Appx. H.1.14. In this work, 57 of 77 listed lines in [27] were observed. 23 lines in [27] had been listed without an assignment. Of these, the 14 lines listed at 218.3, 273.3, 749.2, 861.5, 1023.1, 2027.1, 2061.4, 2136.2, 2159.7, 2352.8, 2403.9, 2453.6, 2581.2 and 2603.1 keV were also observed in this work and found to belong to the ^{141}Pr(n,n'γ)^{141}Pr reaction [174]. Another unassigned line listed at 1825.2 keV [27], unspecified in [65, 174], was also related to inelastic scattering on ^{141}Pr in this work as all other origins were carefully excluded.

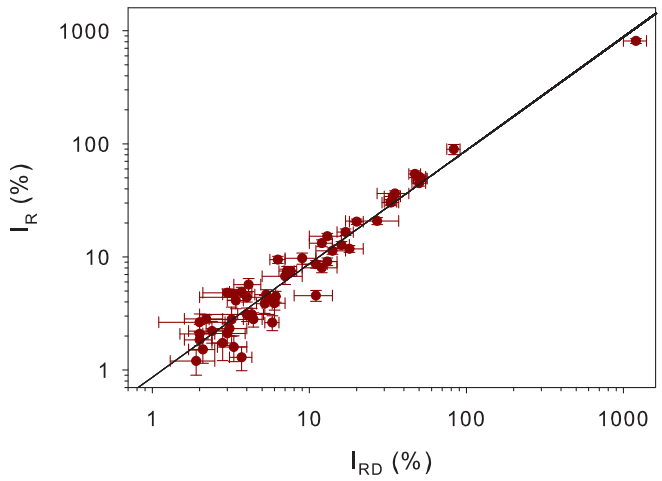


Figure 6.22: Relationship between the relative intensities I_R of the prompt γ-rays induced by fast-neutron inelastic scattering (n,n'γ) reactions on Pr (^{141}Pr) measured in this work and the relative intensities I_{RD} tabulated in the Atlas [27]. The solid line represents the fit of the data with Eq. (4.32).

For the γ-rays at 1506.0, 2082.1, 2104.8, 2135.5 and 2354.3 keV significant interferences from escape peaks were found using Eq. (4.24). Aforementioned peaks were interfered by the lines at 2017.2 (^{141}Pr, SE), 3103.1 (^{37}Cl, DE), 2614 (^{208}Pb, SE), 2645.3 (^{35}Cl, SE) and 2864 keV (^{35}Cl, SE) with contributions to the net counts of $(3.5 \pm 0.5)\%$, $(56 \pm 18)\%$, $(60 \pm 4)\%$, $(41 \pm 3)\%$ and $(17.6 \pm 3.6)\%$, respectively.

A total of 20 γ-lines listed in [27] were not observed in the measurement performed with FaNGaS. These include the lines tabulated at energies of 179.6, 268.3, 277.5, 302.1, 339.9, 352.7, 523.6, 558.6, 723.6, 893.0, 981.7, 1140.3, 1292.6, 1696.8, 1961.9, 2282.9, 2313.8, 2414.4, 2462.4 and 2559.6 keV. For all of the aforementioned lines plausible data is available in [65, 174], except the lines at 179.6, 268.3, 277.5, 1140.3, 2282.9, 2414.4, 2462.4 and 2559.6 keV. At energies of 179.6, 268.3, 277.5, 2282.9, 2414.4, 2462.4 and 2559.6 keV no γ-ray peak with relevant statistics was observed in the spectrum. Missing data in [65, 174] might provide support that these lines probably do not belong to ^{141}Pr. The lines listed at energies of 302.1, 339.9, 352.7, 523.6, 558.6, 723.6 and 893.0 keV, respectively, had relative intensities ranging between 1.3 and 4.0% [27]. Their absence in this work was attributed to

the lower Pr mass irradiated (0.561 g vs. 9.2 g in [27]). In fact, the level of many of those lines was also excited in the FaNGaS measurement. For example, the line at 352.7 keV was accompanied by the line observed in this work at 2061.0 keV from the same level at 2206.0 keV above g.s. [174]. The lines at 981.7, 1140.3, 1292.6, 1696.8, 1961.9 and 2313.8 could not be uniquely identified in this work due to interferences with ^{208}Pb, ^{70}Ge, ^{40}Ar and ^{116m}In, ^{74}Ge, ^{35}Cl and ^{14}N, respectively. From the aforementioned lines only the 1140.3-keV line is not specified in [65, 174]. For the γ-lines at 1140.3, 2414.4 and 2559.6 keV definitely a mistake done by Demidov et al. has to be concluded: neither the level energies nor the γ-ray energies provided in the Atlas [27] are found in [65, 174]. A discrepancy between the level energies in the Atlas [27] based on [175] and those given in [65, 174] was observed for many lines. This could be reasoned in inaccurate or incomplete nuclear data at that time.

On the other hand, 14 new lines were identified in this work. These include the lines at 311.2, 948.5, 974.6, 1264.3, 1872.3, 2042.9, 2082.1, 2119.1, 2267.1, 2419.5, 2437.1, 2563.6, 3111.6 and 3127.7 keV. From these, all are listed in [174]. The line observed at 948.5 keV might not be observed by Demidov et al. due to a close-lying interference from their background [27]. The line at 974.6 keV could not be seen uniquely due to a doublet structure in [27] with the line listed at 972.2 keV. The observed line at 1264.3 keV came from an excited level with 2382.2 keV above g.s. [174], from which also the line at 861.0 keV was emitted. As the latter one was also reported in [27], it is surprising that the 1264.3-keV line had not been observed by Demidov et al. The same observation probably applies also to the lines at 311.2, 1872.3, 2042.9 and 2437.1 keV, for which other lines from the respective excited levels had been observed by Demidov et al. Absence of the remaining γ-rays in the Atlas [27] is assumed to be reasoned in the different level excitation due to the different neutron-energy spectra. Obviously, there were levels excited in this work, which had not been excited by Demidov et al. and vice versa. The line at 2082.1 keV had a strong interference from the DE of the 3103.1-keV line from the ^{37}Cl(n,n'γ)^{37}Cl reaction, i.e. 56% contribution to the net counts. A line was suspected as the SE and the DE of the 3103.1-keV line seemed to be equal in intensity when looking in details into the spectrum (see Appx. G.5). According to [174] this line is plausible and refers to a direct transition to g.s.

The intensity plot is given in Fig. 6.22. The coefficients for the fit with Eq. (4.32) are a= 0.86 $\pm$ 0.07 and b= 1.00 $\pm$ 0.03. The average intensity ratio I_R/I_{RD} is 0.91 $\pm$ 0.27, indicating a reasonable agreement.

An intensity ratio of 0.78 $\pm$ 0.40 implies that the line observed at 2601.5 keV could correspond to the line at 2603.1 keV reported in the Atlas [27]. However, according to [174, 176] there exist two very close levels, one at 2601.2 and the other one at 2603.7 keV with γ-rays of 2601.3 and 2603.1 keV both corresponding to an E1 transition. Excitation of the 2601.2-keV level should be accompanied by another line at 2455.7 keV [174, 176], which is lower in intensity. This line might be present next

to the 2452.7-keV line but no fit with significant counting statistics could be done. Vice versa, excitation of the 2603.7-keV level is accompanied by a line at 2458.7 keV, which had not been observed by Demidov. Nevertheless, in fact the γ-ray reported in this work matches better to the 2601.3-keV level, whereas that one from Demidov et al. is closer to the 2603.1-keV level. Therefore, although the relative intensities agree quite well, those γ-rays might correspond to different transitions.

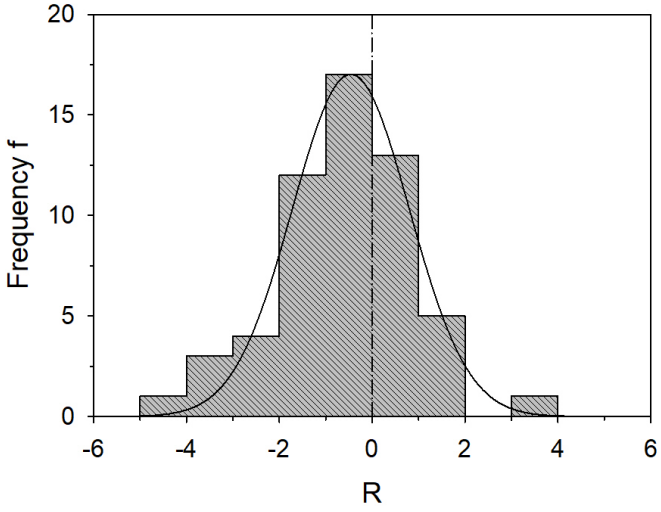


Figure 6.23: Comparison of the relative intensities of the prompt γ-rays induced by fast-neutron inelastic scattering on Pr obtained in this work with the data tabulated in the Atlas [27] in the form of a histogram of the residuals R in units of standard deviation (σ) calculated with Eq. (4.33). The values of R are given in Appx. H.1.14. The solid line represents the fit of the data with a Gaussian according to Eq. (4.34).

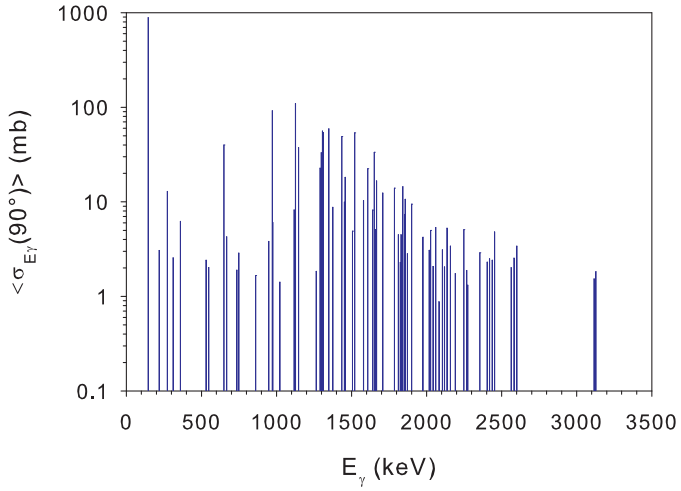


Figure 6.24: Effective isotopic partial γ-ray production cross sections $\langle\sigma_{E\gamma}(90°)\rangle$ of Pr (^{141}Pr) calculated after Eq. (4.1) as a function of the γ-ray energy E_γ. Uncertainties are given in Appx. H.1.14.

The histogram plot is depicted in Fig. 6.23. The fit of the data agrees at the

1.3σ level and the Gaussian centroid is aligned at R_0= -0.459 ± 0.068, indicating a probable systematic effect.

The values of $\langle\sigma_{E\gamma}(90°)\rangle$, calculated after Eq. (4.1) using a fast-neutron flux of 1.13 × 10^8 cm^{-2} s^{-1}, are given in column 4 of Appx. H.1.14. Additionally, they are plotted as a function of the γ-ray energy in Fig. 6.24. The total value of the effective isotopic partial cross sections, (1.85 ± 0.17) b, is similar to the effective reaction cross section derived with NJOY as given in Appx. C.2, i.e. (1.52 ± 0.15) b. This might imply that the anisotropy, on average, was small at a measuring angle of 90° in the case of Pr.

6.3.8 Neodymium (Nd)

The measurement of $NdCl_3$ resulted in the identification of 111 prompt γ-rays of Nd induced by inelastic scattering reactions of fast neutrons. These γ-rays are depicted in the measured spectrum (see Appx. G.6) and their data are given from Appx. H.1.15 to H.1.22. From the aforementioned lines 14 were associated to ^{142}Nd, 13 to ^{143}Nd, 26 to ^{144}Nd, 7 to ^{145}Nd , 24 to ^{146}Nd, 8 to ^{148}Nd and 11 to ^{150}Nd. The remaining 8 lines were found to be fed by two isotopes (multi-isotope lines) each with significant contributions, as given in Appx. H.1.22. With respect to [132] and [133] no pure (n,γ) lines of Nd were observed. However, for 52 (n,n'γ) lines contribution of (n,γ) reactions in ^{35}Cl, ^{142}Nd, ^{143}Nd and ^{145}Nd were checked. Contributions were found to range between 0.02 and 28.7%. For 7 lines, contributions below 1% to the net counts were neglected. Inspection of data in [133], in addition to [132], resulted in the identification of a few further interferences that were also corrected.

Intensities of γ-lines were calculated relative to the 696-keV line of ^{144}Nd (100%), which is a direct transition to g.s. from the first 2^+ level at 696.6 keV [173]. They are given together with the values determined in [27] in columns 3 and 6 of Appx. H.1.15 to H.1.22. In this work, 39 of 44 listed lines in [27] were observed. 19 lines in [27] had been listed without a clear assignment. Of these, the lines listed at energies of 262.3, 334.2, 582.5, 657.9, 676.6, 748.0, 789.8, 921.7, 946.6, 971.0, 1149.8, 1162.0, 1247.5 and 1333.1 keV were observed with acceptable statistics and found to belong to inelastic scattering reactions in Nd with respect to data provided in [65], i.e. [173, 177–182].

For the γ-rays at 1671.8 (^{144}Nd) and 2135.1 keV (^{143}Nd) significant interferences from escape peaks were found using Eq. (4.24). Aforementioned lines were interfered by the DE of the 2693.0-keV line of ^{35}Cl and the SE of the 2645.0-keV line of ^{35}Cl with contributions to the net counts of (20.1 ± 4.1)% and (54 ± 5)%, respectively. For the lines at 813.7 and 864.0 keV from the ^{144}Nd(n,n'γ)^{144}Nd reaction, interfered by the SE of ^{146}Nd (1323.4 keV) and the SE of $^{144+146}$Nd (1376.6 keV), contributions of (0.29 ± 0.02)% and (0.42 ± 0.02)% were neglected.

The 5 tentatively assigned γ-lines in [27] listed at energies of 326.4, 439.1, 630.8, 1212.0 and 1466 keV were not observed in this work. The line at 326.4 keV, given

with a questionmark and the comment "bg?" in [27], had been associated to a background line of ^{73}Ge [27]. The data for the lines at 439.1, 630.8 and 1466 keV must be reviewed carefully as, surprisingly, corresponding background lines are given in the Atlas [27] at 440.0 (^{23}Na), 630.8 (origin unclear) and 1463.3 keV (^{72}Ge). Absence of the line at 439.1 keV and the fact that no justified transitions are proposed in [65] provide support that this line does not belong to Nd. At 630.8 and 1212.0 keV no relevant line was identified in the spectrum, but transitions might be possible [65]. Observation of a line around 1466 keV was hindered by the 1463-keV line arising from the ^{72}Ge(n,n'γ)^{72}Ge reaction in the HPGe crystal, but might be also possible with regard to [65].

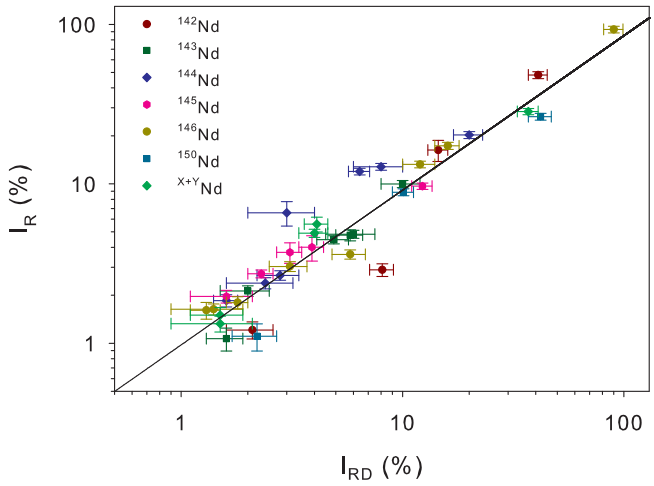


Figure 6.25: Relationship between the relative intensities I_R of the prompt γ-rays induced by fast-neutron inelastic scattering (n,n'γ) reactions on Nd measured in this work and the relative intensities I_{RD} tabulated in the Atlas [27]. The solid line represents the fit of the data with Eq. (4.32).

On the other hand, the irradiation of Nd resulted in the identification of 72 new γ-lines. All corresponding transitions are specified in [65] and from these 10 were assigned to ^{142}Nd, 7 to ^{143}Nd, 18 to ^{144}Nd, 2 to ^{145}Nd, 16 to ^{146}Nd, 8 to ^{148}Nd, 8 to ^{150}Nd and another 3 lines to a reaction fed by two isotopes. Demidov et al. had observed only one single transition corresponding to the ^{148}Nd(n,n'γ)^{148}Nd reaction (301.7 keV [27]). Besides the fact that these lines had small relative intensities below 5% in this work, this observation might also be attributed to the anisotropy in γ-ray emission of ^{148}Nd, that is expected to be different in the measurement by Demidov et al. owing the differences in the neutron-energy spectra. The lines observed at energies of 301.2, 722.0, 946.2, 1249.2 and 1376.6 keV were assigned to two different isotopes of Nd in this work, i.e. $^{144+148}$Nd, $^{148+150}$Nd, $^{146+148}$Nd, $^{145+148}$Nd and $^{144+146}$Nd, respectively. The 946.2- and 1249.2-keV lines were unassigned and the lines at 301.2, 722.0 and 1376.6 keV had been assigned to ^{148}Nd, ^{150}Nd and ^{146}Nd in [27]. In fact, in this work the three aforementioned lines of Demidov et al. were

also fed by the isotopes ^{144}Nd, ^{144}Nd and ^{148}Nd as other lines at 2073.1, 778.3 and 1022.4 keV from the same levels (2901.4 and 2093.3 keV in ^{144}Nd [178], respectively, and 1023.2 keV in ^{148}Nd [181]) were clearly identified.

The lines observed at 882.4 and 1333.0 keV, assigned to the ^{146}Nd(n,n'γ)^{146}Nd reaction, could not be observed by Demidov et al. due to close-lying background interferences reported at 880.9 (^{206}Pb) and 1332.6 keV (^{60}Ni) [27]. Observation of the new line at 1170.7 keV from the ^{148}Nd(n,n'γ)^{148}Nd reaction might be hindered in [27] by a background line reported at 1173.1 keV from ^{60}Ni. Observation of the new lines at 474.0 (^{146}Nd), 527.0 (^{148}Nd), 720.0 (^{150}Nd) and 922.8 keV (^{148}Nd) was related to the better energy resolution of the FaNGaS spectrometer, resulting in resolving the doublets for lines given at energies of 476.6, 525.5, 722.7 and 921.7 keV, respectively, in [27].

Another line listed in Appx. H.1.15, observed at 502.0 keV, was not assigned as no plausible transition was identified in [65]. In fact, this line might correspond to a new transition not included in the NuDat 3.0 [65] database yet, as the counting statistics were acceptable (18.5% uncertainty).

The intensity plot is given in Fig. 6.25 for all lines. The values for the fit coefficients with Eq. (4.32) are a= 0.98 ± 0.10 and b= 0.97 ± 0.05, respectively. The average intensity ratio I_R/I_{RD} is 1.03 ± 0.34, indicating a reasonable agreement between the two measurements.

The line at 476.6 keV in [27] was evaluated as a doublet of the lines at 474.0 and 476.2 keV in this work. However, the resulting intensity ratio compared to the Atlas [27] shows a strong disagreement with 2.19 ± 0.80. This was unexpected as the line in the Atlas is marked with a "m", indicating it was fed by two or more transitions [27]. Nevertheless, it is unclear how Demidov et al. could draw this conclusion. It could also imply that the corresponding level of the 474.0-keV line (E^*= 1517.6 keV [180]) had not been excited with Demidov's spectrum. This possibility cannot be ruled out with certainty, as the relaxation of this level is not accompanied by another line of considerable intensity [180].

With respect to [132], strong interferences from (n,γ) reactions in ^{142}Nd and ^{143}Nd reactions were expected for the observed 617.4-, 696.0-, 741.6-, 813.7- and 864.0-keV lines. For the first three of the aforementioned lines the intensity ratios relative to Demidov's work are close to one. For the latter two ones, however, ratios of 1.87 ± 0.22 and 1.60 ± 0.41 might imply an incorrect or missing interference correction in [27]. In fact, it is unclear if and how Demidov et al. have handled interferences from (n,γ) reactions. From the Atlas [27], however, it is evident that thermal neutron data listed in [29] (for elements with $Z \leq 46$) and [30] (for elements from Z= 47 to Z= 67, i.e. Ag to Ho) had been considered for corrections. In [30] data is listed from different sources. Absolute intensities of (34 ± 1)%, (84 ± 5)%, (75 ± 6)%, (12.6 ± 0.1)% and (10.8 ± 0.1)% were determined for aforementioned γ-lines in order of increasing energy according to data provided in [132]. Compared

to the intensities listed in [30] from private communication with Rasmussen et al., i.e. 23.7, 62, 5.90, 8.87 and 8.82%, a considerable discrepancy between the nuclear data can be observed. Besides the fact that it is unclear if and which of the different values listed in [30] Demidov et al. might have used in order to correct for (n,γ) interferences, the used data seems to be inaccurate compared to the most recent data listed in [132]. Nevertheless, presence of (n,γ) lines is clear from the examination of their spectra, but the interferences might be much severe compared to this work as their spectrum might comprise higher thermal and epithermal neutron-flux values. Unfortunately, their neutron-energy spectrum is not characterized below 0.5 MeV [28].

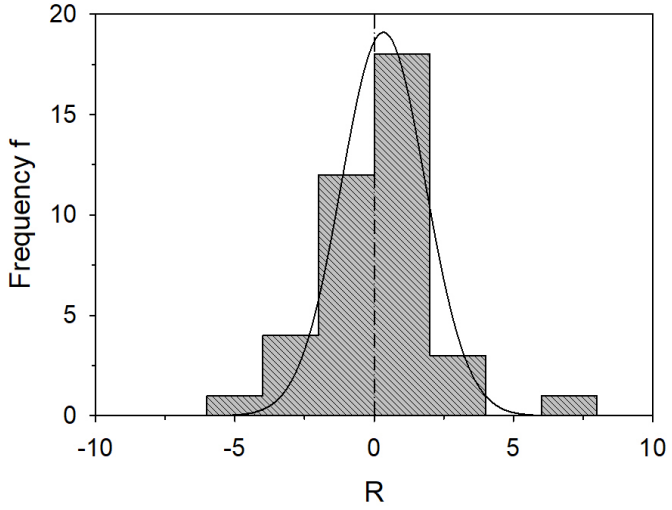


Figure 6.26: Comparison of the relative intensities of the prompt γ-rays induced by fast-neutron inelastic scattering on Nd obtained in this work with the data tabulated in the Atlas [27] in the form of a histogram of the residuals R in units of standard deviation (σ) calculated with Eq. (4.33). The values of R are given in Appx. H.1.15 to H.1.22. The solid line represents the fit of the data with a Gaussian according to Eq. (4.34).

The residual histogram is given in Fig. 6.26. The fit of the data agrees at the 1.5σ level and the Gaussian centroid is aligned at R= 0.333 ± 0.122, indicating a probable systematic effect.

The effective isotopic partial γ-ray production cross sections, calculated after Eq. (4.1), are plotted as a function of the γ-ray energy in Fig. 6.27. The total value of the isotopic partial cross sections was determined as (1.00 ± 0.10) b, (0.90 ± 0.10) b, (2.50 ± 0.24) b, (0.88 ± 0.11) b, (3.20 ± 0.31) b, (0.70 ± 0.12) b and (2.94 ± 0.30) b for the ^{142}Nd(n,n'γ)^{142}Nd, ^{143}Nd(n,n'γ)^{143}Nd , ^{144}Nd(n,n'γ)^{144}Nd, ^{145}Nd(n,n'γ)^{145}Nd, ^{146}Nd(n,n'γ)^{146}Nd, ^{148}Nd(n,n'γ)^{148}Nd and ^{150}Nd(n,n'γ)^{150}Nd reactions. The effective reaction cross sections obtained with NJOY as listed in Appx. C.2 are (0.96 ± 0.09) b, (1.25 ± 0.11) b, (1.59 ± 0.15) b, (2.00 ± 0.21) b, (1.92 ± 0.19) b, (2.15 ± 0.22) b and (2.41 ± 0.25) b, respectively. Neglecting the lines fed

by two isotopes, one might conclude a significant anisotropy in all reactions except for the isotope ^{142}Nd for which both values are almost identical, on average.

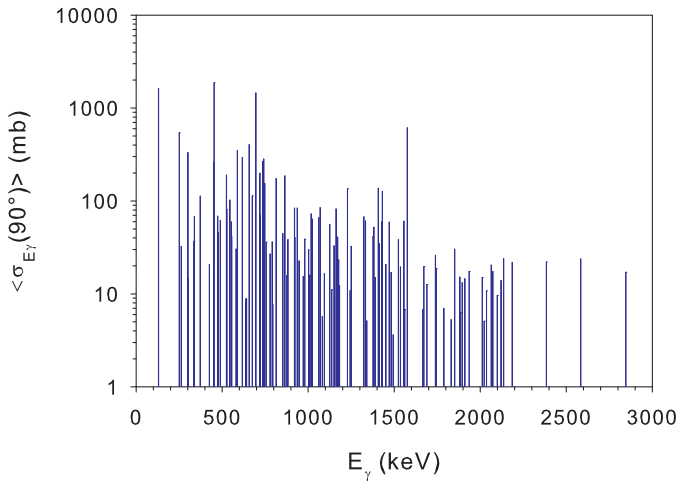


Figure 6.27: Effective isotopic partial γ-ray production cross sections $\langle\sigma_{E\gamma}(90°)\rangle$ of Nd calculated after Eq. (4.1) as a function of the γ-ray energy E_γ. Uncertainties are given in Appx. H.1.15 to H.1.22.

6.3.9 Samarium (Sm)

A total of 141 prompt γ-rays of Sm induced by fast-neutron inelastic scattering were identified. These γ-rays are depicted in Appx. G.7 and their data are given from Appx. H.1.23 to H.1.30. From the observed lines 6 were assigned to ^{144}Sm, 12 to ^{147}Sm, 30 to ^{148}Sm, 9 to ^{149}Sm , 20 to ^{150}Sm, 25 to ^{152}Sm and 14 to ^{154}Sm. The remaining 25 lines correspond to multi-isotope lines and they were found to be fed by two or three isotopes each with significant contributions. With respect to [132] and [133] several pure (n,γ) lines were identified, as given in Table 6.6. A total of 780 γ-rays from (n,γ) reactions in Sm are listed in [133]. Each single line was checked carefully for possible interferences and the counts produced by capture were calculated according to Eqs. (4.26) and (4.30). For 70 γs contributions of neutron capture to the net counts from 1% up to about 100% were determined. γ-lines with contributions above 90% were assumed to be pure capture γ-rays. With respect to Table 6.6 the capture γs from the ^{152}Sm(n,γ)^{153}Sm reaction show a systematic discrepancy in intensity compared to thermal neutron data [132, 133] above 90 keV, which is probably attributed to the high resonance capture cross sections. To correct for this deviation, a mean intensity ratio of 0.30 $\pm$ 0.06, derived with the data of 12 capture lines from 127.2 to 5831.5 keV given in Table 6.6, was used as a scaling factor for the counts produced by the capture reaction in ^{152}Sm.

Intensities of γ-lines were calculated relative to the 550-keV line of ^{148}Sm (100%), which is a direct transition to g.s. from the first 2^+ level at 550.3 keV [181]. They are given together with the values determined in [27] in columns 3 and 6 of Appx.

H.1.23 to H.1.30. For Sm, Demidov et al. had carried out measurements with isotopic enriched samples (for ^{144}Sm, ^{148}Sm, ^{150}Sm, ^{152}Sm and ^{154}Sm) in addition to the measurement of a Sm sample with natural isotope abundances (Sm_2O_3 [27]). Compared to the latter measurement, 63 of 73 lines listed in [27] were identified in this work. 13 of 73 lines in [27] had been listed as tentative assignments. From these, the lines at 215.1, 222.8, 320.6, 461.5, 716.5, 969.4 and 1408.9 keV were observed and related to (n,n'γ) transitions in Sm according to data given in [65, 178, 181–186]. Surprisingly, however, except the aforementioned 461.5-, 969.4- and 1408.9-keV lines these γ-rays had not been observed in the isotopic measurements of Demidov et al.

For the line at 1251.0 keV from ^{147}Sm a significant contribution to the net counts, i.e. $(69 \pm 3)\%$, from the SE of the 1763.5-keV line resulting from the ^{35}Cl(n,n'γ)^{35}Cl reaction was calculated according to Eq. (4.24).

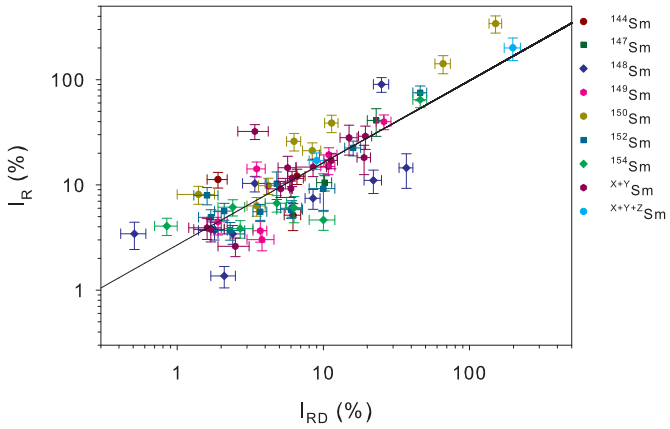


Figure 6.28: Relationship between the relative intensities I_R of the prompt γ-rays induced by fast-neutron inelastic scattering (n,n'γ) reactions on Sm measured in this work and the relative intensities I_{RD} tabulated in the Atlas [27]. The solid line represents the fit of the data with Eq. (4.32).

The γ-lines listed at energies of 158.7, 197.4, 228.5, 297.7, 361.6, 535.8, 563.2, 930.0, 1096.5 and 1204 keV in [27] were not observed in this work. Absence of the unassigned lines at 228.5 and 361.6 keV and plausible data provided in [65] suggests that these lines do not belong to Sm. Curiously, the two aforementioned lines had not been observed in Demidov's isotopic measurements. The line at 930.0 keV could not be identified uniquely due to an interference from the ^{35}Cl(n,n'γ)^{35}Cl reaction. The assignment of the 930.0-keV line by Demidov et al. to ^{154}Sm had been confirmed by their isotopic measurement as well as with this work, since the measured 745.5-keV line belongs to the same level (E^*= 1012.4 keV [65, 186]). For the lines at 158.7, 197.4, 297.7, 535.8, 563.2, 1096.5 and 1204 keV strong background interferences were identified with respect to [34, 141] and [27]. Possible transitions are provided in [65] for all of these lines. In particular, correct assignment is assumed for the lines at 158.7, 297.7, 563.2 and 1096.5 keV as these had been recognized by

Demidov et al. in their isotopic measurements. Nevertheless, those lines should be reviewed carefully owing the aforementioned background interferences. The line at 535.8 keV, assigned to the ^{149}Sm(n,n'γ)^{149}Sm reaction in [27], is plausible as the line at 557.6 keV belonging to the same level (E^*= 558.4 keV [65, 184]) was clearly observed in this work.

The lines listed at 127.3 and 166.5 keV were listed without any assignment by Demidov et al. Both lines were observed and found to belong to the (n,γ) reactions in ^{152}Sm and ^{150}Sm with absolute intensities of 7.4 and 9.9% [132], respectively.

On the other hand, the irradiation of Sm resulted in the identification of 83 new lines. All corresponding transitions are specified in [65] and from these 4 were assigned to ^{144}Sm, 10 to ^{147}Sm, 21 to ^{148}Sm, 2 to ^{149}Sm, 12 to ^{150}Sm, 16 to ^{152}Sm, 8 to ^{154}Sm and 10 to more than one contributing isotope (see Appx. H.1.30). A total of 50 of those lines had been confirmed by the isotopic measurements performed by Demidov et al. Absence of the remaining 33 lines in Demidov's measurement is probably related to differences in the neutron-energy spectra and hence in the excitation processes of the nuclei. The absence of the lines identified at 761.8 (^{150}Sm), 869.4 ($^{148+150+152}$Sm), 951.9 (^{149}Sm) and 983.6 keV (^{144}Sm) also in the isotopic measurements might be reasoned in possible background interferences with respect to [27]. Identification of the lines at 747.6 (^{148}Sm), 838.9 (^{154}Sm), 919.0 (^{152}Sm), 1111.9 (^{152}Sm), 1196.9 (^{147}Sm) and 1170.4 keV ($^{150+152}$Sm) resulted from the resolution of doublets given at energies of 745.8, 840.5, 920.1, 1114, 1194 and 1172 keV in [27]. At energies of 405.4, 550.2, 664.0, 857.6, 903.5, 1047.4 and 1392.6 keV in this work additional doublets might be possible but this possibility was not considered as serious when comparing the relative intensities. The line at 550.2 keV in [27] associated to ^{148}Sm could correspond to a doublet resolved in this work with two lines at 549.6 and 552.4 keV both from ^{148}Sm, respectively. This doublet (if present in [27]) might slightly influence relative intensities obtained in this work, as the net counts of the 552.4-keV line are about 15.2% of the net counts of the 549.6-keV line.

The intensity plot is depicted in Fig. 6.28 for all lines. The values of the fit parameters according to Eq. (4.32) are a= 2.69 ± 0.38 and b= 0.78 ± 0.06, respectively. The average intensity ratio I_R/I_{RD} is 2.12 ± 1.54, clearly indicating a pronounced discrepancy between the two measurements.

The γ-lines observed in this work at 147.3 ($^{150+152}$Sm), 320.6 (^{152}Sm), 397.3 (^{144}Sm), 571.2 (^{148}Sm) and 629.3 keV (^{148}Sm) were found to have significant interferences from (n,γ) reactions in Sm. Contributions of (114 ± 28)%, (95 ± 26)%, (99 ± 37)%, (117 ± 27)% and (98 ± 23)% were found. Hence, although those lines might in principle also be fed by plausible (n,n'γ) transitions listed in [65], all of them are assumed to be pure (n,γ) lines in this work. The lines at 320.6 (unassigned), 397.3 (^{149}Sm) and 629.3 (^{148}Sm) had been also identified by Demidov et al. The 320.6-keV line was probably also in the Demidov measurement a neutron capture line from the ^{152}Sm(n,γ)^{153}Sm reaction with 2.9% absolute intensity [133]. The two latter ones

had been assigned to inelastic scattering reactions in ^{149}Sm and ^{148}Sm, respectively. In the isotopic measurement of ^{148}Sm Demidov used the same line as a reference for intensities as in the elemental measurement (550.2-keV line). The intensity of (25 ± 3)% for the 629.3-keV line from the elemental measurement is in disagreement to that one derived from the isotopic measurement, i.e. (14.2 ± 0.7) [27]. This could imply that no proper corrections for neutron capture were carried out by Demidov et al. In fact, the 550-keV line was also strongly interfered by (n,γ) mainly in the isotope ^{147}Sm (550.1 keV [133]) but also in ^{149}Sm (548.3 keV [133]), ^{150}Sm (550.9 keV [133]) and ^{154}Sm (551.2 keV [133]), respectively, with an overall contribution to net counts of (62 ± 15)%. With respect to [30], the capture line at 550 keV is listed with a questionmark and an intensity of 1.2%. The intensity is in good agreement with the value derived from [132], i.e. (1.12 ± 0.07)%. Therefore, it is very likely that Demidov et al. did not correct this line as its presence was uncertain at that time. Nevertheless, neglection of any (n,γ) interference corrections yields an average intensity ratio of I_R/I_{RD}= 0.99 ± 0.73, which can, besides the large uncertainty, be considered as another hint for missing or inaccurate capture corrections in the Atlas [27].

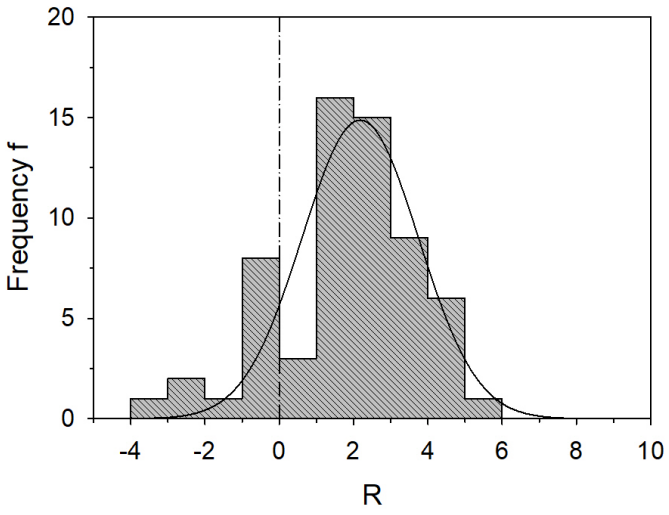


Figure 6.29: Comparison of the relative intensities of the prompt γ-rays induced by fast-neutron inelastic scattering (n,n'γ) reactions on Sm obtained in this work with the data tabulated in the Atlas [27] in the form of a histogram of the residuals R in units of standard deviation (σ) calculated with Eq. (4.33). The values of R are given in Appx. H.1.23 to H.1.30. The solid line represents the fit of the data with a Gaussian according to Eq. (4.34).

The (n,γ) lines listed at 127.3 and 166.5 keV in [27] were given with relative intensities of (4.6 ± 1.0)% and (2.7 ± 0.8)%, respectively. In this work intensities of (18.0 ± 2.9)% and (4.7 ± 0.2)% were determined. However, relative intensities of (6.9 ± 0.3)% and (1.8 ± 0.1)% were obtained when the reference line at 549.6 keV was uncorrected. The fact that the intensities from this work compare better

to the work of Demidov et al. if no (n,γ) corrections were performed is considered as another hint for missing or inaccurate corrections in [27].

The residual histogram is shown in Fig. 6.29. The fit of the data agrees at the 1.6σ level and the Gaussian centroid is aligned at R_0= 2.179 $\pm$ 0.238, indicating a strong systematic effect.

Figure 6.30 shows the intensity ratios with and without the corrections for (n,γ) reactions. The relative intensities agree much better to the data from Demidov et al. when any (n,γ) corrections were neglected. In fact, neglecting neutron capture interferences, there are still a few γ-lines with considerable deviations in intensity ratio. These comprise the lines at 504.9 ($^{149+150}$Sm), 583.5 (^{150}Sm), 636.2 (^{154}Sm), 736.9 (^{150}Sm), 968.3 (^{148}Sm) and 1046.0 keV (^{150}Sm). In this work all of these lines were free of escape peak interferences and background interferences were corrected accordingly. Additionally, since all of the aforementioned lines had interferences from (n,γ) reactions in Sm, this might imply different capture contributions of epithermal and fast neutrons in the work of Demidov et al. owing their different neutron-energy spectrum. The fits for the peaks at 504.9 and 1046.0 keV were difficult in this work due to the 511-keV annihilation peak and the triangular-shaped peak of ^{70}Ge.

In addition, Fig. 6.31 shows a histogram of the residuals R for the two sets of data for the case where (n,γ) interferences were not corrected. In this case, the data sets agree at the 2.7σ level, which is much worse to when the corrections were applied (1.6σ level). The shift of the Gaussian centroid, however, is smaller with R_0= -1.662 $\pm$ 0.391, indicating that the systematic effect becomes less.

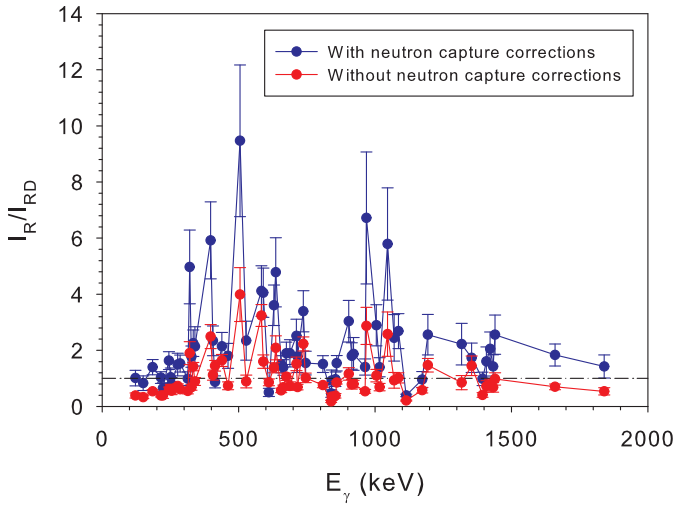


Figure 6.30: Intensity ratio of γ-lines induced by inelastic scattering in Sm compared to data listed in the Atlas [27] with (blue curve) and without (red curve) neutron capture corrections.

Normalizing the net counts to reference lines used by Demidov et al. in the isotopic measurements (1659.8 keV for ^{144}Sm, 550.2 keV for ^{148}Sm, 333.9 keV for ^{150}Sm, 563.2 keV for ^{152}Sm and 839.8 keV for ^{154}Sm) yielded average intensity ratios

of (2.3 ± 0.6)%, (4.2 ± 0.6)%, (8.3 ± 2.2)%, (7.6 ± 1.1)%, (0.5 ± 0.1)% and (0.9 ± 0.3)% for the lines listed at 505.6, 584.3, 637.0, 737.5, 969.4 and 1047.4 keV in the elemental measurement [27]. These ratios agree quite well to that ones from the isotopic measurements, i.e. (2.3 ± 0.2)%, (1.7 ± 0.1)%, (10.2 ± 0.7)%, (7.5 ± 0.5)%, (0.17 ± 0.06)% and (1.5 ± 0.2)%. However, one should be aware that the isotopic measurements did not use isotopic pure samples. Instead, other isotopes were still present with about 1% abundance, which could also induce γ-lines. Comparison of the relative intensities obtained in this work to those from Demidov's isotopic measurements yielded average ratios of 16.6, 6.4, 2.8, 2.3 and 5.5 for lines related to the inelastic scattering in ^{144}Sm, ^{148}Sm, ^{150}Sm, ^{152}Sm and ^{154}Sm.

In fact, the differences in relative intensity compared to Demidov et al. might also be attributed to the differences in the neutron-energy spectra. As the neutrons at the IRT reactor and in this work excited the nuclei differently, various levels were excited. In fact, certain peaks might also be fed by other (n,n'γ) transitions not recognized in both works. Especially in the case of an element as Sm with many isotopes and high level densities, this possibility cannot be excluded.

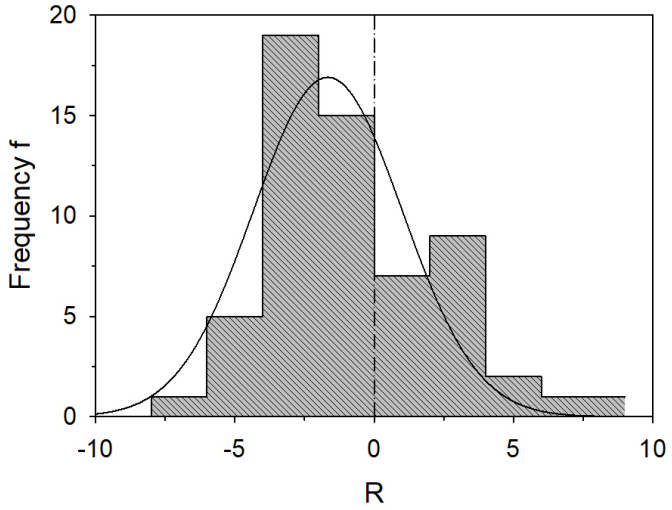


Figure 6.31: Comparison of the relative intensities of the prompt γ-rays induced by fast-neutron inelastic scattering (n,n'γ) reactions on Sm obtained in this work with the data tabulated in the Atlas [27] in the form of a histogram of the residuals R in units of standard deviation (σ) calculated with Eq. (4.33). The values of R were calculated neglecting any (n,γ) interferences. The solid line represents the fit of the data with a Gaussian according to Eq. (4.34).

The values of $\langle\sigma_{E\gamma}(90°)\rangle$, calculated after Eq. (4.1) with a fast-neutron flux of 1.13 × 10^8 cm^{-2} s^{-1}, are given in Appx. H.1.23 to H.1.30 and they are plotted as a function of the γ-ray energy in Fig. 6.32. The total value of the isotopic partial cross sections was determined as (2.09 ± 0.30) b, (0.98 ± 0.20) b, (4.98 ± 0.72) b, (1.36 ± 0.14) b, (15.06 ± 1.97) b, (1.43 ± 0.17) b and (1.41 ± 0.14) b for the ^{144}Sm(n,n'γ)^{144}Sm, ^{147}Sm(n,n'γ)^{147}Sm, ^{148}Sm(n,n'γ)^{148}Sm, ^{149}Sm(n,n'γ)^{149}Sm,

^{150}Sm(n,n'γ)^{150}Sm, ^{152}Sm(n,n'γ)^{152}Sm and ^{154}Sm(n,n'γ)^{154}Sm reactions. The effective reaction values obtained with NJOY and given in Appx. C.2 are (0.97 ± 0.09) b, (2.01 ± 0.21) b, (1.85 ± 0.18) b, (2.24 ± 0.24) b, (2.13 ± 0.22) b, (2.26 ± 0.23) b and (2.35 ± 0.24) b, respectively. Neglecting the contribution of multi-isotope lines, remarkable anisotropy might be deduced for the inelastic scattering reaction on ^{150}Sm.

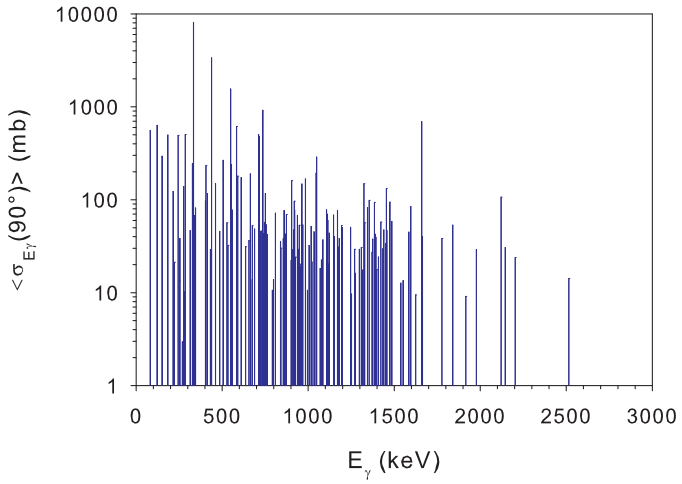


Figure 6.32: Effective isotopic partial γ-ray production cross sections $\langle\sigma_{E\gamma}(90°)\rangle$ of Sm calculated after Eq. (4.1) as a function of the γ-ray energy E_γ. Uncertainties are given in Appx. H.1.23 to H.1.30.

6.3.10 Terbium (Tb)

A total of 124 prompt γ-lines from the ^{159}Tb(n,n'γ)^{159}Tb reaction were found. These γ-rays are depicted in the recorded γ-ray spectrum given in Appx. G.8 and their data are given in Appx. H.1.31. As marked in the spectrum, 26 lines from the ^{159}Tb(n,γ)^{160}Tb reaction were identified [132]. Additionally, 27 lines (23 prompt [132] and 4 delayed [159]) were found to have interferences with lines of neutron capture in Tb and 5 lines were found to have interferences with the ^{35}Cl(n,γ)^{36}Cl reaction. The corresponding contributions to the net counts range between 1.7 and 53%.

γ-ray intensities were calculated relative to the 331-keV line of ^{159}Tb (100%), which is emitted from a $(7/2)^-$ level at 388.4 keV above g.s. [158]. They are given together with the values determined in [27] in columns 3 and 6 of Appx. H.1.31. Compared to the work of Demidov et al. [27], 54 from 60 listed lines were identified. The lines listed at energies of 154.0, 194.1, 272.9, 282.7, 339.2, 451.3 and 464.6 keV in [27], respectively, were either unassigned or assigned to the (n,γ) reaction in ^{159}Tb. Based on [132], all of those lines except the 272.9-keV line were found to belong to the (n,γ) reaction in Tb and all of them were also observed in this work. In fact, the 272.9-keV line was assigned to the ^{159}Tb(n,n'γ)^{159}Tb reaction, as it is specified in [65, 158] and belongs to the same level (E^*= 891.3 keV) as the

line observed at 753.2 keV. γ-rays with energies of 260.9, 274.8, 596.4, 608.2, 617.5 and 1003.0 keV given in [27] were not observed. Only the lines at 274.8 and 617.5 keV had been assigned to fast-neutron inelastic scattering in [27]. The 274.8-keV line is justified, as another line at 753.2 keV, emitted from the same level with 891.3 keV above g.s. [158], was observed. The line at 617.5 keV in [27] is plausible with respect to data in [65, 158]. However, it is surprising that the HPGe detector in this work providing the better energy resolution did not resolve a doublet with the close-lying line at 615.6 keV (reported at 615.4 keV in [27]). Nevertheless, a relative intensity of (36 $\pm$ 2)% for the line at 615.6 keV in this work compares well with the summed up intensity for the 615.4- and 617.5-keV lines in [27] of (34 $\pm$ 10)%. The intensity of these close-lying lines with respect to each other might differ in the two measurements due to differences in the excitation process related to the different neutron-energy spectra. For the lines at 596.4 and 608.2 keV, assigned to (n,γ) and unassigned in [27], respectively, no plausible (n,n'γ) transition of Tb is proposed in [65, 158]. The 596.4-keV line is even not listed as a possible (n,γ) line in [132]. However, both lines appear in the background analysis in the work of Demidov et al. [27]. The unassigned lines at 260.9 and 1003.0 keV in [27] and missing data in [65] help providing support that these lines do not belong to Tb. The line at 1003.0 keV might correspond to the line observed at 1005.8 keV in this work.

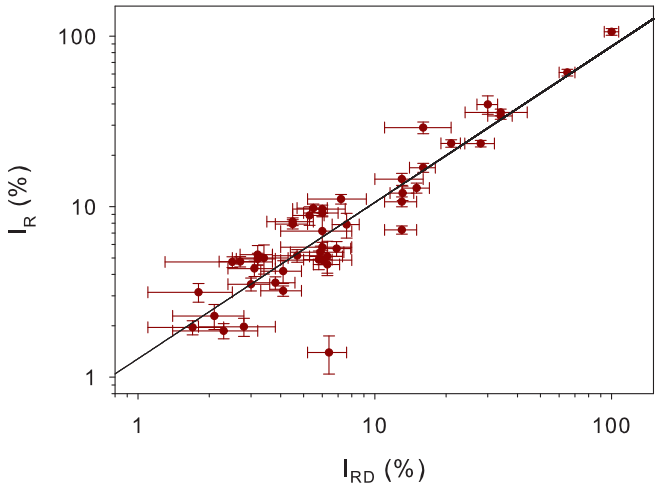


Figure 6.33: Relationship between the relative intensities I_R of the prompt γ-rays induced by fast-neutron inelastic scattering (n,n'γ) reactions on Tb measured in this work and the relative intensities I_{RD} tabulated in the Atlas [27]. The solid line represents the fit of the data with Eq. (4.32).

The 1253.8-keV line was corrected for the SE from the 1762.7-keV line of ^{35}Cl with Eq. (4.24), yielding a contribution of 23.4% to the net counts.

On the other hand, compared to [27] 76 new γ-lines were identified. The identification of new lines is mainly associated to the better energy resolution of the FaNGaS spectrometer and the higher mean neutron energy. In contrast to [27],

doublets in the lines given by Demidov et al. at energies of 184.2, 305.2, 947.0, 1094.1, 1195.1 and 1276.7 keV were resolved. The new line at 1131.1 keV might correspond to another doublet with the line observed at 1134.6 keV (1133.4 keV in [27]). The new lines at 57.9, 66.3, 79.3, 90.3 and 103.4 keV could not be seen by Demidov et al. as their measurement had been limited to a γ energy threshold of 120 keV [27]. The line at 66.3 keV had a strong background interference (97% of the net counts), but data is given as it belongs to the excited level at 454.6 keV above g.s. [158], from which the line at 317.0 keV was clearly observed. The new lines at 440.3, 590.5, 1173.3 and 1534.7 keV could probably not be observed by Demidov et al. due to background interferences [27], which were not present in the spectrum measured in this work.

It is worth to mention that from all 124 observed γ-lines a total of 76 is not specified in [65, 158] yet. Of those, 16 are listed in the Atlas [27], providing support that those lines belong to inelastic scattering in Tb. Acceptable statistics and intensities of the remaining 60 lines as well as thorough exclusion of any other origins or interferences, however, unambiguously provides support that those γ-rays must also be attributed to the ^{159}Tb(n,n'γ)^{159}Tb reaction. Therefore, those new lines make an important contribution to the expansion of existing decay schemes for Tb.

The intensity plot is depicted in Fig. 6.33 for all lines. The values of the fit parameters of Eq. (4.32) are a= 1.27 ± 0.17 and b= 0.92 ± 0.06. The average intensity ratio I_R/I_{RD} is 1.16 ± 0.39, indicating a reasonable agreement between the two measurements.

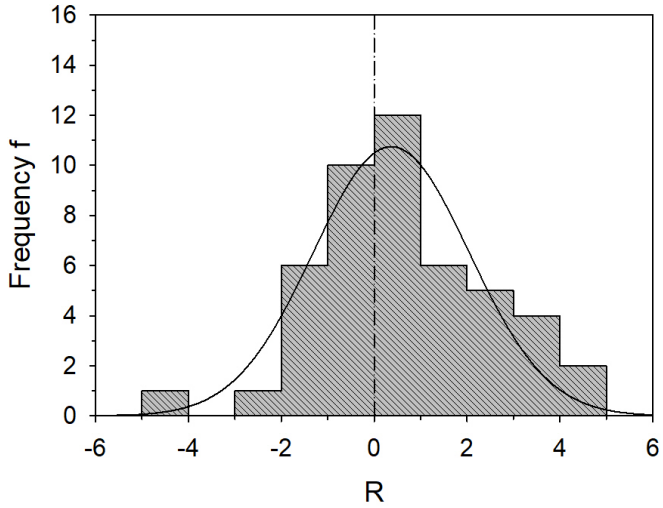


Figure 6.34: Comparison of the relative intensities of the prompt γ-rays induced by fast-neutron inelastic scattering (n,n'γ) reactions on Tb obtained in this work with the data tabulated in the Atlas [27] in the form of a histogram of the residuals R in units of standard deviation (σ) calculated with Eq. (4.33). The values of R are given in Appx. H.1.31. The solid line represents the fit of the data with a Gaussian after Eq. (4.34).

The residual histogram is shown in Fig. 6.34. The fit of the data agrees at the 1.6σ level and the Gaussian centroid is aligned at $R_0 = 0.000 \pm 0.262$, indicating a small probable systematic effect.

The values of $\langle\sigma_{E\gamma}(90°)\rangle$, calculated after Eq. (4.1) with a fast-neutron flux of 1.13×10^8 cm^{-2} s^{-1}, are given in Appx. H.1.31 and plotted as a function of the γ-ray energy in Fig. 6.35. The total value of the effective isotopic partial cross section, (3.44 ± 0.40) b, is much higher compared to the effective reaction cross section derived with NJOY as given in Appx. C.2, i.e. (1.98 ± 0.21) b. This might imply a considerable anisotropy in γ-ray emission, on average, at a measuring angle of 90° in the case of Tb.

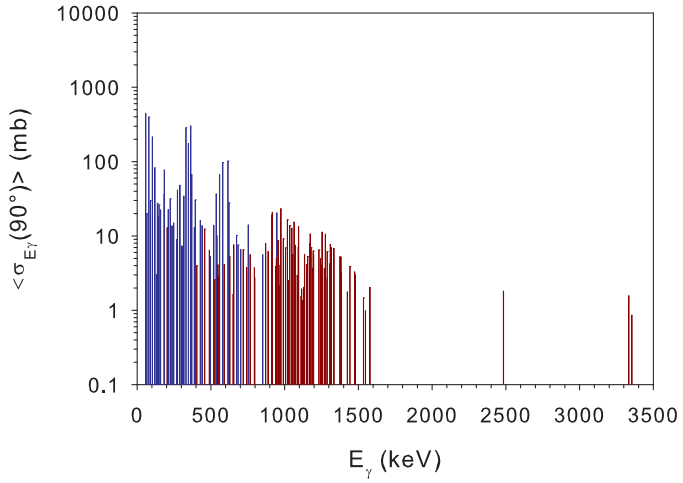


Figure 6.35: Effective isotopic partial γ-ray production cross sections $\langle\sigma_{E\gamma}(90°)\rangle$ of Tb (^{159}Tb) calculated after Eq. (4.1) as a function of the γ-ray energy E_γ. Lines in red are proposed as new lines with respect to data in [65]. Uncertainties are given in Appx. H.1.31.

6.3.11 Dysprosium (Dy)

A total of 150 prompt γ-rays issued from inelastic scattering reactions were identified. These γ-rays are depicted in the γ-ray spectrum shown in Appx. G.9 and their data are given from Appx. H.1.32 to H.1.36. From the observed lines 12 were assigned to ^{161}Dy, 46 to ^{162}Dy, 30 to ^{163}Dy and 48 to ^{164}Dy. The remaining 14 lines were associated to be fed by two or more isotopes as given in Appx. H.1.36. With respect to [132] and [133] several pure (n,γ) lines were identified, as given in Table 6.9. A total of 847 γ-rays from (n,γ) reactions in Dy are listed in [133]. Each single line was checked carefully for possible interferences of neutron capture and the net counts produced in (n,γ) lines were calculated according to Eqs. (4.26) and (4.30). For 99 lines relevant contributions to the net counts were found. For the isotopes ^{161}Dy and ^{162}Dy the amount of calculated counts of neutron capture lines exceeded the measured counts for certain γ-lines by factors of up to 3. With regard to Table 6.9 the intensity ratio of neutron capture lines of those isotopes follows no trend and

is rather random. Therefore, instead of taking a mean value as in the case of Sm, for the two isotopes of Dy the lowest intensity ratios were used as scaling factors to calculate neutron capture counts. These factors were 0.47 ± 0.27 for ^{161}Dy and 0.33 ± 0.21 for ^{162}Dy. The uncertainties were neglected in the conservative correction process for the net counts produced by neutron capture. γ-lines with contributions above 90% were assumed to be pure neutron capture γ-rays.

Intensities of γ-lines were calculated relative to the 754-keV line of ^{164}Dy (100%), which is emitted from the first 3^+ level at 828.2 keV above g.s. [187]. They are given together with the values determined in [27] in columns 3 and 6 of Appx. H.1.32 to H.1.36. For Dy, Demidov et al. had carried out measurements with isotopic enriched samples (for ^{162}Dy and ^{164}Dy) in addition to the measurement of a Dy sample with natural isotope abundances (Dy_2O_3 [27]). Compared to the latter measurement, 81 of all 92 lines listed in [27] were identified. 31 of 92 lines were listed as tentative assignments (no level data) in [27], of which 23 lines were observed in this work and assigned as (n,n'γ) transitions in Dy according to data given in [65]. Relation of the 11 lines at energies of 245.3, 371.3, 548.5, 633.6, 728.5, 842.7, 842.7, 1195.2, 1251.9, 1585.1 and 1735.4 keV to inelastic scattering reactions in Dy had been clearly confirmed by the isotopic measurements (level data available) [27]. The 6 lines at 326.0, 538.5, 569.7, 728.5, 1224.0 and 1273.6 keV are listed in the isotopic measurements without level data. The line at 842.7 keV was assigned to $^{162+164}$Dy(n,n'γ)$^{162+164}$Dy, although no corresponding line in the isotope measurement of ^{162}Dy had been observed. In fact, however, this line was also fed by ^{164}Dy, as the most intense line at 1124.6 keV from the same level (E^*= 1390.5 keV [187]) was clearly observed in this work. This observation emphasizes again the differences in the excitation processes, related to the different neutron-energy spectra. For the line at 1252.6 keV from ^{162}Dy a significant contribution to the net counts, i.e. (31 ± 3)%, from the SE of the 1763.4-keV line resulting from ^{35}Cl(n,n'γ)^{35}Cl was found.

The γ-lines in [27] at 326.0, 538.5, 569.7, 606.8, 846.6, 1217.4, 1224.0, 1273.6, 1369.8 and 1705.6 keV were not observed in this work. The lines at 326.0, 1217.4, 1224.0 and 1273.6 keV had been observed also in the isotopic measurements of Demidov et al. For the lines at 326.0, 1224.0 and 1273.6 keV no level data was given by Demidov et al., also in the isotope measurements. Plausible data is found in [65] except for the 1273.6-keV line. Absence of this line in this work implies a possible misattribution by Demidov et al. The line at 1217.4 keV was assigned to ^{162}Dy in Demidov's elemental measurement, although it was only observed in the isotope measurement of ^{164}Dy. The line at 326.0 keV was not observed in this work due to a background interference (^{70}Ge [34]). The line at 1217.4 keV was interfered by the 1219.2-keV line of ^{35}Cl(n,n'γ)^{35}Cl. The 1224.0-keV line was probably not detected due to the low mass of the sample. The lines at 538.5, 569.7, 606.8, 846.6 and 1705.6 keV were not observed due to background interferences [34, 141]. For all of these

lines possible transitions are included in [65]. Although no other intense lines from suggested levels were observed, it is difficult to judge if those lines are misattributions by Demidov et al. or had been observed, as the excitation process differs. Transitions related to ^{162}Dy and ^{164}Dy could be mostly excluded from the isotopic measurements performed in [27]. The line at 1369.8 keV reported in [27] could correspond to a line at 1371.0 keV given in the ENSDF file of the ^{164}Dy(n,n'γ)^{164}Dy reaction [187] and unplaced in the decay scheme. Aforementioned lines are not assumed to be produced by (n,γ) reactions in Dy, as they should have also been observed in this work then.

Compared to [27] 71 new γ-lines, all specified in [65], were identified. The identification of new lines is mainly associated to the better energy resolution and the higher mean neutron energy. Observation of new γs below 120 keV is related to the lower γ energy threshold of Demidov's measurement [27]. In contrast to [27], doublets in the lines given by Demidov et al. at energies of 267.4, 294.7, 310.0, 548.5, 980.6, 1556.4 and 1585.1 keV were resolved. The new lines at 238.2, 607.9 and 982.6 keV could probably not be observed by Demidov et al. due to background interferences [27]. The lines observed at energies of 235.6, 1308.6, 1319.6, 1901.5, 1919.0, 1982.6 and 1999.6 keV associated to ^{162}Dy(n,n'γ)^{162}Dy and the lines at 308.5, 522.7, 610.6, 982.6, 1001.8, 1515.8, 1543.6, 1554.0, 1581.6, 1666.4, 1836.2, 1859.3, 1905.1 and 1980.0 keV related to ^{164}Dy(n,n'γ)^{164}Dy, respectively, had also been observed in the isotopic measurements of Demidov et al., thereby confirming a correct assignment in this work.

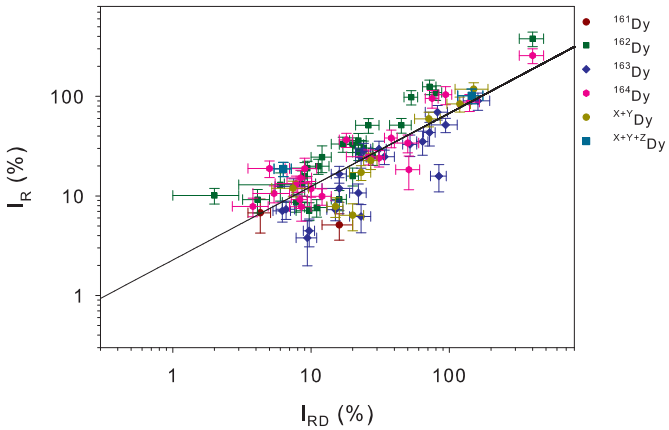


Figure 6.36: Relationship between the relative intensities I_R of the prompt γ-rays induced by fast-neutron inelastic scattering (n,n'γ) reactions on Dy measured in this work and the relative intensities I_{RD} tabulated in the Atlas [27]. The solid line represents the fit of the data with Eq. (4.32).

The intensity plot is depicted in Fig. 6.36 for all lines. The values of the fit coefficients in Eq. (4.32) are a= 2.27 ± 0.41 and b= 0.74 ± 0.06. The average intensity ratio I_R/I_{RD} is 1.14 ± 0.77, indicating an acceptable agreement between

the two measurements.

The lines observed at 337.8 and 495.8 keV, both associated to ^{163}Dy(n,n'γ)^{163}Dy, and the lines at 975.4 and 1025.8 keV, associated to ^{162}Dy(n,n'γ)^{162}Dy, were found to have significant interferences from (n,γ) reactions in Dy. Contributions of (106 $\pm$ 35)%, (161 $\pm$ 59)%, (108 $\pm$ 41)% and (102 $\pm$ 42)% were found, in order of increasing energy. The line at 337.8 keV was emitted from a level at 766.2 keV above g.s. [65], from which also another line at 414.4 keV was observed. The latter one has a contribution of (n,γ) of (76 $\pm$ 25)%. Taking the large uncertainty into account, it might be possible that this level was fed only by neutron capture. For the 495.8-keV line (E^*= 884.3 keV [188]) another line at 532.3 keV was also observed and issued from the inelastic scattering in ^{163}Dy. The latter one was interfered by a line of same energy from ^{162}Dy(n,γ)^{163}Dy with a contribution to the net counts of (23.7 $\pm$ 7.8)%. The intensities for epithermal neutron capture might differ in the two measurements owing the differences in the neutron-energy spectra. The line at 975.4 keV had been observed in the isotopic measurement of ^{162}Dy by Demidov et al. The reference line at 754.3 keV of ^{164}Dy was interfered mainly by a (n,γ) line of same energy from ^{163}Dy(n,γ)^{164}Dy, with a contribution to the net counts of (50 $\pm$ 15)%. Neglection of any neutron capture interference corrections did not approximately halve the intensity ratio but yielded an average intensity ratio of I_R/I_{RD}= 0.82 $\pm$ 0.43. Therefore, in contrast to Sm, an incomplete and inaccurate correction for neutron capture interferences is assumed in the Demidov measurement of Dy.

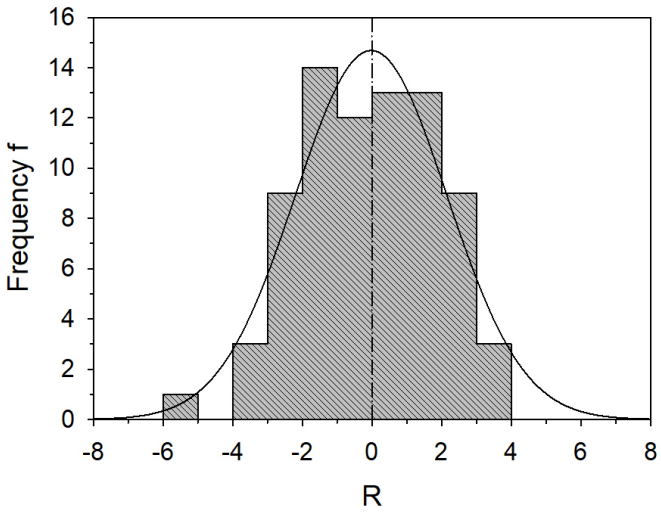


Figure 6.37: Comparison of the relative intensities of the prompt γ-rays induced by fast-neutron inelastic scattering (n,n'γ) reactions on Dy obtained in this work with the data tabulated in the Atlas [27] in the form of a histogram of the residuals R in units of standard deviation (σ) calculated with Eq. (4.33). The values of R are given in Appx. H.1.32 to H.1.36. The solid line represents the fit of the data with a Gaussian according to Eq. (4.34).

The residual histogram is shown in Fig. 6.37. The fit of the data agrees at the

2.2σ level and the Gaussian centroid is aligned at R_0= -0.027 ± 0.186.

Similar to the case of Sm, Fig. 6.38 shows the intensity ratios with and without the corrections for neutron capture. In contrast to Sm, it cannot be concluded that a neglection of interferences arising from (n,γ) yields a much improved intensity ratio on average. For a few lines above 1 MeV the agreement becomes better when neutron capture is disregarded. This implies that neutron capture, at least for several lines, had been corrected by Demidov et al. According to Fig. 6.38, a significant mismtach in intensity with factors higher than two is found for the lines observed in this work at 371.2 (^{161}Dy), 1252.6 (^{162}Dy), 548.2 (^{164}Dy), 761.3 (^{164}Dy), 1684.6 (^{164}Dy), 1722.7 (^{164}Dy) and 646.9 keV ($^{162+163+164}$Dy). For the lines that belong either to ^{162}Dy or ^{164}Dy, a comparison between the elemental and isotopic tables given in [27] can be done, to check the consistency. The line at 1722.7 keV was unassigned in the elemental measurement in [27] and not observed in the isotope measurement. This line was emitted from a level at 1796.7 keV above g.s. [187] and accompanied by another line from the same level observed at 1554.0 keV. It is surprising, that the latter one was also seen in the isotope measurement of Demidov et al. Absence of the much more intense 1722.7-keV line indicates an imprecise analysis of Demidov et al. For the lines at 761.3, 1252.6 and 1684.6 keV intensities of (37 ± 6), (1.1 ± 0.3) and (0.9 ± 0.2)% are listed in [27] for the isotope measurements. Values derived from the elemental measurement, i.e. (18.8 ± 4.3)%, (0.50 ± 0.27) and (0.95 ± 0.33), respectively, indicate inconsistency for the 761.3- and 1252.6-keV lines, respectively.

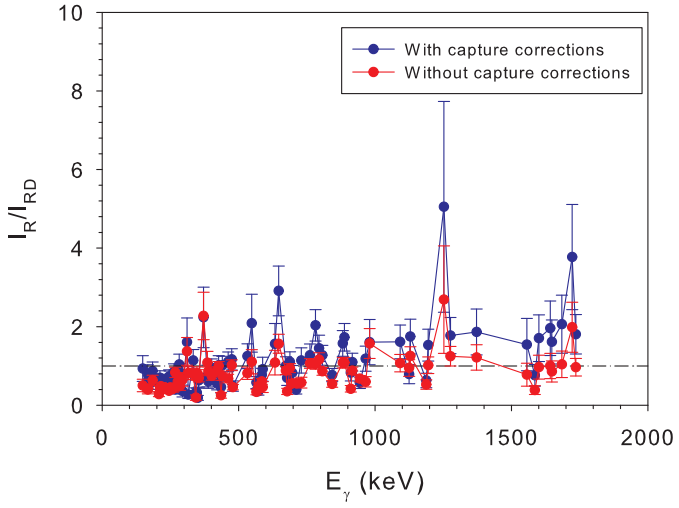


Figure 6.38: Intensity ratio of γ-lines induced by inelastic scattering in Dy compared to data listed in the Atlas [27] with (blue curve) and without (red curve) neutron capture corrections.

Comparison of the relative intensities obtained in this work to those from Demidov's isotopic measurements, for all lines observed in both works, yields average ratios of 1.7 and 2.8 for the inelastic scattering in ^{162}Dy and ^{164}Dy.

Differences in relative intensity compared to Demidov et al. might also be a

consequence of the different neutron-energy spectra. As the fast neutrons in both works excite the nuclei in a different way, different levels are excited. In fact, certain levels could also be fed by other (n,n'γ) transitions not recognized. For elements as Dy with many isotopes and high level densities, this possibility cannot be excluded.

The lines at 167.2, 244.7, 588.3, 677.6, 911.2, 965.6, 1585.7 and 1684.6 keV were free of any (n,γ) interferences and have no or relatively weak background interferences. Intensities were determined relative to the 244.7-keV line and compared with Demidov's data. Intensities of (477 ± 87)%, (31 ± 9)%, (31 ± 7)%, (40 ± 8)%, (48 ± 10)%, (30 ± 6)% and (32 ± 7)%, respectively, were derived. They are mostly in good agreement with those derived from the Atlas [27], i.e. (441 ± 141)%, (25.0 ± 6.2)%, (32 ± 8)%, (35 ± 9)%, (29.4 ± 7.8)%, (50 ± 12)% and (11.2 ± 3.8)%, respectively. This observation indicates a systematic effect due to interferences of (n,γ) reactions.

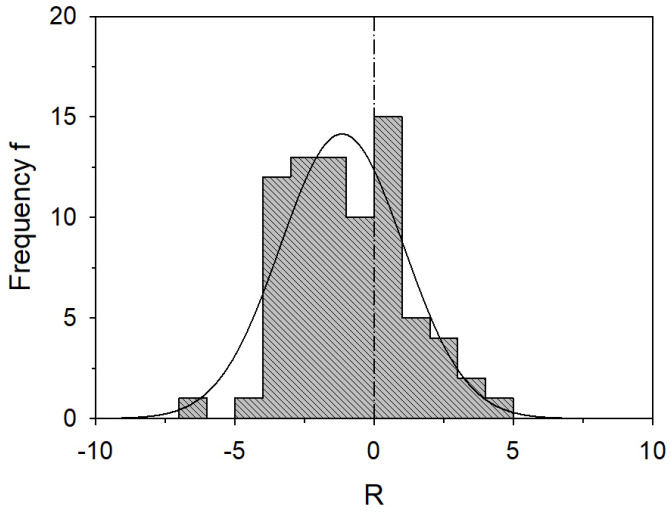


Figure 6.39: Comparison of the relative intensities of the prompt γ-rays induced by fast-neutron inelastic scattering (n,n'γ) reactions on Dy obtained in this work with the data tabulated in the Atlas [27] in the form of a histogram of the residuals R in units of standard deviation (σ) calculated with Eq. (4.33). The values of R were calculated neglecting any (n,γ) interferences. The solid line represents the fit of the data with a Gaussian according to Eq. (4.34).

The residual histogram is shown in Fig. 6.39 for the case of neglection of (n,γ) interferences. The two data sets agree now at the 2.0σ level, which is not much less compared to the case where neutron capture is accounted for. However, the shift of the Gaussian centroid is higher with the Gaussian centroid being aligned at R_0= -1.372 ± 0.265. Besides the fact that detailed information on the correction processes is absent in [27], there are two aspects that one should be aware of and critically review: **(i)** it is unlikely that the databases for capture lines, i.e. [29, 30], were complete in those days, and secondly **(ii)** it might be that the values available in those days were inaccurate compared to those listed in [132, 133].

The values of $\langle\sigma_{E\gamma}(90°)\rangle$, calculated after Eq. (4.1) using a fast-neutron flux of 1.13 × 10^8 cm^{-2} s^{-1}, are given in Appx. H.1.32 to H.1.36 and plotted as a function of the γ-ray energy in Fig. 6.40. The total value of the isotopic partial cross sections was determined as (1.26 ± 0.15) b, (3.06 ± 0.38) b, (1.67 ± 0.27) b and (2.66 ± 0.39) b for the ^{161}Dy(n,n'γ)^{161}Dy, ^{162}Dy(n,n'γ)^{162}Dy, ^{163}Dy(n,n'γ)^{163}Dy and ^{164}Dy(n,n'γ)^{164}Dy reactions. The effective reaction values obtained with NJOY (see also Appx. C.2) are (2.80 ± 0.30) b, (2.59 ± 0.27) b, (2.82 ± 0.31) b and (2.62 ± 0.28) b, respectively. Neglecting the contribution of multi-isotope lines, significant anisotropy might be deduced for the inelastic scattering reaction on Dy except for ^{164}Dy.

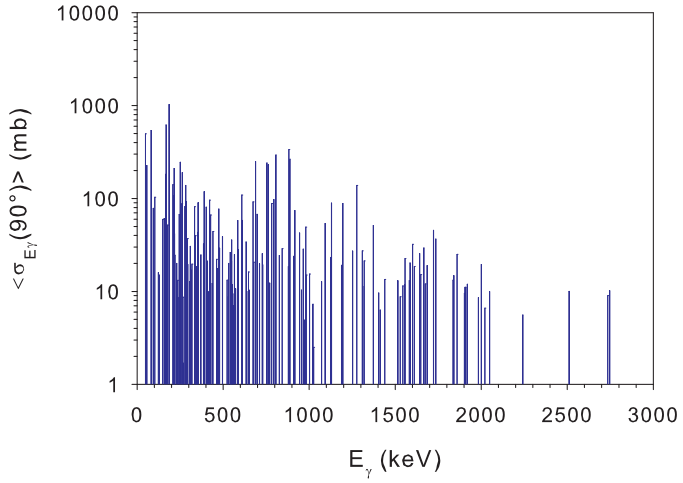


Figure 6.40: Effective isotopic partial γ-ray production cross sections $\langle\sigma_{E\gamma}(90°)\rangle$ of Dy calculated after Eq. (4.1) as a function of the γ-ray energy E_γ. Uncertainties are given in Appx. H.1.32 to H.1.36.

6.4 Detection limits

The detection limits using the γ-lines with the highest relative intensity, calculated with Eqs. (4.1), (4.35) and (4.36), are given in Table 6.11. The values represent the minimum mass of an element that can be identified with an uncertainty in the counting statistics of 50%, i.e. c= 0.5 in Eqs. (4.35) and (4.36). In addition, any beam attenuation effects were neglected, i.e. f_n and $f_{E\gamma}$ were set to unity in Eq. (4.1).

Except for C and O, the DL is in the range of a few mg. Generally, for very thin samples of thicknesses well below 1 mm PGNAA is expected to provide higher sensitivity than the PGAINS method, owing the high (n,γ) cross sections and high thermal or cold neutron fluxes available at research reactors. Nevertheless, assuming equal measurement conditions (in particular equal neutron fluxes at sample position), the ratio (denoted as σ-Ratio in Table 6.11) of effective cross sections between the PGAINS and PGNAA technique could indicate which method has the higher

sensitivity for the identification of a given element. Corresponding values above one for C, O and Ce imply that PGAINS has a higher sensitivity compared to PGNAA even for thin samples composed of these elements.

Table 6.11: Detection limits for all elements investigated within this work as well as effective γ-ray production cross sections for the most intense lines in this work and from thermal neutron capture (n,γ) reactions listed in [132].

Z	PGAINS with FaNGaS (this work)			PGNAA [132]		σ-Ratio
	^{A}Z, E_γ (keV)	$\langle\sigma_{E\gamma}(90°)\rangle$ (mb)	DL (mg)	^{A}Z, E_γ (keV)	$\langle\sigma_{E\gamma}\rangle$ (mb)	(PGAINS/ PGNAA)
C	^{12}C, 4441.1	14.4	13	^{12}C, 4945.3	2.6	**5.5**
O	^{16}O, 6129.3	2.2	62	^{16}O, 870.7	0.2	**12**
Cl	^{35}Cl, 1763.1	70	1.8	^{35}Cl, 1164.9	11,759	$5.9 \cdot 10^{-3}$
Ca	^{40}Ca, 29.8	157	4.8	^{40}Ca, 1942.7	363	0.5
La	^{139}La, 165.7	574	0.6	^{139}La, 1596.2(d)	5,845	0.1
Ce	^{140}Ce, 1596.0	666	0.7	^{140}Ce, 662.0	272	**2.4**
Pr	^{141}Pr, 145.3	889	0.4	^{141}Pr, 176.9	1,060	0.8
Nd	^{144}Nd, 696.0	354[a]	2.1	^{143}Nd, 696.5	273,399	0.01
Sm	^{150}Sm, 333.4	1,269[a]	0.6	^{149}Sm, 334.0	$3.5 \cdot 10^{7}$	$2.0 \cdot 10^{-4}$
Tb	^{159}Tb, 57.9	445	1.2	^{159}Tb, 75.1	1,780	0.2
Dy	^{162}Dy, 184.8	289[a]	1.6	^{164}Dy, 184.3	146,000	$2.0 \cdot 10^{-3}$

[a] effective elemental cross sections calculated after Eq. (4.28) and listed in Appx. H.2

7. Fast-neutron filter design

During irradiation, fast neutrons are scattered from the sample (elastic and inelastic scattering) towards the HPGe detector. Their interactions with the active volume of the Ge crystal lead to an increase of the background in the recorded γ-ray spectrum and to γ-ray interferences.

In addition, irradiation of large objects generates a high γ flux, which leads to a high detector dead time or even to a saturation of the detector preamplifier. In this case, no valuable information can be gained from the measurement. Therefore, in order to reduce the fast-neutron-induced background and to ensure a reasonable γ flux reaching the detector, a neutron/γ filter must be placed into the detector collimator opening of the FaNGaS spectrometer. The design and optimization of such a filter was investigated numerically with the MCNP6 code and also complemented by simple analytical models.

The strategy of this design optimization as well as major outcomes are the subject of this chapter.

7.1 Triangular peaks of Ge

Irradiation of Ge detectors with neutrons of energies in the MeV range results in inelastic scattering reactions with Ge nuclei. The induced recoil atoms deposit their energy in the active crystal volume. This energy adds up to the energy of the deexcitation γ-rays interacting in the crystal. As a result, the FEP of a γ-ray is broadened up to about 40 keV and the shape becomes triangular [189–191].

As depicted in Figs. 5.10 and 7.1, triangular peaks are observed at energies of 69, 563, 596, 692, 834, 1040, 1109, 1204 and 1464 keV. Since inelastic scattering is isotope-specific, the associated energy threshold can differ significantly for isotopes of an element. By default, version 6.1 of the MCNP code uses ENDF/B-VII.1 cross-section libraries [115, 117]. The threshold energy for inelastic scattering and the γ-ray energies of Ge isotopes are given in Table 7.1.

Table 7.1: Threshold energy for inelastic scattering E_{thr} according to the ENDF/B-VII.1 library [50, 115] and γ-ray energy E_γ of Ge isotopes (^{A}Z). The abundance of the isotopes is denoted as h.

^{A}Z	h (%)	E_{thr} (MeV)	E_γ (keV)
^{70}Ge	20.5	1.05	1040
^{72}Ge	27.4	0.70	692, 834, 1464
^{73}Ge	7.8	0.013	69
^{74}Ge	36.5	0.60	596, 1204
^{76}Ge	7.4	0.57	563, 1109

In order to verify that inelastic scattering starts at the right threshold energies in the MCNP6 code, several simple simulations were performed. A cube of Ge with a volume of $5 \times 5 \times 5$ cm^3 was irradiated by a point source of 10^8 monoenergetic neutrons. The resulting spectra were obtained with the F8 pulse-height tally and γ-rays are shown in Fig. 7.1 for incident neutron energies of 0.01, 0.1, 0.6 and 1.2 MeV. Observation of triangular peaks is in agreement with the threshold energies given in Table 7.1.

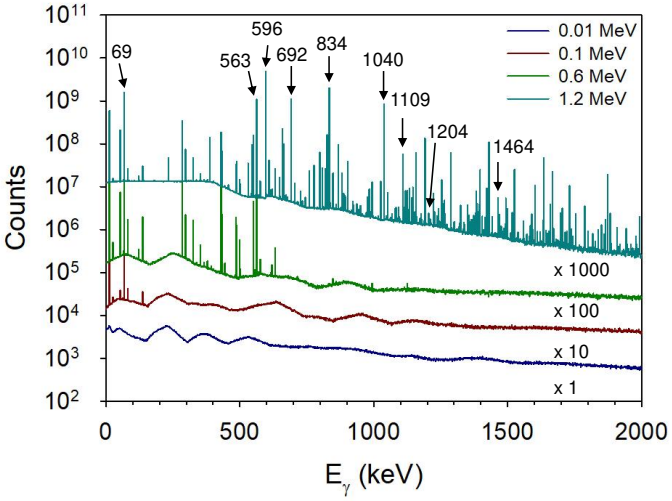


Figure 7.1: γ-ray spectra from MCNP6 simulations for a Ge cube of $5 \times 5 \times 5$ cm^3 irradiated with neutrons of energies: 0.01, 0.1, 0.6 and 1.2 MeV. Marked peaks show a triangular shape in measured spectra. Each simulation ran 10^8 primary neutrons.

7.2 Filter materials

On the one hand, materials suitable for shielding against fast neutrons must have properties of an efficient neutron moderator. Therefore, with regard to Chapter 2, potential materials are characterized by a low mass number A, a high scattering cross section σ_s and a low absorption cross section σ_a. A standard material fulfilling the aforementioned conditions is polyethylene (PE), which is used as first choice for

neutron shielding purposes.

On the other hand, a filter needs at least one isotope that provides a high value of σ_a in order to absorb thermalized neutrons. Converting the fast-neutron beam directed towards the detector into a beam of thermal or cold neutrons is no proper solution, as thermal neutron capture reactions in the Ge crystal result in many γ-lines in the spectrum. Usually two reactions are exploited to capture thermalized neutrons: the ^{6}Li(n,t)^{4}He and the ^{10}B(n,α)^{7}Li reaction, both with considerably high thermal neutron capture cross sections of 938 and 3,847 b [9].

Table 7.2: Densities, total macroscopic cross sections and main γ-rays of considered filter materials. The macroscopic cross sections were calculated with microscopic cross sections provided in [192], obtained by interpolation. Uncertainties were found to be negligible.

Material	Density ρ (g cm^{-3})	Macroscopic cross section (cm^{-1})		γ-rays	
		Σ_{th}[a]	Σ_{fast}[b]	Reaction	E_γ (keV)
PE, $(C_2H_4)_n$	0.93	2.634	0.301	^{1}H(n,γ)^{2}H	2223
LiH	0.82	2.393	0.281	^{1}H(n,γ)^{2}H	2223
LiH with 90% ^{6}Li	0.82	54.733	0.269	^{1}H(n,γ)^{2}H	2223
PE with 20 wt% B_2O_3	1.01	10.542	0.148	^{10}B(n,α)^{7}Li	478
				^{1}H(n,γ)^{2}H	2223
PE with 20 wt% B_4C	1.01	11.849	0.166	^{10}B(n,α)^{7}Li	478
				^{1}H(n,γ)^{2}H	2223
B_4C	2.52	2.435	0.266	^{10}B(n,α)^{7}Li	478

[a] for a neutron energy E_n of 0.025 eV
[b] for a neutron energy E_n of 2.0 MeV

In addition, presence of the filter material should not show up in the recorded γ-ray spectrum. In principle, a filter consisting of Sm or Dy seems ideal at a first sight owing the high capture cross sections of ^{149}Sm (67,894 b [9]) and ^{164}Dy (2,622 b [9]). However, as observed in the measurements presented in this work and with respect to data in [132, 133], these materials will literally flood the whole spectrum with neutron capture γ-lines. Consequently, a proper filter material is also characterized by a moderate γ-ray emission, if at all.

All investigated filter materials are given in Table 7.2 with important characteristics. Differences in the density between natural LiH and LiH enriched with ^{6}Li were neglected. The same density for B_2O_3 and B_4C incorporated into PE was assumed. The 2223-keV γ-ray from the ^{1}H(n,γ)^{2}H reaction will be always present in experimental measurements due to the BPE shielding of the spectrometer. The (n,t) reaction on ^{6}Li is not accompanied by γ-ray emission. The (n,γ) reactions in ^{6}Li and ^{7}Li are not relevant as their thermal cross sections, i.e. 0.039 and 0.045 b [9], respectively, are too small compared to the large cross section of the (n,t) reaction given above.

7.3 Strategy

For optimization of the fast-neutron filter, the analytical and numerical studies were conducted in three steps. The applied method is illustrated in Fig. 7.2.

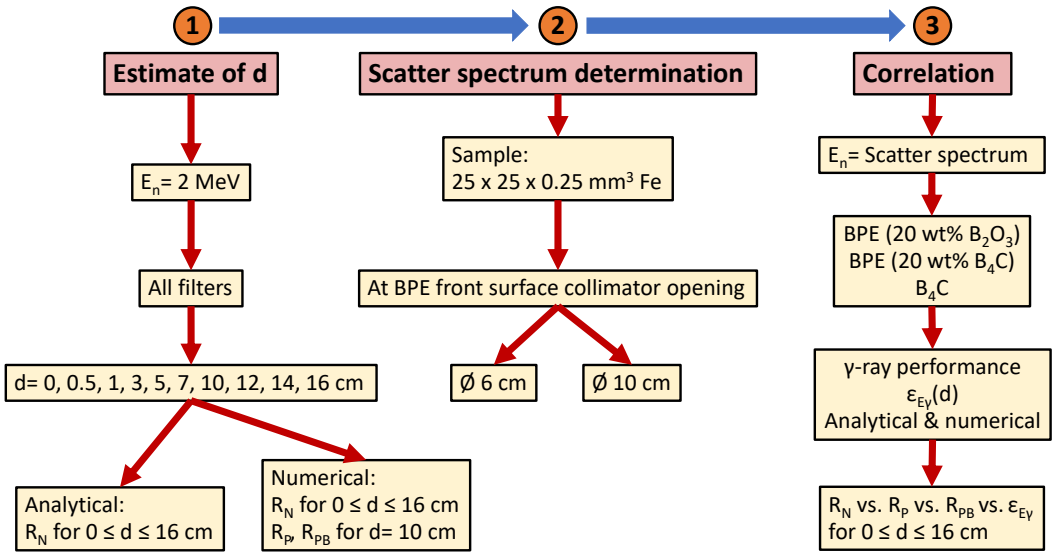


Figure 7.2: Illustration of the strategy for the fast-neutron filter optimization of the FaNGaS spectrometer.

In a first step, a qualitative estimate of the required filter thickness was determined, aiming for a reduction in the scattered fast-neutron flux down to 10%. Thicknesses were derived for monoenergetic neutrons of 2 MeV energy.

In a second step, the actual scatter spectrum impinging on the front surface of the BPE shielding was determined numerically. Although the absolute magnitude of scattered neutrons depends on the sample composition, this task was solved for a Fe foil, as experimental data is available [34]. Scatter spectra were obtained for two detector collimator opening diameters, 6 and 10 cm, respectively.

In a third and last step, the determined scatter spectrum served as an input in the simulations. Focussing on filters that contain B, correlations between all important parameters were done. In particular, in this step the impact of the filter materials with regard to the FEP efficiency of the detector was investigated.

Three parameters were introduced (see Fig. 7.2) and derived from the simulations and analytical calculations to characterize the effectiveness of the considered filter material, namely the: **fast-neutron flux fraction $\mathbf{R_N}$**, the **peak-count fraction $\mathbf{R_P}$** and the **total-count fraction $\mathbf{R_{PB}}$**.

All of these parameters are a function of the filter thickness d, i.e. $f(d)$, and they are quantities relative to the case without a filter material being present (d= 0 cm). Therefore, the quantities listed above give the fast-neutron flux (R_N), the peak

counts (R_P) and the total counts (R_{PB}) in the simulated γ-ray spectra as a function of the filter thickness d relative to a simulation without a filter in the collimation opening of the spectrometer.

7.4 Filter length estimation

A conservative estimate of the filter thickness is obtained by using an energy of the scattered neutrons of 2 MeV, which is close to the average energy of the incident neutron-energy spectrum at sample position, i.e. 2.3 MeV.

7.4.1 Analytical approach

The analytical approach used a parallel beam of monoenergetic neutrons whose attenuation is described by Eq. (4.14). For a neutron energy of 2 MeV the total macroscopic cross sections σ_t of the filter materials were calculated after Eq. (2.10) from the ENDF/B-VIII.0 data library [112] provided at the web application of the JANIS software [192]. The values of Σ_t are given in Table 7.2 for the considered filter materials. Differences to the previous data library, i.e. ENDF/B-VII.1 [115, 117], were found to be negligible. Tabulated values of microscopic cross sections given in [192] were interpolated between 1 and 3 MeV with a step of 2 MeV.

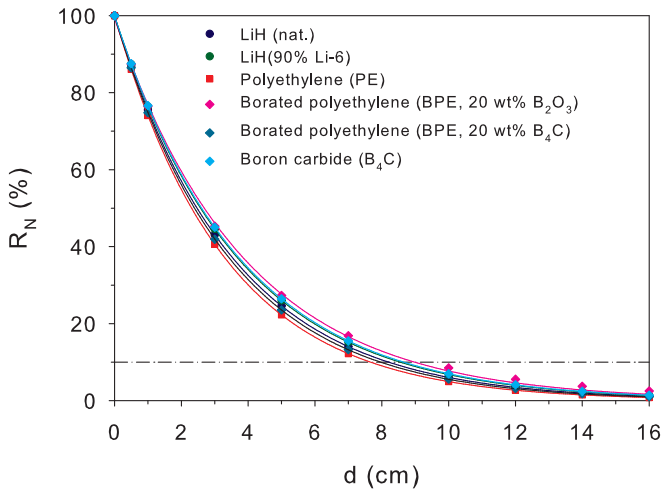


Figure 7.3: Dependence of the fast-neutron fraction R_N for 2 MeV neutrons on the thickness d of different filter materials obtained from analytical calculations according to Eq. (4.14). The solid lines represent the fit of the data with a simple decay function like Eq. (4.14). The dash-dotted line corresponds to a value of R_N of 10%.

The fraction of fast neutrons, i.e. the beam transmission, was calculated for all values of d specified in Fig. 7.2 and then fitted with a simple decay equation like Eq. (4.14) (see Fig. 7.3). As expected, the parameter in the exponential term of the fit perfectly equals the respective total macroscopic cross sections.

According to Fig. 7.3, the filter materials show the same beam attenuation, but with some larger differences for thicknesses between 2 and 12 cm. Approximately 8 to 9 cm of filter material is required to attenuate the fast-neutron beam intensity to 10%.

7.4.2 Numerical approach

A numerical solution is provided by simulation with the MCNP6 code from a simplified model of the FaNGaS spectrometer (see Fig. 7.4). This model includes the outer BPE shielding with the detector collimator opening and the inserted BPE collimator as well as the inner lead shielding. A monoenergetic neutron source of 2 MeV energy was placed 67 cm away from the detector front surface. Note that the detector front surface in Fig. 7.4 (Ge crystal) is placed 1 mm in front of the 30 cm long collimation tract.

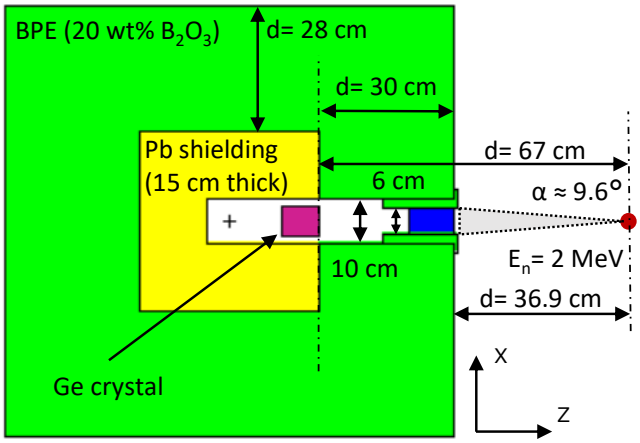


Figure 7.4: Simplified model of the FaNGaS spectrometer for the simulation with the MCNP6 code. The filter is depicted in blue.

From the technical drawing given in Appx. I, the HPGe detector was modeled as a simple Ge cylinder with a diameter of 6.4 cm and a length of 8.3 cm. Simulations were performed with 10^8 or 10^9 primary neutrons.

The planar opening angle (α) from the neutron source towards the collimator opening (at a diameter of 6 cm) is about 9.6°, while the solid angle Ω subtended is approximately 0.02 sr ($< 1\%$ of a 4π sphere). Therefore, in order to increase the statistics of the simulations, the neutron emission was restricted to a cone predicted by the aforementioned solid angle (forward-focussed beam). This emission was confirmed with a FMESH4 tally placed at the BPE front surface and the resulting spatial distribution of neutrons is illustrated in Fig. 7.5.

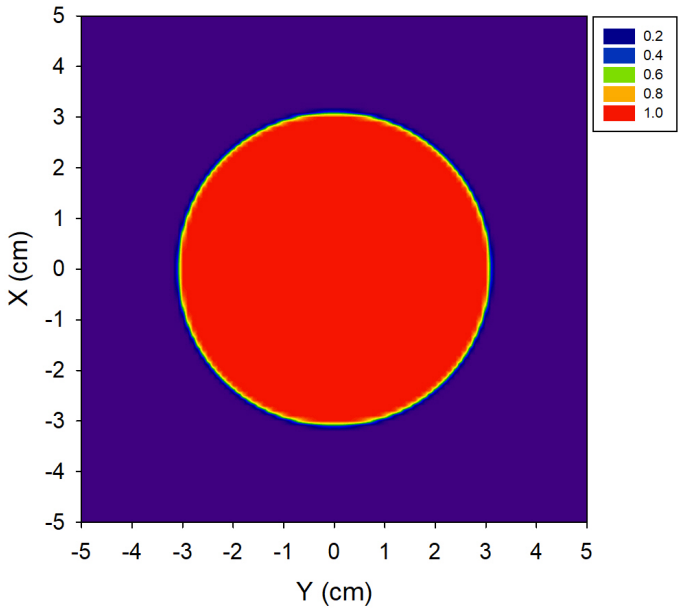


Figure 7.5: Spatial neutron distribution in the XY plane at the front surface of the BPE shielding. The neutron beam was directed along the Z-axis and the colour scale reflects relative neutron-flux values normalized to the maximum. A total of 10^9 primary neutrons were run.

Fast-neutron fraction

The fraction of fast neutrons passing through a filter material of thickness d was determined by counting the number of fast neutrons crossing the front surface of the Ge crystal using the F1 tally (particle current) in the MCNP6 code. The neutron transport cutoff-energy was set to 20 keV and the fast-neutron flux was defined for the energy range 0.6 to 2 MeV. As the distance between the rear side of the filter material and the detector front surface changes with the filter thickness a certain fraction of scattered neutrons is expected to be absorbed in the BPE shielding and thereby lost. This distance travelled by the neutrons, which is at least about 14 cm, is supposed to ensure a parallel (uncollided) beam of neutrons reaching the F1 tally. This assumption enables the comparison with the results obtained from the analytical solution given in Fig. 7.3. The dependence of the fast-neutron flux fraction R_N on the thickness of the various filter materials obtained with 10^8 primary neutrons from the numerical simulations is shown in Fig. 7.6.

The values of the reduction of the fast neutrons obtained by numerical and analytical calculation agree well with each other for small filter thicknesses of all filter materials but show large discrepancies for larger filter thicknesses, with deviations ranging between 0.2 and 68%. The increase of the deviation as a function of the filter material thickness is reasoned in two aspects: first of all (i), the F1 tally counted neutrons with energies between 20 keV and 2 MeV. The analytical solution considers only 2 MeV neutrons. Secondly (i), the distance between the rear side of

the filter material and the detector front surface decreases with increasing the filter thickness in the simulations. From the numerical simulation, an attenuation of the fast neutrons of 10% was achieved for material thicknesses between 8 and 9 cm.

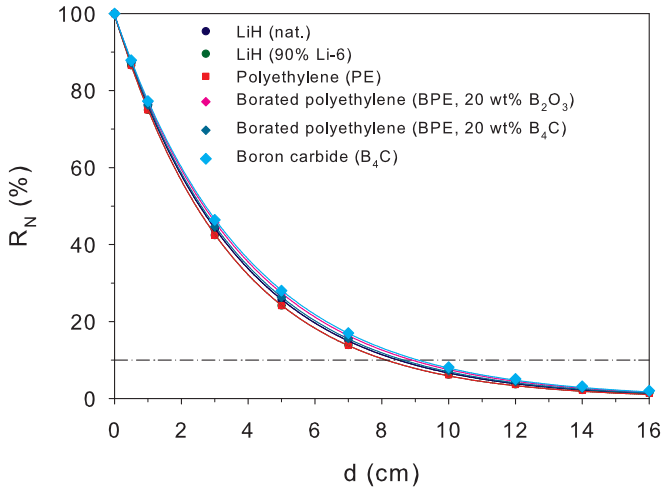


Figure 7.6: Dependence of the fast-neutron fraction R_N for 2 MeV neutrons on the thickness d of different filter materials obtained from numerical simulations with the MCNP6 code. The solid lines represent the fit of the data with a simple decay function like Eq. (4.14). The dash-dotted line corresponds to a value of R_N of 10%.

Neutron-energy spectra

The neutron-energy spectra at the front surface of the detector were determined for the filter materials with a thickness of 10 cm by means of corresponding F1 tallies. The simulations were performed with 10^9 primary neutrons and without neutron energy-cutoff. The obtained spectra are shown in Fig. 7.7.

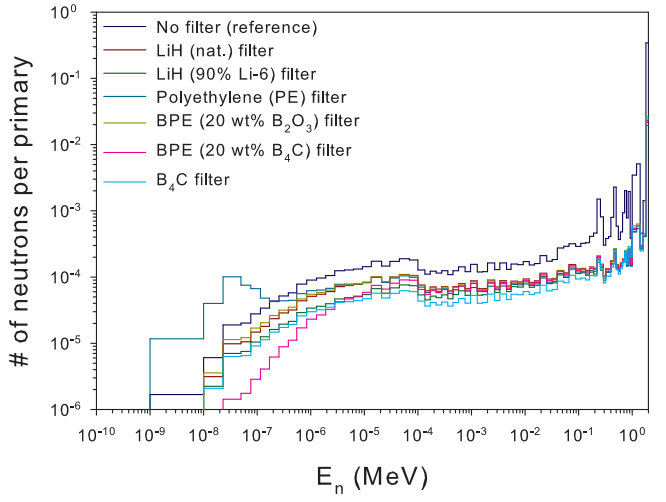


Figure 7.7: Simulated neutron-energy spectra at the detector front surface for all considered filter materials with a thickness of 10 cm induced by 2-MeV neutrons. A total 10^9 primary neutrons were run in the simulations.

Besides small differences on an absolute scale, the shape of the neutron-energy spectra is very similar for all filter materials except for PE. For this material an increase of the neutron flux is observed below 1 eV, as this material does not contain any element with a strong absorption cross section for low-energy neutrons. Despite a good attenuation of the fast neutrons, PE is not an ideal filter material due to a high emission of 2.22-MeV γ-rays of the $^{1}H(n,\gamma)^{2}H$ reaction generating an increased background in the γ-ray spectrum and due to an increased activation of Ge with thermalized neutrons. Doping PE with 20 wt% B_4C instead of B_2O_3 removes thermalized neutrons more efficiently, due to a higher B (boron) content.

Peak- and total- count fraction

As the net counts of a γ-line are directly proportional to the neutron flux, both reduction in the fast-neutron flux (R_N) and line counts (R_P) should correlate. To verify the expected proportionality between R_N and R_P, γ-ray spectra in the energy range 0 to 3 MeV were simulated using the F8 tally (energy deposition) for the various filter materials with a thickness of 10 cm. The simulations were done with 10^9 primary neutrons with a neutron transport energy-cutoff of 10^{-10} MeV. As an example, the γ-ray spectra obtained without filter, a PE and a BPE filter with 20 wt% B_4C are given in Fig. 7.8. The filter materials reduced the Compton background as well as the net counts of γ-lines significantly.

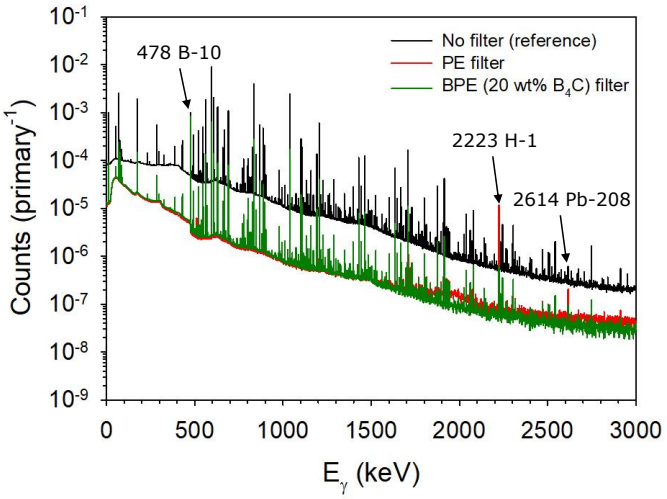


Figure 7.8: γ-ray spectra simulated in MCNP6 with F8 pulse-height tallies without a filter, a PE filter and a BPE filter with 20 wt% B_4C, each of 10 cm thickness. A total of 10^9 primary neutrons were run.

The fraction of peak counts (R_P) as well as the fast-neutron flux fraction (R_N) are given for all filters in Table 7.3. The reduction of the net counts of the γ-lines of Ge isotopes induced by fast neutrons (triangular peaks) agrees very well with the reduction of the fast-neutron flux impinging on the detector surface, thereby confirming the proportionality between these parameters.

Table 7.3: Fraction of peak counts R_P of relevant γ-lines in % for all considered filter materials with a thickness of 10 cm.

E_γ (keV)	^AZ	LiH (nat.) $\mathbf{R_N = 6.93\%}$	LiH (90% ^{6}Li) $\mathbf{R_N = 6.19\%}$	PE $\mathbf{R_N = 6.17\%}$	BPE (20 wt% B_2O_3) $\mathbf{R_N = 7.79\%}$	BPE (20 wt% B_4C) $\mathbf{R_N = 7.24\%}$	B_4C $\mathbf{R_N = 8.15\%}$
69	^{73}Ge	7.86 ± 0.09	7.03 ± 0.11	7.03 ± 0.11	8.58 ± 0.05	8.16 ± 0.10	8.92 ± 0.07
563	^{76}Ge	6.81 ± 0.09	6.08 ± 0.11	6.06 ± 0.12	7.54 ± 0.15	7.16 ± 0.12	8.10 ± 0.10
596	^{74}Ge	6.77 ± 0.46	6.04 ± 0.43	6.02 ± 0.37	7.49 ± 0.48	7.10 ± 0.31	8.05 ± 0.58
692	^{72}Ge	7.00 ± 0.09	6.27 ± 0.06	6.24 ± 0.13	7.74 ± 0.18	7.31 ± 0.06	8.28 ± 0.13
834	^{72}Ge	6.65 ± 0.20	5.92 ± 0.21	5.91 ± 0.18	7.37 ± 0.20	7.01 ± 0.42	7.95 ± 0.24
1040	^{70}Ge	6.61 ± 0.65	5.87 ± 0.62	5.86 ± 0.61	7.33 ± 0.64	6.93 ± 0.54	7.89 ± 0.70
1109	^{76}Ge	6.46 ± 11	5.75 ± 0.09	5.74 ± 0.11	7.12 ± 0.14	6.68 ± 0.33	7.68 ± 0.14
1204	^{74}Ge	6.55 ± 0.09	5.82 ± 0.28	5.80 ± 0.11	7.22 ± 0.31	6.82 ± 0.10	7.83 ± 0.14
1464	^{72}Ge	6.45 ± 0.21	5.71 ± 0.19	5.70 ± 0.07	7.13 ± 0.12	6.72 ± 0.10	7.77 ± 0.08
Average value $\overline{\mathbf{R_P}}$		**6.79 ± 0.41**	**6.05 ± 0.38**	**6.04 ± 0.38**	**7.50 ± 0.42**	**7.10 ± 0.42**	**8.05 ± 0.35**
478	^{10}B	79 ± 2	60 ± 2	86 ± 2	88 ± 2	89 ± 2	61 ± 2
2223	^{1}H	83 ± 2	65 ± 2	449 ± 10	95 ± 3	21 ± 1	62 ± 2
2614	^{208}Pb	24 ± 5	20 ± 4	46 ± 8	30 ± 5	19 ± 3	22 ± 4

In addition, the total counts in the γ-ray spectrum integrated from 0 to 3 MeV were compared to the result obtained from a reference simulation without any filter material. The total counts were reduced by a factor of 8.8 ± 0.7 for the natural LiH filter, 10.5 ± 0.9 for the enriched LiH filter (90% ^{6}Li), 8.9 ± 0.6 for the PE filter, 7.9 ± 0.6 for the BPE filter with 20 wt% B_2O_3, 8.2 ± 0.7 for the BPE filter with 20 wt% B_4C and 8.5 ± 0.7 for the B_4C filter. Therefore, on average, a filter of 10 cm reduces the total counts by a factor of about 9 below a γ-ray energy of 3 MeV. This factor corresponds to a reduction of the γ background to 11.4% (R_{PB}), which is smaller than the reduction of the fast-neutron flux. This observation is plausible since the counts in the γ-ray spectra do not only originate from fast-neutron-induced reactions but also through other reaction channels induced by thermalized neutrons such as (n,γ).

The variation of the value of R_P for the 478-keV line of the ^{10}B(n,α)^{7}Li and the ^{1}H(n,γ)^{2}H reactions for the different filter materials reflects both the effectiveness of the considered filter to reduce the fast-neutron flux as well as the B and H (hydrogen) contents, respectively.

For the 2614-keV line from the ^{208}Pb(n,n'γ)^{208}Pb reaction no correlation between the net counts and the fast-neutron flux was observed. The most intense capture line of the ^{207}Pb(n,γ)^{208}Pb reaction, listed at 7367.78 keV in [132], is accompanied by another line at 2614.53 keV according to [65, 193]. The intensity of the latter is only approximately 0.2% compared to the line at 7367.78 keV. In the measured background spectrum, a line at 7367 keV of ^{207}Pb was observed [34]. With the net counts of this line and the information given above it can be concluded that the contribution of neutron capture in ^{207}Pb relative to inelastic scattering on ^{208}Pb is well below 0.1% and hence negligible. The fact that R_P in Table 7.3 is much higher for PE compared to other filters, suggests that the counts evaluated in the MCNP6 simulations correspond mainly to the ^{207}Pb(n,γ)^{208}Pb reaction. To evaluate this observation further, several simulations were conducted as shown in Table 7.4.

Table 7.4: Numerical simulations performed with the MCNP6 code to investigate the ^{208}Pb(n,n'γ)^{208}Pb reaction. A $5 \times 5 \times 5$ cm^3 cube of Pb was irradiated by 10^8 monoenergetic neutrons of energy E_n. E_{cut} is the neutron-transport cutoff energy.

Simulation	E_n	E_{cut}	PE layer	R_N (%)	R_P(2614 keV) (%)
1	2 MeV	0 eV	-	-	-
2	2 MeV	20 keV	-	-	-
3 (relative to 1)	2 MeV	0 eV	10 cm	12.6 ± 0.4	51 ± 2
4 (relative to 2)	2 MeV	20 keV	10 cm	12.5 ± 0.3	10.3 ± 0.6
5 (relative to 1)	1 eV	0 eV	-	-	3320 ± 62
6 (relative to 2)	1 eV	20 keV	-	-	3320 ± 61

Basically, a cube made of Pb with the dimensions of $5 \times 5 \times 5$ cm^3 was irradiated by monoenergetic beams of fast (2 MeV) and thermal (1 eV) neutrons, respectively. The fast-neutron flux fraction R_N and the peak-count fraction R_P were determined relative to two reference simulations. These simulations differ only in the transport energy-cutoff. In addition, for fast neutrons a 10 cm thick layer made of PE was placed in front of the Pb cube to investigate the effect of thermalized neutrons reaching the Pb cube. From Table 7.4 one can clearly conclude that the net counts of the 2614-keV line increase with an increasing amount of thermal neutrons traversing the Pb cube. It was found that the ^{208}Pb(n,n'γ)^{208}Pb reaction was not simulated by the MCNP6 code, as the corresponding ENDF reaction identifier (i.e. MT= 4) is missing for Pb. Therefore, the counts in the 2614-keV line evaluated in Tables 7.3 and 7.4 are only produced by radiative neutron capture. Nevertheless, γ-ray production data in MCNP6 is questionable, since no relevant line was observed in the simulations at a γ-ray energy of 7367 keV.

Based on the outcomes in this section, PE and LiH (both, natural and enriched) were disregarded from now on as suitable filter materials. PE results in the undesired production of thermal neutrons and does not provide an isotope with a high thermal neutron capture cross section. LiH was no longer considered since the ^{6}Li(n,α)^{3}H reaction produces tritium, which is a major concern in nuclear facilities.

7.5 Scatter neutron spectrum

The outcomes of the investigations presented above are valuable on a quantitative scale but only for monoenergetic neutrons. However, unambiguously the outer shielding of the spectrometer will be exposed to a spatial neutron-energy distribution, related to the scattering properties of the sample.

As the second step of the strategy depicted in Fig. 7.2, the spectrum of the scattered neutrons was investigated by means of numerical simulations. These assume a 0.25 mm thick Fe foil as sample as described in [34].

7.5.1 Variance reduction approach

The MCNP6 code requires to run at least 10^8 primary particles to sample the neutron-energy distribution at sample position correctly. As the solid angle Ω subtended from the sample towards the collimator opening is only about 0.02 sr, the scattering of a neutron towards the detector is expected to be an extremely rare event. Hence, the determination of the scatter spectrum from thermal up to fast neutron energies requires the application of some special techniques. As will be seen in the following, only approximately 10^{-6} neutrons per second per primary scatter towards the collimator opening. This implies that one single simulation considering the complete neutron-energy distribution from 10^{-10} MeV to 20 MeV would at least have to run 10^{14} primary neutrons to achieve acceptable statistics. For this number of particles the expected and estimated computing time exceeds one whole year by far, even with techniques such as CPU threading and parallelising on a standard cluster.

Therefore, to ensure reasonable simulation times, instead of one full simulation each neutron-energy range (thermal, epithermal, fast) was simulated individually with corresponding emission probabilities in each bin. The total neutron flux per primary source neutron in each bin i (cm^{-2} $\mathrm{primary}^{-1}$) is the sum of those three simulations, but with proper scaling factors:

$$\Phi_{tot,i} = \Phi_{th,i} \times \left(\frac{\Phi_{Th}}{\Phi_{Tot}}\right)_{Exp} + \Phi_{epi,i} \times \left(\frac{\Phi_{Epi}}{\Phi_{Tot}}\right)_{Exp} + \Phi_{fast,i} \times \left(\frac{\Phi_{Fast}}{\Phi_{Tot}}\right)_{Exp}, \quad (7.1)$$

where capitalized subscripts of the neutron flux Φ refer to experimental values and lowercase subscripts refer to numerical neutron-flux values in the considered neutron-energy bin i. Running a total of 10^9 primary neutrons in each simulation, the final result equals that one obtained with 10^{14} particles for the whole spectrum, but with much less computing time. To obtain the neutron flux in units of cm^{-2} s^{-1} for every bin, the values of $\Phi_{tot,i}$ in Eq. (7.1) were multiplied by the total number of neutrons impinging on the Fe sample per second, i.e. $\Phi_{Tot} \times S_{Fe}$ (S_{Fe}= 6.25 cm^2).

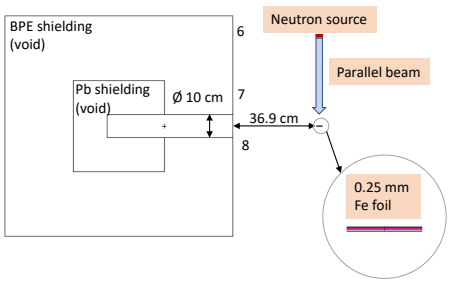


Figure 7.9: MCNP6 model used to determine the spectrum of neutrons scattered from a Fe sample. Material cells of the FaNGaS spectrometer are empty. The numbers 6, 7 and 8 represent surface numbers used for F1 tallies in MCNP6.

To save further computing time, the simulations were performed with empty voids as shown in Fig. 7.9.

7.5.2 Neutron flux at collimator opening

The spectra of scattered neutrons were simulated with the F1 tally at a collimator opening of 6 and 10 cm at the front surface of the BPE shielding (with surfaces 8 and 7 given in Fig. 7.9, respectively). The obtained spectra are depicted in Fig. 7.10. The shape of the experimental sample spectrum is conserved and the differences between the two scatter spectra are negligible.

The uncertainties in each energy bin are shown in Fig. 7.10. At that point one must distinguish between the uncertainty from the simulation and the effective uncertainty resulting after processing of the data with Eq. (7.1). Due to large errors in the experimental thermal and epithermal neutron flux values the uncertainty is rather large. Between 10^{-7} and 10^{-6} MeV it is extremely high. However, the contribution of neutrons in those bins was found to be negligible.

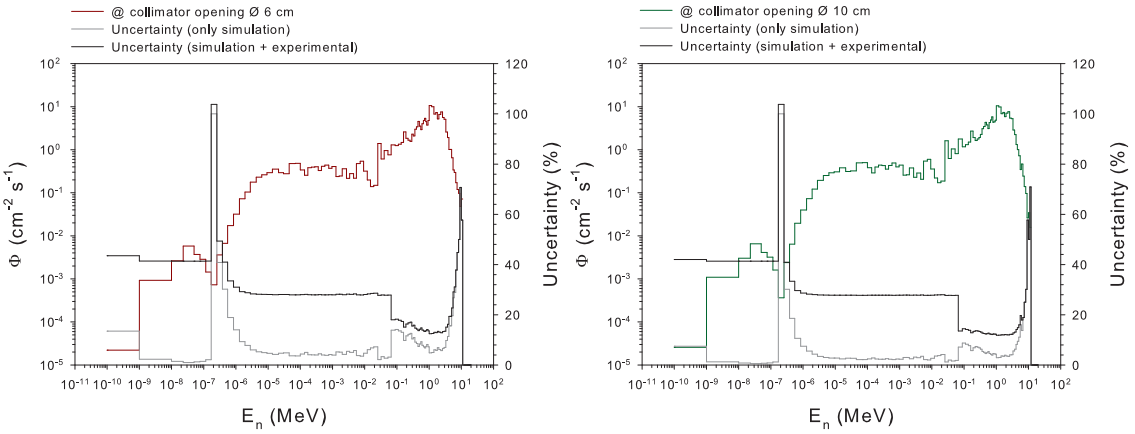


Figure 7.10: Neutron-energy spectrum and statistical uncertainties for each energy bin for the neutron scatter spectra obtained by numerical simulations with the MCNP6 code for collimator openings of 6 (left picture) and 10 cm (right picture) diameter.

For both diameters of 6 and 10 cm at the collimator opening of the BPE front surface shielding the derived neutron flux values are given in Table 7.5. The experimental neutron-energy spectrum at sample position comprises of approximately 0.003% thermal, 2.5% epithermal and 97.5% fast neutrons (see Table 5.1). In contrast to this, the spectrum of scattered neutrons has slightly shifted towards lower neutron energies, leading to a reduction in the average energy from 2.30 to about 1.30 MeV (flux-weighted average). This observation is explained with Table 7.5, as the relative fraction of epithermal neutrons in the whole spectrum has increased compared to the neutron spectrum at sample position.

Table 7.5: Absolute flux values of neutrons scattered towards the collimator opening derived by means of MCNP6 simulations for a Fe sample (S= 2.5 × 2.5 cm^2, d= 0.025 cm) for all considered neutron-energy ranges. Values in % below the flux values give the fraction relative to the total scatter neutron flux.

Collimator opening		Neutron flux Φ (cm^{-2} s^{-1})			
⌀ (cm)	S (cm^2)	Φ_{th} × 10^{-2}	Φ_{epi}	Φ_{fast}	Φ_{tot}
6	28.3	1.7 ± 0.7	13.9 ± 4.1	135 ± 22	149 ± 26
		(0.01%)	(9.4%)	(90.6%)	(100%)
10	78.5	1.9 ± 0.8	15.2 ± 4.4	140 ± 21	155 ± 26
		(0.01%)	(9.8%)	(90.2%)	(100%)

In addition, Table 7.6 gives for all neutron-energy ranges (thermal, epithermal, fast) the ratio of the scatter neutron flux to the experimental neutron flux at sample position. The values in Table 7.6 imply that approximately one out of one million neutrons hitting the sample per second and per square centimeter scatters towards the collimator opening at the BPE front surface of the spectrometer shielding. In addition, this tendency is observed to decrease with increasing energy. Table 7.5 also shows that the contribution of thermal neutrons is completely negligible, as after one minute of irradiation approximately only one single thermal neutron scatters towards the collimator opening. Hence, observation of radiative neutron capture (n,γ) lines associated to isotopes of Ge will mostly be related to scattered epithermal neutrons or moderated fast neutrons.

Table 7.6: Ratio of the flux values from neutrons scattered by the Fe foil towards the collimator opening, i.e. Φ(scatter), to the experimental neutron flux values at sample position, i.e. Φ(incident).

Collimator opening		Φ(scatter)/Φ(incident) × 10^{-6}			
⌀ (cm)	S (cm^2)	Thermal	Epithermal	Fast	Total
6	28.3	5.5	4.7	1.2	1.3
10	78.5	6.1	5.2	1.2	1.3

Scatter pattern

The spatial distribution of the scattered neutrons at the front surface of the BPE shielding was determined with a FMESH4 card. A spatial XYZ-binning of 100 × 100 × 1 was applied for -15 cm ≤ X ≤ 15 cm and -15 cm ≤ Y ≤ 15 cm at Z= 50.0 cm (the collimator opening is centered at X= 0 and Y= 0; Z= 50.0 cm corresponds to the outer surface of the BPE shielding). For thermal, epithermal and fast-neutron energy ranges 10^9 neutrons were run. The scatter patterns are given in Fig. 7.11 and look the same for all neutrons. However, the statistics are observed to become worse towards higher energies. This observation reflects Table 7.6 and is related to the fact that the elastic scattering cross sections fall down with increasing energy,

or vice versa: the penetration power of neutrons rises as a function of energy.

Nevertheless, the patterns could be described as a lung with a "shadow" of the sample along the vertical collimator axis (Y-axis). Noteworthy, the width of this shadow is much bigger than the sample thickness. Fortunately, local peaks in the neutron-flux density appear in regions around the collimator opening, where 30 cm of BPE are available to moderate and absorb the scattered neutrons.

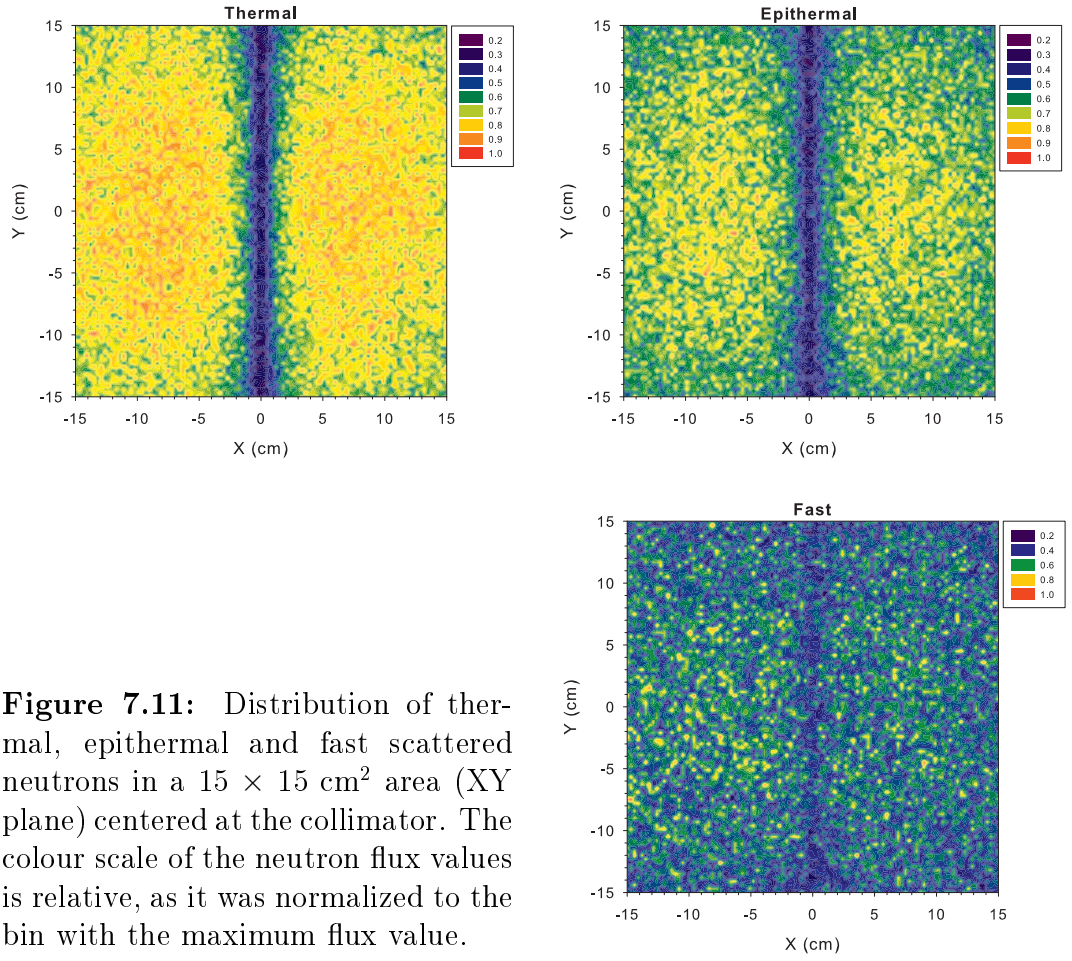


Figure 7.11: Distribution of thermal, epithermal and fast scattered neutrons in a 15 × 15 cm^2 area (XY plane) centered at the collimator. The colour scale of the neutron flux values is relative, as it was normalized to the bin with the maximum flux value.

Dependence on sample thickness

The variation of the scattered fast neutrons was investigated as a function of the thickness of the Fe foil. The results are shown in Fig. 7.12. As expected, the magnitude of scattered neutrons increased with increasing sample thickness. This increase resembles a linear dependence on the thickness, at least for a few several cm. Within the aforementioned linear region doubling of the sample thickness approximately also doubles the scatter neutron flux. In fact, a saturation level of scattered neutrons is achieved around a sample thickness of 10 cm, which corresponds to the maximum length covered by the field of view (solid-angle coverage) of the HPGe detector.

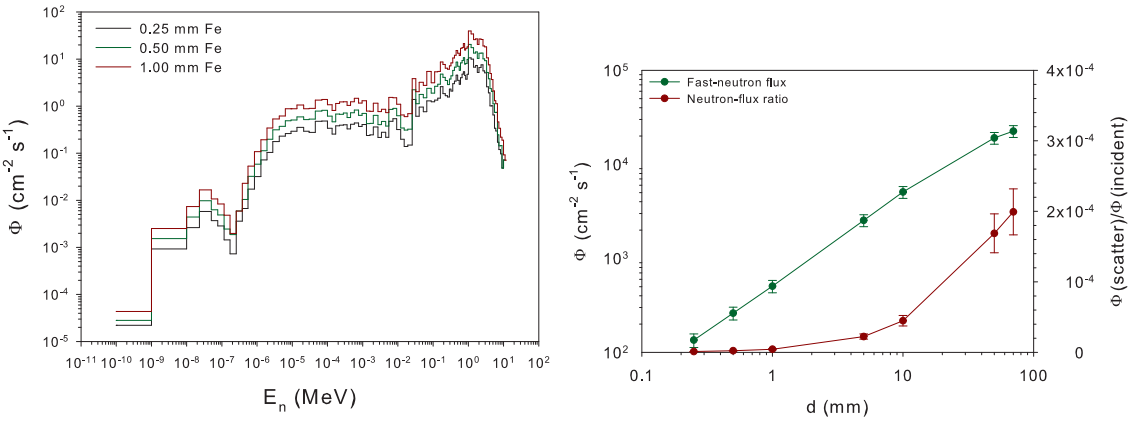


Figure 7.12: Variation of the scatter neutron spectrum at a collimator opening of 6 cm diameter for Fe foils of 0.25, 0.5 and 1 mm thickness as a function of the sample thickness (left picture). Dependence of the scattered fast-neutron flux for Fe samples and the ratio between the scattered fast-neutron-flux Φ(scatter) and the incident fast-neutron flux at sample position Φ(incident) as a function of the sample thickness (0.25 to 70 mm).

Dependence on sample material

All neutron flux values given in Table 7.5 were determined using a thin Fe foil. However, the amount of scattered neutrons strongly depends on the scattering properties of the sample, in particular the macroscopic scattering cross section (Σ_s). To investigate the variation of the scatter neutron flux at a collimator opening of 6 cm as a function of Σ_s, Al, Ti and Cu samples of 1, 10 and 50 mm thickness, in addition to Fe, were simulated with the MCNP6 code. For a thickness of 0.25 mm Fig. 7.13 shows the corresponding fast-neutron scatter spectra at a collimator opening of 6 cm. Figure 7.13 implies that the shape of the energy distribution from fast neutrons scattered towards the detector is relatively independent from the sample composition.

For each thickness of 1, 10 and 50 mm of the above mentioned samples the dependence of the scattered fast-neutron flux on the value of Σ_s, normalized to that one of Fe, is illustrated in Fig. 7.14.

The fact that the individual data points in Fig. 7.14 are equally distributed with respect to each other for all thicknesses, indicates an almost linear dependence between the sample thickness and the scatter neutron flux for the Al, Ti and Cu samples in addition to the Fe sample (see also Fig. 7.12). Surprisingly, however, the value of the scatter neutron flux does not follow a perfect linear dependence on the value of Σ_s. This observation might be reasoned in the different anisotropy patterns of the respective elastic and inelastic scattering processes. Nevertheless, accounting also for the uncertainties of the neutron flux values, the data points in Fig. 7.14 can be fitted by a simple linear fit as indicated by the solid lines.

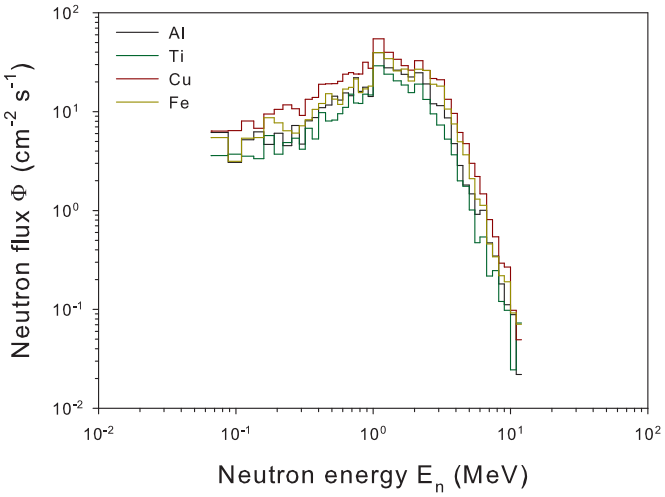


Figure 7.13: Fast-neutron scatter spectra at a collimator opening of 6 cm for Al, Ti, Cu and Fe samples of 0.25 mm thickness and a surface area of 2.5 × 2.5 cm^2 obtained by numerical simulations with the MCNP6 code.

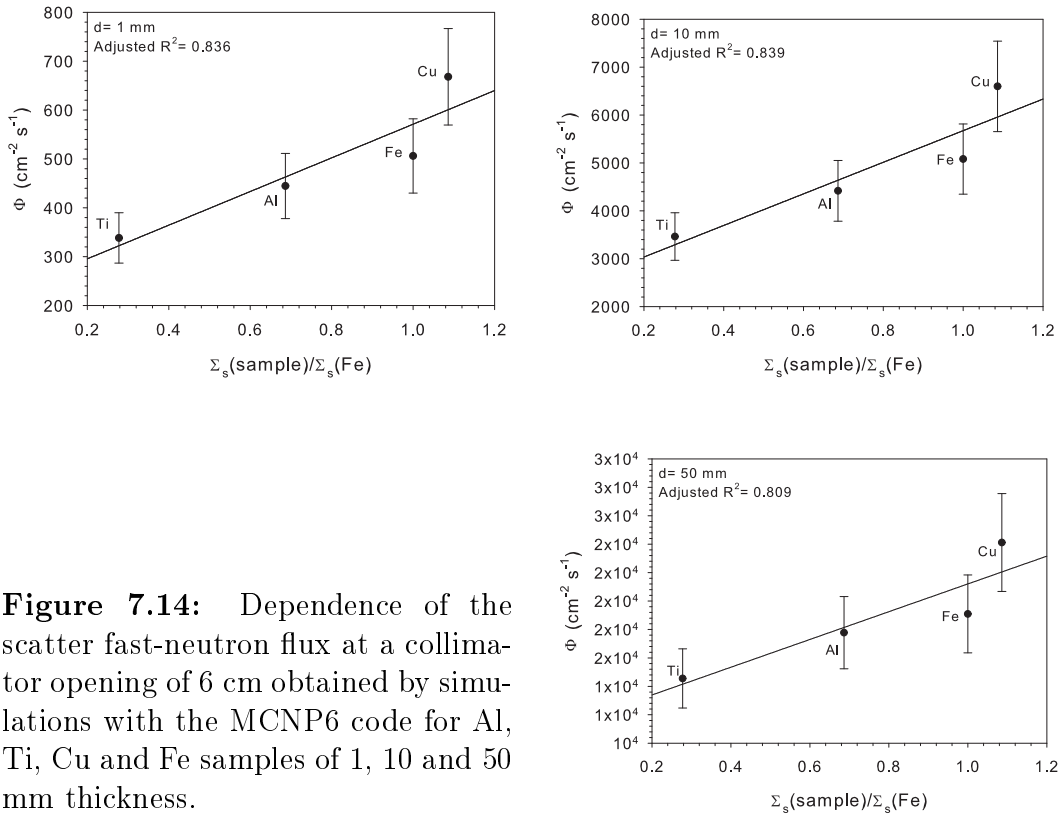


Figure 7.14: Dependence of the scatter fast-neutron flux at a collimator opening of 6 cm obtained by simulations with the MCNP6 code for Al, Ti, Cu and Fe samples of 1, 10 and 50 mm thickness.

7.5.3 Neutron flux at detector front surface

Compared to the neutron flux incident on the BPE front surface, the neutron flux arriving at the front surface of the HPGe detector is expected to be further reduced due to scattering of neutrons into the shielding materials. The flux of fast neutrons at the detector front surface was determined by two complementary methods.

In a first method, for a collimator opening of 6 cm the scatter neutron spectrum induced by fast neutrons impinging on a 0.25 mm thick Fe sample obtained with a previous simulation was used as an input neutron source in another simulation. This latter simulation yielded a fast-neutron flux of (48 ± 8) cm^{-2} s^{-1}.

In a second method, the simulation of the Fe foil as depicted in Fig. 7.9 was repeated applying a F1 tally at the front surface of the HPGe crystal. This simulation provided a value of (44 ± 7) cm^{-2} s^{-1}. As both results agree well, the emission without any specified angular distribution in the first method is reasonable. For a Fe foil of 0.25 mm thickness an average fast-neutron flux of (46 ± 11) cm^{-2} s^{-1} was determined at the front surface of the Ge crystal. Compared to the flux of (135 ± 22) cm^{-2} s^{-1} at the collimator opening this corresponds to a reduction by a factor around 3.

The flux of scattered fast neutrons mainly depends on the composition (Σ_s) and thickness of the sample placed into the beam. However, even without a sample a certain fraction of neutrons scatters towards the detector. The average fast-neutron flux in the Ge crystal was estimated in a previous work on FaNGaS [141] as 11 cm^{-2} s^{-1}. This value was determined from the triangular 596-keV line of ^{74}Ge, with a fission-spectrum average cross section of 1.112 b and an intensity of about 63.7%. The difference in the fast-neutron flux at sample position given in [141], i.e. (1.01 ± 0.04) × 10^8 cm^{-2} s^{-1}, was considered as negligible compared to the value of (1.13 ± 0.04) × 10^8 cm^{-2} s^{-1} in this work.

For the effective fast-neutron flux reaching the front surface of the HPGe detector the contribution without sample (background) must be also considered. In fact, the value of the scattering factor f_s indicates the increase in the scattered neutron flux for a given sample. Since an average value of $\overline{f_s}$= 1.20 ± 0.12 was derived from the measurement of the Fe foil [20], this implies that about 20% of the total scattered neutron flux is induced by the Fe foil. Using a fast-neutron flux of 46 ± 11 cm^{-2} s^{-1} for the Fe foil, a background neutron flux of 230 ± 60 cm^{-2} s^{-1} is concluded. To estimate the average fast-neutron flux inside the Ge crystal the neutron self-shielding factor f_n must be considered. Assuming a mean energy of 1.3 MeV for scattered neutrons and using ENDF/B-VIII.0 data given in [50], Eqs. (2.10) and (4.16) estimate a self-shielding factor of f_n= 0.437. This value implies a sample neutron flux of 101 ± 26 cm^{-2} s^{-1}, which is in strong disagreement with the value of 11 cm^{-2} s^{-1} given in [141]. Regarding the aforementioned disagreement, one should be aware of the following aspects: the cross section of 1.112 b used in [141] is valid for a fission-neutron spectrum average. In fact, however, the shape and mean energy of the scattered neutrons is unknown. In addition, it is unclear how the intensity of 63.7% used in [141] was derived from the Atlas [27]. Furthermore, it is uncertain if 100% counting efficiency of the γs in [141] is justified to assume. On the other hand, the aforementioned aspects make an accurate determination of the neutron self-shielding almost impossible.

Nevertheless, the value of the average fast-neutron flux within the HPGe crystal ($\Phi_s(HPGe)$) can be estimated by the following relationship:

$$\Phi_s(HPGe) = \Phi_{s,bkg}(HPGe) \cdot \frac{\dot{C}_{E\gamma,sample}(596\,keV)}{\dot{C}_{E\gamma,bkg}(596\,keV)}, \tag{7.2}$$

where $\Phi_{s,bkg}(HPGe)$ is the average fast-neutron flux in the Ge crystal without sample and $\dot{C}_{E\gamma,sample}(596\,keV)$ and $\dot{C}_{E\gamma,bkg}(596\,keV)$ are the count rates of the 596-keV line of ^{74}Ge with and without a sample in the neutron beam, respectively.

The accumulated irradiation time the HPGe detector can be used without signifcant radiation damage can be estimated using a value of $\Phi_{s,bkg}(HPGe)$= 101 cm^{-2} s^{-1} deduced in this work and a neutron fluence of 10^9 cm^{-2} suggested as threshold dose in the literature [152]. A time of about 115 days is concluded.

7.6 Neutron performance

With the scatter spectrum derived from a 0.25 mm thick Fe sample at a collimator opening of 6 cm in the previous section it was possible to simulate the performance of the boron-containing filter materials for a polychromatic neutron beam. Relative emission probabilities in each bin of the neutron-energy distribution used in MCNP6 were derived from the aforementioned simulation. Analogous to the investigations of the monochromatic 2-MeV neutron beam the fast-neutron fraction R_N, the peak-count fraction R_P and the total-count fraction R_{PB} were determined.

Fast-neutron fraction

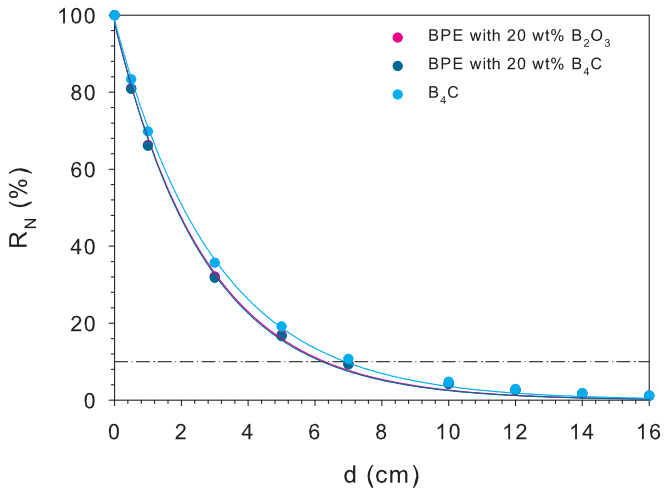


Figure 7.15: Variation of the fast-neutron fraction R_N with the filter thickness d for the fast-neutron scatter spectrum derived at a collimator opening of 6 cm with MCNP6 for irradiation of a 0.25 mm thick Fe sample. The data points were approximated with a simple decay function like Eq. (4.14).

The fraction of fast neutrons transmitted through a certain filter thickness is given in Fig. 7.15. Compared to the results for 2 MeV energy, less filter material is required to reduce the beam intensity to the same level as the mean energy of scattered fast neutrons is around 1.3 MeV.

Neutron-energy spectra

Exemplary, the neutron-energy spectra for BPE filters with 20 wt% B_2O_3 of thicknesses ranging between 0.5 and 16 cm are shown in Fig. 7.16. In addition, the spectra of all three boron-containing filter materials are depcited for a thickness of 7 cm in Fig. 7.16.

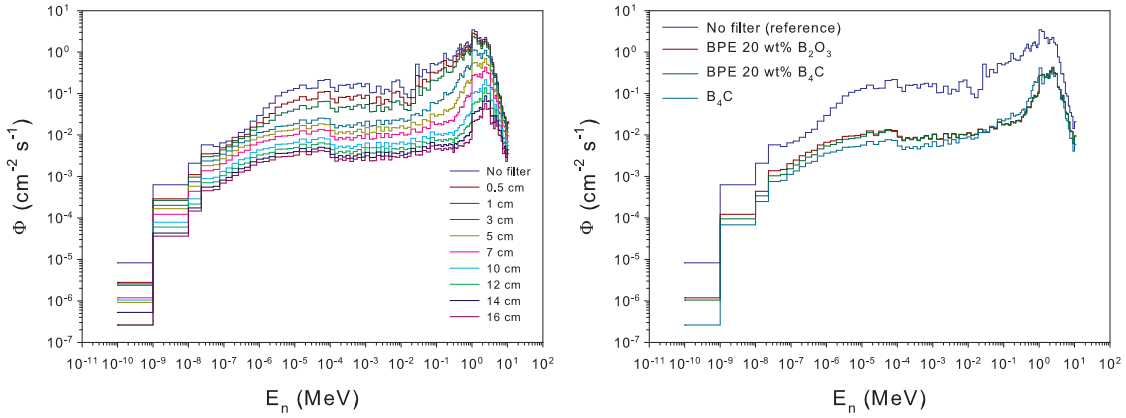


Figure 7.16: Neutron-energy spectra obtained with a F1 (current) tally in the MCNP6 code at the front surface of the detector. The neutron-energy distribution used in the simulation corresponds to that one obtained from the simulation of a 0.25 mm thick Fe sample at a collimator opening of 6 cm. The left plot shows the variation of the neutron flux as a function of the thickness for a BPE filter with 20 wt% B_2O_3. The right plot depicts the neutron spectrum for all three considered boron-containing filters at a thickness of 7 cm. A total of 10^9 primary neutrons were run.

On the one hand, the spectrum shape is conserved over different filter thicknesses. On the other hand, the absolute differences between the three boron-containing filters are negligible.

Peak- and total-count fraction

The values of the peak-count fractions, i.e. R_P, are given in Table 7.7 for all three boron-containing filters and a thickness of 10 cm. In contrast to the monoenergetic 2-MeV case, the average values of R_P for all considered (n,n'γ) reactions of Ge rather disagree with the respective fast-neutron flux fraction R_N. In addition, they strongly depend on the isotope.

Table 7.7: Fraction of peak counts R_P of relevant γ-lines in % for boron-containing filter materials with a thickness of 10 cm. The neutron-energy distribution derived with a 0.25 mm thick Fe sample for a collimator opening of 6 cm was used in the numerical simulations.

E_γ (keV)	^{A}Z	Reaction	BPE (20 wt% B_2O_3) $\mathbf{R_N = 4.40\%}$	BPE (20 wt% B_4C) $\mathbf{R_N = 4.20\%}$	B_4C $\mathbf{R_N = 4.78\%}$
69	^{73}Ge	(n,n'γ)	3.52 ± 0.04	3.40 ± 0.03	4.37 ± 0.07
563	^{76}Ge	(n,n'γ)	6.17 ± 0.31	5.95 ± 0.08	6.21 ± 0.15
596	^{74}Ge	(n,n'γ)	6.37 ± 0.55	6.15 ± 0.60	6.35 ± 0.58
692	^{72}Ge	(n,n'γ)	6.13 ± 0.09	5.90 ± 0.04	6.28 ± 0.13
834	^{72}Ge	(n,n'γ)	7.14 ± 0.22	6.90 ± 0.12	6.63 ± 0.08
1040	^{70}Ge	(n,n'γ)	7.92 ± 0.22	7.64 ± 0.04	6.96 ± 0.14
1109	^{76}Ge	(n,n'γ)	7.74 ± 0.64	7.64 ± 0.53	6.98 ± 0.25
1204	^{74}Ge	(n,n'γ)	7.89 ± 1.62	7.57 ± 1.45	7.01 ± 1.32
1464	^{72}Ge	(n,n'γ)	8.58 ± 0.22	8.45 ± 0.41	7.80 ± 0.22
Mean value of $\overline{\mathbf{R_P}}$			**6.83 ± 1.43**	**6.62 ± 1.41**	**6.51 ± 0.89**
478	^{10}B	(n,α)	49 ± 2	49 ± 2	34 ± 1
2223	^{1}H	(n,γ)	58 ± 3	46 ± 3	35 ± 2
2614	^{208}Pb	(n,n'γ)	25 ± 1	28 ± 1	26 ± 2

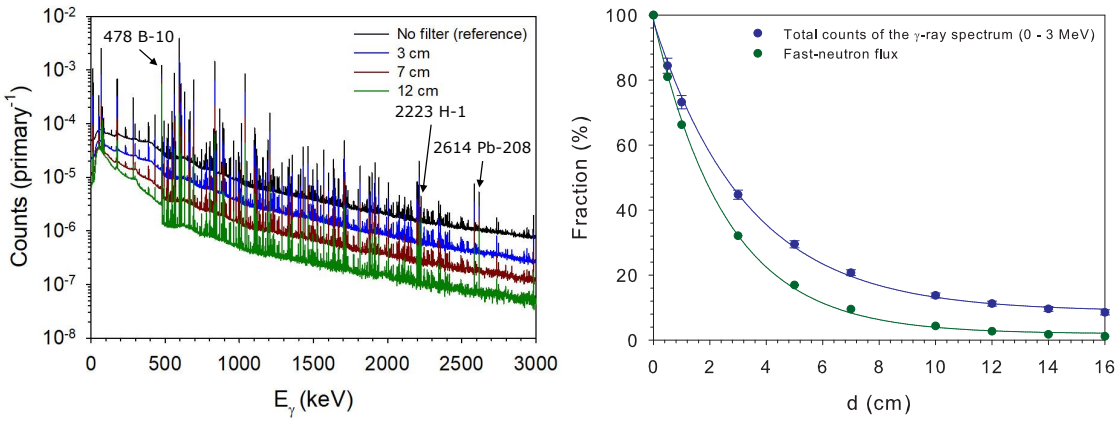


Figure 7.17: Simulated γ-ray spectrum for a BPE filter with 20 wt% B_2O_3 and different thicknesses (left plot), and the variation of the total counts below 3 MeV as a function of the thickness for the same filter material (right plot). A total of 10^9 primary neutrons were run.

The simulated γ-ray spectrum for the BPE filter with 20 wt% B_2O_3, obtained using a F8 tally in the MCNP6 code, is shown in Fig. 7.17. With increasing thickness the total count reduction is less at lower γ-ray energies compared to higher energies. The relative fraction of total counts as a function of the thickness is also given in Fig. 7.17. For a thickness of 10 cm the total counts integrated between 0 and 3

MeV are reduced by a factor of 7.3 ± 0.4, 7.3 ± 0.4 and 8.4 ± 0.5 for the BPE filter with 20 wt% B_2O_3, that one with 20 wt% B_4C and the B_4C filter. With respect to monoenergetic 2-MeV neutrons the counts are reduced less.

Figure 7.18 complements Table 7.7, as it shows the dependence of the reduction in peak counts as a function of the filter thickness for the BPE filter with 20 wt% B_2O_3. It also shows that the agreement between the count reduction and the fast-neutron flux reduction strongly depends on the considered isotope.

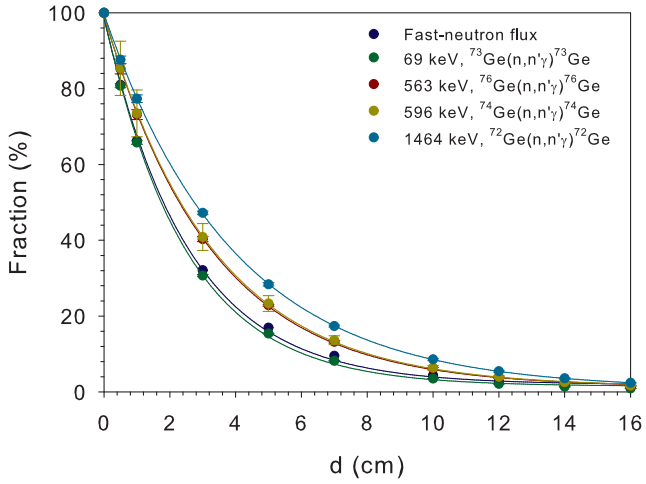


Figure 7.18: Fast-neutron flux fraction and peak-count fraction of a BPE filter with 20 wt% B_2O_3 for different γ-lines of Ge isotopes from inelastic scattering reactions.

With respect to Fig. 7.18 and data given in Table 7.7, the fast-neutron flux reduction agrees with the peak-count reduction best for ^{73}Ge. The ENDF/B-VIII.0 cross sections for the inelastic scattering (MT= 4) for Ge isotopes are depicted in Fig. 7.19 for the energy range of the fast-neutron scatter spectrum, i.e. from 0.06 up to 11 MeV. According to Fig. 7.19 this might be attributed to two reasons: first (i), the cross section covers the whole energy range of the fast-neutron scatter spectrum. Secondly (ii), the average flux reduction does not correspond to every single neutron-energy bin. There are always neutrons that are attenuated more or less than that value. However, with respect to the respective cross sections those neutrons might have a stronger contribution to the reaction rate. It is worth to mention that, in the case of the ^{73}Ge(n,n'γ)^{73}Ge reaction, neutrons around the average energy of 1.3 MeV for the cross section approximately correspond to the average flux reduction given in Table 7.7.

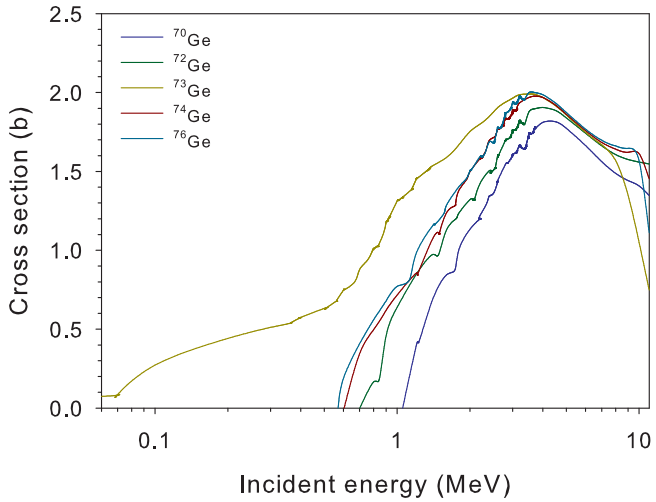


Figure 7.19: Inelastic scattering cross sections (MT= 4) from the ENDF/B-VIII.0 [112] evaluation for every isotope of Ge.

7.7 Gamma-ray performance

The presence of the filter in the opening of the detector collimator will absorb also the γ radiation emitted from the sample and, thus, reduce its detection probability. The dependence of the FEP efficiency of the HPGe detector on the filter thickness was investigated by means of numerical simulation with the MCNP6 code. In these simulations, a detailed model of the detector was used for the energy deposition of γs in the Ge crystal.

7.7.1 HPGe detector model

The geometry model of the HPGe detector implemented into MCNP6 was written based on the technical drawing provided by ORTEC, which is given in Appx. I, together with some important detector specifications. The resulting geometry is depicted in Fig. 7.20 and the input is given in Appx. K.1.

Compared to the technical drawing several slight deviations and assumptions were done. The deviations are due to errors or missing dimensions and include: the nominal radius at the end of the crystal hole was modeled with 5.1 instead of 5.0 mm. The horizontal spacing between the inner and outer Al housing was chosen to be 5.2 mm (undefined in the technical drawing). The vertical excess length of the outer Al housing was set to 0.755 cm.

The aforementioned assumptions include: the composition of the dead layers was modeled with a 50-50 ratio of atoms (in reality there will be a concentration gradient). The 0.3 micron thick Ge/B dead layer was not considered for the crystal front surface. The inner of the crystal hole was filled with copper to account for the electromechanical cooling of the detector ("cold finger").

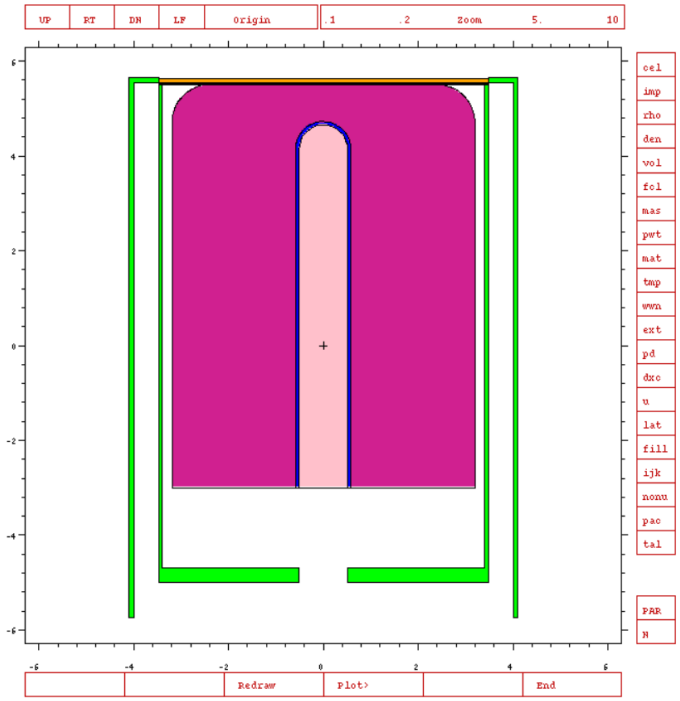


Figure 7.20: HPGe detector model implemented into MCNP6. The model is based on the technical drawing given in Appx. I.

7.7.2 Numerical full-energy-peak efficiency

Detection efficiencies of γ-ray detectors are usually determined experimentally with isotropic sources emitting γs of different energies. Owing the small solid angle subtended from the sample to the detector the deposition of γ energy in the Ge crystal is a rare event associated with poor statistics. Definition of the source as a distribution of several discrete energies will further reduce the statistics. For this reason, in the simulations with MCNP6 a forward-focussed source (cone shape) was defined. In this case, γ-rays were only emitted along Z-axis into the solid-angle fraction of interest, i.e. beam paths that reach the crystal. The source comprised 26 γs with energies ranging from 10 keV up to 8 MeV, each with equal emission probabilities. A F8 tally was used to obtain the γ-ray spectrum. The data was also corrected for the solid angle, to get a result that is equivalent to that one obtained with an isotropic source. Therefore, MCNP6 values were multiplied by the ratio of the solid-angle coverage of the defined emission cone (i.e. 7.14×10^{-3} sr) to that one of a full sphere (4π). This factor was determined as 5.68×10^{-4}.

The γ-ray energy dependence of the FEP efficiency determined without any filter materials in the collimator opening is compared with the experimentally one obtained in Fig. 7.21. In addition, the result obtained with isotropic γ sources (26 individual simulations) is depicted.

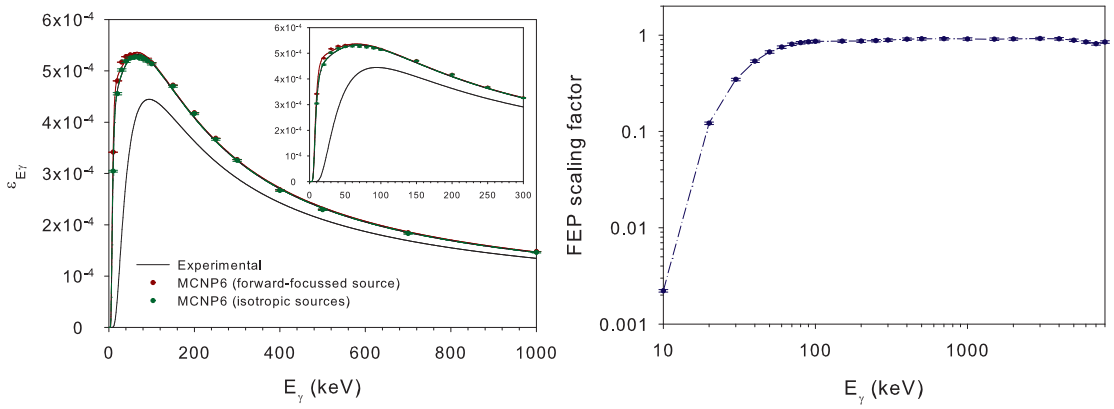


Figure 7.21: Comparison of the experimental FEP efficiency curve with the simulated FEP efficiency curves obtained with MCNP6 for a single forward-focussed γ source and isotropic sources considering 26 γ energies between 10 keV and 8 MeV (left picture). Energy-dependent scaling factors used to adjust the numerical solution of the forward-focussed source to the experimental solution (right picture). A total of 10^8 primaries were run in the simulations.

Comparing the solution using the forward-focussed source in Fig. 7.21 with the experimental FEP, for an energy range between 100 keV and 8 MeV smaller deviations between 9.1% (700 keV) and 23.1% (7000 keV) were observed. Below 100 keV γ energy the deviation increases drastically up to 45,000% at 10 keV. The use of the forward-focussed source was justified, as the relative deviation compared to the solution with the isotropic sources varies from 0.2 to 3.4% between 100 keV and 8 MeV and from 0.5 to 12.2% below 100 keV. In fact, deviations in the low-energy range of γ-rays are frequently observed in the literature [194, 195]. These low-energetic γs are very sensitive to details such as the dead layers [196]. In fact, it is not possible to construct a dead layer with high precision. Deviations might also be due to different densities of the materials or the atom ratios in the dead layers. Nevertheless, the experimental solution is correct, and therefore consideration of the ratios in the FEP efficiency yielded correction factors. Application of these factors in the processing of results from MCNP6 lead to correct values. The correction factors used to scale the solution using the forward-focussed γ source are depicted as a function of the γ-ray energy in Fig. 7.21.

The error made by neglecting the Ge/B dead layer at the crystal front surface was found to be negligible and far below 1% over the considered energy range between 10 keV and 8 MeV. In fact, the front-surface dead layer should only play a significant role in p-type HPGe detectors, where the thicker dead layer is outside.

7.7.3 Analytical full-energy-peak efficiency

The geometrical situation for the analytical solution of the γ-ray efficiency for a small sample is depicted in Fig. 7.22.

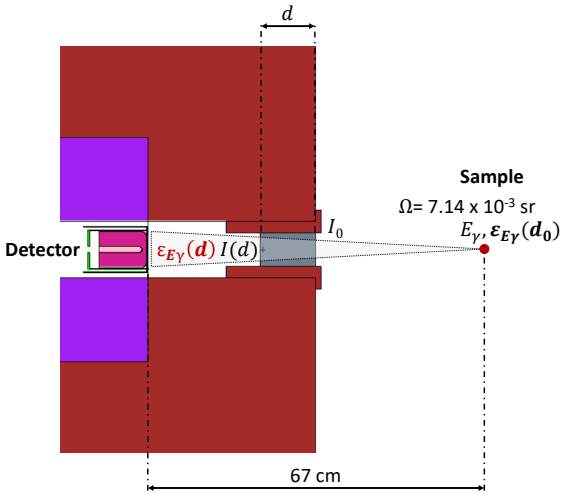


Figure 7.22: Geometrical illustration of the situtation for the determination of the analytical FEP efficiency. The filter is shown in grey colour. A modified excerpt from the MCNP6 geometry plotter is shown.

The solid angle subtended from the sample towards the detector was 7.14×10^{-3} sr. Therefore, it was reasonable to consider a far-field geometry for the collimated γ-ray beam impinging on the filter. The attenuation of the γ-rays by the filter material of thickness d is described by an exponential decay function according to Eq. (4.9). The resulting value for the FEP efficiency with a filter might be estimated by the product of the FEP efficiency value without filter multiplied by the γ-ray transmission in the filter, which can be given by:

$$\epsilon_{E\gamma}(d) = \epsilon_{E\gamma}(d_0) \cdot exp\left(-\mu_m \cdot \rho \cdot d\right), \tag{7.3}$$

with $\epsilon_{E\gamma}(d)$ as the FEP efficiency with use of a filter of thickness d and $\epsilon_{E\gamma}(d_0)$ as the FEP efficiency without any filter material placed in the collimator opening. The mass attenuation coefficients μ_m were taken from XCOM [92], taking coherent scattering into account.

Additionally, numerical simulations with the MCNP6 code were carried out for the three boron-containing filter materials. For thicknesses of 3, 7 and 12 cm, respectively, the analytical and numerical results for the aforementioned filters are given in Fig. 7.23.

The analytical and numerical solutions agree very well with each other, justifying the use of the simple analytical model. The absolute difference averaged over all filters, thicknesses and energies above 60 keV is below 1%. Generally, the deviation in the value of $\epsilon_{E\gamma}$ for both solutions was observed to rise with increasing filter thickness and towards lower γ-ray energies.

Comparing the fitted curves of the analytical FEP efficiencies as given in Fig. 7.23 illustrates that, apart from a reduction in the FEP efficiency value with increasing thickness, for the γ attenuation it makes no significant difference if 20 wt% of B_2O_3 or B_4C is incorporated into PE. However, a severe attenuation effect for

low-energy γs in the case of the pure B_4C filter is evident due to a relatively high material density of 2.52 g cm^{-3}.

As illustrated in Fig. 7.23 it is justified to use the simple analytical model of Eq. (7.3) to estimate the FEP efficiency with use of a filter material in the collimator opening of the spectrometer, thus, avoiding time-consuming numerical simulations. However, to provide flexibility for future user operation at FaNGaS the parameters a_0 to a_8 in Eq. (5.1) of the FEP efficiency curves must be expressed as a function of the filter thickness d, i.e. they must be parametrized. The aforementioned parameters were found to show a perfect linear behaviour with different slopes and values of 1 for the coefficients of determination. Hence, the dependence of the parameters on the thickness d is adequately described by:

$$a_i(d) = b_{0,i} + b_{1,i} \cdot d, \tag{7.4}$$

where a_i is the considered parameter (a_0 to a_8) and $b_{0,i}$ and $b_{1,i}$ are the corresponding fit coefficients.

For all three boron-containing filters the fit coefficients are provided from Appx. J.2 to J.4.

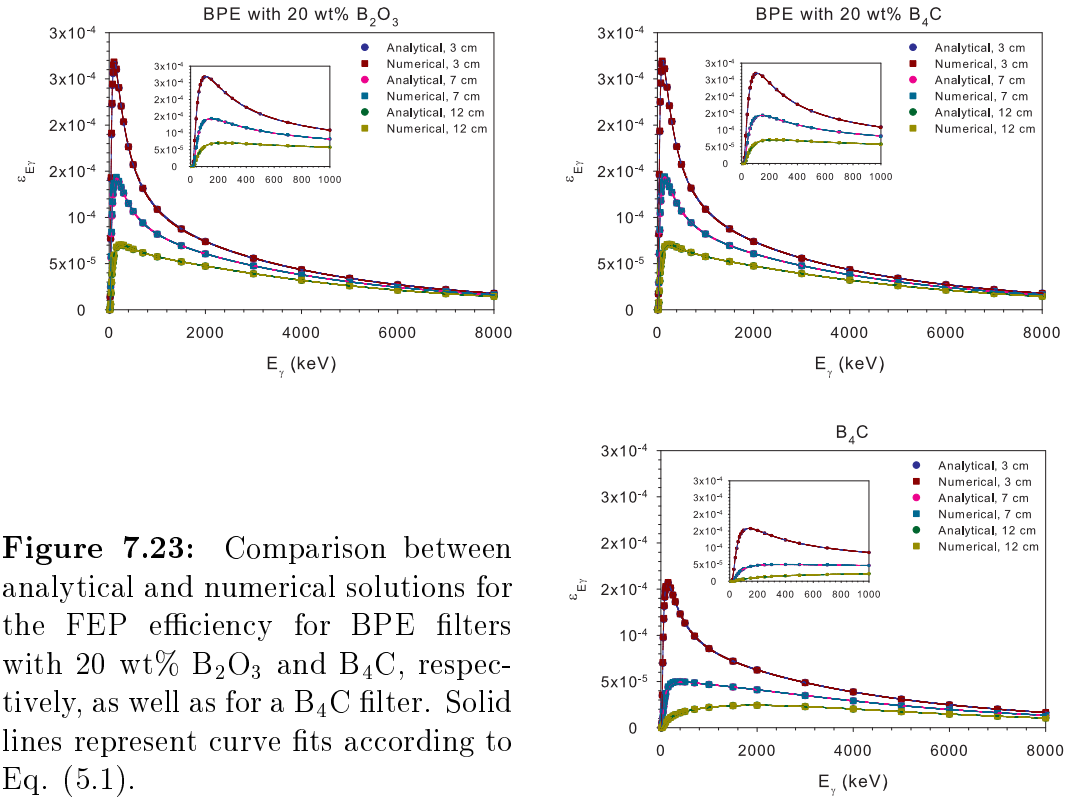


Figure 7.23: Comparison between analytical and numerical solutions for the FEP efficiency for BPE filters with 20 wt% B_2O_3 and B_4C, respectively, as well as for a B_4C filter. Solid lines represent curve fits according to Eq. (5.1).

For the case of the BPE filter with 20 wt% B_2O_3, Fig. 7.24 shows the analytical FEP efficiency as a function of the energy for all thicknesses that were considered.

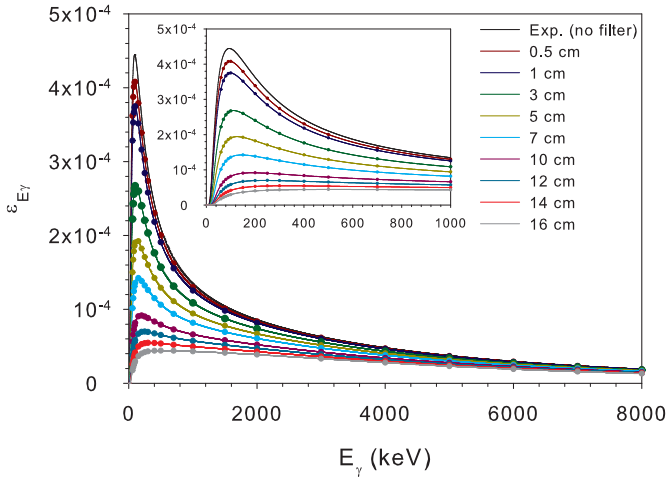


Figure 7.24: Analytically determined FEP efficiency for BPE filters with 20 wt% B_2O_3 and various thicknesses. Solid lines represent curve fits according to Eq. (5.1).

Based on the γ-ray performance characteristics, the BPE filter with 20 wt% B_4C and the B_4C filter were disregarded from now on. The differences in borating PE with 20 wt% B_2O_3 or B_4C are negligible, but the latter material is not so common and availability is difficult. Pure B_4C shows a pronounced γ attenuation due to its high density.

7.8 Proposed material and method

Based on all investigations described above, PE borated with 20 wt% B_2O_3 is suggested as the prime choice for the filter material due to two reasons: **(i)**, this is a standard material characterized by uncomplicated availability and routinely use in various neutron-shielding applications. **(ii)**, this material is already in use for the outer shielding of the FaNGaS spectrometer.

To provide as much flexibility as possible, sets of disc-like filters with different thicknesses should be produced. This would allow to stack the discs to the required thickness. Unfortunately, experimental verification of the obtained results was not possible due to the shut down of FRM II. This should be made as soon as the reactor is back in operation.

Figure 7.25 shows the variation of the scattered fast-neutron flux, the peak counts averaged over all inelastic scattering reactions on Ge and the total counts integrated between 0 and 3 MeV as a function of the filter thickness d. In addition, it illustrates the decrease of relative efficiency (at 1.33 MeV from ^{60}Co) of the HPGe detector with increasing values of d. The placement of a few centimeters of BPE with 20 wt% B_2O_3 into the collimator opening significantly reduces the amount of scattered fast neutrons reaching the detector front surface. With regard to an optimum thickness, however, in the case of large samples the γ radiation emitted from

the sample represents the bottleneck. Since the latter one influences the detector dead time the choose of the filter thickness will be mainly done to prevent saturation of the detector. Nevertheless, the placement of a filter into the collimator opening will always be a compromise between reduction in scattered fast neutrons and loss in counting efficiency. Furthermore, the optimum filter thickness can vary substantially with respect to the energy of the investigated γs.

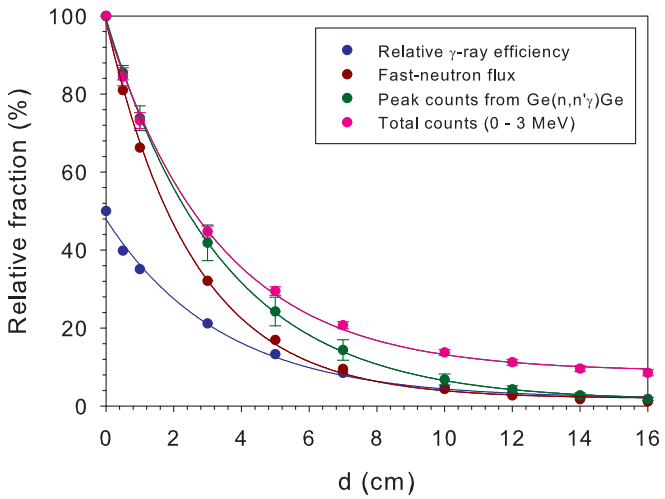


Figure 7.25: Dependence of the relative γ-ray efficiency (at 1.33 MeV from ^{60}Co), the scattered fast-neutron flux, the peak counts from inelastic scattering on Ge (averaged over all γ energies and isotopes) and the total counts (integrated between 0 and 3 MeV) on the thickness d of a filter made of BPE with 20 wt% B_2O_3.

8. Large-sample analytics

The high penetration power of fast neutrons enables the measurement of samples with thicknesses of several centimeters, which is an advantage compared to PGNAA based on cold or thermal neutrons. However, the determination of the elemental composition of large samples requires knowledge on the attenuation of fast neutrons and γs within the sample, i.e. the neutron self-shielding, f_n, and the γ-ray self absorption, $f_{E\gamma}$, respectively. In this chapter, a method is proposed to estimate these two quantities for a rectangular-shaped sample of unknown composition assuming a homogeneous element distribution.

8.1 Concept

The measurement of a sample with rectangular shape is schematically represented in Fig. 8.1. The sample is centered on the neutron beam axis and on the symmetry axis of the coaxial HPGe detector. The neutron beam and the front surface S of the sample have the same size, meaning that the sample is fully irradiated. The maximum size of the neutron beam is 6×6 cm^2 and can be reduced with the MLC in order to fit the dimension of the sample front surface. The field of view of the collimated HPGe detector allows to detect γ radiation emitted from a sample with a maximum length of 10 cm. Therefore, the maximum volume of a sample that can be assayed is $6 \times 6 \times 10$ cm^3.

According to Eq. (4.15), the fast-neutron flux averaged over the sample volume can be given by: $\Phi_s = \Phi_0 \cdot f_n$ with Φ_0 as the incident neutron flux and f_n as the neutron self-shielding factor. Since multiple neutron scattering is not negligible in large samples Eqs. (4.16) and (4.17) are not applicable to derive the value of f_n (see also Fig. 4.3). Therefore, numerical simulations with the MCNP6 code were carried out to find a relationship between f_n and the total macroscopic cross section Σ_t of the sample. The latter can be obtained experimentally by measuring the transmission of the fast neutrons with a suitable neutron detector: $n_T = n_0 \cdot exp(-\Sigma_t \cdot l)$ with n_T as the number of transmitted neutrons, n_0 the number of neutrons counted without sample and l the length of the sample. If the sample is tilted by an angle of 45° relative to the neutron beam axis, then the effective thickness e defined in Eq. (4.11) must be used instead of l.

The γ-ray self-absorption is determined by means of Eq. (4.10) with the mass attenuation coefficient μ_m of standard concrete as a reference since the sample composition is unknown. The average density of the sample is derived from its mass m and volume V, respectively. The sample is assumed to be homogeneous.

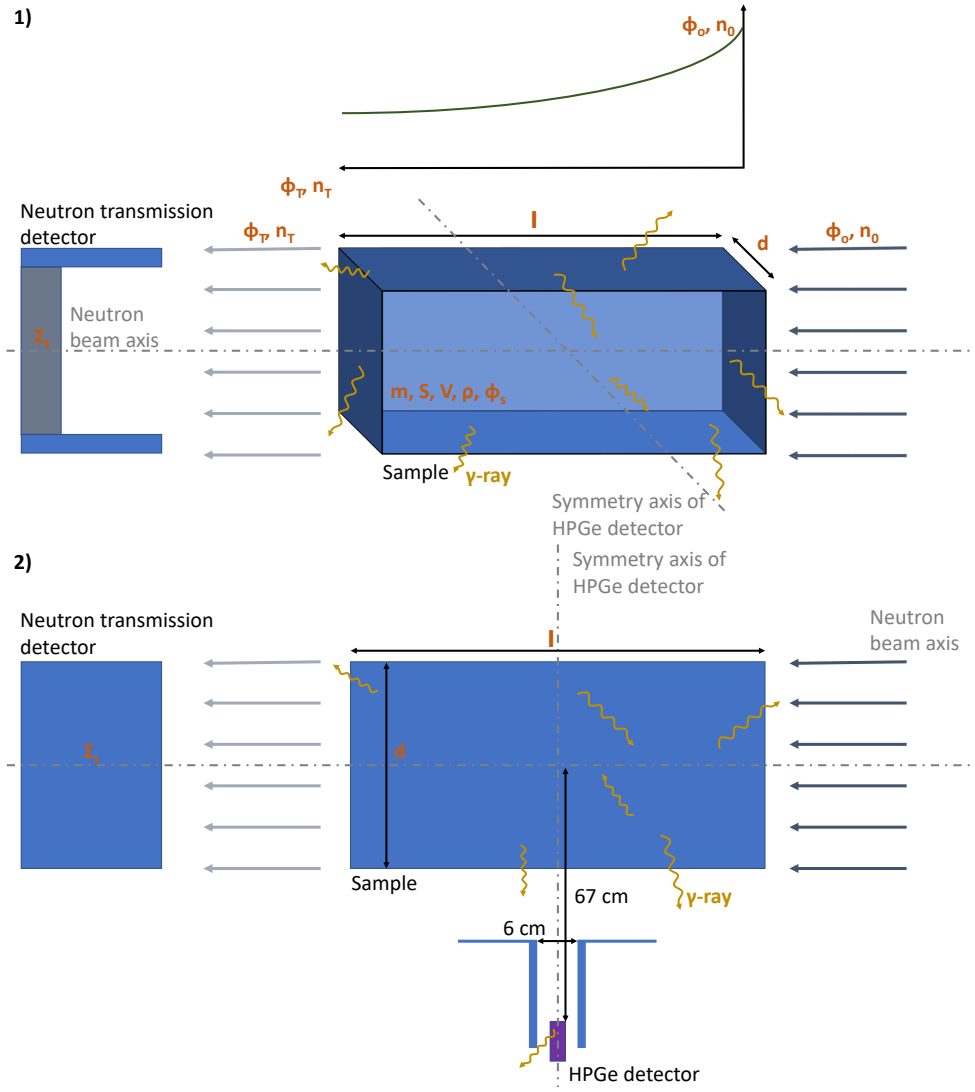


Figure 8.1: Schematic representation of the irradiation of a large rectangular-shaped sample. The top picture shows a view from the side along neutron beam direction, whereas the bottom picture depicts a view from top.

8.2 Gamma attenuation

For γs, the validity of Eq. (4.10) to calculate γ-ray self-absorption factors $f_{E\gamma}$ for voluminous samples was investigated by means of numerical simulations with the MCNP6 code. In the latter ones, Al samples with quadratic surface areas S of 0.5 $\times$ 0.5, 1 $\times$ 1, 2.5 $\times$ 2.5, 3 $\times$ 3, 4 $\times$ 4, 5 $\times$ 5 and 6 $\times$ 6 cm^2 as well as lengths l of 0.1, 0.5, 1, 5 and 10 cm along neutron beam direction were considered. The simulations were conducted as described in Chapter 4 and a uniformly distributed γ source over

the sample volume with discrete energies of 0.1, 0.5, 1, 3 and 5 MeV was used. An exemplary input file is provided in Appx. K.8 (d= 2.5 cm, l= 5 cm, S= 2.5 × 2.5 cm^2).

The determined $f_{E\gamma}$ values are depicted in Fig. 8.2 as a function of the sample length l and a fixed surface area of 2.5 × 2.5 cm^2. The analytical and numerical solutions show a good agreement, thereby confirming validity of Eq. (4.10). However, a larger discrepancy was observed around 100 keV energy of the γs and a small length l of the sample below 1 cm.

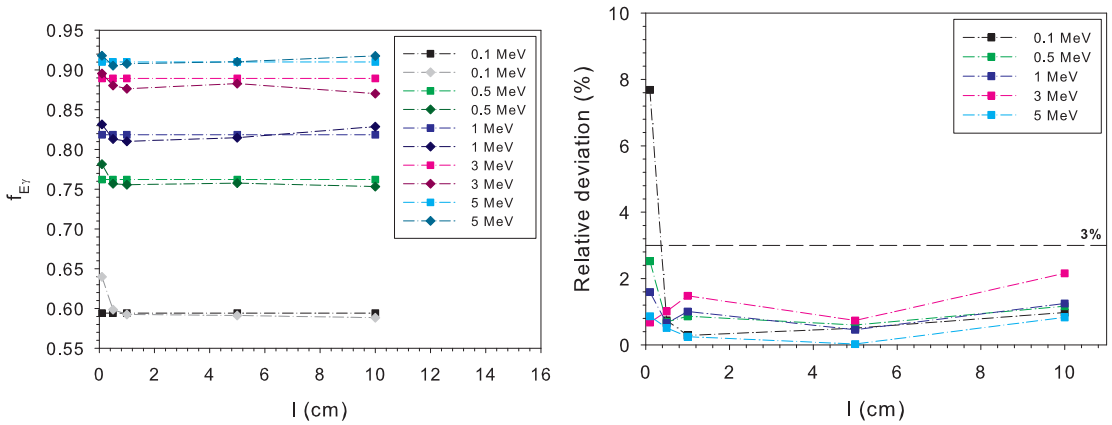


Figure 8.2: Comparison of the analytical γ-ray self-absorption factors $f_{E\gamma}$ for Al samples (μ_m values of Al taken from XCOM [92]) with a surface area of 2.5 × 2.5 cm^2 calculated after Eq. (4.10) with the values derived by numerical simulations with the MCNP6 code. The left plot gives the results as a function of the sample length l for energies of 0.1, 0.5, 1, 3 and 5 MeV and the right plot shows the deviation of the numerical solutions relative to the analytical ones. In the left plot analytical data points are given with square symbols whereas numerical data points are given with diamond symbols. A total of 10^8 primary γs were run in each simulation.

In addition, Fig. 8.3 shows the variation of the γ-ray self-absorption factors as a function of the sample thickness d for a fixed length l of 5 cm. The solution obtained with Eq. (4.10) is in good agreement with the solution derived with the MCNP6 code. However, a deviation above 10% was observed for γ-ray energies around 100 keV and the maximum thickness of 6 cm. The deviations observed in Figs. 8.2 and 8.3 were assumed to be reasoned in a faulty or incomplete γ transport in the simulations with the MCNP6 code since various works in the literature suggest problems with the specified framework conditions [127–130].

Nevertheless, the decent consistency between the simple analytical model and the numerical simulations suggests that the γ-ray self-absorption effect can be reasonably estimated by means of Eq. (4.10) also in the case of large and thick samples.

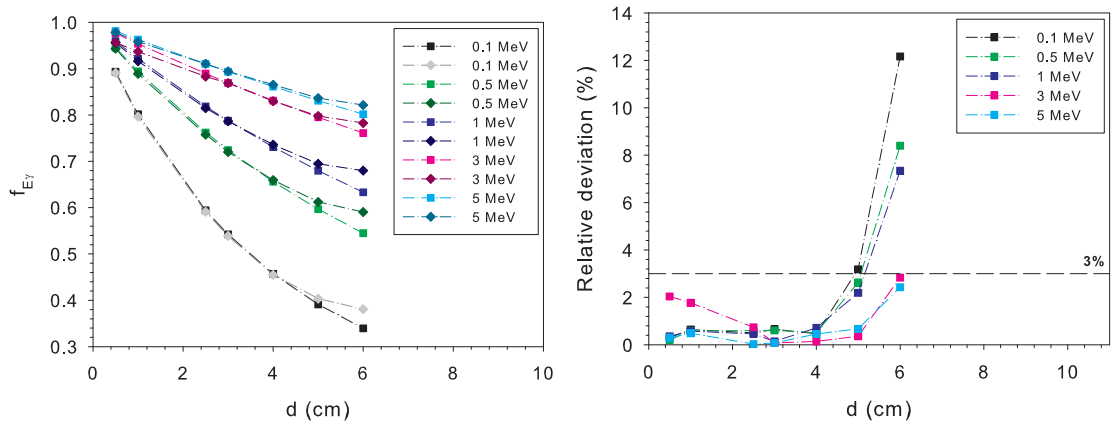


Figure 8.3: Comparison of the analytical γ-ray self-absorption factors $f_{E\gamma}$ for 5 cm long Al samples (μ_m values of Al taken from XCOM [92]) calculated after Eq. (4.10) with the values derived by numerical simulations with the MCNP6 code. The left plot gives the results as a function of the sample thickness d for energies of 0.1, 0.5, 1, 3 and 5 MeV and the right plot shows the deviation of the numerical solutions relative to the analytical ones. In the left plot, analytical data points are given with square symbols whereas numerical data points are given with diamond symbols. A total of 10^8 primary γs were run in each simulation.

8.2.1 Mass attenuation coefficient of concrete

Typical applications of FaNGaS comprise the measurement of archaeological or geological samples. These samples mostly provide signatures of mineral elements such as O, Ca or Fe. Figure 8.4 shows the variation of the mass attenuation coefficient μ_m (taken from XCOM [92]) as a function of the γ-ray energy for the case of ordinary concrete and several selected sample materials. Ordinary concrete, termed as type I according to the American Society of Testing and Materials (ASTM), mainly comprises of 55 wt% tricalcium silicate ($3CaO{\cdot}SiO_2$), 17 wt% dicalcium silicate ($2CaO{\cdot}SiO_2$), 10 wt% tricalcium aluminate ($3CaO{\cdot}Al_2O_3$) and 7 wt% tetracalcium aluminoferrite ($4CaO{\cdot}Al_2O_3{\cdot}Fe_2O_3$) [197]. Aforementioned sample materials were chosen to cover a wide range of densities, i.e. 1.44 g cm^{-3} for $(C_2H_3Cl)_n$, 2.71 g cm^{-3} for $CaCO_3$ and 7.87 g cm^{-3} for Fe. Data of a $LaCl_3{\cdot}7H_2O$ sample (ρ= 2.23 g cm^{-3}) is given to show the effect of an increased H content.

With regard to Chapter 2 the large deviations observed below 0.1 MeV are reasoned in the strong dependence of the photoelectric effect on the atomic number Z of the absorber material. Proportionality of the pair production process to the square of the atomic number, i.e. Z^2, is responsible for deviations above 10 MeV. For γ-ray energies between 0.5 and 4 MeV, however, the value of μ_m is almost independent of the considered absorber material. This is reasoned in the fact that the cross section for Compton scattering has a simple linear dependence on the atomic number Z. The corresponding μ_m value is practically independent of Z and directly

proportional to the electron density (electrons per gram), which varies by only 20% from the lightest to the heavy elements [198]. Consequently, the mass attenuation coefficients of ordinary concrete can serve to determine the concentrations of different elements within a large and unknown sample.

In order to quantify the uncertainty associated to the estimate of $f_{E\gamma}$ using the μ_m values of ordinary concrete, for several γ-ray energies between 0.2 and 6 MeV the deviations of selected samples relative to the concrete sample were calculated. In order to cover a wide range of densities between about 1 and 9 g cm^{-3}, the following sample materials were considered: $(C_2H_3Cl)_n$, $LaCl_3{\cdot}7H_2O$, $PrCl_3{\cdot}7H_2O$, Al, Ti, Fe, Cu, La and Ce. The exact values of the densities for the aforementioned samples are provided in Table 8.1.

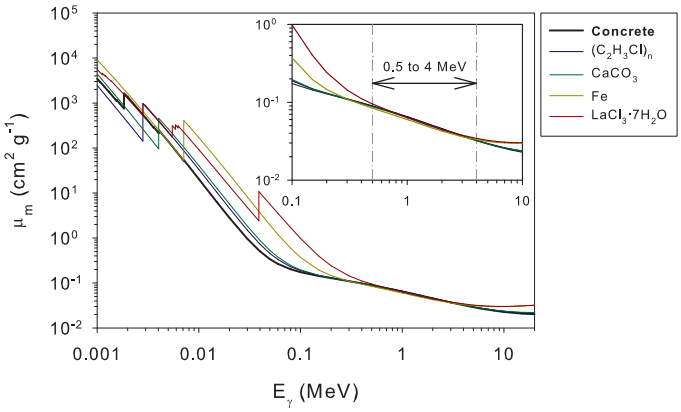


Figure 8.4: Dependence of the mass attenuation coefficient μ_m of ordinary concrete, $(C_2H_3Cl)_n$, $CaCO_3$, Fe and $LaCl_3{\cdot}7H_2O$ as a function of the γ-ray energy E_γ. The values were taken from the XCOM database of NIST [92].

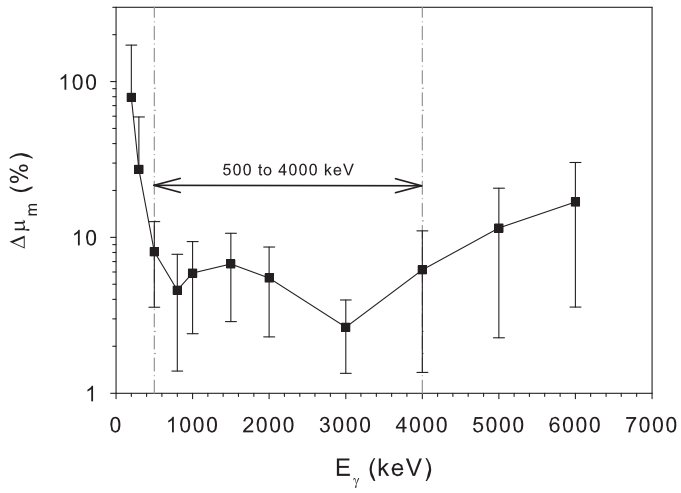


Figure 8.5: Dependence of the deviation in mass attenuation coefficients of several sample materials (averaged values) relative to these ones of ordinary concrete ($\Delta\mu_m$) on the γ-ray energy E_γ. Values for μ_m were taken from the XCOM database of NIST [92].

The deviation between the mass attenuation coefficients of the sample materials given above relative to these from an ordinary concrete sample, denoted as $\Delta\mu_m$, is shown in Fig. 8.5. Besides large uncertainties, between 0.5 and 4 MeV the deviations are below 10% with an average value for $\Delta\mu_m$ of 5.7% in this region. Since the values of μ_m, however, enter an exponential term in the calculation of self-absorption factors and these in turn depend on the sample thickness, the average uncertainty in μ_m cannot serve as a proper uncertainty estimate in the calculated self-absorption factors.

The variation of $\Delta f_{E\gamma}$ is depicted in Fig. 8.6 as a function of the γ-ray energy and the sample thickness for $(C_2H_3Cl)_n$, Ti, Cu and $LaCl_3{\cdot}7H_2O$. Generally, the deviations increase towards lower γ-ray energies and higher sample thicknesses. In addition, the deviations are further increased with increasing densities. The $LaCl_3{\cdot}7H_2O$ sample shows significant deviations at low γ-ray energies due to the high H content, whose μ_m values are very different compared to other elements [92].

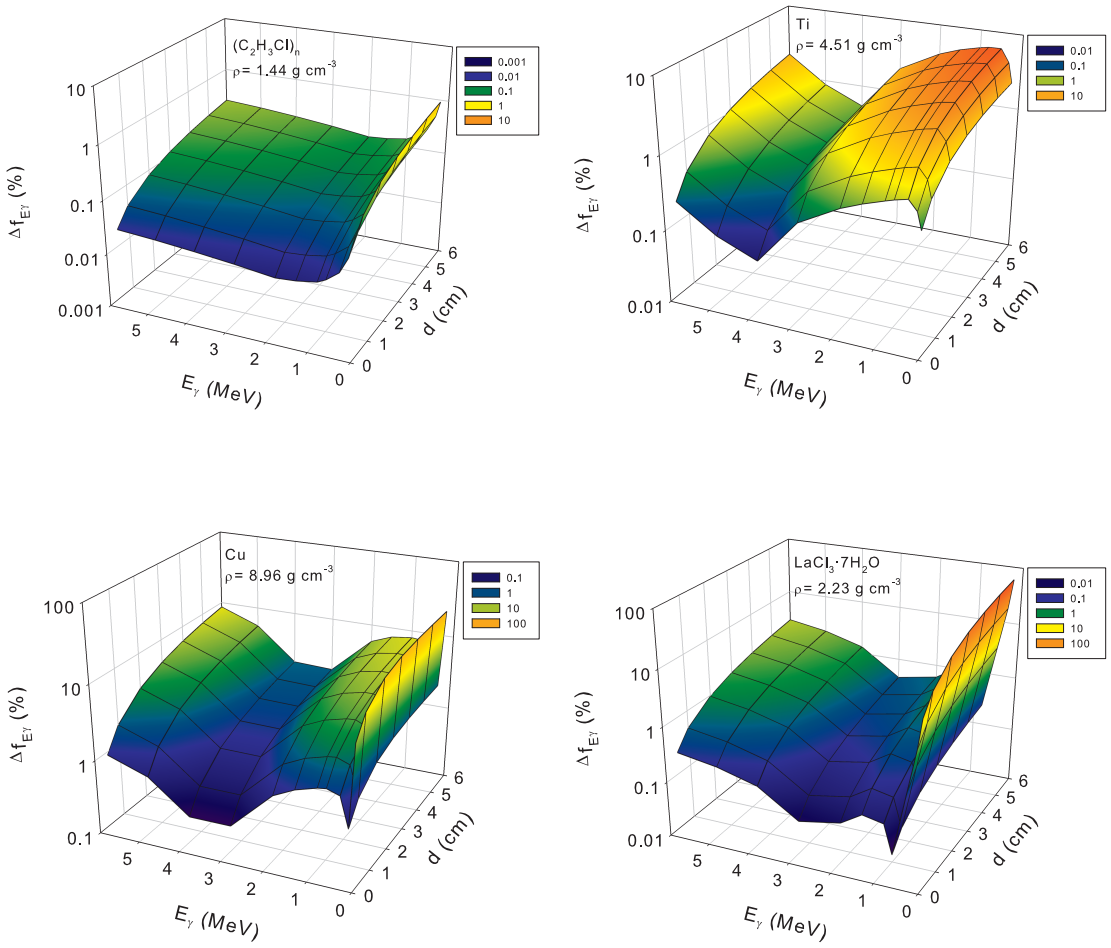


Figure 8.6: Dependence of the deviation in γ-ray self absorption factors $\Delta f_{E\gamma}$ on the γ-ray energy E_γ and the sample thickness d for a $(C_2H_3Cl)_n$, Ti, Cu and $LaCl_3{\cdot}7H_2O$ sample.

Figure 8.7 shows the variation of $\Delta f_{E\gamma}$ values averaged over all considered sample materials for different thicknesses. In agreement with Fig. 8.6, the deviations increase with increasing thicknesses. The right plot of Fig. 8.7 shows the data averaged over all considered thicknesses. Besides large uncertainties, an average uncertainty of 2.1% is obtained for the energy range 0.5 to 4 MeV. Therefore, it is reasonable to take the mass attenuation coefficients of ordinary concrete for the elemental analysis of unknown samples for the aforementioned energy range.

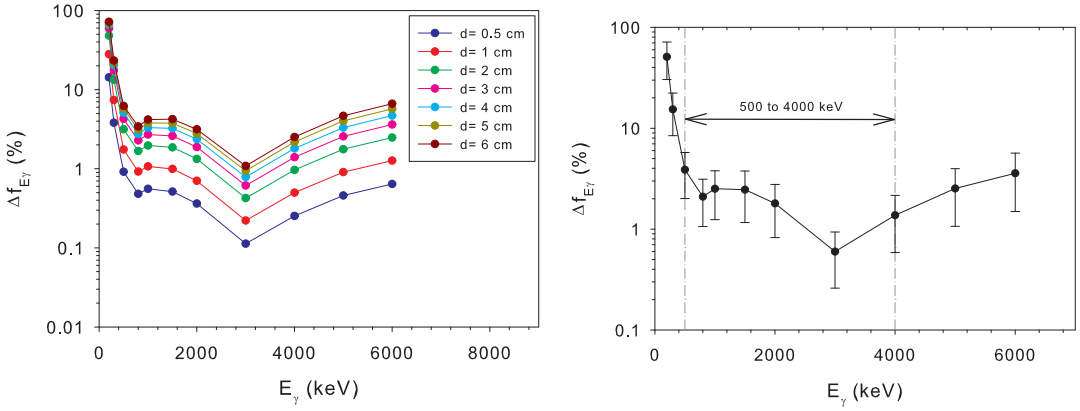


Figure 8.7: Dependence of the deviation in γ-ray self absorption factors $\Delta f_{E\gamma}$ on the γ-ray energy E_γ averaged over a $(C_2H_3Cl)_n$, $LaCl_3{\cdot}7H_2O$, $PrCl_3{\cdot}7H_2O$, Al, Ti, Fe, Cu, La and Ce sample for different sample thicknesses d (left plot) and dependence of the deviation $\Delta f_{E\gamma}$ averaged over all aforementioned samples and the thicknesses d for each γ-ray energy.

8.3 Neutron attenuation

As illustrated in Fig. 8.1 and with regard to Eqs. (4.16) and (4.17), proper determination of neutron self-shielding factors f_n requires knowledge of the total macroscopic cross section Σ_t. Therefore, a neutron transmission measurement is mandatory. Multiple neutron scattering cannot be neglected in the case of large samples and the aforementioned equations are invalid for the case of a neutron-energy distribution, since multiple tracklength contributions of neutrons in different energy bins occur. Using the effective macroscopic cross sections corresponding to the fast-neutron-energy distribution at sample position in the aforementioned equations does also not provide reasonable estimates for the neutron self-shielding factors (see Fig. 4.3). Hence, numerical simulations were performed with the MCNP6 code to derive a relationship between Σ_t and f_n. Table 8.1 gives the density as well as effective macroscopic cross sections for total and scattering reactions for all samples considered in the simulations.

Column 5 of Table 8.1 gives the ratio of Σ_s/Σ_t. This value is approximately one, independent of the sample matrix. Consequently, one can conclude that the

fast neutrons at FaNGaS are basically just scattering, with the elastic scattering dominating over inelastic scattering (see also Appx. E). A transmission measurement as described in Fig. 8.1 would therefore also provide information on the scattering properties of the sample.

Table 8.1: Effective macroscopic cross sections for total (Σ_t) and scattering (Σ_s) reactions calculated after Eq. (2.14) for all samples considered in the numerical simulations and a fast-neutron-energy distribution corresponding to that one at sample position.

Sample	ρ (g cm^{-3})	Σ_s (cm^{-1})	Σ_t (cm^{-1})	Σ_s/Σ_t
$(C_2H_3Cl)_n$	1.44	0.248	0.250	0.994
$CaCO_3$	2.71	0.203	0.208	0.977
$LaCl_3{\cdot}7H_2O$	2.23	0.295	0.297	0.992
$CeCl_3$	3.97	0.142	0.144	0.986
$PrCl_3{\cdot}7H_2O$	2.25	0.297	0.299	0.992
$NdCl_3$	4.13	0.146	0.149	0.976
$SmCl_3{\cdot}7H_2O$	2.38	0.322	0.325	0.992
$TbCl_3{\cdot}6H_2O$	4.35	0.506	0.511	0.990
$DyCl_3{\cdot}6H_2O$	2.56	0.297	0.299	0.991
Al	2.70	0.188	0.189	0.998
Ca	1.55	0.061	0.065	0.936
Ti	4.51	0.182	0.183	0.998
Fe	7.87	0.274	0.275	0.997
Cu	8.96	0.298	0.300	0.992
In	7.31	0.202	0.208	0.973
La	6.18	0.165	0.165	0.999
Ce	6.76	0.187	0.183	1.019
Pr	6.8	0.185	0.185	0.997
Nd	7.0	0.190	0.191	0.995
Sm	7.52	0.193	0.195	0.990
Tb	8.25	0.198	0.203	0.977
Dy	8.55	0.213	0.215	0.990

Neutron self-shielding factors were derived with the MCNP6 code as described in Chapter 4. To assess reliability of the results, a small benchmark with PHITS (Particle and Heavy Ion Transport code System, version 3.29) [199] was conducted. These simulations considered an Al sample with a surface area S of 2.5 × 2.5 cm^2 and sample lengths l along neutron beam direction of 0.1, 1, 3, 5, 7 and 10 cm. The T-Track tally was applied in PHITS as the equivalent to the F4 tally in MCNP6 to derive volume-averaged flux values. The corresponding f_n values derived from the simulations described above are given in Table 8.2. For sample lengths below

1 cm the two codes provide identical values with deviations lower than 0.1%. It is assumed that larger deviations above 1 cm are associated to the different physics models used for the treatment of elastic and inelastic scattering. The deviations in the neutron reaction libraries, i.e. ENDF/B-VIII.0 [112] in MCNP6 and JENDL4.0 [114] in PHITS were found to be negligible.

Table 8.2: Comparison between the numerical neutron self-shielding factors f_n derived for the fast-neutron-energy distribution at sample position with the MCNP6 and PHITS codes for the case of an Al sample. A total of 10^8 and 1.6×10^8 primary neutrons in the MCNP6 and PHITS simulations, respectively, were observed to yield converged results without relevant uncertainties.

Length l (cm)	Neutron self-shielding factor f_n		
	MCNP6 (version 6.1)	PHITS (version 3.29)	Deviation (%)
0.1	1.0179	1.0176	0.03
1	1.0382	1.0376	0.06
3	0.949	0.822	13.4
5	0.838	0.655	21.8
7	0.737	0.565	23.3
10	0.612	0.478	21.8

8.3.1 Three-step parametrization

As the MCNP6 code is considered to deliver reliable values of f_n based on [101], a huge set of simulations was performed for all sample materials given in Table 8.1 (see also Appx. K.9). In these simulations a rectangular-shaped geometry with a quadratic surface was assumed. In total, the results of 792 simulations were exploited, each between about 5 and 10 minutes running time on average for 10^8 primary source neutrons. Four quadratic surface areas S, i.e. 1×1, 2.5×2.5, 3×3 and 6×6 cm^2 as well as several thicknesses along neutron beam direction (l) ranging between 0.025 and 10 cm were considered. The aim of the aforementioned simulations was to feed a three-step parametrization that allows to estimate the neutron self-shielding effect for a large rectangular-shaped sample of unknown element concentrations. The resulting model is a function of the sample length l, the surface area S and the total effective macroscopic cross section Σ_t.

From the 22 sample materials listed in Table 8.1, 6 samples contain water or H, hence enabling neutron moderation processes. Therefore, the results of the three-step parametrization were differentiated between dry (hydrogen-free or unhydrated) and hydrated (hydrogen-containing) samples. Parametrization of the hydrated samples must be considered as a cautious attempt, since only six data points were available to satisfy statistics.

The variation of the f_n values determined by means of numerical simulations with the MCNP6 code is illustrated in Fig. 8.8 as a function of the sample length l

and surface area S exemplary for the case of a Ca ($\Sigma_t = 0.065$ cm^{-1}), Al ($\Sigma_t = 0.189$ cm^{-1}), Cu ($\Sigma_t = 0.300$ cm^{-1}) and $LaCl_3{\cdot}7H_2O$ ($\Sigma_t = 0.297$ cm^{-1}) sample. Generally, the f_n factors decrease with increasing values of l since more and more neutrons are absorbed or scatter off from the sample. They increase as a function of S since more material becomes available in the case of scattering events lateral to the incident neutron beam direction.

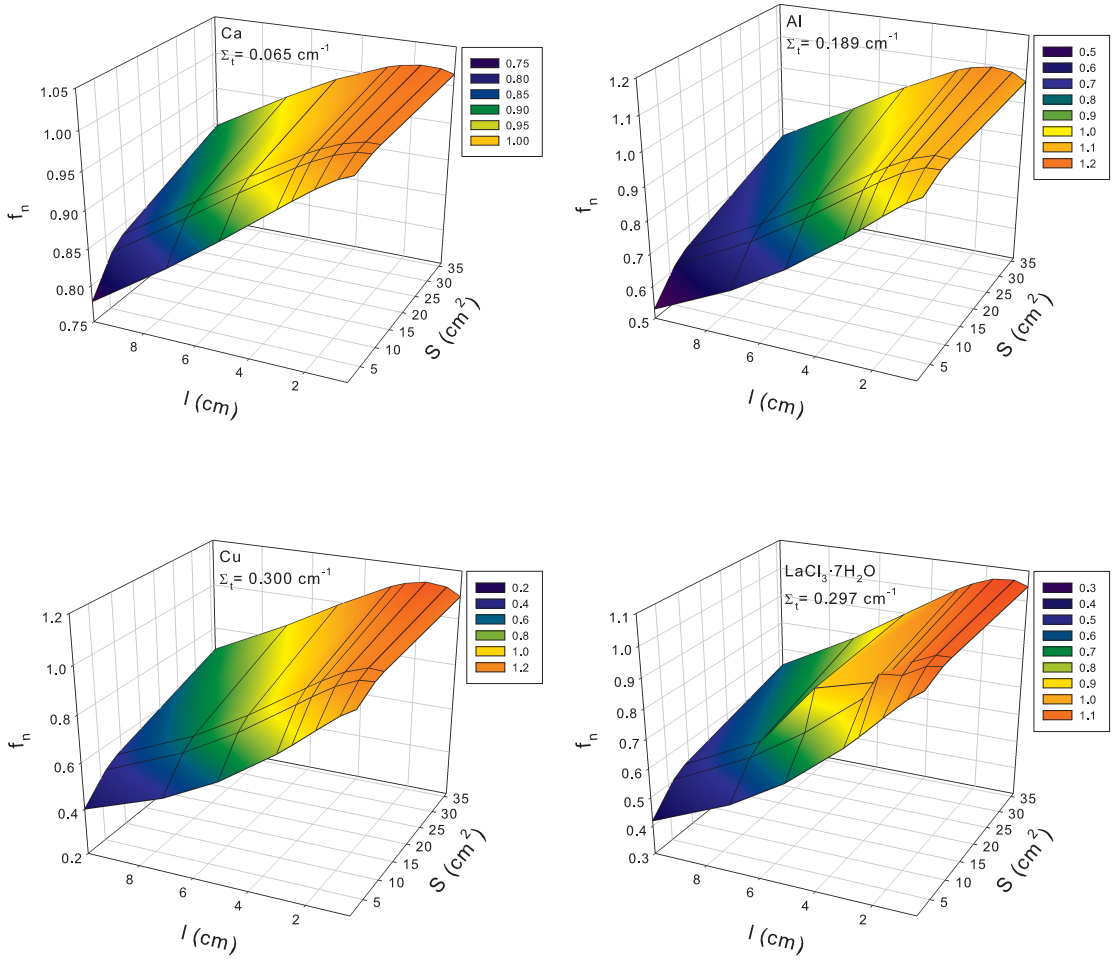


Figure 8.8: Dependence of the neutron self-shielding factor f_n on the sample length l and the quadratic surface area S for a Ca, Al, Cu and $LaCl_3{\cdot}7H_2O$ sample derived with numerical simulations assuming the fast-neutron-energy distribution at sample position.

First step

In a first step, for each considered surface area S and each length l the simulated values of f_n were plotted against the corresponding values of Σ_t. Exemplary, these plots are shown for a surface area of 6×6 cm^2 and lengths of 0.5, 2.5 and 7 cm in Fig. 8.9. Although the data points scatter, a linear trend is clearly observed in Fig. 8.9. Therefore, the points of the dry and hydrated samples were fitted with a

simple linear curve fit. The ordinate section was set to one and the output of this first step was the slope u of the fits for each length and each surface area.

The parametrized self-shielding factor can then be expressed as:

$$f_n = 1 + u \cdot \Sigma_t. \tag{8.1}$$

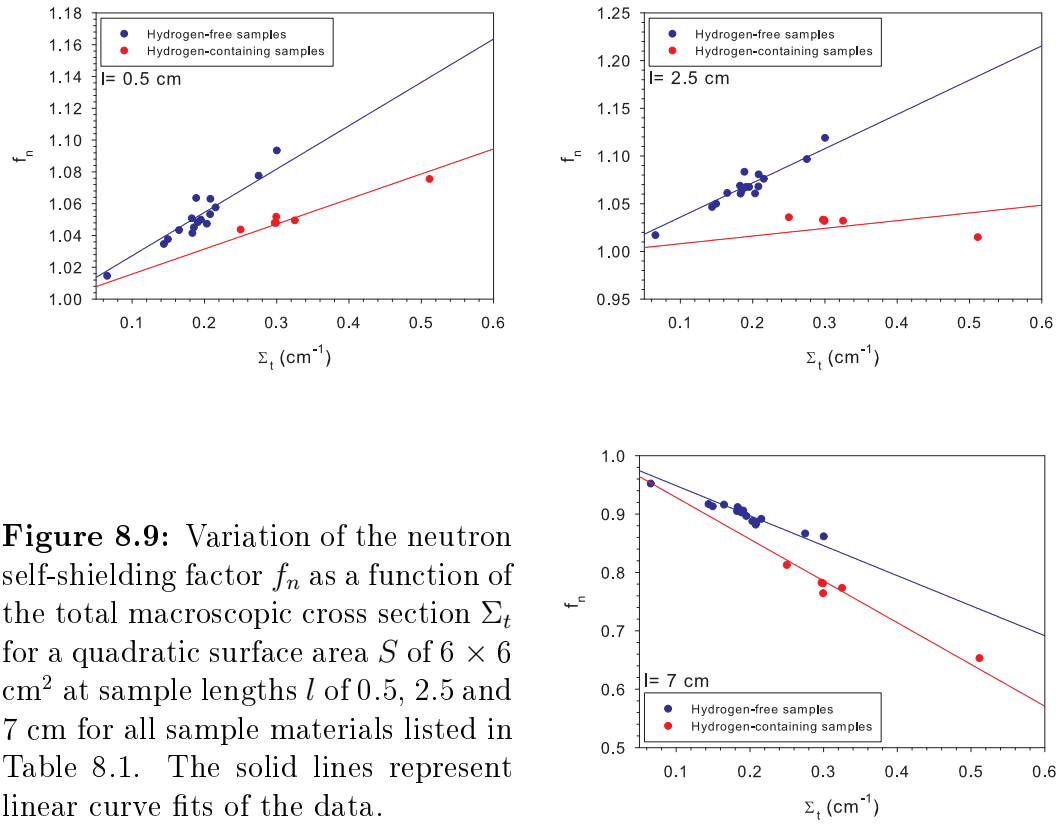


Figure 8.9: Variation of the neutron self-shielding factor f_n as a function of the total macroscopic cross section Σ_t for a quadratic surface area S of 6×6 cm^2 at sample lengths l of 0.5, 2.5 and 7 cm for all sample materials listed in Table 8.1. The solid lines represent linear curve fits of the data.

Second step

The output of the first step, i.e. the slope u of which the neutron self-shielding factors f_n vary depending on the value of Σ_t, served as the input for the second step in the parametrization process. In this step, the slope u was plotted versus the length l for each surface area S. The results for each surface area are depicted in Fig. 8.10 and the data points were fitted with an exponential linear combination:

$$u = a_0 + a_1 \cdot exp(-a_2 \cdot l) + a_3 \cdot l. \tag{8.2}$$

As evident from Fig. 8.10, for a surface area of 1 cm^2 no fits after Eq. (8.2) with converging results were found. In fact, a change in the trendline is observed at very small surface areas as the right hand tail is no longer linear. In particular, this is observed for the hydrated samples containing H. Therefore, a surface area of 1 cm^2 was disregarded in the parametrization process but the validity of the final model is checked for this area later.

The output of the second step were the fit parameters a_0 to a_3 of Eq. (8.2) for each surface area.

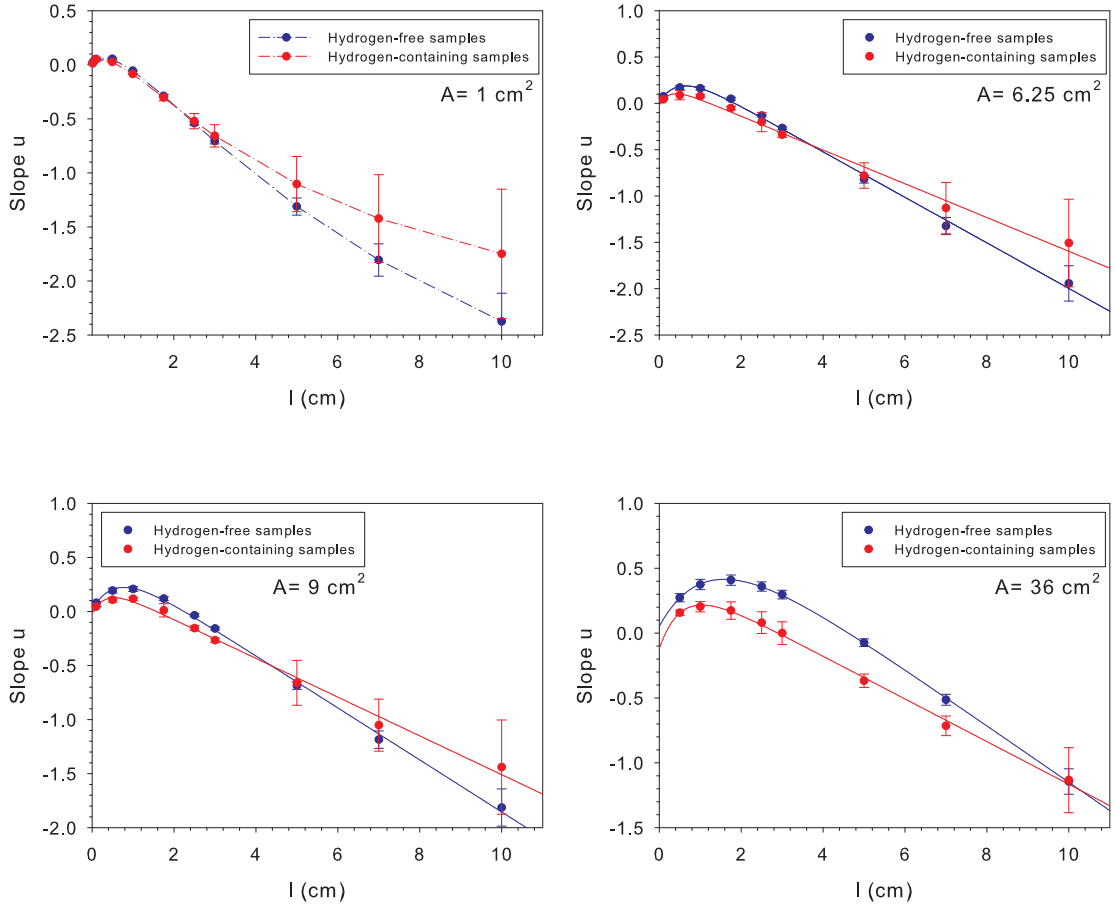


Figure 8.10: Variation of the slope u from Eq. (8.1) as a function of the sample length l for quadratic surface areas of 1, 6.25, 9 and 36 cm^2 for dry (hydrogen-free) and hydrated (hydrogen-containing) samples. The solid lines represent the curve fits after Eq. (8.2).

Third step

In the third and last step the fit parameters a_0 to a_3 of Eq. (8.2) were fitted against all surface areas S except 1 cm^2, which is depicted in Fig. 8.11. Taking the error margins into account, the parameters can be adequately described by a simple linear curve fit, as in the first parametrization step. The output of the third step were the ordinate section $y_{0,i}$ and the slope u_i of each parameter.

The parameters a_0 to a_3 of Eq. (8.2) are described by:

$$a_i = y_{0,i} + u_i \cdot S. \tag{8.3}$$

The fit parameters $y_{0,i}$ and u_i are given in Table 8.3 for i= 0 to i= 3.

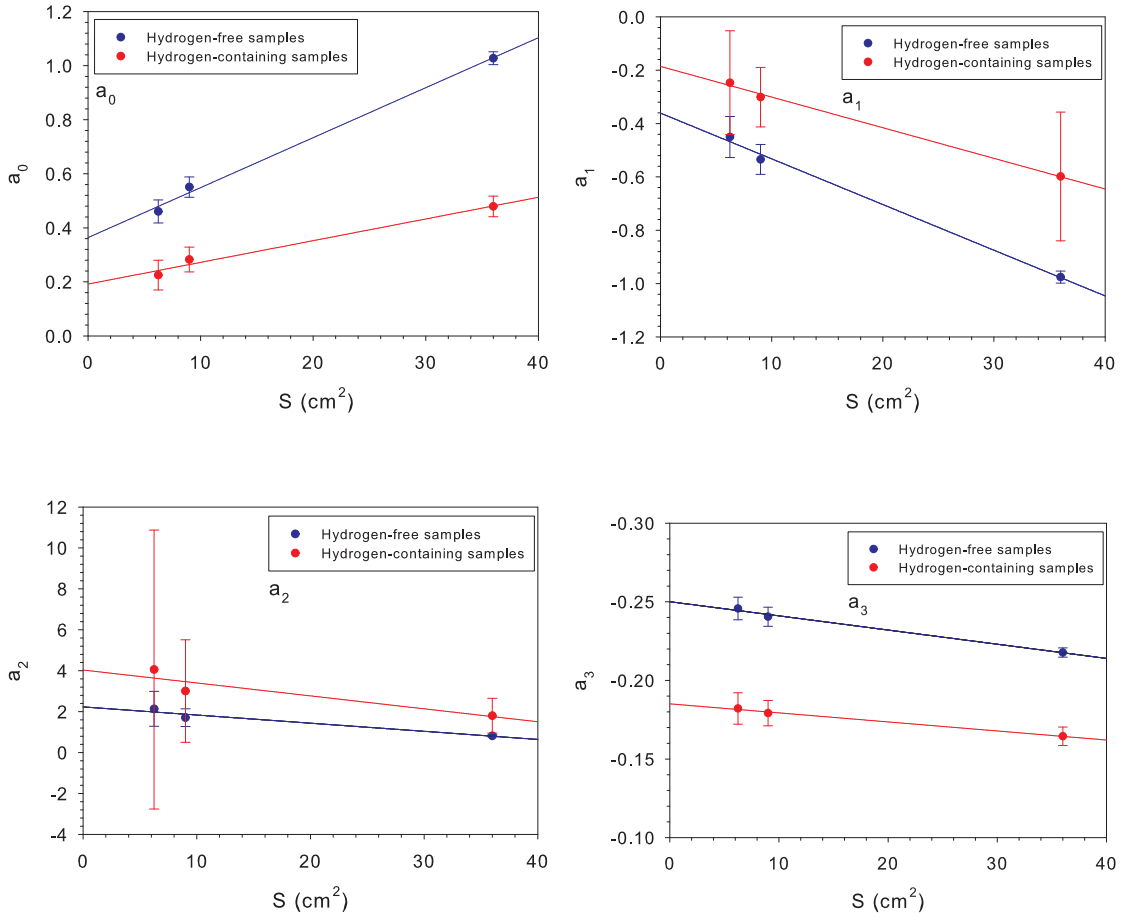


Figure 8.11: Variation of the fit parameters a_0 to a_3 from Eq. (8.2) as a function of the sample surface area S. The solid lines represent linear curve fits of the data.

Table 8.3: Fit parameters $y_{0,i}$ and u_i of Eq. (8.3) for all parameters a_0 to a_3 defined in Eq. (8.2) for the dry and hydrated samples listed in Tab. 8.1.

Parameter a_i	$y_{0,i}$	u_i
Dry samples (hydrogen-free)		
a_0	0.3637 ± 0.0262	0.0185 ± 0.0012
a_1	-0.3609 ± 0.0246	-0.0171 ± 0.0011
a_2	2.2317 ± 0.2140	-0.0398 ± 0.0098
a_3	-0.2501 ± 0.0018	0.0009 ± 0.0001
Hydrated samples (hydrogen-containing)		
a_0	0.1918 ± 0.0237	0.0080 ± 0.0011
a_1	-0.1857 ± 0.0148	-0.0115 ± 0.0007
a_2	4.0344 ± 0.5827	-0.0632 ± 0.0268
a_3	-0.1851 ± 0.0009	0.00058 ± 0.00004

8.3.2 Uncertainty estimation

Similar to the investigation of the γ attenuation in large samples the uncertainty of neutron self-shielding factors determined after Eqs. (8.1), (8.2) and (8.3) was quantified with respect to the exact solution provided by the individual numerical simulations performed with the MCNP6 code. The deviation in the neutron self-shielding factors determined with the suggested model compared to the numerical simulations, denoted as Δf_n, is illustrated in Fig. 8.12 as a function of the sample length l and surface area S for the case of a Ca, Al, Cu and $LaCl_3{\cdot}7H_2O$ sample. The dependence of Δf_n on the total macroscopic cross section Σ_t is observed to be negligible. Generally, it increases towards higher values of the sample length l. At fixed values of l the highest deviation is usually found at surface areas of 1 cm^2.

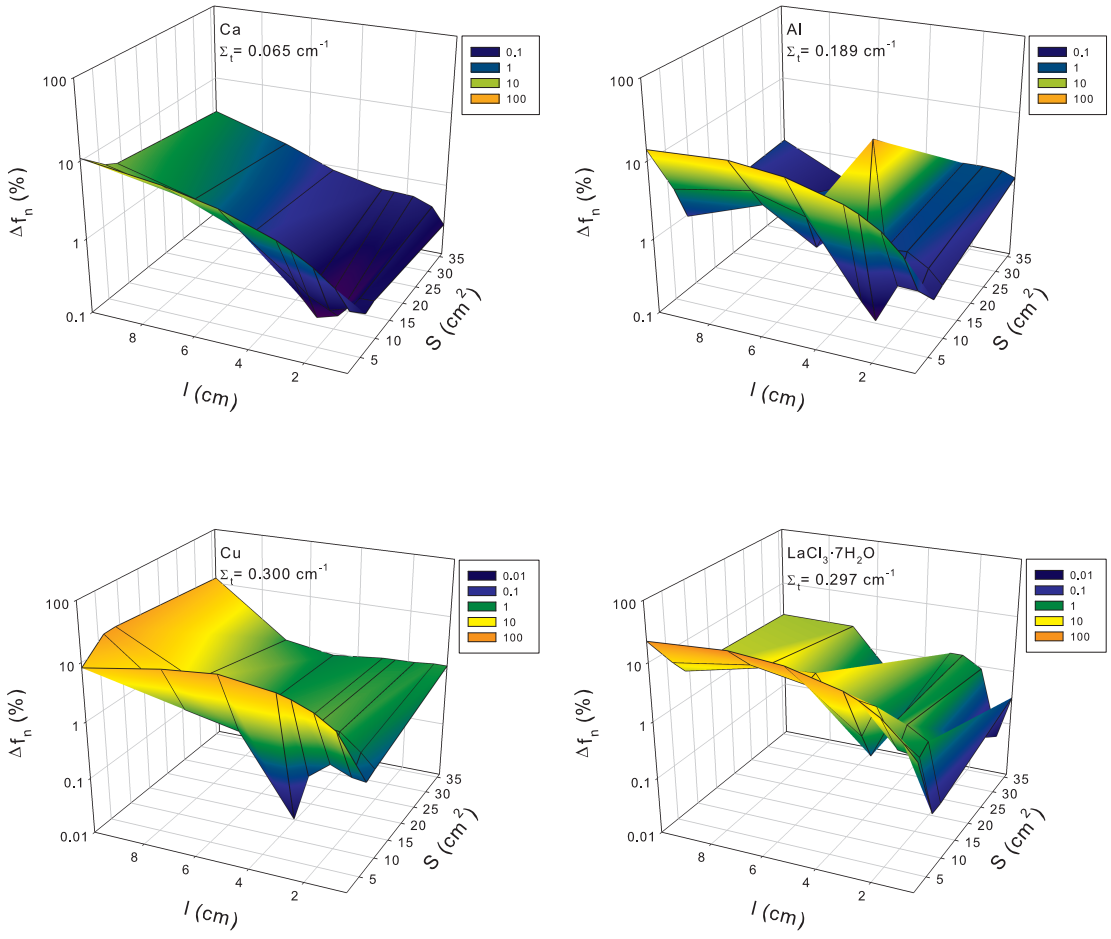


Figure 8.12: Dependence of the deviation in neutron self-shielding factors Δf_n on the sample length l and surface area S for a Ca, Al, Cu and $LaCl_3{\cdot}7H_2O$ sample.

For values of l between 0.5 and 10 cm above a sample surface area S of 6.25 cm^2, for dry samples the value of Δf_n ranges between 0.005% (Nd, S= 36 cm^2, l= 2.5 cm) and 25.4% (Al, S= 9 cm^2, l= 3 cm). For hydrated samples it ranges between

0.004% ($PrCl_3 \cdot 7H_2O$, S= 36 cm^2, l= 1 cm) and 48% ($TbCl_3 \cdot 6H_2O$, S= 6.25 cm^2, l= 10 cm). For surface areas below 6.25 cm^2, i.e. 1 cm^2, for dry samples the value of Δf_n ranges between 0.63% (Ca, S= 1 cm^2, l= 0.5 cm) and 17.3% (Sm, S= 1 cm^2, l= 7 cm). For hydrated samples it ranges between 1.27% ($(C_2H_3Cl)_n$, S= 1 cm^2, l= 0.5 cm) and 46% ($TbCl_3 \cdot 6H_2O$, S= 1 cm^2, l= 10 cm).

The values of Δf_n, averaged over all samples at lengths l between 0.5 and 10 cm, are given in Fig. 8.13 for surface areas of 1 cm^2 and areas of 6.25, 9 and 36 cm^2 (averaged) for dry and hydrated samples as a function of l. The high maximum values of Δf_n given above are rare exceptions, which is also emphasized by the much smaller mean values around a few percent above surface areas of 6.25 cm^2 and around 10% for surface areas below (i.e. 1 cm^2), as depicted in Fig. 8.13. Therefore, the uncertainty of the suggested model after Eqs. (8.1), (8.2) and (8.3) used to estimate neutron self-shielding factors f_n for large samples can be assessed differentiating between dry and hydrated samples as well as sample surface areas below and above 6.25 cm^2. For dry samples the uncertainty is estimated as: 7.8% below and 1.2% above S= 6.25 cm^2. For hydrated samples the uncertainty is estimated as: 13.6% below and 2.3% above S= 6.25 cm^2. The good agreement between the derived model and the individual numerical simulations enables to extrapolate validity of this model also to small surface areas of 1 cm^2, for which no proper fit was found in Fig. 8.10.

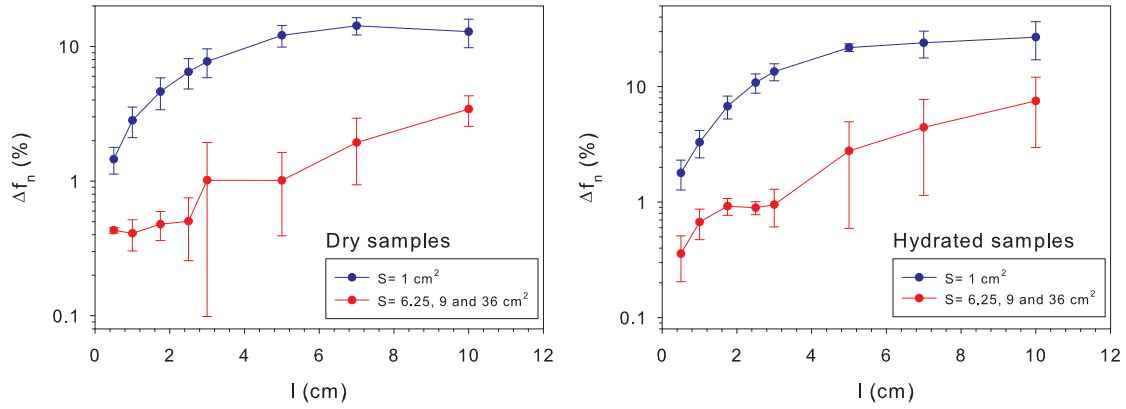


Figure 8.13: Dependence of the deviation in neutron self-shielding factors Δf_n averaged over the samples listed in Table 8.1 for surface areas of 1 cm^2 and 6.25, 9 and 36 cm^2 (averaged) as a function of l for dry (left plot) and hydrated (right plot) samples.

8.4 Proposed approach

Based on the investigations presented in this chapter, Fig. 8.14 illustrates schematically the proposed approach for γ and neutron attenuation corrections for the elemental analysis of homogeneous large samples with FaNGaS at FRM II.

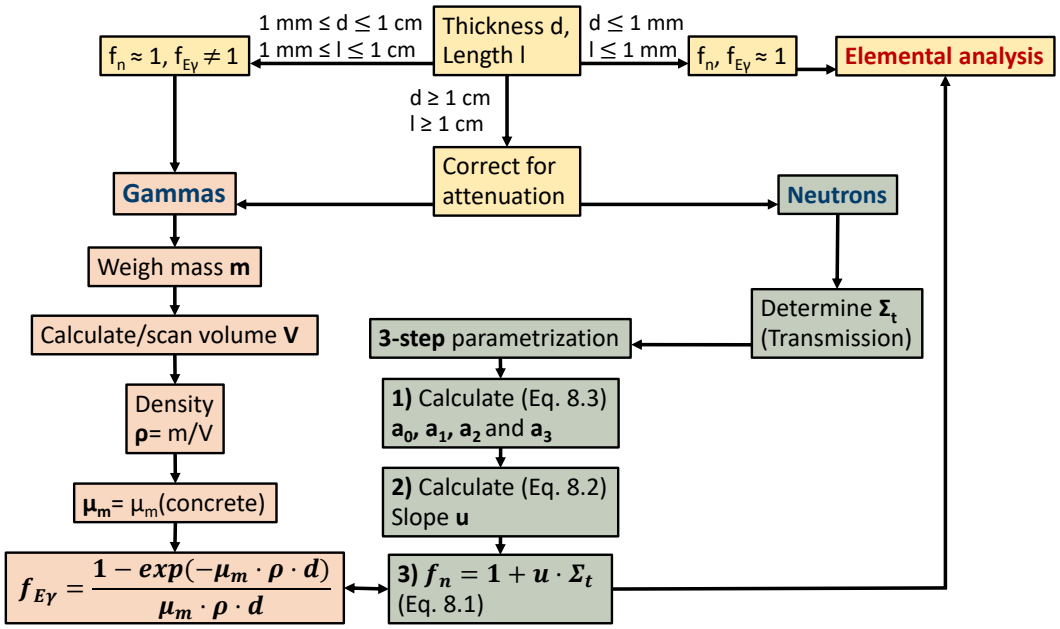


Figure 8.14: Scheme of the proposed approach for γ and neutron attenuation corrections in large rectangular-shaped samples.

Generally, for thin samples with lengths l and thicknesses d well below 1 mm one could neglect both γ-ray self-absorption and neutron self-shielding. Lengths between 1 mm and 1 cm are observed to not reduce the intensity of fast neutrons significantly. However, especially at low γ energies, one has to correct for the γ attenuation within the sample. For values of l and d above 1 cm relevant attenuation corrections are expected for both γs and neutrons.

For the γs one has to determine the sample density ρ first of all, simply by weighing the object's mass m and calculation of the volume V. According to Fig. 8.4 the mass attenuation coefficient μ_m of ordinary concrete can be used for γ-ray energies between 0.5 and 4 MeV to determine the element matrix. The self-absorption factor $f_{E\gamma}$ can then be calculated by the simple analytical model as given by Eq. (4.10).

For the neutrons, first of all a transmission measurement must be done in order to obtain the sample-specific value of Σ_t. The neutron beam profile can be reduced by the MLC to irradiate only a certain fraction of the sample. This fraction also has a rectangular-shaped geometry and the presented three-step parametrization might still be applicable as long as signal contributions produced from the material outside the incident neutron beam dimension are negligible.

Depending on the sample surface area S one can determine the fit coefficients a_0 to a_3 after Eq. (8.3) with the coefficients provided in Table 8.3. Using Eq. (8.2) then allows to calculate the slope u of the fit from the f_n factors against the total effective macroscopic cross sections Σ_t. With the value of Σ_t obtained from the transmission measurement Eq. (8.1) can be used to quantify a self-shielding factor f_n.

The uncertainties assigned to the estimated values of $f_{E\gamma}$ and f_n are given in Table 8.4 together with the uncertainties of experimental parameters required to determine the elemental composition of the sample. The counting statistics for a certain line at an energy E_γ are not included in Table 8.4. However, for intense γ-lines with counting statistics well below 1%, the total uncertainty in the analysis of large samples can be estimated as 4% for dry and hydrated samples, at sample surface areas greater or equal to 6.25 cm^2. At surface areas below 6.25 cm^2 the composition of large samples can be estimated with uncertainties of 9% and 14% for dry and hydrated samples, respectively.

Therefore, the suggested models for γ and neutron attenuation corrections in large samples must be considered as valuable methods in view of the absence of any a priori information on unknown samples.

Table 8.4: Budgeting of the relevant uncertainties for the measurement of large samples with FaNGaS. The uncertainty related to the counting statistics of a given γ-line must be additionally taken into account.

Parameter	Uncertainty (%)
Full-energy-peak (FEP) efficiency	3
γ-ray self-absorption factor $f_{E\gamma}$	2
Fast-neutron flux	4
Neutron self-shielding factor f_n (dry samples)	8 ($S < 6.25$ cm^2), 1 ($S \geq 6.25$ cm^2)
Neutron self-shielding factor f_n (hydrated samples)	14 ($S < 6.25$ cm^2), 2 ($S \geq 6.25$ cm^2)
Total (dry samples)	9 ($S < 6.25$ cm^2), 4 ($S \geq 6.25$ cm^2)
Total (hydrated samples)	14 ($S < 6.25$ cm^2), 4 ($S \geq 6.25$ cm^2)

For sample geometries other than a rectangular shape analytical equations to estimate the γ-ray self-absorption factors $f_{E\gamma}$ are provided in the literature [1]. Regarding the neutron self-shielding factors f_n, in principle, the three-step parametrization could be repeated for any other geometry. However, besides the demanding and time-consuming efforts of such a parametrization, a method independent of the sample geometry might be given by the so-called fixed point formulation approach. The only input in this are ratios of measured and modeled photopeak areas and a detailed description can be found in [200, 201]. The aforementioned method might be in particular useful in case of irregular-shaped samples. Inhomogeneity can be investigated using a 2D transmission detector providing a sufficient spatial resolution.

9. Results and Discussion

In this chapter the major outcomes of this work are presented and discussed separately for the experimental and numerical results. Additionally, short- and long-term goals concerning the further development and future activities of the FaNGaS instrument are given in an outlook.

9.1 Experimental results

The final result of all endeavours put into the analysis of the prompt γ-ray spectra presented in this work is summarized in Table 9.1. From all of the measurements a total of 779 fast-neutron-induced prompt γ-lines were identified and evaluated to derive fast-neutron spectrum-averaged (effective) γ-ray production cross sections for an angle of 90° between the incident neutron beam axis and detector.

Compared to the work of Demidov et al. [27], this work provides 272 additional fast-neutron-induced γ-lines (compare columns 2 and 5 in Table 9.1). This is mainly attributed to the better energy resolution of the HPGe detector with respect to the Ge(Li) detector utilized by Demidov et al. as well as in differences related to the neutron-energy spectra at sample position. Furthermore, this work emphasizes the need for a meticulous validation of the data listed in the Atlas [27] as at least 29 of 507 considered lines were found to correspond to wrong assignments. On the other hand, 88 lines (compare columns 3 and 5 in Table 9.1) from the Atlas [27] were not observed in the measurements performed with FaNGaS. The absence of the aforementioned lines is mostly attributed to background interferences, the DL, or the different excitation of nuclei associated to the differences in the neutron-energy spectra.

Additionally, the majority of all observed γ-lines is listed and compiled in NuDat 3.0 [65]. However, as can be concluded from Table 9.1, the measurements with FaNGaS resulted in 92 new lines (compare columns 2 and 4 in Table 9.1). Besides the fact that several of these lines were also measured by Demidov et al. and thereby confirmed, any other reaction channels than (n,n'γ) were carefully excluded.

Table 9.1: Overview on the final results of this work compared to the Atlas [27].

Element	γ-rays					Confidence level
	This work			Atlas [27]		in intensity (σ)
	Total[a]	Listed in Atlas [27]	Listed in NuDat 3.0 [65]	Total	Ruled out by this work[b]	
C	1	1	1	1	0	-
O	2	2	2	2	0	-
Cl[c]	29	19	29	27	2	0.8
Ca	35	29	34	35	2	1.2
La	54	43	41	51	4	1.3
Ce	58	31	58	45	4	1.2
Pr	71	57	70	77	8	1.3
Nd	111	39	110	44	2	1.5
Sm	141	63(58[d])	141	73	2	1.6
Tb	124	54(48[e])	48	60	4	1.6
Dy	153	81(79[f])	153	92	1	2.2
Σ=	**779**	419(406)	687	**507**	29	

[a] only (n,n'γ), (n,pγ) and (n,αγ) lines
[b] γ-lines for which observation in the Atlas [27] was questionable but possible data is provided in [65] and relevant signals are marked in Demidov's spectra were not considered as certainly ruled out; which lines were ruled out is evident from the discussion in Chapter 6
[c] data averaged over the RE chloride spectra
[d] the lines at 127.3 and 166.5 keV in [27] were assigned to (n,γ) reactions in ^{152}Sm and ^{150}Sm, the lines at 320.6, 397.7 and 629.9 keV were found to be issued mainly by (n,γ) reactions in this work
[e] the lines at 154.0, 194.1, 282.7, 339.2, 451.3 and 464.6 keV in [27] were observed and assigned to the ^{159}Tb(n,γ)^{160}Tb reaction
[f] the lines at 338.6 and 495.1 keV in [27] were mainly issued by (n,γ) reactions in this work

In this work, the neutron-energy spectrum at sample position had to be redetermined in the thermal and epithermal neutron-energy ranges, respectively, which is related to the upgrade of the new MLC of MEDAPP. The new neutron flux values were calculated by exploiting several neutron capture lines from the ^{159}Tb(n,γ)^{160}Tb and the ^{35}Cl(n,γ)^{36}Cl reactions in the acquired $TbCl_3 \cdot 6H_2O$ spectrum. Plausibility of the obtained values of $\Phi_{th} = (3.16 \pm 1.28) \times 10^3$ cm^{-2} s^{-1} and $\Phi_{epi} = (2.94 \pm 0.77) \times 10^6$ cm^{-2} s^{-1}, respectively, was confirmed based on data evaluated from several (n,γ) lines detected in other RE chloride spectra. The fast-neutron flux at sample position was $\Phi_{fast} = (1.13 \pm 0.04) \times 10^8$ cm^{-2} s^{-1}. Compared to a previous version with the old MLC [34] the fast-neutron flux was reduced by about 20%, which was verified by the measurement of Fe using the three strongest lines at 846.9, 1238.3 and 1810.9 keV from the ^{56}Fe(n,n'γ)^{56}Fe reaction. The acceptable agreement between this and Demidov's work, with the confidence level in intensity ranging between 0.8 and 2.2σ in Table 9.1, implies reliability of aforementioned neutron-flux values especially in view of the numerously identified interferences arising from (n,γ) lines.

Assuming the same intensities of (n,γ) lines produced by thermal neutrons also for epithermal and fast neutrons is convenient to correct for interferences and it was found to be a reasonable practice mostly. However, in the case of elements

with high resonance cross sections such as Sm and Dy in particular, a strong effect on the incident neutron energy was observed. In such cases the aforementioned assumption was actually found to be invalid. Nevertheless, since data for irradations of the corresponding elements with pure beams of epithermal and fast neutrons, respectively, is indispensable but absent in the literature, foregoing assumptions were without an alternative.

The experimental results obtained in this work also demonstrate reproducibility of FaNGaS measurements. In particular, the consistency in effective isotopic partial γ-ray production cross sections $\langle\sigma_{E\gamma}(90°)\rangle$ related to fast-neutron-induced γ-lines of Cl derived with the PVC spectrum and with all RE chloride spectra is remarkable. Averaging obtained data over all Cl-containing samples improved the data quality significantly. The confidence level in intensity compared to the Atlas [27] improved from 1.0σ (PVC sample) to 0.8σ, accompanied by the observation of more Cl lines related to the higher masses in the RE chloride samples.

In particular, consistency of FaNGaS was also shown with the analysis of prompt γ-lines from the ^{12}C(n,n'γ)^{12}C, ^{16}O(n,n'γ)^{16}O and ^{18}O(n,n'γ)^{18}O reactions, respectively. Effective isotopic partial γ-ray production cross sections of (14.4 $\pm$ 3.3) mb and (12.8 $\pm$ 2.3) mb obtained for the 4.44-MeV Doppler-broadened line of ^{12}C from the measurement of the $CaCO_3$ and the PVC sample, respectively, compare well to each other. Effective cross sections of (2.20 $\pm$ 0.37) mb and (201 $\pm$ 28) mb related to fast-neutron inelastic scattering reactions in ^{16}O and ^{18}O are very similar to the respective values of (2.56 $\pm$ 0.20) mb and (200 $\pm$ 24) mb, averaged over the spectra of the hydrated RE chloride samples.

The major aim of the experimental part in this work was to extract γ-ray production cross sections for the elements listed in Table 9.1 based on prompt γ-ray spectra previously measured with the FaNGaS instrument. The analysis of these spectra was rather non-trivial and represented a great challenge. In fact, many simplifications and assumptions had to be done. In addition, the analysis of the experimental data had to be supported by means of advanced numerical simulations and processing of nuclear data. In view of the considerable consistency between this work and the work carried out by Demidov et al. and, in particular, the reproducibility of the FaNGaS instrument demonstrated several times, the major motivation that has driven this work has to be considered as successful. Additionally, as a byproduct, the outcomes of this work are of immense value for nuclear spectroscopy, as the multitude of unreported lines adds decisive value to create and update nuclear decay and level schemes of nuclides. The same applies to γ-lines ruled out by this work. The inclusion of the experimental data into the EXFOR database [39] as well as numerous publications [20, 21, 37] ensure availability and benefit for a broad community in nuclear science and technology.

9.2 Numerical results

Numerical computer simulations were performed with the goal to optimize the FaNGaS instrument with regard to the irradiation of large samples. Irradiation of these differs drastically to the case of thin foils or compressed powder samples: first (i), the number of scattered neutrons and emitted γs reaching the detector crystal is increased. Secondly (ii), neutron self-shielding and γ-ray self-absorption are significant and must be corrected properly.

Therefore, numerical simulations served the purpose to design a fast-neutron filter and to develop an analytical model for neutron and γ beam attenuation effects in large samples.

Fast-neutron/gamma filter

In order to ensure reasonable dead times of the detector preamplifier and to reduce the magnitude of triangular-shaped γ-lines of Ge induced by fast-neutron inelastic scattering reactions in the HPGe crystal, simulations with the MCNP6 code were performed.

In a first step, these simulations considered different filter materials: LiH (nat.), LiH (90% ^{6}Li), PE, BPE with 20 wt% B_2O_3 and B_4C, respectively, as well as a pure B_4C filter. Assuming a parallel beam of monoenergetic 2-MeV neutrons, about 8 to 9 cm of the aforementioned filters would be required to reduce the intensity of the scattered neutrons to 10%. Both the PE and LiH filters were disregarded, since PE is incapable to capture thermalized neutrons efficiently and Li results in the production of tritium (^{3}H), which is reviewed critically at FRM II.

In a second step, assuming a 0.25 mm thick Fe sample as described in [34], the actual scatter spectrum of fast neutrons was estimated. The mean neutron energy was found to be around 1.30 MeV and a fast-neutron flux of Φ_{fast}= (135 ± 22) cm^{-2} s^{-1} at the collimator opening (⌀ 6 cm) and Φ_{fast}= (46 ± 11) cm^{-2} s^{-1} at the HPGe detector front surface, respectively, were concluded. Although the shape of the scatter spectra was found to be more or less independent of the considered sample, the magnitude of scattered fast neutrons was found to depend almost linearly on the sample thickness and the effective macroscopic scattering cross section (Σ_s). Absence of ideal proportionality between the reduction in the scattered fast-neutron flux and the peak counts of (n,n'γ) lines from Ge is related to the overlapping of the energy distribution of scattered neutrons and the corresponding excitation functions.

To study the impact of the boron-containing filter materials on the released γ radiation, a realistic model of the HPGe detector was implemented into MCNP6 based on the technical drawing provided by the detector supplier. A systematic deviation between the experimentally determined full-energy-peak (FEP) efficiency and that one derived with MCNP6 was observed. However, after adjusting the

MCNP6 results to the experimental FEP values, it was found that the FEP by using a filter of thickness d can be reasonably estimated with the simple analytical model.

As a result of all simulations and considerations, finally a BPE filter with 20 wt% B_2O_3 was proposed. This standard material is characterized by an uncomplicated availability and it is already in use at FaNGaS as the outer shielding of the spectrometer.

Large-sample analytics

A simple analytical model was proposed in Chapter 8 to quantify neutron self-shielding and γ-ray self-absorption in the case of large samples. The model was developed assuming a rectangular-shaped sample of quadratic surface area. The density of the sample will be estimated by weighing and determination of its volume. The effective total macroscopic cross section (Σ_t) is supposed to be derived from a neutron transmission measurement.

It was found that the mass attenuation coefficient μ_m of ordinary concrete can be used to yield justified estimates of the γ-ray self-absorption factor within a γ-ray energy range of 0.5 to 4 MeV with an uncertainty of about 2%. For the neutrons, a total of 792 simulations were performed with the MCNP6 code to derive a relationship between the value of the neutron self-shielding factor f_n and Σ_t by means of a three-step parametrization. A total of 16 different dry (hydrogen-free) and 6 hydrated (hydrogen-containing) samples were considered with thicknesses along incident neutron beam direction ranging between 0.025 and 10 cm as well as quadratic surface areas of 1, 6.25, 9 and 36 cm^2. Depending on the dimensions and the ab- or presence of H, the value of f_n can be reasonably estimated with uncertainties ranging between 1 and 14%.

The aim of the introduced analytical model is to make time-consuming computer simulations of neutron and γ beam attenuation effects in large samples redundant and to provide a first basis for further efforts into this direction. Experimental verification is indispensable to assess the achievement of this goal.

9.3 Outlook

Due to the long shut down of FRM II, in a first measurement campaign the fast-neutron flux at sample position will be verified by measuring the same Fe foil as reported in [34]. The modifications of the thermal and epithermal component of the neutron-energy spectrum concluded in this work, related to the new MLC, should also be verified. Hence, the whole neutron-energy spectrum ranging from energies of 10^{-10} up to 20 MeV should be measured. Besides the foil activation technique used in [34], monitoring of the neutron flux with further neutron-spectrum unfolding methods such as Bonner sphere spectrometers (BSS) [202] could be useful.

Thin metal foils (d= 0.25 mm, purity > 99.99%) of the elements Sc, V, Co, Zn, Eu, Gd, Ho, Er, Tm, Yb and Lu were already ordered and delivered by Thermo Fisher Scientific. They will be irradiated once fast neutrons are available at FRM II and effective γ-ray production cross sections will be extracted as described within this work. Furthermore, the results for the elements La, Pr, Nd, Sm and Dy will be published in the near future.

The efficiency of the fast-neutron filter, to be placed into the collimator opening of the HPGe detector, will be verified experimentally at FRM II. Discs made of BPE with 20 wt% B_2O_3 and different thicknesses will be produced by the workshop of JCNS-2.

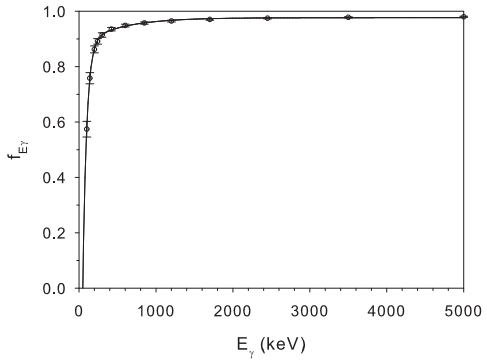
The effective γ-ray production cross sections as well as relative intensities obtained in this work are specific to the neutron-energy spectrum at sample position. Cross sections of other elements that have not been measured yet will be evaluated for the fast-neutron energy spectrum of FaNGaS for the intensities given in the Atlas [27]. Since the intensities in the Atlas [27] are also given relative to the 847-keV line from the ^{56}Fe(n,n'γ)^{56}Fe reaction, this could be investigated.

Regarding large-sample analytics, the validity of the analytical model proposed in this work will be tested once beamtime is available at FaNGaS. Therefore, different neutron transmission detectors will be examined in the experimental room of MEDAPP. Additionally, the fixed point formalism [200, 201] used for quantification of large samples shall be investigated in detail. Special emphasize will be dedicated to the case of samples with an inhomogeneous element matrix.

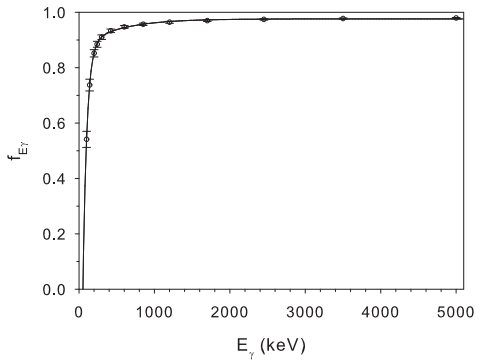
The ultimate aim of all aforementioned activities is to make FaNGaS available for future user operation and to facilitate the analysis of acquired γ-ray spectra. To ensure efficiency of this, a computer algorithm shall be developed that might be supported by artificial intelligence.

Appendices

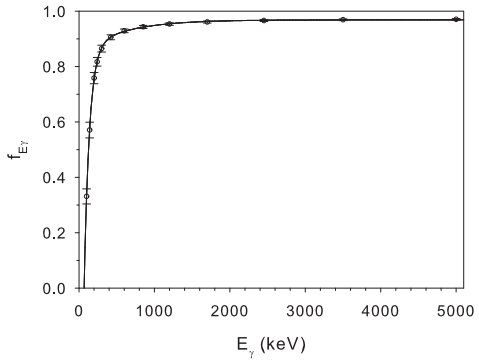
A. Gamma-ray self-absorption correction curves



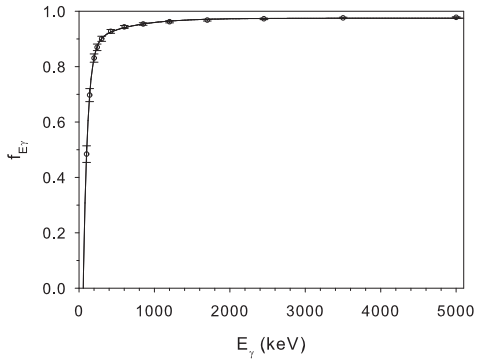
A.1 : Dependence of the γ-ray self-absorption factor $f_{E\gamma}$ on the γ-ray energy E_γ for the $LaCl_3 \cdot 7H_2O$ sample. The solid line represents the fit of the data with Eq. (4.12). The fit coefficients are a_0= -1.4201 $\pm$ 0.1571, a_1= 2.2959 $\pm$ 0.1499, a_2= 0.0197 $\pm$ 0.0008, a_3= 0.1008 $\pm$ 0.0098 and a_4= 0.0020 $\pm$ 0.0003.



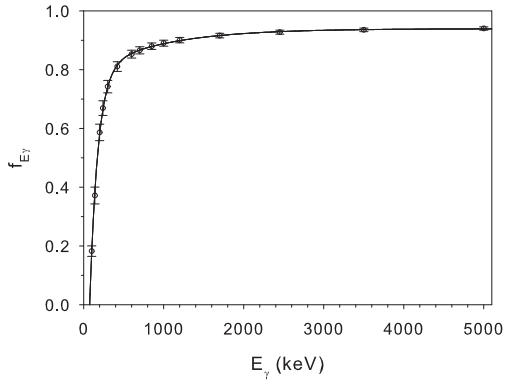
A.2 : Dependence of the γ-ray self-absorption factor $f_{E\gamma}$ on the γ-ray energy E_γ for the $PrCl_3 \cdot 7H_2O$ sample. The solid line represents the fit of the data with Eq. (4.12). The fit coefficients are a_0= -1.4765 $\pm$ 0.1432, a_1= 0.1057 $\pm$ 0.0104, a_2= 0.0020 $\pm$ 0.0002, a_3= 2.3469 $\pm$ 0.1356 and a_4= 0.0191 $\pm$ 0.0007.



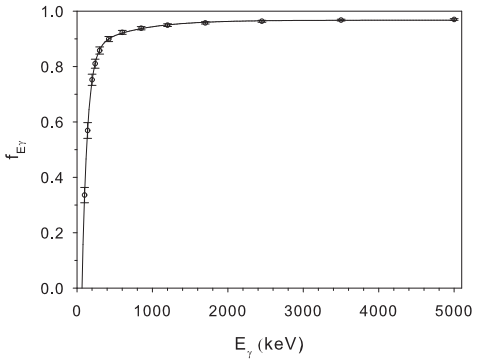
A.3 : Dependence of the γ-ray self-absorption factor $f_{E\gamma}$ on the γ-ray energy E_γ for the $NdCl_3$ sample. The solid line represents the fit of the data with Eq. (4.12). The fit coefficients are a_0= -1.3968 ± 0.0443, a_1= 0.1213 ± 0.0082, a_2= 0.0018 ± 0.0001, a_3= 2.2442 ± 0.0384 and a_4= 0.0143 ± 0.0002.



A.4 : Dependence of the γ-ray self-absorption factor $f_{E\gamma}$ on the γ-ray energy E_γ for the $SmCl_3 \cdot 7H_2O$ sample. The solid line represents the fit of the data with Eq. (4.12). The fit coefficients are a_0= -1.5019 ± 0.1139, a_1= 0.1131 ± 0.0107, a_2= 0.0020 ± 0.0002, a_3= 2.3635 ± 0.1060 and a_4= 0.0178 ± 0.0006.



A.5 : Dependence of the γ-ray self-absorption factor $f_{E\gamma}$ on the γ-ray energy E_γ for the $TbCl_3 \cdot 6H_2O$ sample. The solid line represents the old fit of the data with Eq. (4.12). The fit coefficients are a_0= -0.8829 ± 0.0528, a_1= 0.1558 ± 0.0187, a_2= 0.0011 ± 0.0002, a_3= 1.6665 ± 0.0416 and a_4= 0.0098 ± 0.0004.



A.6 : Dependence of the γ-ray self-absorption factor $f_{E\gamma}$ on the γ-ray energy E_γ for the $DyCl_3{\cdot}6H_2O$ sample. The solid line represents the fit of the data with Eq. (4.12). The fit coefficients are a_0= -1.3188 ± 0.0482, a_1= 0.1247 ± 0.0084, a_2= 0.0017 ± 0.0001, a_3= 2.1617 ± 0.0421 and a_4= 0.0141 ± 0.0003.

B. Average scattering factors

B.1 : Average scattering factor $\overline{f_s}$ for the measured $(C_2H_3Cl)_n$ sample.

E_γ	Reaction	Source material	Count rate (s^{-1})		f_s
(keV)			Background	$(C_2H_3Cl)_n$	
139.7	$^{74}Ge(n,\gamma)^{75m}Ge$	HPGe crystal	9.84 ± 0.11	9.65 ± 0.06	0.98 ± 0.01
1014.2	$^{27}Al(n,n'\gamma)^{27}Al$	HPGe housing	0.68 ± 0.01	0.71 ± 0.02	1.05 ± 0.04
1697.0	$^{74}Ge(n,n'\gamma)^{74}Ge$	HPGe crystal	0.24 ± 0.01	0.21 ± 0.01	0.88 ± 0.05
2222.9	$^{1}H(n,\gamma)^{2}H$	BPE shielding	0.23 ± 0.01	0.27 ± 0.01	1.18 ± 0.04
2614.6	$^{208}Pb(n,n'\gamma)^{208}Pb$	Lead shielding	0.66 ± 0.02	0.71 ± 0.01	1.07 ± 0.04
Average value $\overline{f_s}$					**1.03 ± 0.10**

B.2 : Average scattering factor $\overline{f_s}$ for the measured $CaCO_3$ sample.

E_γ	Reaction	Source material	Count rate (s^{-1})		f_s
(keV)			Background	$CaCO_3$	
139.7	$^{74}Ge(n,\gamma)^{75m}Ge$	HPGe crystal	9.84 ± 0.11	23.82 ± 0.12	2.42 ± 0.03
1014.2	$^{27}Al(n,n'\gamma)^{27}Al$	HPGe housing	0.68 ± 0.01	1.67 ± 0.03	2.48 ± 0.06
1697.0	$^{74}Ge(n,n'\gamma)^{74}Ge$	HPGe crystal	0.24 ± 0.01	0.47 ± 0.01	1.91 ± 0.08
2222.9	$^{1}H(n,\gamma)^{2}H$	BPE shielding	0.23 ± 0.01	0.40 ± 0.01	1.73 ± 0.08
2614.6	$^{208}Pb(n,n'\gamma)^{208}Pb$	Lead shielding	0.66 ± 0.02	1.33 ± 0.02	2.00 ± 0.07
Average value $\overline{f_s}$					**2.11 ± 0.29**

B.3 : Average scattering factor $\overline{f_s}$ for the measured $LaCl_3 \cdot 7H_2O$ sample.

E_γ	Reaction	Source material	Count rate (s^{-1})		f_s
(keV)			Background	$LaCl_3 \cdot 7H_2O$	
139.7	$^{74}Ge(n,\gamma)^{75m}Ge$	HPGe crystal	9.84 ± 0.11	15.46 ± 0.54	1.57 ± 0.06
1014.4	$^{27}Al(n,n'\gamma)^{27}Al$	HPGe housing	0.68 ± 0.01	0.90 ± 0.06	1.34 ± 0.10
1697.2	$^{74}Ge(n,n'\gamma)^{74}Ge$	HPGe crystal	0.24 ± 0.01	0.34 ± 0.01	1.40 ± 0.07
2223.3	$^{1}H(n,\gamma)^{2}H$	BPE shielding	0.23 ± 0.01	0.34 ± 0.01	1.50 ± 0.07
2614.6	$^{208}Pb(n,n'\gamma)^{208}Pb$	Lead shielding	0.66 ± 0.02	0.92 ± 0.01	1.39 ± 0.05
Average value $\overline{f_s}$					**1.44 ± 0.08**

B.4 : Average scattering factor $\overline{f_s}$ for the measured $CeCl_3$ sample.

E_γ	Reaction	Source material	Count rate (s^{-1})		f_s
(keV)			Background	$CeCl_3$	
139.7	$^{74}Ge(n,\gamma)^{75m}Ge$	HPGe crystal	9.84 ± 0.11	16.01 ± 0.10	1.63 ± 0.02
1014.3	$^{27}Al(n,n'\gamma)^{27}Al$	HPGe housing	0.68 ± 0.01	1.26 ± 0.04	1.86 ± 0.06
1697.1	$^{74}Ge(n,n'\gamma)^{74}Ge$	HPGe crystal	0.24 ± 0.01	0.25 ± 0.02	1.01 ± 0.09
2222.8	$^{1}H(n,\gamma)^{2}H$	BPE shielding	0.23 ± 0.01	0.32 ± 0.02	1.40 ± 0.08
2614.6	$^{208}Pb(n,n'\gamma)^{208}Pb$	Lead shielding	0.66 ± 0.02	0.79 ± 0.02	1.20 ± 0.05
Average value $\overline{f_s}$					**1.42 ± 0.30**

B.5 : Average scattering factor $\overline{f_s}$ for the measured $PrCl_3 \cdot 7H_2O$ sample.

E_γ	Reaction	Source material	Count rate (s^{-1})		f_s
(keV)			Background	$PrCl_3 \cdot 7H_2O$	
139.7	$^{74}Ge(n,\gamma)^{75m}Ge$	HPGe crystal	9.84 ± 0.11	17.30 ± 0.17	1.76 ± 0.03
1014.2	$^{27}Al(n,n'\gamma)^{27}Al$	HPGe housing	0.68 ± 0.01	1.11 ± 0.04	1.64 ± 0.06
1696.5	$^{74}Ge(n,n'\gamma)^{74}Ge$	HPGe crystal	0.24 ± 0.01	0.47 ± 0.01	1.93 ± 0.08
2222.8	$^{1}H(n,\gamma)^{2}H$	BPE shielding	0.23 ± 0.01	0.39 ± 0.02	1.70 ± 0.08
2614.6	$^{208}Pb(n,n'\gamma)^{208}Pb$	Lead shielding	0.66 ± 0.02	0.90 ± 0.01	1.36 ± 0.05
Average value $\overline{f_s}$					**1.68 ± 0.18**

B.6 : Average scattering factor $\overline{f_s}$ for the measured $NdCl_3$ sample.

E_γ	Reaction	Source material	Count rate (s^{-1})		f_s
(keV)			Background	$NdCl_3$	
139.7	$^{74}Ge(n,\gamma)^{75m}Ge$	HPGe crystal	9.84 ± 0.11	17.83 ± 0.23	1.81 ± 0.03
1014.2	$^{27}Al(n,n'\gamma)^{27}Al$	HPGe housing	0.68 ± 0.01	1.16 ± 0.04	1.72 ± 0.06
1697.1	$^{74}Ge(n,n'\gamma)^{74}Ge$	HPGe crystal	0.24 ± 0.01	0.41 ± 0.03	1.70 ± 0.12
2223.0	$^{1}H(n,\gamma)^{2}H$	BPE shielding	0.23 ± 0.01	0.41 ± 0.02	1.81 ± 0.11
2614.6	$^{208}Pb(n,n'\gamma)^{208}Pb$	Lead shielding	0.66 ± 0.02	0.92 ± 0.02	1.38 ± 0.06
Average value $\overline{f_s}$					**1.68 ± 0.16**

B.7 : Average scattering factor $\overline{f_s}$ for the measured $SmCl_3 \cdot 7H_2O$ sample.

E_γ	Reaction	Source material	Count rate (s^{-1})		f_s
(keV)			Background	$SmCl_3 \cdot 7H_2O$	
139.7	$^{74}Ge(n,\gamma)^{75m}Ge$	HPGe crystal	9.84 ± 0.11	16.90 ± 0.08	1.72 ± 0.02
1014.3	$^{27}Al(n,n'\gamma)^{27}Al$	HPGe housing	0.68 ± 0.01	1.42 ± 0.06	2.11 ± 0.10
1697.2	$^{74}Ge(n,n'\gamma)^{74}Ge$	HPGe crystal	0.24 ± 0.01	0.33 ± 0.02	1.36 ± 0.10
2222.8	$^{1}H(n,\gamma)^{2}H$	BPE shielding	0.23 ± 0.01	0.38 ± 0.03	1.67 ± 0.14
2614.6	$^{208}Pb(n,n'\gamma)^{208}Pb$	Lead shielding	0.66 ± 0.02	0.91 ± 0.03	1.37 ± 0.06
Average value $\overline{f_s}$					**1.64 ± 0.28**

B.8 : Average scattering factor $\overline{f_s}$ for the measured $DyCl_3 \cdot 6H_2O$ sample.

E_γ	Reaction	Source material	Count rate (s^{-1})		f_s
(keV)			Background	$DyCl_3 \cdot 6H_2O$	
139.7	$^{74}Ge(n,\gamma)^{75m}Ge$	HPGe crystal	9.84 ± 0.11	17.02 ± 0.12	1.73 ± 0.02
1014.5	$^{27}Al(n,n'\gamma)^{27}Al$	HPGe housing	0.68 ± 0.01	1.24 ± 0.06	1.84 ± 0.09
1697.2	$^{74}Ge(n,n'\gamma)^{74}Ge$	HPGe crystal	0.24 ± 0.01	0.41 ± 0.03	1.68 ± 0.12
2223.1	$^{1}H(n,\gamma)^{2}H$	BPE shielding	0.23 ± 0.01	0.24 ± 0.02	1.07 ± 0.11
2614.6	$^{208}Pb(n,n'\gamma)^{208}Pb$	Lead shielding	0.66 ± 0.02	0.93 ± 0.03	1.40 ± 0.07
Average value $\overline{f_s}$					**1.54 ± 0.28**

C. Microscopic cross sections (tables)

C.1 : Microscopic cross sections of C, O, Cl and Ca. The values of the (n,tot) reactions are elemental and they were calculated as the sum of isotopic cross sections multiplied with the corresponding isotopic abundance. Values from JANIS [9] are mean values from various data libraries.

Energy range (MeV)	Thermal		Epithermal	Fast	
	10^{-10} - 1.42 × 10^{-7}		1.42 × 10^{-7} - 0.06	0.06 - 20	
Flux Φ (cm^{-2} s^{-1})	(3.16 ± 1.28) × 10^3		(2.94 ± 0.77) × 10^6	(1.13 ± 0.04) × 10^8	
Cross section $\langle\sigma\rangle$	$\langle\sigma_{th}\rangle$ (mb) (NJOY)	$\langle\sigma_{th}\rangle$ (mb) (JANIS)	$\langle\sigma_{epi}\rangle$ (mb) (NJOY)	$\langle\sigma_{fast}\rangle$ (mb) (NJOY)	$\langle\sigma_{fast}\rangle$ (mb) (JANIS)
Carbon					
$^{12}C(n,\gamma)^{13}C$	3.37(163)	3.61(21)	0.04(1)	0.043(4)	0.032(14)
$^{12}C(n,n'\gamma)^{12}C$	-	-	-	12.45(106)	12.22(19)
$^{13}C(n,\gamma)^{14}C$	1.31(64)	1.85(84)	0.016(2)	0.013(1)	0.022(16)
$^{13}C(n,n'\gamma)^{13}C$	-	-	-	9.79(84)	N.A.
C(n,tot), values in b	4.96(230)	5.58(1)	4.71(81)	2.28(27)	2.40(1)
Oxygen					
$^{16}O(n,\gamma)^{17}O$	0.15(7)	0.19(1)	0.014(3)	0.07(1)	0.11(8)
$^{16}O(n,n'\gamma)^{16}O$	-	-	-	8.49(72)	4.85(10)
$^{16}O(n,p\gamma)^{16}N$	-	-	-	0.07(1)	0.042(4)

C.1 : (continued).

Energy range (MeV)	Thermal		Epithermal	Fast	
	10^{-10} - 1.42 × 10^{-7}		1.42 × 10^{-7} - 0.06	0.06 - 20	
Flux Φ (cm^{-2} s^{-1})	(3.16 ± 1.28) × 10^3		(2.94 ± 0.77) × 10^6	(1.13 ± 0.04) × 10^8	
Cross section $\langle\sigma\rangle$	$\langle\sigma_{th}\rangle$ (mb) (NJOY)	$\langle\sigma_{th}\rangle$ (mb) (JANIS)	$\langle\sigma_{epi}\rangle$ (mb) (NJOY)	$\langle\sigma_{fast}\rangle$ (mb) (NJOY)	$\langle\sigma_{fast}\rangle$ (mb) (JANIS)
^{17}O(n,γ)^{18}O	3.34(162)	1.86(161)	0.04(1)	0.21(2)	0.16(7)
^{17}O(n,n'γ)^{17}O	-	-	-	78(7)	N.A.
^{18}O(n,γ)^{19}O	0.13(7)	0.13(6)	0.0017(2)	0.23(2)	0.12(8)
^{18}O(n,n'γ)^{18}O	-	-	-	347(32)	57(73)
O(n,tot), values in b	3.92(184)	4.45(4)	3.76(66)	2.56(31)	2.79(1)
Chlorine					
^{35}Cl(n,γ)^{36}Cl	38,035(1)	43,609(14)	370(5)	0.72(19)	0.77(31)
^{35}Cl(n,n'γ)^{35}Cl	-	-	-	238(21)	N.A.
^{35}Cl(n,pγ)^{35}S	418(203)	485(6)	29(5)	119(11)	102(7)
^{35}Cl(n,αγ)^{32}P	0.070(34)	0.0800(1)	0.0009(1)	21.75(188)	30.70(1644)
^{37}Cl(n,γ)^{38}Cl	395(195)	433.1(2)	5.78(86)	0.44(5)	0.46(17)
^{37}Cl(n,n'γ)^{37}Cl	-	-	-	177(15)	N.A.
Cl(n,tot), values in b	45.41(2160)	51.73(4)	4.75(63)	2.84(25)	2.77(5)
Calcium					
^{40}Ca(n,γ)^{41}Ca	358(174)	409(1)	10.38(176)	1.41(16)	1.55(31)
^{40}Ca(n,n'γ)^{40}Ca	-	-	-	49.07(422)	N.A.
^{40}Ca(n,pγ)^{40}K	-	-	-	122(11)	110(7)
^{40}Ca(n,αγ)^{37}Ar	2.17(105)	1.54(119)	0.03(1)	44(4)	41(4)
^{42}Ca(n,γ)^{43}Ca	596(289)	683(1)	15.31(255)	2.44(30)	3.22(82)
^{42}Ca(n,n'γ)^{42}Ca	-	-	-	495(44)	N.A.
^{43}Ca(n,γ)^{44}Ca	10,176(4,937)	8543(2706)	178(28)	2.20(29)	4.05(164)
^{43}Ca(n,n'γ)^{43}Ca	-	-	-	744(71)	N.A.
^{44}Ca(n,γ)^{45}Ca	775(376)	889(4)	12.54(188)	1.11(14)	1.44(38)
^{44}Ca(n,n'γ)^{44}Ca	-	-	-	602(55)	N.A.
^{46}Ca(n,γ)^{47}Ca	646(313)	691(89)	8.52(120)	0.49(6)	1.12(90)
^{46}Ca(n,n'γ)^{46}Ca	-	-	-	521(47)	N.A.
^{48}Ca(n,γ)^{49}Ca	953(463)	1,092(3)	10.99(150)	0.21(2)	0.21(6)
^{48}Ca(n,n'γ)^{48}Ca	-	-	-	93(8)	N.A.
Ca(n,tot), values in b	2.96(138)	3.76(20)	1.89(31)	2.81(29)	2.89(7)

C.2 : Microscopic cross sections of La, Ce, Pr, Nd, Sm, Tb and Dy. The values of the (n,tot) reactions are elemental and they were calculated as the sum of isotopic cross sections multiplied with the corresponding isotopic abundance. Values from JANIS [9] are mean values from various data libraries.

Energy range (MeV)	Thermal		Epithermal	Fast	
	10^{-10} - 1.42 × 10^{-7}		1.42 × 10^{-7} - 0.06	0.06 - 20	
Flux Φ (cm^{-2} s^{-1})	(3.16 ± 1.28) × 10^3		(2.94 ± 0.77) × 10^6	(1.13 ± 0.04) × 10^8	
Cross section $\langle\sigma\rangle$	$\langle\sigma_{th}\rangle$ (b) (NJOY)	$\langle\sigma_{th}\rangle$ (b) (JANIS)	$\langle\sigma_{epi}\rangle$ (b) (NJOY)	$\langle\sigma_{fast}\rangle$ (b) (NJOY)	$\langle\sigma_{fast}\rangle$ (b) (JANIS)
Lanthanum					
^{138}La(n,γ)^{139}La	49.91(2421)	57.23(8)	9.84(131)	0.027(4)	0.040(7)
^{138}La(n,n'γ)^{138}La	-	-	-	1.39(14)	N.A.
^{139}La(n,γ)^{140}La	7.88(382)	9.03(8)	0.58(8)	0.0067(8)	0.0068(5)

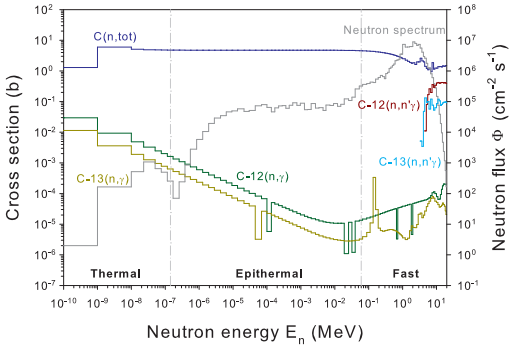
C.2 : (continued).

Energy range (MeV)	Thermal		Epithermal	Fast	
	10^{-10} - 1.42 × 10^{-7}		1.42 × 10^{-7} - 0.06	0.06 - 20	
Flux Φ (cm^{-2} s^{-1})	(3.16 ± 1.28) × 10^{3}		(2.94 ± 0.77) × 10^{6}	(1.13 ± 0.04) × 10^{8}	
Cross section ⟨σ⟩	⟨σ_{th}⟩ (b) (NJOY)	⟨σ_{th}⟩ (b) (JANIS)	⟨σ_{epi}⟩ (b) (NJOY)	⟨σ_{fast}⟩ (b) (NJOY)	⟨σ_{fast}⟩ (b) (JANIS)
^{139}La(n,n'γ)^{139}La	-	-	-	1.33(13)	1.17(9)
La(n,tot)	18.12(860)	20.76(127)	6.55(110)	6.15(69)	6.01(13)
Cerium					
^{136}Ce(n,γ)^{137}Ce	6.50(316)	6.73(120)	5.55(76)	0.133(15)	0.116(20)
^{136}Ce(n,n'γ)^{136}Ce	-	-	-	1.43(14)	N.A.
^{138}Ce(n,γ)^{139}Ce	0.90(44)	1.07(7)	0.82(14)	0.085(10)	0.061(29)
^{138}Ce(n,n'γ)^{138}Ce	-	-	-	1.37(13)	N.A.
^{140}Ce(n,γ)^{141}Ce	0.50(24)	0.56(2)	0.011(2)	0.0060(7)	0.0075(14)
^{140}Ce(n,n'γ)^{140}Ce	-	-	-	0.92(8)	N.A.
^{142}Ce(n,γ)^{143}Ce	0.84(41)	0.97(1)	0.050(9)	0.0072(9)	0.0064(12)
^{142}Ce(n,n'γ)^{142}Ce	-	-	-	1.18(11)	N.A.
Ce(n,tot)	4.08(172)	3.74(82)	9.16(124)	6.31(62)	6.19(18)
Praseodymium					
^{141}Pr(n,γ)^{142}Pr	10.03(487)	11.46(7)	1.38(21)	0.017(2)	0.017(2)
^{141}Pr(n,n'γ)^{141}Pr	-	-	-	1.52(15)	1.42(5)
Pr(n,tot)	12.74(614)	14.57(52)	23.72(393)	6.38(71)	6.30(13)
Neodymium					
^{142}Nd(n,γ)^{143}Nd	16.29(790)	18.68(3)	0.120(18)	0.0233(26)	0.0284(47)
^{142}Nd(n,n'γ)^{142}Nd	-	-	-	0.96(9)	N.A.
^{143}Nd(n,γ)^{144}Nd	282(137)	323(1)	5.01(70)	0.044(5)	0.053(7)
^{143}Nd(n,n'γ)^{143}Nd	-	-	-	1.25(11)	N.A.
^{144}Nd(n,γ)^{145}Nd	3.14(1.52)	3.61(2)	0.31(5)	0.020(2)	0.025(4)
^{144}Nd(n,n'γ)^{144}Nd	-	-	-	1.59(15)	N.A.
^{145}Nd(n,γ)^{146}Nd	36.62(1777)	44.48(337)	9.14(124)	0.039(5)	0.051(3)
^{145}Nd(n,n'γ)^{145}Nd	-	-	-	2.00(21)	N.A.
^{146}Nd(n,γ)^{147}Nd	1.30(63)	1.46(4)	0.25(4)	0.020(3)	0.027(8)
^{146}Nd(n,n'γ)^{146}Nd	-	-	-	1.92(19)	N.A.
^{148}Nd(n,γ)^{149}Nd	2.25(109)	2.57(3)	1.22(18)	0.022(3)	0.027(4)
^{148}Nd(n,n'γ)^{148}Nd	-	-	-	2.15(22)	N.A.
^{150}Nd(n,γ)^{151}Nd	0.91(44)	1.06(5)	1.25(18)	0.017(2)	0.020(2)
^{150}Nd(n,n'γ)^{150}Nd	-	-	-	2.41(25)	N.A.
Nd(n,tot)	59(22)	67(1)	33.39(289)	6.53(32)	6.44(7)
Samarium					
^{144}Sm(n,γ)^{145}Sm	1.42(69)	1.63(1)	0.12(2)	0.056(6)	0.061(9)
^{144}Sm(n,n'γ)^{144}Sm	-	-	-	0.97(9)	N.A.
^{147}Sm(n,γ)^{148}Sm	49.74(2413)	57.12(27)	36.29(488)	0.095(13)	0.146(28)
^{147}Sm(n,n'γ)^{147}Sm	-	-	-	2.01(21)	N.A.
^{148}Sm(n,γ)^{149}Sm	2.09(101)	2.40(1)	2.97(41)	0.054(7)	0.072(11)
^{148}Sm(n,n'γ)^{148}Sm	-	-	-	1.85(18)	N.A.
^{149}Sm(n,γ)^{150}Sm	61,550(28,524)	68,250(557)	68(9)	0.160(23)	0.223(23)
^{149}Sm(n,n'γ)^{149}Sm	-	-	-	2.24(24)	N.A.
^{150}Sm(n,γ)^{151}Sm	87(42)	101(3)	17.53(233)	0.081(11)	0.093(5)
^{150}Sm(n,n'γ)^{150}Sm	-	-	-	2.13(22)	N.A.
^{152}Sm(n,γ)^{153}Sm	180(87)	206.8(2)	128(16)	0.060(8)	0.075(10)
^{152}Sm(n,n'γ)^{152}Sm	-	-	-	2.26(23)	N.A.
^{154}Sm(n,γ)^{155}Sm	7.26(352)	8.38(7)	2.98(41)	0.028(4)	0.036(4)

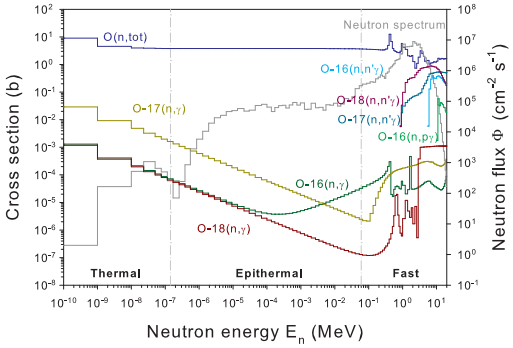
C.2 : (continued).

Energy range (MeV)	Thermal		Epithermal	Fast	
	10^{-10} - 1.42 × 10^{-7}		1.42 × 10^{-7} - 0.06	0.06 - 20	
Flux Φ (cm^{-2} s^{-1})	(3.16 ± 1.28) × 10^{3}		(2.94 ± 0.77) × 10^{6}	(1.13 ± 0.04) × 10^{8}	
Cross section $\langle\sigma\rangle$	$\langle\sigma_{th}\rangle$ (b) (NJOY)	$\langle\sigma_{th}\rangle$ (b) (JANIS)	$\langle\sigma_{epi}\rangle$ (b) (NJOY)	$\langle\sigma_{fast}\rangle$ (b) (NJOY)	$\langle\sigma_{fast}\rangle$ (b) (JANIS)
^{154}Sm(n,n'γ)^{154}Sm	-	-	-	2.35(24)	N.A.
Sm(n,tot)	8,632(3967)	9,542(28)	152(14)	6.64(32)	6.72(6)
Terbium					
^{159}Tb(n,γ)^{160}Tb	20.41(990)	23.37(24)	20.63(287)	0.146(20)	0.171(15)
^{159}Tb(n,n'γ)^{159}Tb	-	-	0.056(11)	1.98(21)	N.A.
Tb(n,tot)	27.35(1315)	31.21(26)	32.46(484)	6.50(73)	6.72(11)
Dysprosium					
^{156}Dy(n,γ)^{157}Dy	29.12(1410)	33.45(19)	37.62(507)	0.34(4)	0.40(2)
^{156}Dy(n,n'γ)^{156}Dy	-	-	-	2.24(23)	N.A.
^{158}Dy(n,γ)^{159}Dy	37.10(1803)	42.49(10)	13.48(190)	0.20(3)	0.23(3)
^{158}Dy(n,n'γ)^{158}Dy	-	-	-	2.34(24)	N.A.
^{160}Dy(n,γ)^{161}Dy	49.18(2383)	57.08(206)	44.24(583)	0.15(2)	0.17(1)
^{160}Dy(n,n'γ)^{160}Dy	-	-	-	2.44(25)	N.A.
^{161}Dy(n,γ)^{162}Dy	517(251)	592(5)	38.02(514)	0.088(13)	0.128(6)
^{161}Dy(n,n'γ)^{161}Dy	-	-	-	2.80(31)	N.A.
^{162}Dy(n,γ)^{163}Dy	170(82)	196(2)	89(11)	0.061(8)	0.070(9)
^{162}Dy(n,n'γ)^{162}Dy	-	-	-	2.59(27)	N.A.
^{163}Dy(n,γ)^{164}Dy	109(53)	128(5)	29.07(405)	0.044(7)	0.066(4)
^{163}Dy(n,n'γ)^{163}Dy	-	-	-	2.83(31)	N.A.
^{164}Dy(n,γ)^{165}Dy	2,281(1,109)	2,619(2)	4.12(60)	0.023(3)	0.028(5)
^{164}Dy(n,n'γ)^{164}Dy	-	-	-	2.63(28)	N.A.
Dy(n,tot)	907(359)	1,038(2)	65(5)	6.79(38)	6.94(5)

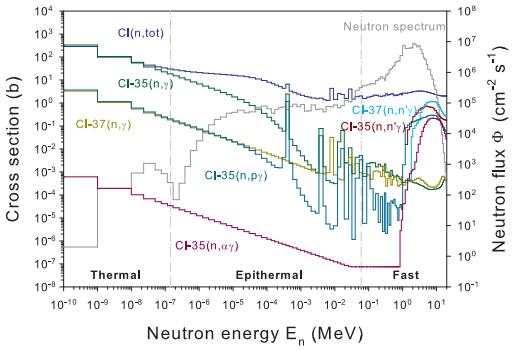
D. Microscopic cross sections (plots)



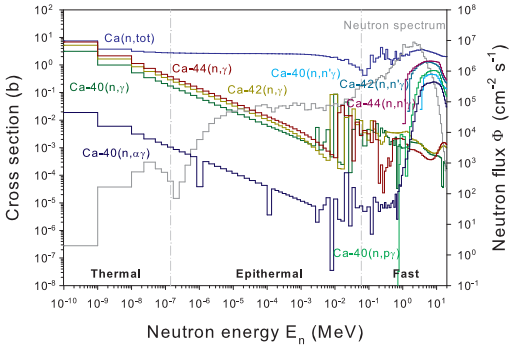
D.1 : Neutron-energy spectrum at sample position (right scale of Y-axis) and neutron-energy dependence of the NJOY grouped microscopic cross sections $\sigma_i(E)$ (left scale of Y-axis) for total (n,tot), radiative capture (n,γ) and fast-neutron inelastic scattering (n,n'γ) reactions for C.



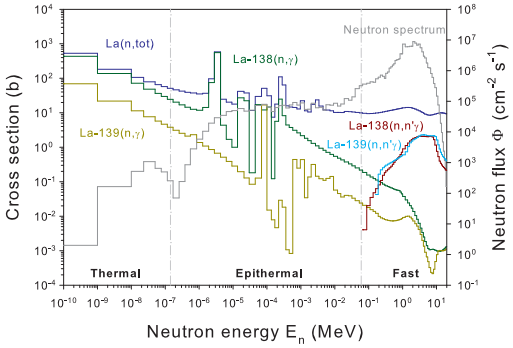
D.2 : Neutron-energy spectrum at sample position (right scale of Y-axis) and neutron-energy dependence of the NJOY grouped microscopic cross sections $\sigma_i(E)$ (left scale of Y-axis) for total (n,tot), radiative capture (n,γ), fast-neutron inelastic scattering (n,n'γ) and (n,pγ) reactions for O.



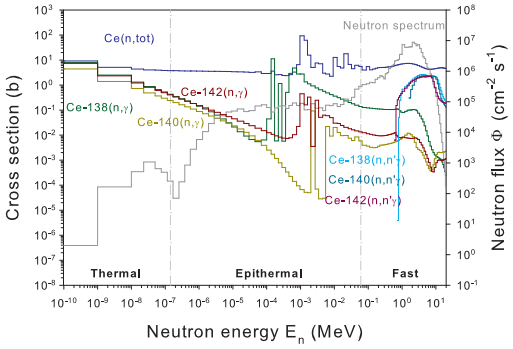
D.3 : Neutron-energy spectrum at sample position (right scale of Y-axis) and neutron-energy dependence of the NJOY grouped microscopic cross sections $\sigma_i(E)$ (left scale of Y-axis) for total (n,tot), radiative capture (n,γ), fast-neutron inelastic scattering (n,n'γ), (n,pγ) and (n,$\alpha\gamma$) reactions for Cl.



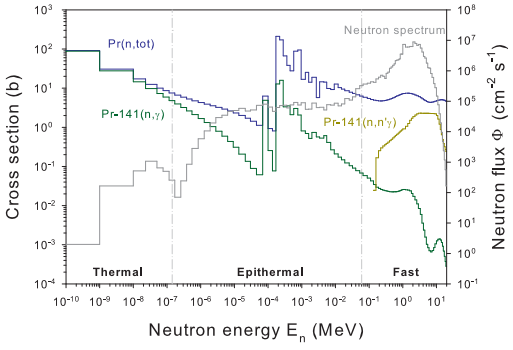
D.4 : Neutron energy spectrum at sample position (right scale of Y-axis) and neutron-energy dependence of the NJOY grouped microscopic cross sections $\sigma_i(E)$ (left scale of Y-axis) for total (n,tot), radiative capture (n,γ), fast-neutron inelastic scattering (n,n'γ), (n,pγ) and (n,$\alpha\gamma$) reactions for Ca.



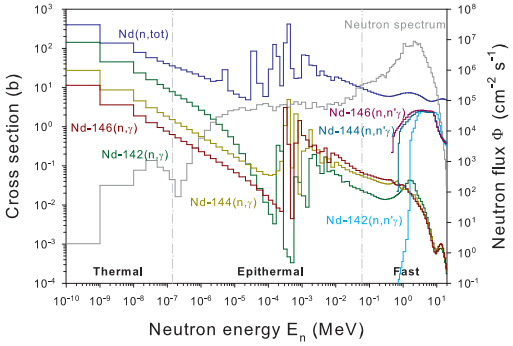
D.5 : Neutron-energy spectrum at sample position (right scale of Y-axis) and neutron-energy dependence of the NJOY grouped microscopic cross sections $\sigma_i(E)$ (left scale of Y-axis) for total (n,tot), radiative capture (n,γ) and fast-neutron inelastic scattering (n,n'γ) reactions for La.



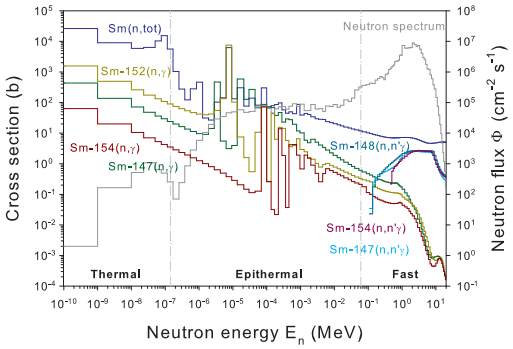
D.6 : Neutron-energy spectrum at sample position (right scale of Y-axis) and neutron-energy dependence of the NJOY grouped microscopic cross sections $\sigma_i(E)$ (left scale of Y-axis) for total (n,tot), radiative capture (n,γ) and fast-neutron inelastic scattering (n,n'γ) reactions for Ce.



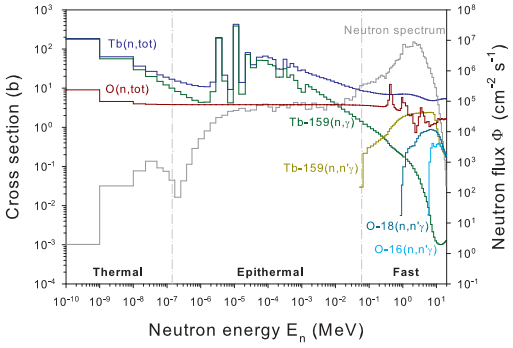
D.7 : Neutron-energy spectrum at sample position (right scale of Y-axis) and neutron-energy dependence of the NJOY grouped microscopic cross sections $\sigma_i(E)$ (left scale of Y-axis) for total (n,tot), radiative capture (n,γ) and fast-neutron inelastic scattering (n,n'γ) reactions for Pr.



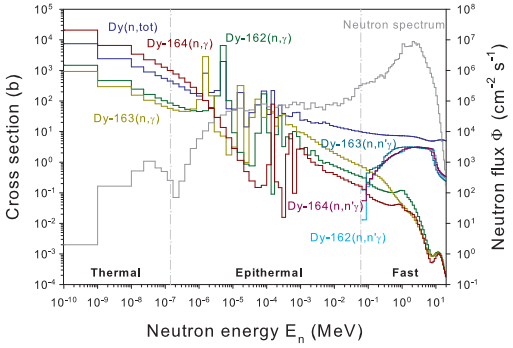
D.8 : Neutron-energy spectrum at sample position (right scale of Y-axis) and neutron-energy dependence of the NJOY grouped microscopic cross sections $\sigma_i(E)$ (left scale of Y-axis) for total (n,tot), radiative capture (n,γ) and fast-neutron inelastic scattering (n,n'γ) reactions for Nd.



D.9 : Neutron-energy spectrum at sample position (right scale of Y-axis) and neutron-energy dependence of the NJOY grouped microscopic cross sections $\sigma_i(E)$ (left scale of Y-axis) for total (n,tot), radiative capture (n,γ) and fast-neutron inelastic scattering (n,n'γ) reactions for Sm.



D.10 : Neutron-energy spectrum at sample position (right scale of Y-axis) and neutron-energy dependence of the NJOY grouped microscopic cross sections $\sigma_i(E)$ (left scale of Y-axis) for total (n,tot), radiative capture (n,γ) and fast-neutron inelastic scattering (n,n'γ) reactions for Tb.



D.11 : Neutron-energy spectrum at sample position (right scale of Y-axis) and neutron-energy dependence of the NJOY grouped microscopic cross sections $\sigma_i(E)$ (left scale of Y-axis) for total (n,tot), radiative capture (n,γ) and fast-neutron inelastic scattering (n,n'γ) reactions for Dy.

E. Macroscopic cross sections

E.1 : Macroscopic cross sections for elastic scattering, inelastic scattering, scattering (total), radiative capture and total for all samples listed in Table 6.1. For thermal neutrons values derived with microscopic cross sections given in JANIS [9] were preferred, for epithermal and fast neutrons those obtained with NJOY.

Energy range (MeV)	Thermal		Epithermal	Fast	
	10^{-10} - 1.42 × 10^{-7}		1.42 × 10^{-7} - 0.06	0.06 - 20	
Flux Φ (cm^{-2} s^{-1})	(3.16 ± 1.28) × 10^{3}		(2.94 ± 0.77) × 10^{6}	(1.13 ± 0.04) × 10^{8}	
Cross section Σ (cm^{-1})	NJOY	JANIS	NJOY	NJOY	JANIS
$CaCO_3$					
Elastic scattering Σ_{el}	0.315(55)	0.3606(1)	0.285(12)	0.202(24)	0.2173(2)
Inelastic scattering Σ_{inel}	-	-	-	0.0015(1)	1.97(3) × 10^{-4}
Scattering Σ_s	0.315(55)	0.3606(1)	0.285(12)	0.203(24)	0.2175(2)
Radiative capture Σ_{cap}	0.0061(2)	0.0069(1)	1.718(8) × 10^{-4}	2.67(31) × 10^{-5}	3.07(3) × 10^{-5}
Total Σ_t	0.321(38)	0.368(1)	0.291(13)	0.208(25)	0.2216(2)
$(C_2H_3Cl)_n$					
Elastic scattering Σ_{el}	1.568(694)	1.765(41)	0.964(130)	0.245(30)	0.267(3)
Inelastic scattering Σ_{inel}	-	-	-	0.0034(3)	3.35(5) × 10^{-4}
Scattering Σ_s	1.568(694)	1.765(41)	0.964(130)	0.248(30)	0.267(3)
Radiative capture Σ_{cap}	0.413(7)	0.4739(2)	0.0041(1)	1.17(24) × 10^{-5}	1.22(43) × 10^{-4}
Total Σ_t	1.985(948)	2.245(2)	0.978(168)	0.250(30)	0.271(1)
$LaCl_3{\cdot}7H_2O$					
Elastic scattering Σ_{el}	1.777(846)	2.005(7)	1.115(192)	0.287(35)	0.317(2)
Inelastic scattering Σ_{inel}	-	-	-	0.0075(7)	0.0044(3)
Scattering Σ_s	1.777(846)	2.005(7)	1.115(192)	0.295(35)	0.321(2)
Radiative capture Σ_{cap}	0.357(22)	0.4092(4)	0.0054(4)	0.35(5) × 10^{-4}	0.37(7) × 10^{-4}
Total Σ_t	2.138(1.021)	2.419(7)	1.121(193)	0.297(36)	0.325(2)
$CeCl_3$					
Elastic scattering Σ_{el}	0.506(242)	0.560(9)	0.218(36)	0.125(14)	0.124(3)
Inelastic scattering Σ_{inel}	-	-	-	0.0170(15)	N.A.
Scattering Σ_s	0.506(242)	0.560(9)	0.218(36)	0.142(14)	0.124(3)
Radiative capture Σ_{cap}	0.847(4)	0.971(1)	0.0085(2)	8.258(1180) × 10^{-5}	9.514(2250) × 10^{-5}
Total Σ_t	1.400(683)	1.542(10)	0.227(38)	0.144(16)	0.141(4)
$PrCl_3{\cdot}7H_2O$					
Elastic scattering Σ_{el}	1.757(837)	1.980(4)	1.179(202)	0.289(35)	0.318(1)

E.1 : (continued).

Energy range (MeV)	Thermal		Epithermal	Fast	
	10^{-10} - 1.42×10^{-7}		1.42×10^{-7} - 0.06	0.06 - 20	
Flux Φ cm^{-2} s^{-1}	$(3.16 \pm 1.28) \times 10^{3}$		$(2.94 \pm 0.77) \times 10^{6}$	$(1.13 \pm 0.04) \times 10^{8}$	
Cross section Σ (cm^{-1})	NJOY	JANIS	NJOY	NJOY	JANIS
Inelastic scattering Σ_{inel}	-	-	-	0.0082(8)	0.0053(2)
Scattering Σ_s	1.757(837)	1.980(4)	1.179(202)	0.297(35)	0.323(1)
Radiative capture Σ_{cap}	0.3659(253)	0.4194(4)	0.0083(8)	$0.73(10) \times 10^{-4}$	$0.75(14) \times 10^{-4}$
Total Σ_t	2.126(1016)	2.404(5)	1.187(204)	0.299(36)	0.327(2)
$NdCl_3$					
Elastic scattering Σ_{el}	0.664(300)	0.746(11)	0.454(73)	0.124(14)	0.126(2)
Inelastic scattering Σ_{inel}	-	-	-	0.0220(21)	N.A.
Scattering Σ_s	0.664(300)	0.746(11)	0.454(73)	0.146(14)	0.126(2)
Radiative capture Σ_{cap}	1.317(209)	1.514(5)	0.041(2)	$3.648(357) \times 10^{-4}$	$4.445(579) \times 10^{-4}$
Total Σ_t	2.031(961)	2.272(13)	0.495(77)	0.149(16)	0.160(4)
$SmCl_3 \cdot 7H_2O$					
Elastic scattering Σ_{el}	2.041(964)	2.284(7)	1.520(247)	0.311(36)	0.339(1)
Inelastic scattering Σ_{inel}	-	-	-	$1.170(106) \cdot 10^{-2}$	$1.300(64) \times 10^{-4}$
Scattering Σ_s	2.041(964)	2.284(7)	1.520(247)	0.322(36)	0.339(1)
Radiative capture Σ_{cap}	32.47(1490)	36.03(29)	0.196(25)	$2.796(386) \times 10^{-4}$	$3.752(522) \times 10^{-4}$
Total Σ_t	34.51(1603)	38.21(11)	1.717(272)	0.325(38)	0.354(2)
$TbCl_3 \cdot 6H_2O$					
Elastic scattering Σ_{el}	2.992(1425)	3.372(5)	1.915(329)	0.487(60)	0.536(2)
Inelastic scattering Σ_{inel}	-	-	$6.74 \pm 1.33 \times 10^{-6}$	0.0189(19)	$2.08(1) \times 10^{-3}$
Scattering Σ_s	2.992(1425)	3.372(5)	1.915(329)	0.506(60)	0.536(2)
Radiative capture Σ_{cap}	0.776(82)	0.990(2)	0.151(20)	$1.04(14) \times 10^{-3}$	$1.22(11) \times 10^{-3}$
Total Σ_t	3.775(1.804)	4.271(7)	2.067(350)	0.511(62)	0.559(3)
$DyCl_3 \cdot 6H_2O$					
Elastic scattering Σ_{el}	2.102(997)	2.364(11)	1.172(198)	0.283(34)	0.312(1)
Inelastic scattering Σ_{inel}	-	-	$8.41(166) \times 10^{-5}$	0.014(1)	$1.22(6) \times 10^{-4}$
Scattering Σ_s	2.102(997)	2.364(11)	1.172(198)	0.297(34)	0.312(1)
Capture Σ_{cap}	3.691(1622)	4.239(13)	0.164(21)	$2.298(326) \times 10^{-4}$	$3.039(306) \times 10^{-4}$
Total Σ_t	5.797(2792)	6.609(17)	1.336(220)	0.299(35)	0.327(1)

F. Reaction rates

F.1 : Reaction rates in the $(C_2H_3Cl)_n$ and $CaCO_3$ sample. Values for thermal neutrons were derived with cross sections given in JANIS [9], all others were obtained with NJOY.

Energy range (MeV)	Thermal		Epithermal		Fast	
	10^{-10} - 1.42×10^{-7}		1.42×10^{-7} - 0.06		0.06 - 20	
Flux Φ (cm^{-2} s^{-1})	$(3.16 \pm 1.28) \times 10^{3}$		$(2.94 \pm 0.77) \times 10^{6}$		$(1.13 \pm 0.04) \times 10^{8}$	
Reaction rate R ($=\Phi \cdot \langle\sigma\rangle \cdot f_n$)	(atom^{-1} s^{-1})	(%)	(atom^{-1} s^{-1})	(%)	(atom^{-1} s^{-1})	(%)
$(C_2H_3Cl)_n$						
$^{12}C(n,\gamma)^{13}C$	$1.14(47) \times 10^{-23}$	0.2	$1.29(39) \times 10^{-22}$	2.6	$4.89(63) \times 10^{-21}$	97.2
$^{12}C(n,n'\gamma)^{12}C$	-	-	-	-	$1.41(16) \times 10^{-18}$	100
$^{13}C(n,\gamma)^{14}C$	$5.85(356) \times 10^{-24}$	0.4	$4.80(144) \times 10^{-23}$	3.1	$1.50(19) \times 10^{-21}$	96.5
$^{13}C(n,n'\gamma)^{13}C$	-	-	-	-	$1.11(13) \times 10^{-18}$	100
C(n,tot)	$1.76(71) \times 10^{-20}$	≈ 0	$1.38(44) \times 10^{-17}$	5.1	$2.57(36) \times 10^{-21}$	94.9

F.1 : (continued).

Energy range	Thermal		Epithermal		Fast	
(MeV)	10^{-10} - 1.42×10^{-7}		1.42×10^{-7} - 0.06		0.06 - 20	
Flux Φ (cm^{-2} s^{-1})	$(3.16 \pm 1.28) \times 10^{3}$		$(2.94 \pm 0.77) \times 10^{6}$		$(1.13 \pm 0.04) \times 10^{8}$	
Reaction rate R ($=\Phi \cdot \langle\sigma\rangle \cdot f_n$)	(atom^{-1} s^{-1})	(%)	(atom^{-1} s^{-1})	(%)	(atom^{-1} s^{-1})	(%)
^{35}Cl(n,γ)^{36}Cl	$1.38(56) \times 10^{-19}$	10.5	$1.09(29) \times 10^{-18}$	83.3	$8.09(219) \times 10^{-20}$	6.2
^{35}Cl(n,n'γ)^{35}Cl	-	-	-	-	$2.69(32) \times 10^{-17}$	100
^{35}Cl(n,pγ)^{35}S	$1.53(62) \times 10^{-21}$	0.01	$8.62(267) \times 10^{-20}$	0.6	$1.34(16) \times 10^{-17}$	99.3
^{35}Cl(n,$\alpha\gamma$)^{32}P	$2.53(102) \times 10^{-25}$	≈ 0	$2.55(76) \times 10^{-24}$	≈ 0	$2.46(29) \times 10^{-18}$	≈ 100
^{37}Cl(n,γ)^{38}Cl	$1.37(55) \times 10^{-21}$	2.0	$1.70(51) \times 10^{-20}$	25.1	$4.93(68) \times 10^{-20}$	72.9
^{37}Cl(n,n'γ)^{37}Cl	-	-	-	-	$1.99(23) \times 10^{-17}$	100
Cl(n,tot)	$1.63(66) \times 10^{-19}$	0.05	$1.40(41) \times 10^{-17}$	4.2	$3.21(37) \times 10^{-16}$	95.8
$CaCO_3$						
^{12}C(n,γ)^{13}C	$1.14(47) \times 10^{-23}$	0.2	$1.29(39) \times 10^{-22}$	2.6	$4.89(63) \times 10^{-21}$	97.2
^{12}C(n,n'γ)^{12}C	-	-	-	-	$1.41(16) \times 10^{-18}$	100
^{13}C(n,γ)^{14}C	$5.85(356) \times 10^{-24}$	0.4	$4.80(144) \times 10^{-23}$	3.1	$1.50(19) \times 10^{-21}$	96.5
^{12}C(n,n'γ)^{12}C	-	-	-	-	$1.11(13) \times 10^{-18}$	100
C(n,tot)	$1.76(71) \times 10^{-20}$	≈ 0	$1.38(44) \times 10^{-17}$	5.1	$2.57(36) \times 10^{-21}$	94.9
^{16}O(n,γ)^{17}O	$5.88(240) \times 10^{-25}$	≈ 0	$4.10(133) \times 10^{-23}$	0.5	$7.52(103) \times 10^{-21}$	99.4
^{16}O(n,n'γ)^{16}O	-	-	-	-	$9.59(111) \times 10^{-19}$	100
^{16}O(n,pγ)^{16}N	-	-	-	-	$7.36(88) \times 10^{-21}$	100
^{17}O(n,γ)^{18}O	$5.86(560) \times 10^{-24}$	0.03	$1.20(36) \times 10^{-22}$	0.5	$2.33(30) \times 10^{-20}$	99.5
^{17}O(n,n'γ)^{17}O	-	-	-	-	$8.79(106) \times 10^{-18}$	100
^{18}O(n,γ)^{19}O	$4.03(240) \times 10^{-25}$	≈ 0	$4.92(147) \times 10^{-24}$	0.02	$2.56(30) \times 10^{-20}$	≈ 100
^{18}O(n,n'γ)^{18}O	-	-	-	-	$3.92(47) \times 10^{-17}$	100
O(n,tot)	$1.40(57) \times 10^{-20}$	≈ 0	$1.10(35) \times 10^{-17}$	3.7	$2.89(42) \times 10^{-16}$	96.3
^{40}Ca(n,γ)^{41}Ca	$1.29(52) \times 10^{-21}$	0.7	$3.05(96) \times 10^{-20}$	15.9	$1.60(22) \times 10^{-19}$	83.4
^{40}Ca(n,n'γ)^{40}Ca	-	-	-	-	$5.55(64) \times 10^{-18}$	100
^{40}Ca(n,pγ)^{40}K	-	-	-	-	$1.37(16) \times 10^{-17}$	100
^{40}Ca(n,$\alpha\gamma$)^{37}Ar	$4.85(424) \times 10^{-24}$	≈ 0	$9.79(297) \times 10^{-23}$	≈ 0	$4.97(58) \times 10^{-18}$	≈ 100
^{42}Ca(n,γ)^{43}Ca	$2.15(87) \times 10^{-21}$	0.7	$4.50(140) \times 10^{-20}$	13.9	$2.76(40) \times 10^{-19}$	85.4
^{42}Ca(n,n'γ)^{42}Ca	-	-	-	-	$5.60(67) \times 10^{-17}$	100
^{43}Ca(n,γ)^{44}Ca	$2.70(139) \times 10^{-20}$	3.4	$5.22(160) \times 10^{-19}$	65.4	$2.49(38) \times 10^{-19}$	31.2
^{43}Ca(n,n'γ)^{43}Ca	-	-	-	-	$8.41(104) \times 10^{-17}$	100
^{44}Ca(n,γ)^{45}Ca	$2.80(114) \times 10^{-21}$	1.7	$3.68(112) \times 10^{-20}$	22.4	$1.25(18) \times 10^{-19}$	75.9
^{44}Ca(n,n'γ)^{44}Ca	-	-	-	-	$6.80(82) \times 10^{-17}$	100
^{46}Ca(n,γ)^{47}Ca	$2.18(93) \times 10^{-21}$	2.6	$2.50(75) \times 10^{-20}$	30.1	$5.58(81) \times 10^{-20}$	67.2
^{46}Ca(n,n'γ)^{46}Ca	-	-	-	-	$5.89(71) \times 10^{-17}$	100
^{48}Ca(n,γ)^{49}Ca	$3.45(139) \times 10^{-21}$	5.7	$3.23(96) \times 10^{-20}$	53.8	$2.43(31) \times 10^{-20}$	40.5
^{48}Ca(n,n'γ)^{48}Ca	-	-	-	-	$1.05(12) \times 10^{-17}$	100
Ca(n,tot)	$1.19(48) \times 10^{-20}$	≈ 0	$5.54(172) \times 10^{-18}$	1.7	$3.17(41) \times 10^{-16}$	98.3

F.2 : Reaction rates in the RE chloride samples listed in Tab. 6.1. Values for thermal neutrons were derived with cross sections given in JANIS [9], all others were obtained with NJOY.

Energy range	Thermal		Epithermal		Fast	
(MeV)	10^{-10} - 1.42×10^{-7}		1.42×10^{-7} - 0.06		0.06 - 20	
Flux Φ (cm^{-2} s^{-1})	$(3.16 \pm 1.28) \times 10^{3}$		$(2.94 \pm 0.77) \times 10^{6}$		$(1.13 \pm 0.04) \times 10^{8}$	
Reaction rate R ($=\Phi \cdot \langle\sigma\rangle \cdot f_n$)	(atom^{-1} s^{-1})	(%)	(atom^{-1} s^{-1})	(%)	(atom^{-1} s^{-1})	(%)
$LaCl_3 \cdot 7H_2O$						
$^{16}O(n,\gamma)^{17}O$	$3.53(144) \times 10^{-24}$	0.05	$6.96(225) \times 10^{-23}$	0.90	$7.62(105) \times 10^{-21}$	99.05
$^{16}O(n,n'\gamma)^{16}O$	-	-	-	-	$9.73(112) \times 10^{-19}$	100
$^{16}O(n,p\gamma)^{16}N$	-	-	-	-	$7.46(90) \times 10^{-21}$	100
$^{17}O(n,\gamma)^{18}O$	$3.52(336) \times 10^{-23}$	0.15	$2.04(61) \times 10^{-22}$	0.86	$2.36(30) \times 10^{-20}$	98.99
$^{17}O(n,n'\gamma)^{17}O$	-	-	-	-	$8.92(107) \times 10^{-18}$	100
$^{18}O(n,\gamma)^{19}O$	$2.42(144) \times 10^{-24}$	0.01	$8.35(249) \times 10^{-24}$	0.03	$2.60(30) \times 10^{-20}$	99.96
$^{18}O(n,n'\gamma)^{18}O$	-	-	-	-	$3.97(48) \times 10^{-17}$	100
O(n,tot)	$8.42(341) \times 10^{-20}$	0.03	$1.87(59) \times 10^{-17}$	5.99	$2.94(43) \times 10^{-16}$	93.98
$^{35}Cl(n,\gamma)^{36}Cl$	$8.26(334) \times 10^{-19}$	30.00	$1.84(49) \times 10^{-18}$	67.02	$8.20(222) \times 10^{-20}$	2.98
$^{35}Cl(n,n'\gamma)^{35}Cl$	-	-	-	-	$2.73(32) \times 10^{-17}$	100
$^{35}Cl(n,p\gamma)^{35}S$	$9.18(372) \times 10^{-21}$	0.07	$1.46(45) \times 10^{-19}$	1.06	$1.36(16) \times 10^{-17}$	98.87
$^{35}Cl(n,\alpha\gamma)^{32}P$	$1.52(61) \times 10^{-24}$	≈ 0	$4.32(129) \times 10^{-24}$	≈ 0	$2.49(29) \times 10^{-18}$	≈ 100
$^{37}Cl(n,\gamma)^{38}Cl$	$8.20(332) \times 10^{-21}$	9.43	$2.88(87) \times 10^{-20}$	33.08	$5.00(69) \times 10^{-20}$	57.49
$^{37}Cl(n,n'\gamma)^{37}Cl$	-	-	-	-	$2.02(24) \times 10^{-17}$	100
Cl(n,tot)	$9.79(396) \times 10^{-19}$	0.28	$2.37(70) \times 10^{-17}$	6.76	$3.25(38) \times 10^{-16}$	92.96
$^{138}La(n,\gamma)^{138}La$	$1.08(44) \times 10^{-18}$	2.04	$4.90(145) \times 10^{-17}$	92.08	$3.13(50) \times 10^{-18}$	5.88
$^{138}La(n,n'\gamma)^{138}La$	-	-	-	-	$1.60(20) \times 10^{-16}$	100
$^{139}La(n,\gamma)^{140}La$	$1.71(69) \times 10^{-19}$	4.44	$2.91(86) \times 10^{-18}$	75.72	$7.63(109) \times 10^{-19}$	19.83
$^{139}La(n,n'\gamma)^{139}La$	-	-	-	-	$1.53(19) \times 10^{-16}$	100
La(n,tot)	$3.93(161) \times 10^{-19}$	0.05	$3.26(102) \times 10^{-17}$	4.42	$7.05(96) \times 10^{-16}$	95.53
$CeCl_3$						
$^{35}Cl(n,\gamma)^{36}Cl$	$1.10(44) \times 10^{-19}$	8.52	$1.10(29) \times 10^{-18}$	85.16	$8.14(221) \times 10^{-20}$	6.32
$^{35}Cl(n,n'\gamma)^{35}Cl$	-	-	-	-	$2.71(32) \times 10^{-17}$	100
$^{35}Cl(n,p\gamma)^{35}S$	$1.22(49) \times 10^{-21}$	0.01	$8.70(269) \times 10^{-20}$	0.64	$1.35(16) \times 10^{-17}$	99.35
$^{35}Cl(n,\alpha\gamma)^{32}P$	$2.02(82) \times 10^{-25}$	≈ 0	$2.57(77) \times 10^{-24}$	≈ 0	$2.47(29) \times 10^{-18}$	≈ 100
$^{37}Cl(n,\gamma)^{38}Cl$	$1.09(44) \times 10^{-21}$	1.61	$1.71(52) \times 10^{-20}$	25.25	$4.96(68) \times 10^{-20}$	73.14
$^{37}Cl(n,n'\gamma)^{37}Cl$	-	-	-	-	$2.01(23) \times 10^{-17}$	100
Cl(n,tot)	$1.30(53) \times 10^{-19}$	0.04	$1.41(42) \times 10^{-17}$	4.18	$3.23(38) \times 10^{-16}$	95.78
$^{136}Ce(n,\gamma)^{137}Ce$	$1.70(75) \times 10^{-20}$	0.05	$1.65(49) \times 10^{-17}$	52.02	$1.52(21) \times 10^{-17}$	47.93
$^{136}Ce(n,n'\gamma)^{136}Ce$	-	-	-	-	$1.63(20) \times 10^{-16}$	100
$^{138}Ce(n,\gamma)^{139}Ce$	$2.71(111) \times 10^{-21}$	0.02	$2.43(77) \times 10^{-18}$	20.07	$9.66(135) \times 10^{-18}$	79.91
$^{138}Ce(n,n'\gamma)^{138}Ce$	-	-	-	-	$1.56(19) \times 10^{-16}$	100
$^{140}Ce(n,\gamma)^{141}Ce$	$1.42(58) \times 10^{-21}$	0.20	$3.26(103) \times 10^{-20}$	4.56	$6.82(95) \times 10^{-19}$	95.24
$^{140}Ce(n,n'\gamma)^{140}Ce$	-	-	-	-	$1.05(12) \times 10^{-16}$	100
$^{142}Ce(n,\gamma)^{143}Ce$	$2.44(99) \times 10^{-21}$	0.25	$1.49(48) \times 10^{-19}$	15.36	$8.19(116) \times 10^{-19}$	84.39
$^{142}Ce(n,n'\gamma)^{142}Ce$	-	-	-	-	$1.34(16) \times 10^{-16}$	100
Ce(n,tot)	$9.43(433) \times 10^{-21}$	≈ 0	$2.72(81) \times 10^{-17}$	3.65	$7.17(90) \times 10^{-16}$	96.35
$PrCl_3 \cdot 7H_2O$						
$^{16}O(n,\gamma)^{17}O$	$3.51(143) \times 10^{-24}$	0.05	$6.98(226) \times 10^{-23}$	0.91	$7.62(105) \times 10^{-21}$	99.05
$^{16}O(n,n'\gamma)^{16}O$	-	-	-	-	$9.73(112) \times 10^{-19}$	100
$^{16}O(n,p\gamma)^{16}N$	-	-	-	-	$7.46(90) \times 10^{-21}$	100
$^{17}O(n,\gamma)^{18}O$	$3.49(334) \times 10^{-23}$	0.15	$2.05(61) \times 10^{-22}$	0.86	$2.36(30) \times 10^{-20}$	98.99
$^{17}O(n,n'\gamma)^{17}O$	-	-	-	-	$8.92(107) \times 10^{-18}$	100
$^{18}O(n,\gamma)^{19}O$	$2.40(143) \times 10^{-24}$	0.01	$8.38(250) \times 10^{-24}$	0.03	$2.60(30) \times 10^{-20}$	99.96

F.2 : (continued).

Energy range	Thermal		Epithermal		Fast	
(MeV)	10^{-10} - 1.42×10^{-7}		1.42×10^{-7} - 0.06		0.06 - 20	
Flux Φ (cm^{-2} s^{-1})	$(3.16 \pm 1.28) \times 10^{3}$		$(2.94 \pm 0.77) \times 10^{6}$		$(1.13 \pm 0.04) \times 10^{8}$	
Reaction rate R	(atom^{-1} s^{-1})	(%)	(atom^{-1} s^{-1})	(%)	(atom^{-1} s^{-1})	(%)
$(=\Phi \cdot \langle\sigma\rangle \cdot f_n)$						
^{18}O(n,n'γ)^{18}O	-	-	-	-	$3.97(48) \times 10^{-17}$	100
O(n,tot)	$8.36(339) \times 10^{-20}$	0.03	$1.88(59) \times 10^{-17}$	6.01	$2.94(43) \times 10^{-16}$	93.96
^{35}Cl(n,γ)^{36}Cl	$8.20(332) \times 10^{-19}$	29.79	$1.85(49) \times 10^{-18}$	67.22	$8.20(222) \times 10^{-20}$	2.98
^{35}Cl(n,n'γ)^{35}Cl	-	-	-	-	$2.73(32) \times 10^{-17}$	100
^{35}Cl(n,pγ)^{35}S	$9.12(369) \times 10^{-21}$	0.07	$1.47(45) \times 10^{-19}$	1.07	$1.36(16) \times 10^{-17}$	98.87
^{35}Cl(n,$\alpha\gamma$)^{32}P	$1.51(61) \times 10^{-24}$	≈ 0	$4.34(129) \times 10^{-24}$	≈ 0	$2.49(29) \times 10^{-18}$	≈ 100
^{37}Cl(n,γ)^{38}Cl	$8.14(330) \times 10^{-21}$	9.36	$2.89(87) \times 10^{-20}$	33.17	$5.00(69) \times 10^{-20}$	57.47
^{37}Cl(n,n'γ)^{37}Cl	-	-	-	-	$2.02(24) \times 10^{-17}$	100
Cl(n,tot)	$9.73(394) \times 10^{-19}$	0.28	$2.37(70) \times 10^{-17}$	6.78	$3.25(38) \times 10^{-16}$	92.94
^{141}Pr(n,γ)^{142}Pr	$2.16(87) \times 10^{-19}$	2.37	$6.90(210) \times 10^{-18}$	75.88	$1.98(29) \times 10^{-18}$	21.74
^{141}Pr(n,n'γ)^{141}Pr	-	-	-	-	$1.75(22) \times 10^{-16}$	100
Pr(n,tot)	$2.74(111) \times 10^{-19}$	0.03	$1.19(37) \times 10^{-16}$	13.95	$7.31(99) \times 10^{-16}$	86.01
$NdCl_3$						
^{35}Cl(n,γ)^{36}Cl	$1.12(45) \times 10^{-19}$	8.56	$1.10(29) \times 10^{-18}$	85.18	$8.18(222) \times 10^{-20}$	6.26
^{35}Cl(n,n'γ)^{35}Cl	-	-	-	-	$2.72(32) \times 10^{-17}$	100
^{35}Cl(n,pγ)^{35}S	$1.24(50) \times 10^{-21}$	0.01	$8.82(273) \times 10^{-20}$	0.65	$1.35(16) \times 10^{-17}$	99.34
^{35}Cl(n,$\alpha\gamma$)^{32}P	$2.05(83) \times 10^{-25}$	≈ 0	$2.61(78) \times 10^{-24}$	≈ 0	$2.48(29) \times 10^{-18}$	≈ 100
^{37}Cl(n,γ)^{38}Cl	$1.11(45) \times 10^{-21}$	1.63	$1.74(53) \times 10^{-20}$	25.42	$4.98(68) \times 10^{-20}$	72.95
^{37}Cl(n,n'γ)^{37}Cl	-	-	-	-	$2.02(24) \times 10^{-17}$	100
Cl(n,tot)	$1.33(54) \times 10^{-19}$	0.04	$1.43(42) \times 10^{-17}$	4.22	$3.24(38) \times 10^{-16}$	95.74
^{142}Nd(n,γ)^{143}Nd	$4.79(194) \times 10^{-20}$	1.56	$3.60(109) \times 10^{-19}$	11.75	$2.65(36) \times 10^{-18}$	86.68
^{142}Nd(n,n'γ)^{142}Nd	-	-	-	-	$1.10(13) \times 10^{-16}$	100
^{143}Nd(n,γ)^{144}Nd	$8.30(336) \times 10^{-19}$	3.96	$1.51(45) \times 10^{-17}$	71.93	$5.04(74) \times 10^{-18}$	24.10
^{143}Nd(n,n'γ)^{143}Nd	-	-	-	-	$1.43(17) \times 10^{-16}$	100
^{144}Nd(n,γ)^{145}Nd	$9.25(375) \times 10^{-21}$	0.29	$9.43(297) \times 10^{-19}$	29.55	$2.24(33) \times 10^{-18}$	70.16
^{144}Nd(n,n'γ)^{144}Nd	-	-	-	-	$1.82(23) \times 10^{-16}$	100
^{145}Nd(n,γ)^{146}Nd	$1.14(47) \times 10^{-19}$	0.36	$2.75(82) \times 10^{-17}$	85.81	$4.43(69) \times 10^{-18}$	13.83
^{145}Nd(n,n'γ)^{145}Nd	-	-	-	-	$2.29(30) \times 10^{-16}$	100
^{146}Nd(n,γ)^{147}Nd	$3.75(152) \times 10^{-21}$	0.12	$7.53(240) \times 10^{-19}$	24.65	$2.30(35) \times 10^{-18}$	75.23
^{146}Nd(n,n'γ)^{146}Nd	-	-	-	-	$2.20(28) \times 10^{-16}$	100
^{148}Nd(n,γ)^{149}Nd	$6.60(267) \times 10^{-21}$	0.11	$3.68(111) \times 10^{-18}$	59.90	$2.46(38) \times 10^{-18}$	39.99
^{148}Nd(n,n'γ)^{148}Nd	-	-	-	-	$2.46(32) \times 10^{-16}$	100
^{150}Nd(n,γ)^{151}Nd	$2.73(111) \times 10^{-21}$	0.05	$3.76(113) \times 10^{-18}$	66.09	$1.92(30) \times 10^{-18}$	33.86
^{150}Nd(n,n'γ)^{150}Nd	-	-	-	-	$2.76(36) \times 10^{-16}$	100
Nd(n,tot)	$1.73(70) \times 10^{-19}$	0.02	$1.00(28) \times 10^{-16}$	11.86	$7.46(69) \times 10^{-16}$	88.12
$SmCl_3 \cdot 7H_2O$						
^{16}O(n,γ)^{17}O	$1.96(80) \times 10^{-25}$	≈ 0	$6.91(223) \times 10^{-23}$	0.89	$7.64(105) \times 10^{-21}$	99.10
^{16}O(n,n'γ)^{16}O	-	-	-	-	$9.75(113) \times 10^{-19}$	100
^{16}O(n,pγ)^{16}N	-	-	-	-	$7.48(90) \times 10^{-21}$	100
^{17}O(n,γ)^{18}O	$1.95(186) \times 10^{-24}$	0.01	$2.03(60) \times 10^{-22}$	0.85	$2.36(31) \times 10^{-20}$	99.14
^{17}O(n,n'γ)^{17}O	-	-	-	-	$8.94(108) \times 10^{-18}$	100
^{18}O(n,γ)^{19}O	$1.34(80) \times 10^{-25}$	≈ 0	$8.29(247) \times 10^{-24}$	0.03	$2.60(30) \times 10^{-20}$	99.97
^{18}O(n,n'γ)^{18}O	-	-	-	-	$3.98(48) \times 10^{-17}$	100
O(n,tot)	$4.67(189) \times 10^{-21}$	≈ 0	$1.86(59) \times 10^{-17}$	5.94	$2.94(43) \times 10^{-16}$	94.06
^{35}Cl(n,γ)^{36}Cl	$4.58(185) \times 10^{-20}$	2.34	$1.83(48) \times 10^{-18}$	93.46	$8.23(223) \times 10^{-20}$	4.20
^{35}Cl(n,n'γ)^{35}Cl	-	-	-	-	$2.74(33) \times 10^{-17}$	100
^{35}Cl(n,pγ)^{35}S	$5.10(206) \times 10^{-22}$	≈ 0	$1.45(45) \times 10^{-19}$	1.05	$1.36(16) \times 10^{-17}$	98.94
^{35}Cl(n,$\alpha\gamma$)^{32}P	$8.41(340) \times 10^{-26}$	≈ 0	$4.29(128) \times 10^{-24}$	≈ 0	$2.50(29) \times 10^{-18}$	≈ 100

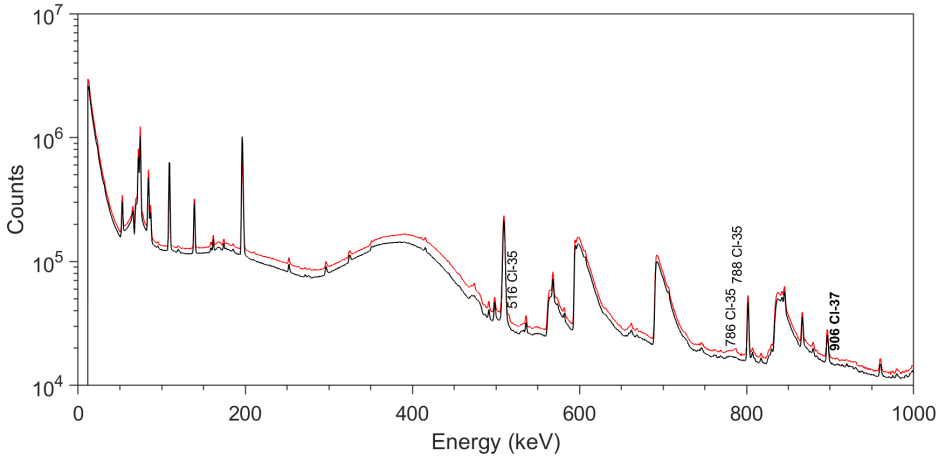
F.2 : (continued).

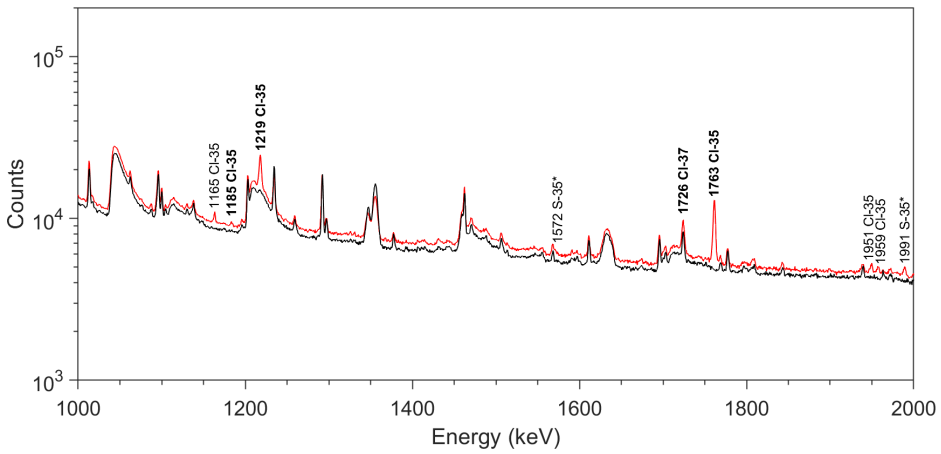
Energy range	Thermal		Epithermal		Fast	
(MeV)	10^{-10} - 1.42 × 10^{-7}		1.42 × 10^{-7} - 0.06		0.06 - 20	
Flux Φ (cm^{-2} s^{-1})	(3.16 ± 1.28) × 10^{3}		(2.94 ± 0.77) × 10^{6}		(1.13 ± 0.04) × 10^{8}	
Reaction rate R (=$\Phi \cdot \langle\sigma\rangle \cdot f_n$)	(atom^{-1} s^{-1})	(%)	(atom^{-1} s^{-1})	(%)	(atom^{-1} s^{-1})	(%)
^{37}Cl(n,γ)^{38}Cl	4.55(184) × 10^{-22}	0.57	2.85(86) × 10^{-20}	36.07	5.01(69) × 10^{-20}	63.36
^{37}Cl(n,n'γ)^{37}Cl	-	-	-	-	2.03(24) × 10^{-17}	100
Cl(n,tot)	5.43(220) × 10^{-20}	0.02	2.35(69) × 10^{-17}	6.71	3.26(38) × 10^{-16}	93.27
^{144}Sm(n,γ)^{145}Sm	1.71(69) × 10^{-21}	0.02	5.89(193) × 10^{-19}	8.37	6.45(89) × 10^{-18}	91.61
^{144}Sm(n,n'γ)^{144}Sm	-	-	-	-	1.12(13) × 10^{-16}	100
^{147}Sm(n,γ)^{148}Sm	6.00(243) × 10^{-20}	0.03	1.79(53) × 10^{-16}	94.21	1.10(18) × 10^{-17}	5.75
^{147}Sm(n,n'γ)^{147}Sm	-	-	-	-	2.31(30) × 10^{-16}	100
^{148}Sm(n,γ)^{149}Sm	2.52(102) × 10^{-21}	0.01	1.47(44) × 10^{-17}	70.41	6.17(94) × 10^{-18}	29.58
^{148}Sm(n,n'γ)^{148}Sm	-	-	-	-	2.12(27) × 10^{-16}	100
^{149}Sm(n,γ)^{150}Sm	7.17(290) × 10^{-17}	16.91	3.34(99) × 10^{-16}	78.77	1.83(30) × 10^{-17}	4.32
^{149}Sm(n,n'γ)^{149}Sm	-	-	-	-	2.57(34) × 10^{-16}	100
^{150}Sm(n,γ)^{151}Sm	1.07(43) × 10^{-19}	0.11	8.66(256) × 10^{-17}	90.22	9.29(143) × 10^{-18}	9.67
^{150}Sm(n,n'γ)^{150}Sm	-	-	-	-	2.45(31) × 10^{-16}	100
^{152}Sm(n,γ)^{153}Sm	2.17(88) × 10^{-19}	0.03	6.34(186) × 10^{-16}	98.90	6.86(105) × 10^{-18}	1.07
^{152}Sm(n,n'γ)^{152}Sm	-	-	-	-	2.59(34) × 10^{-16}	100
^{154}Sm(n,γ)^{155}Sm	8.81(357) × 10^{-21}	0.05	1.47(44) × 10^{-17}	81.79	3.27(50) × 10^{-18}	18.16
^{154}Sm(n,n'γ)^{154}Sm	-	-	-	-	2.70(35) × 10^{-16}	100
Sm(n,tot)	1.00(41) × 10^{-17}	0.66	7.51(210) × 10^{-16}	49.29	7.63(70) × 10^{-16}	50.05
$TbCl_3 \cdot 6H_2O$						
^{16}O(n,γ)^{17}O	6.37(260) × 10^{-24}	0.08	8.50(275) × 10^{-23}	1.13	7.45(103) × 10^{-21}	98.79
^{16}O(n,n'γ)^{16}O	-	-	-	-	9.50(110) × 10^{-19}	100
^{16}O(n,pγ)^{16}N	-	-	-	-	7.29(88) × 10^{-21}	100
^{17}O(n,γ)^{18}O	6.34(606) × 10^{-23}	0.27	2.50(74) × 10^{-22}	1.07	2.30(30) × 10^{-20}	98.66
^{17}O(n,n'γ)^{17}O	-	-	-	-	8.71(105) × 10^{-18}	100
^{18}O(n,γ)^{19}O	4.36(260) × 10^{-24}	0.02	1.02(30) × 10^{-23}	0.04	2.54(30) × 10^{-20}	99.94
^{18}O(n,n'γ)^{18}O	-	-	-	-	3.88(47) × 10^{-17}	100
O(n,tot)	1.52(61) × 10^{-19}	0.05	2.29(72) × 10^{-17}	7.38	2.87(42) × 10^{-16}	92.57
^{35}Cl(n,γ)^{36}Cl	1.49(60) × 10^{-18}	38.95	2.25(60) × 10^{-18}	58.95	8.02(217) × 10^{-20}	2.10
^{35}Cl(n,n'γ)^{35}Cl	-	-	-	-	2.67(32) × 10^{-17}	100
^{35}Cl(n,pγ)^{35}S	1.66(67) × 10^{-20}	0.12	1.79(55) × 10^{-19}	1.33	1.33(16) × 10^{-17}	98.55
^{35}Cl(n,αγ)^{32}P	2.73(111) × 10^{-24}	≈ 0	5.28(157) × 10^{-24}	≈ 0	2.43(28) × 10^{-18}	≈ 100
^{37}Cl(n,γ)^{38}Cl	1.48(60) × 10^{-20}	14.97	3.52(106) × 10^{-20}	35.59	4.89(67) × 10^{-20}	49.44
^{37}Cl(n,n'γ)^{37}Cl	-	-	-	-	1.98(23) × 10^{-17}	100
Cl(n,tot)	1.77(72) × 10^{-18}	0.51	2.89(85) × 10^{-17}	8.30	3.18(37) × 10^{-16}	91.20
^{159}Tb(n,γ)^{160}Tb	7.98(323) × 10^{-19}	0.56	1.26(37) × 10^{-16}	88.01	1.63(26) × 10^{-17}	11.43
^{159}Tb(n,n'γ)^{159}Tb	-	-	3.45(114) × 10^{-19}	0.16	2.21(29) × 10^{-16}	99.84
Tb(n,tot)	1.07(43) × 10^{-18}	0.12	1.98(60) × 10^{-16}	21.34	7.28(100) × 10^{-16}	78.55
$DyCl_3 \cdot 6H_2O$						
^{16}O(n,γ)^{17}O	1.92(78) × 10^{-24}	0.02	8.89(287) × 10^{-23}	1.16	7.58(104) × 10^{-21}	98.82
^{16}O(n,n'γ)^{16}O	-	-	-	-	9.67(112) × 10^{-19}	100
^{16}O(n,pγ)^{16}N	-	-	-	-	7.42(89) × 10^{-21}	100
^{17}O(n,γ)^{18}O	1.91(182) × 10^{-23}	0.08	2.61(78) × 10^{-22}	1.10	2.34(30) × 10^{-20}	98.82
^{17}O(n,n'γ)^{17}O	-	-	-	-	8.86(107) × 10^{-18}	100
^{18}O(n,γ)^{19}O	1.31(78) × 10^{-24}	0.01	1.07(32) × 10^{-23}	0.04	2.58(30) × 10^{-20}	99.95
^{18}O(n,n'γ)^{18}O	-	-	-	-	3.95(48) × 10^{-17}	100
O(n,tot)	4.57(185) × 10^{-20}	0.01	2.39(76) × 10^{-17}	7.57	2.92(42) × 10^{-16}	92.41
^{35}Cl(n,γ)^{36}Cl	4.48(181) × 10^{-19}	15.53	2.36(62) × 10^{-18}	81.64	8.16(221) × 10^{-20}	2.83
^{35}Cl(n,n'γ)^{35}Cl	-	-	-	-	2.71(32) × 10^{-17}	100

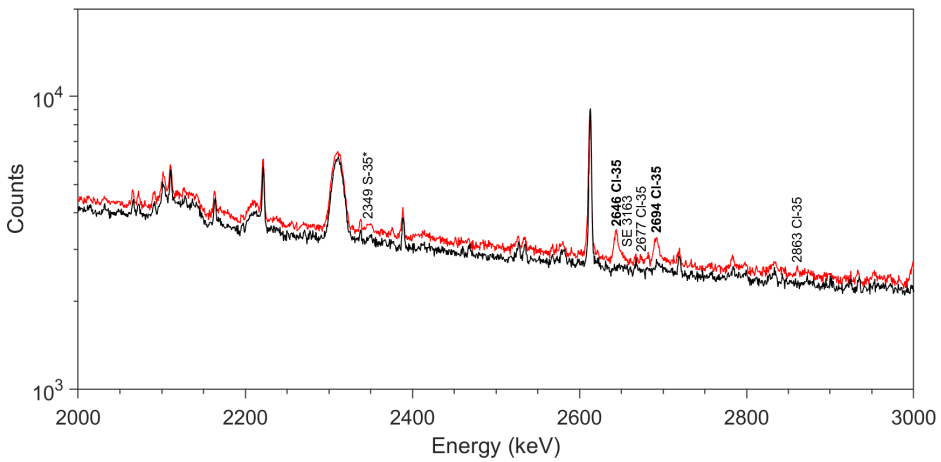
F.2 : (continued).

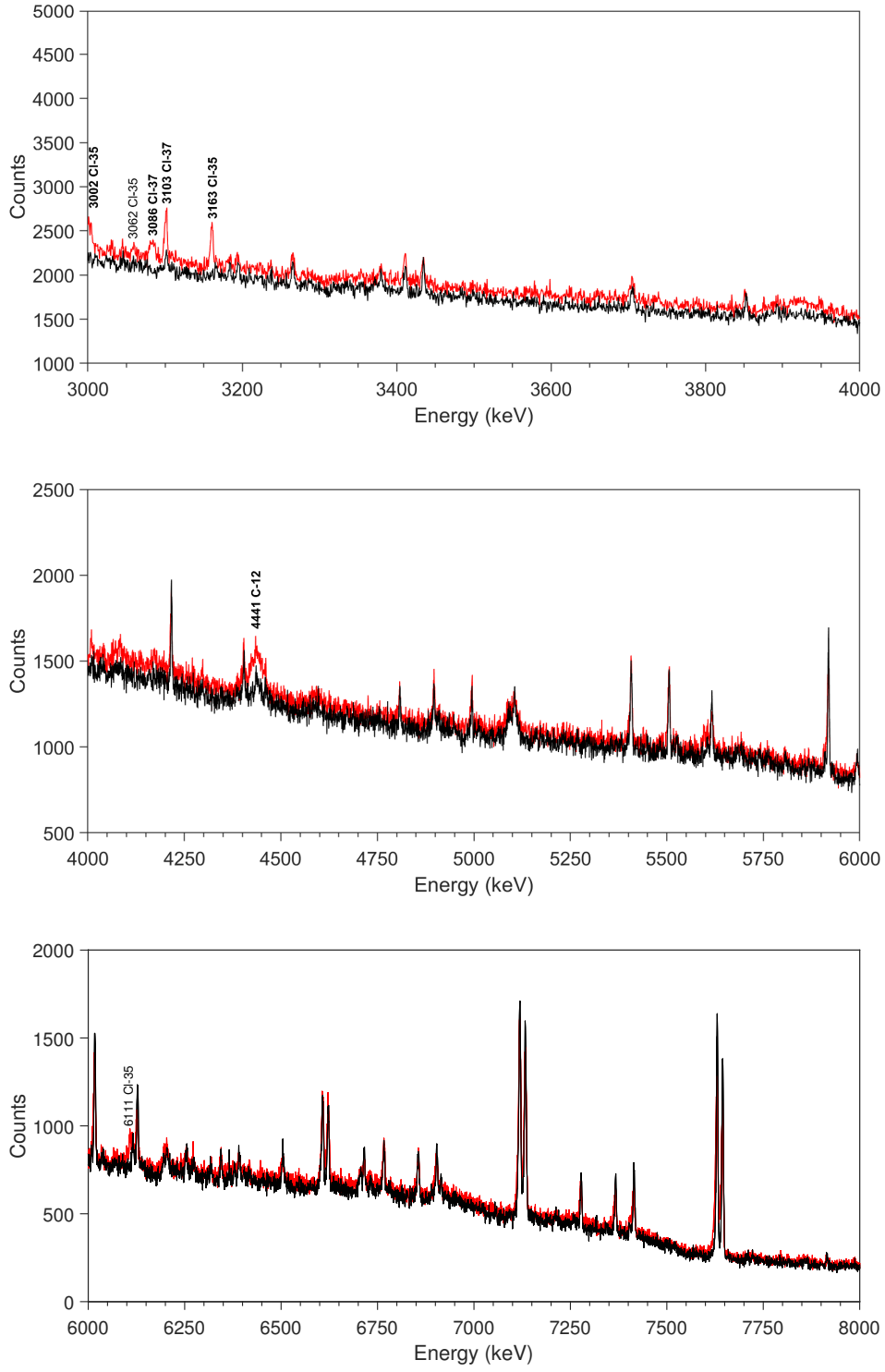
Energy range	Thermal		Epithermal		Fast	
(MeV)	10^{-10} - 1.42 $\times$ 10^{-7}		1.42 $\times$ 10^{-7} - 0.06		0.06 - 20	
Flux Φ (cm^{-2} s^{-1})	(3.16 $\pm$ 1.28) $\times$ 10^{3}		(2.94 $\pm$ 0.77) $\times$ 10^{6}		(1.13 $\pm$ 0.04) $\times$ 10^{8}	
Reaction rate R ($=\Phi \cdot \langle\sigma\rangle \cdot f_n$)	(atom^{-1} s^{-1})	(%)	(atom^{-1} s^{-1})	(%)	(atom^{-1} s^{-1})	(%)
^{35}Cl(n,pγ)^{35}S	4.99(202) $\times$ 10^{-21}	0.04	1.87(58) $\times$ 10^{-19}	1.36	1.35(16) $\times$ 10^{-17}	98.60
^{35}Cl(n,$\alpha\gamma$)^{32}P	8.23(333) $\times$ 10^{-25}	≈ 0	5.52(165) $\times$ 10^{-24}	≈ 0	2.48(29) $\times$ 10^{-18}	≈ 100
^{37}Cl(n,γ)^{38}Cl	4.45(180) $\times$ 10^{-21}	4.89	3.68(111) $\times$ 10^{-20}	40.43	4.97(68) $\times$ 10^{-20}	54.68
^{37}Cl(n,n'γ)^{37}Cl	-	-	-	-	2.01(24) $\times$ 10^{-17}	100
Cl(n,tot)	5.32(215) $\times$ 10^{-19}	0.15	3.02(89) $\times$ 10^{-17}	8.54	3.24(38) $\times$ 10^{-16}	91.31
^{156}Dy(n,γ)^{157}Dy	3.44(139) $\times$ 10^{-19}	0.12	2.39(71) $\times$ 10^{-16}	86.07	3.84(58) $\times$ 10^{-17}	13.81
^{156}Dy(n,n'γ)^{156}Dy	-	-	-	-	2.55(33) $\times$ 10^{-16}	100
^{158}Dy(n,γ)^{159}Dy	4.37(177) $\times$ 10^{-19}	0.40	8.58(257) $\times$ 10^{-17}	78.47	2.31(35) $\times$ 10^{-17}	21.13
^{158}Dy(n,n'γ)^{158}Dy	-	-	-	-	2.66(34) $\times$ 10^{-16}	100
^{160}Dy(n,γ)^{161}Dy	5.86(238) $\times$ 10^{-19}	0.20	2.82(83) $\times$ 10^{-16}	94.01	1.74(26) $\times$ 10^{-17}	5.80
^{160}Dy(n,n'γ)^{160}Dy	-	-	-	-	2.78(36) $\times$ 10^{-16}	100
^{161}Dy(n,γ)^{162}Dy	6.08(246) $\times$ 10^{-18}	2.36	2.42(72) $\times$ 10^{-16}	93.77	1.00(17) $\times$ 10^{-17}	3.88
^{161}Dy(n,n'γ)^{161}Dy	-	-	2.03(67) $\times$ 10^{-18}	0.63	3.19(43) $\times$ 10^{-16}	99.37
^{162}Dy(n,γ)^{163}Dy	2.01(81) $\times$ 10^{-18}	0.35	5.64(165) $\times$ 10^{-16}	98.44	6.90(106) $\times$ 10^{-18}	1.20
^{162}Dy(n,n'γ)^{162}Dy	-	-	-	-	2.95(38) $\times$ 10^{-16}	100
^{163}Dy(n,γ)^{164}Dy	1.32(54) $\times$ 10^{-18}	0.69	1.85(55) $\times$ 10^{-16}	96.71	4.97(84) $\times$ 10^{-18}	2.60
^{163}Dy(n,n'γ)^{163}Dy	-	-	-	-	3.22(43) $\times$ 10^{-16}	100
^{164}Dy(n,γ)^{165}Dy	2.69(109) $\times$ 10^{-17}	48.24	2.62(79) $\times$ 10^{-17}	47.06	2.62(40) $\times$ 10^{-18}	4.70
^{164}Dy(n,n'γ)^{164}Dy	-	-	-	-	2.99(39) $\times$ 10^{-16}	100
Dy(n,tot)	1.07(43) $\times$ 10^{-17}	0.89	4.11(113) $\times$ 10^{-16}	34.39	7.74(74) $\times$ 10^{-16}	64.72

G. Experimental gamma-ray spectra

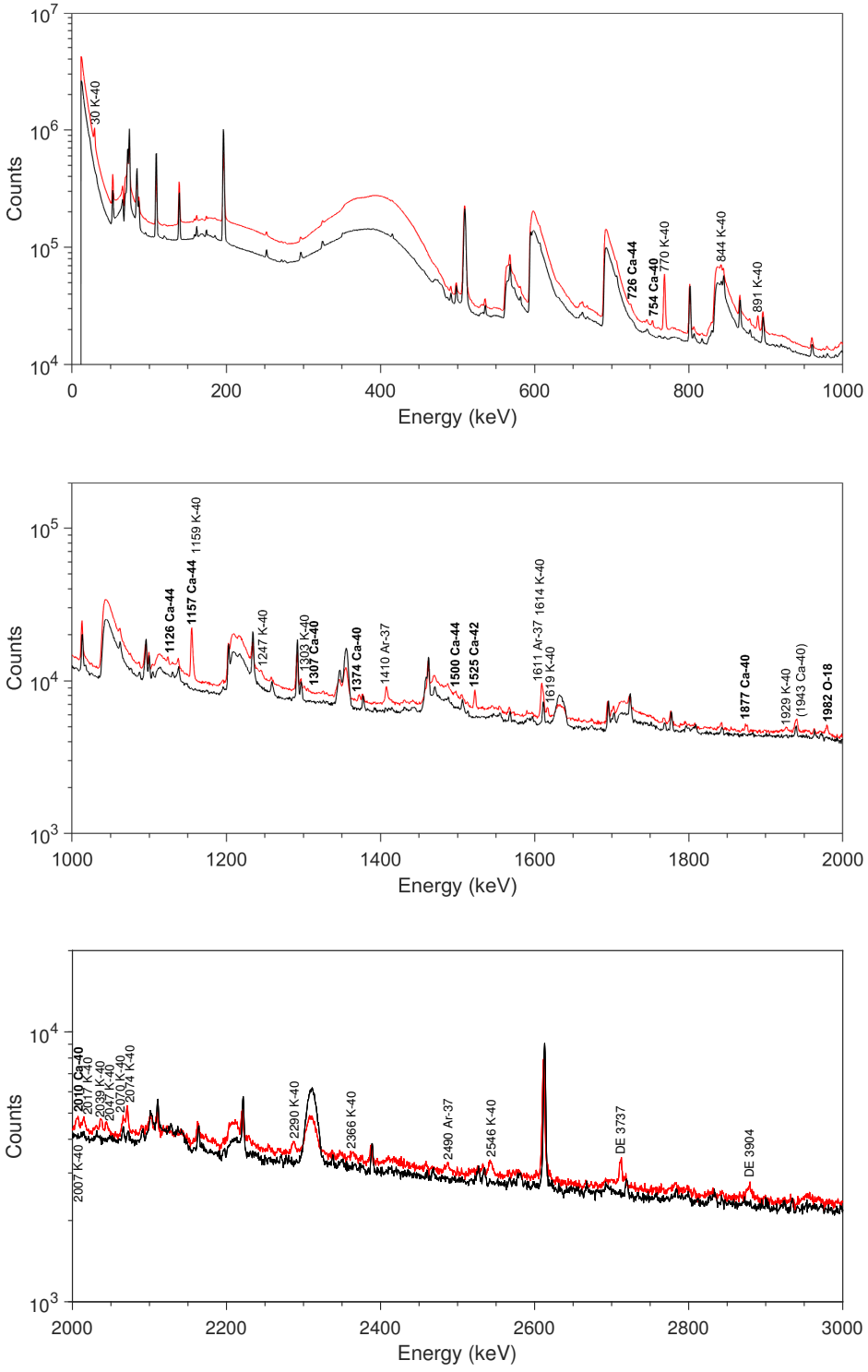


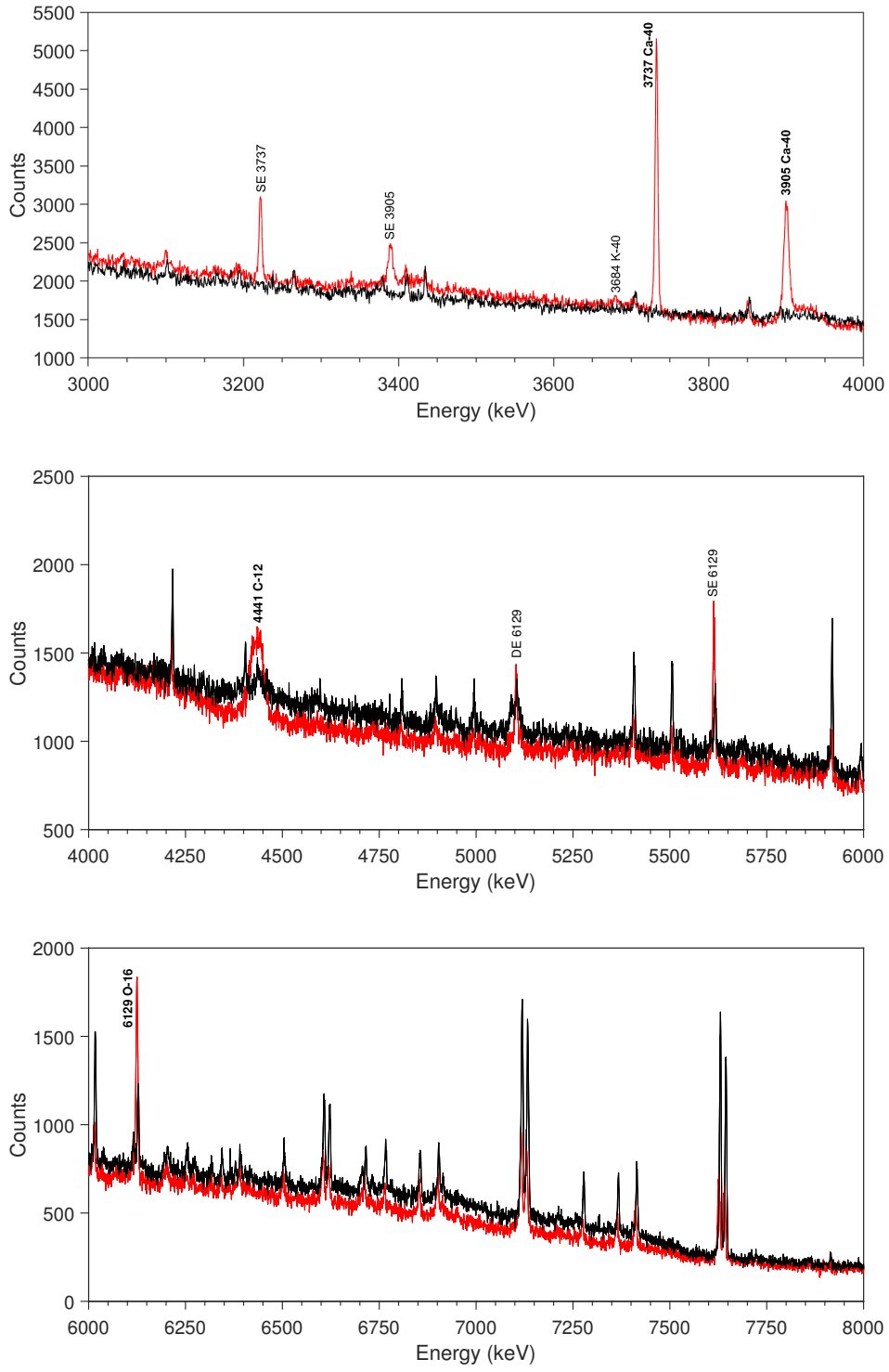




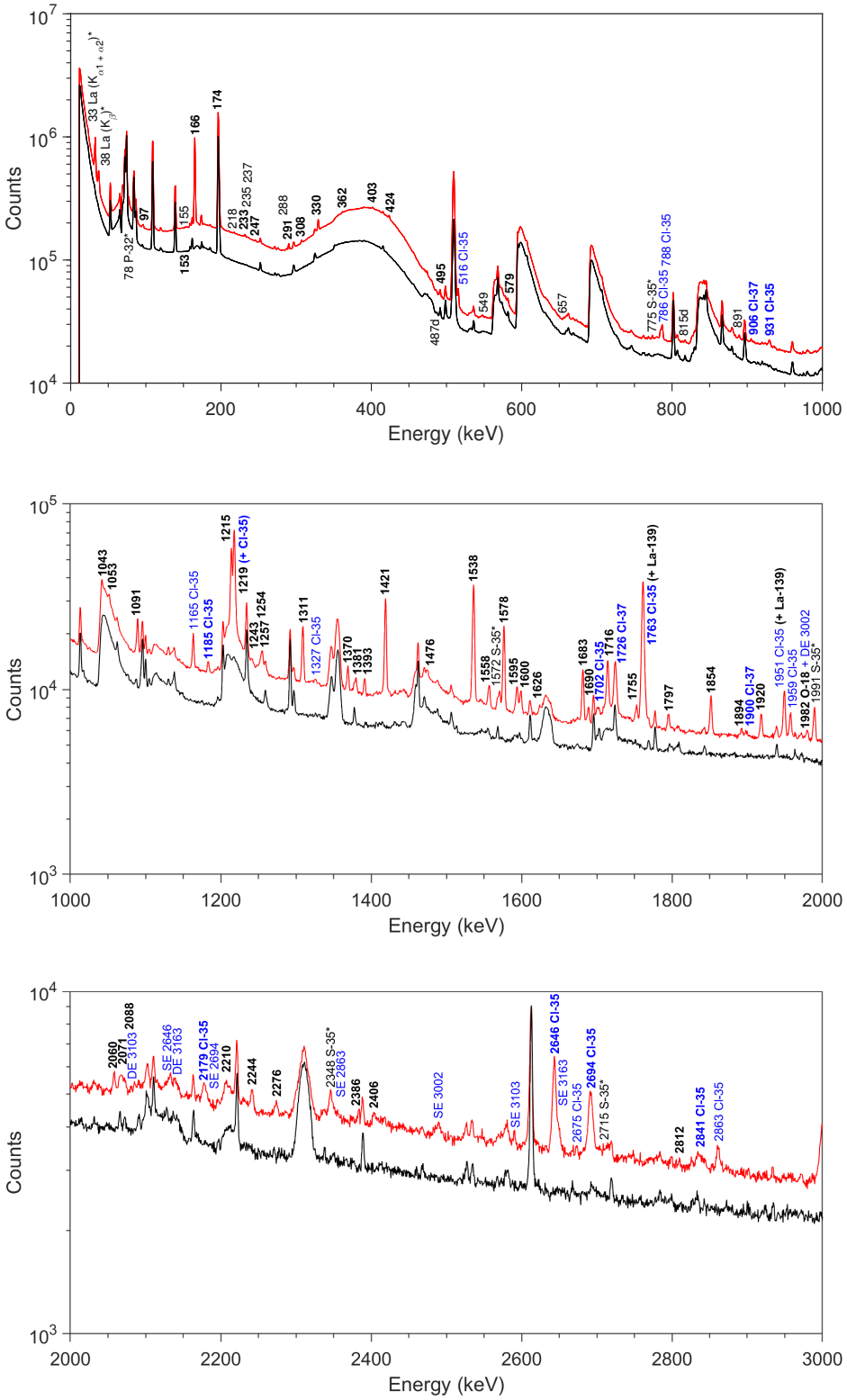


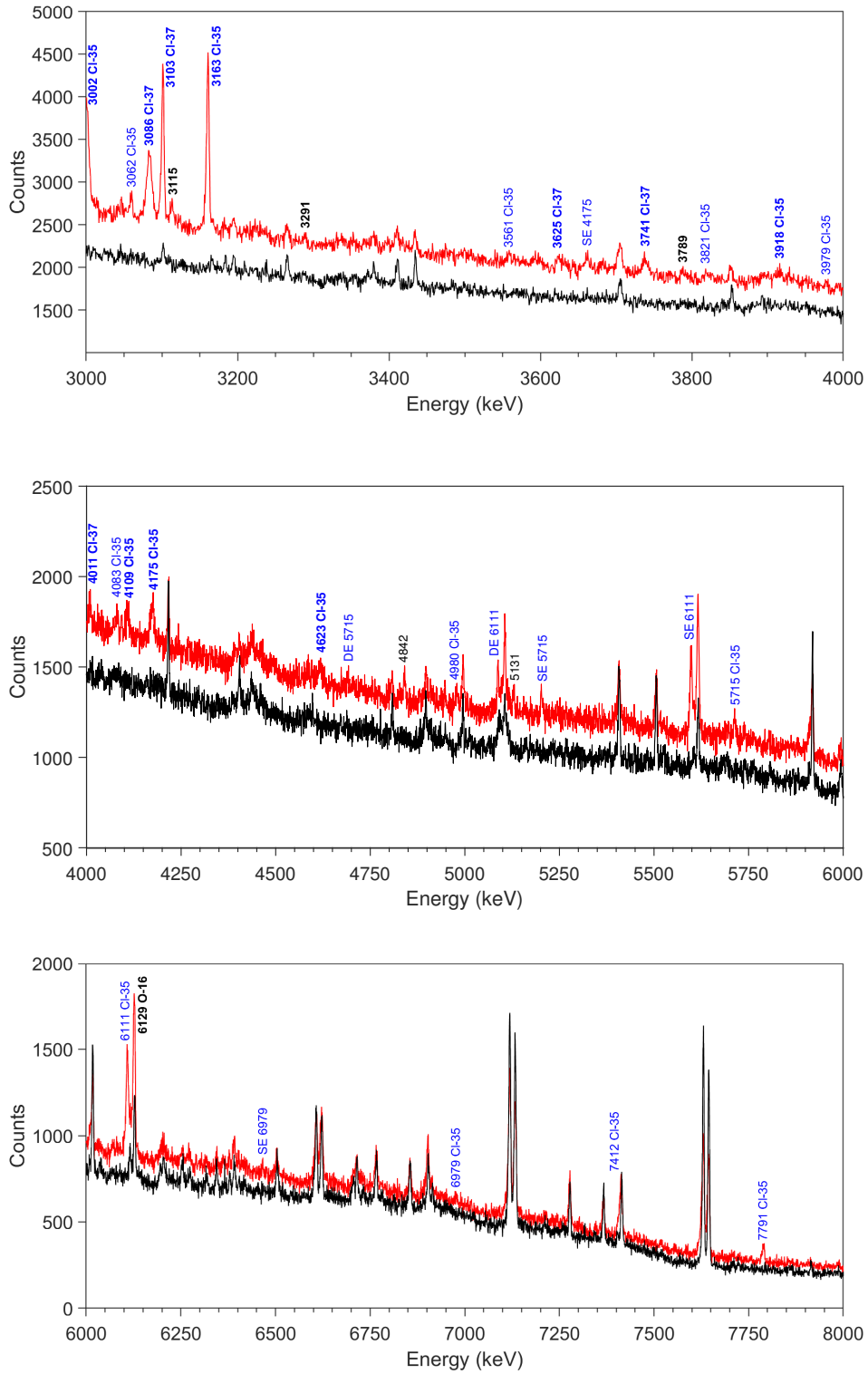
G.1 : γ-ray spectra in the energy range 0-8000 keV recorded during 55,478 s live time for the PVC sample (red) and 51,506 s for the active background (black). Prompt γ-rays of inelastic scattering in C and Cl are written in black and bold, γ-rays from (n,γ) reactions are written in black. Lines of S-35 and P-32 are due to (n,pγ) and (n,$\alpha\gamma$) reactions in Cl and are written in black with asterisks. Abbreviations SE and DE indicate single and double escape peaks, respectively.


Counts
Energy (keV)
30 K-40
726 Ca-44
754 Ca-40
770 K-40
844 K-40
891 K-40
1126 Ca-44
1157 Ca-44
1159 K-40
1247 K-40
1307 K-40
1307 Ca-40
1374 Ca-40
1410 Ar-37
1500 Ca-44
1525 Ca-42
1611 Ar-37
1614 K-40
1619 K-40
1877 Ca-40
1929 K-40
(1943 Ca-40)
1982 O-18
2007 K-40
2010 Ca-40
2017 K-40
2039 K-40
2047 K-40
2074 K-40
2290 K-40
2366 K-40
2490 Ar-37
2546 K-40
DE 3737
DE 3904

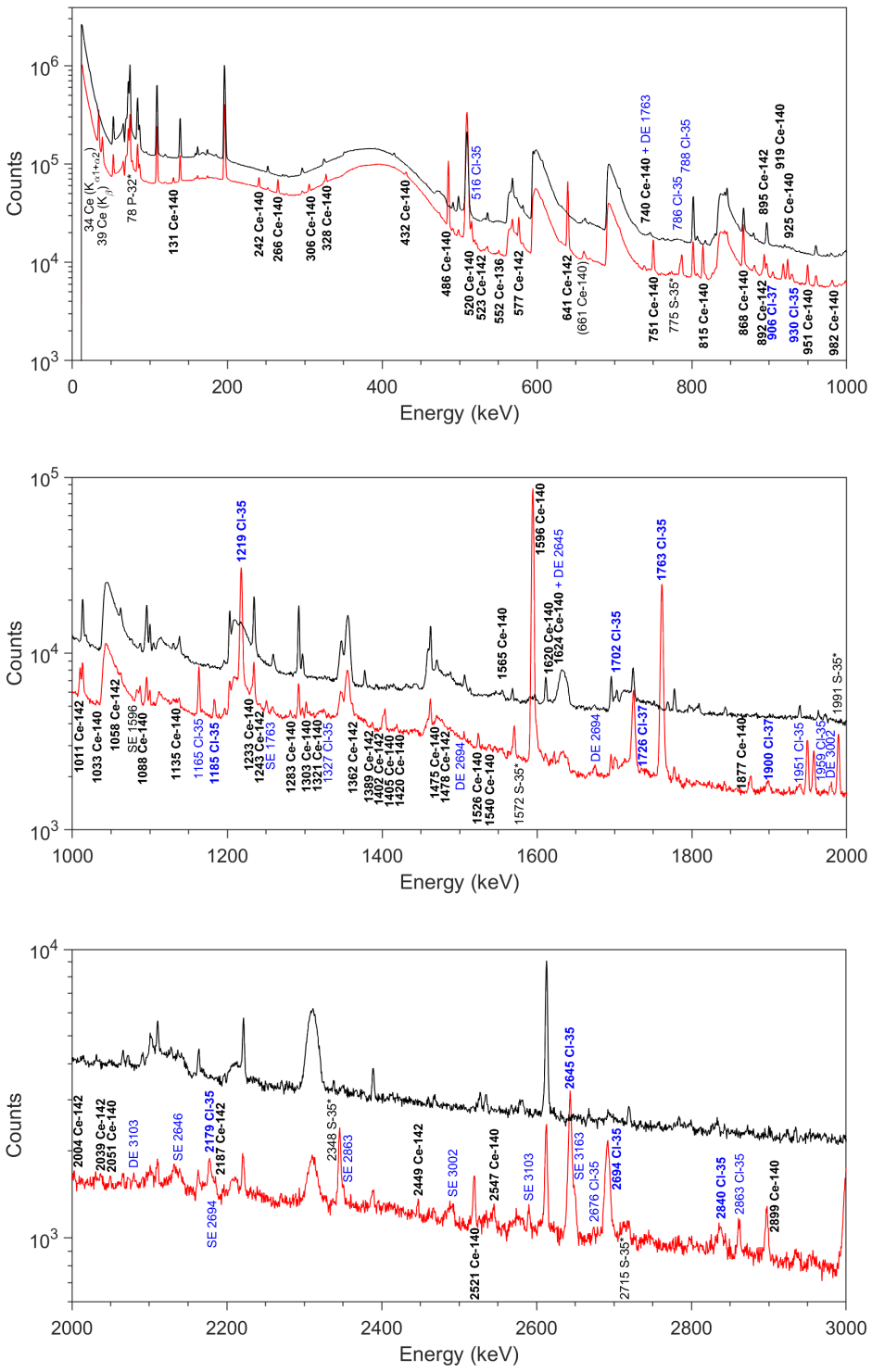


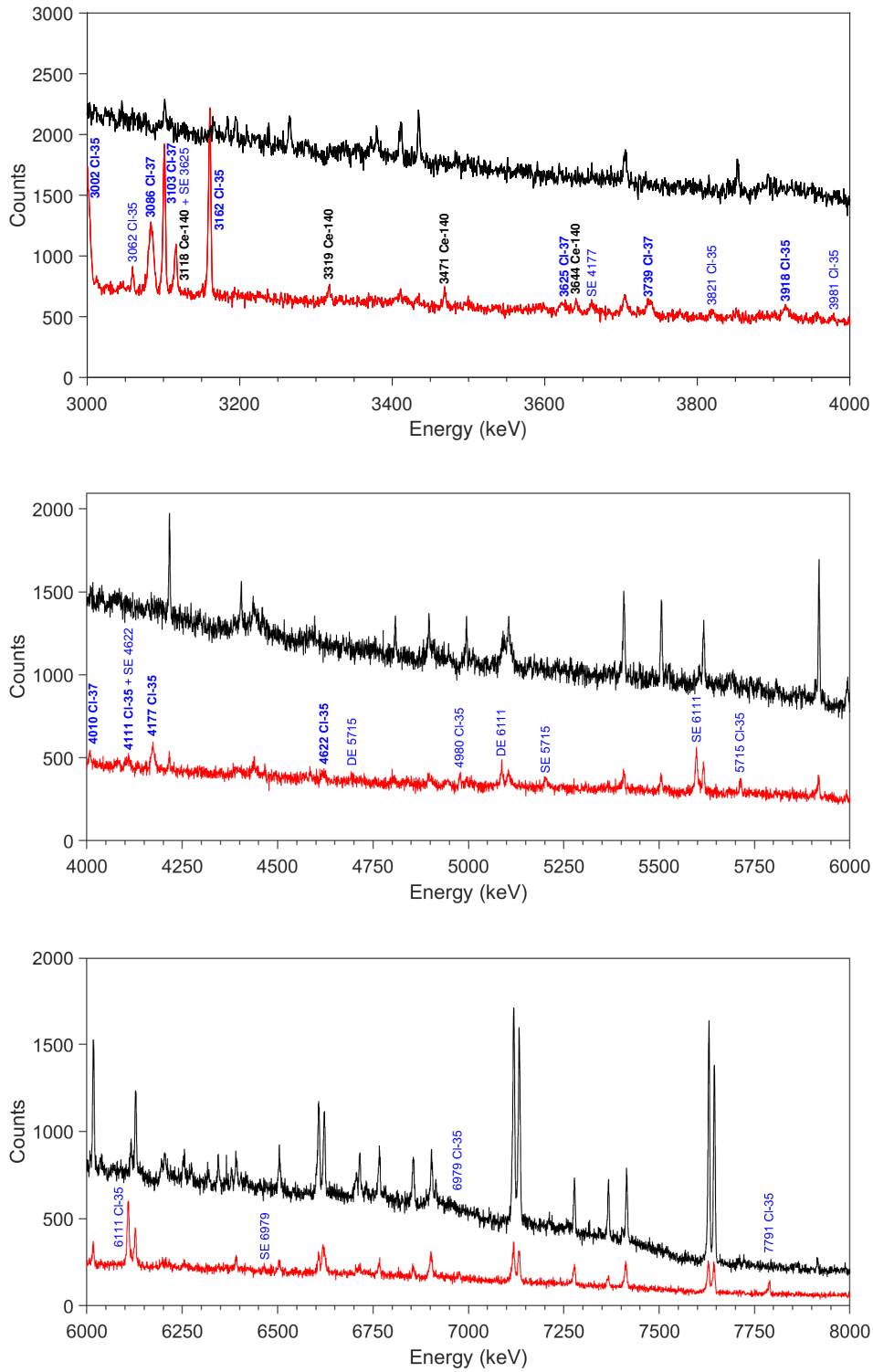
G.2 : γ-ray spectra in the energy range 0-8000 keV acquired during 23,240 s live time for the $CaCO_3$ sample (red) and 51,506 s for the active background (black). Prompt γ-rays induced by (n,pγ) reactions (K-40) and (n,$\alpha\gamma$) reactions (Ar-37) are written in black. Prompt γ-rays issued from (n,n'γ) inelastic scattering of fast neutrons are written in bold. The strongest prompt γ-ray of the (n,γ) reaction in Ca-40 might be present and is marked in black and brackets. Abbreviations SE and DE indicate single and double escape peaks, respectively.


Counts
Energy (keV)
33 La (Kα1+α2)*
38 La (Kβ)*
78 P-32*
97
153
155
166
174
218
233
235
237
247
288
291
308
330
362
403
424
487d
495
516 Cl-35
549
579
657
775 S-35*
786 Cl-35
788 Cl-35
815d
891
906 Cl-37
931 Cl-35
1043
1053
1091
1165 Cl-35
1185 Cl-35
1215
1219 (+ Cl-35)
1243
1254
1257
1311
1327 Cl-35
1370
1383
1393
1421
1476
1538
1558
1572 S-35*
1578
1595
1600
1626
1683
1690
1702 Cl-35
1716
1728 Cl-37
1755
1763 Cl-35 (+ La-139)
1797
1854
1894
1900 Cl-37
1920
1951 Cl-35 (+ La-139)
1959 Cl-35
1982 O-18 + DE 3002
1991 S-35*
2060
2071
2088
DE 3103
SE 2646
DE 3163
2179 Cl-35
SE 2694
2210
2244
2276
2348 S-35*
SE 2863
2386
2406
SE 3002
SE 3103
2646 Cl-35
SE 3163
2675 Cl-35
2694 Cl-35
2715 S-35*
2812
2841 Cl-35
2863 Cl-35

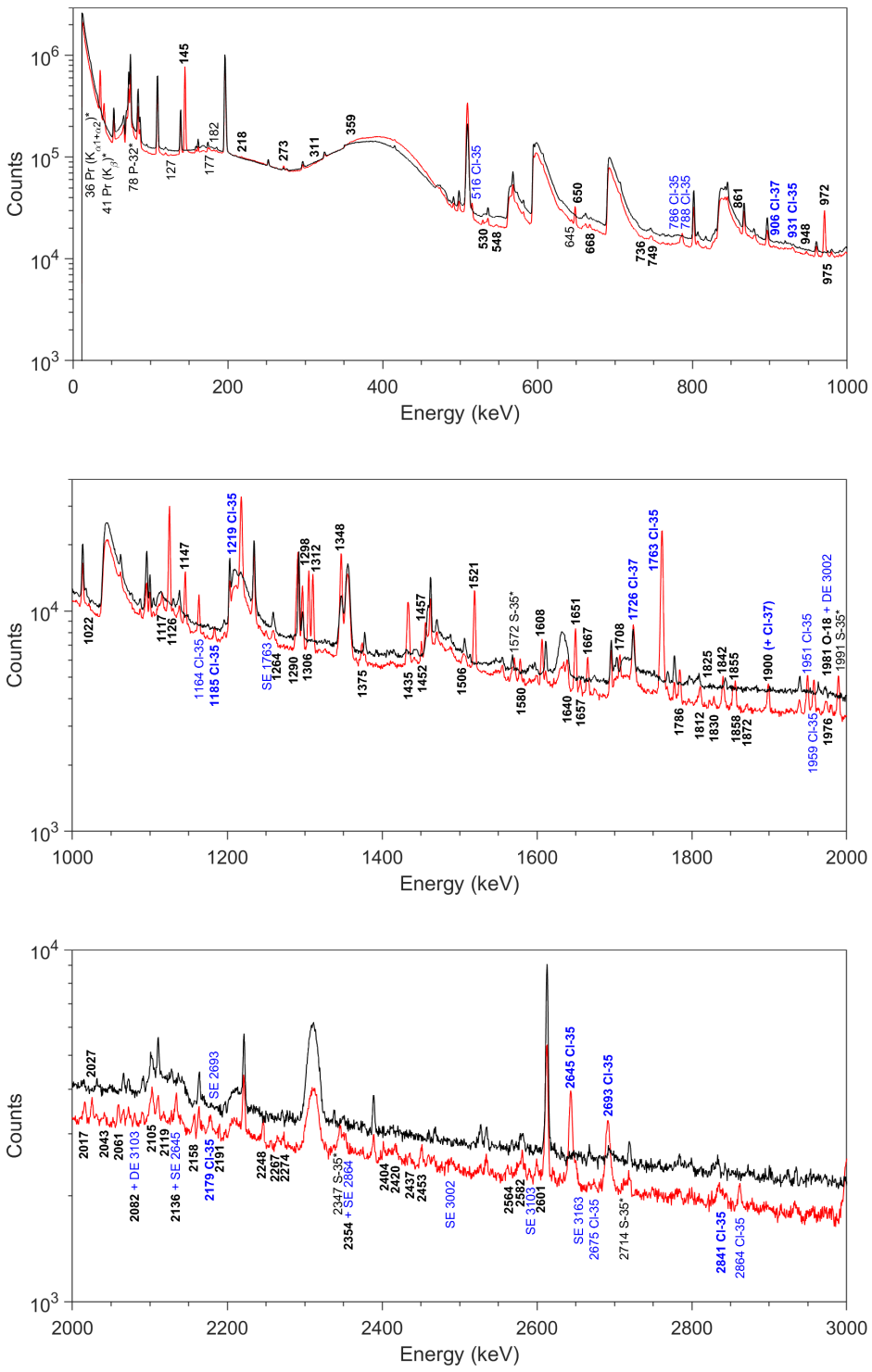


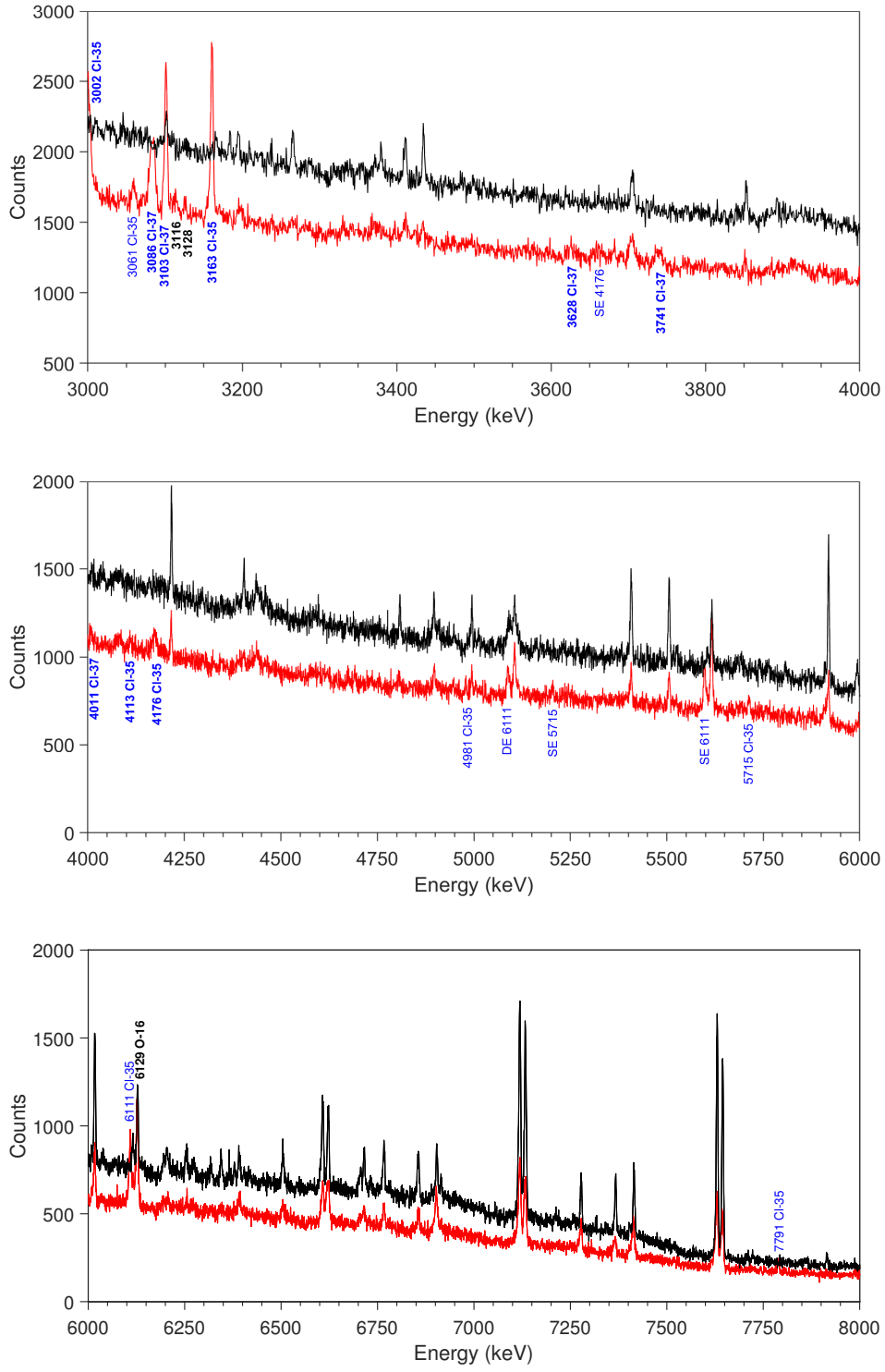
G.3 : γ-ray spectra in the energy range 0-8000 keV acquired during 39,357 s live time for $LaCl_3{\cdot}7H_2O$ (red) and 51,506 s (black) for the active background (black). Prompt γ-rays of inelastic scattering in La-139 and O are written in black and bold, γ-rays from (n,γ) reactions are written in black. γ-rays of Cl are written in blue, bold if (n,n'γ) reaction. Lines of S-35 and P-32 are due to (n,pγ) and (n,$\alpha\gamma$) reactions in Cl and are written in black with asterisks. X-rays are also written in black with asterisks and denoted with K. Abbreviations SE and DE indicate single and double escape peaks, respectively.


Counts
Energy (keV)
34 Ce (K_α1+α2)
39 Ce (K_β)
78 P-32*
131 Ce-140
242 Ce-140
266 Ce-140
306 Ce-140
328 Ce-140
432 Ce-140
486 Ce-140
516 Cl-35
520 Ce-140
523 Ce-142
552 Ce-136
577 Ce-142
641 Ce-142
(661 Ce-140)
740 Ce-140 + DE 1763
751 Ce-140
775 S-35*
786 Cl-35
788 Cl-35
815 Ce-140
868 Ce-140
892 Ce-142
895 Ce-142
906 Cl-37
919 Ce-140
925 Ce-140
930 Cl-35
951 Ce-140
982 Ce-140
1011 Ce-142
1033 Ce-140
1058 Ce-142
SE 1596
1088 Ce-140
1135 Ce-140
1165 Cl-35
1185 Cl-35
1219 Cl-35
1233 Ce-140
1243 Ce-142
SE 1763
1283 Ce-140
1303 Ce-140
1321 Ce-140
1327 Cl-35
1362 Ce-142
1389 Ce-142
1402 Ce-142
1405 Ce-140
1420 Ce-140
1475 Ce-140
1478 Ce-142
DE 2694
1526 Ce-140
1540 Ce-140
1565 Ce-140
1572 S-35*
1596 Ce-140
1620 Ce-140
1624 Ce-140 + DE 2645
1702 Cl-35
1726 Cl-37
1763 Cl-35
DE 2694
1877 Ce-140
1900 Cl-37
1951 Cl-35
1959 Cl-35
DE 3002
1991 S-35*
2004 Ce-142
2039 Ce-142
2051 Ce-140
DE 3103
SE 2646
2179 Cl-35
2187 Ce-142
SE 2694
2348 S-35*
SE 2863
2449 Ce-142
SE 3002
2521 Ce-140
2547 Ce-140
SE 3103
2645 Cl-35
SE 3163
2676 Cl-35
2694 Cl-35
2715 S-35*
2840 Cl-35
2863 Cl-35
2899 Ce-140

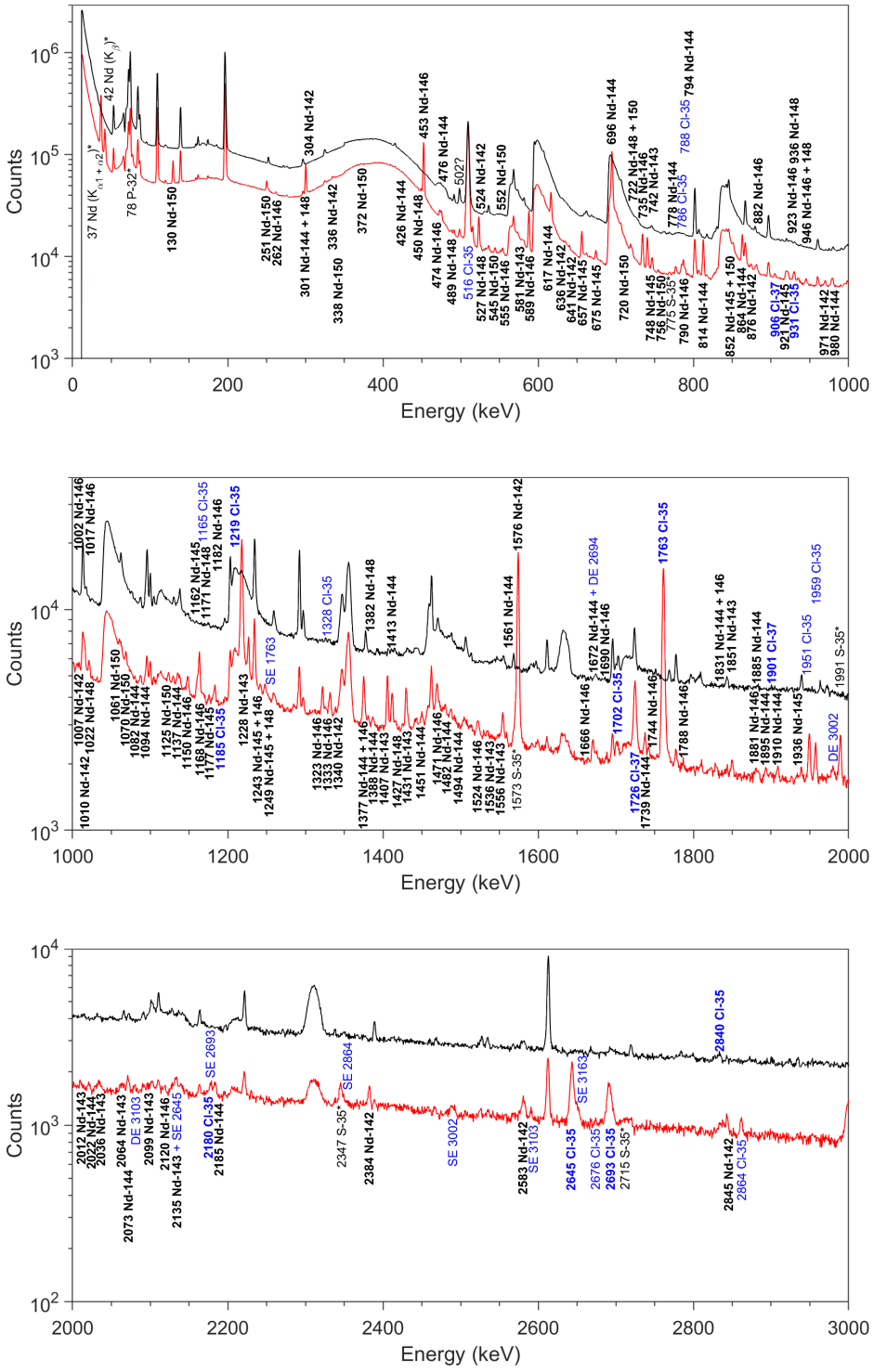


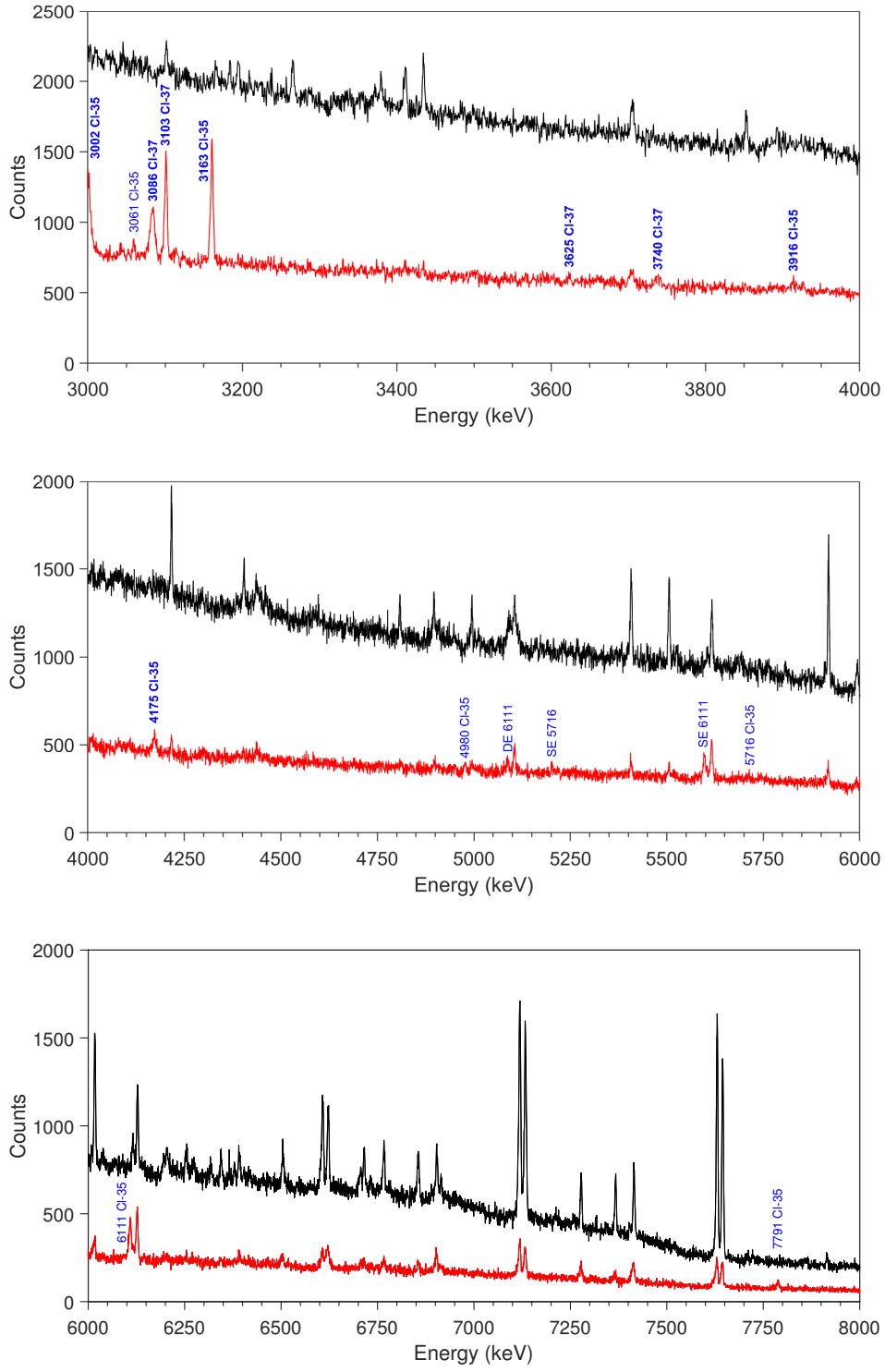
G.4 : γ-ray spectra in the energy range 0-8000 keV acquired during 9,743 s live time for $CeCl_3$ (red) and 51,506 s for the active background (black). Prompt γ-rays of inelastic scattering in Ce are written in black and bold. The strongest prompt γ-ray of the (n,γ) reaction in Ce-140 might be present and is marked in black and brackets. γ-rays of Cl are written in blue, bold if (n,n'γ) reaction. Lines of S-35 and P-32 are due to (n,pγ) and (n,$\alpha\gamma$) reactions in Cl and are written in black with asterisks. X-rays are also written in black with asterisks and denoted with K. Abbreviations SE and DE indicate single and double escape peaks, respectively.


Counts
Energy (keV)
36 Pr (K$_{\alpha1+\alpha2}$)*
41 Pr (K$_\beta$)*
78 P-32*
127
145
177
182
218
273
311
359
516 Cl-35
530
548
645
650
668
726
749
786 Cl-35
788 Cl-35
861
906 Cl-37
931 Cl-35
948
972
975
1022
1117
1126
1147
1164 Cl-35
1185 Cl-35
1219 Cl-35
SE 1783
1264
1290
1306
1312
1348
1375
1435
1452
1457
1506
1521
1572 S-35*
1580
1608
1640
1657
1651
1667
1708
1726 Cl-37
1763 Cl-35
1786
1812
1830
1825
1842
1855
1858
1872
1900 (+ Cl-37)
1951 Cl-35
1959 Cl-35
1976
1981 O-18 + DE 3002
1991 S-35*
2017
2027
2043
2061
2082 + DE 3103
2105
2119
2136 + SE 2645
2158
2179 Cl-35
2191
SE 2693
2248
2267
2274
2347 S-35*
2354 + SE 2864
2404
2420
2437
2453
SE 3002
2564
2582
SE 3103
2601
2645 Cl-35
SE 3163
2675 Cl-35
2714 S-35*
2693 Cl-35
2841 Cl-35
2864 Cl-35

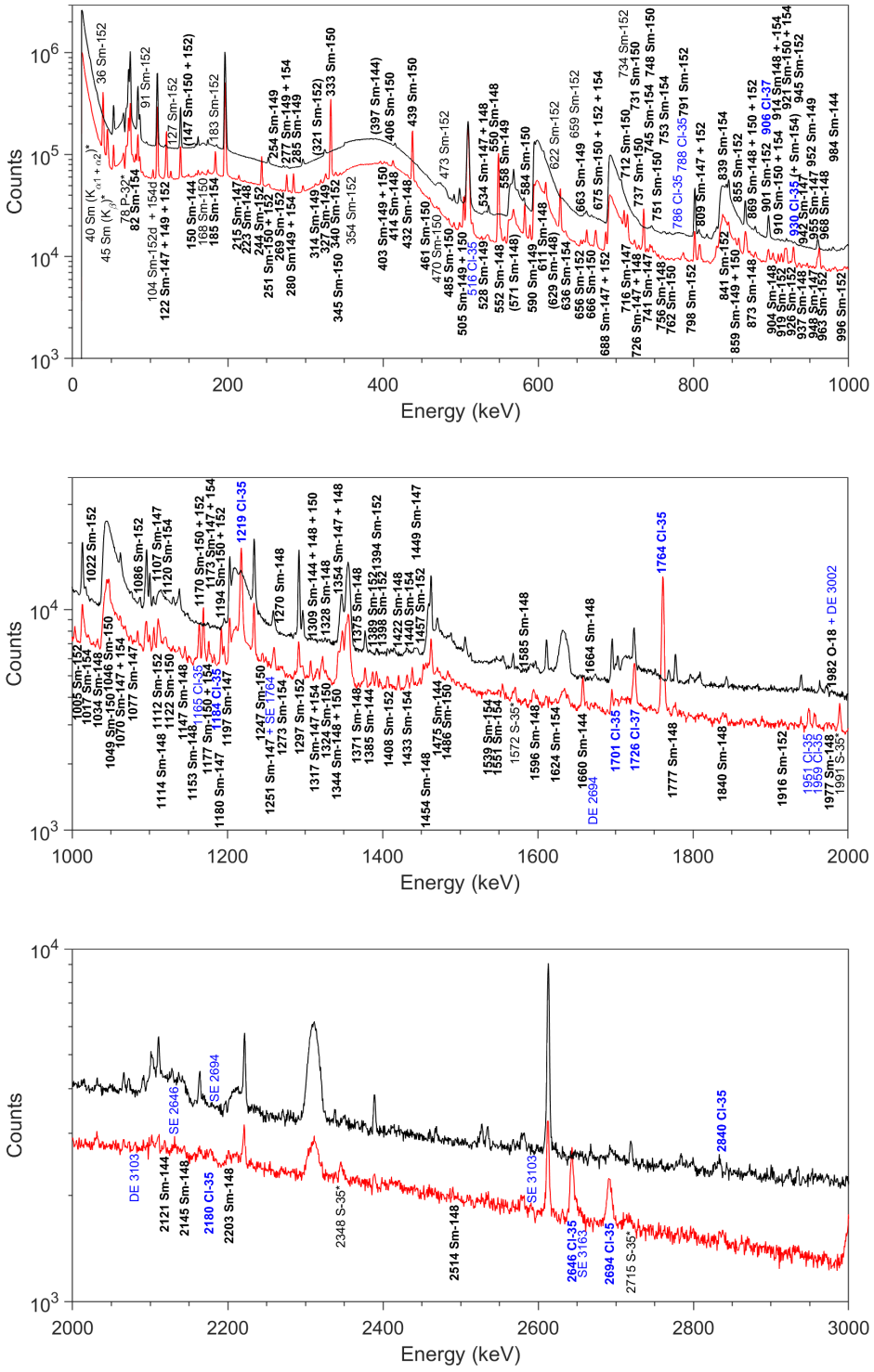


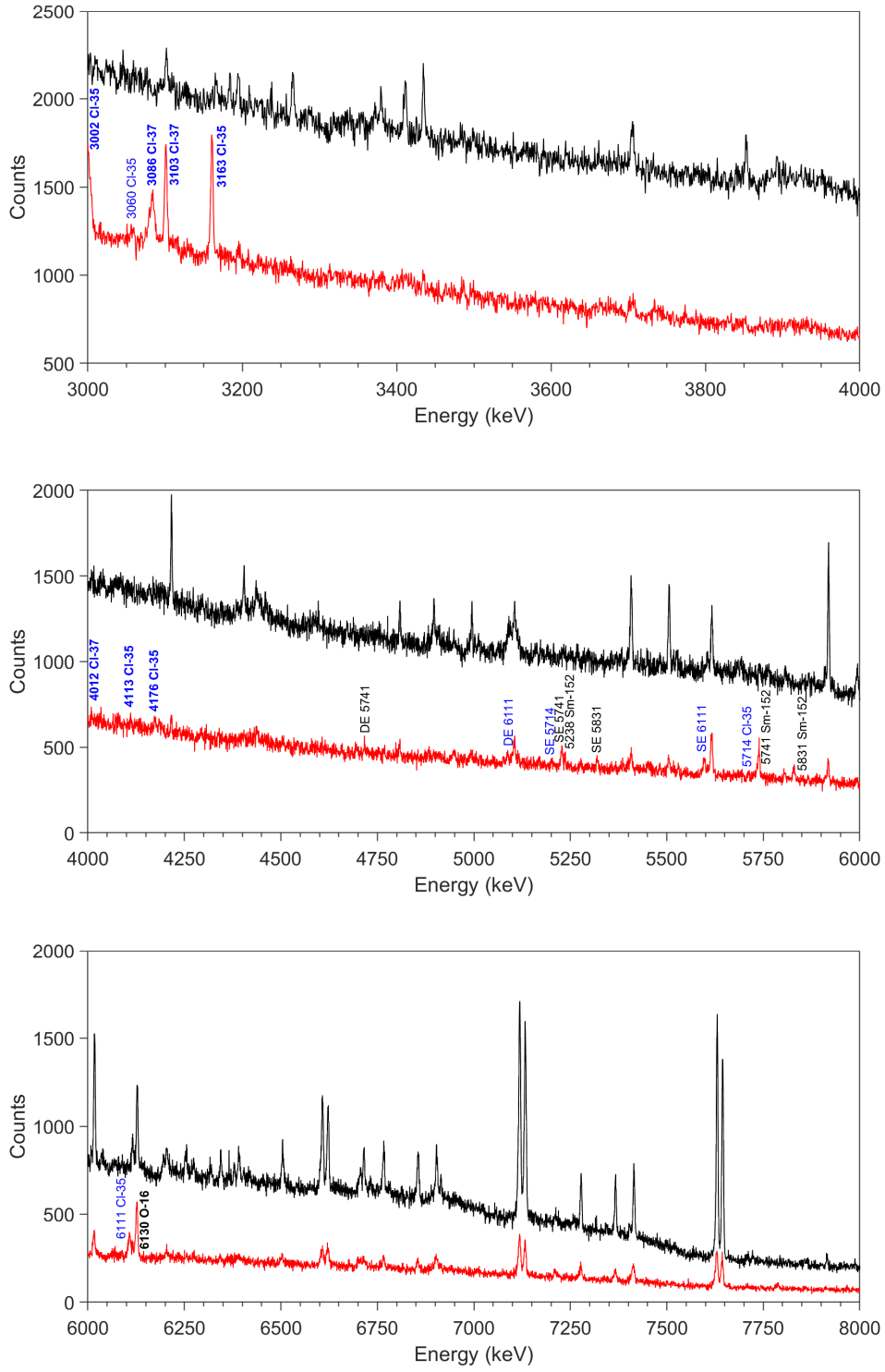
G.5 : γ-ray spectra in the energy range 0-8000 keV acquired during 22,580 s live time for $PrCl_3 \cdot 7H_2O$ (red) and 51,506 s for the active background (black). Prompt γ-rays of inelastic scattering in Pr-141 and O are written in black and bold, γ-rays from (n,γ) reactions are written in black. γ-rays of Cl are written in blue, bold if (n,n'γ) reaction. Lines of S-35 and P-32 are due to (n,pγ) and (n,$\alpha\gamma$) reactions in Cl and are written in black with asterisks. X-rays are also written in black with asterisks and denoted with K. Abbreviations SE and DE indicate single and double escape peaks, respectively.


Counts
Energy (keV)
37 Nd (Kα1 + α2)*
42 Nd (Kβ)*
78 P-32*
130 Nd-150
251 Nd-150
262 Nd-146
301 Nd-144 + 148
304 Nd-142
336 Nd-142
338 Nd-150
372 Nd-150
426 Nd-144
450 Nd-148
453 Nd-146
474 Nd-146
476 Nd-144
489 Nd-148
516 Cl-35
5022
524 Nd-142
527 Nd-148
545 Nd-150
552 Nd-150
555 Nd-146
581 Nd-143
589 Nd-146
617 Nd-144
636 Nd-142
641 Nd-142
657 Nd-145
675 Nd-145
696 Nd-144
720 Nd-150
722 Nd-146
735 Nd-148 + 150
742 Nd-143
748 Nd-145
756 Nd-150
775 S-35*
778 Nd-144
788 Cl-35
788 Cl-35
790 Nd-146
794 Nd-144
814 Nd-144
852 Nd-145 + 150
864 Nd-144
876 Nd-142
882 Nd-146
906 Cl-37
923 Nd-145
931 Cl-35
923 Nd-146
936 Nd-148
946 Nd-146 + 148
971 Nd-142
980 Nd-144
1002 Nd-146
1007 Nd-142
1010 Nd-142
1017 Nd-146
1022 Nd-148
1061 Nd-150
1070 Nd-150
1082 Nd-144
1094 Nd-144
1125 Nd-150
1137 Nd-144
1153 Nd-146
1159 Nd-145
1171 Nd-145
1185 Cl-35
1162 Nd-145
1165 Cl-35
1171 Nd-148
1182 Nd-146
1219 Cl-35
1228 Nd-143
1243 Nd-145 + 146
1249 Nd-145 + 148
SE 1763
1323 Nd-146
1328 Cl-35
1333 Nd-148
1340 Nd-142
1377 Nd-144 + 146
1382 Nd-148
1388 Nd-144
1407 Nd-143
1413 Nd-144
1427 Nd-148
1431 Nd-143
1451 Nd-144
1471 Nd-146
1482 Nd-144
1494 Nd-144
1524 Nd-146
1536 Nd-143
1556 Nd-143
1561 Nd-144
1573 S-35*
1576 Nd-142
1666 Nd-146
1672 Nd-144 + DE 2694
1690 Nd-146
1702 Cl-35
1726 Cl-37
1739 Nd-144
1744 Nd-146
1763 Cl-35
1788 Nd-146
1831 Nd-144 + 146
1851 Nd-143
1881 Nd-146
1885 Nd-144
1895 Nd-144
1901 Cl-37
1910 Nd-144
1936 Nd-145
1951 Cl-35
1959 Cl-35
1991 S-35*
DE 3002
2012 Nd-143
2032 Nd-144
2036 Nd-143
2064 Nd-143
DE 3103
2073 Nd-144
2099 Nd-143
2120 Nd-146
2135 Nd-143 + SE 2645
2180 Cl-35
SE 2693
2185 Nd-144
2347 S-35*
SE 2864
2384 Nd-142
SE 3002
2583 Nd-142
SE 3103
2645 Cl-35
SE 3163
2676 Cl-35
2693 Cl-35
2715 S-35*
2840 Cl-35
2845 Nd-142
2864 Cl-35

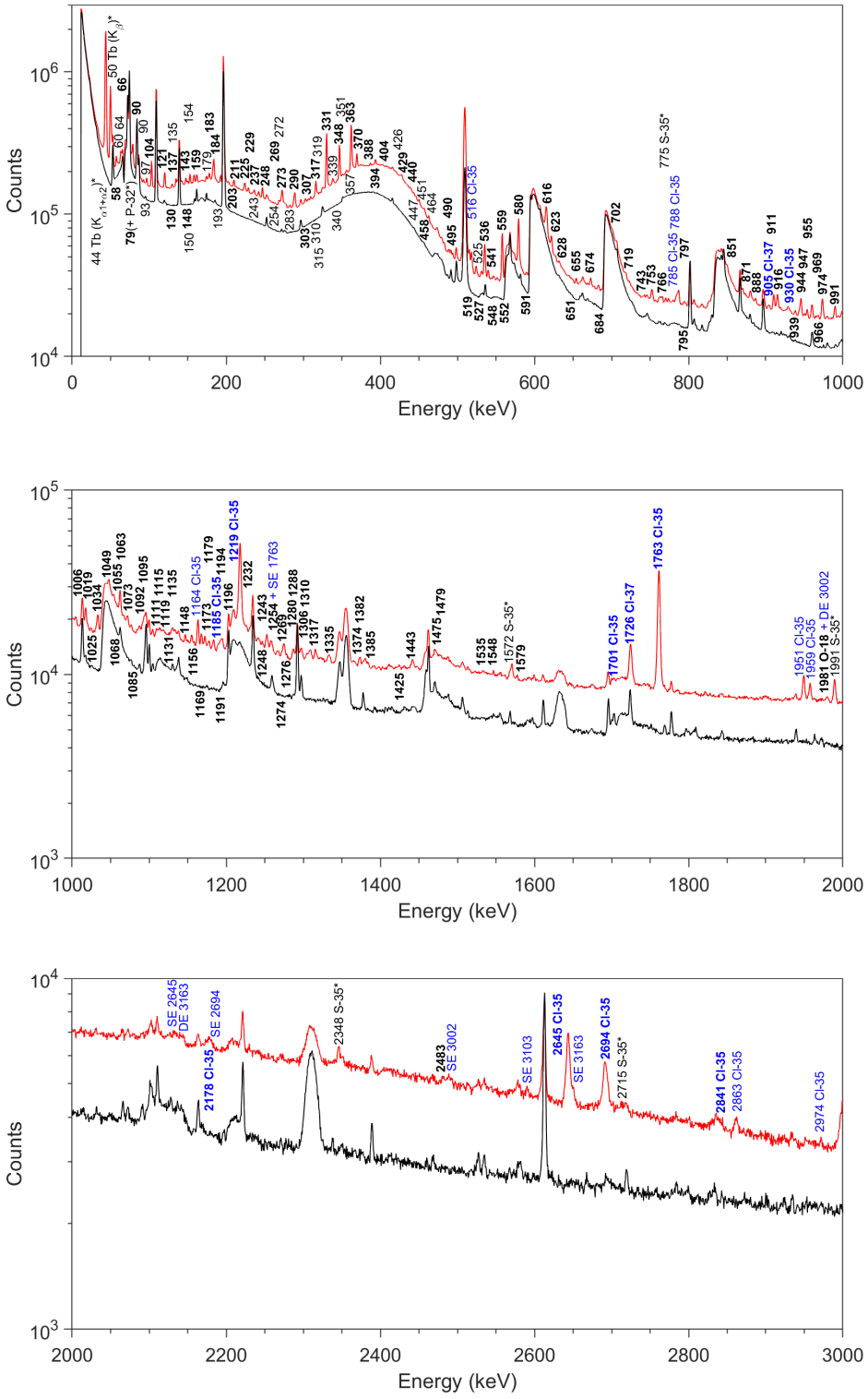


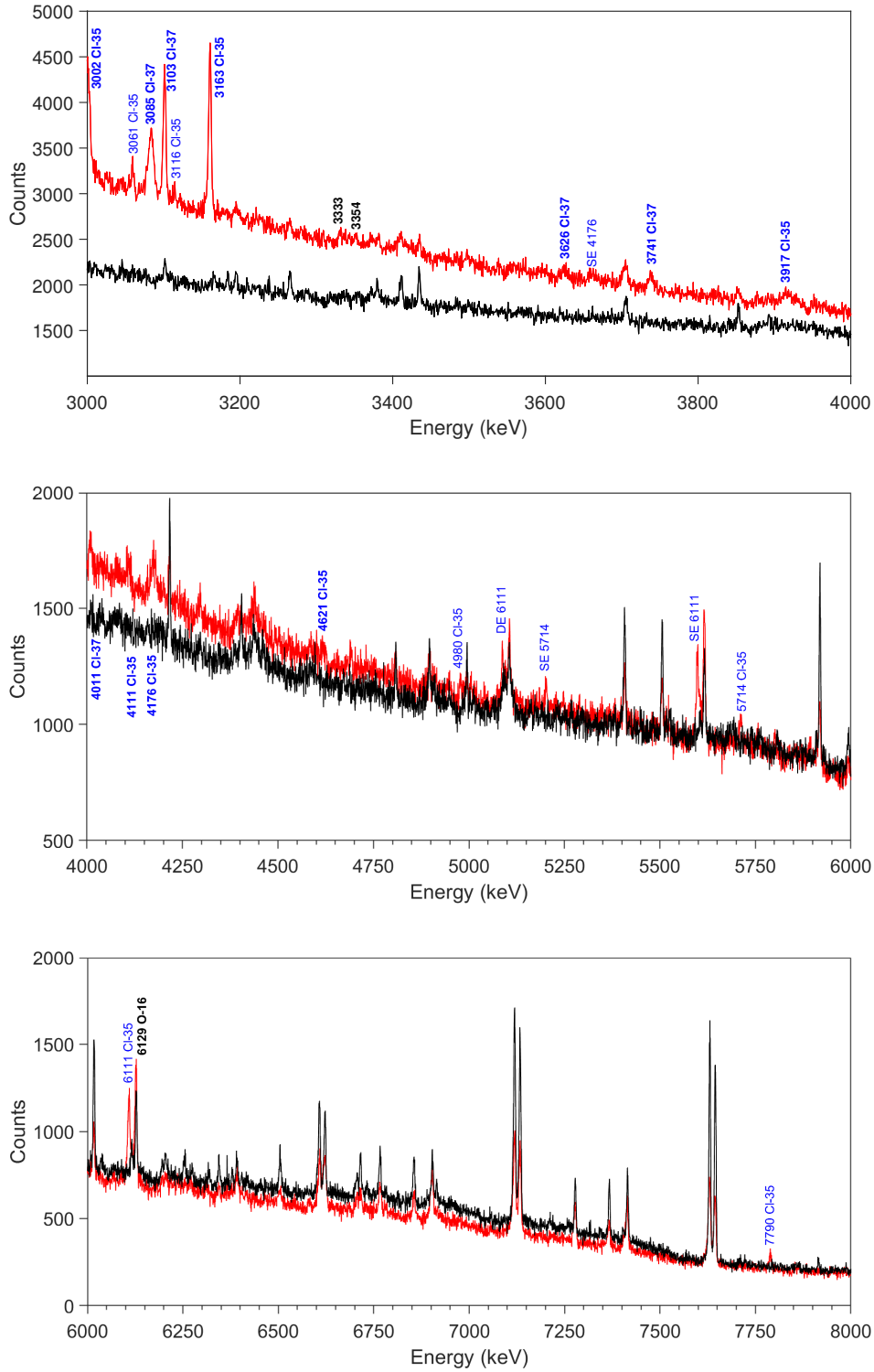
G.6 : γ-ray spectra in the energy range 0-8000 keV acquired during 8,886 s live time for $NdCl_3$ (red) and 51,506 s for the active background (black). Prompt γ-rays of inelastic scattering in Nd are written in black and bold, γ-rays from (n,γ) reactions are written in black. γ-rays of Cl are written in blue, bold if (n,n'γ) reaction. Lines of S-35 and P-32 are due to (n,pγ) and (n,$\alpha\gamma$) reactions in Cl and are written in black with asterisks. X-rays are also written in black with asterisks and denoted with K. Abbreviations SE and DE indicate single and double escape peaks, respectively.


Counts
Energy (keV)
40 Sm (Kα1 + α2)*
45 Sm (Kβ)*
36 Sm-152
78 P-32*
82 Sm-154
91 Sm-152
104 Sm-152d + 154d
122 Sm-147 + 149 + 152
127 Sm-152
(147 Sm-150 + 152)
150 Sm-144
168 Sm-150
183 Sm-152
185 Sm-154
215 Sm-147
223 Sm-148
244 Sm-152
251 Sm-150 + 152
254 Sm-149
269 Sm-152
277 Sm-149 + 154
280 Sm149 + 154
285 Sm-149
314 Sm-149
321 Sm-152)
327 Sm-149
333 Sm-150
340 Sm-152
345 Sm-150
354 Sm-152
(397 Sm-144)
403 Sm-149 + 150
406 Sm-150
414 Sm-148
432 Sm-148
439 Sm-150
461 Sm-150
470 Sm-150
473 Sm-152
485 Sm-150
505 Sm-149 + 150
513 Sm-150
528 Sm-149
534 Sm-147 + 148
550 Sm-149
552 Sm-148
558 Sm-149
(571 Sm-148)
584 Sm-150
590 Sm-149
611 Sm-148
622 Sm-152
(629 Sm-148)
636 Sm-154
656 Sm-152
659 Sm-152
663 Sm-149
666 Sm-150
675 Sm-150 + 152 + 154
688 Sm-147 + 152
716 Sm-147
726 Sm-147 + 148
734 Sm-152
712 Sm-150
731 Sm-150
737 Sm-150
741 Sm-147
745 Sm-154
748 Sm-150
751 Sm-150
753 Sm-154
756 Sm-148
762 Sm-150
786 Cl-35
788 Cl-35
791 Sm-152
798 Sm-152
809 Sm-147 + 152
839 Sm-154
841 Sm-152
855 Sm-152
859 Sm-149 + 150
869 Sm-148 + 150 + 152
873 Sm-148
901 Sm-152
906 Cl-37
904 Sm-148
910 Sm-150 + 154
914 Sm148 + -154
919 Sm-152
921 Sm-150 + 154
926 Sm-152
930 Cl-35 (+ Sm-154)
937 Sm-148
942 Sm-147
943 Sm-152
948 Sm-147
955 Sm-147
952 Sm-149
963 Sm-147
968 Sm-148
984 Sm-144
996 Sm-152
1005 Sm-152
1017 Sm-154
1022 Sm-152
1034 Sm-148
1049 Sm-150
1070 Sm-147 + 154
1077 Sm-147
1086 Sm-152
1107 Sm-147
1112 Sm-152
1114 Sm-148
1120 Sm-154
1122 Sm-150
1147 Sm-148
1153 Sm-148
1165 Cl-35
1170 Sm-150 + 152
1173 Sm-147 + 154
1177 Sm-150 + 154
1180 Sm-147
1184 Cl-35
1194 Sm-150 + 152
1197 Sm-147
1219 Cl-35
1247 Sm-150
1251 Sm-147
+ SE 1764
1270 Sm-148
1273 Sm-154
1297 Sm-152
1309 Sm-144 + 148 + 150
1317 Sm-147 +154
1324 Sm-150
1328 Sm-148
1344 Sm-148 + 150
1354 Sm-147 + 148
1371 Sm-148
1375 Sm-148
1385 Sm-144
1389 Sm-152
1394 Sm-152
1398 Sm-152
1408 Sm-152
1422 Sm-148
1433 Sm-154
1440 Sm-154
1449 Sm-147
1454 Sm-148
1457 Sm-152
1475 Sm-144
1486 Sm-150
1538 Sm-154
1551 Sm-154
1572 S-35*
1585 Sm-148
1596 Sm-148
1624 Sm-154
1660 Sm-144
DE 2694
1664 Sm-148
1701 Cl-35
1726 Cl-37
1764 Cl-35
1777 Sm-148
1840 Sm-148
1916 Sm-152
1951 Cl-35
1959 Cl-35
1977 Sm-148
1991 S-35*
1982 O-18 + DE 3002
DE 3103
2121 Sm-144
SE 2646
2145 Sm-148
SE 2694
2180 Cl-35
2203 Sm-148
2348 S-35*
2514 Sm-148
SE 3103
2646 Cl-35
SE 3163
2694 Cl-35
2715 S-35*
2840 Cl-35

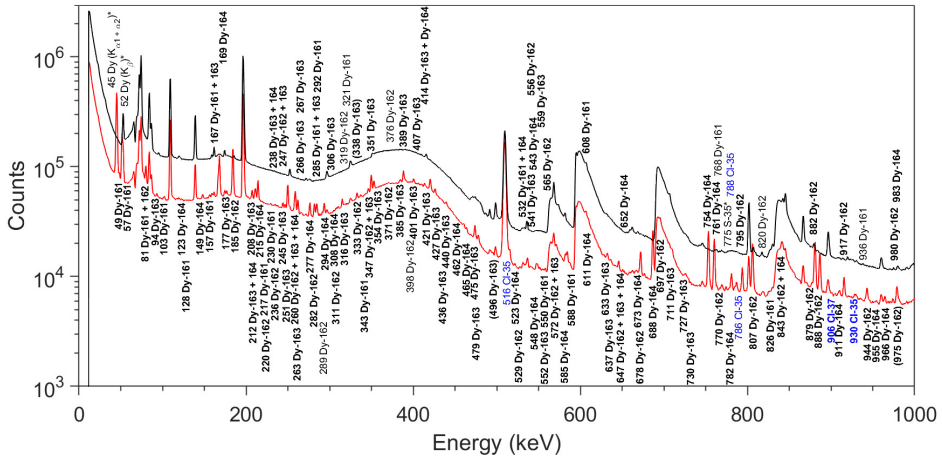


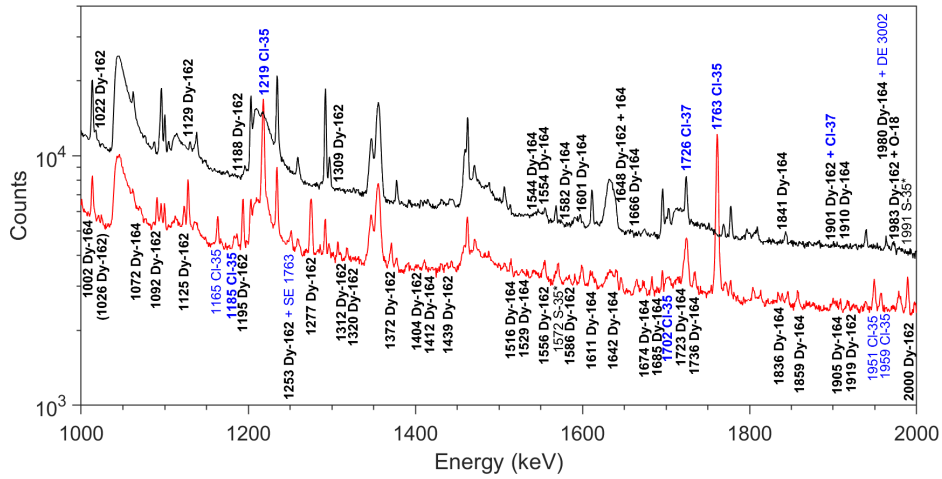
G.7 : γ-ray spectra in the energy range 0-8000 keV acquired during 10,209 s live time for $SmCl_3 \cdot 7H_2O$ (red) and 51,506 s for the active background (black). Prompt γ-rays of inelastic scattering in Sm and O are written in black and bold, γ-rays from (n,γ) reactions are written in black. Lines written in brackets were found to be mainly issued by (n,γ) reactions of Sm in this work. γ-rays of Cl are written in blue, bold if (n,n'γ) reaction. Lines of S-35 and P-32 are due to (n,pγ) and (n,$\alpha\gamma$) reactions in Cl and are written in black with asterisks. X-rays are also written in black with asterisks and denoted with K. Abbreviations SE and DE indicate single and double escape peaks, respectively, and the abbreviation d stands for delayed.

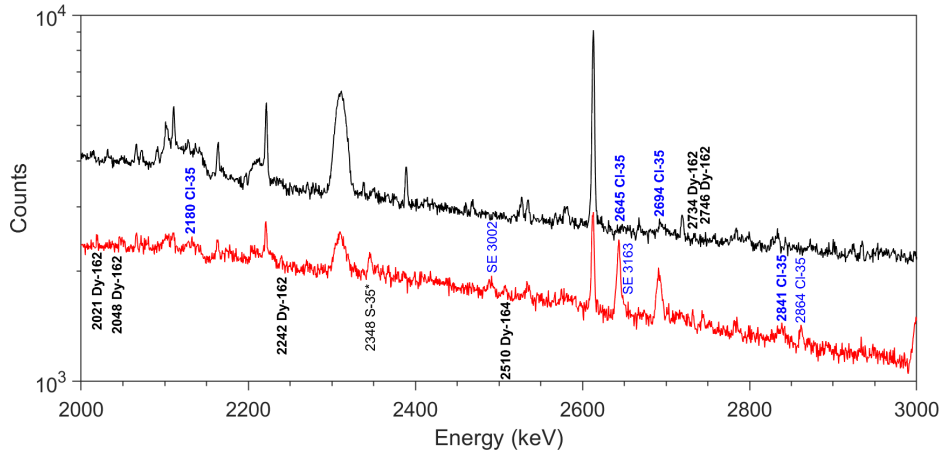

Counts
Energy (keV)
44 Tb (K$_{\alpha1+\alpha2}$)*
50 Tb (K$_\beta$)*
79(+ P-32*)
516 Cl-35
775 S-35*
785 Cl-35 788 Cl-35
1164 Cl-35
1185 Cl-35
1219 Cl-35
+ SE 1763
1701 Cl-35
1726 Cl-37
1763 Cl-35
1951 Cl-35
1959 Cl-35
1981 O-18 + DE 3002
1991 S-35*
SE 2645
DE 3163
SE 2694
2178 Cl-35
2348 S-35*
2483
SE 3002
SE 3103
2645 Cl-35
SE 3163
2694 Cl-35
2715 S-35*
2841 Cl-35
2863 Cl-35
2974 Cl-35

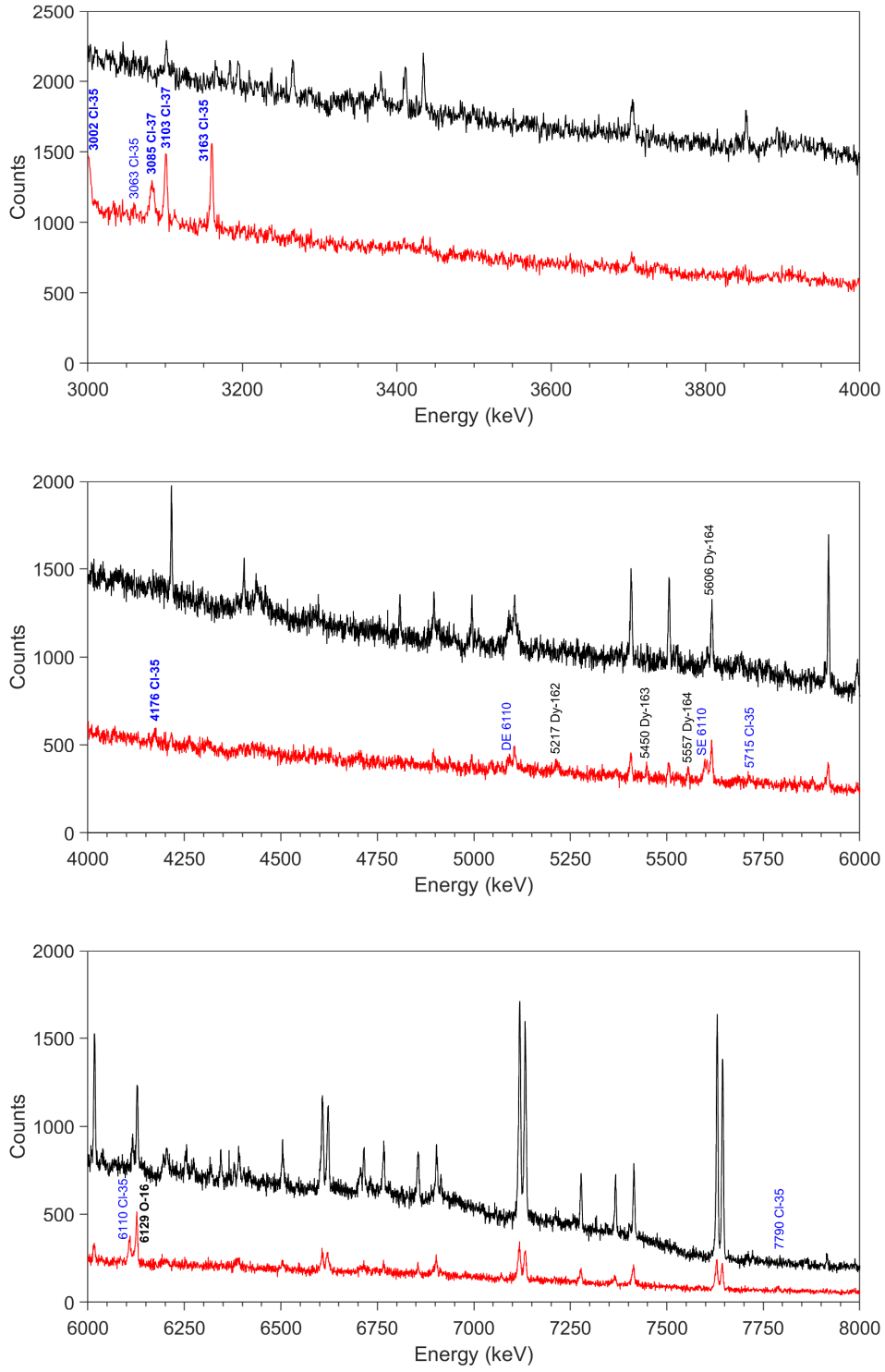


G.8 : γ-ray spectra in the energy range 0-8000 keV acquired during 27,879 s live time for $TbCl_3{\cdot}6H_2O$ (red) and 51,506 s for the active background (black). Prompt γ-rays of inelastic scattering in Tb-159 and O are written in black and bold, γ-rays from (n,γ) reactions are written in black. γ-rays of Cl are written in blue, bold if (n,n'γ) reaction. Lines of S-35 and P-32 are due to (n,pγ) and (n,$\alpha\gamma$) reactions in Cl and are written in black with asterisks. X-rays are also written in black with asterisks and denoted with K. Abbreviations SE and DE indicate single and double escape peaks, respectively.


Counts
Energy (keV)
45 Dy (K$_{\alpha1+\alpha2}$)*
52 Dy (K$_\beta$)*
49 Dy-161
57 Dy-161
81 Dy-161 + 162
94 Dy-163
103 Dy-161
128 Dy-161
123 Dy-164
149 Dy-164
157 Dy-161
167 Dy-161 + 163
169 Dy-164
177 Dy-163
185 Dy-162
212 Dy-163 + 164
220 Dy-162
208 Dy-163
217 Dy-161
230 Dy-161
236 Dy-162
238 Dy-163 + 164
245 Dy-163
247 Dy-162 + 163
260 Dy-162 + 163 + 164
263 Dy-163
266 Dy-163
267 Dy-163
277 Dy-164
282 Dy-162
285 Dy-161 + 163
289 Dy-162
292 Dy-161
294 Dy-164
306 Dy-163
308 Dy-164
311 Dy-162
321 Dy-161
338 Dy-163
343 Dy-161
347 Dy-162 + 163
351 Dy-163
354 Dy-163
371 Dy-162
376 Dy-162
389 Dy-163
398 Dy-162
401 Dy-163
407 Dy-163
414 Dy-163 + Dy-164
436 Dy-163
440 Dy-163
427 Dy-163
421 Dy-163
465 Dy-164
475 Dy-163
479 Dy-163
(496 Dy-163)
516 Cl-35
523 Dy-164
529 Dy-162
532 Dy-161 + 164
541 Dy-163
543 Dy-164
548 Dy-164
550 Dy-161
552 Dy-163
556 Dy-162
559 Dy-163
565 Dy-162
572 Dy-162 + 163
585 Dy-164
588 Dy-161
608 Dy-161
611 Dy-164
632 Dy-164
637 Dy-163
633 Dy-163
647 Dy-162 + 163 + 164
673 Dy-164
678 Dy-162
688 Dy-164
697 Dy-162
711 Dy-163
727 Dy-163
730 Dy-163
754 Dy-164
761 Dy-164
768 Dy-161
775 S-35*
788 Cl-35
770 Dy-162
782 Dy-164
786 Cl-35
795 Dy-162
807 Dy-162
820 Dy-162
826 Dy-161
843 Dy-162 + 164
873 Dy-162
882 Dy-162
888 Dy-164
905 Cl-37
911 Dy-164
917 Dy-162
930 Cl-35
938 Dy-161
944 Dy-162
965 Dy-164
966 Dy-164
(975 Dy-162)
980 Dy-162
983 Dy-164


Counts
Energy (keV)
1022 Dy-162
1129 Dy-162
1188 Dy-162
1219 Cl-35
1309 Dy-162
1544 Dy-164
1554 Dy-164
1582 Dy-164
1601 Dy-164
1648 Dy-162 + 164
1666 Dy-164
1726 Cl-37
1763 Cl-35
1841 Dy-164
1901 Dy-162 + Cl-37
1910 Dy-164
1980 Dy-164 + DE 3002
1983 Dy-162 + O-18
1991 S-35*
2000 Dy-162
1002 Dy-164
(1026 Dy-162)
1072 Dy-164
1092 Dy-162
1125 Dy-162
1165 Cl-35
1185 Cl-35
1195 Dy-162
1253 Dy-162 + SE 1763
1277 Dy-162
1312 Dy-162
1320 Dy-162
1372 Dy-162
1404 Dy-162
1412 Dy-164
1439 Dy-162
1516 Dy-164
1529 Dy-164
1556 Dy-162
1572 S-35*
1586 Dy-162
1611 Dy-164
1642 Dy-164
1674 Dy-164
1686 Dy-164
1702 Cl-35
1723 Dy-164
1736 Dy-164
1836 Dy-164
1859 Dy-164
1905 Dy-164
1919 Dy-162
1951 Cl-35
1959 Cl-35*


Counts
Energy (keV)
2180 Cl-35
2645 Cl-35
2694 Cl-35
2734 Dy-162
2746 Dy-162
2021 Dy-162
2048 Dy-162
2242 Dy-162
2348 S-35*
SE 3002
SE 3163
2510 Dy-164
2841 Cl-35
2864 Cl-35



G.9 : γ-ray spectra in the energy range 0-8000 keV acquired during 8,980 s live time for $DyCl_3{\cdot}6H_2O$ (red) and 51,506 s for the active background (black). Prompt γ-rays of inelastic scattering in Dy and O are written in black and bold, γ-rays from (n,γ) reactions are written in black. Lines written in brackets were found to be mainly issued by (n,γ) reactions of Dy in this work. γ-rays of Cl are written in blue, bold if (n,n'γ) reaction. Lines of S-35 and P-32 are due to (n,pγ) and (n,$\alpha\gamma$) reactions in Cl and are written in black with asterisks. X-rays are also written in black with asterisks and denoted with K. Abbreviations SE and DE indicate single and double escape peaks, respectively.

H. Gamma-ray production cross sections

H.1 Isotopic partial

H.1.1 : Prompt γ-rays of C, O and Ca induced by fast neutrons on $CaCO_3$.

Reaction (E_{thr})	This work				From Atlas [27]		R
	E_γ (keV)	$P_{E\gamma}(90°)/\epsilon_{E\gamma}$ $\times$ 10^{-8} (count)	I_R(relative) (%)	$\langle\sigma_{E_\gamma}(90°)\rangle$ (mb)	E_γ (keV)	I_R(relative) (%)	
^{12}C(n,n'γ)^{12}C (4.81 MeV)[d]	4441.14 ± 0.42[a,b]	5.39 ± 1.14	100	14.4 ± 3.3	4438 ± 2	109[c]	-
^{16}O(n,n'γ)^{16}O (6.43 MeV)[d]	6129.32 ± 0.22[a]	2.50 ± 0.37	547 ± 121	2.20 ± 0.37	6129.3 ± 1.0	595 ± 120	-0.28
^{18}O(n,n'γ)^{18}O (6.43 MeV)[d]	1981.69 ± 0.18	0.46 ± 0.05	100	201 ± 28	1983.0 ± 0.4	100	-
^{40}Ca(n,n'γ)^{40}Ca (3.44 MeV)	754.41 ± 0.07[a]	0.53 ± 0.03	13.5 ± 0.9	1.45 ± 0.14	755.0 ± 0.4	15 ± 3	-0.48
	1307.49 ± 0.26	0.16 ± 0.03	3.93 ± 0.88	0.42 ± 0.10	-	-	-
	1374.32 ± 0.13	0.36 ± 0.03	8.99 ± 0.89	0.97 ± 0.12	1375.7 ± 1.0	10 ± 2	-0.46
	1876.91 ± 0.19	0.35 ± 0.04	8.78 ± 1.09	0.95 ± 0.13	1877.5 ± 0.9	7.8 ± 1.2	0.61
	2009.76 ± 0.23[e]	0.28 ± 0.04	6.96 ± 0.95	0.75 ± 0.12	-	-	-
	3736.89 ± 0.13	5.28 ± 0.17	133 ± 6	14.3 ± 1.2	3736.9 ± 0.8	123 ± 9	0.93
	3904.76 ± 0.28[b]	3.96 ± 0.14	100	10.8 ± 0.9	3904.2	100	-
^{42}Ca(n,n'γ)^{42}Ca (1.56 MeV)	1524.62 ± 0.07	0.87 ± 0.05	22.1 ± 1.4	355 ± 34	1524.4 ± 0.4	20 ± 3	0.63
^{44}Ca(n,n'γ)^{44}Ca (1.18 MeV)	726.17 ± 0.11[a]	0.50 ± 0.07	12.5 ± 1.9	46 ± 8	726.3 ± 1.0	12 ± 3	0.14
	1126.03 ± 0.11	0.34 ± 0.03	8.51 ± 0.85	31 ± 4	1125.5 ± 1.0	8.2 ± 2.0	0.14
	1156.78 ± 0.05	3.90 ± 0.14	98 ± 5	359 ± 31	1156.9 ± 0.5	87 ± 6	1.48
	1499.88 ± 0.28	0.21 ± 0.04	5.38 ± 0.93	19.6 ± 3.7	1500.6 ± 0.8	4.6 ± 1.2	0.52
^{40}Ca(n,pγ)^{40}K (0.54 MeV)	29.78 ± 0.05[f]	63 ± 4	1589 ± 121	171 ± 18	-	-	-
	769.89 ± 0.07[a]	9.56 ± 0.29	241 ± 41	26 ± 2	770.3 ± 0.2	204 ± 10	2.49
	843.54 ± 0.06[a]	0.86 ± 0.15	21.7 ± 3.9	2.34 ± 0.45	-	-	-
	891.19 ± 0.05	1.66 ± 0.07	42 ± 2	4.52 ± 0.41	891.6 ± 0.4	59 ± 7	-2.30
	1158.93 ± 0.10	0.83 ± 0.06	20 ± 2	2.27 ± 0.23	1159.1 ± 0.8	26 ± 4	-1.15
	1247.29 ± 0.16	0.27 ± 0.03	6.77 ± 0.90	0.73 ± 0.11	1247.5 ± 0.6	7.5 ± 2.2	-0.31
	1302.88 ± 0.18	0.27 ± 0.04	6.76 ± 0.93	0.73 ± 0.11	1303.0 ± 0.6	8.1 ± 2.0	-0.61
	1613.58 ± 0.12[a]	0.04 ± 0.01	1.06 ± 0.17	0.11 ± 0.02	-	-	-
	1618.68 ± 0.15	0.39 ± 0.04	9.89 ± 1.08	1.06 ± 0.14	1616.8 ± 1.0[g]	17 ± 4	-1.72
	1929.02 ± 0.22	0.17 ± 0.03	4.29 ± 0.66	0.46 ± 0.08	1929.2 ± 1.6	6.1 ± 1.0	-1.51
	2007.13 ± 0.30	0.22 ± 0.04	5.43 ± 0.92	0.58 ± 0.11	2007.8 ± 0.9[h]	8.3 ± 1.3	-1.80
	2017.39 ± 0.21[a]	0.17 ± 0.05	4.40 ± 1.20	0.47 ± 0.13	2017.8 ± 0.9	5.8 ± 1.2	-0.82
	2039.49 ± 0.19	0.38 ± 0.04	9.68 ± 1.00	1.04 ± 0.13	2040.4 ± 1.0	8.0 ± 1.3	1.02
	2046.72 ± 0.24	0.29 ± 0.04	7.43 ± 0.95	0.80 ± 0.12	2047.8 ± 1.5	4.8 ± 1.1	1.81
	2069.85 ± 0.30	0.32 ± 0.04	7.99 ± 1.15	0.86 ± 0.14	2068.3 ± 1.6	6.0 ± 1.2	1.20
	2073.55 ± 0.12[a]	0.45 ± 0.08	11.3 ± 2.1	1.22 ± 0.24	2073.4 ± 1.0	13 ± 2	-0.57
	2289.66 ± 0.21[i]	0.28 ± 0.02	6.95 ± 0.67	0.75 ± 0.09	2289.8 ± 1.2	11 ± 2	-1.92
	2366.25 ± 0.50	0.18 ± 0.04	4.54 ± 0.98	0.49 ± 0.11	2366.6 ± 2.0	4.8 ± 1.0	-0.19
	2545.64 ± 0.27	0.52 ± 0.06	13.2 ± 1.5	1.42 ± 0.19	2545.1 ± 1.0	14 ± 2	-0.31
	3683.79 ± 0.37	0.16 ± 0.03	4.15 ± 0.71	0.45 ± 0.08	-	-	-
^{40}Ca(n,$\alpha\gamma$)^{37}Ar (0 MeV)	1409.61 ± 0.10[a]	0.74 ± 0.04	18.8 ± 1.1	2.02 ± 0.19	1409.8	21 ± 3	-0.70
	1611.24 ± 0.08	1.65 ± 0.07	42 ± 2	4.47 ± 0.40	1611.2 ± 0.6[j]	48 ± 5	-0.95
	2490.24 ± 0.27	0.17 ± 0.03	4.41 ± 0.73	0.47 ± 0.08	2490.0 ± 1.0	9 ± 2	-2.16

E_{thr} is the threshold energy of the considered reaction taken from [55, 114], E_γ is the γ-ray energy, $P_{E\gamma}(90°)/\epsilon_{E\gamma}$ the net counts in the γ-ray peak divided by the full-energy-peak (FEP) efficiency and the γ-ray self-absorption factor, I_R the relative intensity of the γ-rays and $\langle\sigma_{E_\gamma}(90°)\rangle$ is the fast-neutron spectrum-averaged isotopic partial cross section for γ-ray production at an angle of 90° between neutron beam and detector determined with Eq. (4.1). R is the residual calculated by means of Eq. (4.33)

[a] corrected for background interferences

[b] Doppler-broadened; short-lived transitions in the femtosecond range [65]

[c] unclear how this intensity is obtained, it might be a mistake or the absolute intensity determined with the effective cross section. From this work the absolute intensity is 107% by using an effective cross section for fission neutrons of roughly 12 mb [9] with an angular-distribution correction factor of $W(90°)= 1$

[d] only elemental data available from [55, 114]

H.1.1 : (continued).

[e] ^{40}Ca(n,γ)^{41}Ca excluded and no clear identification in [65], cautious assumption. With regard to the neutron-energy spectrum used in this work it is questionable if this line really comes from the high level at 7623.11 keV or if it is transition not captured in [65] yet
[f] $P_{E\gamma}(90°)/(\epsilon_{E\gamma} \times f_{E\gamma})$ with $f_{E\gamma}$= 0.731 ± 0.022
[g] wrong level energy assigned by Demidov et al.
[h] cautious assumption that this is the line from the ^{40}Ca(n,pγ)^{40}K reaction due to a relatively low excitation level energy of 2807.88 keV and well agreement to peak energy of 2007.71 keV given in [65, 97]. Despite roughly 2 keV difference in energy, it might also be the same line as observed in this work at 2009.76 keV assigned to the ^{40}Ca(n,n'γ)^{40}Ca reaction as the uncertainty is high and the relative intensities are comparable
[i] weak interference from the ^{40}Ca(n,n'γ)^{40}Ca reaction possible [97]
[j] 1611 and 1614 keV

H.1.2 : Prompt γ-rays of ^{35}Cl, ^{37}Cl, ^{35}S and ^{12}C induced by fast neutrons on PVC.

Reaction (E_{thr})	This work				From Atlas [27]		R
	E_γ (keV)	$P_{E\gamma}(90°)/\epsilon_{E\gamma} \times 10^{-8}$ (count)	I_R(relative) (%)	$\langle\sigma_{E_\gamma}(90°)\rangle$ (mb)	E_γ (keV)	I_R(relative) (%)	
^{35}Cl(n,n'γ)^{35}Cl	1184.94 ± 0.16	0.17 ± 0.03	4.31 ± 0.69	2.51 ± 0.44	1184.72 ± 0.15[a]	3.8 ±0.4	0.65
(1.25 MeV)	1219.32 ± 0.05	3.87 ± 0.14	100	**58 ± 5**	1219.52 ± 0.10	100	-
	1763.05 ± 0.07	4.62 ± 0.15	119 ± 6	70 ± 6	1763.27 ± 0.10	129 ± 4	-1.36
	2646.08 ± 0.16	0.98 ± 0.05	25.3 ± 1.6	**14.7 ± 1.4**	2645.7 ± 0.2	25.7 ± 1.5	-0.19
	2694.35 ± 0.18[b,c]	0.64 ± 0.15	16.5 ± 3.9	9.58 ± 2.35	2694.0 ± 0.2	19.1 ± 1.5	-0.64
	3002.46 ± 0.55	0.79 ± 0.08	20.4 ± 2.1	11.9 ± 1.5	3002.2 ± 0.2	15.5 ± 1.5	1.92
	3162.76 ± 0.13	0.59 ± 0.05	15.3 ± 1.3	**8.92 ± 0.98**	3162.52 ± 0.15	16.3 ± 1.5	-0.49
^{37}Cl(n,n'γ)^{37}Cl	905.78 ± 0.39	0.11 ± 0.03	2.89 ± 0.82	**5.27 ± 1.54**	906.64 ± 0.15	2.9 ± 0.4	-0.01
(1.77 MeV)	1725.60 ± 0.19[b]	0.79 ± 0.05	20.6 ± 1.3	37 ± 4	1726.50 ± 0.10	25 ± 2	-1.87
	3086.3 ± 0.55[c]	0.46 ± 0.10	12.0 ± 2.6	22 ± 5	3086.3 ± 0.3	11.2 ± 1.0	0.28
	3103.24 ± 0.18[b]	0.46 ± 0.08	11.8 ± 2.2	**22 ± 4**	3103.29 ± 0.15	14.6 ± 1.5	-1.04
^{35}Cl(n,pγ)^{35}S	1572.83 ± 0.33	0.20 ± 0.03	5.17 ± 0.78	3.01 ± 0.50	1572.32 ± 0.13	5.9 ± 0.5	-0.79
(0 MeV)	1991.02 ± 0.17	0.34 ± 0.04	8.73 ± 1.05	5.08 ± 0.71	1991.43 ± 0.15	11.6 ± 1.0	-1.98
	2348.54 ± 0.37[c]	0.17 ± 0.03	4.41 ± 0.77	**2.57 ± 0.48**	2347.9 ± 0.4	6.6 ± 0.6	-2.24
^{12}C(n,n'γ)^{12}C	4440.96 ± 0.15 [b,c]	2.22 ± 0.37	100	12.8 ± 2.3	4438 ± 2	109[e]	-
(4.81 MeV)[d]							

E_{thr} is the threshold energy of the considered reaction taken from [55, 114], E_γ is the γ-ray energy, $P_{E\gamma}(90°)/\epsilon_{E\gamma}$ the net counts in the γ-ray peak divided by the full-energy-peak (FEP) efficiency , I_R the relative intensity (relative to the 1219-keV line of ^{35}Cl, 100%) of the γ-rays and $\langle\sigma_{E_\gamma}(90°)\rangle$ is the fast-neutron spectrum-averaged isotopic partial cross section for γ-ray production at an angle of 90° between neutron beam and detector determined with Eq. (4.1). R is the residual calculated by means of Eq. (4.33)
[a] unassigned by Demidov et al.
[b] corrected for background interferences
[c] Doppler-broadened; short-lived transitions in the femtosecond range [64, 163, 164]
[d] only elemental data available from [55, 114]
[e] unclear how this intensity is obtained, it might be a mistake or the absolute intensity determined with the effective cross section. From this work the absolute intensity is 107% by using an effective cross section for fission neutrons of roughly 12 mb [9] with an angular-distribution correction factor of $W(90°)$= 1

H.1.3 : Prompt γ-rays of ^{35}Cl, ^{37}Cl, ^{35}S and ^{32}P induced by fast neutrons on $LaCl_3 \cdot 7H_2O$.

Reaction (E_{thr})	This work				From Atlas [27]		R
	E_γ (keV)	$P_{E\gamma}(90°)/(\epsilon_{E\gamma} \times f_{E\gamma}) \times 10^{-8}$ (count)	I_R(relative) (%)	$\langle\sigma_{E_\gamma}(90°)\rangle$ (mb)	E_γ (keV)	I_R(relative) (%)	
^{35}Cl(n,n'γ)^{35}Cl	930.80 ± 0.11[a]	0.57 ± 0.10	3.94 ± 0.86	2.30 ± 0.41	930.5 ± 0.5	3.0 ± 1.0	0.72
(1.25 MeV)	1184.65 ± 0.09	0.64 ± 0.04	4.46 ± 0.62	2.60 ± 0.16	1184.72 ± 0.15[b]	3.8 ±0.4	0.90
	1219.24 ± 0.06	14.45 ± 1.79	100	58 ± 7[c]	1219.52 ± 0.10	100	-
	1701.89 ± 0.14[a]	0.13 ± 0.02	0.89 ± 0.19	0.52 ± 0.09	-	-	-
	1762.92 ± 0.07[d]	20.1 ± 2.6	139 ± 25	81 ± 11	1763.27 ± 0.10	129 ± 4	0.41
	2179.28 ± 0.28	0.56 ± 0.06	3.86 ± 0.63	2.25 ± 0.24	2180.8 ± 0.3[e]	6.2 ± 0.6	-2.69
	2645.76 ± 0.13	3.92 ± 0.75	27 ± 6	15.8 ± 3.0	2645.7 ± 0.2	25.7 ± 1.5	0.22
	2694.03 ± 0.17[a,f]	2.38 ± 0.09	16.4 ± 2.1	9.57 ± 0.36	2694.0 ± 0.2	19.1 ± 1.5	-1.02

H.1.3 : (continued).

Reaction (E_{thr})	This work				From Atlas [27]		R
	E_γ (keV)	$P_{E\gamma}(90°)/(\epsilon_{E\gamma} \times f_{E\gamma})$ $\times 10^{-8}$ (count)	I_R(relative) (%)	$\langle\sigma_{E_\gamma}(90°)\rangle$ (mb)	E_γ (keV)	I_R(relative) (%)	
	2840.72 ± 0.51[f]	0.33 ± 0.05	2.30 ± 0.45	1.34 ± 0.20	2840.3 ± 0.4	5.4 ± 0.6	-4.13
	3002.03 ± 0.18[f]	2.73 ± 0.10	18.9 ± 2.4	11.0 ± 0.4	3002.2 ± 0.2	15.5 ± 1.5	1.19
	3162.66 ± 0.10	2.44 ± 0.10	16.9 ± 2.2	9.84 ± 0.41	3162.52 ± 0.15	16.3 ± 1.5	0.23
	3918.14 ± 0.87[f]	0.16 ± 0.04	1.07 ± 0.32	0.62 ± 0.17	-	-	-
	4109.11 ± 0.16[g,h]	0.26 ± 0.07	1.83 ± 0.56	1.06 ± 0.30	-	-	-
	4175.18 ± 0.16[i]	0.75 ± 0.08	5.17 ± 0.83	3.01 ± 0.31	-	-	-
	4623.38 ± 0.22[f]	0.44 ± 0.09	3.02 ± 0.71	1.76 ± 0.35	-	-	-
^{37}Cl(n,n'γ)^{37}Cl	906.42 ± 0.13	0.38 ± 0.05	2.65 ± 0.45	4.82 ± 0.57	906.64 ± 0.15	2.9 ± 0.4	-0.42
(1.77 MeV)	1726.49 ± 0.14[a]	3.19 ± 0.31	22 ± 3	40 ± 4	1726.50 ± 0.10	25 ± 2	-0.72
	1900.29 ± 0.40[f]	0.23 ± 0.05	1.58 ± 0.42	2.88 ± 0.67	-	-	-
	3085.65 ± 0.17[j]	1.69 ± 0.10	11.7 ± 1.6	21 ± 1	3086.3 ± 0.3	11.2 ± 1.0	0.26
	3103.35 ± 0.10[a]	1.80 ± 0.34	12.4 ± 2.8	23 ± 4	3103.29 ± 0.15	14.6 ± 1.5	-0.68
	3625.37 ± 0.11[f]	0.22 ± 0.05	1.54 ± 0.41	2.80 ± 0.67	-	-	-
	3740.67 ± 0.12[f,k]	0.29 ± 0.06	2.01 ± 0.50	3.67 ± 0.78	3742.9 ± 0.5	3.0 ± 1.0	-0.88
	4011.23 ± 0.64	0.23 ± 0.05	1.57 ± 0.43	2.86 ± 0.69	-	-	-
^{35}Cl(n,pγ)^{35}S	775.08 ± 0.04	0.25 ± 0.04	1.74 ± 0.37	1.01 ± 0.18	775.0 ± 0.2	1.3 ± 0.3	0.93
(0 MeV)	1572.38 ± 0.09	0.93 ± 0.04	6.42 ± 0.84	3.74 ± 0.16	1572.32 ± 0.13	5.9 ± 0.5	0.53
	1991.21 ± 0.10	1.70 ± 0.07	11.8 ± 1.5	6.86 ± 0.27	1991.43 ± 0.15	11.6 ± 1.0	0.10
	2348.50 ± 0.25	0.68 ± 0.06	4.67 ± 0.70	2.72 ± 0.23	2347.9 ± 0.4	6.6 ± 0.6	-2.09
	2716.38 ± 0.68[f,l]	0.18 ± 0.04	1.24 ± 0.34	0.72 ± 0.17	-	-	-
^{35}Cl(n,$\alpha\gamma$)^{32}P	77.77 ± 0.09	4.66 ± 0.80	32 ± 7	18.8 ± 3.2	-	-	-
(0 MeV)							

E_{thr} is the threshold energy of the considered reaction taken from [55, 114], E_γ is the γ-ray energy, $P_{E\gamma}(90°)/(\epsilon_{E\gamma} \times f_{E\gamma})$ the net counts in the γ-ray peak divided by the full-energy-peak (FEP) efficiency and the γ-ray self-absorption factor, I_R the relative intensity (relative to the 1219-keV line of ^{35}Cl, 100%) of the γ-rays and $\langle\sigma_{E_\gamma}(90°)\rangle$ is the fast-neutron spectrum-averaged isotopic partial cross section for γ-ray production at an angle of 90° between neutron beam and detector determined with Eq. (4.1). R is the residual calculated by means of Eq. (4.33). Lines marked in red were not considered for average values

[a] corrected for background interferences

[b] unassigned by Demidov et al.

[c] net counts calculated with effective partial isotopic cross section from PVC measurement, i.e. (58 ± 5) mb

[d] interference from ^{139}La(n,n'γ)^{139}La corrected (4.2% of net counts) with intensity from Atlas [27]

[e] maybe uncorrected interference in [27] from the SE from the 2694.0-keV line of ^{35}Cl

[f] Doppler-broadened; short-lived transitions in the femtosecond range [65]

[g] corrected for contribution of SE from 4623.4-keV line (23.8% of net counts)

[h] interference from ^{139}La(n,γ)^{140}La corrected (3.4% of net counts)

[i] might be fed from two close-lying short-lived levels [163]; possible, but unlikely to come from the ^{37}Cl(n,n'γ)^{37}Cl reaction [164]

[j] interference from ^{139}La(n,γ)^{140}La corrected (3.2% of net counts)

[k] interference from ^{139}La(n,γ)^{140}La corrected (9.3% of net counts)

[l] interference from ^{139}La(n,γ)^{140}La corrected (3.0% of net counts)

H.1.4 : Prompt γ-rays of ^{35}Cl, ^{37}Cl, ^{35}S and ^{32}P induced by fast neutrons on $CeCl_3$.

Reaction (E_{thr})	This work				From Atlas [27]		R
	E_γ (keV)	$P_{E\gamma}(90°)/(\epsilon_{E\gamma} \times f_{E\gamma})$ $\times 10^{-8}$ (count)	I_R(relative) (%)	$\langle\sigma_{E_\gamma}(90°)\rangle$ (mb)	E_γ (keV)	I_R(relative) (%)	
^{35}Cl(n,n'γ)^{35}Cl	930.29 ± 0.10[a]	0.37 ± 0.08	3.16 ± 0.72	2.26 ± 0.51	930.5 ± 0.5	3.0 ± 1.0	0.13
(1.25 MeV)	1184.64 ± 0.08	0.47 ± 0.03	4.03 ± 0.30	2.89 ± 0.19	1184.72 ± 0.15[b]	3.8 ±0.4	0.47
	1219.25 ± 0.06[c]	11.62 ± 0.35	100	72 ± 2	1219.52 ± 0.10	100	-
	1701.73 ± 0.14[a]	0.12 ± 0.04	1.06 ± 0.34	0.76 ± 0.24	-	-	-
	1762.92 ± 0.08[d]	13.26 ± 0.43	114 ± 5	82 ± 3	1763.27 ± 0.10	129 ± 4	-2.31
	2179.10 ± 0.21	0.37 ± 0.03	3.22 ± 0.28	2.31 ± 0.19	2180.8 ± 0.3[e]	6.2 ± 0.6	-4.50
	2645.20 ± 0.12	2.51 ± 0.11	21.6 ± 1.2	15.4 ± 0.7	2645.7 ± 0.2	25.7 ± 1.5	-2.19
	2693.78 ± 0.13[a,f]	2.03 ± 0.63	17.4 ± 5.4	12.5 ± 3.9	2694.0 ± 0.2	19.1 ± 1.5	-0.30
	2839.60 ± 0.39[f]	0.25 ± 0.03	2.11 ± 0.26	1.51 ± 0.18	2840.3 ± 0.4	5.4 ± 0.6	-5.02
	3002.32 ± 0.12[f]	2.04 ± 0.09	17.6 ± 0.9	12.6 ± 0.5	3002.2 ± 0.2	15.5 ± 1.5	1.17
	3162.46 ± 0.11	1.68 ± 0.06	14.4 ± 0.7	10.3 ± 0.4	3162.52 ± 0.15	16.3 ± 1.5	-2.65
	3918.46 ± 0.47[f]	0.12 ± 0.02	1.05 ± 0.17	0.75 ± 0.12	-	-	-
	4110.81 ± 0.25[g]	0.27 ± 0.05	2.30 ± 0.43	1.65 ± 0.31	-	-	-

H.1.4 : (continued).

Reaction (E_{thr})	This work				From Atlas [27]		R
	E_γ (keV)	$P_{E\gamma}(90°)/(\epsilon_{E\gamma} \times f_{E\gamma})$ $\times 10^{-8}$ (count)	I_R(relative) (%)	$\langle\sigma_{E_\gamma}(90°)\rangle$ (mb)	E_γ (keV)	I_R(relative) (%)	
	4176.65 ± 0.75[h]	0.61 ± 0.05	5.22 ± 0.46	3.74 ± 0.31	-	-	-
	4622.17 ± 0.23[f]	0.30 ± 0.04	2.61 ± 0.38	1.87 ± 0.27	-	-	-
^{37}Cl(n,n'γ)^{37}Cl	905.65 ± 0.08	0.29 ± 0.02	2.53 ± 0.20	5.66 ± 0.41	906.64 ± 0.15	2.9 ± 0.4	-0.83
(1.77 MeV)	1726.17 ± 0.08[a,d,i]	2.38 ± 0.09	20.5 ± 1.0	46 ± 2	1726.50 ± 0.10	25 ± 2	-2.01
	1899.99 ± 0.28[f,i]	0.12 ± 0.03	1.06 ± 0.25	2.38 ± 0.56	-	-	-
	3085.91 ± 0.14[f]	1.17 ± 0.05	10.0 ± 0.5	22 ± 1	3086.3 ± 0.3	11.2 ± 1.0	-1.02
	3103.17 ± 0.11[a]	1.29 ± 0.05	11.1 ± 0.5	25 ± 1	3103.29 ± 0.15	14.6 ± 1.5	-2.17
	3625.48 ± 0.90[f]	0.24 ± 0.04	2.07 ± 0.34	4.65 ± 0.74	-	-	-
	3739.47 ± 0.18[f]	0.31 ± 0.04	2.65 ± 0.32	5.93 ± 0.68	3742.9 ± 0.5	3.0 ± 1.0	-0.33
	4010.30 ± 0.32	0.16 ± 0.02	1.37 ± 0.20	3.08 ± 0.43	-	-	-
^{35}Cl(n,pγ)^{35}S	774.83 ± 0.18[i]	0.13 ± 0.03	1.13 ± 0.24	0.81 ± 0.17	775.0 ± 0.2	1.3 ± 0.3	-0.44
(0 MeV)	1572.05 ± 0.10	0.65 ± 0.04	5.57 ± 0.38	3.99 ± 0.25	1572.32 ± 0.13	5.9 ± 0.5	-0.52
	1990.92 ± 0.09	1.19 ± 0.04	10.2 ± 0.5	7.33 ± 0.25	1991.43 ± 0.15	11.6 ± 1.0	-1.23
	2347.62 ± 0.11[i]	0.51 ± 0.04	4.39 ± 0.35	3.14 ± 0.23	2347.9 ± 0.4	6.6 ± 0.6	-3.19
	2714.90 ± 0.50	0.10 ± 0.02	0.82 ± 0.20	0.59 ± 0.15	-	-	-
^{35}Cl(n,$\alpha\gamma$)^{32}P	77.97 ± 0.06	5.17 ± 0.54	45 ± 5	32 ± 3	-	-	-
(0 MeV)							

E_{thr} is the threshold energy of the considered reaction taken from [55, 114], E_γ is the γ-ray energy, $P_{E\gamma}(90°)/(\epsilon_{E\gamma} \times f_{E\gamma})$ the net counts in the γ-ray peak divided by the full-energy-peak (FEP) efficiency and the γ-ray self-absorption factor, I_R the relative intensity (relative to the 1219-keV line of ^{35}Cl, 100%) of the γ-rays and $\langle\sigma_{E_\gamma}(90°)\rangle$ is the fast-neutron spectrum-averaged isotopic partial cross section for γ-ray production at an angle of 90° between neutron beam and detector determined with Eq. (4.1). R is the residual calculated by means of Eq. (4.33)
[a]corrected for background interferences
[b]unassigned by Demidov et al.
[c]negligible interference from the ^{140}Ce(n,n'γ)^{140}Ce reaction, but other interference in [65] is assumed as the cross section differs much compared to that derived from the PVC measurement
[d]possible interference from the ^{142}Ce(n,n'γ)^{142}Ce reaction
[e]maybe uncorrected interference in [27] from the SE from the 2693.8-keV line of ^{35}Cl
[f]Doppler-broadened; short-lived transitions in the femtosecond range [65]
[g]corrected for contribution of SE from 4622.2-keV line (32.6% of net counts)
[h]might be fed from two close-lying short-lived levels [163]; possible, but unlikely to come from the ^{37}Cl(n,n'γ)^{37}Cl reaction [164]
[i]interference from the ^{140}Ce(n,n'γ)^{140}Ce reaction corrected with intensities given in the ENSDF file in [160]

H.1.5 : Prompt γ-rays of ^{35}Cl, ^{37}Cl, ^{35}S and ^{32}P induced by fast neutrons on $PrCl_3 \cdot 7H_2O$.

Reaction (E_{thr})	This work				From Atlas [27]		R
	E_γ (keV)	$P_{E\gamma}(90°)/(\epsilon_{E\gamma} \times f_{E\gamma})$ $\times 10^{-8}$ (count)	I_R(relative) (%)	$\langle\sigma_{E_\gamma}(90°)\rangle$ (mb)	E_γ (keV)	I_R(relative) (%)	
^{35}Cl(n,n'γ)^{35}Cl	930.56 ± 0.34[a]	0.29 ± 0.08	2.91 ± 0.73	2.05 ± 0.51	930.5 ± 0.5	3.0 ± 1.0	-0.07
(1.25 MeV)	1184.57 ± 0.13	0.36 ± 0.03	3.66 ± 0.31	2.58 ± 0.20	1184.72 ± 0.15[b]	3.8 ±0.4	-0.29
	1219.14 ± 0.06	9.80 ± 0.30	100	70 ± 2	1219.52 ± 0.10	100	-
	1762.77 ± 0.09[c]	11.08 ± 0.39	113 ± 5	80 ± 3	1763.27 ± 0.10	129 ± 4	-2.41
	2179.32 ± 0.27	0.27 ± 0.03	2.80 ± 0.33	1.98 ± 0.23	2180.8 ± 0.3[d]	6.2 ± 0.6	-4.95
	2645.26 ± 0.13	2.19 ± 0.08	22 ± 1	15.8 ± 0.6	2645.7 ± 0.2	25.7 ± 1.5	-1.80
	2693.31 ± 0.16[a,c]	1.89 ± 0.54	19.3 ± 5.5	13.6 ± 3.8	2694.0 ± 0.2	19.1 ± 1.5	0.03
	2841.05 ± 0.56[c]	0.18 ± 0.04	1.89 ± 0.40	1.33 ± 0.28	2840.3 ± 0.4	5.4 ± 0.6	-4.87
	3001.76 ± 0.15[c]	1.71 ± 0.07	17.4 ± 0.9	12.3 ± 0.5	3002.2 ± 0.2	15.5 ± 1.5	1.10
	3162.62 ± 0.11	1.45 ± 0.07	14.8 ± 0.8	10.4 ± 0.5	3162.52 ± 0.15	16.3 ± 1.5	-0.87
	4112.87 ± 0.19	0.18 ± 0.05	1.84 ± 0.52	1.30 ± 0.37	-	-	-
	4175.65 ± 0.70[e,f]	0.16 ± 0.03	1.66 ± 0.36	1.17 ± 0.25	-	-	-
^{37}Cl(n,n'γ)^{37}Cl	905.81 ± 0.13	0.14 ± 0.02	1.39 ± 0.21	3.06 ± 0.46	906.64 ± 0.15	2.9 ± 0.4	-3.33
(1.77 MeV)	1725.97 ± 0.08[a]	1.94 ± 0.36	19.8 ± 3.7	44 ± 8	1726.50 ± 0.10	25 ± 2	-1.24
	3085.81 ± 0.23[c]	1.21 ± 0.08	12.4 ± 0.9	27 ± 2	3086.3 ± 0.3	11.2 ± 1.0	0.88
	3103.09 ± 0.16[a]	1.09 ± 0.27	11.1 ± 2.7	25 ± 6	3103.29 ± 0.15	14.6 ± 1.5	-1.11
	3627.93 ± 0.49[c,g]	0.09 ± 0.03	0.91 ± 0.31	2.01 ± 0.69	-	-	-
	3740.88 ± 0.16[c,h]	0.29 ± 0.05	3.01 ± 0.54	6.63 ± 1.18	3742.9 ± 0.5	3.0 ± 1.0	0.01

H.1.5 : (continued).

Reaction (E_{thr})	This work				From Atlas [27]		R
	E_γ (keV)	$P_{E\gamma}(90°)/(\epsilon_{E\gamma} \times f_{E\gamma})$ $\times 10^{-8}$ (count)	I_R(relative) (%)	$\langle\sigma_{E_\gamma}(90°)\rangle$ (mb)	E_γ (keV)	I_R(relative) (%)	
	4010.53 ± 0.55[i]	0.09 ± 0.02	0.91 ± 0.25	2.01 ± 0.54	-	-	-
^{35}Cl(n,pγ)^{35}S	1572.20 ± 0.11	0.57 ± 0.04	5.80 ± 0.42	4.09 ± 0.27	1572.32 ± 0.13	5.9 ± 0.5	-0.14
(0 MeV)	1990.85 ± 0.10	1.07 ± 0.04	10.9 ± 0.5	7.66 ± 0.30	1991.43 ± 0.15	11.6 ± 1.0	-0.64
	2347.47 ± 0.22	0.37 ± 0.04	3.76 ± 0.39	2.65 ± 0.26	2347.9 ± 0.4	6.6 ± 0.6	-3.97
	2714.06 ± 0.70[c]	0.11 ± 0.04	1.14 ± 0.37	0.81 ± 0.26	-	-	-
^{35}Cl(n,αγ)^{32}P	77.79 ± 0.09	3.17 ± 0.59	32 ± 6	23 ± 4	-	-	-
(0 MeV)							

E_{thr} is the threshold energy of the considered reaction taken from [55, 114], E_γ is the γ-ray energy, $P_{E\gamma}(90°)/(\epsilon_{E\gamma} \times f_{E\gamma})$ the net counts in the γ-ray peak divided by the full-energy-peak (FEP) efficiency and the γ-ray self-absorption factor, I_R the relative intensity (relative to the 1219-keV line of ^{35}Cl, 100%) of the γ-rays and $\langle\sigma_{E_\gamma}(90°)\rangle$ is the fast-neutron spectrum-averaged isotopic partial cross section for γ-ray production at an angle of 90° between neutron beam and detector determined with Eq. (4.1). R is the residual calculated by means of Eq. (4.33)
[a]corrected for background interferences
[b]unassigned by Demidov et al.
[c]Doppler-broadened; short-lived transitions in the femtosecond range [65]
[d]maybe uncorrected interference in [27] from the SE from the 2693.3-keV line of ^{35}Cl
[e]might be fed from two close-lying short-lived levels [163]; possible, but unlikely to come from the ^{37}Cl(n,n'γ)^{37}Cl reaction [164]
[f]interference from ^{141}Pr(n,γ)^{142}Pr corrected (11.8% of net counts)
[g]interference from ^{141}Pr(n,γ)^{142}Pr corrected (8.7% of net counts)
[h]interference from ^{141}Pr(n,γ)^{142}Pr corrected (2.7% of net counts)
[i]interference from ^{141}Pr(n,γ)^{142}Pr corrected (17.8% of net counts)

H.1.6 : Prompt γ-rays of ^{35}Cl, ^{37}Cl, ^{35}S and ^{32}P induced by fast neutrons on $NdCl_3$.

Reaction (E_{thr})	This work				From Atlas [27]		R
	E_γ (keV)	$P_{E\gamma}(90°)/(\epsilon_{E\gamma} \times f_{E\gamma})$ $\times 10^{-8}$ (count)	I_R(relative) (%)	$\langle\sigma_{E_\gamma}(90°)\rangle$ (mb)	E_γ (keV)	I_R(relative) (%)	
^{35}Cl(n,n'γ)^{35}Cl	931.41 ± 0.06[a,b]	0.31 ± 0.06	4.52 ± 0.90	3.07 ± 0.61	930.5 ± 0.5	3.0 ± 1.0	1.13
(1.25 MeV)	1184.55 ± 0.13	0.27 ± 0.02	3.89 ± 0.37	2.64 ± 0.24	1184.72 ± 0.15[c]	3.8 ±0.4	0.16
	1219.33 ± 0.09[d]	6.95 ± 0.21	100	68 ± 2	1219.52 ± 0.10	100	-
	1701.81 ± 0.17[a]	0.10 ± 0.02	1.48 ± 0.33	1.01 ± 0.22	-	-	-
	1763.00 ± 0.08	7.40 ± 0.25	106 ± 5	72 ± 2	1763.27 ± 0.10	129 ± 4	-3.57
	2179.52 ± 0.24	0.23 ± 0.02	3.36 ± 0.35	2.28 ± 0.23	2180.8 ± 0.3[e]	6.2 ± 0.6	-4.08
	2645.01 ± 0.14	1.56 ± 0.07	22 ± 1	15.2 ± 0.7	2645.7 ± 0.2	25.7 ± 1.5	-1.71
	2692.98 ± 0.22[a,f]	1.24 ± 0.05	17.8 ± 0.9	12.1 ± 0.5	2694.0 ± 0.2	19.1 ± 1.5	-0.72
	2840.22 ± 0.28[f]	0.14 ± 0.02	2.00 ± 0.26	1.36 ± 0.17	2840.3 ± 0.4	5.4 ± 0.6	-5.21
	3001.56 ± 0.21[f]	1.26 ± 0.06	18.2 ± 1.0	12.3 ± 0.6	3002.2 ± 0.2	15.5 ± 1.5	1.47
	3162.56 ± 0.12	0.98 ± 0.04	14.0 ± 0.8	9.54 ± 0.44	3162.52 ± 0.15	16.3 ± 1.5	-1.33
	3916.26 ± 0.21[f]	0.09 ± 0.03	1.36 ± 0.46	0.93 ± 0.31	-	-	-
	4174.68 ± 0.23[g]	0.23 ± 0.04	3.24 ± 0.56	2.20 ± 0.37	-	-	-
^{37}Cl(n,n'γ)^{37}Cl	906.02 ± 0.15	0.16 ± 0.02	2.25 ± 0.32	4.78 ± 0.67	906.64 ± 0.15	2.9 ± 0.4	-1.27
(1.77 MeV)	1726.21 ± 0.08[a]	1.40 ± 0.17	20 ± 2	43 ± 5	1726.50 ± 0.10	25 ± 2	-1.52
	1900.91 ± 0.46[f]	0.08 ± 0.02	1.12 ± 0.28	2.38 ± 0.59	-	-	-
	3086.43 ± 0.13[f]	0.73 ± 0.04	10.5 ± 0.7	22 ± 1	3086.3 ± 0.3	11.2 ± 1.0	-0.58
	3103.40 ± 0.14[a]	0.75 ± 0.04	10.8 ± 0.6	23 ± 1	3103.29 ± 0.15	14.6 ± 1.5	-2.35
	3625.41 ± 0.17[f]	0.09 ± 0.03	1.35 ± 0.45	2.87 ± 0.96	-	-	-
	3740.27 ± 0.18[f]	0.16 ± 0.03	2.37 ± 0.47	5.03 ± 0.98	3742.9 ± 0.5	3.0 ± 1.0	-0.57
^{35}Cl(n,pγ)^{35}S	774.59 ± 0.19	0.09 ± 0.02	1.33 ± 0.30	0.91 ± 0.20	775.0 ± 0.2	1.3 ± 0.3	0.08
(0 MeV)	1572.95 ± 0.11[h]	0.67 ± 0.04	9.61 ± 0.67	6.53 ± 0.41	1572.32 ± 0.13	5.9 ± 0.5	4.43
	1991.08 ± 0.10	0.63 ± 0.03	9.13 ± 0.54	6.20 ± 0.31	1991.43 ± 0.15	11.6 ± 1.0	-2.17
	2347.24 ± 0.18	0.27 ± 0.03	3.88 ± 0.40	2.63 ± 0.26	2347.9 ± 0.4	6.6 ± 0.6	-3.78
	2714.75 ± 0.69[f]	0.09 ± 0.02	1.36 ± 0.29	0.92 ± 0.20	-	-	-
^{35}Cl(n,αγ)^{32}P	77.88 ± 0.05[i]	4.50 ± 0.39	65 ± 6	44 ± 4	-	-	-

E_{thr} is the threshold energy of the considered reaction taken from [55, 114], E_γ is the γ-ray energy, $P_{E\gamma}(90°)/(\epsilon_{E\gamma} \times f_{E\gamma})$ the net counts in the γ-ray peak divided by the full-energy-peak (FEP) efficiency and the γ-ray self-absorption factor, I_R the relative intensity (relative to the 1219-keV line of ^{35}Cl, 100%) of the γ-rays and $\langle\sigma_{E_\gamma}(90°)\rangle$ is the fast-neutron spectrum-averaged isotopic partial cross section for γ-ray production at an angle of 90° between neutron beam and detector determined with Eq. (4.1). R is the residual calculated by means of Eq. (4.33). Lines marked in red were not considered for average values

H.1.6 : (continued).

Reaction (E_{thr})	This work				From Atlas [27]		R
	E_γ (keV)	$P_{E\gamma}(90°)/(\epsilon_{E\gamma} \times f_{E\gamma})$ $\times$ 10^{-8} (count)	I_R(relative) (%)	$\langle\sigma_{E_\gamma}(90°)\rangle$ (mb)	E_γ (keV)	I_R(relative) (%)	
(0 MeV)							

[a] corrected for background interferences
[b] uncorrected interference according to [182] from ^{150}Nd(n,n'γ)^{150}Nd at E^*= 1062.1 keV
[c] unassigned by Demidov et al.
[d] interference possible according to [173] possible from ^{142}Nd(n,n'γ)^{142}Nd at E^*= 3318.7 keV
[e] maybe uncorrected interference in [27] from the SE from the 2693.0-keV line of ^{35}Cl
[f] Doppler-broadened; short-lived transitions in the femtosecond range [65]
[g] might be fed from two close-lying short-lived levels [163]; possible, but unlikely to come from the ^{37}Cl(n,n'γ)^{37}Cl reaction [164]
[h] uncorrected interference according to [178] from ^{144}Nd(n,n'γ)^{144}Nd at E^*= 2888.0 keV
[i] interference possible according to [173] from ^{142}Nd(n,n'γ)^{142}Nd at E^*= 2513.9 keV

H.1.7 : Prompt γ-rays of ^{35}Cl, ^{37}Cl, ^{35}S and ^{32}P induced by fast neutrons on $SmCl_3 \cdot 7H_2O$.

Reaction (E_{thr})	This work				From Atlas [27]		R
	E_γ (keV)	$P_{E\gamma}(90°)/(\epsilon_{E\gamma} \times f_{E\gamma})$ $\times$ 10^{-8} (count)	I_R(relative) (%)	$\langle\sigma_{E_\gamma}(90°)\rangle$ (mb)	E_γ (keV)	I_R(relative) (%)	
^{35}Cl(n,n'γ)^{35}Cl	929.93 ± 0.07[a,b]	0.49 ± 0.05	9.31 ± 0.93	6.36 ± 0.60	930.5 ± 0.5	3.0 ± 1.0	4.62
(1.25 MeV)	1184.41 ± 0.17	0.21 ± 0.04	3.91 ± 0.77	2.67 ± 0.52	1184.72 ± 0.15[c]	3.8 ±0.4	0.12
	1219.28 ± 0.08	5.29 ± 0.17	100	68 ± 2	1219.52 ± 0.10	100	-
	1701.46 ± 0.29[a]	0.06 ± 0.02	1.08 ± 0.45	0.74 ± 0.30	-	-	-
	1763.53 ± 0.30	5.79 ± 0.28	109 ± 6	75 ± 4	1763.27 ± 0.10	129 ± 4	-2.61
	2179.88 ± 0.39	0.15 ± 0.02	2.82 ± 0.47	1.93 ± 0.32	2180.8 ± 0.3[d]	6.2 ± 0.6	-4.42
	2645.63 ± 0.19	1.00 ± 0.05	19.0 ± 1.1	12.9 ± 0.6	2645.7 ± 0.2	25.7 ± 1.5	-3.60
	2693.93 ± 0.19[a,e]	1.01 ± 0.04	19.0 ± 1.0	13.0 ± 0.6	2694.0 ± 0.2	19.1 ± 1.5	-0.05
	2839.97 ± 0.35[e]	0.11 ± 0.02	2.00 ± 0.38	1.36 ± 0.26	2840.3 ± 0.4	5.4 ± 0.6	-4.78
	3002.24 ± 0.27[e]	1.08 ± 0.06	20 ± 1	13.9 ± 0.8	3002.2 ± 0.2	15.5 ± 1.5	2.39
	3162.89 ± 0.16	0.71 ± 0.03	13.4 ± 0.8	9.18 ± 0.44	3162.52 ± 0.15	16.3 ± 1.5	-1.70
	4176.02 ± 0.54[f]	0.11 ± 0.02	1.98 ± 0.41	1.35 ± 0.28	-	-	-
^{37}Cl(n,n'γ)^{37}Cl	906.09 ± 0.22	0.15 ± 0.03	2.74 ± 0.55	5.86 ± 1.15	906.64 ± 0.15	2.9 ± 0.4	-0.23
(1.77 MeV)	1726.28 ± 0.12[a]	1.02 ± 0.15	19.2 ± 2.9	41 ± 6	1726.50 ± 0.10	25 ± 2	-1.65
	3085.68 ± 0.28[e]	0.54 ± 0.05	10.2 ± 1.0	22 ± 2	3086.3 ± 0.3	11.2 ± 1.0	-0.69
	3103.16 ± 0.17[a]	0.56 ± 0.12	10.5 ± 2.3	22 ± 5	3103.29 ± 0.15	14.6 ± 1.5	-1.48
^{35}Cl(n,pγ)^{35}S	1572.41 ± 0.16	0.29 ± 0.03	5.46 ± 0.63	3.73 ± 0.41	1572.32 ± 0.13	5.9 ± 0.5	-0.54
(0 MeV)	1990.79 ± 0.13	0.58 ± 0.04	10.9 ± 0.9	7.45 ± 0.55	1991.43 ± 0.15	11.6 ± 1.0	-0.52
	2347.92 ± 0.30	0.22 ± 0.03	4.10 ± 0.56	2.80 ± 0.37	2347.9 ± 0.4	6.6 ± 0.6	-3.05
	2715.44 ± 0.67[e]	0.11 ± 0.03	2.10 ± 0.56	1.43 ± 0.38	-	-	-
^{35}Cl(n,$\alpha\gamma$)^{32}P	77.92 ± 0.07	2.12 ± 0.36	40 ± 7	27 ± 5	-	-	-
(0 MeV)							

E_{thr} is the threshold energy of the considered reaction taken from [55, 114], E_γ is the γ-ray energy, $P_{E\gamma}(90°)/(\epsilon_{E\gamma} \times f_{E\gamma})$ the net counts in the γ-ray peak divided by the full-energy-peak (FEP) efficiency and the γ-ray self-absorption factor, I_R the relative intensity (relative to the 1219-keV line of ^{35}Cl, 100%) of the γ-rays and $\langle\sigma_{E_\gamma}(90°)\rangle$ is the fast-neutron spectrum-averaged isotopic partial cross section for γ-ray production at an angle of 90° between neutron beam and detector determined with Eq. (4.1). R is the residual calculated by means of Eq. (4.33). Lines marked in red were not considered for average values
[a] corrected for background interferences
[b] interference from (n,n'γ) corrected with intensity from Atlas [27]; further interferences are likely with respect to data in [65]
[c] unassigned by Demidov et al.
[d] maybe uncorrected interference in [27] from the SE from the 2693.9-keV line of ^{35}Cl
[e] Doppler-broadened; short-lived transitions in the femtosecond range [65]
[f] might be fed from two close-lying short-lived levels [163]; possible, but unlikely to come from the ^{37}Cl(n,n'γ)^{37}Cl reaction [164]

H.1.8 : Prompt γ-rays of ^{35}Cl, ^{37}Cl and ^{35}S induced by fast neutrons on $TbCl_3{\cdot}6H_2O$.

Reaction (E_{thr})	This work				From Atlas [27]		R
	E_γ (keV)	$P_{E\gamma}(90°)/(\epsilon_{E\gamma} \times f_{E\gamma})$ $\times$ 10^{-8} (count)	I_R(relative) (%)	$\langle\sigma_{E_\gamma}(90°)\rangle$ (mb)	E_γ (keV)	I_R(relative) (%)	
^{35}Cl(n,n'γ)^{35}Cl	930.19 ± 0.14[a]	0.51 ± 0.14	3.15 ± 0.86	2.16 ± 0.58	930.5 ± 0.5	3.0 ± 1.0	0.12
(1.25 MeV)	1184.87 ± 0.12	0.65 ± 0.07	4.03 ± 0.43	2.76 ± 0.28	1184.72 ± 0.15[b]	3.8 ±0.4	0.40
	1219.06 ± 0.06	16.17 ± 0.49	100	68 ± 2	1219.52 ± 0.10	100	-
	1701.49 ± 0.23[a]	0.21 ± 0.05	1.28 ± 0.30	0.88 ± 0.20	-	-	-
	1762.72 ± 0.09	18.12 ± 0.60	112 ± 5	77 ± 3	1763.27 ± 0.10	129 ± 4	-2.64
	2178.44 ± 0.52	0.33 ± 0.05	2.02 ± 0.31	1.38 ± 0.21	2180.8 ± 0.3[c]	6.2 ± 0.6	-6.21
	2645.25 ± 0.15	3.80 ± 0.14	23 ± 1	16.0 ± 0.6	2645.7 ± 0.2	25.7 ± 1.5	-1.18
	2693.70 ± 0.15[a,d]	2.44 ± 0.10	15.1 ± 0.8	10.3 ± 0.4	2694.0 ± 0.2	19.1 ± 1.5	-2.38
	2841.04 ± 0.50[d]	0.23 ± 0.04	1.43 ± 0.26	0.97 ± 0.17	2840.3 ± 0.4	5.4 ± 0.6	-6.08
	3001.84 ± 0.15[d]	2.89 ± 0.13	17.9 ± 1.0	12.2 ± 0.6	3002.2 ± 0.2	15.5 ± 1.5	1.33
	3162.53 ± 0.15	2.27 ± 0.13	14.0 ± 0.9	9.60 ± 0.57	3162.52 ± 0.15	16.3 ± 1.5	-1.28
	3917.15 ± 0.82[d]	0.19 ± 0.04	1.17 ± 0.25	0.80 ± 0.17	-	-	-
	4111.47 ± 0.29	0.18 ± 0.05	1.14 ± 0.30	0.78 ± 0.21	-	-	-
	4176.05 ± 0.26[e]	0.69 ± 0.09	4.29 ± 0.58	2.94 ± 0.38	-	-	-
	4621.45 ± 0.23[d]	0.45 ± 0.08	2.77 ± 0.51	1.89 ± 0.35	-	-	-
^{37}Cl(n,n'γ)^{37}Cl	905.05 ± 0.11	0.53 ± 0.05	3.26 ± 0.33	6.97 ± 0.67	906.64 ± 0.15	2.9 ± 0.4	0.69
(1.77 MeV)	1725.96 ± 0.09[a]	3.17 ± 0.69	19.6 ± 4.3	42 ± 9	1726.50 ± 0.10	25 ± 2	-1.13
	1901.00 ± 0.52[d]	0.26 ± 0.05	1.60 ± 0.29	3.41 ± 0.62	-	-	-
	3084.96 ± 0.45[d]	1.81 ± 0.10	11.2 ± 0.7	24 ± 1	3086.3 ± 0.3	11.2 ± 1.0	-0.02
	3102.99 ± 0.13[a]	1.67 ± 0.07	10.3 ± 0.6	22 ± 1	3103.29 ± 0.15	14.6 ± 1.5	-2.67
	3626.31 ± 0.19[d]	0.28 ± 0.07	1.76 ± 0.45	3.77 ± 0.94	-	-	-
	3740.96 ± 0.19[d]	0.42 ± 0.07	2.62 ± 0.47	5.61 ± 0.99	3742.9 ± 0.5	3.0 ± 1.0	-0.34
	4010.94 ± 0.68	0.29 ± 0.05	1.78 ± 0.31	3.80 ± 0.66	-	-	-
^{35}Cl(n,pγ)^{35}S	774.80 ± 0.12	0.34 ± 0.03	2.12 ± 0.21	1.45 ± 0.14	775.0 ± 0.2	1.3 ± 0.3	2.25
(0 MeV)	1571.98 ± 0.13	1.16 ± 0.08	7.16 ± 0.55	4.90 ± 0.35	1572.32 ± 0.13	5.9 ± 0.5	1.70
	1990.80 ± 0.11	1.74 ± 0.08	10.8 ± 0.6	7.36 ± 0.34	1991.43 ± 0.15	11.6 ± 1.0	-0.71
	2347.51 ± 0.18	0.60 ± 0.05	3.71 ± 0.36	2.54 ± 0.23	2347.9 ± 0.4	6.6 ± 0.6	-4.14
	2714.93 ± 0.48[d]	0.20 ± 0.05	1.25 ± 0.29	0.85 ± 0.19	-	-	-

E_{thr} is the threshold energy of the considered reaction taken from [55, 114], E_γ is the γ-ray energy, $P_{E\gamma}(90°)/(\epsilon_{E\gamma} \times f_{E\gamma})$ the net counts in the γ-ray peak divided by the full-energy-peak (FEP) efficiency and the γ-ray self-absorption factor, I_R the relative intensity (relative to the 1219-keV line of ^{35}Cl, 100%) of the γ-rays and $\langle\sigma_{E_\gamma}(90°)\rangle$ is the fast-neutron spectrum-averaged isotopic partial cross section for γ-ray production at an angle of 90° between neutron beam and detector determined with Eq. (4.1). R is the residual calculated by means of Eq. (4.33)

[a] corrected for background interferences

[b] unassigned by Demidov et al.

[c] maybe uncorrected interference in [27] from the SE from the 2693.7-keV line of ^{35}Cl

[d] Doppler-broadened; short-lived transitions in the femtosecond range [65]

[e] might be fed from two close-lying short-lived levels [163]; possible, but unlikely to come from the ^{37}Cl(n,n'γ)^{37}Cl reaction [164]

H.1.9 : Prompt γ-rays of ^{35}Cl, ^{37}Cl and ^{35}S induced by fast neutrons on $DyCl_3{\cdot}6H_2O$.

Reaction (E_{thr})	This work				From Atlas [27]		R
	E_γ (keV)	$P_{E\gamma}(90°)/(\epsilon_{E\gamma} \times f_{E\gamma})$ $\times$ 10^{-8} (count)	I_R(relative) (%)	$\langle\sigma_{E_\gamma}(90°)\rangle$ (mb)	E_γ (keV)	I_R(relative) (%)	
^{35}Cl(n,n'γ)^{35}Cl	930.24 ± 0.48[a]	0.17 ± 0.02	4.15 ± 0.55	2.44 ± 0.31	930.5 ± 0.5	3.0 ± 1.0	1.01
(1.25 MeV)	1185.32 ± 0.43[b]	0.14 ± 0.02	3.55 ± 0.51	2.08 ± 0.29	1184.72 ± 0.15[c]	3.8 ±0.4	-0.38
	1219.18 ± 0.06[d]	4.03 ± 0.14	100	59 ± 2	1219.52 ± 0.10	100	-
	1702.01 ± 0.45[a]	0.06 ± 0.02	1.61 ± 0.42	0.94 ± 0.24	-	-	-
	1763.43 ± 0.27	5.13 ± 0.24	127 ± 8	75 ± 4	1763.27 ± 0.10	129 ± 4	-0.21
	2180.33 ± 0.53	0.10 ± 0.02	2.53 ± 0.61	1.48 ± 0.36	2180.8 ± 0.3[e]	6.2 ± 0.6	-4.28
	2645.38 ± 0.16	1.05 ± 0.08	26 ± 2	15.2 ± 1.2	2645.7 ± 0.2	25.7 ± 1.5	0.11
	2693.53 ± 0.30[a,f]	0.85 ± 0.04	21 ± 1	12.3 ± 0.6	2694.0 ± 0.2	19.1 ± 1.5	0.95
	2840.64 ± 0.31[b,f,g]	0.10 ± 0.02	2.36 ± 0.43	1.38 ± 0.24	2840.3 ± 0.4	5.4 ± 0.6	-4.12
	3001.90 ± 0.22[f]	0.87 ± 0.04	22 ± 1	12.6 ± 0.6	3002.2 ± 0.2	15.5 ± 1.5	3.03

H.1.9 : (continued).

Reaction (E_{thr})	This work				From Atlas [27]		R
	E_γ (keV)	$P_{E\gamma}(90°)/(\epsilon_{E\gamma} \times f_{E\gamma})$ $\times 10^{-8}$ (count)	I_R(relative) (%)	$\langle\sigma_{E_\gamma}(90°)\rangle$ (mb)	E_γ (keV)	I_R(relative) (%)	
	3162.76 ± 0.17	0.65 ± 0.03	16.1 ± 1.0	9.47 ± 0.47	3162.52 ± 0.15	16.3 ± 1.5	-0.08
	4176.30 ± 0.38[h]	0.20 ± 0.04	5.03 ± 0.99	2.95 ± 0.57	-	-	-
^{37}Cl(n,n'γ)^{37}Cl	905.86 ± 0.32	0.10 ± 0.03	2.37 ± 0.76	4.35 ± 1.39	906.64 ± 0.15	2.9 ± 0.4	-0.61
(1.77 MeV)	1725.65 ± 0.08[a,d]	0.57 ± 0.04	14.2 ± 1.1	26 ± 2	1726.50 ± 0.10	25 ± 2	-4.73
	3085.09 ± 0.36[f]	0.50 ± 0.05	12.3 ± 1.3	23 ± 2	3086.3 ± 0.3	11.2 ± 1.0	0.71
	3103.27 ± 0.17[a,i]	0.49 ± 0.03	12.1 ± 0.9	22 ± 2	3103.29 ± 0.15	14.6 ± 1.5	-1.44
^{35}Cl(n,pγ)^{35}S	775.52 ± 0.11	0.14 ± 0.02	3.47 ± 0.48	2.03 ± 0.27	775.0 ± 0.2	1.3 ± 0.3	3.84
(0 MeV)	1572.37 ± 0.14[b]	0.35 ± 0.03	8.57 ± 0.86	5.02 ± 0.47	1572.32 ± 0.13	5.9 ± 0.5	2.68
	1991.01 ± 0.10	0.50 ± 0.03	12.3 ± 0.8	7.21 ± 0.43	1991.43 ± 0.15	11.6 ± 1.0	0.54
	2347.77 ± 0.26	0.21 ± 0.03	5.16 ± 0.67	3.02 ± 0.38	2347.9 ± 0.4	6.6 ± 0.6	-1.61

E_{thr} is the threshold energy of the considered reaction taken from [55, 114], E_γ is the γ-ray energy, $P_{E\gamma}(90°)/(\epsilon_{E\gamma} \times f_{E\gamma})$ the net counts in the γ-ray peak divided by the full-energy-peak (FEP) efficiency and the γ-ray self-absorption factor, I_R the relative intensity (relative to the 1219-keV line of ^{35}Cl, 100%) of the γ-rays and $\langle\sigma_{E_\gamma}(90°)\rangle$ is the fast-neutron spectrum-averaged isotopic partial cross section for γ-ray production at an angle of 90° between neutron beam and detector determined with Eq. (4.1). R is the residual calculated by means of Eq. (4.33). Lines marked in red were not considered for average values

[a] corrected for background interferences

[b] interference from ^{161}Dy(n,γ)^{162}Dy corrected (7.5% of net counts)

[c] unassigned by Demidov et al.

[d] interference from (n,n'γ) reactions of Dy corrected with intensities from [27]

[e] maybe uncorrected interference in [27] from the SE from the 2693.5-keV line of ^{35}Cl

[f] Doppler-broadened; short-lived transitions in the femtosecond range [65]

[g] interference from ^{164}Dy(n,γ)^{165}Dy corrected (5.5% of net counts)

[h] might be fed from two close-lying short-lived levels [163]; possible, but unlikely to come from the ^{37}Cl(n,n'γ)^{37}Cl reaction [164]

[i] interference from ^{164}Dy(n,γ)^{165}Dy corrected (1.7% of net counts)

H.1.10 : Prompt γ-rays of ^{35}Cl, ^{37}Cl, ^{35}S and ^{32}P induced by fast neutrons on RE chloride samples listed in Table 6.1. All given values are averaged over all samples.

Reaction (E_{thr})	This work			From Atlas [27]		R
	E_γ (keV)	I_R(relative) (%)	$\langle\sigma_{E_\gamma}(90°)\rangle$ (mb)	E_γ (keV)	I_R(relative) (%)	
^{35}Cl(n,n'γ)^{35}Cl	930.58 ± 0.43[a]	3.46 ± 0.49	**2.24 ± 0.13**	930.5 ± 0.5	3.0 ± 1.0	0.42
(1.25 MeV)	1184.72 ± 0.28	3.93 ± 0.27	**2.60 ± 0.23**	1184.72 ± 0.15[b]	3.8 ±0.4	0.28
	1219.21 ± 0.09	100	68 ± 4	1219.52 ± 0.10	100	-
	1701.73 ± 0.20[a]	1.23 ± 0.25	**0.81 ± 0.16**	-	-	-
	1763.04 ± 0.29	117 ± 11	**77 ± 3**	1763.27 ± 0.10	129 ± 4	-1.01
	2179.41 ± 0.55	2.95 ± 0.56	**1.94 ± 0.35**	2180.8 ± 0.3[c]	6.2 ± 0.6	-3.98
	2645.36 ± 0.24	23.1 ± 2.5	15.2 ± 1.0	2645.7 ± 0.2	25.7 ± 1.5	-0.87
	2693.61 ± 0.34[a,d]	18.0 ± 1.8	**11.9 ± 1.3**	2694.0 ± 0.2	19.1 ± 1.5	-0.47
	2840.46 ± 0.51[d]	2.01 ± 0.29	**1.32 ± 0.15**	2840.3 ± 0.4	5.4 ± 0.6	-5.10
	3001.95 ± 0.25[d]	18.8 ± 1.4	**12.4 ± 0.8**	3002.2 ± 0.2	15.5 ± 1.5	1.61
	3162.64 ± 0.14	14.8 ± 1.2	9.77 ± 0.43	3162.52 ± 0.15	16.3 ± 1.5	-0.77
	3917.43 ± 0.79[d]	1.16 ± 0.12	**0.78 ± 0.11**	-	-	-
	4111.06 ± 1.35	1.78 ± 0.42	**1.20 ± 0.32**	-	-	-
	4175.79 ± 0.63[e]	3.80 ± 1.41	**2.48 ± 0.87**	-	-	-
	4622.60 ± 0.70[d]	2.80 ± 0.17	**1.84 ± 0.06**	-	-	-
^{37}Cl(n,n'γ)^{37}Cl	905.84 ± 0.40	2.46 ± 0.53	5.07 ± 1.15	906.64 ± 0.15	2.9 ± 0.4	-0.67
(1.77 MeV)	1726.10 ± 0.25[a]	19.4 ± 2.3	**40 ± 6**	1726.50 ± 0.10	25 ± 2	-1.86
	1900.55 ± 0.42[d]	1.34 ± 0.25	**2.76 ± 0.43**	-	-	-
	3085.65 ± 0.46[d]	11.2 ± 0.9	**23 ± 2**	3086.3 ± 0.3	11.2 ± 1.0	0.01
	3103.20 ± 0.13[a]	11.2 ± 0.7	23 ± 1	3103.29 ± 0.15	14.6 ± 1.5	-2.04
	3625.92 ± 0.98[d]	1.53 ± 0.39	**3.22 ± 0.91**	-	-	-
	3740.45 ± 0.54[d]	2.53 ± 0.33	**5.37 ± 1.00**	3742.9 ± 0.5	3.0 ± 1.0	-0.44

H.1.10 : (continued).

Reaction (E_{thr})	This work			From Atlas [27]		R
	E_γ (keV)	I_R(relative) (%)	$\langle\sigma_{E_\gamma}(90°)\rangle$ (mb)	E_γ (keV)	I_R(relative) (%)	
	4010.96 ± 0.53	1.41 ± 0.29	**2.96 ± 0.57**	-	-	-
^{35}Cl(n,pγ)^{35}S	774.96 ± 0.32	1.96 ± 0.83	**1.24 ± 0.45**	775.0 ± 0.2	1.3 ± 0.3	0.75
(0 MeV)	1572.23 ± 0.17	6.50 ± 1.09	**4.24 ± 0.52**	1572.32 ± 0.17	5.9 ± 0.5	0.50
	1990.95 ± 0.14	10.9 ± 1.0	**7.15 ± 0.45**	1991.43 ± 0.15	11.6 ± 1.0	-0.54
	2347.72 ± 0.38	4.24 ± 0.49	2.79 ± 0.20	2347.9 ± 0.4	6.6 ± 0.6	-3.04
	2715.08 ± 0.71[d]	1.32 ± 0.39	**0.89 ± 0.27**	-	-	-
^{35}Cl(n,$\alpha\gamma$)^{32}P	77.86 ± 0.08	37 ± 5	**25 ± 5**	-	-	-
(0 MeV)						

E_{thr} is the threshold energy of the considered reaction taken from [55, 114], E_γ is the γ-ray energy, I_R the relative intensity (relative to the 1219-keV line of ^{35}Cl, 100%) of the γ-rays and $\langle\sigma_{E_\gamma}(90°)\rangle$ is the fast-neutron spectrum-averaged isotopic partial cross section for γ-ray production at an angle of 90° between neutron beam and detector determined with Eq. (4.1). R is the residual calculated by means of Eq. (4.33). Cross sections written in bold are proposed

[a]corrected for background interferences

[b]unassigned by Demidov et al.

[c]maybe uncorrected interference in [27] from the SE from the 2693.6-keV line of ^{35}Cl

[d]Doppler-broadened; short-lived transitions in the femtosecond range [65]

[e]might be fed from two close-lying short-lived levels [163]; possible, but unlikely to come from the ^{37}Cl(n,n'γ)^{37}Cl reaction [164]

H.1.11 : Prompt γ-rays of ^{139}La induced by inelastic scattering of fast neutrons.

This work				From Atlas [27]		I_R (This work)/I_R (Demidov)	R
E_γ (keV)	$P_{E\gamma}(90°)/(\epsilon_{E\gamma}\times f_{E\gamma})\times 10^{-8}$ (count)	I_R(relative) (%)	$\langle\sigma_{E_\gamma}(90°)\rangle$ (mb)	E_γ (keV)	I_R(relative) (%)		
97.11 ± 0.05	0.98 ± 0.06	11.0 ± 0.8	8.98 ± 0.92	-	-	-	-
153.43 ± 0.12[a]	0.29 ± 0.04	3.24 ± 0.48	2.65 ± 0.44	-	-	-	-
165.73 ± 0.04[b]	63 ± 2	702 ± 31	574 ± 48	165.85 ± 0.10[c]	930 ± 150	0.76 ± 0.13	-1.49
174.44 ± 0.04[b,d]	2.28 ± 0.19	26 ± 2	21 ± 2	174.6 ± 0.2	20 ± 5	1.28 ± 0.34	1.02
232.60 ± 0.06	0.73 ± 0.05	8.14 ± 0.60	6.65 ± 0.68	232.5 ± 0.6	9.1 ± 1.0	0.89 ± 0.12	-0.82
246.55 ± 0.08[a]	0.33 ± 0.03	3.73 ± 0.40	3.05 ± 0.39	-	-	-	-
290.83 ± 0.04[b]	1.54 ± 0.07	17.3 ± 0.9	14.1 ± 1.3	291.3 ± 0.2	16.5 ± 1.5	1.05 ± 0.11	0.43
307.92 ± 0.05[b]	0.76 ± 0.05	8.55 ± 0.60	6.99 ± 0.70	308.3 ± 0.3	10.6 ± 1.5	0.81 ± 0.13	-1.27
330.14 ± 0.04[c,e]	4.52 ± 0.18	51 ± 3	41 ± 4	330.7 ± 0.1	54 ± 5	0.94 ± 0.10	-0.58
362.43 ± 0.10	0.58 ± 0.07	6.52 ± 0.81	5.33 ± 0.77	363.1 ± 0.2	8.9 ± 1.0	0.73 ± 0.12	-1.85
402.61 ± 0.07	1.08 ± 0.10	12.1 ± 1.2	9.86 ± 1.19	403.8 ± 0.2	9.8 ± 1.5	1.23 ± 0.22	1.19
424.43 ± 0.05	1.77 ± 0.12	19.8 ± 1.4	16.2 ± 1.7	425.2 ± 0.2	20 ± 3	0.99 ± 0.17	-0.05
495.22 ± 0.12[c,e]	0.32 ± 0.06	3.56 ± 0.70	2.91 ± 0.61	-	-	-	-
579.35 ± 0.07	0.34 ± 0.04	3.86 ± 0.43	3.15 ± 0.42	581.3 ± 0.5	7 ± 2	0.55 ± 0.17	-1.53
1042.90 ± 0.07[f]	1.82 ± 0.08	20 ± 1	16.7 ± 1.5	1043.1 ± 0.3	15 ± 4	1.36 ± 0.37	1.30
1052.85 ± 0.08[b]	0.74 ± 0.06	8.29 ± 0.71	6.77 ± 0.76	1054.2 ± 0.8	8 ± 3	1.04 ± 0.40	0.09
1090.70 ± 0.06[d]	2.62 ± 0.34	29 ± 4	24 ± 4	1090.97 ± 0.10	33 ± 3	0.89 ± 0.14	-0.73
1215.50 ± 0.06[b]	13.50 ± 0.44	151 ± 7	124 ± 10	1215.49 ± 0.10	137 ± 15	1.11 ± 0.13	0.87
1219.24 ± 0.06[b,g]	5.77 ± 0.72	65 ± 8	53 ± 8	1219.10 ± 0.10	80 ± 10	0.81 ± 0.15	-1.17
1242.78 ± 0.19[a]	0.30 ± 0.06	3.33 ± 0.65	2.72 ± 0.57	-	-	-	-
1254.12 ± 0.31	0.56 ± 0.10	6.29 ± 1.15	5.14 ± 1.01	-	-	-	-
1256.57 ± 0.14	1.47 ± 0.13	16.5 ± 1.6	13.5 ± 1.6	1256.0	25 ± 3[h]	0.91 ± 0.22	-0.40
1310.65 ± 0.07	4.60 ± 0.15	52 ± 2	42 ± 4	1310.64 ± 0.15	48 ± 5	1.07 ± 0.12	0.65
1370.49 ± 0.08[e]	1.36 ± 0.07	15.3 ± 0.9	12.5 ± 1.2	1370.5 ± 0.2	16.6 ± 1.5	0.92 ± 0.10	-0.74
1381.38 ± 0.12[b]	0.74 ± 0.06	8.26 ± 0.72	6.75 ± 0.76	1381.1 ± 0.2	6.6 ± 0.7	1.25 ± 0.17	1.65
1392.84 ± 0.09[d]	0.77 ± 0.04	8.63 ± 0.57	7.06 ± 0.69	1392.4 ± 0.2	8.7 ± 0.8	0.99 ± 0.11	-0.07
1420.53 ± 0.07[d]	8.91 ± 0.28	100	82 ± 7	1420.56 ± 0.10	100	-	-

H.1.11 : (continued).

This work				From Atlas [27]		I_R (This work)/I_R (Demidov)	R
E_γ (keV)	$P_{E\gamma}(90°)/(\epsilon_{E\gamma} \times f_{E\gamma}) \times 10^{-8}$ (count)	I_R(relative) (%)	$\langle\sigma_{E_\gamma}(90°)\rangle$ (mb)	E_γ (keV)	I_R(relative) (%)		
1476.28 ± 0.14	0.86 ± 0.07	9.64 ± 0.83	7.88 ± 0.88	1476.1 ± 0.4	6.6 ± 0.7	1.46 ± 0.20	2.80
1537.86 ± 0.07[b]	14.38 ± 0.44	161 ± 7	132 ± 11	1537.69 ± 0.10	144 ± 14	1.12 ± 0.12	1.11
1558.33 ± 0.08[d]	1.13 ± 0.17	12.7 ± 2.0	10.3 ± 1.8	1558.5 ± 0.2	11.8 ± 1.2	1.07 ± 0.20	0.37
1578.16 ± 0.07	6.85 ± 0.22	77 ± 3	63 ± 5	1578.09 ± 0.10	72 ± 7	1.07 ± 0.11	0.61
1595.20 ± 0.13[d,e]	1.37 ± 0.11	15.4 ± 1.4	12.6 ± 1.4	1595.6	18 ± 3	0.85 ± 0.16	-0.80
1600.27 ± 0.14[d,e]	1.01 ± 0.06	11.3 ± 0.8	9.22 ± 0.93	1600.9 ± 0.6	10 ± 2	1.13 ± 0.24	0.60
1625.55 ± 0.22[a,d,e]	0.23 ± 0.03	2.61 ± 0.35	2.13 ± 0.32	1626.7 ± 0.8	3.1 ± 0.4	0.84 ± 0.16	-0.92
1683.10 ± 0.08	2.99 ± 0.11	34 ± 2	27 ± 2	1683.1 ± 0.2	35 ± 4	0.96 ± 0.12	-0.34
1690.49 ± 0.13	0.74 ± 0.08	8.33 ± 0.89	6.80 ± 0.87	1690.6 ± 0.3	10.4 ± 1.5	0.80 ± 0.14	-1.19
1716.14 ± 0.09	3.72 ± 0.19	42 ± 2	34 ± 3	1716.11 ± 0.10	37 ± 4	1.13 ± 0.14	1.00
1754.60 ± 0.11	0.80 ± 0.05	8.94 ± 0.59	7.30 ± 0.71	1755.0 ± 0.4	10.4 ± 1.2	0.86 ± 0.11	-1.09
1797.09 ± 0.11[d]	0.45 ± 0.03	5.03 ± 0.36	4.11 ± 0.41	1797.1 ± 0.4	7.1 ± 0.8	0.71 ± 0.09	-2.36
1853.68 ± 0.09	1.88 ± 0.08	21 ± 1	17.3 ± 1.5	1853.64 ± 0.10	22 ± 2	0.96 ± 0.10	-0.39
1894.28 ± 0.23	0.38 ± 0.05	4.28 ± 0.53	3.50 ± 0.50	1894.0	4.7 ± 0.6	0.91 ± 0.16	-0.52
1920.41 ± 0.10	1.10 ± 0.05	12.4 ± 0.6	10.1 ± 0.9	1920.7 ± 0.2	12.5 ± 1.5	0.99 ± 0.13	-0.09
2060.22 ± 0.14	0.50 ± 0.04	5.56 ± 0.49	4.54 ± 0.51	2060.9 ± 0.5	6.6 ± 0.8	0.84 ± 0.13	-1.11
2070.58 ± 0.32[a]	0.39 ± 0.05	4.43 ± 0.53	3.62 ± 0.51	2071.4 ± 0.6	3.7 ± 0.5	1.20 ± 0.22	-1.11
2087.60 ± 0.27[a]	0.37 ± 0.05	4.11 ± 0.55	3.36 ± 0.51	-	-	-	-
2209.63 ± 0.47[a,d]	0.24 ± 0.05	2.71 ± 0.58	2.22 ± 0.50	2210.5 ± 0.8	12 ± 2	0.23 ± 0.06	-4.46
2243.79 ± 0.16[a]	0.45 ± 0.04	5.01 ± 0.43	4.09 ± 0.46	2244.6 ± 1.0	2.8 ± 0.5	1.79 ± 0.35	3.37
2275.87 ± 0.28[d]	0.26 ± 0.08	2.88 ± 0.89	2.36 ± 0.75	2276.2 ± 1.2	4.4 ± 1.0	0.66 ± 0.25	-1.13
2385.58 ± 0.24	0.25 ± 0.04	2.80 ± 0.42	2.29 ± 0.38	2386.8 ± 1.0[i]	7.4 ± 2.0	0.38 ± 0.12	-2.25
2406.04 ± 0.29[a]	0.28 ± 0.04	3.09 ± 0.44	2.52 ± 0.40	2407.0 ± 1.2	6.3 ± 2.0	0.49 ± 0.17	-1.57
2812.07 ± 0.38[a,e]	0.09 ± 0.03	1.03 ± 0.28	0.84 ± 0.24	-	-	-	-
3115.34 ± 0.36[a,e]	0.19 ± 0.04	2.08 ± 0.44	1.70 ± 0.38	-	-	-	-
3290.76 ± 0.60[a]	0.15 ± 0.04	1.66 ± 0.40	1.35 ± 0.34	-	-	-	-
3789.49 ± 0.68[a]	0.16 ± 0.04	1.82 ± 0.47	1.49 ± 0.40	-	-	-	-

E_γ is the γ-ray energy, $P_{E\gamma}(90°)/(\epsilon_{E\gamma} \times f_{E\gamma})$ the net counts in the γ-ray peak divided by the full-energy-peak (FEP) efficiency and the γ-ray self-absorption factor, I_R the relative intensity (relative to the 1421-keV line of ^{139}La, 100%) of the γ-rays and $\langle\sigma_{E_\gamma}(90°)\rangle$ is the fast-neutron spectrum-averaged isotopic partial cross section for γ-ray production at an angle of 90° between neutron beam and detector determined with Eq. (4.1). R is the residual calculated by means of Eq. (4.33)
[a] γ-ray not listed in [170]; any other origins than ^{139}La(n,n'γ)^{139}La excluded
[b] (n,γ) interference below 1%, neglected
[c] maybe unresolved (n,γ) capture line of ^{139}La by Demidov at 163 keV [132]
[d] corrected for background interference
[e] (n,γ) interference above 1%, corrected
[f] imprecise fit at tip of ^{70}Ge triangle at 1040 keV
[g] corrected for contribution of the ^{35}Cl(n,n'γ)^{35}Cl reaction with the partial cross section deduced from the PVC measurement, i.e. (58 ± 5) mb
[h] 1254 and 1257 keV (unresolved doublet by Demidov)
[i] possible uncorrected interference by the 2390-keV line of ^{116m}In

H.1.12 : Prompt γ-rays of ^{136}Ce and ^{140}Ce induced by inelastic scattering of fast neutrons.

This work				From Atlas [27]		I_R (This work)/I_R (Demidov)	R
E_γ (keV)	$P_{E\gamma}(90°)/(\epsilon_{E\gamma} \times f_{E\gamma}) \times 10^{-8}$ (count)	I_R(relative) (%)	$\langle\sigma_{E_\gamma}(90°)\rangle$ (mb)	E_γ (keV)	I_R(relative) (%)		
551.54 ± 0.08[a]	0.17 ± 0.02	0.40 ± 0.05	1230 ± 171	-	-	-	-
131.00 ± 0.04	1.29 ± 0.05	3.07 ± 0.16	20 ± 2	131.3 ± 0.4	3.3 ± 0.8	0.93 ± 0.23	-0.28
241.63 ± 0.03	1.75 ± 0.06	4.17 ± 0.19	28 ± 2	241.91 ± 0.10	6.5 ± 0.7	0.64 ± 0.07	-3.22
266.16 ± 0.03	2.24 ± 0.08	5.33 ± 0.25	35 ± 3	266.61 ± 0.10	6.2 ± 0.6	0.86 ± 0.09	-1.34

H.1.12 : (continued).

This work				From Atlas [27]		I_R (This work)/I_R (Demidov)	R
E_γ (keV)	$P_{E\gamma}(90°)/(\epsilon_{E\gamma} \times f_{E\gamma}) \times 10^{-8}$ (count)	I_R(relative) (%)	$\langle\sigma_{E_\gamma}(90°)\rangle$ (mb)	E_γ (keV)	I_R(relative) (%)		
306.38 ± 0.04	1.13 ± 0.05	2.69 ± 0.14	17.9 ± 1.6	306.91 ± 0.15	3.3 ± 0.3	0.81 ± 0.09	-1.85
328.17 ± 0.04	1.81 ± 0.09	4.30 ± 0.25	29 ± 3	328.67 ± 0.15	5.9 ± 0.6	0.73 ± 0.09	-2.46
431.85 ± 0.05[b]	0.96 ± 0.06	2.29 ± 0.16	15.2 ± 1.5	432.44 ± 0.15	3.0 ± 0.4	0.76 ± 0.11	-1.65
486.35 ± 0.03[c]	13.6 ± 0.5	32 ± 1	215 ± 18	487.06 ± 0.05	37 ± 4	0.87 ± 0.10	-1.10
520.38 ± 0.10[c,d]	0.24 ± 0.04	0.57 ± 0.09	3.81 ± 0.65	-	-	-	-
739.64 ± 0.12[e]	0.18 ± 0.02	0.42 ± 0.04	2.80 ± 0.35	740.0 ± 0.6	0.38 ± 0.15	1.11 ± 0.45	0.26
751.15 ± 0.04	2.22 ± 0.07	5.27 ± 0.24	35 ± 3	751.65 ± 0.10	5.1 ± 0.5	1.03 ± 0.11	0.31
815.32 ± 0.04	2.00 ± 0.06	4.76 ± 0.21	32 ± 3	815.84 ± 0.10	4.6 ± 0.5	1.03 ± 0.12	0.29
867.52 ± 0.04[c]	2.99 ± 0.65	7.11 ± 1.56	47 ± 11	867.8 ± 0.2	6.5 ± 1.0	1.09 ± 0.29	0.33
919.12 ± 0.05	0.85 ± 0.03	2.02 ± 0.10	13.5 ± 1.2	919.5 ± 0.2	2.1 ± 0.3	0.96 ± 0.15	-0.25
924.83 ± 0.05[c]	1.13 ± 0.04	2.68 ± 0.12	17.8 ± 1.5	925.1 ± 0.2	2.9 ± 0.4	0.92 ± 0.13	-0.53
950.60 ± 0.05	1.05 ± 0.04	2.50 ± 0.13	16.7 ± 1.5	950.84 ± 0.15	2.3 ± 0.2	1.09 ± 0.11	0.86
982.22 ± 0.11[c]	0.25 ± 0.07	0.60 ± 0.16	4.01 ± 1.10	983.1 ± 0.4	0.64 ± 0.08	0.94 ± 0.28	-0.21
1032.90 ± 0.36[f]	0.10 ± 0.03	0.24 ± 0.07	1.62 ± 0.49	-	-	-	-
1088.30 ± 0.13[c]	0.45 ± 0.15	1.07 ± 0.35	7.13 ± 2.39	-	-	-	-
1135.20 ± 0.26	0.18 ± 0.03	0.42 ± 0.06	2.80 ± 0.46	-	-	-	-
1232.84 ± 0.16	0.28 ± 0.03	0.66 ± 0.08	4.40 ± 0.62	1233.6 ± 0.4	0.7 ± 0.2	0.94 ± 0.29	-0.18
1282.72 ± 0.19	0.12 ± 0.02	0.29 ± 0.05	1.91 ± 0.37	-	-	-	-
1303.20 ± 0.10	0.29 ± 0.03	0.69 ± 0.07	4.60 ± 0.55	1304.0 ± 0.8	0.8 ± 0.2	0.86 ± 0.23	-0.52
1321.17 ± 0.60[f]	0.23 ± 0.04	0.53 ± 0.10	3.56 ± 0.70	-	-	-	-
1404.93 ± 0.09[d]	0.45 ± 0.03	1.08 ± 0.08	7.19 ± 0.74	-	-	-	-
1420.19 ± 0.21	0.11 ± 0.02	0.26 ± 0.05	1.74 ± 0.34	-	-	-	-
1474.71 ± 0.29[c,f]	0.13 ± 0.02	0.32 ± 0.05	2.12 ± 0.38	-	-	-	-
1525.70 ± 0.11	0.25 ± 0.02	0.58 ± 0.06	3.88 ± 0.47	1526.4 ± 0.5	0.49 ± 0.10	1.19 ± 0.27	0.81
1539.85 ± 0.32[b,f]	0.09 ± 0.02	0.21 ± 0.06	1.39 ± 0.39	-	-	-	-
1565.14 ± 0.31[b]	0.11 ± 0.03	0.27 ± 0.06	1.82 ± 0.42	-	-	-	-
1595.98 ± 0.07	42 ± 1	100	666 ± 56	1596.20	100	-	-
1619.75 ± 0.32	0.10 ± 0.03	0.25 ± 0.07	1.65 ± 0.48	1620.5 ± 1.0	0.23 ± 0.08	1.08 ± 0.48	0.16
1623.62 ± 0.16[e]	0.14 ± 0.02	0.33 ± 0.04	2.23 ± 0.32	-	-	-	-
1877.26 ± 0.16	0.27 ± 0.02	0.65 ± 0.05	4.34 ± 0.48	-	-	-	-
2051.08 ± 0.32	0.06 ± 0.02	0.14 ± 0.04	0.92 ± 0.25	-	-	-	-
2521.41 ± 0.14	0.43 ± 0.03	1.01 ± 0.07	6.73 ± 0.69	2521.3 ± 0.5	1.4 ± 0.2	0.72 ± 0.12	-1.82
2546.63 ± 0.26	0.16 ± 0.02	0.38 ± 0.06	2.55 ± 0.42	2547.4 ± 0.8	0.57 ± 0.18	0.67 ± 0.23	-0.99
2899.46 ± 0.14	0.46 ± 0.03	1.10 ± 0.07	7.30 ± 0.71	2900.1 ± 0.7	1.1 ± 0.2	1.00 ± 0.19	-0.01
3118.15 ± 0.13[e]	0.39 ± 0.02	0.93 ± 0.06	6.20 ± 0.62	3120.4 ± 1.2[g]	0.56 ± 0.12	1.66 ± 0.37	2.73
3319.29 ± 0.25	0.13 ± 0.02	0.31 ± 0.04	2.08 ± 0.31	-	-	-	-
3471.02 ± 0.24	0.16 ± 0.02	0.39 ± 0.04	2.60 ± 0.35	-	-	-	-
3643.53 ± 0.37[b]	0.09 ± 0.02	0.23 ± 0.05	1.50 ± 0.34	-	-	-	-

E_γ is the γ-ray energy, $P_{E\gamma}(90°)/(\epsilon_{E\gamma} \times f_{E\gamma})$ the net counts in the γ-ray peak divided by the full-energy-peak (FEP) efficiency and the γ-ray self-absorption factor, I_R the relative intensity (relative to the 1596-keV line of ^{140}Ce, 100%) of the γ-rays and $\langle\sigma_{E_\gamma}(90°)\rangle$ is the fast-neutron spectrum-averaged isotopic partial cross section for γ-ray production at an angle of 90° between neutron beam and detector determined with Eq. (4.1). R is the residual calculated by means of Eq. (4.33)

[a] γ-ray of ^{136}Ce

[b] interference from ^{142}Ce(n,n'γ)^{142}Ce possible with respect to [173]

[c] corrected for background interference

[d] doublet with ^{142}Ce

[e] corrected for escape peak interference

[f] somewhat cautious assignment, as relative intensities differ considerably compared to data given in [160]

[g] wrong level energy assigned by Demidov et al. [27]

H.1.13 : Prompt γ-rays of ^{142}Ce induced by inelastic scattering of fast neutrons.

This work				From Atlas [27]		I_R (This work)/I_R (Demidov)	R
E_γ (keV)	$P_{E\gamma}(90°)/(\epsilon_{E\gamma} \times f_{E\gamma}) \times 10^{-8}$ (count)	I_R(relative) (%)	$\langle\sigma_{E_\gamma}(90°)\rangle$ (mb)	E_γ (keV)	I_R(relative) (%)		
522.88 ± 0.08	0.25 ± 0.03	0.59 ± 0.08	32 ± 5	522.0 ± 0.3	0.83 ± 0.15[a]	1.40 ± 0.39	1.31
577.46 ± 0.04	2.15 ± 0.09	5.11 ± 0.26	272 ± 24	578.1 ± 0.2	6.3 ± 0.8	0.81 ± 0.11	-1.41
640.63 ± 0.03	10.6 ± 0.3	25.0 ± 1.1	1333 ± 112	641.23 ± 0.06	29 ± 3	0.86 ± 0.10	-1.23
892.16 ± 0.13	0.23 ± 0.02	0.56 ± 0.06	30 ± 4	-	-	-	-
894.56 ± 0.05	1.29 ± 0.05	3.06 ± 0.15	163 ± 14	894.76 ± 0.15	4.1 ± 0.5[b]	0.88 ± 0.15	-0.96
1011.07 ± 0.06	0.76 ± 0.03	1.81 ± 0.10	96 ± 9	1011.5 ± 0.3	2.6 ± 0.4	0.70 ± 0.11	-1.91
1058.13 ± 0.27[c]	0.09 ± 0.03	0.21 ± 0.07	11.3 ± 3.8	1059.0	0.63 ± 0.15	0.34 ± 0.14	-2.53
1243.20 ± 0.29[d]	0.10 ± 0.02	0.24 ± 0.06	12.6 ± 3.1	-	-	-	-
1362.36 ± 0.14	0.42 ± 0.03	0.99 ± 0.08	53 ± 6	-	-	-	-
1388.59 ± 0.17	0.12 ± 0.03	0.30 ± 0.07	15.7 ± 3.9	-	-	-	-
1402.36 ± 0.12	0.30 ± 0.02	0.71 ± 0.06	38 ± 4	1404.3 ± 0.3	1.9 ± 0.2[e]	0.94 ± 0.14	-2.12
1478.43 ± 0.26[f]	0.14 ± 0.02	0.32 ± 0.05	17.1 ± 3.1	-	-	-	-
2004.15 ± 0.37	0.06 ± 0.02	0.15 ± 0.04	7.84 ± 2.03	-	-	-	-
2038.77 ± 0.34	0.09 ± 0.02	0.21 ± 0.04	11.3 ± 2.2	-	-	-	-
2186.63 ± 0.41	0.13 ± 0.02	0.31 ± 0.06	16.6 ± 3.4	-	-	-	-
2448.81 ± 0.19	0.09 ± 0.02	0.22 ± 0.04	11.8 ± 2.2	-	-	-	-

E_γ is the γ-ray energy, $P_{E\gamma}(90°)/(\epsilon_{E\gamma} \times f_{E\gamma})$ the net counts in the γ-ray peak divided by the full-energy-peak (FEP) efficiency and the γ-ray self-absorption factor, I_R the relative intensity (relative to the 1596-keV line of ^{140}Ce, 100%) of the γ-rays and $\langle\sigma_{E_\gamma}(90°)\rangle$ is the fast-neutron spectrum-averaged isotopic partial cross section for γ-ray production at an angle of 90° between neutron beam and detector determined with Eq. (4.1). R is the residual calculated by means of Eq. (4.33)
[a]520 and 523 keV (unresolved doublet by Demidov)
[b]892 and 895 keV (unresolved doublet by Demidov)
[c]must be reviewed with caution, as a line at 1637 keV from the same excited level [65, 173] is not reported in [27]
[d]probably from E^*= 3423.6 keV [173]; main line at 2782.2 keV in [173] might have been not observed due to lower efficiency
[e]1402 and 1405 keV (unresolved doublet by Demidov)
[f]corrected for background interference

H.1.14 : Prompt γ-rays of ^{141}Pr induced by inelastic scattering of fast neutrons.

This work				From Atlas [27]		I_R (This work)/I_R (Demidov)	R
E_γ (keV)	$P_{E\gamma}(90°)/(\epsilon_{E\gamma} \times f_{E\gamma}) \times 10^{-8}$ (count)	I_R(relative) (%)	$\langle\sigma_{E_\gamma}(90°)\rangle$ (mb)	E_γ (keV)	I_R(relative) (%)		
145.30 ± 0.03	54 ± 2	812 ± 40	889 ± 75	145.45 ± 0.05	1200 ± 200	0.68 ± 0.12	-1.90
218.42 ± 0.11	0.19 ± 0.05	2.80 ± 0.81	3.06 ± 0.91	218.3 ± 0.5	3.2 ± 0.9	0.87 ± 0.35	-0.33
272.88 ± 0.04[a]	0.79 ± 0.05	11.8 ± 0.8	12.9 ± 1.3	273.3 ± 0.2	18 ± 4	0.65 ± 0.15	-1.52
311.22 ± 0.36	0.16 ± 0.03	2.34 ± 0.42	2.56 ± 0.49	-	-	-	-
359.35 ± 0.11[b]	0.38 ± 0.05	5.68 ± 0.75	6.22 ± 0.92	359.8 ± 0.6	4.1 ± 0.8	1.39 ± 0.33	1.45
530.11 ± 0.11[a]	0.15 ± 0.03	2.21 ± 0.48	2.42 ± 0.55	530.88 ± 0.10	2.4 ± 0.7	0.92 ± 0.34	-0.23
547.86 ± 0.23[b]	0.12 ± 0.02	1.85 ± 0.33	2.02 ± 0.38	546.4 ± 0.3	2.0 ± 0.4	0.92 ± 0.25	-0.30
649.52 ± 0.04	2.44 ± 0.10	36 ± 2	40 ± 4	650.34 ± 0.10	35 ± 8	1.04 ± 0.24	0.17
668.48 ± 0.07[a]	0.26 ± 0.03	3.90 ± 0.51	4.27 ± 0.63	668.88 ± 0.10	6.0 ± 1.0	0.65 ± 0.14	-1.87
735.73 ± 0.29	0.12 ± 0.03	1.73 ± 0.52	1.90 ± 0.58	736.0 ± 0.3	2.8 ± 0.4	0.62 ± 0.21	-1.63
748.72 ± 0.15[a]	0.18 ± 0.03	2.62 ± 0.39	2.87 ± 0.47	749.21 ± 0.10	5.8 ± 0.6	0.45 ± 0.08	-4.42
860.96 ± 0.12[a]	0.10 ± 0.02	1.52 ± 0.37	1.66 ± 0.42	861.5 ± 0.2	2.1 ± 0.4	0.72 ± 0.22	-1.07
948.47 ± 0.13	0.23 ± 0.04	3.49 ± 0.60	3.82 ± 0.71	-	-	-	-
971.64 ± 0.05[a]	5.63 ± 0.18	84 ± 4	92 ± 8	972.24 ± 0.10	83 ± 8[c]	1.08 ± 0.15	-3.14
974.64 ± 0.11[b]	0.37 ± 0.03	5.51 ± 0.49	6.04 ± 0.68	-	-	-	-
1022.47 ± 0.14	0.09 ± 0.02	1.29 ± 0.31	1.42 ± 0.35	1023.1 ± 0.2	3.7 ± 0.6	0.35 ± 0.10	-3.56
1117.10 ± 0.10[a]	0.50 ± 0.05	7.50 ± 0.74	8.22 ± 0.99	1117.65 ± 0.10	7.6 ± 0.7	0.99 ± 0.13	-0.09
1126.40 ± 0.05	6.70 ± 0.21	100	110 ± 9	1126.90 ± 0.10	100	-	-
1146.80 ± 0.06	2.30 ± 0.09	34 ± 2	38 ± 3	1147.24 ± 0.10	34 ± 4	1.01 ± 0.13	0.07

H.1.14 : (continued).

This work				From Atlas [27]		I_R (This work)/I_R (Demidov)	R
E_γ (keV)	$P_{E\gamma}(90°)/(\epsilon_{E\gamma} \times f_{E\gamma}) \times 10^{-8}$ (count)	I_R(relative) (%)	$\langle\sigma_{E_\gamma}(90°)\rangle$ (mb)	E_γ (keV)	I_R(relative) (%)		
1264.30 ± 0.24	0.11 ± 0.02	1.68 ± 0.33	1.84 ± 0.38	-	-	-	-
1290.31 ± 0.08	1.39 ± 0.08	21 ± 1	23 ± 2	1290.0 ± 0.4	27 ± 10	0.77 ± 0.29	-0.62
1298.18 ± 0.06[a]	2.02 ± 0.09	30 ± 2	33 ± 3	1298.74 ± 0.10	33 ± 4	0.92 ± 0.12	-0.64
1306.45 ± 0.06	3.42 ± 0.11	51 ± 3	56 ± 5	1306.85 ± 0.10	50 ± 5	1.02 ± 0.11	0.20
1311.61 ± 0.06	3.31 ± 0.11	49 ± 3	54 ± 5	1312.13 ± 0.10	51 ± 5	0.97 ± 0.11	-0.29
1347.98 ± 0.06[a]	3.62 ± 0.21	54 ± 4	59 ± 6	1348.70 ± 0.10	47 ± 4	1.15 ± 0.13	1.29
1375.23 ± 0.11[d]	0.54 ± 0.05	8.00 ± 0.75	8.76 ± 1.02	1375.7 ± 0.3	12 ± 3	0.67 ± 0.18	-1.29
1434.83 ± 0.09[a]	3.00 ± 0.13	45 ± 3	49 ± 4	1435.34	50 ± 5	0.90 ± 0.10	-0.91
1451.73 ± 0.09	0.61 ± 0.04	9.09 ± 0.71	9.95 ± 1.03	1452.21 ± 0.10	13 ± 2	0.70 ± 0.12	-1.84
1456.89 ± 0.08[a]	1.11 ± 0.06	16.6 ± 1.1	18.2 ± 1.7	1457.52 ± 0.10	17 ± 2	0.98 ± 0.13	-0.18
1506.04 ± 0.19[e]	0.30 ± 0.03	4.47 ± 0.50	4.89 ± 0.64	1506.9 ± 0.5	6.1 ± 0.2	0.73 ± 0.09	-3.04
1520.68 ± 0.07	3.29 ± 0.11	49 ± 3	54 ± 5	1521.13 ± 0.10	51 ± 5	0.96 ± 0.11	-0.34
1579.61 ± 0.09	0.63 ± 0.04	9.45 ± 0.68	10.3 ± 1.0	1580.2 ± 1.0	6.3 ± 0.7	1.50 ± 0.20	3.23
1607.78 ± 0.08	1.37 ± 0.05	20 ± 1	22 ± 2	1608.30 ± 0.10	20 ± 2	1.02 ± 0.12	0.21
1640.18 ± 0.11[a,d]	0.50 ± 0.05	7.48 ± 0.74	8.19 ± 0.98	1641.2 ± 0.2	7.2 ± 0.8	1.04 ± 0.15	0.26
1651.03 ± 0.08	2.05 ± 0.08	31 ± 2	33 ± 3	1651.48 ± 0.10	33 ± 3	0.93 ± 0.10	-0.71
1657.19 ± 0.14	0.31 ± 0.03	4.66 ± 0.51	5.10 ± 0.65	1658.0 ± 0.2	3.3 ± 0.5	1.41 ± 0.26	1.91
1666.81 ± 0.08	1.02 ± 0.05	15.2 ± 0.9	16.7 ± 1.5	1667.28 ± 0.10	13 ± 3	1.17 ± 0.28	0.71
1708.19 ± 0.09	0.76 ± 0.04	11.3 ± 0.7	12.4 ± 1.2	1708.75 ± 0.10	14 ± 3	0.81 ± 0.18	-0.87
1785.90 ± 0.09[d]	0.85 ± 0.05	12.8 ± 0.9	14.0 ± 1.4	1786.45 ± 0.10	16 ± 2	0.80 ± 0.11	-1.48
1811.92 ± 0.14[a]	0.28 ± 0.03	4.11 ± 0.43	4.50 ± 0.56	1812.9 ± 0.2	5.8 ± 0.6	0.71 ± 0.10	-2.28
1824.57 ± 0.27[f]	0.14 ± 0.03	2.09 ± 0.45	2.29 ± 0.51	1825.2 ± 0.3	2.0 ± 0.5	1.04 ± 0.34	0.13
1829.99 ± 0.22	0.28 ± 0.04	4.11 ± 0.63	4.50 ± 0.75	1830.5 ± 0.3	3.4 ± 0.4	1.21 ± 0.23	0.95
1841.80 ± 0.11	0.89 ± 0.05	13.2 ± 0.9	14.5 ± 1.4	1842.22 ± 0.10	12 ± 2	1.10 ± 0.20	0.56
1854.68 ± 0.16	0.45 ± 0.07	6.74 ± 1.04	7.38 ± 1.25	1854.9 ± 0.6	7 ± 2	0.96 ± 0.31	-0.12
1857.62 ± 0.14	0.65 ± 0.07	9.72 ± 1.10	10.7 ± 1.4	1858.4 ± 0.5	9 ± 2	1.08 ± 0.27	0.32
1872.30 ± 0.24	0.17 ± 0.03	2.59 ± 0.48	2.83 ± 0.56	-	-	-	-
1900.19 ± 0.11[g]	0.58 ± 0.04	8.62 ± 0.65	9.44 ± 0.96	1900.90 ± 0.10	11 ± 2	0.78 ± 0.15	-1.13
1975.79 ± 0.29	0.26 ± 0.05	3.87 ± 0.70	4.23 ± 0.81	1975.7 ± 0.3	5.2 ± 0.6	0.74 ± 0.16	-1.45
2017.21 ± 0.19[a]	0.19 ± 0.03	2.81 ± 0.40	3.07 ± 0.49	2018.8 ± 0.5	4.4 ± 0.6	0.64 ± 0.13	-2.20
2026.63 ± 0.15	0.30 ± 0.03	4.55 ± 0.51	4.98 ± 0.65	2027.1 ± 0.3	11 ± 3	0.41 ± 0.12	-2.12
2042.87 ± 0.31[d]	0.13 ± 0.02	1.89 ± 0.33	2.07 ± 0.38	-	-	-	-
2060.97 ± 0.16	0.33 ± 0.03	4.90 ± 0.48	5.37 ± 0.64	2061.4 ± 0.3	3.7 ± 0.6	1.33 ± 0.25	1.57
2082.08 ± 0.29[e]	0.05 ± 0.01	0.80 ± 0.20	0.88 ± 0.23	-	-	-	-
2104.82 ± 0.19[a,e]	0.19 ± 0.01	2.84 ± 0.23	3.11 ± 0.33	2105.3 ± 1.0	2.2 ± 0.6	1.29 ± 0.37	0.99
2119.11 ± 0.34	0.13 ± 0.03	1.87 ± 0.39	2.05 ± 0.45	-	-	-	-
2135.54 ± 0.15[e]	0.32 ± 0.02	4.81 ± 0.39	5.27 ± 0.56	2136.2 ± 0.7	3.0 ± 0.9	1.60 ± 0.50	1.84
2158.33 ± 0.24[d]	0.21 ± 0.03	3.11 ± 0.41	3.40 ± 0.50	2159.7 ± 0.5	4.3 ± 0.8	0.72 ± 0.16	-1.33
2191.22 ± 0.27	0.11 ± 0.03	1.60 ± 0.41	1.75 ± 0.47	2192.7 ± 1.5	3.3 ± 0.7	0.48 ± 0.16	-2.10
2247.71 ± 0.15	0.31 ± 0.03	4.64 ± 0.48	5.08 ± 0.63	2248.8 ± 0.5	5.3 ± 0.8	0.88 ± 0.16	-0.70
2267.07 ± 0.43	0.12 ± 0.03	1.72 ± 0.44	1.88 ± 0.49	-	-	-	-
2273.95 ± 0.36[a]	0.08 ± 0.02	1.21 ± 0.30	1.32 ± 0.34	2274.6 ± 0.5	1.9 ± 0.6	0.63 ± 0.21	-1.04
2354.29 ± 0.36[e]	0.18 ± 0.03	2.64 ± 0.49	2.89 ± 0.57	2352.8 ± 0.5	2.0 ± 0.9	1.32 ± 0.64	0.63
2403.74 ± 0.33	0.14 ± 0.03	2.11 ± 0.46	2.31 ± 0.52	2403.9 ± 0.5	3.0 ± 0.9	0.70 ± 0.26	-0.88
2419.53 ± 0.37	0.15 ± 0.04	2.29 ± 0.56	2.51 ± 0.64	-	-	-	-
2437.12 ± 0.32	0.15 ± 0.03	2.20 ± 0.39	2.41 ± 0.46	-	-	-	-
2452.70 ± 0.19	0.29 ± 0.02	4.40 ± 0.41	4.82 ± 0.55	2453.6 ± 1.0	4 ± 2	1.10 ± 0.56	0.20
2563.55 ± 0.32	0.12 ± 0.02	1.84 ± 0.34	2.02 ± 0.40	-	-	-	-
2582.26 ± 0.25[a]	0.16 ± 0.02	2.32 ± 0.32	2.54 ± 0.39	2581.2 ± 1.5	3.1 ± 0.9	0.75 ± 0.24	-0.82
2601.50 ± 0.25	0.21 ± 0.03	3.11 ± 0.43	3.40 ± 0.52	2603.1 ± 1.0	4 ± 2	0.78 ± 0.40	-0.44
3115.56 ± 0.70[d]	0.09 ± 0.03	1.40 ± 0.40	1.54 ± 0.45	-	-	-	-
3127.71 ± 0.43	0.11 ± 0.03	1.67 ± 0.44	1.83 ± 0.50	-	-	-	-

H.1.14 : (continued).

E_γ is the γ-ray energy, $P_{E\gamma}(90°)/(\epsilon_{E\gamma} \times f_{E\gamma})$ the net counts in the γ-ray peak divided by the full-energy-peak (FEP) efficiency and the γ-ray self-absorption factor, I_R the relative intensity (relative to the 1126-keV line of ^{141}Pr, 100%) of the γ-rays and $\langle\sigma_{E_\gamma}(90°)\rangle$ is the fast-neutron spectrum-averaged isotopic partial cross section for γ-ray production at an angle of 90° between neutron beam and detector determined with Eq. (4.1). R is the residual calculated by means of Eq. (4.33)
[a]corrected for background interference
[b]corrected for (n,γ) interference from Pr
[c]972 and 975 keV (unresolved doublet by Demidov)
[d]corrected for (n,γ) interference from Cl
[e]corrected for escape peak interference
[f]γ-ray not listed in [65, 174]; any other origins than ^{141}Pr(n,n'γ)^{141}Pr excluded
[g]corrected for contribution of the ^{37}Cl(n,n'γ)^{37}Cl reaction with the partial cross section deduced from the $CeCl_3$ measurement, i.e. (2.38 ± 0.56) mb

H.1.15 : Prompt γ-rays of ^{142}Nd induced by inelastic scattering of fast neutrons.

This work				From Atlas [27]		I_R (This work)/I_R (Demidov)	R
E_γ (keV)	$P_{E\gamma}(90°)/(\epsilon_{E\gamma} \times f_{E\gamma})$ × 10^{-8} (count)	I_R(relative) (%)	$\langle\sigma_{E_\gamma}(90°)\rangle$ (mb)	E_γ (keV)	I_R(relative) (%)		
303.87 ± 0.12	0.18 ± 0.03	1.15 ± 0.17	14.7 ± 2.4	-	-	-	-
335.79 ± 0.07	0.45 ± 0.04	2.89 ± 0.26	37 ± 4	334.2 ± 0.3	8.1 ± 1.0	0.36 ± 0.05	-5.04
502.05 ± 0.19[a]	0.10 ± 0.02	0.66 ± 0.13	-	-	-	-	-
524.34 ± 0.05	2.32 ± 0.08	14.9 ± 0.7	190 ± 16	525.49 ± 0.10	14.5 ± 1.5[b]	1.12 ± 0.21	0.62
636.09 ± 0.27	0.11 ± 0.03	0.69 ± 0.20	8.81 ± 2.62	-	-	-	-
641.41 ± 0.16	0.11 ± 0.03	0.69 ± 0.19	8.83 ± 2.49	-	-	-	-
875.56 ± 0.11	0.19 ± 0.02	1.24 ± 0.14	15.8 ± 2.1	-	-	-	-
970.79 ± 0.12[c]	0.19 ± 0.02	1.21 ± 0.15	15.4 ± 2.2	971.0 ± 0.7	2.1 ± 0.5	0.58 ± 0.15	-1.70
1006.72 ± 0.17[c,d]	0.14 ± 0.03	0.93 ± 0.18	11.9 ± 2.4	-	-	-	-
1009.62 ± 0.16	0.19 ± 0.02	1.25 ± 0.14	15.9 ± 2.2	-	-	-	-
1340.09 ± 0.14[d]	0.06 ± 0.01	0.40 ± 0.09	5.11 ± 1.15	-	-	-	-
1575.61 ± 0.07	7.48 ± 0.29	48 ± 2	613 ± 53	1575.85 ± 0.15	41 ± 4	1.18 ± 0.13	1.54
2384.14 ± 0.14	0.27 ± 0.02	1.73 ± 0.15	22 ± 3	-	-	-	-
2583.26 ± 0.25[c]	0.29 ± 0.03	1.87 ± 0.19	24 ± 3	-	-	-	-
2845.33 ± 0.17[e]	0.21 ± 0.02	1.34 ± 0.12	17.1 ± 2.0	-	-	-	-

E_γ is the γ-ray energy, $P_{E\gamma}(90°)/(\epsilon_{E\gamma} \times f_{E\gamma})$ the net counts in the γ-ray peak divided by the full-energy-peak (FEP) efficiency and the γ-ray self-absorption factor, I_R the relative intensity (relative to the 696-keV line of ^{146}Nd, 100%) of the γ-rays and $\langle\sigma_{E_\gamma}(90°)\rangle$ is the fast-neutron spectrum-averaged isotopic partial cross section for γ-ray production at an angle of 90° between neutron beam and detector determined with Eq. (4.1). R is the residual calculated by means of Eq. (4.33)
[a]line is attributed to Nd, but not listed in [65]
[b]524 and 527 keV (unresolved doublet by Demidov)
[c]corrected for background interference
[d]corrected for (n,γ) interference from Nd
[e]corrected for (n,γ) interference from Cl

H.1.16 : Prompt γ-rays of ^{143}Nd induced by inelastic scattering of fast neutrons.

This work				From Atlas [27]		I_R (This work)/I_R (Demidov)	R
E_γ (keV)	$P_{E\gamma}(90°)/(\epsilon_{E\gamma} \times f_{E\gamma})$ × 10^{-8} (count)	I_R(relative) (%)	$\langle\sigma_{E_\gamma}(90°)\rangle$ (mb)	E_γ (keV)	I_R(relative) (%)		
580.62 ± 0.19	0.17 ± 0.03	1.07 ± 0.18	30 ± 5	583.5 ± 0.6	1.6 ± 0.3	0.67 ± 0.17	-1.52
741.59 ± 0.04[a]	1.55 ± 0.06	9.98 ± 0.51	283 ± 25	742.3 ± 0.3	10 ± 2	1.00 ± 0.21	-0.01
1227.95 ± 0.06	0.74 ± 0.05	4.76 ± 0.38	135 ± 14	1228.1 ± 0.4	5.8 ± 0.8	0.82 ± 0.13	-1.17
1407.06 ± 0.07[b]	0.75 ± 0.04	4.83 ± 0.28	137 ± 13	1408.0 ± 0.8	6.0 ± 1.5	0.81 ± 0.21	-0.77
1431.14 ± 0.08[b]	0.69 ± 0.03	4.47 ± 0.26	127 ± 12	1431.8 ± 0.6	4.9 ± 0.8	0.91 ± 0.16	-0.51
1536.06 ± 0.30	0.11 ± 0.02	0.69 ± 0.13	19.4 ± 3.9	-	-	-	-

H.1.16 : (continued).

This work				From Atlas [27]		I_R (This work)/I_R (Demidov)	R
E_γ (keV)	$P_{E\gamma}(90°)/(\epsilon_{E\gamma} \times f_{E\gamma}) \times 10^{-8}$ (count)	I_R(relative) (%)	$\langle\sigma_{E_\gamma}(90°)\rangle$ (mb)	E_γ (keV)	I_R(relative) (%)		
1556.00 ± 0.10[a,b]	0.33 ± 0.02	2.13 ± 0.16	60 ± 6	1557.0 ± 1.2	2.0 ± 0.5	1.06 ± 0.28	0.25
1851.40 ± 0.19[a]	0.17 ± 0.02	1.07 ± 0.16	30 ± 5	-	-	-	-
2011.76 ± 0.32	0.08 ± 0.02	0.54 ± 0.13	15.0 ± 3.8	-	-	-	-
2035.61 ± 0.35[a,b,c]	0.06 ± 0.01	0.38 ± 0.07	10.8 ± 2.2	-	-	-	-
2063.50 ± 0.53	0.11 ± 0.03	0.72 ± 0.17	20 ± 5	-	-	-	-
2098.61 ± 0.39[b]	0.05 ± 0.01	0.34 ± 0.07	9.63 ± 2.00	-	-	-	-
2135.15 ± 0.21[a,d]	0.14 ± 0.01	0.87 ± 0.08	25 ± 3	-	-	-	-

E_γ is the γ-ray energy, $P_{E\gamma}(90°)/(\epsilon_{E\gamma} \times f_{E\gamma})$ the net counts in the γ-ray peak divided by the full-energy-peak (FEP) efficiency and the γ-ray self-absorption factor, I_R the relative intensity (relative to the 696-keV line of ^{146}Nd, 100%) of the γ-rays and $\langle\sigma_{E_\gamma}(90°)\rangle$ is the fast-neutron spectrum-averaged isotopic partial cross section for γ-ray production at an angle of 90° between neutron beam and detector determined with Eq. (4.1). R is the residual calculated by means of Eq. (4.33)

[a] corrected for (n,γ) interference from Nd

[b] corrected for background interference

[c] corrected for (n,γ) interference from Cl

[d] corrected for contribution of SE from 2645 keV (54% of net counts)

H.1.17 : Prompt γ-rays of ^{144}Nd induced by inelastic scattering of fast neutrons.

This work				From Atlas [27]		I_R (This work)/I_R (Demidov)	R
E_γ (keV)	$P_{E\gamma}(90°)/(\epsilon_{E\gamma} \times f_{E\gamma}) \times 10^{-8}$ (count)	I_R(relative) (%)	$\langle\sigma_{E_\gamma}(90°)\rangle$ (mb)	E_γ (keV)	I_R(relative) (%)		
426.02 ± 0.16[a]	0.22 ± 0.04	1.42 ± 0.26	21 ± 4	-	-	-	-
476.15 ± 0.14[a,b]	0.49 ± 0.07	3.16 ± 0.47	46 ± 8	476.6	3.0 ± 1.0[c]	2.19 ± 0.80	3.27
617.41 ± 0.04[a]	3.14 ± 0.12	20 ± 1	294 ± 26	618.04 ± 0.12	20 ± 3	1.01 ± 0.16	0.08
695.97 ± 0.04[a]	15.53 ± 0.49	100	1450 ± 123	696.60 ± 0.15	100	-	-
778.31 ± 0.08[a]	0.29 ± 0.02	1.85 ± 0.16	27 ± 3	778.6 ± 0.6	1.6 ± 0.2	1.16 ± 0.18	0.97
793.91 ± 0.26	0.08 ± 0.02	0.53 ± 0.13	7.65 ± 2.03	-	-	-	-
813.68 ± 0.04[a]	1.86 ± 0.07	12.0 ± 0.6	173 ± 15	814.2 ± 0.2	6.4 ± 0.7	1.87 ± 0.22	6.15
864.01 ± 0.04[a]	1.99 ± 0.07	12.8 ± 0.6	186 ± 16	864.5 ± 0.2	8 ± 2	1.60 ± 0.41	2.29
979.93 ± 0.09[a,b]	0.41 ± 0.03	2.67 ± 0.18	39 ± 4	980.7 ± 0.5	2.8 ± 0.6	0.95 ± 0.21	-0.21
1081.63 ± 0.22	0.06 ± 0.01	0.39 ± 0.09	5.68 ± 1.43	-	-	-	-
1094.28 ± 0.22	0.18 ± 0.02	1.14 ± 0.15	16.5 ± 2.5	-	-	-	-
1136.65 ± 0.12[a,b]	0.12 ± 0.01	0.76 ± 0.08	11.1 ± 1.5	-	-	-	-
1388.42 ± 0.23	0.16 ± 0.02	1.03 ± 0.15	15.0 ± 2.5	-	-	-	-
1413.11 ± 0.08[a,b]	0.37 ± 0.03	2.39 ± 0.19	35 ± 4	1413.3 ± 1.0	2.4 ± 0.8	0.99 ± 0.34	-0.02
1451.26 ± 0.18	0.22 ± 0.03	1.43 ± 0.19	21 ± 3	-	-	-	-
1481.70 ± 0.19[a]	0.18 ± 0.02	1.17 ± 0.15	17.0 ± 2.5	-	-	-	-
1493.55 ± 0.25[a,b]	0.04 ± 0.01	0.25 ± 0.07	3.62 ± 0.98	-	-	-	-
1560.80 ± 0.14[a]	0.07 ± 0.01	0.47 ± 0.07	6.80 ± 1.13	-	-	-	-
1671.75 ± 0.12[a,d]	0.21 ± 0.02	1.35 ± 0.11	19.6 ± 2.1	-	-	-	-
1739.24 ± 0.12	0.28 ± 0.03	1.79 ± 0.18	26 ± 3	-	-	-	-
1885.01 ± 0.46[a,b]	0.07 ± 0.02	0.44 ± 0.13	6.34 ± 1.92	-	-	-	-
1894.91 ± 0.24[a]	0.14 ± 0.02	0.91 ± 0.15	13.2 ± 2.4	-	-	-	-
1910.03 ± 0.23[a]	0.16 ± 0.02	1.00 ± 0.16	14.5 ± 2.5	-	-	-	-
2022.40 ± 0.39[a,e]	0.05 ± 0.02	0.35 ± 0.11	5.07 ± 1.58	-	-	-	-
2073.11 ± 0.18[a,b,e]	0.19 ± 0.02	1.20 ± 0.12	17.4 ± 2.2	-	-	-	-
2185.17 ± 0.23[a]	0.23 ± 0.02	1.50 ± 0.15	22 ± 3	-	-	-	-

H.1.17 : (continued).

E_γ is the γ-ray energy, $P_{E\gamma}(90°)/(\epsilon_{E\gamma} \times f_{E\gamma})$ the net counts in the γ-ray peak divided by the full-energy-peak (FEP) efficiency and the γ-ray self-absorption factor, I_R the relative intensity (relative to the 696-keV line of ^{146}Nd, 100%) of the γ-rays and $\langle\sigma_{E_\gamma}(90°)\rangle$ is the fast-neutron spectrum-averaged isotopic partial cross section for γ-ray production at an angle of 90° between neutron beam and detector determined with Eq. (4.1). R is the residual calculated by means of Eq. (4.33)
[a]corrected for (n,γ) interference from Nd
[b]corrected for background interference
[c]474 and 476 keV (unresolved doublet by Demidov)
[d]corrected for contribution of DE from 2693 keV (20.1% of net counts)
[e]corrected for (n,γ) interference from Cl

H.1.18 : Prompt γ-rays of ^{145}Nd induced by inelastic scattering of fast neutrons.

This work				From Atlas [27]		I_R (This work)/I_R (Demidov)	R
E_γ (keV)	$P_{E\gamma}(90°)/(\epsilon_{E\gamma} \times f_{E\gamma}) \times 10^{-8}$ (count)	I_R(relative) (%)	$\langle\sigma_{E_\gamma}(90°)\rangle$ (mb)	E_γ (keV)	I_R(relative) (%)		
657.01 ± 0.04	1.50 ± 0.05	9.68 ± 0.44	402 ± 34	657.9 ± 0.2	12.3 ± 1.3	0.79 ± 0.09	-1.91
675.18 ± 0.05	0.42 ± 0.02	2.73 ± 0.16	113 ± 10	676.6 ± 0.4	2.3 ± 0.3	1.19 ± 0.17	1.26
747.65 ± 0.05[a]	0.58 ± 0.08	3.72 ± 0.55	155 ± 25	748.0 ± 0.5	3.1 ± 0.4	1.20 ± 0.23	0.91
920.52 ± 0.10[a]	0.31 ± 0.05	2.01 ± 0.32	84 ± 15	921.7± 0.4	3.9 ± 0.5[b]	1.03 ± 0.23	0.16
1161.73 ± 0.14[c]	0.31 ± 0.03	1.97 ± 0.18	82 ± 9	1162.0 ± 1.2	1.6 ± 0.5	1.23 ± 0.40	0.69
1177.06 ± 0.23[a]	0.09 ± 0.02	0.56 ± 0.14	23 ± 6	-	-	-	-
1935.52 ± 0.37[c]	0.07 ± 0.02	0.42 ± 0.13	17.5 ± 5.6	-	-	-	-

E_γ is the γ-ray energy, $P_{E\gamma}(90°)/(\epsilon_{E\gamma} \times f_{E\gamma})$ the net counts in the γ-ray peak divided by the full-energy-peak (FEP) efficiency and the γ-ray self-absorption factor, I_R the relative intensity (relative to the 696-keV line of ^{146}Nd, 100%) of the γ-rays and $\langle\sigma_{E_\gamma}(90°)\rangle$ is the fast-neutron spectrum-averaged isotopic partial cross section for γ-ray production at an angle of 90° between neutron beam and detector determined with Eq. (4.1). R is the residual calculated by means of Eq. (4.33)
[a]corrected for background interference
[b]921 and 923 keV (unresolved doublet by Demidov)
[c]corrected for (n,γ) interference from Cl

H.1.19 : Prompt γ-rays of ^{146}Nd induced by inelastic scattering of fast neutrons.

This work				From Atlas [27]		I_R (This work)/I_R (Demidov)	R
E_γ (keV)	$P_{E\gamma}(90°)/(\epsilon_{E\gamma} \times f_{E\gamma}) \times 10^{-8}$ (count)	I_R(relative) (%)	$\langle\sigma_{E_\gamma}(90°)\rangle$ (mb)	E_γ (keV)	I_R(relative) (%)		
262.34 ± 0.10	0.25 ± 0.03	1.61 ± 0.19	32 ± 5	262.3 ± 0.6	1.3 ± 0.2	1.24 ± 0.24	1.12
453.20 ± 0.03	14.44 ± 0.51	93 ± 4	1866 ± 160	453.94 ± 0.10	90 ± 9	1.03 ± 0.11	0.29
474.00 ± 0.06[a]	0.53 ± 0.05	3.42 ± 0.32	69 ± 8	-	-	-	-
555.02 ± 0.08	0.32 ± 0.03	2.06 ± 0.18	41 ± 5	-	-	-	-
588.84 ± 0.03[b]	2.69 ± 0.11	17.3 ± 0.9	348 ± 31	589.69 ± 0.15	16 ± 2	1.08 ± 0.15	0.61
735.35 ± 0.04[b]	2.06 ± 0.07	13.2 ± 0.6	266 ± 23	736.0 ± 0.3	12 ± 2	1.10 ± 0.19	0.59
790.43 ± 0.09	0.28 ± 0.02	1.80 ± 0.16	36 ± 4	789.8 ± 0.6	1.8 ± 0.2	1.00 ± 0.14	0.01
882.40 ± 0.12	0.30 ± 0.03	1.91 ± 0.18	38 ± 5	-	-	-	-
922.83 ± 0.11[a]	0.31 ± 0.02	1.99 ± 0.17	40 ± 4	-	-	-	-
1002.27 ± 0.15[b]	0.23 ± 0.03	1.50 ± 0.18	30 ± 4	-	-	-	-
1016.54 ± 0.08[b]	0.56 ± 0.03	3.61 ± 0.24	73 ± 7	1015.9	5.8 ± 1.0	0.62 ± 0.12	-2.13
1149.52 ± 0.09[a]	0.25 ± 0.02	1.64 ± 0.13	33 ± 4	1149.8 ± 1.2	1.4 ± 0.5	1.17 ± 0.43	0.45
1168.11 ± 0.26	0.15 ± 0.03	0.94 ± 0.19	18.8 ± 4.0	-	-	-	-
1181.78 ± 0.43	0.10 ± 0.02	0.61 ± 0.14	12.3 ± 3.0	-	-	-	-
1323.38 ± 0.10[b]	0.52 ± 0.03	3.35 ± 0.22	67 ± 7	-	-	-	-
1332.97 ± 0.11	0.47 ± 0.03	3.03 ± 0.22	61 ± 6	1333.1 ± 0.7	3.1 ± 0.6	0.98 ± 0.20	-0.10
1470.91 ± 0.08[a]	0.46 ± 0.07	2.95 ± 0.45	59 ± 10	-	-	-	-
1523.66 ± 0.13	0.30 ± 0.02	1.92 ± 0.17	38 ± 4	-	-	-	-

H.1.19 : (continued).

This work				From Atlas [27]		I_R (This work)/I_R (Demidov)	R
E_γ (keV)	$P_{E\gamma}(90°)/(\epsilon_{E\gamma} \times f_{E\gamma}) \times 10^{-8}$ (count)	I_R(relative) (%)	$\langle\sigma_{E_\gamma}(90°)\rangle$ (mb)	E_γ (keV)	I_R(relative) (%)		
1665.65 ± 0.47	0.05 ± 0.02	0.34 ± 0.10	6.79 ± 2.11	-	-	-	-
1689.51 ± 0.29[b]	0.10 ± 0.02	0.63 ± 0.12	12.6 ± 2.6	-	-	-	-
1743.95 ± 0.18[b]	0.14 ± 0.02	0.93 ± 0.14	18.7 ± 3.1	-	-	-	-
1788.29 ± 0.37[c]	0.05 ± 0.02	0.35 ± 0.10	6.97 ± 2.12	-	-	-	-
1881.47 ± 0.46	0.12 ± 0.03	0.75 ± 0.17	15.1 ± 3.5	-	-	-	-
2119.99 ± 0.48	0.11 ± 0.03	0.69 ± 0.17	13.9 ± 3.5	-	-	-	-

E_γ is the γ-ray energy, $P_{E\gamma}(90°)/(\epsilon_{E\gamma} \times f_{E\gamma})$ the net counts in the γ-ray peak divided by the full-energy-peak (FEP) efficiency and the γ-ray self-absorption factor, I_R the relative intensity (relative to the 696-keV line of ^{146}Nd, 100%) of the γ-rays and $\langle\sigma_{E_\gamma}(90°)\rangle$ is the fast-neutron spectrum-averaged isotopic partial cross section for γ-ray production at an angle of 90° between neutron beam and detector determined with Eq. (4.1). R is the residual calculated by means of Eq. (4.33)
[a]corrected for background interference
[b]corrected for (n,γ) interference from Nd
[c]corrected for (n,γ) interference from Cl

H.1.20 : Prompt γ-rays of ^{148}Nd induced by inelastic scattering of fast neutrons.

This work				From Atlas [27]		I_R (This work)/I_R (Demidov)	R
E_γ (keV)	$P_{E\gamma}(90°)/(\epsilon_{E\gamma} \times f_{E\gamma}) \times 10^{-8}$ (count)	I_R(relative) (%)	$\langle\sigma_{E_\gamma}(90°)\rangle$ (mb)	E_γ (keV)	I_R(relative) (%)		
449.93 ± 0.07	0.68 ± 0.09	4.35 ± 0.61	261 ± 41	-	-	-	-
489.00 ± 0.13[a]	0.16 ± 0.05	1.03 ± 0.29	62 ± 18	-	-	-	-
527.03 ± 0.10	0.21 ± 0.03	1.36 ± 0.20	81 ± 13	-	-	-	-
936.11 ± 0.16[b]	0.22 ± 0.03	1.40 ± 0.18	84 ± 13	-	-	-	-
1022.42 ± 0.15[a,c]	0.17 ± 0.02	1.07 ± 0.14	64 ± 10	-	-	-	-
1170.67 ± 0.34[b,c]	0.11 ± 0.02	0.68 ± 0.16	41 ± 10	-	-	-	-
1382.01 ± 0.28[c]	0.14 ± 0.02	0.87 ± 0.14	52 ± 9	-	-	-	-
1426.71 ± 0.22	0.15 ± 0.03	0.99 ± 0.17	60 ± 11	-	-	-	-

E_γ is the gamma-ray energy, $P_{E\gamma}(90°)/(\epsilon_{E\gamma} \times f_{E\gamma})$ the net counts in the γ-ray peak divided by the full-energy-peak (FEP) efficiency and the γ-ray self-absorption factor, I_R the relative intensity (relative to the 696-keV line of ^{146}Nd, 100%) of the γ-rays and $\langle\sigma_{E_\gamma}(90°)\rangle$ is the fast-neutron spectrum-averaged isotopic partial cross section for γ-ray production at an angle of 90° between neutron beam and detector determined with Eq. (4.1). R is the residual calculated by means of Eq. (4.33)
[a]corrected for background interference
[b]corrected for (n,γ) interference from Cl
[c]corrected for (n,γ) interference from Nd

H.1.21 : Prompt γ-rays of ^{150}Nd induced by inelastic scattering of fast neutrons.

This work				From Atlas [27]		I_R (This work)/I_R (Demidov)	R
E_γ (keV)	$P_{E\gamma}(90°)/(\epsilon_{E\gamma} \times f_{E\gamma}) \times 10^{-8}$ (count)	I_R(relative) (%)	$\langle\sigma_{E_\gamma}(90°)\rangle$ (mb)	E_γ (keV)	I_R(relative) (%)		
130.05 ± 0.03	4.10 ± 0.15	26 ± 1	1615 ± 140	129.97 ± 0.10	42 ± 5	0.63 ± 0.08	-3.02
250.87 ± 0.04	1.38 ± 0.05	8.87 ± 0.44	543 ± 47	251.12 ± 0.10	10.1 ± 1.1	0.88 ± 0.11	-1.04
338.44 ± 0.16	0.17 ± 0.03	1.11 ± 0.21	68 ± 14	338.4 ± 0.6	2.2 ± 0.5	0.50 ± 0.15	-2.01
372.35 ± 0.20	0.29 ± 0.05	1.84 ± 0.34	112 ± 22	-	-	-	-

H.1.21 : (continued).

This work				From Atlas [27]		I_R (This work)/I_R (Demidov)	R
E_γ (keV)	$P_{E\gamma}(90°)/(\epsilon_{E\gamma} \times f_{E\gamma}) \times 10^{-8}$ (count)	I_R(relative) (%)	$\langle\sigma_{E_\gamma}(90°)\rangle$ (mb)	E_γ (keV)	I_R(relative) (%)		
545.22 ± 0.08[a]	0.26 ± 0.02	1.67 ± 0.15	102 ± 12	-	-	-	-
552.47 ± 0.14	0.15 ± 0.02	0.97 ± 0.13	59 ± 9	-	-	-	-
719.95 ± 0.07	0.50 ± 0.03	3.24 ± 0.21	198 ± 19	-	-	-	-
755.59 ± 0.14	0.09 ± 0.02	0.59 ± 0.11	36 ± 7	-	-	-	-
1061.50 ± 0.19	0.17 ± 0.03	1.08 ± 0.22	66 ± 14	-	-	-	-
1069.90 ± 0.11	0.21 ± 0.02	1.38 ± 0.14	85 ± 11	-	-	-	-
1124.78 ± 0.13	0.14 ± 0.02	0.91 ± 0.11	56 ± 8	-	-	-	-

E_γ is the γ-ray energy, $P_{E\gamma}(90°)/(\epsilon_{E\gamma} \times f_{E\gamma})$ the net counts in the γ-ray peak divided by the full-energy-peak (FEP) efficiency and the γ-ray self-absorption factor, I_R the relative intensity (relative to the 696-keV line of ^{146}Nd, 100%) of the γ-rays and $\langle\sigma_{E_\gamma}(90°)\rangle$ is the fast-neutron spectrum-averaged isotopic partial cross section for γ-ray production at an angle of 90° between neutron beam and detector determined with Eq. (4.1). R is the residual calculated by means of Eq. (4.33)
[a]corrected for (n,γ) interference from Nd

H.1.22 : Prompt γ-rays induced by inelastic scattering of fast neutrons in multiple Nd isotopes.

This work				From Atlas [27]		I_R (This work)/I_R (Demidov)	R
E_γ (keV)	$P_{E\gamma}(90°)/(\epsilon_{E\gamma} \times f_{E\gamma}) \times 10^{-8}$ (count)	I_R(relative) (%)	$\langle\sigma_{E_\gamma}(90°)\rangle$ (mb)	E_γ (keV)	I_R (%)		
^{144}Nd + ^{146}Nd							
1376.56 ± 0.07[a,b]	0.76 ± 0.04	4.90 ± 0.28	41 ± 4	1377.2 ± 0.6	4.0 ± 0.6	1.23 ± 0.20	1.36
1830.60 ± 0.31[a,c]	0.10 ± 0.02	0.63 ± 0.12	5.27 ± 1.07	-	-	-	-
^{144}Nd + ^{148}Nd							
301.23 ± 0.03	4.41 ± 0.14	28 ± 1	332 ± 28	301.71 ± 0.10	37 ± 4	0.77 ± 0.09	-2.04
^{145}Nd + ^{146}Nd							
1243.28 ± 0.16	0.12 ± 0.02	0.80 ± 0.14	10.8 ± 2.0	-	-	-	-
^{145}Nd + ^{148}Nd							
1249.25 ± 0.12	0.21 ± 0.02	1.33 ± 0.15	33 ± 4	1247.5 ± 1.5	1.5 ± 0.6	0.88 ± 0.37	-0.28
^{145}Nd + ^{150}Nd							
852.42 ± 0.18	0.28 ± 0.04	1.80 ± 0.29	45 ± 8	-	-	-	-
^{146}Nd + ^{148}Nd							
946.16 ± 0.12	0.23 ± 0.03	1.50 ± 0.17	23 ± 3	946.6 ± 0.8	1.5 ± 0.4	1.00 ± 0.29	0.00
^{148}Nd + ^{150}Nd							
722.01 ± 0.09	0.36 ± 0.03	2.34 ± 0.19	71 ± 8	722.7 ± 0.4	4.1 ± 0.5[d]	1.36 ± 0.22	2.65

E_γ is the γ-ray energy, $P_{E\gamma}(90°)/(\epsilon_{E\gamma} \times f_{E\gamma})$ the net counts in the γ-ray peak divided by the full-energy-peak (FEP) efficiency and the γ-ray self-absorption factor, I_R the relative intensity (relative to the 696-keV line of ^{146}Nd, 100%) of the γ-rays and $\langle\sigma_{E_\gamma}(90°)\rangle$ is the fast-neutron spectrum-averaged isotopic partial cross section for γ-ray production at an angle of 90° between neutron beam and detector determined with Eq. (4.1). R is the residual calculated by means of Eq. (4.33)
[a]corrected for (n,γ) interference from Nd
[b]corrected for background interference
[c]corrected for (n,γ) interference from Cl
[d]720 and 722 keV (unresolved doublet by Demidov)

H.1.23 : Prompt γ-rays of ^{144}Sm induced by inelastic scattering of fast neutrons.

This work				From Atlas [27]		I_R (This work)/I_R (Demidov)	R
E_γ (keV)	$P_{E\gamma}(90°)/(\epsilon_{E\gamma} \times f_{E\gamma}) \times 10^{-8}$ (count)	I_R(relative) (%)	$\langle\sigma_{E_\gamma}(90°)\rangle$ (mb)	E_γ (keV)	I_R(relative) (%)		
149.99 ± 0.06[a]	0.31 ± 0.07	5.16 ± 1.48	294 ± 74	149.8 ± 0.4	6.2 ± 0.8	0.83 ± 0.26	-0.62
397.28 ± 0.07[b,c]	0.67 ± 0.04	11.2 ± 1.9	641 ± 65	397.7 ± 0.4	1.9 ± 0.3	5.92 ± 1.37	4.84
983.56 ± 0.16[c,d]	0.18 ± 0.02	2.93 ± 0.59	167 ± 25	-	-	-	-
1384.92 ± 0.37[d]	0.10 ± 0.02	1.64 ± 0.47	94 ± 24	-	-	-	-
1475.05 ± 0.22	0.10 ± 0.02	1.66 ± 0.39	95 ± 19	-	-	-	-
1659.70 ± 0.11	0.72 ± 0.04	12.1 ± 2.0	690 ± 65	1659.8 ± 0.2	6.6 ± 0.9	1.83 ± 0.39	2.51
2120.54 ± 0.46	0.11 ± 0.03	1.87 ± 0.60	106 ± 31	-	-	-	-

E_γ is the γ-ray energy, $P_{E\gamma}(90°)/(\epsilon_{E\gamma} \times f_{E\gamma})$ the net counts in the γ-ray peak divided by the full-energy-peak (FEP) efficiency and the γ-ray self-absorption factor, I_R the relative intensity (relative to the 550-keV line of ^{148}Sm, 100%) of the γ-rays and $\langle\sigma_{E_\gamma}(90°)\rangle$ is the fast-neutron spectrum-averaged isotopic partial cross section for γ-ray production at an angle of 90° between neutron beam and detector determined with Eq. (4.1). R is the residual calculated by means of Eq. (4.33)

[a] corrected for (n,γ) interference from Sm

[b] assigned as (n,γ) neutron capture line of Sm, as the capture contribution is (99 ± 37)%; net counts, intensity and cross section are calculated under neglection of the capture counts and are given to support the discussion

[c] corrected for background interference

[d] confirmed by Demidov's isotopic measurements [27]

H.1.24 : Prompt γ-rays of ^{147}Sm induced by inelastic scattering of fast neutrons.

This work				From Demidov Atlas [27]		I_R (This work)/I_R (Demidov)	R
E_γ (keV)	$P_{E\gamma}(90°)/(\epsilon_{E\gamma} \times f_{E\gamma}) \times 10^{-8}$ (count)	I_R(relative) (%)	$\langle\sigma_{E_\gamma}(90°)\rangle$ (mb)	E_γ (keV)	I_R(relative) (%)		
215.02 ± 0.05	0.63 ± 0.03	10.5 ± 1.7	123 ± 12	215.11 ± 0.10	10.2 ± 1.2	1.03 ± 0.21	0.15
715.86 ± 0.07[a]	2.45 ± 0.61	41 ± 12	479 ± 125	716.5 ± 0.3	23 ± 3	1.78 ± 0.57	1.45
741.31 ± 0.10[a]	0.22 ± 0.03	3.71 ± 0.80	43 ± 7	-	-	-	-
942.21 ± 0.18	0.15 ± 0.03	2.50 ± 0.58	29 ± 5	-	-	-	-
947.71 ± 0.11[a]	0.27 ± 0.07	4.55 ± 1.37	53 ± 14	-	-	-	-
955.32 ± 0.25	0.10 ± 0.02	1.64 ± 0.46	19.1 ± 4.7	-	-	-	-
1076.67 ± 0.19[b]	0.11 ± 0.03	1.92 ± 0.52	22 ± 5	-	-	-	-
1106.59 ± 0.09[a,b]	0.40 ± 0.03	6.68 ± 1.16	78 ± 8	-	-	-	-
1180.10 ± 0.18	0.20 ± 0.03	3.27 ± 0.66	38 ± 6	-	-	-	-
1196.94 ± 0.09[a,b]	0.26 ± 0.02	4.30 ± 0.72	50 ± 5	-	-	-	-
1250.99 ± 0.23[c]	0.05 ± 0.01	0.83 ± 0.22	9.66 ± 2.21	-	-	-	-
1449.23 ± 0.21	0.17 ± 0.03	2.89 ± 0.66	34 ± 6	-	-	-	-

E_γ is the γ-ray energy, $P_{E\gamma}(90°)/(\epsilon_{E\gamma} \times f_{E\gamma})$ the net counts in the γ-ray peak divided by the full-energy-peak (FEP) efficiency and the γ-ray self-absorption factor, I_R the relative intensity (relative to the 550-keV line of ^{148}Sm, 100%) of the γ-rays and $\langle\sigma_{E_\gamma}(90°)\rangle$ is the fast-neutron spectrum-averaged isotopic partial cross section for γ-ray production at an angle of 90° between neutron beam and detector determined with Eq. (4.1). R is the residual calculated by means of Eq. (4.33)

[a] corrected for (n,γ) interference from Sm

[b] corrected for background interference

[c] corrected for contribution of SE from 1763.5-keV line of ^{35}Cl (69% of net counts)

H.1.25 : Prompt γ-rays of ^{148}Sm induced by inelastic scattering of fast neutrons.

This work				From Atlas [27]		I_R (This work)/I_R (Demidov)	R
E_γ (keV)	$P_{E\gamma}(90°)/(\epsilon_{E\gamma} \times f_{E\gamma}) \times 10^{-8}$ (count)	I_R(relative) (%)	$\langle\sigma_{E_\gamma}(90°)\rangle$ (mb)	E_γ (keV)	I_R(relative) (%)		
222.54 ± 0.13[a]	0.08 ± 0.01	1.37 ± 0.31	21 ± 4	222.8 ± 0.6	2.1 ± 0.4	0.65 ± 0.19	-1.44
413.67 ± 0.05[a]	0.45 ± 0.07	7.45 ± 1.60	116 ± 19	414.2	8.5 ± 1.0	0.88 ± 0.21	-0.56
432.11 ± 0.10[a,b]	0.11 ± 0.02	1.87 ± 0.49	29 ± 7	-	-	-	-
549.60 ± 0.04[a]	5.98 ± 0.94	100	1558 ± 273	550.23 ± 0.10	100	-	-
552.44 ± 0.08[a]	0.91 ± 0.06	15.3 ± 2.6	238 ± 24	-	-	-	-
571.18 ± 0.08[b,c]	0.47 ± 0.04	7.88 ± 1.42	123 ± 15	-	-	-	-
610.66 ± 0.04[a]	0.66 ± 0.13	11.1 ± 2.8	172 ± 36	611.9	22 ± 3	0.50 ± 0.14	-2.67
629.34 ± 0.04[b,c]	5.39 ± 0.19	90 ± 14	1405 ± 120	629.87 ± 0.10	25 ± 3	3.61 ± 0.72	4.42
756.26 ± 0.11	0.21 ± 0.03	3.44 ± 0.69	54 ± 8	-	-	-	-
873.40 ± 0.11[b]	0.27 ± 0.03	4.45 ± 0.87	69 ± 10	-	-	-	-
903.51 ± 0.08	0.62 ± 0.04	10.3 ± 1.7	161 ± 16	903.5	3.4 ± 0.6	3.04 ± 0.74	3.76
937.32 ± 0.10[a]	0.26 ± 0.03	4.36 ± 0.84	68 ± 9	-	-	-	-
968.30 ± 0.14[a]	0.20 ± 0.05	3.43 ± 0.99	53 ± 14	969.4 ± 0.4	0.51 ± 0.10	6.72 ± 2.35	2.92
1033.69 ± 0.22[b]	0.17 ± 0.03	2.90 ± 0.70	45 ± 9	-	-	-	-
1114.09 ± 0.14[d]	0.23 ± 0.05	3.84 ± 1.10	60 ± 15	1114	37 ± 4[e]	0.39 ± 0.04	-3.59
1146.76 ± 0.13[b]	0.26 ± 0.04	4.39 ± 0.91	68 ± 11	-	-	-	-
1152.59 ± 0.27[a,b]	0.15 ± 0.04	2.56 ± 0.72	40 ± 10	-	-	-	-
1269.81 ± 0.52	0.11 ± 0.04	1.88 ± 0.66	29 ± 9	-	-	-	-
1328.16 ± 0.33[a,d,f]	0.22 ± 0.03	3.62 ± 0.79	56 ± 10	-	-	-	-
1370.51 ± 0.27[b]	0.10 ± 0.03	1.75 ± 0.57	27 ± 8	-	-	-	-
1375.15 ± 0.27	0.14 ± 0.03	2.41 ± 0.59	38 ± 8	-	-	-	-
1421.97 ± 0.15	0.22 ± 0.02	3.69 ± 0.70	58 ± 8	1422.9 ± 1.2	1.8 ± 0.4	2.05 ± 0.60	2.34
1454.02 ± 0.13[b]	0.51 ± 0.03	8.48 ± 1.44	132 ± 13	-	-	-	-
1584.75 ± 0.32[b]	0.17 ± 0.03	2.87 ± 0.71	45 ± 9	-	-	-	-
1596.26 ± 0.18[b,d]	0.32 ± 0.03	5.42 ± 0.97	84 ± 10	-	-	-	-
1664.19 ± 0.21[b]	0.15 ± 0.02	2.57 ± 0.56	40 ± 7	-	-	-	-
1776.61 ± 0.31	0.15 ± 0.03	2.45 ± 0.68	38 ± 9	-	-	-	-
1840.12 ± 0.27	0.20 ± 0.03	3.42 ± 0.69	53 ± 8	1842	2.4 ± 0.5	1.42 ± 0.41	1.20
1977.23 ± 0.31	0.11 ± 0.02	1.86 ± 0.48	29 ± 6	-	-	-	-
2145.18 ± 0.49	0.12 ± 0.03	1.96 ± 0.60	31 ± 8	-	-	-	-
2203.06 ± 0.33[b]	0.09 ± 0.02	1.54 ± 0.42	24 ± 6	-	-	-	-
2514.29 ± 0.41[b]	0.05 ± 0.02	0.91 ± 0.30	14.2 ± 4.3	-	-	-	-

E_γ is the γ-ray energy, $P_{E\gamma}(90°)/(\epsilon_{E\gamma} \times f_{E\gamma})$ the net counts in the γ-ray peak divided by the full-energy-peak (FEP) efficiency and the γ-ray self-absorption factor, I_R the relative intensity (relative to the 550-keV line of ^{148}Sm, 100%) of the γ-rays and $\langle\sigma_{E_\gamma}(90°)\rangle$ is the fast-neutron spectrum-averaged isotopic partial cross section for γ-ray production at an angle of 90° between neutron beam and detector determined with Eq. (4.1). R is the residual calculated by means of Eq. (4.33)
[a]corrected for (n,γ) interference from Sm
[b]confirmed by Demidov's isotopic measurements [27]
[c]assigned as (n,γ) neutron capture line of Sm, as the capture contributions are approximately 100%; net counts, intensities and cross sections are calculated under neglection of the capture counts and are given to support the discussion
[d]corrected for background interference
[e]1112 and 1114 keV (unresolved doublet by Demidov)
[f]corrected for (n,γ) interference from Cl

H.1.26 : Prompt γ-rays of ^{149}Sm induced by inelastic scattering of fast neutrons.

This work				From Atlas [27]		I_R (This work)/I_R (Demidov)	R
E_γ (keV)	$P_{E\gamma}(90°)/(\epsilon_{E\gamma} \times f_{E\gamma}) \times 10^{-8}$ (count)	I_R(relative) (%)	$\langle\sigma_{E_\gamma}(90°)\rangle$ (mb)	E_γ (keV)	I_R(relative) (%)		
254.31 ± 0.10[a,b]	0.18 ± 0.03	3.02 ± 0.66	38 ± 7	254.6 ± 0.6	3.8 ± 0.8	0.79 ± 0.24	-0.76
285.43 ± 0.03[b]	2.38 ± 0.08	40 ± 6	504 ± 43	285.84 ± 0.10	26 ± 3	1.53 ± 0.30	1.96

H.1.26 : (continued).

This work				From Atlas [27]		I_R (This work)/I_R (Demidov)	R
E_γ (keV)	$P_{E\gamma}(90°)/(\epsilon_{E\gamma} \times f_{E\gamma}) \times 10^{-8}$ (count)	I_R(relative) (%)	$\langle\sigma_{E_\gamma}(90°)\rangle$ (mb)	E_γ (keV)	I_R(relative) (%)		
313.61 ± 0.10[b]	0.22 ± 0.03	3.67 ± 0.81	46 ± 8	314.4 ± 0.4	3.7 ± 0.4	0.99 ± 0.24	-0.03
326.95 ± 0.05	1.16 ± 0.05	19.3 ± 3.2	245 ± 22	327.8 ± 0.4	10.9 ± 1.5	1.77 ± 0.38	2.41
527.70 ± 0.17	0.27 ± 0.05	4.46 ± 1.12	56 ± 12	528.7 ± 0.8	1.9 ± 0.3	2.34 ± 0.70	2.21
557.63 ± 0.08	0.37 ± 0.04	6.12 ± 1.20	78 ± 11	-	-	-	-
590.21 ± 0.05[b]	0.85 ± 0.04	14.2 ± 2.3	180 ± 16	591.0 ± 0.3	3.5 ± 0.5	4.05 ± 0.88	4.54
663.43 ± 0.05[a,b]	0.90 ± 0.05	15.0 ± 2.5	190 ± 18	664.05 ± 0.10	10.8 ± 1.2	1.39 ± 0.28	1.53
951.93 ± 0.20[b]	0.10 ± 0.02	1.60 ± 0.45	20 ± 5	-	-	-	-

E_γ is the γ-ray energy, $P_{E\gamma}(90°)/(\epsilon_{E\gamma} \times f_{E\gamma})$ the net counts in the γ-ray peak divided by the full-energy-peak (FEP) efficiency and the γ-ray self-absorption factor, I_R the relative intensity (relative to the 550-keV line of ^{148}Sm, 100%) of the γ-rays and $\langle\sigma_{E_\gamma}(90°)\rangle$ is the fast-neutron spectrum-averaged isotopic partial cross section for γ-ray production at an angle of 90° between neutron beam and detector determined with Eq. (4.1). R is the residual calculated by means of Eq. (4.33)
[a]corrected for background interference
[b]corrected for (n,γ) interference from Sm

H.1.27 : Prompt γ-rays of ^{150}Sm induced by inelastic scattering of fast neutrons.

This work				From Atlas [27]		I_R (This work)/I_R (Demidov)	R
E_γ (keV)	$P_{E\gamma}(90°)/(\epsilon_{E\gamma} \times f_{E\gamma}) \times 10^{-8}$ (count)	I_R(relative) (%)	$\langle\sigma_{E_\gamma}(90°)\rangle$ (mb)	E_γ (keV)	I_R(relative) (%)		
333.37 ± 0.05[a]	20.34 ± 2.02	340 ± 63	8077 ± 1022	333.92 ± 0.07	151 ± 15	2.25 ± 0.47	2.92
345.34 ± 0.10[a,b]	0.21 ± 0.03	3.44 ± 0.75	82 ± 14	-	-	-	-
405.83 ± 0.06[a]	0.59 ± 0.05	9.83 ± 1.73	233 ± 26	405.4	4.2 ± 0.6	2.34 ± 0.53	3.08
438.68 ± 0.04[a]	8.46 ± 0.98	142 ± 28	3358 ± 471	439.4	66 ± 8	2.14 ± 0.49	2.63
461.01 ± 0.11[a]	0.38 ± 0.05	6.31 ± 1.27	150 ± 22	461.5 ± 0.6	3.5 ± 0.5	1.80 ± 0.45	2.06
485.40 ± 0.08[a]	0.11 ± 0.02	1.92 ± 0.47	46 ± 9	-	-	-	-
583.58 ± 0.04[a,c]	1.55 ± 0.16	26 ± 5	615 ± 81	584.3	6.3 ± 0.7	4.12 ± 0.90	3.97
666.05 ± 0.14[a,b,c]	0.03 ± 0.01	0.58 ± 0.15	13.8 ± 2.9	-	-	-	-
711.70 ± 0.06[a]	1.26 ± 0.13	21 ± 4	501 ± 66	712.5 ± 0.6	8.4 ± 1.2	2.51 ± 0.59	3.06
730.99 ± 0.07[a,b]	0.12 ± 0.02	1.95 ± 0.44	46 ± 8	-	-	-	-
736.92 ± 0.05[a]	2.31 ± 0.24	39 ± 7	918 ± 120	737.45 ± 0.08	11.4 ± 1.2	3.39 ± 0.73	3.69
747.61 ± 0.08[a,b,c]	0.14 ± 0.01	2.34 ± 0.39	56 ± 6	-	-	-	-
751.02 ± 0.11[a]	0.35 ± 0.03	5.89 ± 1.04	140 ± 16	-	-	-	-
761.76 ± 0.15[a,b,c]	0.11 ± 0.02	1.78 ± 0.39	42 ± 7	-	-	-	-
1046.04 ± 0.09[a,b]	0.48 ± 0.06	8.11 ± 1.57	192 ± 27	1047.4 ± 0.8	1.4 ± 0.4	5.79 ± 2.00	4.14
1048.71 ± 0.09[a]	0.72 ± 0.03	12.1 ± 2.0	287 ± 26	-	-	-	-
1122.23 ± 0.14[a,b]	0.11 ± 0.02	1.84 ± 0.41	44 ± 8	-	-	-	-
1246.57 ± 0.17[a,b]	0.13 ± 0.02	2.13 ± 0.52	50 ± 10	-	-	-	-
1323.85 ± 0.20[a,b]	0.37 ± 0.04	6.26 ± 1.24	148 ± 21	-	-	-	-
1486.18 ± 0.25[a,b,c]	0.15 ± 0.02	2.46 ± 0.51	58 ± 9	-	-	-	-

E_γ is the γ-ray energy, $P_{E\gamma}(90°)/(\epsilon_{E\gamma} \times f_{E\gamma})$ the net counts in the γ-ray peak divided by the full-energy-peak (FEP) efficiency and the γ-ray self-absorption factor, I_R the relative intensity (relative to the 550-keV line of ^{148}Sm, 100%) of the γ-rays and $\langle\sigma_{E_\gamma}(90°)\rangle$ is the fast-neutron spectrum-averaged isotopic partial cross section for γ-ray production at an angle of 90° between neutron beam and detector determined with Eq. (4.1). R is the residual calculated by means of Eq. (4.33)
[a]corrected for (n,γ) interference from Sm
[b]confirmed by Demidov's isotopic measurements [27]
[c]corrected for background interference

H.1.28 : Prompt γ-rays of ^{152}Sm induced by inelastic scattering of fast neutrons.

This work				From Atlas [27]		I_R (This work)/I_R (Demidov)	R
E_γ (keV)	$P_{E\gamma}(90°)/(\epsilon_{E\gamma} \times f_{E\gamma}) \times 10^{-8}$ (count)	I_R(relative) (%)	$\langle\sigma_{E_\gamma}(90°)\rangle$ (mb)	E_γ (keV)	I_R(relative) (%)		
244.37 ± 0.03	4.49 ± 0.14	75 ± 12	492 ± 41	244.66 ± 0.10	46 ± 5	1.63 ± 0.32	2.24
268.81 ± 0.12[a]	0.03 ± 0.01	0.45 ± 0.14	2.97 ± 0.81	-	-	-	-
320.57 ± 0.07[b]	0.48 ± 0.05	7.95 ± 1.48	52 ± 7	320.6 ± 0.6	1.6 ± 0.3	4.97 ± 1.31	4.21
339.80 ± 0.05[a]	0.61 ± 0.15	10.3 ± 3.0	67 ± 17	340.6 ± 0.3	4.8 ± 0.7	2.14 ± 0.70	1.77
655.96 ± 0.07	0.33 ± 0.02	5.56 ± 0.96	36 ± 4	656.5 ± 0.4	3.7 ± 0.4	1.50 ± 0.31	1.79
791.36 ± 0.25[a]	0.10 ± 0.03	1.62 ± 0.50	10.6 ± 3.0	-	-	-	-
798.25 ± 0.13	0.13 ± 0.02	2.12 ± 0.48	13.9 ± 2.5	-	-	-	-
841.12 ± 0.16	0.28 ± 0.07	4.60 ± 1.33	30 ± 8	840.5	10 ± 2[c]	0.92 ± 0.37	-0.20
854.85 ± 0.08[a]	0.35 ± 0.03	5.82 ± 1.02	38 ± 4	-	-	-	-
900.89 ± 0.19[d]	0.20 ± 0.03	3.39 ± 0.71	22 ± 4	-	-	-	-
918.99 ± 0.08[d,e]	0.88 ± 0.05	14.7 ± 2.5	96 ± 10	-	-	-	-
926.00 ± 0.14[d,e]	0.22 ± 0.03	3.67 ± 0.78	24 ± 4	-	-	-	-
944.60 ± 0.20	0.16 ± 0.02	2.61 ± 0.58	17.1 ± 3.0	-	-	-	-
963.31 ± 0.07	1.34 ± 0.05	22 ± 4	147 ± 13	963.30 ± 0.10	16 ± 2	1.41 ± 0.29	1.57
995.84 ± 0.17[a,d,e]	0.10 ± 0.02	1.62 ± 0.39	10.6 ± 2.1	-	-	-	-
1004.76 ± 0.11	0.29 ± 0.03	4.92 ± 0.89	32 ± 4	1005.5 ± 1.6	1.7 ± 0.3	2.89 ± 0.73	3.43
1022.26 ± 0.17[d,e]	0.19 ± 0.02	3.26 ± 0.64	21 ± 3	-	-	-	-
1085.70 ± 0.13	0.34 ± 0.03	5.64 ± 1.03	37 ± 4	1085.8 ± 0.3	2.1 ± 0.3	2.69 ± 0.62	3.31
1111.91 ± 0.09[d,e]	0.64 ± 0.04	10.7 ± 1.8	70 ± 7	-	-	-	-
1296.84 ± 0.20	0.27 ± 0.03	4.46 ± 0.86	29 ± 4	-	-	-	-
1388.67 ± 0.12[d]	0.39 ± 0.03	6.52 ± 1.15	43 ± 5	-	-	-	-
1393.67 ± 0.12[e]	0.36 ± 0.03	6.00 ± 1.07	39 ± 5	1392.6	6.1 ± 1.0	0.98 ± 0.24	-0.07
1398.33 ± 0.20[d]	0.16 ± 0.03	2.70 ± 0.63	17.7 ± 3.3	-	-	-	-
1408.04 ± 0.15[e]	0.22 ± 0.02	3.69 ± 0.70	24 ± 3	1408.9 ± 1.2	2.3 ± 0.6	1.60 ± 0.52	1.50
1457.26 ± 0.15[d,e]	0.42 ± 0.03	7.10 ± 1.23	46 ± 5	-	-	-	-
1915.84 ± 0.36	0.08 ± 0.02	1.39 ± 0.46	9.09 ± 2.74	-	-	-	-

E_γ is the γ-ray energy, $P_{E\gamma}(90°)/(\epsilon_{E\gamma} \times f_{E\gamma})$ the net counts in the γ-ray peak divided by the full-energy-peak (FEP) efficiency and the γ-ray self-absorption factor, I_R the relative intensity (relative to the 550-keV line of ^{148}Sm, 100%) of the γ-rays and $\langle\sigma_{E_\gamma}(90°)\rangle$ is the fast-neutron spectrum-averaged isotopic partial cross section for γ-ray production at an angle of 90° between neutron beam and detector determined with Eq. (4.1). R is the residual calculated by means of Eq. (4.33)
[a]corrected for (n,γ) interference from Sm
[b]assigned as (n,γ) neutron capture line of Sm, as the capture contribution is (95 ± 26)%; net counts, intensity and cross section are calculated under neglection of the capture counts and are given to support the discussion
[c]839 and 841 keV (unresolved doublet by Demidov)
[d]confirmed by Demidov's isotopic measurements [27]
[e]corrected for background interference

H.1.29 : Prompt γ-rays of ^{154}Sm induced by inelastic scattering of fast neutrons.

This work				From Atlas [27]		I_R (This work)/I_R (Demidov)	R
E_γ (keV)	$P_{E\gamma}(90°)/(\epsilon_{E\gamma} \times f_{E\gamma}) \times 10^{-8}$ (count)	I_R(relative) (%)	$\langle\sigma_{E_\gamma}(90°)\rangle$ (mb)	E_γ (keV)	I_R(relative) (%)		
81.90 ± 0.04[a]	4.33 ± 0.19	72 ± 12	558 ± 50	-	-	-	-
184.69 ± 0.03	3.85 ± 0.12	65 ± 10	497 ± 42	185.06 ± 0.06	46 ± 5	1.40 ± 0.27	1.62
636.22 ± 0.08[b]	0.24 ± 0.03	4.06 ± 0.76	31 ± 4	637.0 ± 0.6	0.85 ± 0.15	4.78 ± 1.23	4.14
745.48 ± 0.06[b,c]	0.44 ± 0.03	7.40 ± 1.28	57 ± 6	745.8	6.3 ± 0.8[d]	1.55 ± 0.42	3.32
753.12 ± 0.15[a,b]	0.23 ± 0.03	3.89 ± 0.75	30 ± 4	-	-	-	-
838.90 ± 0.08[a]	0.28 ± 0.04	4.63 ± 0.94	36 ± 5	-	-	-	-
1016.73 ± 0.14[b]	0.40 ± 0.03	6.71 ± 1.20	52 ± 6	1017.6	4.8 ± 0.8	1.40 ± 0.34	1.32
1120.26 ± 0.18[a]	0.16 ± 0.02	2.65 ± 0.56	20 ± 3	-	-	-	-
1272.56 ± 0.48[a]	0.13 ± 0.03	2.10 ± 0.66	16.1 ± 4.6	-	-	-	-

H.1.29 : (continued).

This work				From Atlas [27]		I_R (This work)/I_R (Demidov)	R
E_γ (keV)	$P_{E\gamma}(90°)/(\epsilon_{E\gamma} \times f_{E\gamma}) \times 10^{-8}$ (count)	I_R(relative) (%)	$\langle\sigma_{E_\gamma}(90°)\rangle$ (mb)	E_γ (keV)	I_R(relative) (%)		
1432.95 ± 0.15[c]	0.23 ± 0.02	3.85 ± 0.73	30 ± 4	1432.2 ± 1.6	2.7 ± 0.6	1.43 ± 0.42	1.22
1439.76 ± 0.12	0.37 ± 0.03	6.14 ± 1.08	47 ± 5	1440.4 ± 0.6	2.4 ± 0.5	2.56 ± 0.70	3.14
1538.62 ± 0.38[a]	0.10 ± 0.02	1.65 ± 0.45	12.7 ± 3.0	-	-	-	-
1551.48 ± 0.32[a]	0.10 ± 0.02	1.74 ± 0.49	13.4 ± 3.3	-	-	-	-
1624.42 ± 0.35[a,c]	0.07 ± 0.02	1.23 ± 0.39	9.44 ± 2.72	-	-	-	-

E_γ is the γ-ray energy, $P_{E\gamma}(90°)/(\epsilon_{E\gamma} \times f_{E\gamma})$ the net counts in the γ-ray peak divided by the full-energy-peak (FEP) efficiency and the γ-ray self-absorption factor, I_R the relative intensity (relative to the 550-keV line of ^{148}Sm, 100%) of the γ-rays and $\langle\sigma_{E_\gamma}(90°)\rangle$ is the fast-neutron spectrum-averaged isotopic partial cross section for γ-ray production at an angle of 90° between neutron beam and detector determined with Eq. (4.1). R is the residual calculated by means of Eq. (4.33)
[a]confirmed by Demidov's isotopic measurements [27]
[b]corrected for (n,γ) interference from Sm
[c]corrected for background interference
[d]745 and 748 keV (unresolved doublet by Demidov)

H.1.30 : Prompt γ-rays induced by inelastic scattering of fast neutrons in multiple Sm isotopes.

This work				From Atlas [27]		I_R (This work)/I_R (Demidov)	R
E_γ (keV)	$P_{E\gamma}(90°)/(\epsilon_{E\gamma} \times f_{E\gamma}) \times 10^{-8}$ (count)	I_R(relative) (%)	$\langle\sigma_{E_\gamma}(90°)\rangle$ (mb)	E_γ (keV)	I_R(relative) (%)		
^{147}Sm + ^{148}Sm							
533.88 ± 0.20[a]	0.29 ± 0.05	4.83 ± 1.11	32 ± 6	-	-	-	-
725.57 ± 0.07[b,c]	0.41 ± 0.03	6.85 ± 1.19	46 ± 5	-	-	-	-
1354.18 ± 0.12[a]	0.88 ± 0.09	14.7 ± 2.8	98 ± 13	1352	8.5 ± 2.0	1.73 ± 0.52	1.82
^{147}Sm + ^{152}Sm							
687.89 ± 0.05[c]	0.69 ± 0.04	11.6 ± 1.9	48 ± 5	688.3 ± 0.4	6.1 ± 1.2	1.89 ± 0.49	2.43
809.08 ± 0.06[a]	1.02 ± 0.06	17.1 ± 2.9	72 ± 7	810.5	11.3 ± 1.2	1.51 ± 0.30	1.86
^{147}Sm + ^{152}Sm							
1069.78 ± 0.23	0.23 ± 0.04	3.91 ± 0.89	18.2 ± 3.3	1069.2	1.6 ± 0.4	2.45 ± 0.83	2.37
1172.88 ± 0.20	0.20 ± 0.03	3.30 ± 0.68	15.3 ± 2.4	1172	19 ± 2[d]	0.96 ± 0.29	-0.15
1317.46 ± 0.29	0.23 ± 0.04	3.78 ± 0.90	17.5 ± 3.4	1318.0 ± 0.6	1.7 ± 0.4	2.22 ± 0.74	2.11
^{148}Sm + ^{150}Sm							
1344.48 ± 0.13[b,c]	0.52 ± 0.06	8.71 ± 1.71	82 ± 12	-	-	-	-
^{148}Sm + ^{154}Sm							
914.47 ± 0.08[a,c]	0.55 ± 0.04	9.18 ± 1.59	47 ± 5	913.0	5.1 ± 1.0	1.80 ± 0.47	2.17
^{149}Sm + ^{150}Sm							
402.74 ± 0.07[b,c]	0.70 ± 0.05	11.8 ± 2.0	97 ± 10	-	-	-	-
504.90 ± 0.04[c]	1.92 ± 0.08	32 ± 5	266 ± 23	505.6 ± 0.6	3.4 ± 0.8	9.47 ± 2.70	5.47
859.45 ± 0.06[c]	0.55 ± 0.05	9.25 ± 1.64	76 ± 9	857.6	6.0 ± 1.2	1.54 ± 0.28	1.97
^{149}Sm + ^{154}Sm							
276.65 ± 0.03[a,c]	1.73 ± 0.34	29 ± 7	139 ± 29	277.2	19.4 ± 2.0	1.49 ± 0.40	1.28
280.44 ± 0.10[b,c]	0.13 ± 0.03	2.13 ± 0.66	10.2 ± 2.8	-	-	-	-
^{150}Sm + ^{152}Sm							
147.27 ± 0.11[e]	0.16 ± 0.03	2.71 ± 0.60	13.9 ± 2.4	-	-	-	-
251.17 ± 0.09[c]	0.16 ± 0.02	2.60 ± 0.52	13.4 ± 2.0	251.4 ± 0.6	2.5 ± 0.6	1.04 ± 0.33	0.13
1170.35 ± 0.08[b,c]	0.89 ± 0.09	14.9 ± 2.8	76 ± 10	-	-	-	-
1193.52 ± 0.08[c]	0.61 ± 0.05	10.3 ± 1.9	53 ± 6	1194	5.7 ± 0.8[f]	2.56 ± 0.72	2.42
^{150}Sm + ^{154}Sm							
910.48 ± 0.08[a,b,c]	0.30 ± 0.07	5.00 ± 1.40	29 ± 7	-	-	-	-

H.1.30 : (continued).

This work				From Atlas [27]		I_R (This work)/I_R (Demidov)	R
E_γ (keV)	$P_{E\gamma}(90°)/(\epsilon_{E\gamma} \times f_{E\gamma}) \times 10^{-8}$ (count)	I_R(relative) (%)	$\langle\sigma_{E_\gamma}(90°)\rangle$ (mb)	E_γ (keV)	I_R(relative) (%)		
921.04 ± 0.08[a,c]	0.80 ± 0.13	13.4 ± 3.0	78 ± 14	920.1	15 ± 2[g]	1.87 ± 0.59	1.53
1177.31 ± 0.10[a,b,c]	0.32 ± 0.07	5.35 ± 1.44	31 ± 7	-	-	-	-
^{144}Sm + ^{148}Sm + ^{150}Sm							
1308.80 ± 0.21[b,c]	0.23 ± 0.03	3.80 ± 0.80	31 ± 5	-	-	-	-
^{147}Sm + ^{149}Sm + ^{152}Sm							
121.56 ± 0.03[a,c]	11.97 ± 2.20	200 ± 48	631 ± 126	121.6	198 ± 25	1.01 ± 0.28	0.04
^{148}Sm + ^{150}Sm + ^{152}Sm							
869.40 ± 0.10[b,c]	0.66 ± 0.08	11.1 ± 2.2	43 ± 6	-	-	-	-
^{150}Sm + ^{152}Sm + ^{154}Sm							
674.97 ± 0.05[c]	1.02 ± 0.09	17.0 ± 3.1	52 ± 6	675.44	9.0 ± 1.0	1.89 ± 0.40	2.50

E_γ is the γ-ray energy, $P_{E\gamma}(90°)/(\epsilon_{E\gamma} \times f_{E\gamma})$ the net counts in the γ-ray peak divided by the full-energy-peak (FEP) efficiency and the γ-ray self-absorption factor, I_R the relative intensity (relative to the 550-keV line of ^{148}Sm, 100%) of the γ-rays and $\langle\sigma_{E_\gamma}(90°)\rangle$ is the fast-neutron spectrum-averaged isotopic partial cross section for γ-ray production at an angle of 90° between neutron beam and detector determined with Eq. (4.1). R is the residual calculated by means of Eq. (4.33)
[a]corrected for background interference
[b]confirmed by Demidov's isotopic measurements [27]
[c]corrected for (n,γ) interference from Sm
[d]1170 and 1173 keV (unresolved doublet by Demidov)
[e]assigned as (n,γ) neutron capture line of Sm, as the capture contribution is (114 ± 28)%; net counts, intensity and cross section are calculated under neglection of the capture counts and are given to support the discussion
[f]1194 and 1197 keV (unresolved doublet by Demidov)
[g]919 and 921 keV (unresolved doublet by Demidov)

H.1.31 : Prompt γ-rays of ^{159}Tb induced by inelastic scattering of fast neutrons.

This work				From Atlas [27]		I_R (This work)/I_R (Demidov)	R
E_γ (keV)	$P_{E\gamma}(90°)/(\epsilon_{E\gamma} \times f_{E\gamma}) \times 10^{-8}$ (count)	I_R(relative) (%)	$\langle\sigma_{E_\gamma}(90°)\rangle$ (mb)	E_γ (keV)	I_R(relative) (%)		
57.92 ± 0.06	46 ± 6	156 ± 19	445 ± 63	-	-	-	-
66.27 ± 0.08[a]	2.07 ± 0.53	7.00 ± 1.81	19.9 ± 5.4	-	-	-	-
79.29 ± 0.7[b,c]	41 ± 6	140 ± 20	397 ± 63	-	-	-	-
90.29 ± 0.08[c]	3.09 ± 0.49	10.4 ± 1.7	30 ± 5	-	-	-	-
103.71 ± 0.03[c]	22.3 ± 0.7	75 ± 3	214 ± 18	-	-	-	-
120.74 ± 0.03	8.61 ± 0.61	29 ± 2	83 ± 9	121.3 ± 0.4	16 ± 5	1.82 ± 0.58	2.38
130.31 ± 0.07[c]	0.32 ± 0.05	1.07 ± 0.16	3.04 ± 0.52	-	-	-	-
137.39 ± 0.04	2.87 ± 0.13	9.67 ± 0.53	28 ± 2	137.1 ± 0.6	6.0 ± 1.5	1.61 ± 0.41	2.31
142.83 ± 0.09	1.90 ± 0.16	6.42 ± 0.59	18.3 ± 2.1	-	-	-	-
148.26 ± 0.04	2.72 ± 0.11	9.18 ± 0.47	26 ± 2	149.0	6.0 ± 1.0	1.53 ± 0.27	2.88
158.95 ± 0.05	2.32 ± 0.38	7.84 ± 1.30	22 ± 4	159.0 ± 0.4	7.6 ± 1.0	1.03 ± 0.22	0.15
183.06 ± 0.07[c]	3.77 ± 0.30	12.7 ± 1.1	36 ± 4	-	-	-	-
184.48 ± 0.05[c]	8.00 ± 0.68	27 ± 2	77 ± 9	184.2 ± 0.3	30 ± 3[d]	1.32 ± 0.21	3.23
203.50 ± 0.09[c,e]	1.34 ± 0.15	4.51 ± 0.53	12.8 ± 1.8	-	-	-	-
210.53 ± 0.04[c]	2.34 ± 0.13	7.89 ± 0.49	22 ± 2	210.7 ± 0.6	4.5 ± 0.7	1.75 ± 0.29	3.96
224.67 ± 0.08	3.28 ± 0.19	11.1 ± 0.7	31 ± 3	224.5 ± 0.6	7.2 ± 2.0	1.54 ± 0.44	1.82
229.38 ± 0.05[c]	1.40 ± 0.09	4.73 ± 0.34	13.5 ± 1.4	228.2 ± 0.8	2.5 ± 1.2	1.89 ± 0.92	1.79
237.00 ± 0.05[c]	1.41 ± 0.09	4.75 ± 0.33	13.5 ± 1.4	237.2 ± 0.4	2.7 ± 0.5	1.76 ± 0.35	3.42
247.67 ± 0.04[c]	1.55 ± 0.20	5.23 ± 0.69	14.9 ± 2.2	247.6 ± 0.4	3.2 ± 0.5	1.63 ± 0.33	2.38
269.31 ± 0.07[c]	0.93 ± 0.11	3.14 ± 0.39	8.95 ± 1.29	269.1 ± 0.8	1.8 ± 0.7	1.75 ± 0.71	1.67
273.30 ± 0.05[c]	4.30 ± 0.32	14.5 ± 1.2	41 ± 4	272.9 ± 0.6[f]	13 ± 3	1.12 ± 0.27	0.47
289.77 ± 0.09[c]	5.01 ± 0.25	16.9 ± 1.0	48 ± 4	289.6	16 ± 2	1.06 ± 0.15	0.41
303.40 ± 0.09[c]	0.76 ± 0.11	2.57 ± 0.39	7.31 ± 1.23	-	-	-	-
306.82 ± 0.11[c]	0.76 ± 0.11	2.57 ± 0.39	7.31 ± 1.23	305.2 ± 0.6	6.3 ± 1.0[d]	0.81 ± 0.15	-1.03

H.1.31 : (continued).

This work				From Atlas [27]		I_R (This work)/I_R (Demidov)	R
E_γ (keV)	$P_{E\gamma}(90°)/(\epsilon_{E\gamma} \times f_{E\gamma}) \times 10^{-8}$ (count)	I_R(relative) (%)	$\langle\sigma_{E_\gamma}(90°)\rangle$ (mb)	E_γ (keV)	I_R(relative) (%)		
317.01 ± 0.05[c]	3.56 ± 0.33	12.0 ± 1.2	34 ± 4	317.4 ± 0.3	13.1 ± 1.5	0.92 ± 0.14	-1.03
330.89 ± 0.03	29.6 ± 1.0	100	285 ± 24	331.4 ± 0.3	100	-	-
347.61 ± 0.03[c]	18.11 ± 0.57	61 ± 3	174 ± 15	348.3 ± 0.3	65 ± 5	0.94 ± 0.08	-0.68
362.89 ± 0.07[c]	31 ± 1	106 ± 5	302 ± 25	363.5 ± 0.3	100 ± 7	1.06 ± 0.09	0.70
370.16 ± 0.03[c]	6.96 ± 0.26	23 ± 1	67 ± 6	370.7 ± 0.3	21 ± 2	1.12 ± 0.12	1.07
387.74 ± 0.07	1.36 ± 0.15	4.58 ± 0.51	13.0 ± 1.7	388.3 ± 0.6	6.3 ± 0.8	0.73 ± 0.12	-1.81
394.41 ± 0.04	3.17 ± 0.18	10.7 ± 0.7	30 ± 3	395.1 ± 0.4	13 ± 2	0.82 ± 0.14	-1.09
404.26 ± 0.21[e]	0.41 ± 0.10	1.39 ± 0.35	3.96 ± 1.04	402.6 ± 0.6	6.4 ± 1.2	0.22 ± 0.07	-4.00
428.54 ± 0.09[c]	1.68 ± 0.6	5.67 ± 0.56	16.1 ± 2.0	429.1 ± 0.6	6.9 ± 1.0	0.82 ± 0.13	-1.07
440.26 ± 0.10	1.43 ± 0.15	4.81 ± 0.53	13.7 ± 1.8	-	-	-	-
457.78 ± 0.13[e]	1.28 ± 0.13	4.33 ± 0.45	12.3 ± 1.5	457.7 ± 0.7	3.1 ± 0.7	1.40 ± 0.35	1.49
489.71 ± 0.17[e]	0.67 ± 0.12	2.25 ± 0.42	6.40 ± 1.28	-	-	-	-
494.56 ± 0.18	0.55 ± 0.11	1.87 ± 0.38	5.32 ± 1.13	-	-	-	-
519.24 ± 0.06[c]	1.45 ± 0.18	4.88 ± 0.61	13.9 ± 2.0	520.1 ± 0.6	5.8 ± 0.8	0.84 ± 0.21	-0.91
526.90 ± 0.19[e]	0.27 ± 0.05	0.90 ± 0.17	2.56 ± 0.50	-	-	-	-
536.14 ± 0.04	3.81 ± 0.23	12.9 ± 0.9	37 ± 4	536.8 ± 0.3	15 ± 2	0.86 ± 0.16	-0.98
540.62 ± 0.06	1.04 ± 0.08	3.50 ± 0.30	9.98 ± 1.12	541.7 ± 0.8	3.0 ± 0.6	1.17 ± 0.28	0.75
547.75 ± 0.14[e]	0.42 ± 0.06	1.43 ± 0.21	4.07 ± 0.67	-	-	-	-
552.38 ± 0.20[e]	0.30 ± 0.06	1.01 ± 0.21	2.88 ± 0.62	-	-	-	-
558.76 ± 0.06	6.95 ± 0.21	23 ± 1	67 ± 6	559.6 ± 0.3	28 ± 4	0.84 ± 0.17	-1.10
580.02 ± 0.05	10.01 ± 0.31	34 ± 2	97 ± 8	580.9 ± 0.2	34 ± 4	1.00 ± 0.13	0.01
590.52 ± 0.12[e]	0.43 ± 0.05	1.45 ± 0.19	4.13 ± 0.60	-	-	-	-
615.58 ± 0.06	10.57 ± 0.33	36 ± 2	102 ± 9	615.4 ± 0.6[g]	34 ± 10	1.05 ± 0.34	0.17
622.82 ± 0.04	2.50 ± 0.13	9.79 ± 0.55	28 ± 3	623.5 ± 0.6	5.5 ± 0.8	1.78 ± 0.44	4.43
628.20 ± 0.13[e]	0.55 ± 0.09	1.85 ± 0.30	5.28 ± 0.95	-	-	-	-
650.78 ± 0.15[e,h]	0.17 ± 0.04	0.58 ± 0.14	1.64 ± 0.41	-	-	-	-
655.02 ± 0.11[c,e]	0.79 ± 0.07	2.67 ± 0.27	7.60 ± 0.93	-	-	-	-
673.78 ± 0.10	1.06 ± 0.08	3.57 ± 0.30	10.2 ± 1.1	674.5 ± 0.7	3.8 ± 0.8	0.94 ± 0.22	-0.26
683.79 ± 0.14	0.79 ± 0.06	2.65 ± 0.22	7.55 ± 0.83	-	-	-	-
702.29 ± 0.13	0.69 ± 0.10	2.31 ± 0.34	6.59 ± 1.08	-	-	-	-
719.43 ± 0.18[e]	0.68 ± 0.11	2.28 ± 0.38	6.49 ± 1.18	718.7 ± 0.9	2.1 ± 0.7	1.09 ± 0.37	0.23
743.07 ± 0.18[e]	0.39 ± 0.06	1.32 ± 0.19	3.76 ± 0.62	-	-	-	-
753.24 ± 0.08	1.46 ± 0.11	4.94 ± 0.39	14.1 ± 1.5	753.8 ± 0.7	3.2 ± 0.6	1.54 ± 0.39	2.42
766.45 ± 0.09[e]	0.58 ± 0.05	1.96 ± 0.19	5.57 ± 0.66	765.3 ± 0.9	1.7 ± 0.6	1.15 ± 0.42	0.41
794.81 ± 0.13[e]	0.39 ± 0.05	1.31 ± 0.16	3.72 ± 0.52	-	-	-	-
796.86 ± 0.17[e]	0.28 ± 0.04	0.96 ± 0.15	2.72 ± 0.47	-	-	-	-
851.05 ± 0.15	0.58 ± 0.12	1.96 ± 0.41	5.58 ± 1.23	-	-	-	-
870.97 ± 0.08[e]	0.82 ± 0.10	2.76 ± 0.35	7.86 ± 1.13	-	-	-	-
887.66 ± 0.11[e]	0.64 ± 0.05	2.16 ± 0.20	6.14 ± 0.71	-	-	-	-
911.38 ± 0.08	1.98 ± 0.09	6.68 ± 0.37	19.0 ± 1.7	-	-	-	-
916.09 ± 0.08[e]	2.16 ± 0.10	7.30 ± 0.40	21 ± 2	914.4	13 ± 2	0.56 ± 0.09	-2.79
939.31 ± 0.11[e,i]	0.40 ± 0.05	1.36 ± 0.17	3.86 ± 0.56	-	-	-	-
944.41 ± 0.15[e]	0.52 ± 0.05	1.76 ± 0.19	5.01 ± 0.65	-	-	-	-
946.67 ± 0.06	2.11 ± 0.11	7.11 ± 0.44	20 ± 2	947.0 ± 0.6	5.3 ± 0.8[d]	1.67 ± 0.33	4.41
954.68 ± 0.08[e]	0.91 ± 0.08	3.06 ± 0.29	8.72 ± 1.02	-	-	-	-
965.64 ± 0.16[c]	0.22 ± 0.04	0.76 ± 0.14	2.15 ± 0.43	-	-	-	-
968.80 ± 0.13[e]	0.42 ± 0.06	1.42 ± 0.19	4.03 ± 0.62	-	-	-	-
974.49 ± 0.06[e]	2.42 ± 0.10	8.16 ± 0.42	23 ± 2	975.8 ± 1.0	4.5 ± 1.0	1.81 ± 0.44	3.38
990.87 ± 0.07[e]	0.95 ± 0.06	3.20 ± 0.22	9.12 ± 0.90	991.4 ± 0.8	4.1 ± 0.8	0.78 ± 0.16	-1.08
1005.82 ± 0.10[e]	0.72 ± 0.05	2.42 ± 0.19	6.89 ± 0.74	-	-	-	-
1018.64 ± 0.07[e]	1.71 ± 0.10	5.77 ± 0.40	16.4 ± 1.6	1019.0 ± 0.8	6 ± 2	0.96 ± 0.33	-0.11
1025.40 ± 0.19[e]	0.26 ± 0.04	0.88 ± 0.15	2.52 ± 0.45	-	-	-	-
1034.43 ± 0.12[e,i]	1.44 ± 0.07	4.85 ± 0.29	13.8 ± 1.3	1035.2 ± 1.5	6 ± 2	0.81 ± 0.30	-0.57
1048.82 ± 0.10[e]	1.32 ± 0.10	4.46 ± 0.35	12.7 ± 1.4	-	-	-	-

H.1.31 : (continued).

This work				From Atlas [27]		I_R (This work)/I_R (Demidov)	R
E_γ (keV)	$P_{E\gamma}(90°)/(\epsilon_{E\gamma} \times f_{E\gamma}) \times 10^{-8}$ (count)	I_R(relative) (%)	$\langle\sigma_{E_\gamma}(90°)\rangle$ (mb)	E_γ (keV)	I_R(relative) (%)		
1055.16 ± 0.10[e]	0.59 ± 0.06	1.98 ± 0.23	5.62 ± 0.76	-	-	-	-
1063.30 ± 0.06[e]	1.60 ± 0.13	5.40 ± 0.46	15.4 ± 1.7	1063.7 ± 0.8	5.9 ± 1.5	0.92 ± 0.26	-0.32
1068.07 ± 0.18[e]	0.27 ± 0.04	0.91 ± 0.15	2.59 ± 0.48	-	-	-	-
1072.86 ± 0.09[e]	0.78 ± 0.05	2.62 ± 0.18	7.47 ± 0.75	-	-	-	-
1085.49 ± 0.26[e]	0.31 ± 0.08	1.04 ± 0.29	2.96 ± 0.84	-	-	-	-
1092.27 ± 0.17[e]	0.74 ± 0.13	2.49 ± 0.43	7.08 ± 1.32	-	-	-	-
1094.58 ± 0.13[e]	1.39 ± 0.20	4.69 ± 0.69	13.4 ± 2.2	1094.1 ± 0.8	6 ± 2[d]	1.20 ± 0.48	0.59
1111.13 ± 0.19[e,h]	0.16 ± 0.03	0.54 ± 0.09	1.52 ± 0.27	-	-	-	-
1114.82 ± 0.16[c,e,h]	0.20 ± 0.04	0.68 ± 0.13	1.93 ± 0.41	-	-	-	-
1119.46 ± 0.28[e]	0.14 ± 0.04	0.48 ± 0.12	1.36 ± 0.36	-	-	-	-
1131.10 ± 0.12[e,h,i]	0.21 ± 0.03	0.72 ± 0.11	2.04 ± 0.35	-	-	-	-
1134.65 ± 0.14[e]	0.58 ± 0.07	1.97 ± 0.24	5.62 ± 0.79	1133.4 ± 1.5	2.8 ± 1.0	0.70 ± 0.28	-0.80
1147.96 ± 0.12[e]	0.43 ± 0.05	1.44 ± 0.18	4.10 ± 0.58	-	-	-	-
1156.25 ± 0.11[e]	0.55 ± 0.05	1.87 ± 0.19	5.31 ± 0.67	1156.9 ± 1.5	2.3 ± 0.9	0.81 ± 0.33	-0.47
1168.89 ± 0.09[e,i]	0.83 ± 0.06	2.79 ± 0.23	7.93 ± 0.86	-	-	-	-
1173.25 ± 0.09[e]	1.11 ± 0.09	3.73 ± 0.32	10.6 ± 1.2	-	-	-	-
1178.78 ± 0.13[c,e]	0.72 ± 0.08	2.44 ± 0.29	6.95 ± 0.96	-	-	-	-
1190.69 ± 0.22[e]	0.38 ± 0.05	1.30 ± 0.18	3.69 ± 0.59	-	-	-	-
1193.60 ± 0.18[e]	0.65 ± 0.07	2.20 ± 0.24	6.26 ± 0.81	-	-	-	-
1196.05 ± 0.14[e]	0.59 ± 0.06	1.98 ± 0.21	5.63 ± 0.73	1195.1 ± 1.0	4.1 ± 0.8[d]	1.02 ± 0.25	0.10
1232.42 ± 0.18[e]	0.67 ± 0.10	2.27 ± 0.35	6.47 ± 1.10	-	-	-	-
1243.14 ± 0.31[e]	0.51 ± 0.09	1.74 ± 0.33	4.94 ± 0.99	-	-	-	-
1248.06 ± 0.24[e]	0.42 ± 0.13	1.43 ± 0.43	4.06 ± 1.25	-	-	-	-
1253.82 ± 0.10[e,j]	0.17 ± 0.09	3.95 ± 0.34	11.3 ± 1.3	1255.9 ± 1.0	4.7 ± 1.0	0.84 ± 0.31	-0.71
1269.04 ± 0.13[e]	0.38 ± 0.05	1.28 ± 0.18	3.64 ± 0.58	-	-	-	-
1273.60 ± 0.28[e]	0.36 ± 0.06	1.23 ± 0.21	3.50 ± 0.64	-	-	-	-
1276.05 ± 0.12[c,e]	1.10 ± 0.10	3.70 ± 0.35	10.5 ± 1.2	1276.7 ± 1.0	3.4 ± 0.9[d]	1.45 ± 0.48	1.66
1279.51 ± 0.27[e]	0.28 ± 0.05	0.94 ± 0.17	2.68 ± 0.51	-	-	-	-
1288.19 ± 0.12[e]	0.64 ± 0.06	2.16 ± 0.21	6.16 ± 0.74	-	-	-	-
1306.29 ± 0.24[e]	0.44 ± 0.06	1.49 ± 0.20	4.24 ± 0.65	-	-	-	-
1310.03 ± 0.13[e]	0.80 ± 0.06	2.71 ± 0.22	7.72 ± 0.83	-	-	-	-
1316.99 ± 0.12[e]	0.73 ± 0.05	2.45 ± 0.20	6.99 ± 0.75	-	-	-	-
1334.54 ± 0.17[e]	0.71 ± 0.07	2.40 ± 0.25	6.83 ± 0.86	-	-	-	-
1374.50 ± 0.12[e,i]	0.55 ± 0.04	1.84 ± 0.15	5.25 ± 0.57	-	-	-	-
1381.52 ± 0.16[e]	0.54 ± 0.05	1.82 ± 0.17	5.18 ± 0.62	-	-	-	-
1384.92 ± 0.21[e]	0.33 ± 0.04	1.11 ± 0.14	3.16 ± 0.46	-	-	-	-
1425.35 ± 0.30[e]	0.18 ± 0.04	0.62 ± 0.13	1.76 ± 0.40	-	-	-	-
1442.88 ± 0.12[e]	0.40 ± 0.03	1.36 ± 0.10	3.88 ± 0.39	-	-	-	-
1474.52 ± 0.43[e]	0.34 ± 0.08	1.15 ± 0.26	3.27 ± 0.77	-	-	-	-
1478.87 ± 0.32[e,h]	0.31 ± 0.06	1.05 ± 0.19	2.98 ± 0.58	-	-	-	-
1534.73 ± 0.27[e,h]	0.15 ± 0.03	0.52 ± 0.10	1.47 ± 0.31	-	-	-	-
1548.01 ± 0.16[e]	0.10 ± 0.02	0.35 ± 0.06	0.98 ± 0.20	-	-	-	-
1578.61 ± 0.21[e]	0.21 ± 0.04	0.71 ± 0.12	2.03 ± 0.37	-	-	-	-
2483.50 ± 0.54[e,h]	0.19 ± 0.05	0.63 ± 0.15	1.80 ± 0.46	-	-	-	-
3333.07 ± 0.43[e,h]	0.16 ± 0.04	0.55 ± 0.13	1.57 ± 0.39	-	-	-	-
3353.65 ± 0.58[e,h]	0.09 ± 0.03	0.30 ± 0.11	0.86 ± 0.32	-	-	-	-

E_γ is the γ-ray energy, $P_{E\gamma}(90°)/(\epsilon_{E\gamma} \times f_{E\gamma})$ the net counts in the γ-ray peak divided by the full-energy-peak (FEP) efficiency and the γ-ray self-absorption factor, I_R the relative intensity (relative to the 331-keV line of ^{159}Tb, 100%) of the γ-rays and $\langle\sigma_{E_\gamma}(90°)\rangle$ is the fast-neutron spectrum-averaged isotopic partial cross section for γ-ray production at an angle of 90° between neutron beam and detector determined with Eq. (4.1). R is the residual calculated by means of Eq. (4.33)

[a] emitted from same excited level as 317.01 keV, corrected for strong background interference

[b] corrected for interference from the ^{35}Cl(n,n'γ) reaction: $\langle\sigma_{E_\gamma}(90°)\rangle$= (32 ± 3) mb [21] yields a contribution to the net counts of 1.7%

[c] corrected for (n,γ) interference from Tb

[d] unresolved doublet, intensity of 183.06 & 184.48 keV, 303.40 & 306.82 keV, 944.41 & 946.67 keV, 1092.27 & 1094.58 keV, 1193.60 & 1196.05 keV, 1273.60 & 1276.05 keV

H.1.31 : (continued).

[e]not listed in [65, 158], any other origins than (n,n'γ) excluded
[f]probably interchanged intensities between 272.9 and 274.8 keV
[g]intensity of 615.4 and 617.5 keV
[h]tentative and uncertain suggestion
[i]corrected for (n,γ) interference from Cl
[j]corrected for interference with SE from the 1762.7-keV line of ^{35}Cl (23.4% contribution to the net counts)

H.1.32 : Prompt γ-rays of ^{161}Dy induced by inelastic scattering of fast neutrons.

This work				From Atlas [27]		I_R (This work)/I_R (Demidov)	R
E_γ (keV)	$P_{E\gamma}(90°)/(\epsilon_{E\gamma} \times f_{E\gamma}) \times 10^{-8}$ (count)	I_R(relative) (%)	$\langle\sigma_{E_\gamma}(90°)\rangle$ (mb)	E_γ (keV)	I_R(relative) (%)		
48.62 ± 0.13	2.83 ± 0.71	138 ± 41	495 ± 131	-	-	-	-
56.70 ± 0.20	1.29 ± 0.34	63 ± 19	225 ± 63	-	-	-	-
102.63 ± 0.07	0.59 ± 0.05	29 ± 5	103 ± 13	-	-	-	-
128.46 ± 0.20	0.09 ± 0.03	4.17 ± 1.55	15.0 ± 5.2	-	-	-	-
157.00 ± 0.08[a]	0.35 ± 0.04	17.0 ± 3.2	61 ± 8	-	-	-	-
217.31 ± 0.10	0.24 ± 0.04	11.6 ± 2.5	42 ± 7	-	-	-	-
230.18 ± 0.13[a]	0.11 ± 0.02	5.57 ± 1.22	20 ± 3	-	-	-	-
292.02 ± 0.11[a,b]	0.21 ± 0.03	10.3 ± 2.1	37 ± 6	-	-	-	-
343.25 ± 0.25[a]	0.10 ± 0.03	5.11 ± 1.51	18.4 ± 4.8	344.0 ± 0.4	16 ± 4	0.32 ± 0.12	-2.55
549.62 ± 0.10	0.20 ± 0.02	9.96 ± 1.88	36 ± 5	-	-	-	-
588.34 ± 0.12	0.16 ± 0.04	7.78 ± 2.20	28 ± 7	589.8 ± 0.2	8.5 ± 1.5	0.92 ± 0.31	-0.27
607.85 ± 0.11[a,c]	0.22 ± 0.05	10.7 ± 2.9	39 ± 9	-	-	-	-
826.46 ± 0.26	0.14 ± 0.05	6.77 ± 2.53	24 ± 8	825.9 ± 0.2	4.3 ± 0.8	1.20 ± 0.50	0.42

E_γ is the γ-ray energy, $P_{E\gamma}(90°)/(\epsilon_{E\gamma} \times f_{E\gamma})$ the net counts in the γ-ray peak divided by the full-energy-peak (FEP) efficiency and the γ-ray self-absorption factor, I_R the relative intensity (relative to the 754-keV line of ^{164}Dy, 100%) of the γ-rays and $\langle\sigma_{E_\gamma}(90°)\rangle$ is the fast-neutron spectrum-averaged isotopic partial cross section for γ-ray production at an angle of 90° between neutron beam and detector determined with Eq. (4.1). R is the residual calculated by means of Eq. (4.33)
[a]corrected for (n,γ) interference from Dy
[b]corrected for (n,γ) interference from Cl
[c]corrected for background interference

H.1.33 : Prompt γ-rays of ^{162}Dy induced by inelastic scattering of fast neutrons.

This work				From Atlas [27]		I_R (This work)/I_R (Demidov)	R
E_γ (keV)	$P_{E\gamma}(90°)/(\epsilon_{E\gamma} \times f_{E\gamma}) \times 10^{-8}$ (count)	I_R(relative) (%)	$\langle\sigma_{E_\gamma}(90°)\rangle$ (mb)	E_γ (keV)	I_R(relative) (%)		
184.83 ± 0.03[a,c]	7.14 ± 0.54	348 ± 60	937 ± 102	185.07 ± 0.10	400 ± 80	0.87 ± 0.23	-0.52
219.78 ± 0.10	0.19 ± 0.03	9.09 ± 2.13	24 ± 5	-	-	-	-
235.65 ± 0.10[b,c]	0.09 ± 0.02	4.22 ± 1.06	11.4 ± 2.4	-	-	-	-
282.44 ± 0.03[c]	0.96 ± 0.08	47 ± 8	126 ± 14	282.9 ± 0.2	45 ± 8	1.04 ± 0.26	0.15
310.72 ± 0.14[c]	0.04 ± 0.01	1.79 ± 0.54	4.82 ± 1.31	310.0 ± 0.3	9.0 ± 0.4[d]	1.61 ± 0.62	0.99
333.48 ± 0.04[c]	0.56 ± 0.05	27 ± 5	74 ± 9	334.2 ± 0.3	24 ± 4	1.14 ± 0.28	0.52
371.16 ± 0.22[c]	0.19 ± 0.04	9.17 ± 2.44	25 ± 6	371.3 ± 0.3	4.1 ± 0.9	2.24 ± 0.77	1.95
528.71 ± 0.24[c]	0.07 ± 0.02	3.25 ± 1.05	8.76 ± 2.58	-	-	-	-
556.11 ± 0.16[c]	0.07 ± 0.02	3.50 ± 0.96	9.42 ± 2.26	-	-	-	-
565.27 ± 0.10[c]	0.19 ± 0.03	9.23 ± 2.12	25 ± 5	565.6 ± 0.2	16 ± 2	0.58 ± 0.15	-2.32
677.62 ± 0.09	0.16 ± 0.02	7.65 ± 1.53	21 ± 3	678.0 ± 0.2	11 ± 2	0.70 ± 0.19	-1.33
696.58 ± 0.09[c]	0.47 ± 0.06	23 ± 5	62 ± 9	696.9 ± 0.4	28 ± 3	0.82 ± 0.19	-0.90
770.44 ± 0.10[a,c]	0.09 ± 0.02	4.57 ± 1.08	12.3 ± 2.4	-	-	-	-
794.86 ± 0.05[c]	0.65 ± 0.07	32 ± 6	86 ± 11	795.40 ± 0.10	22 ± 3	1.45 ± 0.33	1.48

H.1.33 : (continued).

This work				From Atlas [27]		I_R (This work)/I_R (Demidov)	R
E_γ (keV)	$P_{E\gamma}(90°)/(\epsilon_{E\gamma} \times f_{E\gamma}) \times 10^{-8}$ (count)	I_R(relative) (%)	$\langle\sigma_{E_\gamma}(90°)\rangle$ (mb)	E_γ (keV)	I_R(relative) (%)		
807.13 ± 0.04[a,c]	2.09 ± 0.14	102 ± 17	274 ± 28	807.54 ± 0.10	80 ± 8	1.27 ± 0.25	1.14
878.70 ± 0.16[c]	0.13 ± 0.03	6.19 ± 1.61	16.7 ± 3.7	-	-	-	-
881.93 ± 0.05[a,c]	2.33 ± 0.19	113 ± 20	305 ± 34	882.34 ± 0.10	72 ± 8	1.57 ± 0.33	1.93
887.82 ± 0.05[c]	1.88 ± 0.13	92 ± 16	247 ± 26	888.18 ± 0.10	53 ± 6	1.73 ± 0.35	2.32
916.72 ± 0.05[a,c]	0.50 ± 0.05	24 ± 4	65 ± 8	917.10 ± 0.10	22 ± 2	1.10 ± 0.23	0.44
944.16 ± 0.06[c]	0.23 ± 0.04	11.4 ± 2.7	31 ± 6	944.4	20 ± 2	0.57 ± 0.15	-2.56
975.38 ± 0.12[a,e]	0.14 ± 0.02	6.70 ± 1.43	-	-	-	-	-
980.10 ± 0.06[a,c]	0.27 ± 0.04	13.0 ± 2.9	35 ± 6	980.6 ± 0.2	12 ± 2[f]	1.61 ± 0.58	1.13
1021.83 ± 0.14[a,c]	0.05 ± 0.01	2.21 ± 0.64	5.96 ± 1.51	-	-	-	-
1025.83 ± 0.13[a,e]	0.13 ± 0.03	6.11 ± 1.69	-	-	-	-	-
1091.96 ± 0.07[c]	0.37 ± 0.03	18.2 ± 3.3	49 ± 6	1092.0	11.3 ± 2.2	1.61 ± 0.43	1.75
1124.63 ± 0.08[a,c]	0.13 ± 0.02	6.17 ± 1.42	16.6 ± 3.1	1124.8 ± 0.2	7.8 ± 1.6	0.79 ± 0.24	-0.76
1129.24 ± 0.06[a,c,g]	0.61 ± 0.06	30 ± 5	80 ± 10	1129.7 ± 0.2	17 ± 3	1.75 ± 0.44	2.06
1187.61 ± 0.12[c]	0.13 ± 0.02	6.12 ± 1.32	16.5 ± 2.8	1187.7 ± 0.2	9.7 ± 1.9	0.63 ± 0.18	-1.55
1195.16 ± 0.11[c]	0.63 ± 0.05	31 ± 5	82 ± 9	1195.20 ± 0.10	20 ± 4	1.53 ± 0.40	1.60
1252.56 ± 0.19[c,h]	0.21 ± 0.02	10.1 ± 1.81	27 ± 3	1251.9	2.0 ± 1.0	5.05 ± 2.68	3.92
1276.50 ± 0.07[c]	0.95 ± 0.07	46 ± 8	124 ± 14	1276.6 ± 0.2	26 ± 5	1.77 ± 0.46	2.13
1308.61 ± 0.17[b,c]	0.19 ± 0.03	9.10 ± 1.96	25 ± 4	-	-	-	-
1311.53 ± 0.22	0.09 ± 0.02	4.20 ± 1.09	11.3 ± 2.5	-	-	-	-
1319.59 ± 0.14[b]	0.16 ± 0.02	7.89 ± 1.52	21 ± 3	-	-	-	-
1372.35 ± 0.11[c]	0.36 ± 0.03	17.5 ± 3.2	47 ± 6	1372.7 ± 0.5	9.4 ± 2.4	1.87 ± 0.58	2.05
1403.95 ± 0.47	0.07 ± 0.02	3.57 ± 1.07	9.62 ± 2.56	-	-	-	-
1438.84 ± 0.34[i]	0.09 ± 0.02	4.30 ± 1.14	11.6 ± 2.7	-	-	-	-
1556.41 ± 0.16[a]	0.17 ± 0.02	8.38 ± 1.74	23 ± 4	1556.4 ± 0.8	8.6 ± 2.2[j]	1.54 ± 0.67	0.91
1585.67 ± 0.19	0.15 ± 0.02	7.52 ± 1.45	20 ± 3	1585.1 ± 1.2	17 ± 3[k]	0.76 ± 0.27	-0.80
1901.48 ± 0.33[b,l]	0.07 ± 0.02	3.54 ± 0.93	9.6 ± 2.2	-	-	-	-
1919.01 ± 0.33[b]	0.09 ± 0.02	4.43 ± 1.22	12.0 ± 2.9	-	-	-	-
1982.58 ± 0.33[b,m]	0.07 ± 0.01	3.18 ± 0.82	8.56 ± 1.89	-	-	-	-
1999.65 ± 0.20[b]	0.15 ± 0.02	7.22 ± 1.55	19.5 ± 3.2	-	-	-	-
2020.85 ± 0.21[c]	0.05 ± 0.01	2.45 ± 0.70	6.60 ± 1.65	-	-	-	-
2048.04 ± 0.27	0.08 ± 0.02	3.69 ± 1.01	9.94 ± 2.37	-	-	-	-
2241.54 ± 0.36[c]	0.04 ± 0.01	2.07 ± 0.74	5.58 ± 1.85	-	-	-	-
2734.31 ± 0.26	0.07 ± 0.02	3.35 ± 0.98	9.02 ± 2.35	-	-	-	-
2746.29 ± 0.34	0.08 ± 0.02	3.76 ± 1.14	10.1 ± 2.7	-	-	-	-

E_γ is the γ-ray energy, $P_{E\gamma}(90°)/(\epsilon_{E\gamma} \times f_{E\gamma})$ the net counts in the γ-ray peak divided by the full-energy-peak (FEP) efficiency and the γ-ray self-absorption factor, I_R the relative intensity (relative to the 754-keV line of ^{164}Dy, 100%) of the γ-rays and $\langle\sigma_{E_\gamma}(90°)\rangle$ is the fast-neutron spectrum-averaged isotopic partial cross section for γ-ray production at an angle of 90° between neutron beam and detector determined with Eq. (4.1). R is the residual calculated by means of Eq. (4.33)

[a] corrected for background interference

[b] confirmed by Demidov's isotopic measurements [27]

[c] corrected for (n,γ) interference from Dy

[d] 308 and 311 keV (unresolved doublet by Demidov)

[e] assigned as (n,γ) line of Dy, as the capture contributions are approximately 100%; net counts and intensities were calculated under neglection of the capture counts and are given to support the discussion

[f] 980 and 983 keV (unresolved doublet by Demidov)

[g] corrected for (n,γ) interference from Cl

[h] corrected for contribution of SE from 1763 keV (31% of net counts)

[i] corrected for contribution of SE from 1951 keV (4.1% of net counts)

[j] 1554 and 1556 keV (unresolved doublet by Demidov)

[k] 1582 and 1586 keV (unresolved doublet by Demidov)

[l] corrected for interference from ^{37}Cl with $\langle\sigma_{E_\gamma}(90°)\rangle$= (2.38 ± 0.56) mb from the $CeCl_3$ measurement [21] (42% contribution to the net counts)

[m] corrected for interference from ^{18}O with $\langle\sigma_{E_\gamma}(90°)\rangle$= (201 ± 28) mb from the $CaCO_3$ measurement [20] (53% contribution to the net counts)

H.1.34 : Prompt γ-rays of ^{163}Dy induced by inelastic scattering of fast neutrons.

This work				From Atlas [27]		I_R (This work)/I_R (Demidov)	R
E_γ (keV)	$P_{E\gamma}(90°)/(\epsilon_{E\gamma} \times f_{E\gamma}) \times 10^{-8}$ (count)	I_R(relative) (%)	$\langle\sigma_{E_\gamma}(90°)\rangle$ (mb)	E_γ (keV)	I_R(relative) (%)		
93.78 ± 0.06[a]	0.59 ± 0.06	29 ± 5	78 ± 10	-	-	-	-
177.39 ± 0.04[a]	0.39[a]± 0.04	19.0 ± 3.5	52 ± 7	-	-	-	-
207.86 ± 0.04[a]	1.06 ± 0.05	52 ± 8	141 ± 13	208.15 ± 0.10	94 ± 20	0.55 ± 0.15	-1.95
244.72 ± 0.05	0.51 ± 0.03	25 ± 4	67 ± 6	245.3 ± 0.2	34 ± 6	0.73 ± 0.18	-1.28
250.52 ± 0.03[a]	1.85 ± 0.23	90 ± 18	246 ± 36	250.94 ± 0.10	161 ± 35	0.56 ± 0.6	-1.80
262.75 ± 0.04[a,b]	1.42 ± 0.09	69 ± 12	189 ± 19	263.20 ± 0.10	82 ± 15	0.85 ± 0.21	-0.67
266.21 ± 0.13[a]	0.07 ± 0.02	3.18 ± 0.92	8.67 ± 2.22	-	-	-	-
267.44 ± 0.14[a]	0.013 ± 0.004	0.62 ± 0.24	1.69 ± 0.60	267.1 ± 0.3	9.4 ± 1.6[c]	0.40 ± 0.12	-2.32
305.71 ± 0.12[a]	0.10 ± 0.02	4.68 ± 1.22	12.8 ± 2.8	-	-	-	-
315.70 ± 0.06[a]	0.13 ± 0.03	6.22 ± 1.95	17.0 ± 4.8	316.2 ± 0.3	23 ± 4	0.27 ± 0.10	-3.77
337.83 ± 0.08[d]	0.30 ± 0.03	14.6 ± 2.8	-	338.6 ± 0.3	12 ± 4	1.22 ± 0.47	0.53
350.55 ± 0.03[a,b]	0.32 ± 0.09	15.8 ± 4.8	43 ± 12	351.22 ± 0.10	84 ± 11	0.19 ± 0.06	-0.67
353.67 ± 0.04[a]	0.67 ± 0.13	33 ± 8	90 ± 18	354.29 ± 0.10	52 ± 6	0.63 ± 0.17	-1.91
385.32 ± 0.07[a]	0.24 ± 0.06	11.9 ± 3.3	33 ± 8	385.8 ± 0.3	16 ± 4	0.75 ± 0.28	-0.79
389.06 ± 0.04[a]	0.89 ± 0.19	43 ± 12	118 ± 27	389.82 ± 0.10	72 ± 7	0.60 ± 0.17	-2.12
401.31 ± 0.05[a]	0.61 ± 0.08	30 ± 6	81 ± 12	402.1 ± 0.2	31 ± 4	0.95 ± 0.23	-0.21
406.94 ± 0.13[a]	0.16 ± 0.04	7.76 ± 2.09	21 ± 5	-	-	-	-
421.08 ± 0.05[a]	0.72 ± 0.16	35 ± 10	96 ± 23	421.90 ± 0.10	64 ± 6	0.55 ± 0.16	-2.56
427.00 ± 0.04[a]	0.48 ± 0.08	23 ± 5	64 ± 12	427.4 ± 0.2	23 ± 2	1.02 ± 0.25	0.07
435.60 ± 0.17[a,e]	0.09 ± 0.02	4.47 ± 1.39	12.2 ± 3.4	436.8 ± 0.3	9.7 ± 0.9	0.46 ± 0.15	-3.16
440.45 ± 0.05[a]	0.33 ± 0.04	16.2 ± 3.1	44 ± 6	441.3 ± 0.3	16 ± 2	1.01 ± 0.23	0.06
478.73 ± 0.04[a]	0.22 ± 0.04	10.7 ± 2.5	29 ± 5	479.4 ± 0.2	22 ± 3	0.49 ± 0.13	-0.67
495.80 ± 0.16[d]	0.29 ± 0.05	14.3 ± 3.2	-	495.1 ± 0.4	5.4 ± 0.8	2.64 ± 0.71	2.70
541.03 ± 0.17	0.20 ± 0.03	9.63 ± 2.24	26 ± 5	-	-	-	-
552.32 ± 0.13[a]	0.09 ± 0.02	4.35 ± 1.04	11.9 ± 2.3	-	-	-	-
558.85 ± 0.10[a]	0.05 ± 0.01	2.58 ± 0.75	7.04 ± 1.82	-	-	-	-
633.30 ± 0.13[a,e]	0.24 ± 0.03	11.7 ± 2.3	32 ± 5	633.6 ± 0.2	7.5 ± 2.0	1.56 ± 0.52	1.38
637.32 ± 0.19[a]	0.08 ± 0.02	3.66 ± 1.16	9.99 ± 2.87	-	-	-	-
710.90 ± 0.13[a]	0.12 ± 0.02	5.92 ± 1.40	16.1 ± 3.1	711.57 ± 0.10	15 ± 2	0.39 ± 0.11	-3.72
726.84 ± 0.19[a,b]	0.19 ± 0.03	9.31 ± 1.95	25 ± 4	-	-	-	-
729.63 ± 0.27[b]	0.15 ± 0.03	7.07 ± 1.70	19.3 ± 3.9	728.5 ± 0.2	6.2 ± 0.9	1.14 ± 0.32	1.45

E_γ is the γ-ray energy, $P_{E\gamma}(90°)/(\epsilon_{E\gamma} \times f_{E\gamma})$ the net counts in the γ-ray peak divided by the full-energy-peak (FEP) efficiency and the γ-ray self-absorption factor, I_R the relative intensity (relative to the 754-keV line of ^{164}Dy, 100%) of the γ-rays and $\langle\sigma_{E_\gamma}(90°)\rangle$ is the fast-neutron spectrum-averaged isotopic partial cross section for γ-ray production at an angle of 90° between neutron beam and detector determined with Eq. (4.1). R is the residual calculated by means of Eq. (4.33)
[a]corrected for (n,γ) interference from Dy
[b]corrected for background interference
[c]266 and 267 keV (unresolved doublet by Demidov)
[d]assigned as capture line of Dy, as the capture contributions are approximately 100%; net counts and intensities were calculated under neglection of the capture counts and are given to support the discussion
[e]corrected for (n,γ) interference from Cl

H.1.35 : Prompt γ-rays of ^{164}Dy induced by inelastic scattering of fast neutrons.

This work				From Atlas [27]		I_R (This work)/I_R (Demidov)	R
E_γ (keV)	$P_{E\gamma}(90°)/(\epsilon_{E\gamma} \times f_{E\gamma}) \times 10^{-8}$ (count)	I_R(relative) (%)	$\langle\sigma_{E_\gamma}(90°)\rangle$ (mb)	E_γ (keV)	I_R(relative) (%)		
123.26 ± 0.16	0.14 ± 0.03	6.58 ± 1.89	15.9 ± 4.0	-	-	-	-
148.65 ± 0.06[a]	1.06 ± 0.05	52 ± 8	141 ± 13	148.7 ± 0.3	26 ± 8	0.93 ± 0.33	-0.19
168.74 ± 0.03[a,b]	5.28 ± 0.38	257 ± 44	619 ± 66	169.0 ± 0.2	400 ± 80	0.64 ± 0.17	-1.57
214.89 ± 0.03[a]	1.79 ± 0.20	87 ± 17	210 ± 29	215.23 ± 0.10	140 ± 25	0.62 ± 0.16	-1.75

H.1.35 : (continued).

This work				From Atlas [27]		I_R (This work)/I_R (Demidov)	R
E_γ (keV)	$P_{E\gamma}(90°)/(\epsilon_{E\gamma} \times f_{E\gamma}) \times 10^{-8}$ (count)	I_R(relative) (%)	$\langle\sigma_{E_\gamma}(90°)\rangle$ (mb)	E_γ (keV)	I_R(relative) (%)		
277.04 ± 0.04[a,b]	0.70 ± 0.09	34 ± 7	82 ± 12	277.6 ± 0.2	50 ± 10	0.68 ± 0.19	-1.32
294.21 ± 0.04[a]	0.17 ± 0.04	8.09 ± 2.49	19.5 ± 5.4	294.7 ± 0.2	51 ± 10[d]	0.36 ± 0.15	-2.70
308.48 ± 0.11[c]	0.26 ± 0.04	12.7 ± 2.9	31 ± 6	-	-	-	-
461.59 ± 0.05[a]	0.19 ± 0.02	9.18 ± 1.70	22 ± 3	462.2 ± 0.4	8.3 ± 1.1	1.11 ± 0.25	0.43
464.94 ± 0.06[a]	0.08 ± 0.02	4.09 ± 1.19	9.85 ± 2.55	-	-	-	-
522.67 ± 0.13[c]	0.11 ± 0.02	5.49 ± 1.48	13.2 ± 3.1	-	-	-	-
543.16 ± 0.29	0.13 ± 0.03	6.56 ± 1.69	15.8 ± 3.5	-	-	-	-
548.18 ± 0.09[a]	0.18 ± 0.02	8.83 ± 1.74	21 ± 3	548.5 ± 0.5	9.0 ± 2.0[e]	2.09 ± 0.73	1.78
585.24 ± 0.05[a]	0.49 ± 0.05	24 ± 5	58 ± 8	585.63 ± 0.10	31 ± 3	0.78 ± 0.16	-1.29
610.57 ± 0.11[a,c]	0.50 ± 0.06	24 ± 5	58 ± 8	-	-	-	-
651.77 ± 0.20	0.09 ± 0.03	4.28 ± 1.42	10.3 ± 3.1	-	-	-	-
673.12 ± 0.04[a]	0.78 ± 0.10	38 ± 8	92 ± 14	673.66 ± 0.10	38 ± 4	1.00 ± 0.23	0.02
687.83 ± 0.04[a]	2.13 ± 0.29	104 ± 21	250 ± 39	688.46 ± 0.10	94 ± 10	1.10 ± 0.26	0.42
754.31 ± 0.04[a]	2.05 ± 0.32	100	241 ± 42	754.86 ± 0.10	100	-	-
761.34 ± 0.04[a]	1.96 ± 0.25	95 ± 19	230 ± 24	761.87 ± 0.10	75 ± 8	1.27 ± 0.29	0.98
781.89 ± 0.05[a]	0.75 ± 0.04	36 ± 6	88 ± 8	782.31 ± 0.10	18 ± 2	2.03 ± 0.40	2.96
911.16 ± 0.11	0.20 ± 0.02	9.93 ± 1.88	24 ± 3	911.4 ± 0.2	12 ± 2	0.83 ± 0.21	-0.75
955.25 ± 0.28	0.09 ± 0.02	4.29 ± 1.24	10.4 ± 2.6	-	-	-	-
965.61 ± 0.10	0.24 ± 0.02	11.8 ± 2.2	29 ± 3	965.1	10 ± 2	1.18 ± 0.32	0.63
982.64 ± 0.20[b,c]	0.13 ± 0.02	6.24 ± 1.40	15.1 ± 2.7	-	-	-	-
1001.84 ± 0.21[a,c]	0.13 ± 0.03	6.38 ± 1.72	15.4 ± 3.6	-	-	-	-
1072.07 ± 0.26[a]	0.11 ± 0.02	5.30 ± 1.30	12.8 ± 2.6	-	-	-	-
1412.18 ± 0.22[a,b]	0.05 ± 0.01	2.61 ± 0.71	6.31 ± 1.50	-	-	-	-
1515.81 ± 0.18[b,c]	0.11 ± 0.02	5.39 ± 1.24	13.0 ± 2.4	-	-	-	-
1528.90 ± 0.34[a]	0.07 ± 0.02	3.63 ± 0.99	8.75 ± 2.08	-	-	-	-
1543.64 ± 0.46[c]	0.10 ± 0.02	4.75 ± 1.34	11.4 ± 2.8	-	-	-	-
1553.96 ± 0.34[c]	0.10 ± 0.02	4.89 ± 1.36	11.8 ± 2.9	-	-	-	-
1581.62 ± 0.28[c]	0.11 ± 0.02	5.43 ± 1.35	13.1 ± 2.7	-	-	-	-
1600.88 ± 0.13[a,b,f]	0.27 ± 0.03	13.3 ± 2.5	32 ± 4	1599.8 ± 0.8	7.8 ± 2.3	1.71 ± 0.60	1.62
1610.82 ± 0.22	0.16 ± 0.02	7.70 ± 1.63	18.6 ±3.0	-	-	-	-
1641.97 ± 0.14[b,f]	0.22 ± 0.03	10.6 ± 2.1	26 ± 4	1642.8 ± 0.8	5.4 ± 1.6	1.96 ± 0.69	1.99
1666.41 ± 0.20[c]	0.25 ± 0.03	12.2 ± 2.3	29 ± 4	-	-	-	-
1674.35 ± 0.29[a,b]	0.10 ± 0.02	5.00 ± 1.27	12.1 ± 2.6	-	-	-	-
1684.63 ± 0.17	0.16 ± 0.02	7.84 ± 1.66	18.9 ± 3.1	1685.8	3.8 ± 1.1	2.06 ± 0.74	2.03
1722.69 ± 0.22[a]	0.39 ± 0.04	18.9 ± 3.6	45 ± 6	1724.0 ± 0.8	5.0 ± 1.5	3.77 ± 1.34	3.58
1735.98 ± 0.15[a]	0.31 ± 0.03	15.2 ± 2.9	37 ± 5	1735.4 ± 0.8	8.4 ± 1.7	1.80 ± 0.50	2.02
1836.16 ± 0.20[a,c]	0.11 ± 0.02	5.49 ± 1.23	13.2 ± 2.4	-	-	-	-
1840.69 ± 0.22	0.13 ± 0.02	6.11 ± 1.37	14.7 ± 2.7	-	-	-	-
1859.35 ± 0.15[c]	0.21 ± 0.03	10.4 ± 2.2	25 ± 4	-	-	-	-
1905.09 ± 0.43[c]	0.09 ± 0.02	4.60 ± 1.27	11.1 ± 2.7	-	-	-	-
1910.13 ± 0.27	0.09 ± 0.02	4.59 ± 1.22	11.1 ± 2.6	-	-	-	-
1980.04 ± 0.23[c]	0.15 ± 0.02	7.36 ± 1.55	17.7 ± 2.9	-	-	-	-
2509.58 ± 0.32	0.09 ± 0.02	4.16 ± 1.02	10.0 ± 2.1	-	-	-	-

E_γ is the γ-ray energy, $P_{E\gamma}(90°)/(\epsilon_{E\gamma} \times f_{E\gamma})$ the net counts in the γ-ray peak divided by the full-energy-peak (FEP) efficiency and the γ-ray self-absorption factor, I_R the relative intensity (relative to the 754-keV line of ^{164}Dy, 100%) of the γ-rays and $\langle\sigma_{E_\gamma}(90°)\rangle$ is the fast-neutron spectrum-averaged isotopic partial cross section for γ-ray production at an angle of 90° between neutron beam and detector determined with Eq. (4.1). R is the residual calculated by means of Eq. (4.33).
[a]corrected for (n,γ) interference from Dy
[b]corrected for background interference
[c]confirmed by Demidov's isotopic measurement [27]
[d]292 and 294 keV (unresolved doublet by Demidov)
[e]548 and 550 keV (unresolved doublet by Demidov)
[f]corrected for (n,γ) interference from Cl

H.1.36 : Prompt γ-rays induced by inelastic scattering of fast neutrons in multiple Dy isotopes.

This work				From Atlas [27]		I_R (This work)/I_R (Demidov)	R
E_γ (keV)	$P_{E\gamma}(90°)/(\epsilon_{E\gamma} \times f_{E\gamma})$ $\times$ 10^{-8} (count)	I_R(relative) (%)	$\langle\sigma_{E_\gamma}(90°)\rangle$ (mb)	E_γ (keV)	I_R(relative) (%)		
^{161}Dy + ^{162}Dy							
80.60 ± 0.06[a]	7.04 ± 0.57	343 ± 60	528 ± 59	-	-	-	-
^{161}Dy + ^{163}Dy							
167.20 ± 0.04[b]	2.42 ± 0.11	118 ± 19	183 ± 16	167.3 ± 0.2	150 ± 40	0.79 ± 0.25	-0.72
285.14 ± 0.04[a]	1.22 ± 0.08	59 ± 10	92 ± 9	285.8 ± 0.2	71 ± 15	0.84 ± 0.23	-0.65
^{161}Dy + ^{164}Dy							
532.33 ± 0.08[a,b]	0.17 ± 0.02	8.24 ± 1.66	22 ± 3	533.7 ± 0.2	6.6 ± 1.0	1.25 ± 0.31	0.84
^{162}Dy + ^{163}Dy							
247.31 ± 0.06[a]	0.33 ± 0.03	16.0 ± 2.8	22 ± 2	247.9 ± 0.2	23 ± 4	0.70 ± 0.17	-1.43
347.00 ± 0.05[a]	0.13 ± 0.03	6.40 ± 1.93	8.7 ± 2.4	347.4 ± 0.3	20 ± 4	0.32 ± 0.12	-3.06
572.25 ± 0.15[a]	0.11 ± 0.02	5.36 ± 1.29	7.27 ± 1.46	572.8 ± 0.3	15 ± 2	0.36 ± 0.10	4.05
^{162}Dy + ^{164}Dy							
842.65 ± 0.06[a,b]	0.43 ± 0.05	21 ± 4	26 ± 4	842.7 ± 0.2	27 ± 3	0.77 ± 0.17	-1.27
1648.06 ± 0.16[a,c]	0.24 ± 0.02	11.9 ± 2.2	15.2 ± 1.8	1649.8 ± 0.8	7.4 ± 2.2	1.61 ± 0.56	1.47
^{163}Dy + ^{164}Dy							
211.68 ± 0.04[a]	1.71 ± 0.13	83 ± 14	106 ± 12	212.06 ± 0.10	119 ± 23	0.70 ± 0.18	-1.32
238.21 ± 0.10	0.14 ± 0.02	6.66 ± 1.48	8.52 ± 1.50	-	-	-	-
414.42 ± 0.07[a]	0.16 ± 0.04	7.73 ± 2.32	9.89 ± 2.66	-	-	-	-
^{162}Dy + ^{163}Dy + ^{164}Dy							
259.54 ± 0.04[a]	1.96 ± 0.14	95 ± 16	83 ± 9	260.00	145 ± 30	0.66 ± 0.18	-1.45
646.86 ± 0.04[a]	0.38 ± 0.02	18.3 ± 3.0	15.9 ± 1.5	647.2 ± 0.2	6.3 ± 0.9	2.91 ± 0.63	3.84

E_γ is the γ-ray energy, $P_{E\gamma}(90°)/(\epsilon_{E\gamma} \times f_{E\gamma})$ the net counts in the γ-ray peak divided by the full-energy-peak (FEP) efficiency and the γ-ray self-absorption factor, I_R the relative intensity (relative to the 754-keV line of ^{164}Dy, 100%) of the γ-rays and $\langle\sigma_{E_\gamma}(90°)\rangle$ is the fast-neutron spectrum-averaged isotopic partial cross section for γ-ray production at an angle of 90° between neutron beam and detector determined with Eq. (4.1) R is the residual calculated by means of Eq. (4.33)
[a]corrected for (n,γ) interference from Dy
[b]corrected for background interference
[c]corrected for (n,γ) interference from Cl

H.2 Elemental

H.2.1 : Prompt γ-rays of La induced by (n,n'γ) and (n,γ) reactions.

E_γ (keV)	Neutron capture interference		$P_{E\gamma}(90°)/(\epsilon_{E\gamma} \times f_{E\gamma})$ $\times$ 10^{-8} (count)	$\langle\sigma^Z_{E\gamma}\rangle$ (mb)
	^AZ	P_{cap}/P_{net} (%)		
330.14 ± 0.04	^{139}La, ^{139}La(d)	1.30 ± 0.24	4.58 ± 0.18	43 ± 4
495.22 ± 0.12	^{139}La	9.22 ± 2.60	0.35 ± 0.07	3.02 ± 0.64
1370.49 ± 0.08	^{35}Cl	1.39 ± 0.30	1.38 ± 0.07	12.2 ± 1.2
1595.20 ± 0.13[a]	^{139}La(d)	2.82 ± 0.91	1.41 ± 0.10	14.4 ± 1.5
1600.27 ± 0.14[a]	^{35}Cl	18.2 ± 4.0	1.23 ± 0.07	9.29 ± 0.92
1625.55 ± 0.22[a]	^{35}Cl	11.5 ± 2.7	0.26 ± 0.03	2.13 ± 0.33
2812.07 ± 0.38	^{35}Cl	25 ± 9	0.12 ± 0.03	0.86 ± 0.24
3115.34 ± 0.36	^{35}Cl, ^{139}La	24 ± 6	0.22 ± 0.04	1.63 ± 0.36

H.2.1 : (continued).

E_γ is the γ-ray energy, $P_{E\gamma}(90°)/(\epsilon_{E\gamma} \times f_{E\gamma})$ the net counts in the γ-ray peak divided by the full-energy-peak (FEP) efficiency and the γ-ray self-absorption factor, ${}^{A}Z$ the isotopes of interfering (n,γ) reactions, P_{cap}/P_{net} the ratio of neutron capture counts to net counts and $\langle\sigma^{Z}_{E\gamma}\rangle$ is the neutron spectrum-averaged elemental partial cross section for γ-ray production at an angle of 90° between neutron beam and detector, calculated after Eq. (4.28)
[a]corrected for background interference

H.2.2 : Prompt γ-rays of Pr induced by (n,n'γ) and (n,γ) reactions.

E_γ (keV)	Neutron capture interference		$P_{E\gamma}(90°)/$ $(\epsilon_{E\gamma} \times f_{E\gamma})$ $\times 10^{-8}$ (count)	$\langle\sigma^{Z}_{E\gamma}\rangle$ (mb)
	${}^{A}Z$	P_{cap}/P_{net} (%)		
359.35 ± 0.11	^{141}Pr	3.70 ± 0.87	0.40 ± 0.05	6.22 ± 0.93
547.86 ± 0.23	^{141}Pr	34 ± 9	0.19 ± 0.03	2.64 ± 0.47
974.64 ± 0.11	^{141}Pr	8.09 ± 1.73	0.40 ± 0.03	6.22 ± 0.71
1375.23 ± 0.11	^{35}Cl	1.39 ± 0.46	0.54 ± 0.05	8.55 ± 1.01
1640.18 ± 0.11[a]	^{35}Cl	2.22 ± 0.74	0.51 ± 0.03	8.00 ± 0.78
1785.90 ± 0.09	^{35}Cl	1.47 ± 0.43	0.87 ± 0.36	13.6 ± 5.7
2042.87 ± 0.31	^{35}Cl	6.44 ± 2.43	0.14 ± 0.02	2.04 ± 0.38

H.2.2 : (continued).

E_γ (keV)	Neutron capture interference		$P_{E\gamma}(90°)/$ $(\epsilon_{E\gamma} \times f_{E\gamma})$ $\times 10^{-8}$ (count)	$\langle\sigma^{Z}_{E\gamma}\rangle$ (mb)
	${}^{A}Z$	P_{cap}/P_{net} (%)		
2158.33 ± 0.24	^{35}Cl	6.64 ± 2.08	0.22 ± 0.03	3.35 ± 0.50
3115.56 ± 0.70	^{35}Cl	18.6 ± 7.3	0.12 ± 0.03	1.55 ± 0.45

E_γ is the γ-ray energy, $P_{E\gamma}(90°)/(\epsilon_{E\gamma} \times f_{E\gamma})$ the net counts in the γ-ray peak divided by the full-energy-peak (FEP) efficiency and the γ-ray self-absorption factor, ${}^{A}Z$ the isotopes of interfering (n,γ) reactions, P_{cap}/P_{net} the ratio of neutron capture counts to net counts and $\langle\sigma^{Z}_{E\gamma}\rangle$ is the neutron spectrum-averaged elemental partial cross section for γ-ray production at an angle of 90° between neutron beam and detector, calculated after Eq. (4.28)
[a]corrected for background interference

H.2.3 : Prompt γ-rays of Nd induced by (n,n'γ) and (n,γ) reactions.

E_γ (keV)	Neutron capture interference		$P_{E\gamma}(90°)/$ $(\epsilon_{E\gamma} \times f_{E\gamma})$ $\times 10^{-8}$ (count)	$\langle\sigma^{Z}_{E\gamma}\rangle$ (mb)
	${}^{A}Z$	P_{cap}/P_{net} (%)		
426.02 ± 0.16	^{143}Nd	6.63 ± 1.73	0.24 ± 0.04	5.11 ± 1.01

H.2.3 : (continued).

E_γ (keV)	Neutron capture interference		$P_{E\gamma}(90°)/$ $(\epsilon_{E\gamma} \times f_{E\gamma})$ $\times 10^{-8}$ (count)	$\langle \sigma^Z_{E\gamma} \rangle$ (mb)
	^{A}Z	P_{cap}/P_{net} (%)		
476.15 ± 0.14[a]	^{143}Nd	9.62 ± 2.74	0.54 ± 0.08	11.8 ± 2.0
545.22 ± 0.08	^{142}Nd	2.84 ± 0.56	0.27 ± 0.02	5.77 ± 0.67
588.84 ± 0.03	^{145}Nd	10.1 ± 2.3	2.99 ± 0.10	65 ± 6
617.41 ± 0.04	^{143}Nd	9.65 ± 1.85	3.48 ± 0.12	75 ± 7
695.97 ± 0.04	^{143}Nd	5.11 ± 0.98	16.37 ± 0.50	354 ± 31
735.35 ± 0.04	^{145}Nd	6.82 ± 2.03	2.21 ± 0.07	48 ± 4
741.59 ± 0.04	^{142}Nd	13.8 ± 1.1	1.80 ± 0.07	39 ± 4
778.31 ± 0.08	^{143}Nd	6.52 ± 1.34	0.31 ± 0.03	6.66 ± 0.77
813.68 ± 0.04	^{143}Nd	6.49 ± 1.25	1.99 ± 0.07	43 ± 4
864.01 ± 0.04	^{143}Nd	6.42 ± 1.24	2.12 ± 0.08	46 ± 4
936.11 ± 0.16	^{35}Cl	2.76 ± 0.72	0.22 ± 0.03	4.74 ± 0.72
979.93 ± 0.09[a]	^{143}Nd	6.91 ± 1.78	0.45 ± 0.03	9.63 ± 0.98
1002.27 ± 0.15	^{143}Nd	1.51 ± 0.33	0.24 ± 0.03	5.11 ± 0.71
1006.72 ± 0.17[a]	^{143}Nd	1.58 ± 0.58	0.15 ± 0.03	3.19 ± 0.66
1016.54 ± 0.08[a]	^{143}Nd, ^{145}Nd	1.96 ± 0.54	0.57 ± 0.03	12.4 ± 1.2
1022.42 ± 0.15[a]	^{143}Nd	1.41 ± 0.47	0.17 ± 0.02	3.63 ± 0.55
1136.65 ± 0.12[a]	^{143}Nd	13.1 ± 3.6	0.14 ± 0.01	2.96 ± 0.39
1161.73 ± 0.14	^{143}Nd	8.20 ± 2.37	0.33 ± 0.03	7.20 ± 0.84
1170.67 ± 0.34	^{35}Cl, ^{143}Nd	11.2 ± 4.2	0.12 ± 0.03	2.42 ± 0.59
1323.38 ± 0.10	^{143}Nd, ^{145}Nd	1.88 ± 0.52	0.53 ± 0.03	11.5 ± 1.2
1340.09 ± 0.14	^{143}Nd	13.5 ± 3.8	0.07 ± 0.02	1.56 ± 0.35
1376.56 ± 0.07[a]	^{143}Nd	2.45 ± 0.54	0.78 ± 0.04	16.9 ± 1.6
1382.01 ± 0.28	^{142}Nd	3.58 ± 0.29	0.14 ± 0.02	3.04 ± 0.54
1413.11 ± 0.08[a]	^{143}Nd	11.6 ± 3.6	0.42 ± 0.03	9.06 ± 0.97
1481.70 ± 0.19	^{143}Nd	7.87 ± 1.78	0.20 ± 0.02	4.28 ± 0.63
1493.55 ± 0.25[a]	^{143}Nd	29 ± 11	0.05 ± 0.01	1.18 ± 0.32
1556.00 ± 0.10[a]	^{142}Nd	4.25 ± 0.47	0.35 ± 0.02	7.54 ± 0.80
1560.80 ± 0.14	^{143}Nd	12.4 ± 3.0	0.08 ± 0.01	1.80 ± 0.30
1671.75 ± 0.12[b]	^{143}Nd	15.9 ± 3.2	0.26 ± 0.02	5.62 ± 0.60
1689.51 ± 0.29	^{143}Nd	2.21 ± 0.59	0.10 ± 0.02	2.16 ± 0.45
1743.95 ± 0.18	^{143}Nd	1.50 ± 0.36	0.15 ± 0.02	3.18 ± 0.54
1788.29 ± 0.37	^{35}Cl	10.5 ± 3.9	0.06 ± 0.02	1.21 ± 0.37
1830.60 ± 0.31	^{35}Cl, ^{143}Nd	8.19 ± 2.45	0.11 ± 0.02	2.23 ± 0.45
1851.40 ± 0.19	^{142}Nd	3.57 ± 1.04	0.17 ± 0.02	3.72 ± 0.62
1885.01 ± 0.46[a]	^{143}Nd	3.22 ± 1.51	0.07 ± 0.02	1.52 ± 0.46
1894.91 ± 0.24	^{143}Nd	6.58 ± 1.65	0.15 ± 0.03	3.26 ± 0.60
1910.03 ± 0.23	^{143}Nd	4.70 ± 1.14	0.16 ± 0.02	3.53 ± 0.61

H.2.3 : (continued).

E_γ (keV)	Neutron capture interference		$P_{E\gamma}(90°)/$	$\langle\sigma^Z_{E\gamma}\rangle$ (mb)
	^AZ	P_{cap}/P_{net} (%)	$(\epsilon_{E\gamma} \times f_{E\gamma})$ $\times$ 10^{-8} (count)	
1935.52 ± 0.37	^{35}Cl	7.76 ± 2.40	0.07 ± 0.02	1.45 ± 0.33
2022.40 ± 0.39	^{35}Cl, ^{143}Nd	12.1 ± 4.1	0.06 ± 0.02	1.25 ± 0.39
2035.61 ± 0.35[a]	^{35}Cl, ^{143}Nd	15.0 ± 5.8	0.07 ± 0.01	1.38 ± 0.28
2073.11 ± 0.18[a]	^{35}Cl, ^{143}Nd	8.52 ± 2.97	0.20 ± 0.02	4.27 ± 0.53
2135.15 ± 0.21[c]	^{143}Nd	3.35 ± 0.69	0.14 ± 0.01	2.93 ± 0.35
2185.17 ± 0.23	^{143}Nd	2.98 ± 0.63	0.24 ± 0.02	5.20 ± 0.66
2845.33 ± 0.17	^{35}Cl	5.43 ± 1.31	0.22 ± 0.02	4.60 ± 0.54

E_γ is the γ-ray energy, $P_{E\gamma}(90°)/(\epsilon_{E\gamma} \times f_{E\gamma})$ the net counts in the γ-ray peak divided by the full-energy-peak (FEP) efficiency and the γ-ray self-absorption factor, ^AZ the isotopes of interfering (n,γ) reactions, P_{cap}/P_{net} the ratio of neutron capture counts to net counts and $\langle\sigma^Z_{E\gamma}\rangle$ is the neutron spectrum-averaged elemental partial cross section for γ-ray production at an angle of 90° between neutron beam and detector, calculated after Eq. (4.27)
[a]corrected for background interference
[b]corrected for contribution of DE from 2693 keV
[c]corrected for contribution of SE from 2645 keV

H.2.4 : Prompt γ-rays of Sm induced by (n,n'γ) and (n,γ) reactions.

E_γ (keV)	Neutron capture interference		$P_{E\gamma}(90°)/$	$\langle\sigma^Z_{E\gamma}\rangle$ (mb)
	^AZ	P_{cap}/P_{net} (%)	$(\epsilon_{E\gamma} \times f_{E\gamma})$ $\times$ 10^{-8} (count)	
121.56 ± 0.03[a]	^{150}Sm, ^{152}Sm, ^{154}Sm	4.16 ± 1.46	12.49 ± 0.39	343 ± 30
149.99 ± 0.06	^{150}Sm, ^{152}Sm	3.38 ± 0.81	0.32 ± 0.03	8.98 ± 1.05
222.54 ± 0.13	^{149}Sm, ^{152}Sm	37 ± 11	0.13 ± 0.02	3.18 ± 0.59
251.17 ± 0.09	^{149}Sm, ^{150}Sm	36 ± 7	0.24 ± 0.03	6.61 ± 0.91
254.31 ± 0.10[a]	^{149}Sm, ^{150}Sm, ^{152}Sm	32 ± 14	0.26 ± 0.04	6.64 ± 1.07
268.81 ± 0.12	^{149}Sm, ^{152}Sm	12.1 ± 3.2	0.16 ± 0.02	4.26 ± 0.67
276.65 ± 0.03[a]	^{150}Sm, ^{152}Sm	17.4 ± 5.6	2.10 ± 0.08	56 ± 5
280.44 ± 0.10	^{150}Sm	49 ± 13	0.25 ± 0.03	5.80 ± 0.82
285.43 ± 0.03	^{149}Sm, ^{150}Sm, ^{152}Sm, ^{154}Sm	3.57 ± 0.54	2.47 ± 0.08	70 ± 6
313.61 ± 0.10	^{150}Sm, ^{152}Sm	32 ± 8	0.32 ± 0.04	8.01 ± 1.29
333.37 ± 0.05	^{149}Sm, ^{150}Sm	40 ± 10	33.7 ± 1.0	967 ± 84
339.80 ± 0.05	^{150}Sm	8.02 ± 1.97	0.67 ± 0.04	18.5 ± 1.9
345.34 ± 0.10	^{149}Sm, ^{150}Sm	38 ± 10	0.33 ± 0.04	9.39 ± 1.41
402.74 ± 0.07	^{149}Sm, ^{150}Sm	15.1 ± 3.6	0.83 ± 0.05	24 ± 2
405.83 ± 0.06	^{149}Sm, ^{150}Sm, ^{152}Sm	20 ± 4	0.73 ± 0.05	20 ± 20
413.67 ± 0.05	^{147}Sm, ^{150}Sm, ^{152}Sm	77 ± 14	1.94 ± 0.08	39 ± 4
432.11 ± 0.10	^{147}Sm, ^{150}Sm	72 ± 19	0.40 ± 0.05	8.23 ± 1.15
438.68 ± 0.04	^{149}Sm, ^{150}Sm, ^{152}Sm, ^{154}Sm	50 ± 11	16.97 ± 0.51	482 ± 42
461.01 ± 0.11	^{149}Sm, ^{150}Sm	7.03 ± 1.67	0.41 ± 0.05	11.5 ± 1.7

H.2.4 : (continued).

E_γ (keV)	Neutron capture interference		$P_{E\gamma}(90°)/$ $(\epsilon_{E\gamma} \times f_{E\gamma})$ $\times 10^{-8}$ (count)	$\langle \sigma^Z_{E\gamma} \rangle$ (mb)
	^AZ	P_{cap}/P_{net} (%)		
485.40 ± 0.08	^{149}Sm	64 ± 16	0.31 ± 0.03	9.09 ± 1.21
504.90 ± 0.04	^{149}Sm	9.53 ± 2.29	2.13 ± 0.07	61 ± 5
549.60 ± 0.04	^{147}Sm, ^{149}Sm, ^{150}Sm, ^{154}Sm	62 ± 15	15.67 ± 0.48	341 ± 30
552.44 ± 0.08	^{152}Sm	1.77 ± 0.47	0.93 ± 0.06	26 ± 3
583.58 ± 0.04[a]	^{149}Sm, ^{152}Sm, ^{154}Sm	48 ± 14	2.96 ± 0.10	84 ± 7
590.21 ± 0.16	^{149}Sm	3.36 ± 0.81	0.28 ± 0.07	7.86 ± 2.02
610.66 ± 0.04	^{147}Sm	78 ± 19	2.98 ± 0.11	60 ± 5
636.22 ± 0.08	^{150}Sm	12.6 ± 3.3	0.28 ± 0.03	7.56 ± 0.97
663.43 ± 0.05[a]	^{150}Sm, ^{154}Sm	1.29 ± 0.21	0.90 ± 0.09	26 ± 3
666.05 ± 0.14[a]	^{149}Sm	3.13 ± 0.76	0.12 ± 0.02	3.29 ± 0.57
674.97 ± 0.05	^{149}Sm, ^{150}Sm	32 ± 8	1.50 ± 0.06	43 ± 4
687.89 ± 0.05	^{149}Sm	1.23 ± 0.30	0.70 ± 0.04	20.0 ± 1.9
711.70 ± 0.06	^{149}Sm	37 ± 9	2.00 ± 0.11	58 ± 6
715.86 ± 0.07	^{150}Sm	1.94 ± 0.48	2.50 ± 0.17	71 ± 8
725.57 ± 0.07	^{154}Sm	5.06 ± 1.15	0.43 ± 0.03	12.1 ± 1.3
730.99 ± 0.07	^{149}Sm	56 ± 14	0.27 ± 0.03	7.68 ± 0.96
736.92 ± 0.05	^{149}Sm, ^{150}Sm	42 ± 16	3.98 ± 0.13	114 ± 10
741.31 ± 0.10	^{154}Sm	1.68 ± 0.44	0.23 ± 0.03	6.41 ± 1.08
745.48 ± 0.06[a]	^{154}Sm	1.86 ± 0.62	0.45 ± 0.03	12.8 ± 1.4
747.61 ± 0.08[a]	^{149}Sm	57 ± 21	0.33 ± 0.04	9.47 ± 1.36
751.02 ± 0.11	^{152}Sm	16.9 ± 13.7	0.35 ± 0.03	9.36 ± 1.08
753.12 ± 0.15	^{150}Sm	5.20 ± 1.36	0.25 ± 0.03	6.87 ± 0.95
761.76 ± 0.15[a]	^{149}Sm	22 ± 8	0.14 ± 0.02	3.92 ± 0.68
791.36 ± 0.25	^{150}Sm	5.12 ± 1.83	0.10 ± 0.03	2.86 ± 0.80
854.85 ± 0.08	^{154}Sm	3.28 ± 0.75	0.36 ± 0.03	10.2 ± 1.2
859.45 ± 0.06	^{149}Sm	31 ± 7	0.80 ± 0.03	23 ± 2
869.40 ± 0.10	^{149}Sm	33 ± 9	0.99 ± 0.10	28 ± 4
910.48 ± 0.08[a]	^{149}Sm, ^{154}Sm	30 ± 16	0.43 ± 0.04	12.2 ± 1.6
914.47 ± 0.08[a]	^{154}Sm	8.42 ± 3.50	0.60 ± 0.04	16.6 ± 1.8
921.04 ± 0.08[a]	^{149}Sm	8.00 ± 2.54	0.87 ± 0.05	25 ± 3
937.32 ± 0.10	^{154}Sm	8.51 ± 2.05	0.28 ± 0.03	7.89 ± 1.08
947.71 ± 0.11	^{150}Sm	4.68 ± 1.19	0.29 ± 0.03	8.00 ± 1.00
951.93 ± 0.20	^{150}Sm	16.0 ± 5.3	0.11 ± 0.03	3.06 ± 0.76
968.30 ± 0.14	^{154}Sm	10.8 ± 2.6	0.23 ± 0.03	6.31 ± 0.89
995.84 ± 0.17[a]	^{149}Sm	30 ± 10	0.14 ± 0.02	3.98 ± 0.65
1016.73 ± 0.14	^{149}Sm	23 ± 6	0.52 ± 0.03	14.9 ± 1.6
1046.04 ± 0.09	^{149}Sm	14.4 ± 4.3	0.57 ± 0.06	16.2 ± 2.20
1048.71 ± 0.09	^{149}Sm	6.77 ± 1.64	0.78 ± 0.03	22 ± 2
1106.59 ± 0.09[a]	^{154}Sm	4.97 ± 1.52	0.42 ± 0.03	11.8 ± 1.3
1122.23 ± 0.14	^{149}Sm	43 ± 11	0.19 ± 0.02	5.54 ± 0.79
1152.59 ± 0.27	^{154}Sm	1.06 ± 0.33	0.15 ± 0.02	4.40 ± 71
1170.35 ± 0.08	^{149}Sm	42 ± 10	1.53 ± 0.06	44 ± 4
1177.31 ± 0.10[a]	^{149}Sm	33 ± 15	0.48 ± 0.03	13.7 ± 1.4
1193.52 ± 0.08	^{149}Sm	32 ± 8	0.91 ± 0.04	26 ± 2

H.2.4 : (continued).

E_γ (keV)	Neutron capture interference		$P_{E\gamma}(90°)/$ $(\epsilon_{E\gamma} \times f_{E\gamma})$ $\times$ 10^{-8} (count)	$\langle\sigma^Z_{E\gamma}\rangle$ (mb)
	^AZ	P_{cap}/P_{net} (%)		
1196.94 ± 0.09[a]	^{149}Sm	23 ± 8	0.34 ± 0.03	9.60 ± 1.10
1246.57 ± 0.17	^{149}Sm	53 ± 14	0.27 ± 0.04	7.74 ± 1.26
1308.80 ± 0.21	^{149}Sm, ^{154}Sm	34 ± 9	0.34 ± 0.04	9.80 ± 1.39
1323.85 ± 0.20	^{149}Sm	36 ± 9	0.59 ± 0.05	16.8 ± 2.0
1328.16 ± 0.33[a]	^{35}Cl, ^{154}Sm	3.30 ± 1.49	0.22 ± 0.03	6.27 ± 1.08
1344.48 ± 0.13	^{147}Sm, ^{154}Sm	42 ± 10	0.90 ± 0.05	22 ± 2
1486.18 ± 0.25[a]	^{149}Sm	39 ± 16	0.24 ± 0.03	6.94 ± 0.97

E_γ is the γ-ray energy, $P_{E\gamma}(90°)/(\epsilon_{E\gamma} \times f_{E\gamma})$ the net counts in the γ-ray peak divided by the full-energy-peak (FEP) efficiency and the γ-ray self-absorption factor, ^AZ the isotopes of interfering (n,γ) reactions, P_{cap}/P_{net} the ratio of neutron capture counts to net counts and $\langle\sigma^Z_{E\gamma}\rangle$ is the neutron spectrum-averaged elemental partial cross section for γ-ray production at an angle of 90° between neutron beam and detector, calculated after Eq. (4.28)
[a]corrected for background interference

H.2.5 : Prompt γ-rays of Tb induced by (n,n'γ) and (n,γ) reactions.

E_γ (keV)	Neutron capture interference		$P_{E\gamma}(90°)/$ $(\epsilon_{E\gamma} \times f_{E\gamma})$ $\times$ 10^{-8} (count)	$\langle\sigma^Z_{E\gamma}\rangle$ (mb)
	^AZ	P_{cap}/P_{net} (%)		
79.29 ± 0.07	^{159}Tb	7.76 ± 1.93	44 ± 6	398 ± 65
90.29 ± 0.08	^{159}Tb	28 ± 7	4.27 ± 0.45	35 ± 5
103.71 ± 0.03	^{159}Tb	3.65 ± 0.85	23.09 ± 0.73	189 ± 17
130.31 ± 0.07	^{159}Tb	53 ± 13	0.68 ± 0.06	5.52 ± 0.66
158.95 ± 0.05[a]	^{159}Tb	21 ± 7	2.95 ± 0.67	24 ± 6
183.06 ± 0.07	^{159}Tb	9.69 ± 2.36	4.17 ± 0.32	34 ± 4
184.48 ± 0.05[a]	^{159}Tb	12.5 ± 4.1	9.14 ± 2.06	75 ± 18
210.53 ± 0.04	^{159}Tb	11.7 ± 2.8	2.65 ± 0.12	22 ± 2
229.38 ± 0.05	^{159}Tb	11.4 ± 2.7	1.58 ±0.09	12.9 ± 1.3
237.00 ± 0.05	^{159}Tb	11.3 ± 2.6	1.59 ± 0.09	13.0 ± 1.3
247.67 ± 0.04	^{159}Tb	52 ± 12	3.23 ± 0.13	26 ± 2
269.31 ± 0.07	^{159}Tb	38 ± 9	1.50 ± 0.12	12.3 ± 1.5
273.30 ± 0.05[a]	^{159}Tb	14.0 ± 4.5	4.99 ± 1.12	41 ± 10
289.77 ± 0.09	^{159}Tb	16.6 ± 3.9	6.01 ± 0.20	49 ± 4
303.40 ± 0.09	^{159}Tb	49 ± 11	1.48 ± 0.14	12.1 ± 1.5
306.82 ± 0.11	^{159}Tb	30 ± 8	1.07 ± 0.16	8.69 ± 1.52
317.01 ± 0.05	^{159}Tb	30 ± 7	5.05 ± 0.30	41 ± 4
347.61 ± 0.03	^{159}Tb	2.21 ± 0.52	18.52 ± 0.57	151 ± 14

H.2.5 : (continued).

E_γ (keV)	Neutron capture interference		$P_{E\gamma}(90°)/$ $(\epsilon_{E\gamma} \times f_{E\gamma})$ $\times$ 10^{-8} (count)	$\langle\sigma^Z_{E\gamma}\rangle$ (mb)
	^AZ	P_{cap}/P_{net} (%)		
362.89 ± 0.07	^{159}Tb	3.70 ± 0.86	32.6 ± 1.0	266 ± 24
370.16 ± 0.03	^{159}Tb	4.40 ± 1.03	7.28 ± 0.27	59 ± 5
404.26 ± 0.21	^{159}Tb	11.4 ± 2.9	0.57 ± 0.14	4.65 ± 1.19
428.54 ± 0.09	^{159}Tb	33 ± 8	2.51 ± 0.14	20 ± 2
519.24 ± 0.06	^{159}Tb	18.6 ± 4.8	1.78 ± 0.20	14.5 ± 2.1
939.31 ± 0.11	^{35}Cl	9.42 ± 2.35	0.44 ± 0.05	4.05 ± 0.59
965.64 ± 0.16	^{159}Tb(d)	22 ± 6	0.29 ± 0.05	147 ± 29
1034.43 ± 0.12	^{35}Cl	1.66 ± 0.37	1.46 ± 0.07	13.5 ± 1.3
1114.82 ± 0.16[a]	^{159}Tb(d)	1.93 ± 0.66	0.71 ± 0.07	38 ± 5
1131.10 ± 0.12[a]	^{35}Cl	42 ± 14	0.36 ± 0.05	3.12 ± 0.53
1168.89 ± 0.09	^{35}Cl	4.34 ± 1.00	0.86 ± 0.06	7.91 ± 0.89
1178.78 ± 0.13	^{159}Tb(d)	4.94 ± 1.27	2.44 ± 0.29	92 ± 13
1276.05 ± 0.12	^{159}Tb(d)	1.69 ± 0.42	1.12 ± 0.10	53 ± 6
1374.50 ± 0.12	^{35}Cl	4.46 ± 1.03	0.57 ± 0.04	5.28 ± 0.59

E_γ is the γ-ray energy, $P_{E\gamma}(90°)/(\epsilon_{E\gamma}\times f_{E\gamma})$ the net counts in the γ-ray peak divided by the full-energy-peak (FEP) efficiency and the γ-ray self-absorption factor, ^AZ the isotopes of interfering (n,γ) reactions, P_{cap}/P_{net} the ratio of neutron capture counts to total counts and $\langle\sigma^Z_{E\gamma}\rangle$ is the neutron spectrum-averaged elemental partial cross section for γ-ray production at an angle of 90° between neutron beam and detector, calculated after Eq. (4.28)
[a]corrected for background interference

H.2.6 : Prompt γ-rays of Dy induced by (n,n'γ) and (n,γ) reactions.

E_γ (keV)	Neutron capture interference		$P_{E\gamma}(90°)/$ $(\epsilon_{E\gamma} \times f_{E\gamma})$ $\times$ 10^{-8} (count)	$\langle\sigma^Z_{E\gamma}\rangle$ (mb)
	^AZ	P_{cap}/P_{net} (%)		
80.61 ± 0.06	^{161}Dy	7.58 ± 2.31	7.62 ± 0.59	237 ± 27
93.78 ± 0.06	^{162}Dy	4.41 ± 1.45	0.64 ± 0.06	20 ± 3
148.65 ± 0.06	^{161}Dy	5.96 ± 1.81	0.53 ± 0.04	16.7 ± 1.8
157.00 ± 0.08	^{164}Dy	2.13 ± 0.76	0.36 ± 0.04	11.3 ± 1.5
168.74 ± 0.03[a]	^{162}Dy, ^{163}Dy	23.6 ± 8.9	6.91 ± 0.23	200 ± 18
177.39 ± 0.04	^{162}Dy, ^{164}Dy	30 ± 9	0.56 ± 0.03	15.6 ± 1.5
184.83 ± 0.03[a]	^{161}Dy, ^{162}Dy, ^{164}Dy	31 ± 9	10.3 ± 0.3	285 ± 25
207.86 ± 0.04	^{162}Dy	1.31 ± 0.41	1.08 ± 0.05	34 ± 3
211.68 ± 0.04	^{161}Dy, ^{162}Dy	12.0 ± 3.2	1.94 ± 0.13	59 ± 6
214.89 ± 0.03	^{163}Dy	35 ± 11	2.76 ± 0.10	76 ± 7
230.18 ± 0.13	^{162}Dy	1.46 ± 0.78	0.12 ± 0.02	3.72 ± 0.64

H.2.6 : (continued).

E_γ (keV)	Neutron capture interference		$P_{E\gamma}(90°)/$	$\langle\sigma^Z_{E\gamma}\rangle$ (mb)
	^AZ	P_{cap}/P_{net} (%)	$(\epsilon_{E\gamma} \times f_{E\gamma})$ $\times 10^{-8}$ (count)	
235.65 ± 0.10	^{161}Dy, ^{162}Dy	37 ± 11	0.14 ± 0.02	3.76 ± 0.70
247.31 ± 0.06	^{161}Dy, ^{162}Dy	21 ± 5	0.42 ± 0.03	11.3 ± 1.2
250.52 ± 0.03	^{162}Dy	37 ± 12	2.96 ± 0.09	80 ± 7
259.54 ± 0.04	^{161}Dy, ^{162}Dy	22 ± 5	2.50 ± 0.12	73 ± 7
262.75 ± 0.04[a]	^{162}Dy	5.15 ± 1.97	1.38 ± 0.09	44 ± 5
266.21 ± 0.13	^{162}Dy	61 ± 21	0.17 ± 0.03	4.01 ± 0.69
267.44 ± 0.14	^{162}Dy	92 ± 34	0.15 ± 0.03	2.94 ± 0.62
277.04 ± 0.04[a]	^{162}Dy, ^{163}Dy	43 ± 16	1.22 ± 0.06	32 ± 3
282.44 ± 0.03	^{161}Dy	25 ± 8	1.28 ± 0.05	37 ± 3
285.14 ± 0.04	^{162}Dy	13.6 ± 4.3	1.41 ± 0.07	43 ± 4
292.02 ± 0.11	^{35}Cl, ^{162}Dy	5.31 ± 1.65	0.22 ± 0.03	7.00 ± 1.11
294.21 ± 0.04	^{163}Dy	85 ± 26	1.11 ± 0.05	23 ± 2
305.71 ± 0.12	^{162}Dy	9.03 ± 3.38	0.11 ± 0.02	3.27 ± 0.73
310.72 ± 0.14	^{161}Dy, ^{162}Dy	85 ± 24	0.24 ± 0.04	4.97 ± 1.00
315.70 ± 0.06	^{162}Dy	83 ± 27	0.77 ± 0.06	15.9 ± 1.8
333.48 ± 0.04	^{161}Dy	27 ± 8	0.77 ± 0.04	22 ± 2
343.25 ± 0.25	^{162}Dy, ^{164}Dy	16.8 ± 6.2	0.13 ± 0.03	3.70 ± 0.96
347.00 ± 0.05	^{162}Dy	80 ± 25	0.65 ± 0.04	13.8 ± 1.4
350.55 ± 0.03[a]	^{162}Dy, ^{164}Dy	88 ± 33	2.71 ± 0.10	51 ± 5
353.67 ± 0.04	^{162}Dy, ^{164}Dy	54 ± 18	1.45 ± 0.07	36 ± 3
371.16 ± 0.22	^{162}Dy	50 ± 17	0.38 ± 0.06	9.57 ± 1.61
385.32 ± 0.07	^{162}Dy, ^{164}Dy	65 ± 22	0.70 ± 0.06	15.7 ± 1.9
389.06 ± 0.04	^{162}Dy	65 ± 21	2.52 ± 0.19	59 ± 7
401.31 ± 0.05	^{162}Dy	35 ± 11	0.94 ± 0.05	26 ± 3
406.94 ± 0.13	^{162}Dy	7.76 ± 1.93	0.23 ± 0.05	6.42 ± 1.38
414.42 ± 0.07	^{162}Dy, ^{164}Dy	76 ± 25	0.65 ± 0.05	13.6 ± 1.6
421.08 ± 0.05	^{162}Dy, ^{164}Dy	68 ± 22	2.29 ± 0.12	52 ± 5
427.00 ± 0.04	^{161}Dy, ^{162}Dy	49 ± 15	0.94 ± 0.06	24 ± 2
435.60 ± 0.17	^{35}Cl, ^{162}Dy	7.51 ± 2.53	0.10 ± 0.03	3.03 ± 0.85
440.45 ± 0.05	^{161}Dy, ^{162}Dy	31 ± 10	0.48 ± 0.03	13.4 ± 1.4
461.59 ± 0.05	^{162}Dy	17.9 ± 5.8	0.23 ± 0.02	6.82 ± 0.80
464.94 ± 0.06	^{164}Dy	70 ± 24	0.28 ± 0.02	5.54 ± 0.55
474.72 ± 0.04	^{161}Dy, ^{162}Dy, ^{164}Dy	42 ± 11	0.99 ± 0.04	26 ± 2
478.73 ± 0.04	^{164}Dy	46 ± 16	0.41 ± 0.02	9.88 ± 0.96
528.71 ± 0.24	^{162}Dy, ^{164}Dy	42 ± 14	0.11 ± 0.03	2.92 ± 0.83
532.33 ± 0.08[a]	^{162}Dy	23 ± 9	0.22 ± 0.03	6.36 ± 0.90
548.18 ± 0.09	^{164}Dy	9.50 ± 3.42	0.20 ± 0.02	6.12 ± 0.87
552.32 ± 0.13	^{162}Dy	15.6 ± 5.6	0.11 ± 0.02	3.18 ± 0.61
556.11 ± 0.16	^{164}Dy	13.7 ± 5.6	0.08 ± 0.02	2.48 ± 0.59
558.85 ± 0.10	^{162}Dy	57 ± 20	0.12 ± 0.02	3.01 ± 0.56

H.2.6 : (continued).

E_γ (keV)	Neutron capture interference		$P_{E\gamma}(90°)/$	$\langle\sigma^Z_{E\gamma}\rangle$ (mb)
	^AZ	P_{cap}/P_{net} (%)	$(\epsilon_{E\gamma} \times f_{E\gamma})$ $\times 10^{-8}$ (count)	
565.27 ± 0.10	^{162}Dy, ^{164}Dy	12.5 ± 4.1	0.22 ± 0.04	6.62 ± 1.21
572.25 ± 0.15	^{161}Dy, ^{162}Dy	62 ±15	0.29 ± 0.04	6.93 ± 1.08
585.24 ± 0.05	^{162}Dy, ^{164}Dy	35 ± 8	0.76 ± 0.05	20 ± 2
607.85 ± 0.11[a]	^{162}Dy	39 ± 16	0.36 ± 0.08	9.72 ± 2.22
610.57 ± 0.11	^{162}Dy	1.56 ± 0.52	0.50 ± 0.06	16.1 ± 2.2
633.30 ± 0.13	^{35}Cl, ^{161}Dy, ^{162}Dy	27 ± 6	0.33 ± 0.04	9.41 ± 1.28
637.32 ± 0.19	^{162}Dy	51 ± 19	0.15 ± 0.03	3.84 ± 0.93
646.86 ± 0.04	^{161}Dy	6.07 ± 1.82	0.40 ± 0.02	12.6 ± 1.2
673.12 ± 0.04	^{162}Dy, ^{163}Dy	42 ± 16	1.36 ± 0.05	36 ± 3
687.83 ± 0.04	^{163}Dy	41 ± 13	3.61 ± 0.17	96 ± 9
696.58 ± 0.09	^{161}Dy, ^{162}Dy	25 ± 7	0.63 ± 0.07	18.2 ± 2.4
710.90 ± 0.10	^{161}Dy, ^{162}Dy	64 ± 16	0.34 ± 0.04	7.95 ± 1.09
726.84 ± 0.19[a]	^{162}Dy	28 ± 12	0.27 ± 0.03	7.54 ± 1.09
754.31 ± 0.04	^{162}Dy, ^{163}Dy	50 ± 15	4.07 ± 0.13	104 ± 9
761.34 ± 0.04	^{163}Dy	40 ± 12	3.25 ± 0.11	87 ± 8
770.44 ± 0.10[a]	^{162}Dy	52 ± 22	0.20 ± 0.02	4.89 ± 0.66
781.89 ± 0.05	^{162}Dy	2.13 ± 0.67	0.77 ± 0.04	25 ± 2
794.86 ± 0.05	^{161}Dy, ^{162}Dy	37 ± 9	1.04 ± 0.05	28 ± 3
807.13 ± 0.04[a]	^{161}Dy, ^{162}Dy	26 ± 9	2.81 ± 0.11	81 ± 7
842.65 ± 0.06[a]	^{161}Dy, ^{162}Dy	28 ± 9	0.59 ± 0.06	16.9 ± 2.2
878.70 ± 0.16	^{161}Dy, ^{162}Dy	35 ± 10	0.19 ± 0.04	5.35 ± 1.12
881.93 ± 0.05[a]	^{161}Dy, ^{162}Dy	27 ± 9	3.17 ± 0.11	91 ± 8
887.82 ± 0.05	^{161}Dy	19.5 ± 5.8	2.34 ± 0.08	69 ± 6
916.72 ± 0.05[a]	^{161}Dy, ^{162}Dy	37 ± 15	0.79 ± 0.04	21 ± 2
944.16 ± 0.06	^{161}Dy	57 ± 17	0.55 ± 0.03	13.4 ± 1.3
980.10 ± 0.06[a]	^{161}Dy	58 ± 22	0.64 ± 0.03	15.5 ± 1.5
1001.84 ± 0.21	^{162}Dy	47 ± 16	0.25 ± 0.04	6.32 ± 1.16
1021.83 ± 0.14[a]	^{161}Dy	44 ± 21	0.08 ± 0.02	2.12 ± 0.51
1072.07 ± 0.26	^{162}Dy	16.2 ± 5.9	0.13 ± 0.02	3.89 ± 0.78
1091.96 ± 0.07	^{161}Dy	24 ± 7	0.49 ± 0.03	14.3 ± 1.4
1124.63 ± 0.08[a]	^{161}Dy	58 ± 25	0.30 ± 0.02	7.33 ± 0.82
1129.24 ± 0.06[a]	^{35}Cl, ^{161}Dy	30 ± 11	0.87 ± 0.05	24 ± 2
1187.61 ± 0.12	^{161}Dy, ^{162}Dy	40 ± 11	0.21 ± 0.02	5.57 ± 0.76
1195.16 ± 0.11	^{161}Dy, ^{162}Dy	24 ± 6	0.83 ± 0.04	24 ± 2
1252.59 ± 0.19[b]	^{162}Dy	7.76 ± 1.93	0.22 ± 0.02	6.89 ± 0.83
1276.50 ± 0.07	^{161}Dy, ^{162}Dy	28 ± 7	1.32 ± 0.06	37 ± 3
1308.61 ± 0.17	^{161}Dy	28 ± 9	0.26 ± 0.03	7.40 ± 1.10
1372.35 ± 0.11	^{161}Dy	23 ± 7	0.47 ± 0.03	13.6 ± 1.40
1412.18 ± 0.22[a]	^{164}Dy	30 ± 15	0.08 ± 0.02	2.07 ± 0.47
1528.90 ± 0.34	^{162}Dy	42 ± 15	0.13 ± 0.02	3.37 ± 0.67

H.2.6 : (continued).

E_γ (keV)	Neutron capture interference		$P_{E\gamma}(90°)/$	$\langle\sigma^Z_{E\gamma}\rangle$ (mb)
	^AZ	P_{cap}/P_{net} (%)	$(\epsilon_{E\gamma} \times f_{E\gamma})$ $\times$ 10^{-8} (count)	
1600.88 ± 0.13[a]	^{35}Cl, ^{162}Dy	11.2 ±3.7	0.31 ± 0.03	9.21 ± 1.21
1648.06 ± 0.16	^{35}Cl, ^{164}Dy	5.38 ± 1.59	0.26 ± 0.02	8.07 ± 0.98
1674.35 ± 0.29[a]	^{164}Dy	15.3 ± 6.9	0.12 ± 0.02	3.57 ± 0.76
1722.69 ± 0.22	^{164}Dy	4.08 ± 1.46	0.40 ± 0.04	12.7 ± 1.7
1735.98 ± 0.15	^{164}Dy	5.89 ± 2.11	0.33 ± 0.04	10.3 ± 1.4
1836.16 ± 0.20	^{164}Dy	12.7 ± 4.8	0.13 ± 0.02	3.87 ± 0.68
2020.85 ± 0.21	^{35}Cl, ^{164}Dy	23 ± 9	0.07 ± 0.01	1.82 ± 0.44
2241.54 ± 0.36	^{164}Dy	29 ± 13	0.06 ± 0.02	1.62 ± 0.51

E_γ is the γ-ray energy, $P_{E\gamma}(90°)/(\epsilon_{E\gamma} \times f_{E\gamma})$ the net counts in the γ-ray peak divided by the full-energy-peak (FEP) efficiency and the γ-ray self-absorption factor, ^AZ the isotopes of interfering (n,γ) reactions, P_{cap}/P_{net} the ratio of neutron capture counts to net counts and $\langle\sigma^Z_{E\gamma}\rangle$ is the neutron spectrum-averaged elemental partial cross section for γ-ray production at an angle of 90° between neutron beam and detector, calculated after Eq. (4.28)

[a]corrected for background interference

[b]corrected for contribution of SE from 1763 keV

I. HPGe detector data sheet

QUALITY ASSURANCE DATA SHEET

GMX Series HPGe (High-Purity Germanium) Coaxial Detector System

Model and Serial Numbers

Detector Model No.	GMX50P4-83-CW-PL		
Cryostat Configuration	CFG-X-COOL-III-230	Ship Date	29-May-14
Dewar Model	No Dewar	Serial No.	53-TN42454A
Preamplifier Model	A232N	When calling Customer Service, always	
Preamplifier Serial No.	13241589	reference the Detector Serial No.	
H. V. Filter Model	138EMI	Sales Order No.	95002117
H. V. Filter Serial No.	13142811		
SMART-1-N Serial No.			

Cryogenic Information

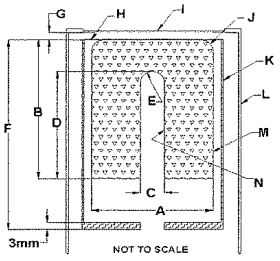
Dewar Capacity	0	Static Holding Time	
Detector Cool-Down Time			

High Voltage Bias

Recommended Operating Bias: NEGATIVE 4000 Volts

Performance Specifications*

	Warranted	Measured	Amp Shape Time
Resolution (FWHM) at 1.33 MeV, ^{60}Co	2.2 keV	1.99 keV	6 µs
Peak-to-Compton Ratio, ^{60}Co	58:1	68:1	6 µs
Relative Efficiency at 1.33 MeV, ^{60}Co	50 %	56.9 %	6 µs
Peak Shape (FWTM/FWHM), ^{60}Co	2.0	2.0	6 µs
*Peak Shape (FWFM/FWHM), ^{60}Co	3.0	2.8	6 µs
*FWFM/FWHM is typical not warranted			
Resolution (FWHM) at 5.9 KeV, ^{55}Fe	N/A eV	N/A eV	µs



E: NOMINAL 5-mm RADIUS

F: 105-mm CUP LENGTH

G: 4-mm SPACE

H: 0.03-mm/0.03-mm Al/Mylar

I: 0.9-mm CARBON FIBER

J: NOMINAL 8-mm RADIUS

K: 0.8-mm Al

L: 1-mm Al

M: 0.3-micron Ge/B DEAD LAYER

N: 700-micron Ge/Li DEAD LAYER

A= 63.9 mm — Crystal Diameter

B= 85.1 mm — Crystal Length

C= 10.2 mm — Hole Diameter

D= 77.1 mm — Hole Depth

OTHER Capsule: NOCA # 11264
Cryo: X-COOL-III-230 # 130503ER

Data Certified By: [signature] DATE 5-28-14

Form no. 0308BK vers. 1

I.1 : Quality assurance data sheet of the ORTEC HPGe detector.

J. Gamma-ray efficiency parametrization

J.1 : Fit coefficients a_0 to a_8 for the experimental full-energy-peak (FEP) efficiency curve depcited in Fig. 5.9 and according to Eq. (5.1).

Fit coefficient	Value
a_0	-1.4342960720028 $\times$ 10^{2}
a_1	1.5658642376457 $\times$ 10^{2}
a_2	-8.0909929841862 $\times$ 10^{1}
a_3	2.4221420178659 $\times$ 10^{1}
a_4	-4.5262516996129
a_5	5.3279317449508 $\times$ 10^{-1}
a_6	-3.8180319039540 $\times$ 10^{-2}
a_7	1.5118234519668 $\times$ 10^{-3}
a_8	-2.5205921253835 $\times$ 10^{-5}

J.2 : Fit coefficients $b_{0,i}$ and $b_{1,i}$ of Eq. (7.4) for all parameters a_0 to a_8 from Eq. (5.1) for the filter material BPE with 20 wt% B_2O_3.

Parameter	Fit coefficients	
	$b_{0,i}$	$b_{1,i}$
a_0	-1.4351024000355 $\times$ 10^{2}	-2.7369812708627 $\times$ 10^{1}
a_1	1.5669228468099 $\times$ 10^{2}	3.3293259700811 $\times$ 10^{1}
a_2	-8.0970045336266 $\times$ 10^{1}	-1.7743613719418 $\times$ 10^{1}
a_3	2.4240708656451 $\times$ 10^{1}	5.3599888994593
a_4	-4.5300769920690	-1.0028417641902
a_5	5.3327344442030 $\times$ 10^{-1}	1.1906014362010 $\times$ 10^{-1}
a_6	-3.8217607800200 $\times$ 10^{-2}	-8.7630821960000 $\times$ 10^{-3}
a_7	1.5134608595000$\times$ 10^{-3}	3.6567017970000 $\times$ 10^{-4}
a_8	-2.5237065800000 $\times$ 10^{-5}	-6.6243788000000 $\times$ 10^{-6}

J.3 : Fit coefficients $b_{0,i}$ and $b_{1,i}$ of Eq. (7.4) for all parameters a_0 to a_8 from Eq. (5.1) for the filter material BPE with 20 wt% B_4C.

Parameter	Fit coefficients	
	$b_{0,i}$	$b_{1,i}$
a_0	-1.4347041538694 $\times 10^{2}$	-2.4779713921416 $\times 10^{1}$
a_1	1.5664025849446 $\times 10^{2}$	3.04332243071121 $\times 10^{1}$
a_2	-8.094069880546 $\times 10^{1}$	-1.6372473038800 $\times 10^{1}$
a_3	2.4231324994738 $\times 10^{1}$	4.9877956063844
a_4	-4.5282255711297	-9.4033296857300 $\times 10^{-1}$
a_5	5.33042190128700 $\times 10^{-1}$	1.1241476520230 $\times 10^{-1}$
a_6	-3.8199744758700 $\times 10^{-2}$	-8.3268079662000 $\times 10^{-3}$
a_7	1.5126804424000$\times 10^{-3}$	3.4952002620000 $\times 10^{-4}$
a_8	-2.5222296000000 $\times 10^{-5}$	-6.3667171000000 $\times 10^{-6}$

J.4 : Fit coefficients $b_{0,i}$ and $b_{1,i}$ of Eq. (7.4) for all parameters a_0 to a_8 from Eq. (5.1) for the filter material B_4C.

Parameter	Fit coefficients	
	$b_{0,i}$	$b_{1,i}$
a_0	-1.4349058060474 $\times 10^{2}$	-4.6323406537571 $\times 10^{1}$
a_1	1.5666638292073 $\times 10^{2}$	5.6718538944284 $\times 10^{1}$
a_2	-8.0955284178892 $\times 10^{1}$	-3.0461682208985 $\times 10^{1}$
a_3	2.4235952249240 $\times 10^{1}$	9.2637683164322
a_4	-4.5291310830582	-1.7431350835365
a_5	5.3315427657190 $\times 10^{-1}$	2.0797644625020 $\times 10^{-1}$
a_6	-3.820832440900 $\times 10^{-2}$	-1.5374745737500 $\times 10^{-2}$
a_7	1.5130518893000 $\times 10^{-3}$	6.4408348030000 $\times 10^{-4}$
a_8	-2.5229262500000 $\times 10^{-5}$	-1.1709066100000 $\times 10^{-5}$

K. MCNP6 input files

K.1: Single and double escape peak MCNP6 simulation of the HPGe crystal of FaNGaS.

```
-------------------------------------------------------------------------------
Escape peak correction simulation for the HPGe crystal of FaNGaS
c Cell cards
1     1 -5.323  (+2 -4 +10 -15) : (+24 -17 +14 -3)  : (-25) $Ge crystal
2     2 -2.929  #1 (+1 -2 +10 -14) : (+14 +23 -24) $700-micron Ge/Li dead layer
3     3 -3.892 #1 #2 (+4 -5 +10 -15) : (-26 +25 -17 +15 #1 #2) $0.3-micron Ge/B
4     4 -2.700  #1 #2 #3 (11 -16 +6 -7) : (+1 -7 +12 -11) &
: (-7 +17 -18) $Inner Al housing
5     4 -2.700 #1 #2 #3 #4 (8 -9 13 -19) : (7 -9 19 -21) $Outer Al housing
```

```
6     5 -1.380 #1 #2 #3 #4 #5 (-7 17 -18) $0.03 mm mylar
7     6 -2.267 #1 #2 #3 #4 #5 #6 -7 19 -20 $Carbon fiber
8     7 -8.960 #1 #2 #3 #4 #5 #6 #7 +10 -15 -1 $Copper cold finger
9     0 -22 #1 #2 #3 #4 #5 #6 #7 #8 $Confining sphere
10    0 +22 $Black hole region outside
c End of cell cards

c Surface cards
c Cylinders
1 CZ 0.51 $Inner diameter Ge cyl (hole) with Ge/Li dead layer
2 CZ 0.58 $700-micron Ge/Li dead layer
3 CZ 2.39497 $Cylinder up to center of curvature tori
4 CZ 3.19497 $Outer diameter Ge cyl without dead layer
5 CZ 3.195 $0.3-micron Ge/B dead layer
6 CZ 3.4 $0.8 mm inner Al housing
7 CZ 3.48 $0.8 mm inner Al housing
8 CZ 4.0 $1.0 mm inner Al housing
9 CZ 4.1 $1.0 mm outer Al housing
c End of cylinders
c Planes
c Below Origin (=half crystal length)
10 PZ -4.255 $Lower Ge crystal plane
11 PZ -5.945 $3 mm Al bottom, inner housing
12 PZ -6.245 $3 mm Al bottom, inner housing
13 PZ -7.0 $Lower ending of outer Al housing
c Above origin
14 PZ 2.895 $Center of spheres # 23 and 24 for inner curvature
15 PZ 3.455 $Lower Ge crystal hole plane in contact with Cu cold finger
16 PZ 4.255 $Upper Ge crystal plane, backside plane
17 PZ 4.258 $0.03 mm Al
18 PZ 4.261 $0.03 mm mylar
19 PZ 4.295 $Lower front of outer Al housing, 4 mm gap
20 PZ 4.385 $0.9 mm carbon fiber
21 PZ 4.395 $1 mm Al housing
c End of planes
c Spheres
22 SPH 0.0   0.0    0.0    20.0 $Confining sphere
23 SPH 0.0   0.0    2.895  0.51 $Nom. radius
24 SPH 0.0   0.0    2.895  0.58 $Nom. radius
c End of spheres
c Tori
25 TZ 0 0 3.455 2.39497 0.80 0.80  $8 mm nom. radius edge, torus
26 TZ 0 0 3.455 2.39497 0.80003 0.80003 $Radius with Ge/B dead layer
c End of tori
c End of surface cards

c Source and physics definition
MPHYS ON
MODE P
```

```
IMP:P 1 1 1 1 1 1 1 1 0
PHYS:P 10 0 0 0 0 J 0
CUT:P J 0.001 $Photon transport cutoff 1 keV, default
c Circular disk source of discrete energies and homogeneous radial distribution
SDEF ERG=d1 POS=0 0 7.1 AXS=0 0 1 EXT=0 RAD=d2 PAR=2 VEC=0 0 -1 DIR=1
SI1 L 1.1 1.3 1.5 1.8 2.3 2.8 3.5 4.0 5.0 6.0 7.0 8.0
SP1 1 1 1 1 1 1 1 1 1 1 1
SI2 -3.195 3.195 $Full coverage of Ge crystal, including dead layer
SP2 0 1
c Tallies
F8:P 1
E8 1E-03 8000i 8.0 $ ~ 1 keV intervals
c End of tallies
c Material cards
M1 32070 0.2050 32072 0.2740 32073 0.0780 32074 0.3650 32076 0.0744 $Ge crystal
M2 32070 0.2050 32072 0.2740 32073 0.0780 32074 0.3650 32076 0.0744 &
3006 0.0740 3007 0.9260 $Ge/Li dead layer, 50-50 ratio
M3 32070 0.2050 32072 0.2740 32073 0.0780 32074 0.3650 32076 0.0744 &
5010 0.1990 5011 0.8010 $Ge/B dead layer, 50-50 ratio
M4 13027 1.00 $Al
M5 6012 9.8900 6013 0.1100 1001 7.9991 1002 0.0092 8016 3.9905 &
8017 0.0015 8018 0.0080 $Mylar, (C10H8O4)n
M6 6012 0.9890 6013 0.0110 $Carbon fiber, ~ C
M7 29063 0.6917 29065 0.3083 $Cu
PRINT 110 $Print of first 50 starting histories
NPS 1E08
```

K.2: Integral ($10^{-10} \leq E_n \leq 20$ MeV) MCNP6 simulation of the neutron moderation in a $TbCl_3{\cdot}6H_2O$ sample.

```
MCNP6 simulation of neutron moderation influence of water in TbCl3·6H2O
c Cell cards
1     1 -4.35  -2 -1 3 4 $Sample
2     0        -2  3 4 1 $Confining sphere
3     0        -2 -3 1 4 $Reference volume 1
4     0        -2 -4 1 3 $Reference volume 2
5     0        2 $Outer world
c End of cell cards

c Surface cards
1 1 RPP -0.443 0.443 -0.443 0.443 -0.30 0.30 $Sample
2 SPH 0.0 0.0 0.0 10.0 $Confining sphere
3 2 RPP -0.433 0.433 -0.443 0.443 -0.30 0.30 $Reference volume 1
4   RPP -0.525 0.525 -0.443 0.443 -9.5 -9.49 $Reference volume 2
c End of surface cards

c Transformations
*TR1 0 0 0 45 90 90 90 0 90 45 90 90 1 $45° rotation around Y-axis
*TR2 0 0 -8.5 45 90 90 90 0 90 45 90 90 1 $45° rotation around Y-axis
```

```
c Source and physics definition
MPHYS ON
IMP:N 1 1 1 1 0
VOL 0.4709976 4187.857513 0.4709976 0.009303
AREA 3.696392 0.5316 0.5316 0.5316 0.5316 0.784996 0.784996 1256.637061 &
3.696392 0.5316 0.5316 0.5316 0.5316 0.784996 0.784996 1.89932 0.00886 0.00886 &
0.0105 0.0105 0.9303 0.9303
SDEF ERG=d1 POS=0 0 -9.80 PAR=1 VEC=0 0 1 DIR=1 X=d2 Y=d3 Z=-9.80
c FaNGaS energy bin structure with rel. probabilities
SI1 H 1.00E-10 1.00E-09 1.00E-08 2.30E-08 5.00E-08 7.60E-08 1.15E-07 1.70E-07 &
2.55E-07 3.80E-07 5.50E-07 8.40E-07 1.28E-06 1.90E-06 2.80E-06 4.25E-06    &
6.30E-06 9.20E-06 1.35E-05 2.10E-05 3.00E-05 4.50E-05 6.90E-05 1.00E-04    &
1.35E-04 1.70E-04 2.20E-04 2.80E-04 3.60E-04 4.50E-04 5.75E-04 7.60E-04    &
9.60E-04 1.28E-03 1.60E-03 2.00E-03 2.70E-03 3.40E-03 4.50E-03 5.50E-03    &
7.20E-03 9.20E-03 1.20E-02 1.50E-02 1.90E-02 2.55E-02 3.20E-02 4.00E-02    &
5.25E-02 6.60E-02 8.80E-02 1.10E-01 1.35E-01 1.60E-01 1.90E-01 2.20E-01    &
2.55E-01 2.90E-01 3.20E-01 3.60E-01 4.00E-01 4.50E-01 5.00E-01 5.50E-01    &
6.00E-01 6.60E-01 7.20E-01 7.80E-01 8.40E-01 9.20E-01 1.00E+00 1.20E+00    &
1.40E+00 1.60E+00 1.80E+00 2.00E+00 2.30E+00 2.60E+00 2.90E+00 3.30E+00    &
3.70E+00 4.10E+00 4.50E+00 5.00E+00 5.50E+00 6.00E+00 6.70E+00 7.40E+00    &
8.20E+00 9.00E+00 1.00E+01 1.10E+01 1.20E+01 1.30E+01 1.40E+01 1.50E+01    &
1.60E+01 1.70E+01 1.80E+01 1.90E+01 2.00E+01
SP1 0.00 4.2134E-09 3.4751E-07 1.0893E-06 2.2583E-06 1.3691E-06 1.0482E-06 &
5.3890E-07 3.1254E-07 1.0709E-06 3.7909E-06 1.2540E-05 2.5914E-05 4.7021E-05 &
8.5940E-05 1.2884E-04 1.5494E-04 2.0627E-04 2.2112E-04 2.5948E-04 2.1181E-04 &
2.2834E-04 3.2596E-04 3.5553E-04 2.8660E-04 2.0617E-04 2.7708E-04 3.2165E-04 &
3.2792E-04 2.6779E-04 3.3741E-04 4.0676E-04 3.3425E-04 3.9463E-04 2.4053E-04 &
2.4575E-04 3.8613E-04 2.7457E-04 2.8326E-04 2.2877E-04 3.4218E-04 3.3067E-04 &
3.8322E-04 3.1262E-04 3.6343E-04 5.4460E-04 4.8447E-04 6.1985E-04 1.1497E-03 &
1.4382E-03 3.1949E-03 3.3908E-03 3.7743E-03 3.6428E-03 4.7283E-03 5.3504E-03 &
6.2503E-03 5.7304E-03 4.8742E-03 7.1728E-03 7.8965E-03 1.0582E-02 1.1695E-02 &
1.3255E-02 1.4664E-02 1.8794E-02 1.9531E-02 2.0076E-02 2.1340E-02 3.0896E-02 &
3.0821E-02 6.4030E-02 5.2591E-02 5.2716E-02 5.4704E-02 5.4341E-02 7.7078E-02 &
6.9182E-02 5.9467E-02 6.4110E-02 4.8716E-02 3.5868E-02 2.5879E-02 2.2706E-02 &
1.5580E-02 1.0985E-02 1.0657E-02 7.0640E-02 5.2627E-02 3.2948E-03 2.4239E-03 &
1.2897E-03 6.6527E-04 3.3640E-04 1.6787E-04 8.3254E-05 4.1281E-05 2.0552E-05 &
1.0292E-05 4.8811E-06 1.4467E-06
SI2 -0.525 0.525
SP2 0 1
SI3 -0.443 0.443
SP3 0 1
c Tallies
F11:N 4.6
E11 1.00E-10 1.00E-09 1.00E-08 2.30E-08 5.00E-08 7.60E-08 1.15E-07 1.70E-07 &
2.55E-07 3.80E-07 5.50E-07 8.40E-07 1.28E-06 1.90E-06 2.80E-06 4.25E-06    &
6.30E-06 9.20E-06 1.35E-05 2.10E-05 3.00E-05 4.50E-05 6.90E-05 1.00E-04    &
1.35E-04 1.70E-04 2.20E-04 2.80E-04 3.60E-04 4.50E-04 5.75E-04 7.60E-04    &
9.60E-04 1.28E-03 1.60E-03 2.00E-03 2.70E-03 3.40E-03 4.50E-03 5.50E-03    &
7.20E-03 9.20E-03 1.20E-02 1.50E-02 1.90E-02 2.55E-02 3.20E-02 4.00E-02    &
```

```
5.25E-02 6.60E-02 8.80E-02 1.10E-01 1.35E-01 1.60E-01 1.90E-01 2.20E-01    &
2.55E-01 2.90E-01 3.20E-01 3.60E-01 4.00E-01 4.50E-01 5.00E-01 5.50E-01    &
6.00E-01 6.60E-01 7.20E-01 7.80E-01 8.40E-01 9.20E-01 1.00E+00 1.20E+00    &
1.40E+00 1.60E+00 1.80E+00 2.00E+00 2.30E+00 2.60E+00 2.90E+00 3.30E+00    &
3.70E+00 4.10E+00 4.50E+00 5.00E+00 5.50E+00 6.00E+00 6.70E+00 7.40E+00    &
8.20E+00 9.00E+00 1.00E+01 1.10E+01 1.20E+01 1.30E+01 1.40E+01 1.50E+01    &
1.60E+01 1.70E+01 1.80E+01 1.90E+01 2.00E+01
FT11 TAG 1
FU11 -1
F21:N 2
E21 1.00E-10 1.00E-09 1.00E-08 2.30E-08 5.00E-08 7.60E-08 1.15E-07 1.70E-07 &
2.55E-07 3.80E-07 5.50E-07 8.40E-07 1.28E-06 1.90E-06 2.80E-06 4.25E-06    &
6.30E-06 9.20E-06 1.35E-05 2.10E-05 3.00E-05 4.50E-05 6.90E-05 1.00E-04    &
1.35E-04 1.70E-04 2.20E-04 2.80E-04 3.60E-04 4.50E-04 5.75E-04 7.60E-04    &
9.60E-04 1.28E-03 1.60E-03 2.00E-03 2.70E-03 3.40E-03 4.50E-03 5.50E-03    &
7.20E-03 9.20E-03 1.20E-02 1.50E-02 1.90E-02 2.55E-02 3.20E-02 4.00E-02    &
5.25E-02 6.60E-02 8.80E-02 1.10E-01 1.35E-01 1.60E-01 1.90E-01 2.20E-01    &
2.55E-01 2.90E-01 3.20E-01 3.60E-01 4.00E-01 4.50E-01 5.00E-01 5.50E-01    &
6.00E-01 6.60E-01 7.20E-01 7.80E-01 8.40E-01 9.20E-01 1.00E+00 1.20E+00    &
1.40E+00 1.60E+00 1.80E+00 2.00E+00 2.30E+00 2.60E+00 2.90E+00 3.30E+00    &
3.70E+00 4.10E+00 4.50E+00 5.00E+00 5.50E+00 6.00E+00 6.70E+00 7.40E+00    &
8.20E+00 9.00E+00 1.00E+01 1.10E+01 1.20E+01 1.30E+01 1.40E+01 1.50E+01    &
1.60E+01 1.70E+01 1.80E+01 1.90E+01 2.00E+01
F12:N 4.6
E12 1.00E-10 1.00E-09 1.00E-08 2.30E-08 5.00E-08 7.60E-08 1.15E-07 1.70E-07 &
2.55E-07 3.80E-07 5.50E-07 8.40E-07 1.28E-06 1.90E-06 2.80E-06 4.25E-06    &
6.30E-06 9.20E-06 1.35E-05 2.10E-05 3.00E-05 4.50E-05 6.90E-05 1.00E-04    &
1.35E-04 1.70E-04 2.20E-04 2.80E-04 3.60E-04 4.50E-04 5.75E-04 7.60E-04    &
9.60E-04 1.28E-03 1.60E-03 2.00E-03 2.70E-03 3.40E-03 4.50E-03 5.50E-03    &
7.20E-03 9.20E-03 1.20E-02 1.50E-02 1.90E-02 2.55E-02 3.20E-02 4.00E-02    &
5.25E-02 6.60E-02 8.80E-02 1.10E-01 1.35E-01 1.60E-01 1.90E-01 2.20E-01    &
2.55E-01 2.90E-01 3.20E-01 3.60E-01 4.00E-01 4.50E-01 5.00E-01 5.50E-01    &
6.00E-01 6.60E-01 7.20E-01 7.80E-01 8.40E-01 9.20E-01 1.00E+00 1.20E+00    &
1.40E+00 1.60E+00 1.80E+00 2.00E+00 2.30E+00 2.60E+00 2.90E+00 3.30E+00    &
3.70E+00 4.10E+00 4.50E+00 5.00E+00 5.50E+00 6.00E+00 6.70E+00 7.40E+00    &
8.20E+00 9.00E+00 1.00E+01 1.10E+01 1.20E+01 1.30E+01 1.40E+01 1.50E+01    &
1.60E+01 1.70E+01 1.80E+01 1.90E+01 2.00E+01
FT12 TAG 1
FU12 -1
F22:N 2
E22 1.00E-10 1.00E-09 1.00E-08 2.30E-08 5.00E-08 7.60E-08 1.15E-07 1.70E-07 &
2.55E-07 3.80E-07 5.50E-07 8.40E-07 1.28E-06 1.90E-06 2.80E-06 4.25E-06    &
6.30E-06 9.20E-06 1.35E-05 2.10E-05 3.00E-05 4.50E-05 6.90E-05 1.00E-04    &
1.35E-04 1.70E-04 2.20E-04 2.80E-04 3.60E-04 4.50E-04 5.75E-04 7.60E-04    &
9.60E-04 1.28E-03 1.60E-03 2.00E-03 2.70E-03 3.40E-03 4.50E-03 5.50E-03    &
7.20E-03 9.20E-03 1.20E-02 1.50E-02 1.90E-02 2.55E-02 3.20E-02 4.00E-02    &
5.25E-02 6.60E-02 8.80E-02 1.10E-01 1.35E-01 1.60E-01 1.90E-01 2.20E-01    &
2.55E-01 2.90E-01 3.20E-01 3.60E-01 4.00E-01 4.50E-01 5.00E-01 5.50E-01    &
6.00E-01 6.60E-01 7.20E-01 7.80E-01 8.40E-01 9.20E-01 1.00E+00 1.20E+00    &
```

```
1.40E+00 1.60E+00 1.80E+00 2.00E+00 2.30E+00 2.60E+00 2.90E+00 3.30E+00    &
3.70E+00 4.10E+00 4.50E+00 5.00E+00 5.50E+00 6.00E+00 6.70E+00 7.40E+00    &
8.20E+00 9.00E+00 1.00E+01 1.10E+01 1.20E+01 1.30E+01 1.40E+01 1.50E+01    &
1.60E+01 1.70E+01 1.80E+01 1.90E+01 2.00E+01
F14:N 3
E14 1.00E-10 1.00E-09 1.00E-08 2.30E-08 5.00E-08 7.60E-08 1.15E-07 1.70E-07 &
2.55E-07 3.80E-07 5.50E-07 8.40E-07 1.28E-06 1.90E-06 2.80E-06 4.25E-06    &
6.30E-06 9.20E-06 1.35E-05 2.10E-05 3.00E-05 4.50E-05 6.90E-05 1.00E-04    &
1.35E-04 1.70E-04 2.20E-04 2.80E-04 3.60E-04 4.50E-04 5.75E-04 7.60E-04    &
9.60E-04 1.28E-03 1.60E-03 2.00E-03 2.70E-03 3.40E-03 4.50E-03 5.50E-03    &
7.20E-03 9.20E-03 1.20E-02 1.50E-02 1.90E-02 2.55E-02 3.20E-02 4.00E-02    &
5.25E-02 6.60E-02 8.80E-02 1.10E-01 1.35E-01 1.60E-01 1.90E-01 2.20E-01    &
2.55E-01 2.90E-01 3.20E-01 3.60E-01 4.00E-01 4.50E-01 5.00E-01 5.50E-01    &
6.00E-01 6.60E-01 7.20E-01 7.80E-01 8.40E-01 9.20E-01 1.00E+00 1.20E+00    &
1.40E+00 1.60E+00 1.80E+00 2.00E+00 2.30E+00 2.60E+00 2.90E+00 3.30E+00    &
3.70E+00 4.10E+00 4.50E+00 5.00E+00 5.50E+00 6.00E+00 6.70E+00 7.40E+00    &
8.20E+00 9.00E+00 1.00E+01 1.10E+01 1.20E+01 1.30E+01 1.40E+01 1.50E+01    &
1.60E+01 1.70E+01 1.80E+01 1.90E+01 2.00E+01
FT14 TAG 1
FU14 -1
F24:N 1
E24 1.00E-10 1.00E-09 1.00E-08 2.30E-08 5.00E-08 7.60E-08 1.15E-07 1.70E-07 &
2.55E-07 3.80E-07 5.50E-07 8.40E-07 1.28E-06 1.90E-06 2.80E-06 4.25E-06    &
6.30E-06 9.20E-06 1.35E-05 2.10E-05 3.00E-05 4.50E-05 6.90E-05 1.00E-04    &
1.35E-04 1.70E-04 2.20E-04 2.80E-04 3.60E-04 4.50E-04 5.75E-04 7.60E-04    &
9.60E-04 1.28E-03 1.60E-03 2.00E-03 2.70E-03 3.40E-03 4.50E-03 5.50E-03    &
7.20E-03 9.20E-03 1.20E-02 1.50E-02 1.90E-02 2.55E-02 3.20E-02 4.00E-02    &
5.25E-02 6.60E-02 8.80E-02 1.10E-01 1.35E-01 1.60E-01 1.90E-01 2.20E-01    &
2.55E-01 2.90E-01 3.20E-01 3.60E-01 4.00E-01 4.50E-01 5.00E-01 5.50E-01    &
6.00E-01 6.60E-01 7.20E-01 7.80E-01 8.40E-01 9.20E-01 1.00E+00 1.20E+00    &
1.40E+00 1.60E+00 1.80E+00 2.00E+00 2.30E+00 2.60E+00 2.90E+00 3.30E+00    &
3.70E+00 4.10E+00 4.50E+00 5.00E+00 5.50E+00 6.00E+00 6.70E+00 7.40E+00    &
8.20E+00 9.00E+00 1.00E+01 1.10E+01 1.20E+01 1.30E+01 1.40E+01 1.50E+01    &
1.60E+01 1.70E+01 1.80E+01 1.90E+01 2.00E+01
c End of tallies
c Material cards
c Definition of TbCl3·6H2O
M1 1001.00c 11.9988 1002.00c 0.0012 8016.00c 5.9856 8017.00c 0.0024 &
8018.00c 0.012 17035.00c 2.2731 17037.00c 0.7269 65159.00c 1
NPS 1E10
```

K.3: MCNP6 simulation of the fast-neutron energy distribution at sample position to derive the self-shielding factor for a $TbCl_3{\cdot}6H_2O$ sample.

```
MCNP6 simulation of fast-neutron self-shielding in TbCl3·6H2O
c Cell cards
1     1 -4.35  -2 -1 $Sample
2     0        #1 -2  +1 $Confining sphere
3     0        +2 $Outer world
```

```
c Surface cards
1 1 RPP -0.443 0.443 -0.443 0.443 -0.30 0.30 $Sample
2 SPH 0.0 0.0 0.0 100.0 $Confining sphere
c End of surface cards

c Transformations
*TR1 0 0 0 45 90 90 90 0 90 45 90 90 1 $ 45° rotation around Y-axis
c Source and physics definition
MPHYS ON
IMP:N 1 1 0
VOL 0.4709976 4188789.734
PHYS:N 20.000001 $20.000001 MeV energy upper transport limit
CUT:N 1E09 6.599999E-02 $6.599999E-02 MeV lower transport limit
SDEF ERG=d1 POS=0 0 -9.80 PAR=1 VEC=0 0 1 DIR=1 X=d2 Y=d3 Z=-9.80
c FaNGaS energy bin structure with rel. probabilities
SI1 H 6.60E-02 8.80E-02 1.10E-01 1.35E-01 1.60E-01 1.90E-01 2.20E-01 &
2.55E-01 2.90E-01 3.20E-01 3.60E-01 4.00E-01 4.50E-01 5.00E-01 5.50E-01    &
6.00E-01 6.60E-01 7.20E-01 7.80E-01 8.40E-01 9.20E-01 1.00E+00 1.20E+00    &
1.40E+00 1.60E+00 1.80E+00 2.00E+00 2.30E+00 2.60E+00 2.90E+00 3.30E+00    &
3.70E+00 4.10E+00 4.50E+00 5.00E+00 5.50E+00 6.00E+00 6.70E+00 7.40E+00    &
8.20E+00 9.00E+00 1.00E+01 1.10E+01 1.20E+01 1.30E+01 1.40E+01 1.50E+01    &
1.60E+01 1.70E+01 1.80E+01 1.90E+01 2.00E+01
SP1 0.00 3.2372E-03 3.4357E-03 3.8242E-03 3.6910E-03 4.7909E-03 &
5.4212E-03 6.3330E-03 5.8062E-03 4.9387E-03 7.2678E-03 8.0010E-03 &
1.0722E-02 1.1850E-02 1.3430E-02 1.4858E-02 1.9043E-02 1.9790E-02 &
2.0342E-02 2.1622E-02 3.1305E-02 3.1229E-02 6.4877E-02 5.3288E-02 &
5.3414E-02 5.5428E-02 5.5060E-02 7.8098E-02 7.0097E-02 6.0255E-02 &
6.4959E-02 4.9361E-02 3.6343E-02 2.6221E-02 2.3007E-02 1.5786E-02 &
1.1130E-02 1.0799E-02 7.1575E-03 5.3323E-03 3.3384E-03 2.4559E-03 &
1.3068E-03 6.7408E-04 3.4086E-04 1.7009E-04 8.4356E-05 4.1827E-05 &
2.0825E-05 1.0428E-05 4.9457E-06 1.4658E-06
SI2 -0.525 0.525
SP2 0 1
SI3 -0.443 0.443
SP3 0 1
c Tallies
F14:N 1
E14 6.60E-02 8.80E-02 1.10E-01 1.35E-01 1.60E-01 1.90E-01 2.20E-01 &
2.55E-01 2.90E-01 3.20E-01 3.60E-01 4.00E-01 4.50E-01 5.00E-01 5.50E-01    &
6.00E-01 6.60E-01 7.20E-01 7.80E-01 8.40E-01 9.20E-01 1.00E+00 1.20E+00    &
1.40E+00 1.60E+00 1.80E+00 2.00E+00 2.30E+00 2.60E+00 2.90E+00 3.30E+00    &
3.70E+00 4.10E+00 4.50E+00 5.00E+00 5.50E+00 6.00E+00 6.70E+00 7.40E+00    &
8.20E+00 9.00E+00 1.00E+01 1.10E+01 1.20E+01 1.30E+01 1.40E+01 1.50E+01    &
1.60E+01 1.70E+01 1.80E+01 1.90E+01 2.00E+01
c End of tallies
c Material cards
c Definition of TbCl3·6H2O
M1 1001.00c 11.9988 1002.00c 0.0012 8016.00c 5.9856 8017.00c 0.0024 &
```

```
8018.00c 0.012 17035.00c 2.2731 17037.00c 0.7269 65159.00c 1
NPS 1E08
```

K.4: MCNP6 simulation of the neutron spectrum at detector position for a 2-MeV neutron beam and a BPE filter with 20 wt% B_2O_3 of 3 cm placed into the collimator opening.

```
Neutron spectrum at detector position with 3.0 cm thick BPE filter
c Cell cards
1     1 -5.323 -2 +6 -7 $Ge crystal
2     3 -1.01 -1 +10 -11 #1 $BPE filter
3     2 -11.340 #1 #2 (+13 -14 -5) : (+13 -14 +5 +3) $Pb shielding
4     3 -1.01 #1 #2 #3 (+14 -15 -8) : (+8 +14 -15 +3 -11) $BPE shielding
5     3 -1.01 #1 #2 #3 #4 (+9 -11 +1 -3) : (+1 -4 +11 -12) $BPE collimator
6     0       #1 #2 #3 #4 #5 -16 $Confining sphere
7     0 +16 $Blackhole region outside
c End of cell cards

c Surface cards
c Cylinders
1 CZ 3.0 $Collimator
2 CZ 3.195 $Detector cross section, including dead layer
3 CZ 5.0 $BPE collimator
4 CZ 7.0 $BPE
c End of cylinders
c Planes
5 PZ 5.0
6 PZ 11.6
7 PZ 19.9 $Neutron catcher/detector, 8.3 cm long ~ crystal volume
8 PZ 20
9 PZ 34 $End of BPE collimator
10 PZ 47.0 $3.0 cm thick filter
11 PZ 50.0 $BPE front surface to sample
12 PZ 51.0 $BPE collimator excess length
c End of planes
c Boxes
13 RPP -5.0 5.0 -5.0 5.0 -5.0 5.0 $Inner Pb shielding RPP
14 RPP -20.0 20.0 -20.0 20.0 -20.0 20.0 $Outer Pb shielding RPP
15 RPP -48.0 48.0 -48.0 48.0 -50.0 50.0 $Outer BPE shielding RPP
c End of boxes
c Spheres
16 SPH 0.0 0.0 0.0 150.0 $Confining sphere
c End of spheres
c End of surface cards

c Source and physics definition
MPHYS ON
MODE N
IMP:N 1 1 1 1 1 1 0
```

```
PHYS:N 20 $20 MeV energy upper transport limit
CUT:N 1E09 0.02 $10 s and 20 keV lower transport limit
c Cone-focussed point source, longitudinal half-opening angle of ~ 4.78°
SDEF ERG=2.0 POS=0 0 +86.9 PAR=1 VEC=0 0 -1 DIR=d1
SI1 0.996526588 1.0 $Cone-shaped beam into collimator
SP1 0 1
c Tallies
F1:N 7 $Detector front surface
E1 1.90E-02 2.55E-02 3.20E-02 4.00E-02 &
5.25E-02 6.60E-02 8.80E-02 1.10E-01 1.35E-01 1.60E-01 1.90E-01 2.20E-01    &
2.55E-01 2.90E-01 3.20E-01 3.60E-01 4.00E-01 4.50E-01 5.00E-01 5.50E-01    &
6.00E-01 6.60E-01 7.20E-01 7.80E-01 8.40E-01 9.20E-01 1.00E+00 1.20E+00    &
1.40E+00 1.60E+00 1.80E+00 2.00E+00 2.30E+00 2.60E+00 2.90E+00 3.30E+00    &
3.70E+00 4.10E+00 4.50E+00 5.00E+00 5.50E+00 6.00E+00 6.70E+00 7.04E+00    &
8.20E+00 9.00E+00 1.00E+01 1.10E+01 1.20E+01 1.30E+01 1.40E+01 1.50E+01    &
1.60E+01 1.70E+01 1.80E+01 1.90E+01 2.00E+01
c End of tallies
c Material cards
M1 32070 0.2050 32072 0.2740 32073 0.0780 32074 0.3650 32076 0.0744 $Ge crystal
M2 82204 0.0140 82206 0.2410 82207 0.2210 82208 0.5240 $Pb shielding
M3 1001 -0.1150 5000 -0.0621 6000 -0.6850 8016 -0.1379 $BPE, 20% B2O3
PRINT 50 110 $Print of cell volumes/areas and first 50 starting histories
NPS 1E08
```

K.5: MCNP6 simulation of the fast-neutron energy distribution at the BPE shielding front surface scattered from a 0.25 mm thick Fe sample.

```
Fast-neutron spectrum scattered towards detector at BPE front surface
c Cell cards
1     0 (+9 -10 -3) : (+9 -10 +3 +2) $Pb shielding
2     0 #1 (+10 -11 -4) : (+4 +10 -11 +2) $BPE shielding
3     0 #1 #2 -2 +6 -7 $Neutron spectrum scorer, 10 cm diameter
4     0 #1 #2 #3 -1 +7 -8 $Neutron spectrum scorer, 6 cm diameter
5     3 -7.874 #1 #2 #3 #4 (-13) (-12) $Fe sample
6     0        #1 #2 #3 #4 #5  -13 $Confining sphere
7     0 +13 $Blackhole region outside
c End of cell cards

c Surface cards
c Cylinders
1 CZ 3.0 $Collimator
2 CZ 5.0 $BPE collimator
c End of cylinders
c Planes
3 PZ 5.0
4 PZ 20
5 PZ 34 $End of BPE collimator
6 PZ 50.0 $Distance detector to sample
7 PZ 50.001 $10 cm diameter detector
```

```
8 PZ 50.002 $6 cm diameter detector
c End of planes
c Boxes
9 RPP -5.0 5.0 -5.0 5.0 -5.0 5.0 $Inner Pb shielding RPP
10 RPP -20.0 20.0 -20.0 20.0 -20.0 20.0 $Outer Pb shielding RPP
11 RPP -48.0 48.0 -48.0 48.0 -50.0 50.0 $Outer BPE shielding RPP
12 RPP -0.0125 0.0125 -1.25 1.25 86.9 89.4 $Fe sample
c End of boxes
c Spheres
13 SPH 0.0 0.0 0.0 150.0 $Confining sphere
c End of spheres
c End of surface cards

c Source and physics definition
MPHYS ON
MODE N
IMP:N 1 1 1 1 1 1 0
PHYS:N 20 $20 MeV energy upper transport limit
CUT:N 1E09 1.0E-10 $10 s and 1.0E-10 MeV lower transport limit
SDEF ERG=d1 POS=10 0 88.15 X=10 Y=d2 Z=d3 PAR=1 VEC=-1 0 0 DIR=1
c FaNGaS neutron-energy bin structure with rel. probabilities
SI1 H 6.60E-02 8.80E-02 1.10E-01 1.35E-01 1.60E-01 1.90E-01 2.20E-01 &
2.55E-01 2.90E-01 3.20E-01 3.60E-01 4.00E-01 4.50E-01 5.00E-01 5.50E-01    &
6.00E-01 6.60E-01 7.20E-01 7.80E-01 8.40E-01 9.20E-01 1.00E+00 1.20E+00    &
1.40E+00 1.60E+00 1.80E+00 2.00E+00 2.30E+00 2.60E+00 2.90E+00 3.30E+00    &
3.70E+00 4.10E+00 4.50E+00 5.00E+00 5.50E+00 6.00E+00 6.70E+00 7.40E+00    &
8.20E+00 9.00E+00 1.00E+01 1.10E+01 1.20E+01 1.30E+01 1.40E+01 1.50E+01    &
1.60E+01 1.70E+01 1.80E+01 1.90E+01 2.00E+01
SP1 0.00 3.2372E-03 3.4357E-03 3.8242E-03 3.6910E-03 4.7909E-03 &
5.4212E-03 6.3330E-03 5.8062E-03 4.9387E-03 7.2678E-03 8.0010E-03 &
1.0722E-02 1.1850E-02 1.3430E-02 1.4858E-02 1.9043E-02 1.9790E-02 &
2.0342E-02 2.1622E-02 3.1305E-02 3.1229E-02 6.4877E-02 5.3288E-02 &
5.3414E-02 5.5428E-02 5.5060E-02 7.8098E-02 7.0097E-02 6.0255E-02 &
6.4959E-02 4.9361E-02 3.6343E-02 2.6221E-02 2.3007E-02 1.5786E-02 &
1.1130E-02 1.0799E-02 7.1575E-03 5.3323E-03 3.3384E-03 2.4559E-03 &
1.3068E-03 6.7408E-04 3.4086E-04 1.7009E-04 8.4356E-05 4.1827E-05 &
2.0825E-05 1.0428E-05 4.9457E-06 1.4658E-06
SI2 -1.25 1.25
SP2 0 1
SI3 86.9 89.4
SP3 0 1
c Tallies
F11:N 12.1 $Neutron-energy spectrum at sample front surface
CF11 5
E11 1.00E-10 1.00E-09 1.00E-08 2.30E-08 5.00E-08 7.60E-08 1.15E-07 1.70E-07 &
2.55E-07 3.80E-07 5.50E-07 8.40E-07 1.28E-06 1.90E-06 2.80E-06 4.25E-06    &
6.30E-06 9.20E-06 1.35E-05 2.10E-05 3.00E-05 4.50E-05 6.90E-05 1.00E-04    &
1.35E-04 1.70E-04 2.20E-04 2.80E-04 3.60E-04 4.50E-04 5.75E-04 7.60E-04    &
9.60E-04 1.28E-03 1.60E-03 2.00E-03 2.70E-03 3.40E-03 4.50E-03 5.50E-03    &
```

```
7.20E-03 9.20E-03 1.20E-02 1.50E-02 1.90E-02 2.55E-02 3.20E-02 4.00E-02    &
5.25E-02 6.60E-02 8.80E-02 1.10E-01 1.35E-01 1.60E-01 1.90E-01 2.20E-01    &
2.55E-01 2.90E-01 3.20E-01 3.60E-01 4.00E-01 4.50E-01 5.00E-01 5.50E-01    &
6.00E-01 6.60E-01 7.20E-01 7.80E-01 8.40E-01 9.20E-01 1.00E+00 1.20E+00    &
1.40E+00 1.60E+00 1.80E+00 2.00E+00 2.30E+00 2.60E+00 2.90E+00 3.30E+00    &
3.70E+00 4.10E+00 4.50E+00 5.00E+00 5.50E+00 6.00E+00 6.70E+00 7.40E+00    &
8.20E+00 9.00E+00 1.00E+01 1.10E+01 1.20E+01 1.30E+01 1.40E+01 1.50E+01    &
1.60E+01 1.70E+01 1.80E+01 1.90E+01 2.00E+01
F21:N 8 $Neutron-energy spectrum at BPE front surface, 6 cm diameter
E21 1.00E-10 1.00E-09 1.00E-08 2.30E-08 5.00E-08 7.60E-08 1.15E-07 1.70E-07 &
2.55E-07 3.80E-07 5.50E-07 8.40E-07 1.28E-06 1.90E-06 2.80E-06 4.25E-06    &
6.30E-06 9.20E-06 1.35E-05 2.10E-05 3.00E-05 4.50E-05 6.90E-05 1.00E-04    &
1.35E-04 1.70E-04 2.20E-04 2.80E-04 3.60E-04 4.50E-04 5.75E-04 7.60E-04    &
9.60E-04 1.28E-03 1.60E-03 2.00E-03 2.70E-03 3.40E-03 4.50E-03 5.50E-03    &
7.20E-03 9.20E-03 1.20E-02 1.50E-02 1.90E-02 2.55E-02 3.20E-02 4.00E-02    &
5.25E-02 6.60E-02 8.80E-02 1.10E-01 1.35E-01 1.60E-01 1.90E-01 2.20E-01    &
2.55E-01 2.90E-01 3.20E-01 3.60E-01 4.00E-01 4.50E-01 5.00E-01 5.50E-01    &
6.00E-01 6.60E-01 7.20E-01 7.80E-01 8.40E-01 9.20E-01 1.00E+00 1.20E+00    &
1.40E+00 1.60E+00 1.80E+00 2.00E+00 2.30E+00 2.60E+00 2.90E+00 3.30E+00    &
3.70E+00 4.10E+00 4.50E+00 5.00E+00 5.50E+00 6.00E+00 6.70E+00 7.40E+00    &
8.20E+00 9.00E+00 1.00E+01 1.10E+01 1.20E+01 1.30E+01 1.40E+01 1.50E+01    &
1.60E+01 1.70E+01 1.80E+01 1.90E+01 2.00E+01
F31:N 7 $Neutron-energy spectrum at BPE front surface, 10 cm diameter
E31 1.00E-10 1.00E-09 1.00E-08 2.30E-08 5.00E-08 7.60E-08 1.15E-07 1.70E-07 &
2.55E-07 3.80E-07 5.50E-07 8.40E-07 1.28E-06 1.90E-06 2.80E-06 4.25E-06    &
6.30E-06 9.20E-06 1.35E-05 2.10E-05 3.00E-05 4.50E-05 6.90E-05 1.00E-04    &
1.35E-04 1.70E-04 2.20E-04 2.80E-04 3.60E-04 4.50E-04 5.75E-04 7.60E-04    &
9.60E-04 1.28E-03 1.60E-03 2.00E-03 2.70E-03 3.40E-03 4.50E-03 5.50E-03    &
7.20E-03 9.20E-03 1.20E-02 1.50E-02 1.90E-02 2.55E-02 3.20E-02 4.00E-02    &
5.25E-02 6.60E-02 8.80E-02 1.10E-01 1.35E-01 1.60E-01 1.90E-01 2.20E-01    &
2.55E-01 2.90E-01 3.20E-01 3.60E-01 4.00E-01 4.50E-01 5.00E-01 5.50E-01    &
6.00E-01 6.60E-01 7.20E-01 7.80E-01 8.40E-01 9.20E-01 1.00E+00 1.20E+00    &
1.40E+00 1.60E+00 1.80E+00 2.00E+00 2.30E+00 2.60E+00 2.90E+00 3.30E+00    &
3.70E+00 4.10E+00 4.50E+00 5.00E+00 5.50E+00 6.00E+00 6.70E+00 7.40E+00    &
8.20E+00 9.00E+00 1.00E+01 1.10E+01 1.20E+01 1.30E+01 1.40E+01 1.50E+01    &
1.60E+01 1.70E+01 1.80E+01 1.90E+01 2.00E+01
c Material cards
M1 82204 0.0140 82206 0.2410 82207 0.2210 82208 0.5240 $Pb shielding
M2 1001 -0.1150 5000 -0.0621 6000 -0.6850 8016 -0.1379 $BPE, 20 wt% B2O3
M3 26054 0.0580 26056 0.9172 26057 0.0220 26058 0.0028 $Fe
PRINT 50 110 $Print of cell volumes/areas and first 50 starting histories
NPS 1E09
```

K.6: MCNP6 simulation of the fast-neutron flux reduction at detector using the fast-neutron scatter spectrum (obtained with simulation of a 0.25 mm thick Fe foil, see also Appx. K.5) and a 3 cm thick BPE filter with 20 wt% B_2O_3.

```
Fast-neutron flux reduction at detector, 3 cm BPE with 20wt% B2O3
c Cell cards
```

```
1     1 -5.323 (+2 -4 +10 -15) : (+24 -16 +14 -3) : (-25) $Ge crystal
2     2 -2.929 #1 (+1 -2 +10 -15) : (+14 +23 -24) $700-micron Ge/Li dead layer
3     3 -3.892 #1 #2 (4 -5 +10 -15) : (-26 +25 #1 #2) &
$0.3-micron Ge/B dead layer
4     4 -2.700 #1 #2 #3 (11 -16 +6 -7) : (+1 -7 +12 -11) : (-7 +16 -17 +26) &
$Al housing
5     4 -2.700 #1 #2 #3 #4 (8 -9 13 -19) : (7 -9 19 -21) $Outer Al housing
6     5 -1.380 #1 #2 #3 #4 #5 (-7 17 -18) $0.03 mm mylar
7     6 -1.800 #1 #2 #3 #4 #5 #6 -7 19 -20 $Carbon fiber
8     7 -8.960 #1 #2 #3 #4 #5 #6 #7 +10 -15 -1 $Copper cold finger
9     0  +18 -32 -5 $Current detector in front of detector
10    8 -11.340 #1 #2 #3 #4 #5 #6 #7 #8 #9 (+33 -34) $Pb shielding
11    9 -1.01 #10 (+34 -35 -27) : (+34 -35 +27 -30 +38) $BPE shielding
12    9 -1.01 #11 (+28 -30 +37 -38) : (+37 -39 +30 -31) $BPE collimator
13    9 -1.01 -37 +29 -30 $BPE filter
14    0 -22 -36 $Current detector
15    0 -22 +35 #12 #14 $Confining sphere 1 (outside BPE)
16    0 #12 #13 (+27 -30 -38) $Confining sphere 2 (inside BPE)
17    0 -33 #1 #2 #3 #4 #5 #6 #7 #8 #9 $Conf. sph. 3 det.
18    0 +22 $Blk hole

c Surface cards
c Cylinders
1 CZ 0.51 $Inner diameter Ge cyl. (hole) with Ge/Li dead layer
2 CZ 0.58 $700-micron Ge/Li dead layer
3 CZ 2.39497
4 CZ 3.19497 $Outer diameter Ge cyl without dead layer
5 CZ 3.195 $0.3-micron Ge/B dead layer
6 CZ 3.4
7 CZ 3.48 $0.8 mm inner Al housing
8 CZ 4.0
9 CZ 4.1 $1.0 mm outer Al housing
c End of cylinders
c Planes
c Below Origin (=half crystal length)
10 PZ -4.255 $Lower Ge crystal plane
11 PZ -5.945
12 PZ -6.245 $3 mm Al bottom, inner housing
13 PZ -7.0 $Lower ending of outer Al housing
c Above origin
14 PZ 2.895
15 PZ 3.455 $Lower Ge crystal hole plane
16 PZ 4.255 $Upper Ge crystal plane, backside plane
17 PZ 4.258 $0.03 mm Al
18 PZ 4.261 $0.03 mm mylar
19 PZ 4.295 $Lower front of outer Al housing
20 PZ 4.385 $0.9 mm carbon fiber
21 PZ 4.395 $1 mm Al housing
22 SPH 0.0 0.0 0.0 150.0 $Confining sphere
```

```
23 SPH 0.0 0.0 2.895 0.51 $Nom. radius
24 SPH 0.0 0.0 2.895 0.58 $Nom. radius
25 TZ 0 0 3.455 2.39497 0.80 0.80 $Nom. radius edge, torus
26 TZ 0 0 3.455 2.39497 0.80003 0.80003
c End of planes
c Continuation after HPGe model, with shielding
27 PZ 4.495 $Begin collimation tract, 0.1 cm spacing to detector front surf.
28 PZ 18.495 $End of BPE collimator
29 PZ 31.495 $ $3.0 cm thick filter
30 PZ 34.495 $BPE front surface to sample
31 PZ 35.495 $BPE collimator excess length
32 PZ 4.262
c End of planes
c Boxes
33 RPP -5.0 5.0 -5.0 5.0 -20.505 4.495 $Inner Pb shielding RPP
34 RPP -20.0 20.0 -20.0 20.0 -35.505 4.495 $Outer Pb shielding RPP
35 RPP -48.0 48.0 -48.0 48.0 -65.505 34.495 $Outer BPE shielding RPP
36 RPP -5 5 -5 5 69.9 70.0 $Current detector
c End of boxes
c Begin of cylinders
37 CZ 3.0
38 CZ 5.0 $BPE collimator
39 CZ 7.0 $BPE
c End of surface cards

c Source definition
MPHYS ON
MODE N
IMP:N 1 1 1 1 1 1 1 1 1 1 1 1 1 1 1 1 0
PHYS:N 20 $20 MeV energy upper transport limit
CUT:N 1E09 0.02 $20 keV lower transport limit
c Cone-focussed point source, longitudinal half-opening angle of ~ 4.80°
SDEF ERG=d1 POS=0 0 +71.255 PAR=1 X=0 Y=0 Z=+71.255 VEC=0 0 -1 DIR=d2
c FaNGaS neutron-energy bin structure with rel. probabilities of scatter spec.
SI1 H 6.60E-02 8.80E-02 1.10E-01 1.35E-01 1.60E-01 1.90E-01 2.20E-01 &
2.55E-01 2.90E-01 3.20E-01 3.60E-01 4.00E-01 4.50E-01 5.00E-01 5.50E-01    &
6.00E-01 6.60E-01 7.20E-01 7.80E-01 8.40E-01 9.20E-01 1.00E+00 1.20E+00    &
1.40E+00 1.60E+00 1.80E+00 2.00E+00 2.30E+00 2.60E+00 2.90E+00 3.30E+00    &
3.70E+00 4.10E+00 4.50E+00 5.00E+00 5.50E+00 6.00E+00 6.70E+00 7.40E+00    &
8.20E+00 9.00E+00 1.00E+01 1.10E+01
SP1 0.00 9.61E-03 9.19E-03 9.98E-03 1.09E-02 1.92E-02 1.37E-02 1.24E-02    &
1.16E-02 1.70E-02 1.55E-02 2.22E-02 2.53E-02 3.36E-02 2.62E-02 2.16E-02    &
2.98E-02 3.55E-02 3.97E-02 3.32E-02 2.77E-02 3.53E-02 7.88E-02 7.39E-02    &
4.99E-02 5.40E-02 3.85E-02 4.88E-02 5.60E-02 4.16E-02 3.77E-02 1.92E-02    &
1.42E-02 7.49E-03 7.52E-03 4.80E-03 2.52E-03 2.20E-03 1.27E-03 8.84E-04    &
7.20E-04 3.59E-04 5.31E-04
SI2 0.9964994810 1.0 $Cone-shaped beam into collimator
SP2 0 1
c Tallies
```

```
F1:N 32
E1 1.90E-02 2.55E-02 3.20E-02 4.00E-02 &
5.25E-02 6.60E-02 8.80E-02 1.10E-01 1.35E-01 1.60E-01 1.90E-01 2.20E-01    &
2.55E-01 2.90E-01 3.20E-01 3.60E-01 4.00E-01 4.50E-01 5.00E-01 5.50E-01    &
6.00E-01 6.60E-01 7.20E-01 7.80E-01 8.40E-01 9.20E-01 1.00E+00 1.20E+00    &
1.40E+00 1.60E+00 1.80E+00 2.00E+00 2.30E+00 2.60E+00 2.90E+00 3.30E+00    &
3.70E+00 4.10E+00 4.50E+00 5.00E+00 5.50E+00 6.00E+00 6.70E+00 7.40E+00    &
8.20E+00 9.00E+00 1.00E+01 1.10E+01 1.20E+01 1.30E+01 1.40E+01 1.50E+01    &
1.60E+01 1.70E+01 1.80E+01 1.90E+01 2.00E+01
c End of tallies
c Material cards
M1 32070 0.2050 32072 0.2740 32073 0.0780 32074 0.3650 32076 0.0744 $Ge crystal
M2 32070 0.2050 32072 0.2740 32073 0.0780 32074 0.3650 32076 0.0744 &
3006 0.0740 3007 0.9260 $Ge/Li dead layer, 50-50 ratio
M3 32070 0.2050 32072 0.2740 32073 0.0780 32074 0.3650 32076 0.0744 &
5010 0.1990 5011 0.8010 $Ge/B dead layer, 50-50 ratio
M4 13027 1.00 $Al
M5 6012 9.8900 6013 0.1100 1001 7.9991 1002 0.0092 8016 3.9905 &
8017 0.0015 $Mylar,(C10H8O4)n
c 8018 0.0080
M6 6012 0.9890 6013 0.011 $Carbon fiber, ~ C
M7 29063 0.6917 29065 0.3083 $Cu
M8 82204 0.0140 82206 0.2410 82207 0.2210 82208 0.5240 $Pb shielding
M9 1001 -0.1150 5010 -0.0114 5011 -0.0507 6000 -0.6850 &
8016 -0.1379 $BPE, 20 wt% B2O3
PRINT 50 110 $Print of cell volumes/areas and first 50 starting histories
NPS 1E08
```

K.7: MCNP6 simulation of the γ and neutron spectrum at the HPGe detector front surface using the scatter spectrum derived with a 0.25 mm thick Fe foil (see also Appx. K.5).

```
Gamma and neutron spectrum at detector, 0.5 cm BPE with 20wt% B2O3
c Cell cards
1     1 -5.323 (+2 -4 +10 -15) : (+24 -16 +14 -3) : (-25) $Ge crystal
2     2 -2.929 #1 (+1 -2 +10 -15) : (+14 +23 -24) $700-micron Ge/Li dead layer
3     3 -3.892 #1 #2 (4 -5 +10 -15) : (-26 +25 #1 #2) &
$0.3-micron Ge/B dead layer
4     4 -2.700 #1 #2 #3 (11 -16 +6 -7) : (+1 -7 +12 -11) : (-7 +16 -17 +26) &
$Al housing
5     4 -2.700 #1 #2 #3 #4 (8 -9 13 -19) : (7 -9 19 -21) $Outer Al housing
6     5 -1.380 #1 #2 #3 #4 #5 (-7 17 -18) $0.03 mm mylar
7     6 -1.800 #1 #2 #3 #4 #5 #6 -7 19 -20 $Carbon fiber
8     7 -8.960 #1 #2 #3 #4 #5 #6 #7 +10 -15 -1 $Copper cold finger
9     0  +18 -32 -5 $Current detector in front of detector
10    8 -11.340 #1 #2 #3 #4 #5 #6 #7 #8 #9 (+33 -34) $Pb shielding
11    9 -1.01 #10 (+34 -35 -27) : (+34 -35 +27 -30 +38) $BPE shielding
12    9 -1.01 #11 (+28 -30 +37 -38) : (+37 -39 +30 -31) $BPE collimator
13    9 -1.01 -37 +29 -30 $BPE filter
```

```
14    0   -22 -36 $Current detector
15    0 -22 +35 #12 #14 $Confining sphere 1 (outside BPE)
16    0  #12 #13 (+27 -30 -38) $Confining sphere 2 (inside BPE)
17    0 -33 #1 #2 #3 #4 #5 #6 #7 #8 #9 $Conf. sph. 3 det
18    0 +22 $Blk hole

c Surface cards
c Cylinders
1 CZ 0.51 $Inner diameter Ge cyl. (hole) with Ge/Li dead layer
2 CZ 0.58 $700-micron Ge/Li dead layer
3 CZ 2.39497
4 CZ 3.19497 $Outer diameter Ge cyl. without dead layer
5 CZ 3.195 $0.3-micron Ge/B dead layer
6 CZ 3.4
7 CZ 3.48 $0.8 mm inner Al housing
8 CZ 4.0
9 CZ 4.1 $1.0 mm outer Al housing
c End of cylinders
c Planes
c Below Origin (=half crystal length)
10 PZ -4.255 $Lower Ge crystal plane
11 PZ -5.945
12 PZ -6.245 $3 mm Al bottom, inner housing
13 PZ -7.0 $Lower ending of outer Al housing
c Above origin
14 PZ 2.895
15 PZ 3.455 $Lower Ge crystal hole plane
16 PZ 4.255 $Upper Ge crystal plane, backside plane
17 PZ 4.258 $0.03 mm Al
18 PZ 4.261 $0.03 mm mylar
19 PZ 4.295 $Lower front of outer Al housing
20 PZ 4.385 $0.9 mm carbon fiber
21 PZ 4.395 $1 mm Al housing
22 SPH 0.0   0.0    0.0    150.0 $Confining sphere
23 SPH 0.0   0.0    2.895  0.51 $Nom. radius
24 SPH 0.0   0.0    2.895  0.58 $Nom. radius
25 TZ 0 0 3.455 2.39497 0.80 0.80 $Nom. radius edge, torus
26 TZ 0 0 3.455 2.39497 0.80003 0.80003
c End of planes
c Continuation after HPGe model, with shielding
27 PZ 4.495 $Begin collimation tract, 0.1 cm spacing to detector front surf.
28 PZ 18.495 $End of BPE collimator
29 PZ 33.995 $ $0.5 cm thick filter
30 PZ 34.495 $BPE front surface to sample
31 PZ 35.495 $BPE collimator excess length
32 PZ 4.262
c End of planes
c Boxes
33 RPP -5.0 5.0 -5.0 5.0 -20.505 4.495 $Inner Pb shielding RPP
```

```
34 RPP -20.0 20.0 -20.0 20.0 -35.505 4.495 $Outer Pb shielding RPP
35 RPP -48.0 48.0 -48.0 48.0 -65.505 34.495 $Outer BPE shielding
36 RPP -5 5 -5 5 69.9 70.0 $Current detector
c End of boxes
c Begin of cylinders
37 CZ 3.0
38 CZ 5.0 $BPE collimator
39 CZ 7.0 $BPE
c End of cylinders
c End of surface cards

c Source and physics definition
MPHYS ON
MODE N P
IMP:N,P 1 1 1 1 1 1 1 1 1 1 1 1 1 1 1 1 1 0
PHYS:N 20 $20 MeV energy upper transport limit
CUT:N 1E09 1.0E-10 $10 s and 1.0E-10 MeV lower transport limit
c Cone-focussed point source, longitudinal half-opening angle of ~ 4.80°
SDEF ERG=d1 POS=0 0 +71.255 PAR=1 X=0 Y=0 Z=+71.255 VEC=0 0 -1 DIR=d2
c FaNGaS neutron-energy bin structure with rel. probabilities of scatter spec.
SI1 H 1.00E-10 1.00E-09 1.00E-08 2.30E-08 5.00E-08 7.60E-08 1.15E-07 1.70E-07 &
2.55E-07 3.80E-07 5.50E-07 8.40E-07 1.28E-06 1.90E-06 2.80E-06 4.25E-06    &
6.30E-06 9.20E-06 1.35E-05 2.10E-05 3.00E-05 4.50E-05 6.90E-05 1.00E-04    &
1.35E-04 1.70E-04 2.20E-04 2.80E-04 3.60E-04 4.50E-04 5.75E-04 7.60E-04    &
9.60E-04 1.28E-03 1.60E-03 2.00E-03 2.70E-03 3.40E-03 4.50E-03 5.50E-03    &
7.20E-03 9.20E-03 1.20E-02 1.50E-02 1.90E-02 2.55E-02 3.20E-02 4.00E-02    &
5.25E-02 6.60E-02 8.80E-02 1.10E-01 1.35E-01 1.60E-01 1.90E-01 2.20E-01    &
2.55E-01 2.90E-01 3.20E-01 3.60E-01 4.00E-01 4.50E-01 5.00E-01 5.50E-01    &
6.00E-01 6.60E-01 7.20E-01 7.80E-01 8.40E-01 9.20E-01 1.00E+00 1.20E+00    &
1.40E+00 1.60E+00 1.80E+00 2.00E+00 2.30E+00 2.60E+00 2.90E+00 3.30E+00    &
3.70E+00 4.10E+00 4.50E+00 5.00E+00 5.50E+00 6.00E+00 6.70E+00 7.40E+00    &
8.20E+00 9.00E+00 1.00E+01 1.10E+01
SP1 0.00 1.50E-07 6.33E-06 1.79E-05 3.96E-05 2.53E-05 1.95E-05 9.80E-06    &
4.91E-06 2.42E-05 4.50E-05 1.16E-04 2.13E-04 4.86E-04 6.97E-04 1.18E-03    &
1.54E-03 1.76E-03 1.97E-03 2.37E-03 1.96E-03 1.86E-03 3.19E-03 3.24E-03    &
2.28E-03 1.71E-03 2.56E-03 2.64E-03 2.69E-03 2.21E-03 2.75E-03 2.95E-03    &
2.48E-03 2.73E-03 1.60E-03 1.65E-03 2.43E-03 1.45E-03 1.87E-03 1.46E-03    &
3.19E-03 3.62E-03 2.14E-03 1.33E-03 9.35E-04 1.00E-03 9.32E-03 4.10E-03    &
6.42E-03 5.11E-03 8.71E-03 8.33E-03 9.04E-03 9.90E-03 1.74E-02 1.24E-02    &
1.12E-02 1.05E-02 1.54E-02 1.41E-02 2.01E-02 2.29E-02 3.05E-02 2.38E-02    &
1.96E-02 2.70E-02 3.22E-02 3.60E-02 3.01E-02 2.51E-02 3.20E-02 7.14E-02    &
6.70E-02 4.52E-02 4.89E-02 3.49E-02 4.42E-02 5.07E-02 3.77E-02 3.42E-02    &
1.74E-02 1.28E-02 6.79E-03 6.82E-03 4.35E-03 2.29E-03 2.00E-03 1.16E-03    &
8.01E-04 6.52E-04 3.25E-04 4.82E-04
SI2 0.9964994810 1.0 $Cone-shaped beam into collimator
SP2 0 1
c Tallies
F1:N 32 $Complete neutron-energy spectrum at det. front surf.
E1 1.00E-10 1.00E-09 1.00E-08 2.30E-08 5.00E-08 7.60E-08 1.15E-07 1.70E-07 &
```

```
2.55E-07 3.80E-07 5.50E-07 8.40E-07 1.28E-06 1.90E-06 2.80E-06 4.25E-06    &
6.30E-06 9.20E-06 1.35E-05 2.10E-05 3.00E-05 4.50E-05 6.90E-05 1.00E-04    &
1.35E-04 1.70E-04 2.20E-04 2.80E-04 3.60E-04 4.50E-04 5.75E-04 7.60E-04    &
9.60E-04 1.28E-03 1.60E-03 2.00E-03 2.70E-03 3.40E-03 4.50E-03 5.50E-03    &
7.20E-03 9.20E-03 1.20E-02 1.50E-02 1.90E-02 2.55E-02 3.20E-02 4.00E-02    &
5.25E-02 6.60E-02 8.80E-02 1.10E-01 1.35E-01 1.60E-01 1.90E-01 2.20E-01    &
2.55E-01 2.90E-01 3.20E-01 3.60E-01 4.00E-01 4.50E-01 5.00E-01 5.50E-01    &
6.00E-01 6.60E-01 7.20E-01 7.80E-01 8.40E-01 9.20E-01 1.00E+00 1.20E+00    &
1.40E+00 1.60E+00 1.80E+00 2.00E+00 2.30E+00 2.60E+00 2.90E+00 3.30E+00    &
3.70E+00 4.10E+00 4.50E+00 5.00E+00 5.50E+00 6.00E+00 6.70E+00 7.40E+00    &
8.20E+00 9.00E+00 1.00E+01 1.10E+01 1.20E+01 1.30E+01 1.40E+01 1.50E+01    &
1.60E+01 1.70E+01 1.80E+01 1.90E+01 2.00E+01
F8:P 1 $Induced gamma spectrum in Ge crystal from 0 - 3 MeV
E8 1E-03 3000i 3.0 $ ~ 1 keV intervals
c End of tallies
c Material cards
M1 32070 0.2050 32072 0.2740 32073 0.0780 32074 0.3650 32076 0.0744 $Ge crystal
M2 32070 0.2050 32072 0.2740 32073 0.0780 32074 0.3650 32076 0.0744 &
3006 0.0740 3007 0.9260 $Ge/Li dead layer, 50-50 ratio
M3 32070 0.2050 32072 0.2740 32073 0.0780 32074 0.3650 32076 0.0744 &
5010 0.1990 5011 0.8010 $Ge/B dead layer, 50-50 ratio
M4 13027 1.00 $Al
M5 6012 9.8900 6013 0.1100 1001 7.9991 1002 0.0092 8016 3.9905 &
8017 0.0015 $Mylar, (C10H8O4)n
c 8018 0.0080
M6 6012 0.9890 6013 0.011 $Carbon fiber, ~ C
M7 29063 0.6917 29065 0.3083 $Cu
M8 82204 0.0140 82206 0.2410 82207 0.2210 82208 0.5240 $Pb shielding
M9 1001 -0.1150 5010 -0.0114 5011 -0.0507 6000 -0.6850 &
8016 -0.1379 $BPE, 20% B2O3
PRINT 50 110 $Print of cell volumes/areas and first 50 starting histories
NPS 1E09
```

K.8: MCNP6 simulation of the γ-ray self-absorption for γs of 0.1, 0.5, 1, 3 and 5 MeV in a 5 cm thick Al sample of S= 2.5 $\times$ 2.5 cm^2.

```
Gamma-ray self-absorption for an Al sample of 50 mm thickness
c Cell cards
1     1 -2.7 -1 -5 -8 -2 $Al sample
2     0 +3 -4 -2 $Reference body 1
3     0 -5 +6 -7 $Reference body 2
4     0  #1 #2 #3 -8 $Inner void region
5     0  +8 $Blackhole region outside
c End of cell cards

c Surface cards
1 RPP -1.25 1.25 -1.25 1.25 -2.5 2.5 $Al sample
2 CX 3.0 $Detector
3 PX 67
```

```
4 PX 68
5 CZ 3.0
6 PZ 67
7 PZ 68
8 SPH 0.0 0.0 0.0 100.0 $Confining sphere
c End of surface cards

c Source and physics definition
MODE P
IMP:P 1 1 1 1 0
VOL 31.25 523567.5256
PHYS:P 5.000001 0 0 0 0 J 0
CUT:P J 0.099999 $Photon transport cutoff 0.099999 MeV
c Uniform gamma-ray emssion in cell 1
SDEF ERG=d1 X=d2 Y=d3 Z=d4 CEL=1 PAR=2
SI1 L 0.1 0.5 1 3 5
SP1 0.2 0.2 0.2 0.2 0.2
SI2 -1.25 1.25
SP2 0 1
SI3 -1.25 1.25
SP3 0 1
SI4 -2.5 2.5
SP4 0 1
c Tallies
F11:P 3
E11 0.049 0.05 0.069 0.07 0.099 0.1 0.139 0.14 0.199 0.2 0.239 0.24 0.299 0.3 &
0.419 0.420 0.599 0.6 0.849 0.85 1.199 1.2 1.699 1.7 2.449 2.45 3.499 3.5 &
4.999 5.0 5.999 6.0
FT11 TAG 1
FU11 -1
F21:P 6
E21 0.049 0.05 0.069 0.07 0.099 0.1 0.139 0.14 0.199 0.2 0.239 0.24 0.299 0.3 &
0.419 0.420 0.599 0.6 0.849 0.85 1.199 1.2 1.699 1.7 2.449 2.45 3.499 3.5 &
4.999 5.0 5.999 6.0
FT21 TAG 1
FU21 -1
c End of tallies
c Material cards
M1 13027.84p 1.0 $Al
PRINT 50 110 170 $Print of cell volumes/areas, first 50 starting histories, &
$and source-distribution frequency table
NPS 1E08
```

K.9: MCNP6 simulation for the parametrization of the fast-neutron self-shielding factor for large samples. The simulation for a 10 mm thick Al sample with S= 2.5 $\times$ 2.5 cm^2 is given.

```
Neutron attenuation for an Al sample of 10 mm thickness
c Cell cards
```

```
1     1 -2.7 -1 -2 $Al sample
2     0 +1 -2 $Inner void region
3     0 +2 $Blackhole region outside
c End of cell cards

c Surface cards
1 RPP -1.25 1.25 -1.25 1.25 -1.0 0 $Al sample
2 SPH 0.0 0.0 0.0 10.0 $Confining sphere
c End of surface cards

c Source and physics definition
MPHYS ON
MODE N
IMP:N 1 1 0
VOL 6.25 4182.5402
PHYS:N 20.000001 $20.000001 MeV energy upper transport limit
CUT:N 1E09 6.599999E-02 $10 s and 6.599999 MeV lower transport limit
c Parallel beam of fast neutrons
SDEF ERG=d1 POS=0 0 1 X=d2 Y=d3 Z=1 PAR=1 VEC=0 0 -1 DIR=1
c FaNGaS neutron-energy bin structure with rel. probabilities
SI1 H 6.60E-02 8.80E-02 1.10E-01 1.35E-01 1.60E-01 1.90E-01 2.20E-01 &
2.55E-01 2.90E-01 3.20E-01 3.60E-01 4.00E-01 4.50E-01 5.00E-01 5.50E-01    &
6.00E-01 6.60E-01 7.20E-01 7.80E-01 8.40E-01 9.20E-01 1.00E+00 1.20E+00    &
1.40E+00 1.60E+00 1.80E+00 2.00E+00 2.30E+00 2.60E+00 2.90E+00 3.30E+00    &
3.70E+00 4.10E+00 4.50E+00 5.00E+00 5.50E+00 6.00E+00 6.70E+00 7.40E+00    &
8.20E+00 9.00E+00 1.00E+01 1.10E+01 1.20E+01 1.30E+01 1.40E+01 1.50E+01    &
1.60E+01 1.70E+01 1.80E+01 1.90E+01 2.00E+01
SP1 0.00 3.23720667625859E-03 3.43569234108028E-03 &
3.82421442525146E-03 3.69103140340141E-03 4.79093699406737E-03 &
5.42119342327392E-03 6.33299589652048E-03 5.80620692246088E-03 &
4.93872718605582E-03 7.26778318160245E-03 8.00100583952963E-03 &
1.07219492966813E-02 1.18497087558955E-02 1.34300040742991E-02 &
1.48577833515518E-02 1.90430240113022E-02 1.97898513865151E-02 &
2.03419164932162E-02 2.16221919935812E-02 3.13051705122817E-02 &
3.12285544728303E-02 6.48773165470218E-02 5.32875294950595E-02 &
5.34135521393908E-02 5.54284823731868E-02 5.50604389687194E-02 &
7.80982375977714E-02 7.00972317582417E-02 6.02545768208715E-02 &
6.49589448507364E-02 4.93607784637386E-02 3.63432121345235E-02 &
2.62213024739194E-02 2.30070090057210E-02 1.57857682779909E-02 &
1.11300908152540E-02 1.07985653361327E-02 7.15751336781262E-03 &
5.33233313826536E-03 3.33838281059952E-03 2.45593788518012E-03 &
1.30676889718468E-03 6.74077939621729E-04 3.40855451028396E-04 &
1.70094767959573E-04 8.43564075492202E-05 4.18273452761879E-05 &
2.08245259379846E-05 1.04283738184097E-05 4.94574435602427E-06 &
1.46580088187767E-06
SI2 -1.25 1.25
SP2 0 1
SI3 -1.25 1.25
SP3 0 1
```

```
c Tallies
F11:N 1.6
E11 6.60E-02 2.00E+01
F21:N 1.6
E21 6.60E-02 2.00E+01
FT21 TAG 1
FU21 -1
F14:N 1
E14 6.60E-02 2.00E+01
F24:N 1
E24 6.60E-02 2.00E+01
FT24 TAG 1
FU24 -1
c End of tallies
c Material cards
M1 13027.00c 1.0 $Al, Lib80x
PRINT 50 110 $Print of cell volumes/areas and first 50 starting histories
NPS 1E08
-------------------------------------------------------------------------------
```

Publications

The outcomes of this work were published in peer-reviewed journals and numerous talks were given to present the current status.

Publications appeared in *peer-reviewed journals*:

- E. Mauerhofer, Z. Ilic, C. Stieghorst, Zs. Révay, E. Vezhlev, **N. Ophoven**, T. H. Randriamalala, T. Brückel (2022). "Prompt gamma rays from fast neutron inelastic scattering on aluminum, titanium and copper". J. Radioanal. Nucl. Chem. 331:3987-4000.
- **N. Ophoven**, Z. Ilic, E. Mauerhofer, T. H. Randriamalala, E. Vezhlev, C. Stieghorst, Zs. Révay, T. Brückel, J. Jolie, E. Strub (2022). "Fast neutron induced gamma rays from (n,n'), (n,p) and (n,α) reactions on $CaCO_3$". J. Radioanal. Nucl. Chem. 331:5729-5740.
- **N. Ophoven**, Z. Ilic, E. Mauerhofer, T. H. Randriamalala, E. Vezhlev, C. Stieghorst, Zs. Révay, T. Brückel, J. Jolie, E. Strub (2023). "Prompt gamma rays from fast neutron induced reactions on cerium and chlorine". J. Radioanal. Nucl. Chem. 332:3133-3145.
- **N. Ophoven**, Z. Ilic, E. Mauerhofer, T. H. Randriamalala, E. Vezhlev, C. Stieghorst, Zs. Révay, J. Jolie, E. Strub (2024). "Prompt gamma rays of terbium induced by inelastic scattering of fission neutrons". J. Radioanal. Nucl. Chem. DOI:10.1007/s10967-023-09344-y

Oral and **poster contributions** to *internal conferences/workshops*:

- **N. Ophoven**. "Measurement of prompt gamma-rays induced by inelastic scattering of fission neutrons with the FaNGaS instrument". 1st JCNS-2 PhD days 2021, 15 - 17 June 2021, Jülich, Germany. (oral + poster)
- **N. Ophoven**. "FaNGaS Instrument Version III - Flux reconstruction & (n,γ) capture line interference corrections". 2nd JCNS-2 PhD days 2021, 1 - 3 December 2021, Jülich, Germany. (oral + poster)
- **N. Ophoven**. "A fast neutron filter for the HPGe detector of FaNGaS: First results with MCNP6". 1st JCNS-2 PhD days 2022, 23 May 2022, Jülich, Germany. (oral)

- **N. Ophoven**. "A fast neutron filter for the HPGe detector of FaNGaS". JCNS-2 seminar, 2 February 2023, Jülich, Germany. (oral + poster)
- **N. Ophoven**. "Photon and neutron attenuation corrections for large-sample analytics with FaNGaS". 1st JCNS-2 PhD days 2023, 2 - 3 August, Jülich, Germany. (oral + poster)

Oral and **poster contributions** to *external conferences/workshops*:

- **N. Ophoven**, Z. Ilic, E. Vezhlev, E. Mauerhofer, J. Jolie, E. Strub. "Fast Neutron-induced Gamma-ray Spectrometry (FaNGaS)". Jahrestagung der GDCh-Fachgruppe Nuklearchemie 2022, 4 - 6 October 2022, Bergisch Gladbach, Germany. (poster)
- **N. Ophoven**, Z. Ilic, E. Mauerhofer, T. H. Randriamalala, E. Vezhlev, C. Stieghorst, Zs. Révay, T. Brückel, J. Jolie, E. Strub (2023). "Fast Neutron-induced Gamma-ray Spectrometry (FaNGaS)". 3rd International Conference on Radioanalytical and Nuclear Chemistry (RANC), 7 - 12 May 2023, Budapest, Hungary. (talk)
- **N. Ophoven**, Z. Ilic, E. Mauerhofer, T. H. Randriamalala, E. Vezhlev, C. Stieghorst, Zs. Révay, T. Brückel, J. Jolie, E. Strub (2023). "Fast Neutron-induced Gamma-ray Spectrometry (FaNGaS)". 17$^{\text{th}}$ International Symposium on Capture Gamma-Ray Spectroscopy and Related Topics - CGS17, 17 - 21 July 2023, Grenoble, France. (**invited talk**)
- **N. Ophoven**, Z. Ilic, E. Vezhlev, E. Mauerhofer, J. Jolie, E. Strub (2022). "Fast Neutron-induced Gamma-ray Spectrometry (FaNGaS)". Poster session of the BCGS, 6 June 2023, Cologne, Germany. (poster)

A more detailed version of the PhD days talks was usually presented to Prof. Dr. Jan Jolie and PD Dr. Erik Strub in the frame of the weekly nuclear chemistry group seminar at about every 6 months:

- 1st Progress Report on 18 May 2021
- 2nd Progress Report on 17 November 2021
- 3rd Progress Report on 24 May 2022
- 4th Progress Report on 6 December 2022

Bibliography

[1] G. L. Molnár, ed. *Handbook of Prompt Gamma Activation Analysis: with Neutron Beams*. Boston, MA: Springer US, 2004. ISBN: 978-1-4757-0997-1.

[2] H. Shahabinejad, N. Vosoughi, and F. Saheli. "Matrix effects corrections in prompt gamma-ray spectra of a PGNAA online analyzer system using artificial neural network". *Prog. Nucl. Energy* 118 (2020), 103146. DOI: 10.1016/j.pnucene.2019.103146.

[3] S. Chen. "A Study on Properties of Novel Metallic Foam for Nuclear Applications". PhD thesis. 2015. DOI: 10.13140/RG.2.1.2700.6804.

[4] R. M. Lindstrom and Zs. Révay. "Prompt gamma neutron activation analysis (PGAA): recent developments and applications". *J. Radioanal. Nucl. Chem.* 314 (2017), 843–858. DOI: 10.1007/s10967-017-5483-8.

[5] L. Zhang, P. Wu, and W. Zhang. "The Review of Prompt Gamma Activation Analysis". *Open Access Libr.* 9 (2022), 1–12. DOI: 10.4236/oalib.1109296.

[6] P. Ghorbani et al. "Neutron beam preparation with Am–Be source for analysis of biological samples with PGNAA method". *J. Radioanal. Nucl. Chem.* 291 (2012), 839–842. DOI: 10.1007/s10967-011-1359-5.

[7] L. Yongsheng et al. "A new Am-Be PGNAA setup for element determination in aqueous solution". *Appl. Radiat. Isot.* 95 (2015), 233–238. DOI: 10.1016/j.apradiso.2014.11.005.

[8] C. Cheng et al. "MCNP benchmark of a ^{252}Cf source-based PGNAA system for bulk sample analysis". *Appl. Radiat. Isot.* 158 (2020), 109045. DOI: 10.1016/j.apradiso.2020.109045.

[9] OECD NEA data bank. *JANIS book of neutron-induced cross-sections*. 2020. URL: https://www.oecd-nea.org/janis/book/book-neutron-2020-09.pdf.

[10] K. Sueki et al. "Nondestructive Determination of Major Elements in a Large Sample by Prompt γ Ray Neutron Activation Analysis". *Anal. Chem.* 68 (1996), 2203–2209. DOI: 10.1021/ac9511051.

[11] I. H. Degenaar et al. "Validation of MCNP for large-sample thermal-beam prompt-gamma neutron activation analysis". *J. Radioanal. Nucl. Chem.* 260 (2004), 311–315. DOI: 10.1023/B:JRNC.0000027102.53688.54.

[12] M. Blaauw, I. H. Degenaar, and J. J. M. de Goeij. "Development of a non-invasive method for the determination of the macroscopic neutron cross sections of a sample matrix in large-sample prompt-gamma neutron activation analysis". *J. Radioanal. Nucl. Chem.* 271 (2007), 765–770. DOI: 10.1007/s10967-007-0339-2.

[13] M. Blaauw and T. Belgya. "Neutron self-shielding correction for prompt gamma neutron activation analysis of large samples". *J. Radioanal. Nucl. Chem.* 265 (2005), 257–259. DOI: 10.1007/s10967-005-0817-3.

[14] K. Sudarshan et al. "A simple method for correcting the neutron self-shielding effect of matrix and improving the analytical response in prompt gamma-ray neutron activation analysis". *Anal. Chim. Acta* 549 (2005), 205–211. DOI: 10.1016/j.aca.2005.06.021.

[15] L. Szentmiklósi et al. "Correction for neutron self-shielding and gamma-ray self-absorption in prompt-gamma activation analysis for large and irregularly shaped samples". *J. Anal. At. Spectrom.* 36 (2021), 103–110. DOI: 10.1039/D0JA00364F.

[16] C. D. Schrader and R. J. Stinner. "Remote analysis of surfaces by neutron-gamma-ray inelastic scattering technique". *J. Geophys. Res.* 66 (1961), 1951. DOI: 10.1029/JZ066i006p01951.

[17] Alan H. Jiggins and Farouk I. Habbani. "Prompt gamma-ray analysis using 3.29 MeV neutron inelastic scattering". *Int. J. Appl. Radiat. Isot.* 27 (1976), 689–693. DOI: 10.1016/0020-708X(76)90013-2.

[18] S. W. Yates et al. "Elemental analysis by gamma-ray detection following inelastic neutron scattering". *J. Radioanal. Chem.* 46 (1978), 343–355. DOI: 10.1007/BF02519900.

[19] B. D. Sowerby. "Elemental analysis by neutron inelastic scatter gamma rays with a radioisotope neutron source". *Nucl. Instrum. Methods* 166 (1979), 571–579. DOI: 10.1016/0029-554X(79)90553-6.

[20] N. Ophoven et al. "Fast neutron induced gamma rays from (n,n'), (n,p) and (n,α) reactions on $CaCO_3$". *J. Radioanal. Nucl. Chem.* 331 (2022), 5729–5740. DOI: 10.1007/s10967-022-08594-6.

[21] N. Ophoven et al. "Prompt gamma rays from fast neutron induced reactions on cerium and chlorine". *J. Radioanal. Nucl. Chem.* 332 (2023), 3133–3145. DOI: 10.1007/s10967-023-08989-z.

[22] M. R. Ahmed et al. "Use of spectroscopy of gamma-radiation from the inelastic scattering of reactor fast neutrons for elemental analysis". *J. Radioanal. Chem.* 23 (1974), 199–203. DOI: 10.1007/BF02514358.

[23] M. R. Ahmed et al. "Investigation of gamma-ray spectra from the inelastic scattering of reactor fast neutrons". *Nucl. Instrum. Methods* 117 (1974), 533–539. DOI: 10.1016/0029-554X(74)90302-4.

[24] A. M. Demidov et al. "The spectrum of γ-rays from the ^{182}W(n,n'γ) reaction with reactor fast neutrons". *Nucl. Phys. A* 237 (1975), 125–141. DOI: 10.1016/0375-9474(75)90467-4.

[25] M. Ahmed, N. Rammo, and A. Demidov. "Distribution of intense lines in gamma-ray spectra from the inelastic scattering of reactor fast neutrons" (1975).

[26] L. I. Govor et al. "On level population in ^{108,110}Pd in the inelastic scattering of reactor fast neutrons". *Nucl. Phys. A* 245 (1975), 13–28. DOI: 10.1016/0375-9474(75)90079-2.

[27] A. M. Demidov et al. *Atlas of Gamma-ray Spectra from the Inelastic Scattering of Reactor Fast Neutrons.* Nuclear Research Institute, Baghdad, Iraq (Moscow, Atomizdat), 1978.

[28] A. M. Hurst et al. "The Baghdad Atlas: A relational database of inelastic neutron-scattering (n,n'γ) data". *Nucl. Instrum. Methods Phys. Res. A* 995 (2021), 165095. DOI: 10.1016/j.nima.2021.165095.

[29] G. A. Bartholomew et al. "Compendium of thermal-neutron-capture γ-ray measurements part I Z≤46". *Nucl. Data Sheets A* 3 (1967), 367–645. DOI: 10.1016/S0550-306X(67)80014-4.

[30] L. V. Groshev et al. "Compendium of thermal-neutron-capture γ-ray measurements part II Z = 47 to Z = 67 (Ag to Ho)". *Nucl. Data Sheets A* 5 (1968), 1–242. DOI: 10.1016/S0550-306X(68)80008-4.

[31] L. Nichol and T. J. Kennett. "Inelastic Neutron Scattering in the Region A = 11–40". *Can. J. Phys.* 50 (1972), 553–562. DOI: 10.1139/p72-075.

[32] M. Rossbach et al. "TANDEM: a mutual cooperation effort for transactinide nuclear data evaluation and measurement". *J. Radioanal. Nucl. Chem.* 304 (2015), 1359–1363. DOI: 10.1007/s10967-015-4001-0.

[33] C. Genreith et al. "Measurement of thermal neutron capture cross sections of ^{237}Np and ^{242}Pu using prompt gamma neutron activation". *J. Radioanal. Nucl. Chem.* 296 (2013), 699–703. DOI: 10.1007/s10967-012-2080-8.

[34] Z. Ilic et al. "Prompt gamma rays induced by inelastic scattering of fission neutrons on iron". *J. Radioanal. Nucl. Chem.* 325 (2020), 641–655. DOI: 10.1007/s10967-020-07271-w.

[35] E. Mauerhofer et al. "Prompt and delayed gamma rays induced by epithermal and fast neutrons with indium". *J. Radioanal. Nucl. Chem.* 331 (2022), 535–546. DOI: 10.1007/s10967-021-08102-2.

[36] E. Mauerhofer et al. "Prompt gamma rays from fast neutron inelastic scattering on aluminum, titanium and copper". *J. Radioanal. Nucl. Chem.* (2022), 3987–4000. DOI: 10.1007/s10967-022-08435-6.

[37] N. Ophoven et al. "Prompt gamma rays of terbium induced by inelastic scattering of fission neutrons". *J. Radioanal. Nucl. Chem.* (2024). DOI: 10.1007/s10967-023-09344-y.

[38] S. Bouat et al. "Detection of hydrate plugs inside submarine pipelines using neutrons". *Nondestruct. Test. Evaluation* 37 (2022), 245–257. DOI: 10.1080/10589759.2021.1990284.

[39] IAEA NDS. *EXFOR: Experimental Nuclear Reaction Data.* URL: https://www-nds.iaea.org/exfor/.

[40] C. Grupen. *Astroparticle Physics.* 2nd ed. Undergraduate Texts in Physics. Cham: Springer, 2020. ISBN: 978-3-030-27341-5.

[41] A. Trkov and D. A. Brown. *ENDF-6 Formats Manual: Data Formats and Procedures for the Evaluated Nuclear Data Files.* United States, 2018. DOI: 10.2172/1425114.

[42] W. S. C. Williams. *Nuclear and Particle Physics.* Reprinted. Oxford science publications. Oxford: Clarendon Press, 1991. ISBN: 9780198520467.

[43] J. K. Shultis and R. E. Faw. *Fundamentals of Nuclear Science and Engineering.* Third edition. Boca Raton: CRC Press, 2017. ISBN: 9781498769297.

[44] J. R. Lamarsh. *Introduction to Nuclear Reactor Theory.* LaGrange Park, III.: American Nuclear Society, 2002. ISBN: 0894480405.

[45] N. J. Carron. *An introduction to the passage of energetic particles through matter.* Boca Raton: Taylor and Francis, 2007. ISBN: 9780429137396.

[46] T. Jevremovic. *Nuclear Principles in Engineering.* 2nd ed. Boston, MA: Springer US, 2009. ISBN: 9780387856087.

[47] A. A. Kamal. *Nuclear Physics.* Graduate texts in physics. Heidelberg, Berlin: Springer, 2014. ISBN: 978-3-642-38654-1.

[48] J. Krugers. *Instrumentation in Applied Nuclear Chemistry.* Boston, MA: Springer US, 1973. ISBN: 978-1-4684-1955-9.

[49] M. F. L'Annunziata. "Nuclear Radiation, Its Interaction with Matter and Radioisotope Decay". In: *Handbook of Radioactivity Analysis.* San Diego: Academic Press, 2003, 1–121. ISBN: 9780124366039.

[50] IAEA-NDS. *ENDF: Evaluated Nuclear Data File.* URL: https://www-nds.iaea.org/exfor/endf.htm.

[51] R. F. Fleming. "Neutron self-shielding factors for simple geometrics". *Int. J. Appl. Radiat. Isot.* 33 (1982), 1263–1268. DOI: 10.1016/0020-708X(82)90247-2.

[52] M. S. Uddin et al. "Fast neutron spectrum unfolding of a TRIGA Mark II reactor and measurement of spectrum-averaged cross sections: integral tests of differential cross sections of neutron threshold reactions". *Radiochim. Acta* 101 (2013), 613–620. DOI: 10.1524/ract.2013.2073.

[53] R. Reifarth et al. "Neutron-induced cross sections". *Eur. Phys. J. Plus* 133 (2018). DOI: 10.1140/epjp/i2018-12295-3.

[54] E. B. Podgorsak. *Radiation Physics for Medical Physicists*. 3rd ed. Cham: Springer, 2016. ISBN: 978-3-319-25380-0.

[55] Nuclear Data Center Japan Atomic Energy Agency. *JENDL-4.0*. URL: https://wwwndc.jaea.go.jp/jendl/j40/j40.html.

[56] N. A. Fedorov et al. "Inelastic scattering of 14.1 MeV neutrons on iron". *Eur. Phys. J. A* 57 (2021), 1–11. DOI: 10.1140/epja/s10050-021-00503-x.

[57] D. N. Grozdanov et al. "Measurement of Angular Distributions of Gamma Rays from the Inelastic Scattering of 14.1-MeV Neutrons by Carbon and Oxygen Nuclei". *Phys. Atom. Nuclei* 81 (2018), 588–594. DOI: 10.1134/S106377881805006X.

[58] T. Yamazaki. "Tables of coefficients for angular distribution of gamma rays from aligned nuclei". *Nucl. Data Sheets A* 3 (1967), 1–23. DOI: 10.1016/S0550-306X(67)80002-8.

[59] J. K. Dickens, J. H. Todd, and D. C. Larson. *Cross sections for production of 70 discrete-energy gamma rays created by neutron interactions with ^{56}Fe for E_n to 40 MeV: Tabulated data*. United States, 1990. DOI: 10.2172/6783246.

[60] E. L. Chupp. *Gamma-Ray Astronomy: Nuclear Transition Region*. Vol. 14. Geophysics and astrophysics monographs. Dordrecht: D. Reidel, 1976. ISBN: 978-90-277-0696-6.

[61] J. F. Ziegler, M. D. Ziegler, and J. P. Biersack. "SRIM – The stopping and range of ions in matter (2010)". *Nucl. Instrum. Methods Phys. Res. B* 268 (2010), 1818–1823. DOI: 10.1016/j.nimb.2010.02.091.

[62] J. F. Ziegler. *SRIM - The Stopping and Range of Ions in Matter*. URL: http://www.srim.org/.

[63] Y. Tsuchikawa et al. "Measurement of Doppler broadening of prompt gamma-rays from various zirconium- and ferro-borons". *Nucl. Instrum. Methods Phys. Res. B* 991 (2021), 164964. DOI: 10.1016/j.nima.2020.164964.

[64] A. Barzilov and P. C. Womble. "Study of Doppler broadening of gamma-ray spectra in 14-MeV neutron activation analysis". *J. Radioanal. Nucl. Chem.* 301 (2014), 811–819. DOI: 10.1007/s10967-014-3189-8.

[65] Brookhaven National Laboratory. *NuDat 3.0 National Nuclear Data Center*. URL: https://www.nndc.bnl.gov/nudat3/.

[66] P. C. Womble et al. "Evaluation of the Doppler-Broadening of Gamma-Ray Spectra from Neutron Inelastic Scattering on Light Nuclei". *AIP Conf. Proc.* 1099 (2009), 624–627. DOI: 10.1063/1.3120114.

[67] Z. Janout, S. Pospíšil, and M. Vobecký. "Observation of a Doppler broadening of the 4438 keV gamma-line of ^{12}C in processes ^{12}C(n,n'γ)^{12}C and ^{9}Be(α,nγ)^{12}C". *J. Radioanal. Chem.* 56 (1980), 71–81. DOI: 10.1007/BF02516939.

[68] S. Marguet. *The Physics of Nuclear Reactors*. Cham: Springer, 2018. ISBN: 978-3-319-59559-7.

[69] W. Greiner. *Quantum Electrodynamics*. Berlin, Heidelberg: Springer, 2009. ISBN: 978-3-540-87560-4.

[70] Walter Greiner. *Quantum Mechanics: An introduction*. 4th ed. Berlin, Heidelberg: Springer, 2001. ISBN: 978-3-540-67458-0.

[71] R. Antoni and L. Bourgois. *Applied Physics of External Radiation Exposure: Dosimetry and Radiation Protection*. Biological and Medical Physics, Biomedical Engineering. Cham: Springer International Publishing AG, 2017. ISBN: 978-3-319-48658-1.

[72] A. Vértes et al., eds. *Handbook of Nuclear Chemistry*. 2nd ed. Heidelberg: Springer, 2011. ISBN: 978-1-4419-0719-6.

[73] S. R. Cherry, M. E. Phelps, and J. A. Sorenson. *Physics in Nuclear Medicine*. 4th ed. Philadelphia: Saunders / Elsevier, 2012. ISBN: 9781416051985.

[74] C. Grupen and I. Buvat. *Handbook of Particle Detection and Imaging*. Berlin, Heidelberg: Springer, 2012. ISBN: 978-3-642-13270-4.

[75] C. Grupen et al. *Particle Detectors*. 2nd ed. Vol. 26. Cambridge Monographs on Particle Physics, Nuclear Physics and Cosmology. Cambridge: Cambridge University Press, 2008. ISBN: 9780521840064.

[76] G. F. Knoll. *Radiation Detection and Measurement*. 3rd ed. New York: Wiley, 2000. ISBN: 9780471073383.

[77] S. N. Ahmed. *Physics and Engineering of Radiation Detection*. 2nd ed. Elsevier, 2015. ISBN: 9780128013632.

[78] A. de Angelis and M. Pimenta. *Introduction to Particle and Astroparticle Physics: Multimessenger Astronomy and its Particle Physics Foundations*. 2nd ed. Undergraduate lecture notes in physics. Cham, Switzerland: Springer International Publishing, 2018. ISBN: 978-3-319-78180-8.

[79] K. Bethge et al. *Medical Applications of Nuclear Physics*. Berlin, Heidelberg: Springer, 2004. ISBN: 978-3-642-05870-7.

[80] Claude Leroy. *Principles of Radiation Interaction in Matter and Detection*. 2nd ed. Singapore: World Scientific Pub. Co, 2009. ISBN: 9789812818294.

[81] W. R. Leo. *Techniques for Nuclear and Particle Physics Experiments: A How-to Approach*. 2nd rev. ed. Berlin, Heidelberg: Springer, 1994. ISBN: 978-3-540-57280-0.

[82] I. Obodovskiy. *Radiation: Fundamentals, Applications, Risks, and Safety*. Elsevier, 2019. ISBN: 9780444639790.

[83] C. M. Davisson. "Interaction of γ-Radiation With Matter". In: *Alpha-, Beta- and Gamma-Ray Spectroscopy*. Ed. by K. Siegbahn. North-Holland Publishing Co, 1968, 37–78. ISBN: 9780720400830.

[84] R. K. Hobbie and B. J. Roth. *Intermediate Physics for Medicine and Biology*. 5th ed. Cham: Springer International Publishing, 2015. ISBN: 978-3-319-12681-4.

[85] G. Ghisellini. *Radiative Processes in High Energy Astrophysics*. Vol. 873. Lecture notes in physics. Cham: Springer, 2013. ISBN: 978-3-319-00611-6.

[86] C. W. Fabjan and H. Schopper. *Particle Physics Reference Library: Detectors for Particles and Radiation*. Vol. 2. Cham: Springer International Publishing, 2020. ISBN: 978-3-030-35317-9.

[87] O. Klein and Y. Nishina. "Über die Streuung von Strahlung durch freie Elektronen nach der neuen relativistischen Quantendynamik von Dirac". *Z. Physik* 52 (1929), 853–868. DOI: 10.1007/BF01366453.

[88] W. Heitler. *The Quantum Theory of Radiation*. 3rd ed. Dover books on physics. New York: Dover Publications Inc., 1984. ISBN: 0486645584.

[89] S. Flügge, ed. *Corpuscles and radiation in matter II/Korpuskeln und Strahlung in Materie II*. vol. 6. Handbuch der Physik. Berlin, Göttingen, Heidelberg: Springer, 1958. ISBN: 978-3-642-45900-9.

[90] T. J. L. Courvoisier. *High Energy Astrophysics: An Introduction*. Astronomy and Astrophysics Library. Berlin, Heidelberg: Springer, 2013. ISBN: 978-3-642-30969-4.

[91] T. Basaglia et al. "Validation of e^+e^- Pair Production Total Cross Sections for Monte Carlo Particle Transport". *IEEE Trans. Nucl. Sci.* 69 (2022), 858–870. DOI: 10.1109/TNS.2022.3154104.

[92] National Institute of Standards and Technology (NIST). *XCOM: Photon Cross Sections Database*. URL: https://physics.nist.gov/PhysRefData/Xcom/html/xcom1.html.

[93] Zs. Révay, T. Belgya, and G. L. Molnár. "Application of Hypermet-PC in PGAA". *J. Radioanal. Nucl. Chem.* 265 (2005), 261–265. DOI: 10.1007/s10967-005-0818-2.

[94] Institute of Isotopes. *Hypermet PC*. URL: https://www.iki.kfki.hu/nuclear/hypc/index_en.shtml.

[95] N. Abgrall et al. "ADC Nonlinearity Correction for the Majorana Demonstrator". *IEEE Trans. Nucl. Sci.* 68 (2021), 359–367. DOI: 10.1109/TNS.2020.3043671.

[96] D. Dallet and J. M. Da Silva, eds. *Dynamic Characterisation of Analogue-To-Digital Converters*. Vol. 860. The Springer International Series in Engineering and Computer Science. Dordrecht: Springer, 2005. ISBN: 0-387-25902-3.

[97] J. Chen. "Nuclear Data Sheets for A=40". *Nucl. Data Sheets* 140 (2017), 1–376. DOI: 10.1016/j.nds.2017.02.001.

[98] J. Romero–Barrientos et al. "Calculation of self–shielding factor for neutron activation experiments using GEANT4 and MCNP". in: vol. 1753. AIP Conference Proceedings. 2016, 080018.

[99] I. F. Gonçalves, E. Martinho, and J. Salgado. "Monte Carlo calculation of epithermal neutron resonance self-shielding factors in wires of different materials". *Appl. Radiat. Isot.* 55 (2001), 447–451. DOI: 10.1016/S0969-8043(01)00089-6.

[100] M. N. Nasrabadi, M. Jalali, and A. Mohammadi. "Calculation of thermal neutron self-shielding correction factors for aqueous bulk sample prompt gamma neutron activation analysis using the MCNP code". *Nucl. Instrum. Methods Phys. Res. B* 263 (2007), 473–476. DOI: 10.1016/j.nimb.2007.06.015.

[101] A. Trkov et al. "On the self-shielding factors in neutron activation analysis". *Nucl. Instrum. Methods Phys. Res. A* 610 (2009), 553–565. DOI: 10.1016/j.nima.2009.08.079.

[102] M. J. Vargas et al. "Monte Carlo simulation of the self-absorption corrections for natural samples in gamma-ray spectrometry". *Appl. Radiat. Isot.* 57 (2002), 893–898. DOI: 10.1016/S0969-8043(02)00220-8.

[103] M. Mohebian, R. Pourimani, and S. M. Modarresi. "Using MCNP Simulation for Self-absorption Correction in HPGe Spectrometry of Soil Samples". *Iran. J. Sci. Technol. Trans. Sci.* 43 (2019), 3047–3052. DOI: 10.1007/s40995-019-00775-5.

[104] A. Kalamara et al. "Monte Carlo MCNP modeling of a HPGe detector and its efficiency for extended sample geometry". *HNPS Adv. Nucl. Phys.* 20 (2019), 134–138. DOI: 10.12681/hnps.2498.

[105] S. Sangaroon et al. "Efficiency calibrations of HPGe detector for PGNAA system". *J. Phys.: Conf. Ser.* 901 (2017), 012133. DOI: 10.1088/1742-6596/901/1/012133.

[106] I. H. Hutchinson. *A Student's Guide to Numerical Methods*. Cambridge University Press, 2015. ISBN: 9781107095670. DOI: 10.1017/CBO9781316155516.

[107] T. Goorley et al. "Initial MCNP6 Release Overview". *Nucl. Technol.* 180 (2012), 298–315. DOI: 10.13182/NT11-135.

[108] J. T. Goorley et al. *Initial MCNP6 Release Overview - MCNP6 version 1.0*. 2013. DOI: 10.2172/1086758.

[109] Y. Wu. *Neutronics of Advanced Nuclear Systems*. Singapore: Springer, 2019. ISBN: 978-981-13-6519-5.

[110] H. D. Lemmel and P. K. McLaughlin. *BROND-22 Russian evaluated neutron reaction data library Summary documentation*. International Atomic Energy Agency (IAEA), 1994. URL: http://inis.iaea.org/search/search.aspx?orig_q=RN:30022845.

[111] Z. Ge et al. "CENDL-3.2: The new version of Chinese general purpose evaluated nuclear data library". *EPJ Web Conf.* 239 (2020), 09001. DOI: 10.1051/epjconf/202023909001.

[112] D. A. Brown et al. "ENDF/B-VIII.0: The 8 th Major Release of the Nuclear Reaction Data Library with CIELO-project Cross Sections, New Standards and Thermal Scattering Data". *Nucl. Data Sheets* 148 (2018), 1–142. DOI: 10.1016/j.nds.2018.02.001.

[113] A. J. M. Plompen et al. "The joint evaluated fission and fusion nuclear data library, JEFF-3.3". *Eur. Phys. J. A* 56 (2020), 1–108. DOI: 10.1140/epja/s10050-020-00141-9.

[114] K. Shibata et al. "JENDL-4.0: A New Library for Nuclear Science and Engineering". *J. Nucl. Sci. Technol.* 48 (2011), 1–30. DOI: 10.1080/18811248.2011.9711675.

[115] M. B. Chadwick et al. "ENDF/B-VII.1 Nuclear Data for Science and Technology: Cross Sections, Covariances, Fission Product Yields and Decay Data". *Nucl. Data Sheets* 112 (2011), 2887–2996. DOI: 10.1016/j.nds.2011.11.002.

[116] J. L. Conlin. *Release of ENDF/B-VIII.0-Based ACE Data Files*. URL: https://permalink.lanl.gov/object/tr?what=info:lanl-repo/lareport/LA-UR-18-24034.

[117] J. L. Conlin. "Release of ENDF/B-VII.1-based Continuous Energy Neutron Cross Section Data Tables for MCNP" (). URL: https://nucleardata.lanl.gov/files/la-ur-20240.pdf.

[118] M. C. White. *Further Notes on MCPLIB03/04 and New MCPLIB63/84*. URL: https://nucleardata.lanl.gov/files/la-ur-12-00018.pdf.

[119] H. G. Hughes and M. R. James. *Advanced Tallies (MCNP6 Class).* 2014. URL: https://mcnp.lanl.gov/pdf_files/TechReport_2014_LANL_LA-UR-14-21281_HughesJames.pdf.

[120] R. E. MacFarlane and A. C. Kahler. "Methods for Processing ENDF/B-VII with NJOY". *Nucl. Data Sheets* 111 (2010), 2739–2890. DOI: 10.1016/j.nds.2010.11.001.

[121] R. Macfarlane et al. *The NJOY Nuclear Data Processing System, Version 2016.* 2017. DOI: 10.2172/1338791.

[122] D. E. Cullen. *Program SIGMA1 (version 79-1): Doppler broaden evaluated cross sections in the evaluated nuclear data file/version B (ENDF/B) format.* 1979. DOI: 10.2172/5254306.

[123] Nuclear Energy Agency (NEA). *JANIS.* URL: https://www.oecd-nea.org/jcms/pl_39910/janis.

[124] P. von der Hardt and H. Röttger. *Neutron Radiography Handbook.* Dordrecht: Springer, 1981. ISBN: 978-94-009-8569-8.

[125] M. Długosz-Lisiecka and H. Bem. "Fast procedure for self-absorption correction for low γ energy radionuclide ^{210}Pb determination in solid environmental samples". *J. Radioanal. Nucl. Chem.* 298 (2013), 495–499. DOI: 10.1007/s10967-012-2404-8.

[126] C. Agarwal et al. "A simple numerical method for gamma-ray self-attenuation correction for samples of common geometries". *Nucl. Instrum. Methods Phys. Res. A* 597 (2008), 198–202. DOI: 10.1016/j.nima.2008.08.147.

[127] M. M. Hiller et al. "Reducing Statistical Uncertainties in Simulated Organ Doses of Phantoms Immersed in Water". *Radiat. Prot. Dosim.* 174 (2017), 439–448. DOI: 10.1093/rpd/ncw240.

[128] J. J. Demarco, R. E. Wallace, and K. Boedeker. "An analysis of MCNP cross-sections and tally methods for low-energy photon emitters". *Phys. Med. Biol.* 47 (2002), 1321–1332. DOI: 10.1088/0031-9155/47/8/307.

[129] M. E. Medhat, S. P. Shirmardi, and V. P. Singh. "Monte Carlo simulation for the estimation of iron in human whole blood and comparison with experimental data". *Pramana* 88 (2017). DOI: 10.1007/s12043-016-1344-1.

[130] Ö. Kilicoglu, H. O. Tekin, and V. P. Singh. "Determination of Mass Attenuation Coefficients of Different Types of Concretes using Monte Carlo Method". *Eur. J. Sci. Technol.* (2019), 591–598. DOI: 10.31590/ejosat.535203.

[131] F. Molina et al. "Energy distribution of the neutron flux measurements at the Chilean Reactor RECH-1 using multi-foil neutron activation and the Expectation Maximization unfolding algorithm". *Appl. Radiat. Isot.* 129 (2017), 28–34. DOI: 10.1016/j.apradiso.2017.08.001.

[132] Zs. Révay et al. "Prompt Gamma-Ray Spectrum Catalog". In: *Handbook of Prompt Gamma Activation Analysis*. Ed. by G. L. Molnár. Boston, MA: Springer US, 2004, 173–364. ISBN: 978-1-4757-0997-1.

[133] International Atomic Energy Agency (IAEA). *PGAA-IAEA Database Viewer*. URL: https://www-nds.iaea.org/pgaa/pgaa7/index.html.

[134] L. A. Currie. "Limits for qualitative detection and quantitative determination. Application to radiochemistry". *Anal. Chem.* 40 (1968), 586–593. DOI: 10.1021/ac60259a007.

[135] V. C. Rogers. "Detection limits for gamma-ray spectral analysis". *Anal. Chem.* 42 (1970), 807–808. DOI: 10.1021/ac60289a010.

[136] M. Korun, B. Vodenik, and B. Zorko. "Calculation of the decision thresholds in gamma-ray spectrometry". *Appl. Radiat. Isot.* 94 (2014), 221–229. DOI: 10.1016/j.apradiso.2014.08.010.

[137] Zs. Révay. "Determining elemental composition using prompt gamma activation analysis". *Anal. Chem.* 81 (2009), 6851–6859. DOI: 10.1021/ac9011705.

[138] F. M. Wagner et al. "The Munich Fission Neutron Therapy Facility MEDAPP at the research reactor FRM II". *Strahlenther. Onkol.* 184 (2008), 643–646. DOI: 10.1007/s00066-008-1878-3.

[139] L. B. Sommer et al. "A new Multi Leaf Collimator for the fission neutron therapy facility at FRM II". *Nucl. Instrum. Methods Phys. Res. A* 1057 (2023), 168717. DOI: 10.1016/j.nima.2023.168717.

[140] T. Bücherl and S. Söllradl. "NECTAR: Radiography and tomography station using fission neutrons". *Journal of large-scale research facilities JLSRF* 1 (2015). DOI: 10.17815/jlsrf-1-45.

[141] T. H. Randriamalala et al. "FaNGaS: A new instrument for (n,n'γ) reaction measurements at FRM II". *Nucl. Instrum. Methods Phys. Res. A* 806 (2016), 370–377. DOI: 10.1016/j.nima.2015.10.026.

[142] Forschungs-Neutronenquelle Heinz Maier-Laibnitz FRM II. *Converter facility*. URL: https://www.frm2.tum.de/en/frm2/the-neutron-source/neutrons/secondary-sources/converter-facility/.

[143] B. E. Watt. "Energy Spectrum of Neutrons from Thermal Fission of U^{235}". *Phys. Rev.* 87 (1952), 1037–1041. DOI: 10.1103/PhysRev.87.1037.

[144] I. Kodeli et al. "Evaluation and use of the prompt fission neutron spectrum and spectra covariance matrices in criticality and shielding". *Nucl. Instrum. Methods Phys. Res. A* 610 (2009), 540–552. DOI: 10.1016/j.nima.2009.08.076.

[145] I. Y. Lee, M. A. Deleplanque, and K. Vetter. "Developments in large gamma-ray detector arrays". *Rep. Prog. Phys.* 66 (2003), 1095–1144. DOI: 10.1088/0034-4885/66/7/201.

[146] D. A. Neamen. *Semiconductor Physics and Devices: Basic Principles.* 4th ed. New York: McGraw-Hill, 2012. ISBN: 0073529583.

[147] B. G. Streetman and S. Banerjee. *Solid State Electronic Devices.* 6th ed. Delhi: Prentice Hall of India, 2005. ISBN: 9788120330207.

[148] T. W. Raudorf and R. H. Pehl. "Effect of charge carrier trapping on germanium coaxial detector line shapes". *Nucl. Instrum. Methods Phys. Res. A* 255 (1987), 538–551. DOI: 10.1016/0168-9002(87)91225-3.

[149] H. W. Kraner, C. Chasman, and K. W. Jones. "Effects produced by fast neutron bombardment of Ge(Li) gamma ray detectors". *Nucl. Instrum. Methods* 62 (1968), 173–183. DOI: 10.1016/0029-554X(68)90431-X.

[150] G. Gilmore. *Practical Gamma-ray Spectroscopy.* 2nd ed. Chichester: Wiley, 2008. ISBN: 9780470861967.

[151] R. H. Pehl et al. "Radiation Damage Resistance of Reverse Electrode GE Coaxial Detectors". *IEEE Trans. Nucl. Sci.* 26 (1979), 321–323. DOI: 10.1109/TNS.1979.4329652.

[152] M. Descovich et al. "Effects of neutron damage on the performance of large volume segmented germanium detectors". *Nucl. Instrum. Methods Phys. Res. A* 545 (2005), 199–209. DOI: 10.1016/j.nima.2005.01.308.

[153] J. Zhang, X. Mo, and X. Cai. "Study of Annealing the Damaged HPGe Detector". *World Journal of Nuclear Science and Technology* 11 (2021), 100–108. DOI: 10.4236/wjnst.2021.112007.

[154] P. N. Peplowski et al. "Radiation damage and annealing of three coaxial n-type germanium detectors: Preparation for spaceflight missions to asteroid 16 Psyche and Mars' moon Phobos". *Nucl. Instrum. Methods Phys. Res. A* 942 (2019), 162409. DOI: 10.1016/j.nima.2019.162409.

[155] Deutsches Institut für Normung e.V. (DIN). *DIN 17640-1 Bleilegierungen für allgemeine Verwendung.* 2004.

[156] P. P. Aguiar-Amado, V. A. Amado, and J. C. Aguiar. "Full-energy peak determination from total efficiency and peak-to-total ratio calculations". *Nucl. Instrum. Methods Phys. Res. A* 990 (2021), 164980. DOI: 10.1016/j.nima.2020.164980.

[157] International Atomic Energy Agency (IAEA). *Codes for radiation damage calculations and neutron spectral adjustment.* URL: https://www-nds.iaea.org/irdf2002/codes/index.htmlx.

[158] C. W. Reich. "Nuclear Data Sheets for A = 159". *Nucl. Data Sheets* 113 (2012), 157–363. DOI: 10.1016/j.nds.2012.01.002.

[159] S. Y. F. Chu, L. P. Ekström, and R. B. Firestone. *The LUND/LBNL Nuclear Data Search Version 2.0, February 1999*. URL: https://nucleardata.nuclear.lu.se/toi/.

[160] N. Nica. "Nuclear Data Sheets for A=140". *Nucl. Data Sheets* 154 (2018), 1–403. DOI: 10.1016/j.nds.2018.11.002.

[161] J. H. Kelley, J. E. Purcell, and C. G. Sheu. "Energy levels of light nuclei A= 12". *Nucl. Phys. A* 968 (2017), 71–253. DOI: 10.1016/j.nuclphysa.2017.07.015.

[162] A. L. Catz and S. Amiel. "Study of lifetimes of nuclear levels by Doppler broadening attenuation using a Ge(Li) gamma-ray spectrometer". *Nucl. Phys. A* 92 (1967), 222–232. DOI: 10.1016/0375-9474(67)90686-0.

[163] J. Chen, J. Cameron, and B. Singh. "Nuclear Data Sheets for A = 35". *Nucl. Data Sheets* 112 (2011), 2715–2850. DOI: 10.1016/j.nds.2011.10.001.

[164] J. Cameron et al. "Nuclear Data Sheets for A = 37". *Nucl. Data Sheets* 113 (2012), 365–514. DOI: 10.1016/j.nds.2012.02.001.

[165] C. Ouellet and B. Singh. "Nuclear Data Sheets for A = 32". *Nucl. Data Sheets* 112 (2011), 2199–2355. DOI: 10.1016/j.nds.2011.08.004.

[166] J. Chen and B. Singh. "Nuclear Data Sheets for A = 42". *Nucl. Data Sheets* 135 (2016), 1–192. DOI: 10.1016/j.nds.2016.06.001.

[167] J. Chen and B. Singh. "Nuclear Structure and Decay Data for A=44 Isobars". *Nucl. Data Sheets* 190 (2023), 1–318. DOI: 10.1016/j.nds.2023.06.001.

[168] J. K. Dickens. "The Neutron Induced Gamma-Ray Reactions in Calcium in the Energy Range 4.85≤ E_n ≤8.05 MeV". *Nucl. Sci. Eng.* 48 (1972), 78–86. DOI: 10.13182/NSE72-A22458.

[169] A. Tellez et al. "Excited states of ^{40}Ca up to 9 MeV". *J. Phys. France* 34 (1973), 281–293. DOI: 10.1051/jphys:01973003404028100.

[170] P. K. Joshi et al. "Nuclear Data Sheets for A = 139". *Nucl. Data Sheets* 138 (2016), 1–292. DOI: 10.1016/j.nds.2016.11.001.

[171] M. Scheck et al. "Dipole strength distributions of the stable odd-mass N=82 isotones ^{139}La and ^{141}Pr". *Phys. Rev. C* 75 (2007). DOI: 10.1103/PhysRevC.75.044313.

[172] E. A. McCutchan. "Nuclear Data Sheets for A=136". *Nucl. Data Sheets* 152 (2018), 331–667. DOI: 10.1016/j.nds.2018.10.002.

[173] T. D. Johnson et al. "Nuclear Data Sheets for A = 142". *Nucl. Data Sheets* 112 (2011), 1949–2127. DOI: 10.1016/j.nds.2011.08.002.

[174] N. Nica. "Nuclear Data Sheets for A=141". *Nucl. Data Sheets* 187 (2023), 1–354. DOI: 10.1016/j.nds.2023.01.002.

[175] R. L. Auble. "Nuclear data sheets for A = 141". *Nucl. Data Sheets* 10 (1973), 151–204. DOI: 10.1016/S0090-3752(73)80005-5.

[176] M. Scheck et al. "Pauli blocking in the low-lying, low-spin states of ^{141}Pr". *Phys. Rev. C* 78 (2008), 034302. DOI: 10.1103/PhysRevC.78.034302.

[177] E. Browne and J. K. Tuli. "Nuclear Data Sheets for A = 143". *Nucl. Data Sheets* 113 (2012), 715–908. DOI: 10.1016/j.nds.2012.02.003.

[178] A. A. Sonzogni. "Nuclear Data Sheets for A = 144". *Nucl. Data Sheets* 93 (2001), 599–762. DOI: 10.1006/ndsh.2001.0015.

[179] E. Browne and J. K. Tuli. "Nuclear Data Sheets for A = 145". *Nucl. Data Sheets* 110 (2009), 507–680. DOI: 10.1016/j.nds.2009.02.001.

[180] Y. Khazov, A. Rodionov, and G. Shulyak. "Nuclear Data Sheets for A = 146". *Nucl. Data Sheets* 136 (2016), 163–452. DOI: 10.1016/j.nds.2016.08.002.

[181] N. Nica. "Nuclear Data Sheets for A = 148". *Nucl. Data Sheets* 117 (2014), 1–229. DOI: 10.1016/j.nds.2014.02.001.

[182] S. K. Basu and A. A. Sonzogni. "Nuclear Data Sheets for A = 150". *Nucl. Data Sheets* 114 (2013), 435–660. DOI: 10.1016/j.nds.2013.04.001.

[183] N. Nica and B. Singh. "Nuclear Data Sheets for A=147". *Nucl. Data Sheets* 181 (2022), 1–474. DOI: 10.1016/j.nds.2022.03.001.

[184] B. Singh and J. Chen. "Nuclear Structure and Decay Data for A=149 Isobars". *Nucl. Data Sheets* 185 (2022), 2–559. DOI: 10.1016/j.nds.2022.10.001.

[185] M. J. Martin. "Nuclear Data Sheets for A = 152". *Nucl. Data Sheets* 114 (2013), 1497–1847. DOI: 10.1016/j.nds.2013.11.001.

[186] C. W. Reich. "Nuclear Data Sheets for A = 154". *Nucl. Data Sheets* 110 (2009), 2257–2532. DOI: 10.1016/j.nds.2009.09.001.

[187] B. Singh and J. Chen. "Nuclear Data Sheets for A=164". *Nucl. Data Sheets* 147 (2018), 1–381. DOI: 10.1016/j.nds.2018.01.001.

[188] C. W. Reich and B. Singh. "Nuclear Data Sheets for A = 163". *Nucl. Data Sheets* 111 (2010), 1211–1469. DOI: 10.1016/j.nds.2010.04.001.

[189] E. Gete et al. "Neutron-induced peaks in Ge detectors from evaporation neutrons". *Nucl. Instrum. Methods Phys. Res. A* 388 (1997), 212–219. DOI: 10.1016/S0168-9002(96)01163-1.

[190] C. Chasman et al. "Measurement of the Energy Loss of Germanium Atoms to Electrons in Germanium at Energies below 100 keV. II". *Phys. Rev.* 154 (1967), 239–244. DOI: 10.1103/PhysRev.154.239.

[191] M. Baginova, P. Vojtyla, and P. P. Povinec. "Investigation of neutron interactions with Ge detectors". *Nucl. Instrum. Methods Phys. Res. A* 897 (2018), 22–31. DOI: 10.1016/j.nima.2018.04.036.

[192] OECD NEA data bank. *JANIS Web*. URL: https://www.oecd-nea.org/janisweb/.

[193] M. J. Martin. "Nuclear Data Sheets for A = 208". *Nucl. Data Sheets* 108 (2007), 1583–1806. DOI: 10.1016/j.nds.2007.07.001.

[194] D. van Ho et al. "Comparison of efficiency calibration techniques of HPGe detector for radioactivity measurement of soil sample in Marinelli geometry". *J. Radioanal. Nucl. Chem.* 331 (2022), 1361–1365. DOI: 10.1007/s10967-021-08187-9.

[195] D. M. Montalván Olivares, M. V. M. Guevara, and F. G. Velasco. "Determination of the HPGe detector efficiency in measurements of radioactivity in extended environmental samples". *Appl. Radiat. Isot.* 130 (2017), 34–42. DOI: 10.1016/j.apradiso.2017.09.017.

[196] M. H. Bölükdemir et al. "Investigation of shape effects and dead layer thicknesses of a coaxial HPGe crystal on detector efficiency by using PHITS Monte Carlo simulation". *Radiat. Phys. Chem.* 189 (2021), 109746. DOI: 10.1016/j.radphyschem.2021.109746.

[197] K. H. J. Buschow, ed. *Encyclopedia of Materials: Science and Technology*. Amsterdam: Elsevier, 2010. ISBN: 9780080523583.

[198] L. J. Verhey and P. L. Petti. "7 - Principles of Radiation Physics". In: *Leibel and Phillips Textbook of Radiation Oncology*. Ed. by R. T. Hoppe et al. Philadelphia: Saunders, 2010, 95–119. ISBN: 978-1-4160-5897-7.

[199] T. Sato et al. "Recent improvements of the particle and heavy ion transport code system – PHITS version 3.33". *J. Nucl. Sci. Technol.* (2023), 1–9. DOI: 10.1080/00223131.2023.2275736.

[200] J. P. Holloway and H. Akkurt. "The fixed point formulation for large sample PGNAA—Part 1: theory". *Nucl. Instrum. Methods Phys. Res. A* 522 (2004), 529–544. DOI: 10.1016/j.nima.2003.11.401.

[201] H. Akkurt, J. P. Holloway, and L. E. Smith. "The fixed point formulation for large sample PGNAA—Part 2: experimental demonstration". *Nucl. Instrum. Methods Phys. Res. A* 522 (2004), 545–557. DOI: 10.1016/j.nima.2003.11.400.

[202] D. J. Thomas and A. V. Alevra. "Bonner sphere spectrometers—a critical review". *Nucl. Instrum. Methods Phys. Res. A* 476 (2002), 12–20. DOI: 10.1016/S0168-9002(01)01379-1.

Erklärung zur Dissertation

Hiermit versichere ich an Eides statt, dass ich die vorliegende Dissertation selbstständig und ohne die Benutzung anderer als der angegebenen Hilfsmittel und Literatur angefertigt habe. Alle Stellen, die wörtlich oder sinngemäß aus veröffentlichten und nicht veröffentlichten Werken dem Wortlaut oder dem Sinn nach entnommen wurden, sind als solche kenntlich gemacht. Ich versichere an Eides statt, dass diese Dissertation noch keiner anderen Fakultät oder Universität zur Prüfung vorgelegen hat; dass sie - abgesehen von unten angegebenen Teilpublikationen und eingebundenen Artikeln und Manuskripten - noch nicht veröffentlicht worden ist sowie, dass ich eine Veröffentlichung der Dissertation vor Abschluss der Promotion nicht ohne Genehmigung des Promotionsausschusses vornehmen werde. Die Bestimmungen dieser Ordnung sind mir bekannt. Darüber hinaus erkläre ich hiermit, dass ich die Ordnung zur Sicherung guter wissenschaftlicher Praxis und zum Umgang mit wissenschaftlichem Fehlverhalten der Universität zu Köln gelesen und sie bei der Durchführung der Dissertation zugrundeliegenden Arbeiten und der schriftlich verfassten Dissertation beachtet habe und verpflichte mich hiermit, die dort genannten Vorgaben bei allen wissenschaftlichen Tätigkeiten zu beachten und umzusetzen. Ich versichere, dass die eingereichte elektronische Fassung der eingereichten Druckfassung vollständig entspricht.

Teilpublikationen

- **N. Ophoven** et al. (2022). "Fast neutron induced gamma rays from (n,n'), (n,p) and (n,α) reactions on $CaCO_3$". J. Radioanal. Nucl. Chem. 331:5729-5740.
- **N. Ophoven** et al. (2023). "Prompt gamma rays from fast neutron induced reactions on cerium and chlorine". J. Radioanal. Nucl. Chem. 332:3133-3145.
- **N. Ophoven** et al. (2024). "Prompt gamma rays of terbium induced by inelastic scattering of fission neutrons". J. Radioanal. Nucl. Chem. DOI: 10.1007/s10967-023-09344-y

Die Dissertation beinhaltet die Gewinnung und Analyse von Primärdaten. Diese Daten sind auf den Servern des JCNS-2 gesichert und auf Anfrage zugänglich.

Jülich, den 08.03.2024

Niklas Ophoven

(Niklas Ophoven)